
STUDY OF NEUTRAL-PION PAIR PRODUCTION IN SINGLE-TAGGED TWO-PHOTON COLLISIONS AT BESIII

DISSERTATION

ZUR ERLANGUNG DES GRADES

„DOKTOR DER NATURWISSENSCHAFTEN“

AM FACHBEREICH FÜR PHYSIK, MATHEMATIK UND INFORMATIK DER
JOHANNES GUTENBERG-UNIVERSITÄT IN MAINZ

VORGELEGT VON

MAX LELLMANN

GEBOREN AM 23. AUGUST 1994 IN BAD EMS

MAINZ, DEN 19.02.2026





Study of Neutral-Pion Pair Production in Single-Tagged Two-Photon Collisions at BESIII © 2026 by Max Lellmann is licensed under CC BY 4.0. To view a copy of this license, visit <https://creativecommons.org/licenses/by/4.0/>

Tag der Abgabe: 19.02.2026
Tag der mündlichen Prüfung: 19.05.2026

This work uses natural units with $\hbar = c = 1$.

Max Lellmann
Institut für Kernphysik
Johann-Joachim-Becher-Weg 45
Johannes Gutenberg-Universität
D-55128 Mainz

Abstract

The anomalous magnetic moment of the muon, $a_\mu = (g - 2)_\mu/2$, is one of the most precisely measured quantities in particle physics and a key test of the Standard Model. The current theoretical uncertainty is dominated by hadronic effects. The calculation of the hadronic Light-by-Light scattering contribution – the coupling of four photons to hadronic states within the muon’s interaction with an external magnetic field – is limited by the knowledge of hadronic two-photon couplings, especially of tensor mesons, at arbitrary photon virtualities, typically described by electromagnetic transition form factors. The hadronic Light-by-Light scattering contribution is the second largest source of uncertainty of the Standard Model prediction of a_μ .

In this work, the singly virtual electromagnetic transition form factors of the scalar $f_0(500)$ and $f_0(980)$ as well as the tensor $f_2(1270)$ are measured using the BESIII detector setup. Especially, the $f_0(500)$ transition form factor is measured for the first time and the $f_0(500)$ and $f_2(1270)$ form factors are determined for the first time in the range $Q^2 = (0.1 - 3.0) \text{ GeV}^2$, most relevant for the Standard Model prediction of the muon’s anomalous magnetic moment. The analysis is based on single-tagged $e^+e^- \rightarrow e^+e^-\pi^0\pi^0$ events, where the pions originate from the fusion of two virtual photons, and one lepton remains undetected, leaving one photon quasi on-shell.

To make use of the full potential of the data, new Monte Carlo generator for hadron production in two-photon scattering, HadroTOPS, has been developed to model the process and perform efficiency corrections. The generator itself is modular and intended to be used in a number of analyses of two-photon reactions. From the selected events, the effective $\gamma\gamma^* \rightarrow \pi^0\pi^0$ cross section is measured over the full helicity angle range and the mass range $W = (0.3 - 2.0) \text{ GeV}$, followed by a partial-wave analysis to extract the transition form factors.

Using the same selection, the doubly virtual $\gamma^*\gamma^* \rightarrow \pi^0\pi^0$ cross section in the $f_2(1270)$ region is measured for the first time. The momentum transfer of the second lepton is reconstructed from energy-momentum conservation via a kinematic fit, enabling the determination of the second virtuality. The reduced virtuality of the second photon compared to a standard double-tagged measurement increases the cross section, making this measurement possible in the first place.

Together, these analyses provide essential new input for improving the Standard Model prediction of the hadronic Light-by-Light contribution to a_μ .

Kurzfassung

Das anomale magnetische Moment des Myons, $a_\mu = (g - 2)_\mu/2$, gehört zu den präzisesten Messgrößen der Teilchenphysik und stellt einen zentralen Test des Standardmodells dar. Die derzeitige theoretische Unsicherheit wird von hadronischen Beiträgen dominiert. Die Genauigkeit der Berechnung des Beitrags der hadronischen Licht-nach-Licht-Streuungen – der Kopplung von vier Photonen an hadronische Zustände innerhalb der Wechselwirkung des Myons mit einem externen Magnetfeld – ist durch das begrenzte Wissen über die hadronischen Zwei-Photonen-Kopplungen, insbesondere von Tensor-Mesonen, bei beliebigen Photonvirtualitäten eingeschränkt, die typischerweise durch elektromagnetische Übergangsformfaktoren beschrieben werden. Die hadronische Licht-an-Licht Streuung stellt die zweitgrößte Fehlerquelle dar.

In dieser Arbeit werden die einfach virtuellen elektromagnetischen Übergangsformfaktoren der skalaren Zustände $f_0(500)$ und $f_0(980)$ sowie des Tensor-Zustands $f_2(1270)$ mit dem BESIII-Detektorsystem gemessen. Erstmals werden die Formfaktoren im Bereich $Q^2 = (0.1 - 3.0) \text{ GeV}^2$ gemessen, der im Kontext der Standardmodellvorhersage von a_μ besonders relevant ist. Die Analyse basiert auf einfach getaggten $e^+e^- \rightarrow e^+e^-\pi^0\pi^0$ -Ereignissen, bei denen die Pionen durch die Fusion zweier virtueller Photonen entstehen und ein Lepton unentdeckt bleibt, sodass ein Photon quasi reell ist. Zur Modellierung des Prozesses und zur Effizienzkorrektur wurde ein neuer Monte-Carlo-Generator für Hadronproduktion Zwei-Photonen-Streuung, HADROTOPS, entwickelt. Der Generator ist modular aufgebaut und für die Anwendung in einer Vielzahl zukünftiger Analysen von Zwei-Photonen-Reaktionen vorgesehen. Aus den selektierten Ereignissen wird der effektive Wirkungsquerschnitt $\gamma\gamma^* \rightarrow \pi^0\pi^0$ über den gesamten Helizitätswinkelbereich und den Massenbereich $W = (0.3 - 2.0) \text{ GeV}$ gemessen. Eine Partialwellenanalyse des Wirkungsquerschnitts ermöglicht anschließend die Extraktion der Übergangsformfaktoren.

Mit derselben Ereignisswahl wird erstmals der doppelt virtuelle Wirkungsquerschnitt $\gamma^*\gamma^* \rightarrow \pi^0\pi^0$ im $f_2(1270)$ -Massenbereich bestimmt. Der Impulsübertrag des zweiten Leptons wird dabei nicht durch direkte Detektion, sondern über Energie-Impuls-Erhaltung mittels eines kinematischen Fits rekonstruiert, wodurch die zweite Virtualität bestimmt werden kann. Die, verglichen mit einer konventionellen double-tag Messung, reduzierte Virtualität des zweiten Photons in dieser neuartigen Ereignisselektion erhöht den Wirkungsquerschnitt und ermöglicht damit erst diese Messung.

Zusammen liefern diese Analysen wesentliche neue Information zur Verbesserung der Standardmodellvorhersage des hadronischen Licht-an-Licht-Beitrags zu a_μ .

Contents

1	Introduction and Motivation	1
1.1	The Standard Model of Particle Physics	1
1.2	The Anomalous Magnetic Moment of the Muon	4
1.2.1	Direct Measurement	5
1.2.2	Standard Model Prediction	7
1.2.3	The Muon Anomaly	19
1.3	The Two-Photon Particle Production Mechanism	20
1.4	The Two-Photon Production of Neutral-Pion Pairs	26
1.5	Goal of this Work	31
2	Development of a Monte Carlo Event Generator for Hadronic Two-Photon Scattering in Electron Collisions	33
2.1	Basic Requirements on Monte Carlo Simulations for the Study of Hadronic Two-Photon Scattering	34
2.2	General Approach	35
2.3	Phase Space Generation	36
2.3.1	Generation of the $e^+e^- \rightarrow e^+e^- \mathcal{M}$ Phase Space	36
2.3.2	Generation of the Final State Hadronic Decay	39
2.3.3	Application of User Cuts and Consistency Checks	41
2.4	Two-Photon Cross Sections and Responses	41
2.4.1	Production through a Single Resonance of a Custom Final State	41
2.4.2	Luminosity Function Mode	44
2.4.3	$e^+e^- \rightarrow e^+e^- \pi\pi$ and $e^+e^- \rightarrow e^+e^- \pi\eta$ Modes	44
2.4.4	$e^+e^- \rightarrow e^+e^- KK$ and $e^+e^- \rightarrow e^+e^- \eta\eta$ Modes	45
2.4.5	$e^+e^- \rightarrow e^+e^- f_1(1285) \rightarrow e^+e^- \eta\pi^+\pi^-$ Mode	47
2.5	Program Structure	47
2.5.1	Double and Quadruple Precision Floating Numbers	49
2.5.2	Input Scheme	49
2.5.3	Output Scheme	49
2.5.4	Implementation of Three Vector and LorentzVector classes	50
2.5.5	Important Variables	50
2.5.6	Important Functions	50
2.6	Running the Simulation	52
2.7	Results	53

2.7.1	Luminosity Functions	53
2.7.2	Fixed Two-Photon Cross Sections and Luminosity Functions	56
2.7.3	Cross Sections of Two-Hadron Final States	56
2.7.4	Cross Sections of the $e^+e^- \rightarrow e^+e^-\pi^0\pi^0$ Process	57
2.7.5	Cross Sections of the $e^+e^- \rightarrow e^+e^-f_1(1285) \rightarrow e^+e^-\eta\pi^+\pi^-$ Process	58
2.8	Summary of the Monte Carlo Event Generator	61
3	The BESIII Experiment	63
3.1	Beijing Electron Positron Collider II	63
3.2	Beijing Spectrometer III	63
3.2.1	Main Drift Chamber	64
3.2.2	Time-of-Flight System	65
3.2.3	Electromagnetic Calorimeter	66
3.2.4	Superconducting Solenoid	66
3.2.5	Muon Chambers	67
3.3	Trigger and Data Acquisition	67
3.4	The BESIII Offline Software System	67
3.5	Further Upgrades and Modifications	68
4	Data Sets and Simulations	71
4.1	Data Sets	71
4.2	Simulation of the Signal Process	71
4.3	Simulation of Other Two-Photon Processes	72
4.4	Simulation of Other Potential Background Processes	72
5	Study of the $\gamma\gamma^* \rightarrow \pi^0\pi^0$ Cross Section	75
5.1	Event Selection and Background Suppression	76
5.1.1	Good Charged Track Selection	76
5.1.2	Particle Identification	77
5.1.3	Photon Candidate Selection	79
5.1.4	Kinematic Fitting	81
5.1.5	Selection of Single-Virtual Events	81
5.1.6	Three Constraint Kinematic Fit	85
5.1.7	Suppression of Two-Photon Backgrounds	86
5.1.8	Total Event Yield	89
5.2	Background Subtraction	89
5.3	Reconstruction Efficiency	93
5.4	Determination of the Two-Photon Luminosity Function	98
5.5	Extraction of the Effective Two-Photon Production Cross Section	103
5.6	Study of Systematic Uncertainties	103
5.6.1	Integrated Luminosity	104
5.6.2	Electron/Positron Detection Efficiency and Particle Identification	104
5.6.3	Pion Detection Efficiency	105
5.6.4	Analysis Constraints	105

5.6.5	Fit of the χ_{3C}^2 Spectra	108
5.6.6	Subtraction of the Two-Photon Background	108
5.6.7	Efficiency Correction	111
5.6.8	Two-Photon Luminosity Function	111
5.6.9	Total Systematic Uncertainty	111
5.7	Measurement of Transition Form Factors	119
5.7.1	Parametrization of the $f_0(500)$ and $f_0(980)$ Amplitudes	120
5.7.2	Parametrization of the $f_2(1270)$ Amplitude	121
5.7.3	Resolution Effects	122
5.7.4	Fit Results	123
5.8	Summary of the Study of the $\gamma\gamma^* \rightarrow \pi^0\pi^0$ Cross Section	125
6	Measurement of the $\gamma^*\gamma^* \rightarrow \pi^0\pi^0$ Cross Section	129
6.1	Event Selection and Background Suppression	130
6.2	Background Subtraction	132
6.3	Reconstruction Efficiency	136
6.4	Calculation Two-Photon Luminosity Functions	136
6.5	Extraction of the Two-Photon Production Cross Section	138
6.6	Study of Systematic Uncertainties	139
6.6.1	Integrated Luminosity	139
6.6.2	Electron/Positron Detection Efficiency and Particle Information	139
6.6.3	Pion Detection Efficiency	140
6.6.4	Analysis Conditions	141
6.6.5	Background Description in the Fits of the χ_{3C}^2 Distributions	143
6.6.6	Efficiency Correction	144
6.6.7	Total Systematic Uncertainty	144
6.7	Summary of the Measurement of the $\gamma^*\gamma^* \rightarrow \pi^0\pi^0$ Cross Section	146
7	Conclusion and Outlook	151
	Bibliography	155
	List of Figures	181
	List of Tables	187
A	Background Subtraction for the $\gamma\gamma^* \rightarrow \pi^0\pi^0$ Process	189
B	Partial-Wave Analysis of the $\gamma\gamma^* \rightarrow \pi^0\pi^0$ Process	195
C	Numerical Results	201
	Danksagung / Acknowledgments	215
	Curriculum Vitae	217
	Publications	219

1 | Introduction and Motivation

Contents

1.1	The Standard Model of Particle Physics	1
1.2	The Anomalous Magnetic Moment of the Muon	4
1.2.1	Direct Measurement	5
1.2.2	Standard Model Prediction	7
1.2.2.1	QED Contributions	7
1.2.2.2	Electroweak Contributions	8
1.2.2.3	Hadronic Vacuum Polarization	9
1.2.2.4	Hadronic Light-by-Light Scattering	11
1.2.3	The Muon Anomaly	19
1.3	The Two-Photon Particle Production Mechanism	20
1.4	The Two-Photon Production of Neutral-Pion Pairs	26
1.5	Goal of this Work	31

1.1 | The Standard Model of Particle Physics

Humans modeling the world to gain a deeper understanding of nature can be traced back to philosophers in Ancient Greece, who might be considered the very first scientists. A solid foundation for the field of physics was, however, laid in the 17th century by the efforts of Galilei and Newton, who introduced methods of repeatable experiments and combined them with mathematics and the classical equations of motion [1, 2]. In the 19th century, Maxwell demonstrated that seemingly different phenomena – electric and magnetic interactions – can be unified under a single formalism [3, 4]. A process that has since evolved into the ongoing quest of simplifying and combining theoretical frameworks in order to develop more robust theories, which are able to describe more phenomena of nature. In the 20th century, Einstein’s theories of special and general relativity changed the understanding of space and time [5–10]. Concurrently, Max Planck’s works on black-body radiation started the rapid development of quantum mechanics [11, 12]. Later, Dirac combined quantum mechanics with the theory of special relativity, resulting in the Dirac equation. This equation describes the movement of a relativistic spin-1/2 particle and its

antimatter counterpart, which has not been observed at this point in time [13–15]. Only five years later, the predicted antimatter counterpart of the electron – the positron – was found, demonstrating the power of Dirac’s theory [16]. This was an early indication that relativistic quantum mechanics might be one building block of a *Theory of Everything*.

Further developments lead to the well-established Standard Model of Particle Physics (SM), which is the theory closest to a *Theory of Everything* – a comprehensive theoretical framework able to describe all phenomena of nature at all scales. It includes all known information about matter and its fundamental interactions, except for gravity. The model was initially proposed by Glashow and Weinberg [17]. Its renormalizability was proven by ’t Hooft [18] and the discovery of asymptotic freedom in quantum chromodynamics by Gross and Wilczek [19, 20] and independently by Politzer [21] further consolidated it as a self-consistent theory.

Today, this theoretical framework is able to describe phenomena of quantum electrodynamics (QED), the weak nuclear force, and quantum chromodynamics (QCD). In the SM, there are twelve fermionic particles of matter (spin-1/2), four force-carrying gauge bosons (spin-1), and the scalar Higgs boson (spin-0). Forces are described by the exchange of gauge bosons. Here, the electromagnetic interaction is mediated by the massless photon γ , which couples to the electric charge of the particles. The weak force is carried by the heavy gauge bosons Z^0 and W^\pm that couple to the weak charge. The eight gluons are the carriers of the strong nuclear force and couple to the color charge. The twelve matter particles can be further divided into quarks (u, d, c, s, t, b) and leptons ($e, \nu_e, \mu, \nu_\mu, \tau, \nu_\tau$). All the twelve matter particles carry the weak charge and can, therefore, interact via the weak force. Since the neutrinos ν do not carry an electric charge, unlike all other particles of matter, they cannot interact via the electromagnetic interaction. Finally, only the quarks and gluons carry color charge, and, thus, are able to interact via the strong force. Figure 1.1 shows a schematic drawing of the particles included in the SM.

The Standard Model is widely regarded as one of the most successful theories in physics. Its predictions have been confirmed with remarkable precision for energies above a few GeV. Most notably, the model’s accuracy is underscored by the experimental observation of all predicted particles, including the heavy gauge bosons [23, 24], the top quark [25], the τ lepton [26], and most recently, the Higgs boson [27, 28]. This experimental validation highlights the exceptional success of the Standard Model.

There are however limitations to the Standard Model. Although not a direct flaw of the Standard Model itself, the large coupling strength of the strong interaction at small energies makes perturbative calculations below a few GeV unfeasible – resulting in model dependent or computationally expensive low energy QCD calculations. The phenomenon of a large QCD coupling at small energies, known as quantum confinement, prevents the free observation of quarks and gluons, which can only exist in color-neutral bound states called hadrons. A significant flaw is the absence of a theory of gravity and other phenomena, which are typically described by the theory of general relativity. Although gravity is negligibly weak at the scale of elementary particles, a *Theory of Everything* must obviously contain it. Astronomical observations, such as the expansion of the universe or the rotational curves of galaxies, indicate the existence of so-called dark energy and

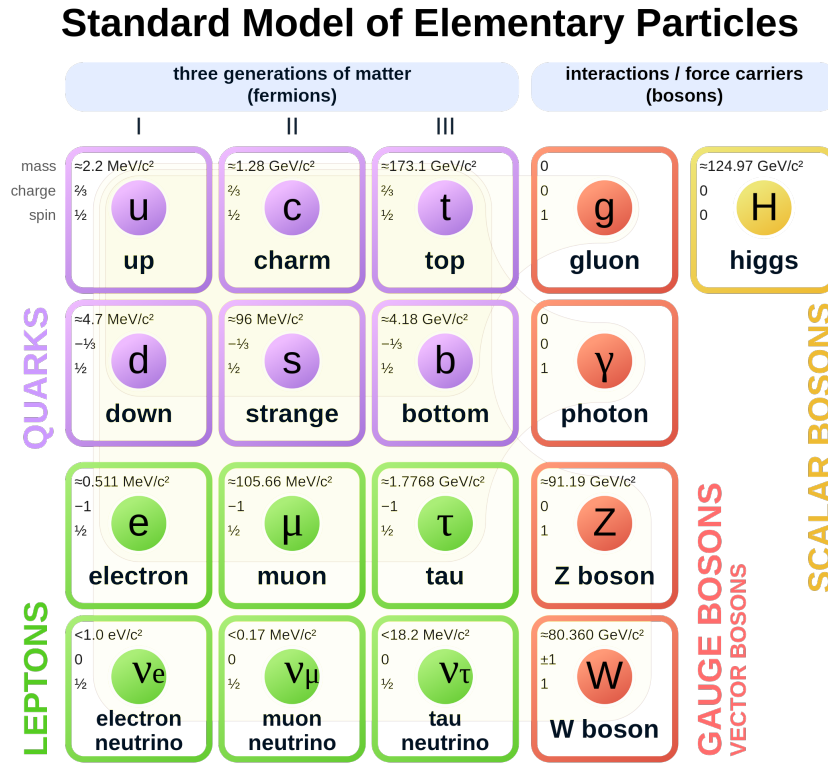


Figure 1.1: Schematic overview of the particles included in the Standard Model [22].

dark matter [29–32] – neither of which is explained in the SM. While the SM is able to predict a matter-antimatter asymmetry in the universe through CP violation and the CKM formalism [33], the observed asymmetries in the universe exceed the SM prediction significantly [34].

Gravity is anticipated to become relevant beyond the TeV energy scale. It is anticipated that the SM is the low-energy limit of the *Theory of Everything*. This does not imply that *New Physics* can only be discovered at high energies. There might be effects at small energies that have not been observed due to limited precision of earlier experiments. To find observations at small energy scales, observables that can be measured and calculated at very high precision are necessary to show a significant deviation. One quantity which is considered to reach this precision is the anomalous magnetic moment of the muon $a_\mu = (g - 2)_\mu/2$. In this observable, a long-standing discrepancy between Standard Model and direct measurement is observed, although some theory predictions suggest the tensions are small [35, 36]. Today, the SM prediction of a_μ is less precise than the direct measurement and limited by the knowledge of photon-hadron couplings at small energy scales.

The goal of this work is to contribute to these efforts by increasing the precision of

the SM prediction of the muon anomalous magnetic moment through the study of the two-photon coupling of neutral pion pairs. The following section explains the latest measurements and SM prediction of the anomalous magnetic moment of the muon and how measurements of two-photon production of hadrons contribute to a more accurate understanding of the SM prediction. Subsequently, the production of hadrons in two-photon scattering in electron-positron collisions is described, and the currently available data is presented. Finally, the specific goal of this work is outlined.

1.2 | The Anomalous Magnetic Moment of the Muon

The movement of a free particle inside a magnetic field is defined via its magnetic moment $\vec{\mu}$. The intrinsic spin \vec{S} of an electrically charged lepton ℓ leads to a magnetic moment of

$$\vec{\mu} = g_\ell \frac{e}{2m_\ell} \vec{S} \quad , \quad (1.1)$$

where m_ℓ is the mass of the lepton, e the elementary charge, and g_ℓ the Landé factor. Relativistic quantum mechanics predicts the Landé factor to be exactly 2 for charged spin-1/2 elementary particles [13, 14]. However, there are more effects that need to be taken into account than just the relativistic movement of a fermion, which is described by Dirac. Due to quantum fluctuations, the actual value of g_ℓ differs from 2. To quantify the effect of said quantum fluctuations, one defines the anomalous magnetic moment

$$a_\ell = \frac{g_\ell - 2}{2} \quad (1.2)$$

as the relative deviation of the Landé factor from the Dirac value. The anomalous magnetic moment of charged leptons can be calculated with high precision. The first-order QED calculation – which is the exchange of one additional photon – has been performed by Julian Schwinger [37]. He found

$$a_\ell^{\text{Schwinger}} = \frac{\alpha}{2\pi} \quad . \quad (1.3)$$

Today, the SM prediction of the anomalous magnetic moment of the muon is performed at great precision. It includes, besides tenth order QED calculations, contributions stemming from the weak interaction and QCD. The SM prediction of a_μ is discussed in Sec. 1.2.2.

The direct measurement of the muon anomalous magnetic moment is one of the most precise measurements of any observable in elementary particle physics. It has been measured at a precision better than 130 ppb [36]. The experimental measurement procedure is explained in detail in Sec. 1.2.1.

Due to this small uncertainty, the observable is considered for high-precision tests of the Standard Model.

1.2.1 | Direct Measurement

The most precise direct measurements of the muon anomalous magnetic moment have been carried out at the Brookhaven National Laboratory and the Fermi National Accelerator Laboratory, both in the United States [36, 38–44]. Both experiments employ the so-called "magic momentum" method, which will be briefly outlined in this section.

The method relies on the injection of muons into a storage ring with a homogeneous magnetic field. The muons are produced from the decay of charged pions. Since the other decay product, the (anti-)neutrino, must be left-handed (right-handed in the case of antineutrino) to participate in the weak interaction, the resulting muons are polarized. Inside the storage ring, the muons undergo relativistic cyclotron motion, so their momentum vector rotates with the angular frequency

$$\vec{\omega}_c = \frac{e}{m_\mu \gamma} \vec{B} \quad , \quad (1.4)$$

where $\gamma = E_\mu/m_\mu$ is the Lorentz factor and \vec{B} the magnetic field.

The muon's spin vector also undergoes an additional Larmor precession. Consequently, the spin precession frequency $\vec{\omega}_s$ is slightly larger than the cyclotron frequency, leading to a gradual de-polarization of the muon ensemble. The difference between these two angular frequencies is called the anomalous precession frequency and is given by

$$\vec{\omega}_a \equiv \vec{\omega}_s - \vec{\omega}_c = \frac{e}{m_\mu} \left[a_\mu \vec{B} - \left(a_\mu - \frac{1}{\gamma^2 - 1} \right) \vec{\beta} \times \vec{E} \right] \quad , \quad (1.5)$$

where β is the muon velocity and \vec{E} the applied electric field.

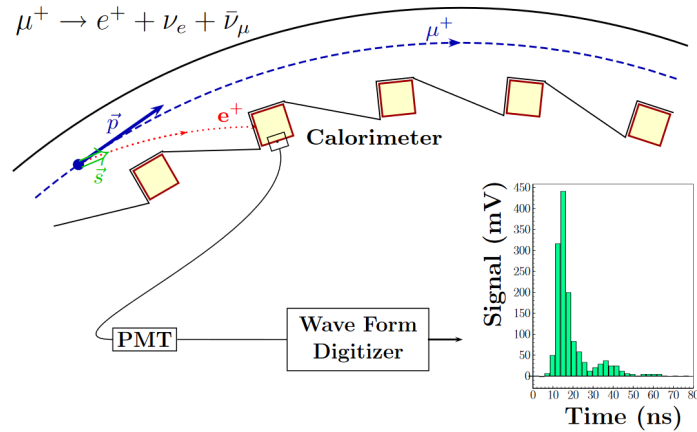


Figure 1.2: Schematic illustration of the storage ring, detector instrumentation, and the decay pattern of a muon inside the storage ring at the BNL and FNAL experiments. Figure is taken from Ref. [45].

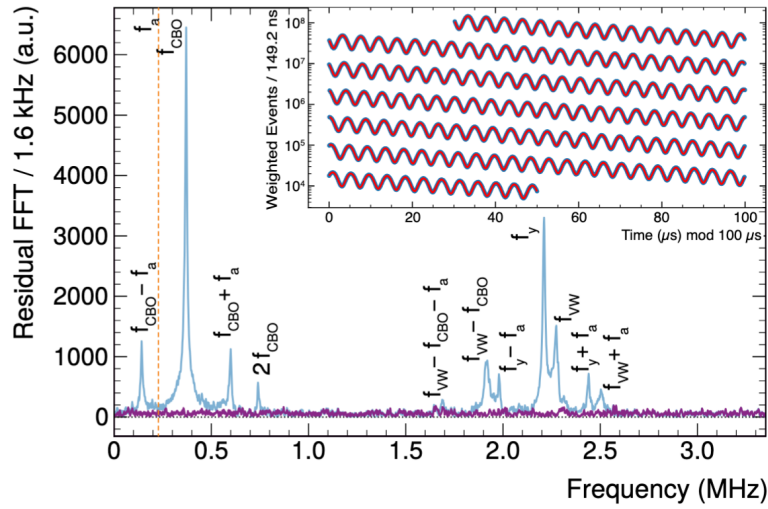


Figure 1.3: Observed event rate as a function of time after injection (inset), and Fourier transform of the residuals from the fits to the last three runs of the FNAL muon $g - 2$ experiment. The blue line shows the result without beam-oscillation effects, while the purple line includes these effects. The dashed line indicates the anomalous precession frequency, and additional peaks correspond to various beam-oscillation modes observed in the data. Figure adapted from Ref. [36].

If the muon momentum is tuned such that $a_\mu \approx \frac{1}{\gamma^2 - 1}$, the electric-field term cancels, and the anomalous precession frequency becomes directly proportional to the anomalous magnetic moment. For an anomalous magnetic moment of $a_\mu = 116592071.5(14.5) \times 10^{-11}$ [36, 38–44], this occurs at a muon energy of $E_\mu \approx 3.1$ GeV [45].

When muons decay inside the storage ring, the emitted electrons (or positrons) are again polarized, since the associated neutrinos (antineutrinos) must be left-handed (right-handed) to participate in the weak interaction. As a result, the momentum of the final-state electron tends to align with the muon’s spin vector at the moment of decay. The lighter and less energetic electrons are deflected more strongly, allowing them to be detected by instrumentation placed inside the storage ring. A schematic drawing of this process is shown in Fig. 1.2.

The count rate recorded by these detectors exhibits an oscillatory behavior that can be directly related to the anomalous precession frequency, and thus to the anomalous magnetic moment of the muon

$$N(t) \propto \exp\left(-\frac{t}{\gamma\tau_\mu}\right) (1 + A \sin(\omega_a t + \phi)) \quad , \quad (1.6)$$

where τ_μ is the muon lifetime and ϕ the phase [45].

The expected time dependence of the event rate is clearly observed in the experiments, as illustrated in the inset of Fig. 1.3. A Fourier transform of the fit residuals, however, reveals significant beam oscillation effects originating from numerous sources, all of which were taken into account in the final iteration of the FNAL analysis (blue line) [36]. After these corrections, the residuals are largely flat, highlighting the considerable effort invested by the experimental collaborations to minimize systematic uncertainties.

The world average is dominated by the combined results of the Fermilab measurements,

$$a_{\mu}^{\text{FNAL}} = 116592070.5(14.8) \times 10^{-11} \quad [36]$$

which, when combined with the final Brookhaven results, yields the world average

$$a_{\mu} = 116592071.5(14.5) \times 10^{-11} \quad [36, 38\text{--}44] \quad ,$$

which has an impressive relative precision of 124 ppb.

A novel approach for a direct measurement of a_{μ} is being developed at J-PARC [46]. Unlike the measurements at Brookhaven and Fermilab, this method will not use the “magic momentum” approach. Instead, it eliminates the need for electric fields required for focusing by employing an ultracold muon beam, thereby providing a crucial, completely independent check of the existing experimental results.

1.2.2 | Standard Model Prediction

The SM prediction of a_{μ} includes contributions from all forces described in the SM. It can be expressed as the sum of contributions from quantum electrodynamics, the electroweak interaction, and quantum chromodynamics, which is in turn split into two contributions:

$$a_{\mu}^{\text{SM}} = a_{\mu}^{\text{QED}} + a_{\mu}^{\text{EW}} + a_{\mu}^{\text{QCD}} \quad . \quad (1.7)$$

While the contributions from QED and the weak interaction are well under control, the hadronic contribution dominates the uncertainty of the SM prediction. In this section, a short overview of the SM prediction of the muon anomalous magnetic moment, as presented in detail in the summary papers of the Muon $g - 2$ Theory Initiative [35, 47], is given in this section. The quoted numbers and primary sources in this section are taken from these two summary papers.

1.2.2.1 | QED Contributions

The leading-order contributions to a_{μ} stem from the electromagnetic interaction. The Schwinger term is the leading QED contribution, corresponding to a pure one-loop, second-order QED correction. The corresponding Feynman diagram is shown in Fig. 1.4. Due to the small coupling of the electromagnetic interaction, this contribution can be calculated with high precision using perturbation theory.

Today, the QED prediction of a_{μ} includes corrections up to tenth order [48, 49]. A relatively recent development is that precise measurements of the fine-structure constant

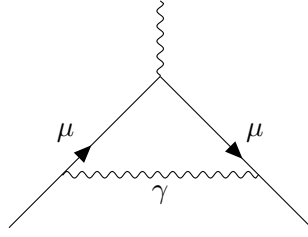


Figure 1.4: Feynman Graph of the leading order QED correction.

a_μ differ by 2.5σ to 5.6σ [50–55], which is now the leading source of uncertainty in the determination of a_μ^{QED} , besides the estimates for the tenth- and twelfth-order corrections [35]. The QED contribution given in Ref. [35] reads

$$a_\mu^{\text{QED}} = 116584718.8(2) \times 10^{-11} \quad .$$

This is the largest contribution to a_μ while at the same time carrying the smallest uncertainty.

1.2.2.2 | Electroweak Contributions

Electroweak contributions to the muon anomalous magnetic moment a_μ^{EW} comprise all SM contributions that are not purely QED or hadronic. These interactions involve at least the propagation of one heavy gauge boson or the Higgs boson. The leading-order Feynman diagrams contributing to a_μ^{EW} are shown in Fig. 1.5. Due to the large masses of the exchange particles, the contributions are heavily suppressed compared to the QED part. Similar to the QED case, the electroweak contributions can be calculated using perturbation theory. Currently, the SM prediction includes all two-loop corrections as well as estimates for some higher-order contributions [56–62]. The Theory Initiative white paper [35] cites a value of

$$a_\mu^{\text{EW}} = 154.4(4) \times 10^{-11} \quad .$$

The uncertainty is of the same order as that of the QED contribution. It is dominated by hadronic effects and estimates of unknown higher-order contributions beyond the two-loop level.

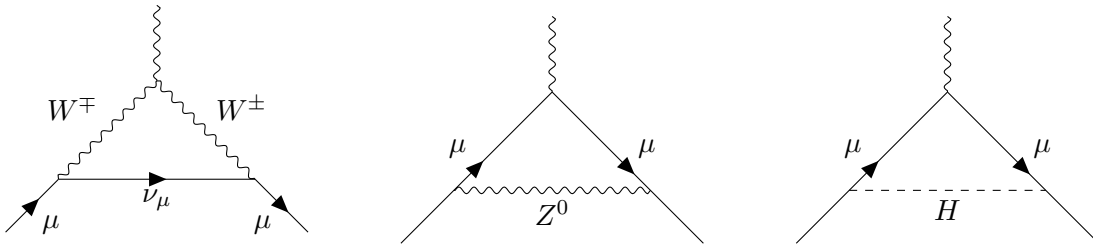


Figure 1.5: Leading-order Feynman graphs of the contributions from the weak interaction to the muon anomalous magnetic moment.

1.2.2.3 | Hadronic Vacuum Polarization

The first of the two hadronic contributions to a_μ is the hadronic vacuum polarization (HVP) contribution. Hadronic vacuum polarization accounts for the formation of quark loops inside photon propagators. The leading-order Feynman diagram is depicted in Fig. 1.6. Due to the generally low energy scales, perturbative calculations are not applicable and alternative methods have to be employed. This contribution is predicted phenomenologically by data-driven approaches on the basis of dispersion relations and from lattice QCD. The phenomenological approaches relate the loop integrals containing vacuum-polarization photon propagators to cross sections of virtual photons decaying into hadrons, which in turn can be measured in electron-positron collisions or inferred from τ decays. The general formula for the calculation of the leading-order (LO) HVP contribution from hadronic cross sections is given by

$$a_\mu^{\text{HVP,LO}} = \frac{\alpha^2}{3\pi^2} \int_{m_\pi^2}^{\infty} ds \frac{K(s)}{s} R(s) \quad , \quad (1.8)$$

where s is the squared center-of-mass energy, $R(s)$ is the hadronic R -ratio defined as

$$R(s) = \frac{\sigma^0(e^+e^- \rightarrow \text{hadrons})}{\sigma^0(e^+e^- \rightarrow \mu^+\mu^-)} \quad , \quad (1.9)$$

m_π is the pion mass, and $K(s)$ is a kernel function [79, 80]. The kernel function slowly increases from 0.68 at $s = 0$ to 1 for $s \rightarrow \infty$. The dominant behavior of the integral arises from the s in the denominator, which gives much larger weight to low-energy contributions compared to high-energy ones. Consequently, precise knowledge of $R(s)$ at small energy scales is essential for the calculation of $a_\mu^{\text{HVP,LO}}$. At low energies, the most relevant contribution to $R(s)$ is the pion form factor. This quantity has been measured by several experimental collaborations in electron-positron collisions [63–78, 81–98] and has been determined from τ decays using isospin approximations [99–103]. Unfortunately, a rather significant spread is observed between some of the most precise results. In particular, the measurements by the CMD-3 collaboration [77, 78] show substantial disagreement with those of BESIII [75], KLOE [70–74], and, to a lesser extent, BaBar [69], as well as with

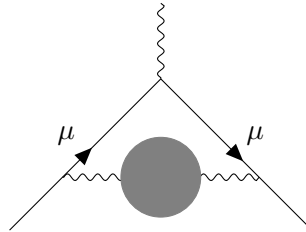


Figure 1.6: Leading-order Feynman graph of the hadronic vacuum polarization contribution. The gray blob represents the complex hadronic interactions that cannot be calculated perturbatively at small energies.

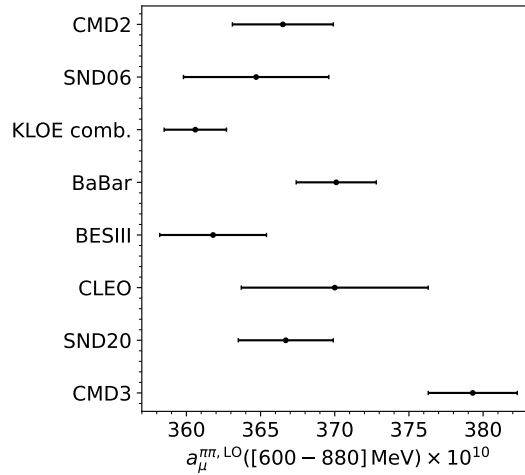


Figure 1.7: Comparison of the leading-order contribution of the pion form factor to the muon anomalous magnetic moment $a_\mu^{\pi\pi, \text{LO}}$ in the energy range $\sqrt{s} = (600 - 880)$ MeV using data by CMD2 [63–66], SND06 [67, 68], BaBar [69], KLOE [70–74], BESIII [75], SND20 [76], and CMD3 [77, 78]. The data points are extracted directly from the experimental data and taken from Ref. [77].

evaluations based on τ data in parts of the energy range. The resulting spread in the prediction of the $\pi^+\pi^-$ contribution to the muon anomalous magnetic moment $a_\mu^{\pi\pi, \text{LO}}$ is illustrated in Fig. 1.7, where the contribution of the pion vector form factor is shown when extracted from different experimental e^+e^- data [63–78].

Due to the large spread observed in phenomenological determinations of $a_\mu^{\text{HVP}, \text{LO}}$ [104–115], which exceeds the uncertainty of the direct measurement of a_μ , the $g - 2$ Theory Initiative does not provide a data-driven estimate of the hadronic vacuum polarization contribution to a_μ in its most recent evaluation of the Standard Model prediction [35].

Instead of relying on data-driven evaluations, the $g - 2$ theory initiative uses a determination of the HVP contribution using lattice QCD calculations. For the SM prediction, the results of eight different lattice QCD collaborations for $a_\mu^{\text{HVP}, \text{LO}}$ [116–132] are averaged. Notably, the BMWc collaboration [118], the RBC/UKQCD collaboration [128], and the Mainz/CLS collaboration [129] have computed the complete leading-order hadronic vacuum polarization contribution to a_μ . In contrast to the data-driven approaches, no significant deviations are observed between the results. The calculations are averaged using five different methods, all of which show excellent consistency. The result quoted in Ref. [35] for the leading-order hadronic vacuum polarization contribution to a_μ is

$$a_\mu^{\text{HVP}, \text{LO}} = (713.2 \pm 6.1) \times 10^{-10} \quad .$$

Besides the leading-order hadronic vacuum polarization contribution, the next-to-leading-order (NLO) and next-to-next-to-leading-order (NNLO) contributions are also considered in Ref. [35]. Despite the tensions in the e^+e^- data, the (N)NLO lattice results are

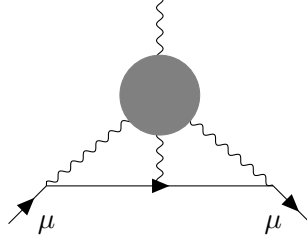


Figure 1.8: Leading-order Feynman graph of the hadronic Light-by-Light scattering contribution. The gray blob represents the complex hadronic interactions that cannot be calculated perturbatively at small energies.

less precise than the data-driven calculations. The NLO result is based on a conservative treatment of the results presented in Ref. [133], accommodating the spread arising from the use of different pion form factor determinations. For the NNLO contribution, the results of Ref. [134] are adopted. The values quoted in Ref. [35] are

$$\begin{aligned} a_{\mu}^{\text{HVP, NLO}} &= (-9.96 \pm 0.13) \times 10^{-10} \\ a_{\mu}^{\text{HVP, NNLO}} &= (1.24 \pm 0.01) \times 10^{-10} \quad . \end{aligned}$$

The MUonE collaboration at CERN is developing a method to directly measure the HVP contribution to a_{μ} using spacelike elastic electron-muon scattering, providing an additional cross-check of the phenomenological and lattice results [135].

1.2.2.4 | Hadronic Light-by-Light Scattering

The leading-order Feynman diagram of the hadronic light-by-light (HLbL) scattering contribution to the muon anomalous magnetic moment is shown in Fig. 1.8. As in the case of the HVP contribution, significant contributions arise from low-momentum regions, and thus perturbative calculations are only possible for a small fraction of the total contribution. Phenomenological and lattice QCD calculations of this contribution are included in the theory prediction of a_{μ} as presented in Ref. [35]. The approaches and results summarized in this reference are outlined in this section. Compared to the HVP contribution, the HLbL contribution is suppressed by an additional power of α and is therefore roughly two orders of magnitude smaller. Consequently, the HLbL prediction does not need to achieve the same level of precision as the HVP calculation to yield a meaningful result. Nonetheless, the calculation is quite involved and often model-dependent.

The starting point for the calculation of a_{μ}^{HLbL} is the description of the coupling via the HLbL tensor, defined as the hadronic Green's function of four electromagnetic currents in pure QCD:

$$\Pi^{\mu\nu\rho\sigma}(q_1, q_2, q_3) = -i \int d^4x d^4y d^4z e^{-i(q_1x + q_2y + q_3z)} \langle 0 | T \{ j^{\mu}(x) j^{\nu}(y) j^{\rho}(z) j^{\sigma}(0) \} | 0 \rangle \quad . \quad (1.10)$$

It includes contributions from the electromagnetic currents of the three lightest quarks:

$$j^\mu = \bar{q}Q\gamma^\mu q \quad q = (u, d, s)^T \quad Q = \text{diag}(2, -1, -1)/3 \quad . \quad (1.11)$$

The helicity amplitudes for off-shell two-photon scattering can be obtained by contracting this tensor with polarization vectors – relating the tensor to experimental observables in hadronic two-photon collisions. In Ref. [136], a decomposition of the HLbL tensor into a set of Lorentz structures $T_i^{\mu\nu\rho\sigma}$ and scalar coefficients Π_i was performed, based on the works presented in Refs. [137, 138], such that the tensor can be expressed as

$$\Pi^{\mu\nu\rho\sigma} = \sum_{i=1}^{54} T_i^{\mu\nu\rho\sigma} \Pi_i \quad . \quad (1.12)$$

The large number of contributing functions can be reduced by accounting for redundancies in the decomposition. In a fully off-shell scattering process, only 41 independent contributions remain, corresponding to the number of independent helicity amplitudes.

The HLbL contribution can be derived from the expression for $\Pi^{\mu\nu\rho\sigma}$ assuming the external photon being on-shell [139]. This leads to the formula

$$a_\mu^{\text{HLbL}} = \frac{\alpha^3}{432\pi^2} \int_0^\infty d\Sigma \Sigma^3 \int_0^1 dr r \int_0^{2\pi} d\phi \phi \sum_{i=1}^{12} T_i(\Sigma, r, \phi) \bar{\Pi}_i(Q_1^2, Q_2^2, Q_3^2, 0) \quad (1.13)$$

with known kernel functions T_i , linear combinations of the coefficients Π_i labeled as $\bar{\Pi}_i$, and Euclidean photon virtualities constructed from Σ , r , and ϕ [136, 140]:

$$\begin{aligned} Q_1^2 &= \frac{\Sigma}{3} \left(1 - \frac{r}{2} \cos \phi - \frac{r}{2} \sqrt{3} \sin \phi \right) \\ Q_2^2 &= \frac{\Sigma}{3} \left(1 - \frac{r}{2} \cos \phi + \frac{r}{2} \sqrt{3} \sin \phi \right) \\ Q_3^2 &= \frac{\Sigma}{3} (1 + r \cos \phi) \quad . \end{aligned} \quad (1.14)$$

Some of the linear combinations of Π_i vanish, so that only 12 functions $\bar{\Pi}_i$ remain nonzero for an on-shell external photon.

Unlike the HVP contribution, the complexity of the HLbL tensor prevents a simple summation over all possible intermediate states. Moreover, the scalar functions $\bar{\Pi}_i$ cannot be measured directly, and therefore for individual intermediate states a relation to physical observables, such as transition form factors (TFFs) or cross sections, needs to be constructed [47]. Within this framework, contributions from one-, two-hadron, etc., intermediate states are incorporated into $\bar{\Pi}_i$ (and thus a_μ^{HLbL}). By considering the suppression of contributions from intermediate states with increasing thresholds, Refs. [136, 140–146] focused on the most important channels and treated them explicitly. This framework allows the HLbL contribution to be unambiguously decomposed as

$$a_\mu^{\text{HLbL}} = a_\mu^{\text{HLbL}, \pi^0\text{-pole}} + a_\mu^{\text{HLbL}, \pi\text{-box}} + a_\mu^{\text{HLbL}, \pi\pi} + \dots \quad , \quad (1.15)$$

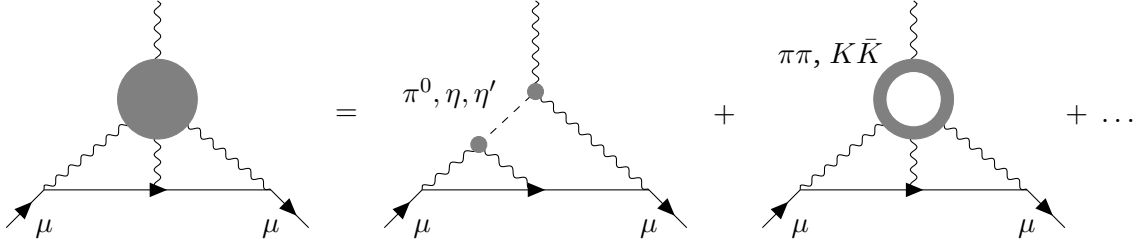


Figure 1.9: Feynman graphs of the leading order long distance contributions to the HLbL contribution to a_μ^{HLbL} [147].

where $a_\mu^{\text{HLbL}, \pi^0\text{-pole}}$ denotes the contribution from the exchange of a π^0 in one of the channels, $a_\mu^{\text{HLbL}, \pi\text{-box}}$ arises from two-pion discontinuities in two channels, and $a_\mu^{\text{HLbL}, \pi\pi}$ describes the two-pion contribution beyond the pion-box term. The inclusion of heavier pseudoscalars, such as η and η' , follows the same strategy as the π^0 -pole contribution, while the exchange of two kaons is treated analogously to the two-pion exchange. The contributions are then calculated individually by connecting them to different experimental inputs. Early counting schemes predicted the contributions of the pseudoscalar poles to be dominant, followed by the effects of pion and kaon boxes [147]. The according Feynman graphs are shown in Fig. 1.9. Combining this with properly evaluated short-distance contributions from QCD [138, 148] allows for a precise estimate of the HLbL contribution to the muon anomalous magnetic moment. In the following section, the various contributions to the phenomenological evaluation of a_μ^{HLbL} , as well as the corresponding lattice-QCD approaches, are briefly discussed.

Short Distance Contributions

The short-distance constraints on a_μ^{HLbL} arise from kinematic regions where two or three photon virtualities in the hadronic tensor become large. They are obtained from an operator product expansion of the electromagnetic quark currents entering the HLbL tensor [138, 148–152].

The short-distance contributions can be divided into two categories. In the pure short-distance region, all photon virtualities are large. The leading-order contribution in this region arises from a perturbative massless quark loop, with subleading contributions from quark masses and gluonic operators. In a mixed region, where two virtualities are large and significantly exceed the other virtuality, the HLbL contribution involves an axial current with two non-perturbative form factors and calculations using operator product expansion (OPE) and effective poles (EP) [35, 138, 148–165].

The Dispersive Approach

For the pseudoscalar pole contribution, the HLbL master formula (Eq. (1.13)) can be rewritten as

$$a_\mu^{\text{PS-pole}} = \left(\frac{\alpha}{\pi}\right)^3 \int dQ_1 dQ_2 d\tau [w_1(Q_1, Q_2, \tau) F(-Q_1^2, -Q_3^2) F(-Q_2^2, 0)] \quad (1.16)$$

$$+ w_2(Q_1, Q_2, \tau) F(-Q_1^2, -Q_2^2) F(-Q_3^2, 0)] \quad ,$$

with $Q_3^2 \equiv Q_1^2 + Q_2^2 + 2\tau Q_1 Q_2$ and known weighting functions $w_{1/2}(Q_1, Q_2, \tau)$ [45, 145, 166, 167]. This approach requires knowledge of the singly- and doubly-virtual transition form factors of the corresponding pseudoscalar state, $F(-Q_1^2, -Q_2^2)$, in the spacelike regime. The weighting functions peak at small momentum transfers, as do all models for the transition form factors. Therefore, the low- Q^2 regime is expected to dominate. In principle, a purely data-driven calculation of the pseudoscalar pole contributions is possible. Unfortunately, the available data are not sufficiently precise, do not cover the entire kinematic range required, or – particularly in the case of doubly-virtual form factors – are simply absent, so that a satisfactory fully data driven determination cannot be achieved [168–174].

Therefore, the transition form factors need to be determined by other means. The asymptotic behavior of pseudoscalar transition form factors is dictated by the Brodsky-Lepage limit [175, 176], while the low-momentum behavior has been studied using dispersive constructions of the transition form factors [144, 145, 177–182]. The combined value used in Ref. [35] is

$$a_\mu^{\text{HLbL, PS-poles}} = 91.2_{-2.4}^{+2.9} \times 10^{-11} \quad .$$

The pion-box contribution can be calculated from Born terms computed using scalar QED, multiplied by the pion vector form factor [136]. Although discrepancies exist in the available data on the pion vector form factor, the precision is still very good, making the uncertainty of the pion-box contribution small [140]:

$$a_\mu^{\text{HLbL, } \pi\text{-box}} = -15.9(2) \times 10^{-11} \quad .$$

Similarly, the box contribution from two-kaon intermediate states can be determined. Since the threshold is higher, these contributions are much smaller compared to the pion-box contribution. A dispersive analysis yields [35, 183]:

$$a_\mu^{\text{HLbL, } K^\pm\text{-box}} = -0.48(1) \times 10^{-11} \quad a_\mu^{\text{HLbL, } K^0\text{-box}} = -0.5(4) \times 10^{-11} \quad .$$

For the pion-rescattering contribution, the HLbL tensor can be connected to the helicity partial waves in the $\gamma^* \gamma^* \rightarrow \pi\pi$ process (charged and neutral pions). In the case of the S -wave pion-rescattering contribution, only two of the five structures in the tensor contain contributions from S -waves [136, 137, 140, 184]. The resulting dispersion relation is given by an Omnès function and requires knowledge of the S -wave $\pi\pi$ scattering phase shift. At low energies, different representations of the phase shift agree well [140, 185–187] and accurately reproduce the parameters of the $f_0(500)$ state, the lightest resonance in the $\gamma^* \gamma^* \rightarrow \pi\pi$ process. The inclusion of the $f_0(980)$ final state requires a coupled-channel approach including the $K\bar{K}$ intermediate states [47], which has been performed in [188, 189]. Combining the results of Refs. [140, 144, 189], an S -wave rescattering contribution of

$$a_\mu^{\text{HLbL, } \pi\pi/K\bar{K}, S\text{-wave}} = -8.7(1.0) \times 10^{-11}$$

was obtained [35]. The impact on the nominal value of a_μ is much smaller than the impact of the pion-box contribution, yet the uncertainty is significantly larger, highlighting the necessity for a more accurate study of the $\gamma^*\gamma^* \rightarrow \pi\pi$ process.

Additionally, Ref. [189] estimated the contribution of the $a_0(980)$ state – a resonance present in the $\gamma^*\gamma^* \rightarrow K\bar{K}$ and $\gamma^*\gamma^* \rightarrow \pi^0\eta$ processes – and Ref. [190] calculated the S -wave $\pi^0\eta$ and $K\bar{K}$ contributions to a_μ^{HLbL} using a dispersive approach and experimental input on $\gamma^*\gamma^* \rightarrow \pi^0\eta$ and $\gamma^*\gamma^* \rightarrow K_S K_S$. The resulting contribution is

$$a_\mu^{\text{HLbL}, \pi^0\eta/K\bar{K}, S\text{-wave}} = -0.44(5) \times 10^{-11} \quad .$$

In total, the contribution of light scalars to the muon anomalous magnetic moment is

$$a_\mu^{\text{HLbL}, \text{scalars}} = -9.1(1.0) \times 10^{-11} \quad .$$

The contribution is much smaller than the one from the pseudoscalar poles, yet the uncertainty is of a similar magnitude.

The contribution of heavier scalars with masses above 1 GeV was estimated using simplified quark models and vector meson dominance ansätze for the transition form factors, combined with determinations of the two-photon widths [189–192]. The contribution quoted in Ref. [35] is

$$a_\mu^{\text{HLbL}, \text{heavy scalars}} = -0.7(4) \times 10^{-11} \quad .$$

For the D -wave (and higher-wave) rescattering contribution to a_μ^{HLbL} , the main complication lies in constructing the $\gamma^*\gamma^* \rightarrow \pi\pi$ partial waves. While there is ample information for on-shell photons (see, for example, Refs. [193–199] and Sec. 1.4), the data for off-shell photons is sparse. Currently, there is only one measurement of the $\gamma\gamma^* \rightarrow \pi^0\pi^0$ process [200] with relatively large photon virtualities above 3 GeV^2 . In Ref. [201], a basis for the calculation of the HLbL tensor for axial mesons has been constructed, allowing the inclusion of such mesons into the calculation while leaving the S -wave contributions unaffected. This framework can also be applied to contributions arising from tensor states. The tensor meson contribution can, in general, be described in a narrow-width approximation in terms of five transition form factors [202]. In Refs. [191, 192], the tensor meson contributions of the $f_2(1270)$, $a_2(1320)$, and $f_2'(1525)$ are calculated using a simple quark model [203], with the scale set to the ρ meson mass at low energies for a more realistic behavior. The resulting contribution is

$$a_\mu^{\text{HLbL}, \text{tensors}} = -2.5(3) \times 10^{-11} \quad .$$

It is important to note that the error estimation is based solely on uncertainties stemming from the radiative widths. A more precise determination of the transition form factors of tensor mesons is therefore of utmost importance.

Since Ref. [201] developed a basis for the calculation of the HLbL tensor, the main complication in the determination of the dispersive approach to calculating $a_\mu^{\text{HLbL}, \text{axial}}$ is the extraction of the relevant transition form factors from data [35]. Spin-1 particles are

forbidden from decaying into two on-shell photons, so there is no direct measurement of the radiative widths of axial mesons. Experimental constraints on the transition form factors of the $f_1(1285)$ have been obtained using a vector meson dominance approach in Refs. [204, 205]. The normalization of the transition form factor and constraints on the symmetric transition form factors are based on a single measurement of $\gamma\gamma^* \rightarrow f_1(1285)$ by the L3 collaboration [206].

An additional complication arises because the short-distance contributions involve axial-vector currents, so the axial-vector contribution must be considered together with the short-distance contributions. The matching of both contributions, discussed in Ref. [35], separates the high- and low-energy regimes by a matching scale and is described in detail in Refs. [191, 192]. The combined result for the subleading contributions is

$$a_\mu^{\text{HLbL, subleading}} = 33.2(7.2) \times 10^{-11} \quad .$$

This represents the largest uncertainty in the dispersive evaluation of the HLbL contribution to a_μ , which in total reads [35]

$$a_\mu^{\text{HLbL, disp.}} = 98.7(7.9) \times 10^{-11} \quad .$$

The dispersive calculations can be cross-checked using different approaches such as holographic QCD [164, 207–221], rational approximants [167, 222–231], chiral theory [232, 233], Regge evaluations [234], and functional methods [235–237].

Generally, the different methods yield results that are consistent with the presented dispersive calculations. When discrepancies appear, they are typically small, covered by the quoted uncertainties, or connected to limitations of the applied model. An important exception arises in the case of the holographic calculation of the tensor-meson contribution to a_μ^{HLbL} . The full tensor contributions are evaluated within holographic QCD using two transition form factors, one of which shows good agreement with the available data [238]. The result is found to be

$$a_\mu^{\text{HLbL, } f_2+a_2+f_2'} = 3.4(4) \times 10^{-11},$$

but it switches sign when one of the transition form factors is set to zero:

$$a_\mu^{\text{HLbL, } f_2+a_2+f_2'} = -4.6(6) \times 10^{-11} \quad .$$

This is a significant deviation – several times larger than the uncertainty of the dispersive determination of the ground-state tensor mesons ($-2.5(3) \times 10^{-11}$). Given that the models otherwise show good agreement, this discrepancy must be taken seriously. Since the substantial differences in the holographic predictions originate from the limited knowledge of the tensor-state transition form factors, precise measurements of these observables are required to resolve the issue.

The aforementioned results can be combined to yield a phenomenological estimate of the hadronic Light-by-Light contribution to a_μ . For most contributions, the presented

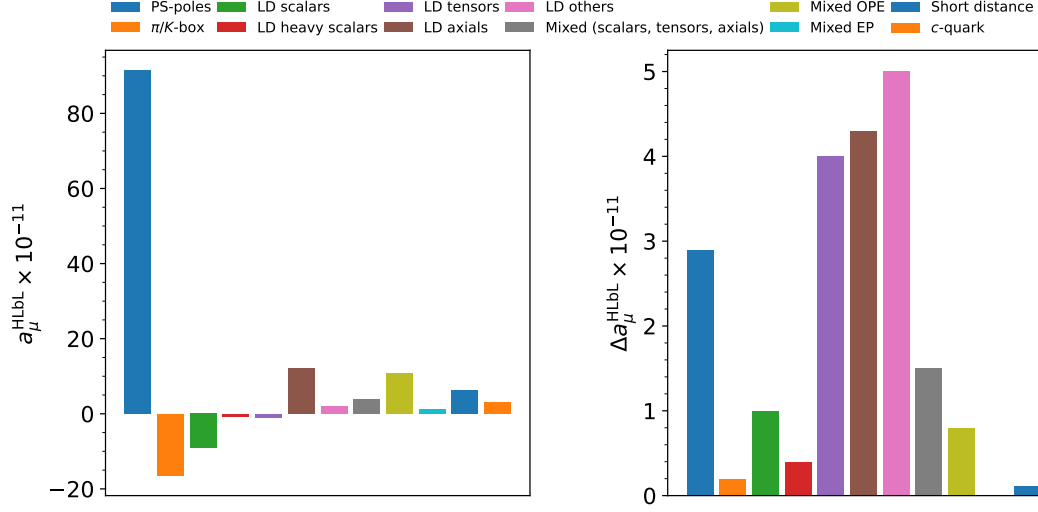


Figure 1.10: Comparison of the different contributions to the central value (left) and the uncertainty of the phenomenologically determined hadronic Light-by-Light contributions to the muon anomalous magnetic moment a_μ^{HLbL} . All numbers are according to Ref. [35].

dispersive predictions are used. In case of the tensor contribution, where the large discrepancies between dispersive and holographic models are observed, a conservative estimate of $-1(4) \times 10^{-11}$ is used, which covers all predictions.

Pure short-distance constraints contribute

$$a_\mu^{\text{short distance}} = 6.2_{-0.3}^{+0.2} \times 10^{-11} \quad .$$

The mixed region is also taken completely from dispersive results. Scalar, tensor, and axial states contribute $3.8(1.5) \times 10^{-11}$, contributions from the operator product expansion dominate with $10.9(0.8) \times 10^{-11}$, and effective poles contribute 1.2×10^{-11} , giving a total of

$$a_\mu^{\text{Mixed}} = 15.9(1.7) \times 10^{-11} \quad .$$

Charm-quark contributions are considered to be purely perturbative [35, 47]:

$$a_\mu^{\text{HLbL, c-quark}} = 3(1) \times 10^{-11} \quad .$$

Adding all contributions, taking into account a large uncertainty for long-distance contributions of other states ($2(5) \times 10^{-11}$) and additional contributions from the variation of the cutoff momentum in the calculation of the short distance contributions (1.9×10^{-11}), one finds a phenomenologically evaluated leading-order HLbL contribution of [35, 136, 140, 145, 148–150, 152, 167, 181, 183, 189–191, 201, 204, 216, 219, 220, 232, 234, 236–239]

$$a_\mu^{\text{HLbL, phen.}} = 103.3(8.8) \times 10^{-11} \quad .$$

The different contributions to central value and uncertainty of $a_\mu^{\text{HLbL, phen.}}$ are depicted in Fig. 1.10. The largest fraction contributing to the central value is the pseudoscalar-pole contribution, followed by the pion- and kaon-boxes and contributions in the mixed region – where only some of the internal photon virtualities are large – and contributions from axial-vector mesons. The uncertainty, however, is completely dominated by the tensor and axial-vector contributions which add significant uncertainties to the long distance and mixed contributions and the long distance contribution of other states. The pseudoscalar poles are the fourth-largest contributor to the uncertainty. It is therefore important to gather as much information as possible on the two-photon coupling of axial and tensor states in the relevant energy range for the HLbL contributions to a_μ .

Finally, the results of Ref. [240] were updated to estimate a next-to-leading order HLbL contribution to the muon anomalous magnetic moment [35]

$$a_\mu^{\text{HLbL, NLO}} = 2.6(6) \times 10^{-11} \quad .$$

Lattice QCD

Similarly to the HVP calculations, the HLbL contribution can be estimated using lattice QCD, to provide a first-principles QCD estimation complementary to the phenomenological calculations.

Lattice QCD can either predict the full HLbL contribution or the contributions of exclusive states. The latter can be calculated, in accordance with the phenomenological approach, from information on the two-photon couplings of hadronic states – most importantly the light pseudoscalars π^0 , η , and η' . The transition form factors of these states have been calculated on the lattice by several groups [241–248]. The results are consistent with one another, with available data, and with phenomenological approaches. For the π^0 , the transition form factor results are precise enough to provide a competitive lattice determination of the HLbL contribution to a_μ . The average value obtained in Ref. [35],

$$a_\mu^{\pi^0\text{-pole}} = 58.8(2.2) \times 10^{-11}$$

shows a 1.3σ discrepancy compared to the phenomenological approach presented in Ref. [146], with similar uncertainties.

While the calculation of transition form factors on the lattice has delivered promising results, which may be combined with phenomenological approaches, a direct calculation of the complete a_μ^{HLbL} on the lattice is also possible. This strategy has been pursued by several groups using different methods [249–253]. The averaged results from Ref. [35],

$$a_\mu^{\text{HLbL, lattice}} = 122.5(9.0) \times 10^{-11} \quad ,$$

are slightly higher than those obtained from phenomenological approaches and show a mild tension of around 1.5σ . The uncertainties of both results are similar. Since the phenomenological and lattice results are generally consistent. They are combined to [35]

$$a_\mu^{\text{HLbL}} = 112.6(9.6) \times 10^{-11} \quad .$$

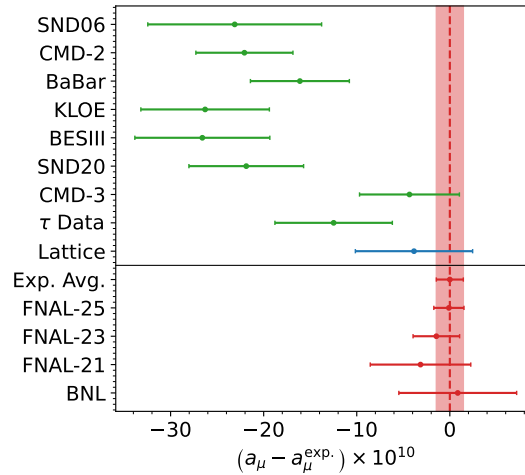


Figure 1.11: Comparison of the Standard Model predictions of the muon anomalous magnetic moment to the experimental measurements and to the world average. The green points represent the results if $a_\mu^{\text{HVP, LO}}$ is evaluated using only the pion form factor data of the respective experiment (values taken from Fig. 83 of Ref. [35]). The blue point shows the result when using the lattice QCD calculations of a_μ^{HVP} . The red points are the direct measurements by Fermilab [36, 38–43] and Brookhaven [44], the red band represents the experimental average of the shown measurements.

Compared to the leading-order HVP contribution, $a_\mu^{\text{HVP, LO}} = 7132(61) \times 10^{-11}$ [35], the HLbL contribution is smaller and currently carries a smaller absolute uncertainty. At present, the uncertainty of the HVP term is dominated by tensions between different experimental determinations of the pion form factor and lattice-QCD results. Once this discrepancy is resolved, a substantial reduction of the HVP uncertainty is anticipated, thereby increasing the importance of an improved determination of the HLbL contribution.

1.2.3 | The Muon Anomaly

By comparing the direct measurement of the muon anomalous magnetic moment to the Standard Model prediction one finds no relevant deviation between the results – that is if the lattice QCD calculation of the hadronic vacuum polarization contribution is used in the Standard Model prediction. As shown in Fig. 1.11, there is a significant deviation of the experimental world average to some of the data-driven calculations and the lattice results, which is, to this date, unsolved. To clarify whether there is a significant deviation between direct measurement and Standard Model prediction and a_μ is an indication of the presence of new physics or if there is agreement between theory and experiment and a_μ is another example for the impressive precision of the Standard Model, the uncertainty of the Standard Model prediction needs to be reduced significantly.

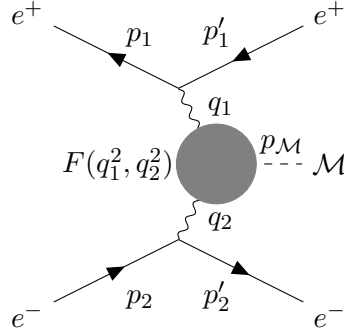


Figure 1.12: Feynman graph of the space-like two-photon process $e^+e^- \rightarrow e^+e^-\mathcal{M}$. The labeling of the vectors is the same used throughout this work.

While the largest uncertainties in the SM prediction stem from the hadronic vacuum polarization contributions, those might become significantly smaller as soon as the discrepancies between the experimental evaluations of the pion-vector form factor and lattice calculations are sorted out. In this case the uncertainties from the hadronic Light-by-Light contribution will become increasingly more important. As demonstrated in this chapter, more detailed studies of two-photon production of hadrons, especially tensor and axial vector states, is necessary.

1.3 | The Two-Photon Particle Production Mechanism

The two-photon production of hadrons is typically studied in electron-positron collisions via the process

$$e^+(p_1) + e^-(p_2) \rightarrow e^+(p'_1) + e^-(p'_2) + \mathcal{M}(p_{\mathcal{M}}) \quad , \quad (1.17)$$

where the hadronic state is produced by the collision of two photons of momentum $q_1 = p_1 - p'_1$ and $q_2 = p_2 - p'_2$ emitted by each lepton and the quantities in the parentheses describe the four-momentum of the respective particle¹. In Fig. 1.12, the Feynman graph of this process is shown. An important note is that in this work the space-like production of hadrons is studied. The timelike process, where the initial state leptons fuse into a virtual photon which later decays into the hadronic state and another (virtual) photon, is typically heavily suppressed compared to the space-like process, since one of the virtualities is fixed to the squared center-of-mass energy and the involved transition form factors, typically rapidly drop at large momentum transfers.

The squared center-of-mass energy is given by $s = (p_1 + p_2)^2$. The mass of the hadronic final state is equal to the two-photon center-of-mass energy $W^2 = p_{\mathcal{M}}^2 = (q_1 + q_2)^2$. Generally, the kinematics in the $e^+e^- \rightarrow e^+e^-\mathcal{M}$ process can be fully characterized by six Lorentz invariants: The already mentioned center-of-mass energy \sqrt{s} and two-photon

¹The definition of the kinematic values described here and throughout this section are used in the entire thesis.

center-of-mass energy W as well as the subsystem center-of-mass energies $s_1 = (p_1 + p_{\mathcal{M}})^2$ and $s_2 = (p_2 + p_{\mathcal{M}})^2$, describing the $e^+e^- \mathcal{M}$ Dalitz plot, and the two-photon virtualities $Q_1^2 = -q_1^2 = -t_1$ and $Q_2^2 = -q_2^2 = -t_2$, which are equal to the momentum transfers of the positron and electron, respectively.

By assuming inclusive production of hadrons, the cross section of the $e^+e^- \rightarrow e^+e^- \mathcal{M}$ process can be directly related to two-photon production cross sections. Ignoring beam polarization, the formula reads [254]

$$d\sigma = \frac{\alpha^2}{8\pi^4 Q_1^2 Q_2^2} \frac{\sqrt{X}}{s(1-4m^2/s)^{1/2}} \frac{d^3\vec{p}'_1}{E'_1} \frac{d^3\vec{p}'_2}{E'_2} \left\{ 4\rho_1^{++} \rho_2^{++} \frac{1}{2} (\sigma_0 + \sigma_2) + \rho_1^{00} \rho_2^{00} \sigma_{\text{LL}} \right. \\ \left. + 2\rho_1^{++} \rho_2^{00} \sigma_{\text{TL}} + 2\rho_1^{00} \rho_2^{++} \sigma_{\text{LT}} + 2(\rho_1^{++} - 1)(\rho_2^{++} - 1) \cos(2\tilde{\phi}) \tau_{\text{TT}} \right. \\ \left. + 8 [(\rho_1^{00} + 1)(\rho_2^{00} + 1)(\rho_1^{++} - 1)(\rho_2^{++} - 1)]^{1/2} \cos \tilde{\phi} \frac{1}{2} (\tau_0 + \tau_1) \right\} .$$

The two-photon production of hadrons is described via the positive cross sections σ_0 , σ_2 , σ_{TL} , σ_{LT} , and σ_{LL} , where the numbers in the subscript refer to helicity and T and L to transversal and longitudinal photon polarization, respectively, and the response functions τ_0 , τ_1 , and τ_{TT} , which can take any sign. In this work the cross section $2\sigma_{\text{TT}} = \sigma_0 + \sigma_2$ and response function $2\tau_{\text{LT}} = \tau_0 + \tau_1$ are used as well. The kinematic factors are given by

$$\rho_1^{++} = \frac{1}{2} \left\{ 1 - \frac{4m^2}{Q_1^2} + \frac{1}{X} (2p_1 \cdot q_2 - q_1 \cdot q_2)^2 \right\} \\ \rho_2^{++} = \frac{1}{2} \left\{ 1 - \frac{4m^2}{Q_2^2} + \frac{1}{X} (2p_2 \cdot q_1 - q_1 \cdot q_2)^2 \right\} \\ \rho_1^{00} = \frac{1}{X} (2p_1 \cdot q_2 - q_1 \cdot q_2)^2 - 1 \\ \rho_2^{00} = \frac{1}{X} (2p_2 \cdot q_1 - q_1 \cdot q_2)^2 - 1 \quad , \quad (1.18)$$

with

$$X = \nu^2 - q_1^2 \cdot q_2^2 \quad (1.19)$$

$$\nu = q_1 \cdot q_2 = \frac{1}{2} (W^2 + Q_1^2 + Q_2^2) \quad . \quad (1.20)$$

The dihedral angle between the lepton scattering planes in the two-photon center-of-mass frame is labeled by $\tilde{\phi}$.

An alternative representation of the cross section can be obtained using the kinematic factors

$$\varepsilon_1 = \frac{\rho_1^{++} - 1}{\rho_1^{++}} \quad \text{and} \quad \varepsilon_2 = \frac{\rho_2^{++} - 1}{\rho_2^{++}} \quad , \quad (1.21)$$

resulting in the formula

$$\begin{aligned}
d\sigma = & \frac{\alpha^2}{8\pi^4 Q_1^2 Q_2^2} \frac{\sqrt{X}}{s(1-4m^2/s)^{1/2}} \cdot \frac{d^3\vec{p}'_1}{E'_1} \cdot \frac{d^3\vec{p}'_2}{E'_2} \frac{4}{(1-\varepsilon_1)(1-\varepsilon_2)} \\
& \times \left\{ \frac{1}{2} (\sigma_0 + \sigma_2) + \left[\varepsilon_1 + \frac{2m^2}{Q_1^2} (1-\varepsilon_1) \right] \left[\varepsilon_2 + \frac{2m^2}{Q_2^2} (1-\varepsilon_2) \right] \sigma_{\text{LL}} \right. \\
& + \left[\varepsilon_2 + \frac{2m^2}{Q_2^2} (1-\varepsilon_2) \right] \sigma_{\text{TL}} + \left[\varepsilon_1 + \frac{2m^2}{Q_1^2} (1-\varepsilon_1) \right] \sigma_{\text{LT}} + \frac{1}{2} \varepsilon_1 \varepsilon_2 \cos(2\tilde{\phi}) \tau_{\text{TT}} \\
& \left. + \left[\varepsilon_1(1+\varepsilon_1) + \frac{4m^2}{Q_1^2} \varepsilon_1(1-\varepsilon_1) \right]^{1/2} \left[\varepsilon_2(1+\varepsilon_2) + \frac{4m^2}{Q_2^2} \varepsilon_2(1-\varepsilon_2) \right]^{1/2} \cos \tilde{\phi} (\tau_0 + \tau_1) \right\} .
\end{aligned} \tag{1.22}$$

In contrast to the inclusive production of hadrons, the exclusive process

$$e^+(p_1) + e^-(p_2) \rightarrow e^+(p'_1) + e^-(p'_2) + \pi^0(\ell_1) + \pi^0(\ell_2) \tag{1.23}$$

preserves full kinematic information of the pion pair, including angular dependencies, which allows for a more differential analysis of the two-photon dynamics. It is most convenient to define all angles in the two-photon center-of-mass frame. Here, and throughout this work, the two-photon center-of-mass system is defined as follows:

The positive z^* axis is defined by the direction of \vec{q}_1^* (the asterisk indicating the two-photon center-of-mass frame). Thus, the negative z^* axis is defined by the remaining photon $\vec{q}_2^* = -\vec{q}_1^*$. The x^*z^* plane is defined such that \vec{p}'_1 lies in this plane with positive

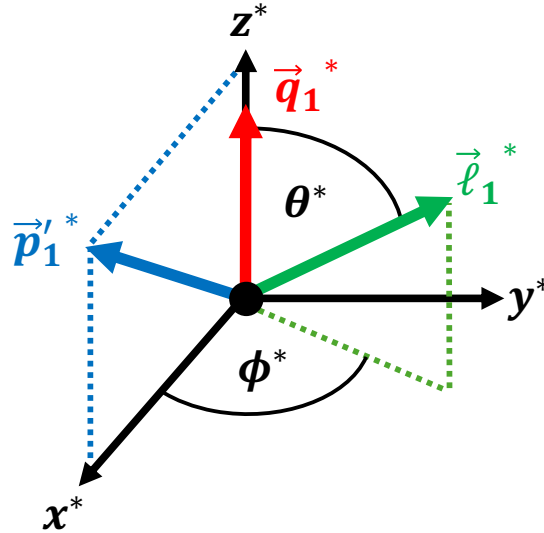


Figure 1.13: Definition of the coordinate system and angles in the two-photon center-of-mass system.

x^* values. The definition of the y^* axis follows from the definition of a right handed coordinate system. The pion helicity angles θ^* and ϕ^* are then equal to polar and azimuthal angles in this system. Figure 1.13 shows the definition of the coordinate system and the angles.

Generally, the definition of the two-photon system remains invariant under the exchange of electron and positron. Especially in single tagged measurements, it is useful to define the coordinates such, that the vectors labeled with 1 are connected to the measured lepton, while the vectors labeled with 2 stem from the non-measured lepton.

The inclusive cross section of two-pion production does not only depend on the pion helicity angles but also on the angles between the hadron planes, defined as the planes produced by the z^* axis and the pion vector $\vec{\ell}^*$, and the lepton planes, defined as the planes containing z^* and \vec{p}_1^* or \vec{p}_2^* .

The angles $\tilde{\phi}_1$ and $\tilde{\phi}_2$ are defined using the transverse lepton momenta

$$\vec{p}_{i\perp}^* = \vec{p}_i^* - (\vec{p}_i^* \cdot \vec{z}^*) \vec{z}^* \quad , \quad (1.24)$$

by the relation

$$\vec{p}_{i\perp}^* \cdot (\vec{z}^* \times \vec{\ell}_1^*) = |\vec{p}_{i\perp}^*| |\vec{\ell}_1^*| \sin \theta^* \sin \tilde{\phi}_i \quad . \quad (1.25)$$

The dihedral angle introduced in Eq. (1.18) is given by $\tilde{\phi} = \tilde{\phi}_2 - \tilde{\phi}_1$ and thus

$$\vec{p}_{1\perp}^* \cdot \vec{p}_{2\perp}^* = |\vec{p}_{1\perp}^*| |\vec{p}_{2\perp}^*| \cos(\tilde{\phi}_2 - \tilde{\phi}_1) = |\vec{p}_{1\perp}^*| |\vec{p}_{2\perp}^*| \cos \tilde{\phi} \quad . \quad (1.26)$$

The cross section formula now contains the differential two-photon cross sections and responses and the angles $\tilde{\phi}_1$ and $\tilde{\phi}_2$. The phase space factor needs to be modified to account for the decay of the intermediate state. For an unpolarized beam it reads [255, 256]

$$\begin{aligned} d\sigma = & \frac{\alpha^2}{8\pi^4 Q_1^2 Q_2^2} \frac{\sqrt{X}}{s\sqrt{1-4m^2/s}} \frac{d^3\vec{p}_1'}{E_1'} \frac{d^3\vec{p}_2'}{E_2'} d\cos\theta^* \frac{4}{(1-\varepsilon_1)(1-\varepsilon_2)} \\ & \times \left\{ \frac{1}{2} \left(\frac{d\sigma_0}{d\cos\theta^*} + \frac{d\sigma_2}{d\cos\theta^*} \right) + \left[\varepsilon_1 + \frac{2m^2}{Q_1^2} (1-\varepsilon_1) \right] \left[\varepsilon_2 + \frac{2m^2}{Q_2^2} (1-\varepsilon_2) \right] \frac{d\sigma_{LL}}{d\cos\theta^*} \right. \\ & + \left[\varepsilon_2 + \frac{2m^2}{Q_2^2} (1-\varepsilon_2) \right] (1 + \varepsilon_1 \cos 2\tilde{\phi}_1) \frac{d\sigma_{TL}}{d\cos\theta^*} \\ & + \left[\varepsilon_1 + \frac{2m^2}{Q_1^2} (1-\varepsilon_1) \right] (1 + \varepsilon_2 \cos 2\tilde{\phi}_2) \frac{d\sigma_{LT}}{d\cos\theta^*} \\ & + \frac{1}{2} \varepsilon_1 \varepsilon_2 \left[\cos 2(\tilde{\phi}_2 - \tilde{\phi}_1) \frac{d\sigma_0}{d\cos\theta^*} + \cos 2(\tilde{\phi}_1 + \tilde{\phi}_2) \frac{d\sigma_2}{d\cos\theta^*} \right] \\ & \left. - \left[\varepsilon_1 \cos 2\tilde{\phi}_1 + \varepsilon_2 \cos 2\tilde{\phi}_2 \right] \frac{d\tau_{T2}}{d\cos\theta^*} \right\} \end{aligned}$$

$$\begin{aligned}
& + \left[\varepsilon_1(1 + \varepsilon_1) + \frac{4m^2}{Q_1^2} \varepsilon_1(1 - \varepsilon_1) \right]^{1/2} \left[\varepsilon_2(1 + \varepsilon_2) + \frac{4m^2}{Q_2^2} \varepsilon_2(1 - \varepsilon_2) \right]^{1/2} \\
& \quad \times \left[\cos(\tilde{\phi}_2 - \tilde{\phi}_1) \left(\frac{d\tau_0}{d \cos \theta^*} + \frac{d\tau_1}{d \cos \theta^*} \right) + \cos(\tilde{\phi}_1 + \tilde{\phi}_2) \left(\frac{d\tau_1}{d \cos \theta^*} - \frac{d\tau_{12}}{d \cos \theta^*} \right) \right] \\
& + \left[\varepsilon_1(1 + \varepsilon_1) + \frac{4m^2}{Q_1^2} \varepsilon_1(1 - \varepsilon_1) \right]^{1/2} \left[\cos \tilde{\phi}_1 \left(\frac{d\tau_{-12}}{d \cos \theta^*} - \frac{d\tau_{1T}}{d \cos \theta^*} \right) \right. \\
& \quad - 2 \left[\varepsilon_2 + \frac{2m^2}{Q_2^2} (1 - \varepsilon_2) \right] \cos \tilde{\phi}_1 \frac{d\tau_{1L}}{d \cos \theta^*} + \varepsilon_2 \cos(\tilde{\phi}_1 + 2\tilde{\phi}_2) \frac{d\tau_{-12}}{d \cos \theta^*} \\
& \quad \left. - \varepsilon_2 \cos(2\tilde{\phi}_2 - \tilde{\phi}_1) \frac{d\tau_{1T}}{d \cos \theta^*} \right] \\
& + \left[\varepsilon_2(1 + \varepsilon_2) + \frac{4m^2}{Q_2^2} \varepsilon_2(1 - \varepsilon_2) \right]^{1/2} \left[\cos \tilde{\phi}_2 \left(\frac{d\tau_{12}}{d \cos \theta^*} - \frac{d\tau_{1T}}{d \cos \theta^*} \right) \right. \\
& \quad - 2 \left[\varepsilon_1 + \frac{2m^2}{Q_1^2} (1 - \varepsilon_1) \right] \cos \tilde{\phi}_2 \frac{d\tau_{-1L}}{d \cos \theta^*} + \varepsilon_1 \cos(2\tilde{\phi}_1 + \tilde{\phi}_2) \frac{d\tau_{12}}{d \cos \theta^*} \\
& \quad \left. - \varepsilon_1 \cos(2\tilde{\phi}_1 - \tilde{\phi}_2) \frac{d\tau_{1T}}{d \cos \theta^*} \right] \Bigg\}. \tag{1.27}
\end{aligned}$$

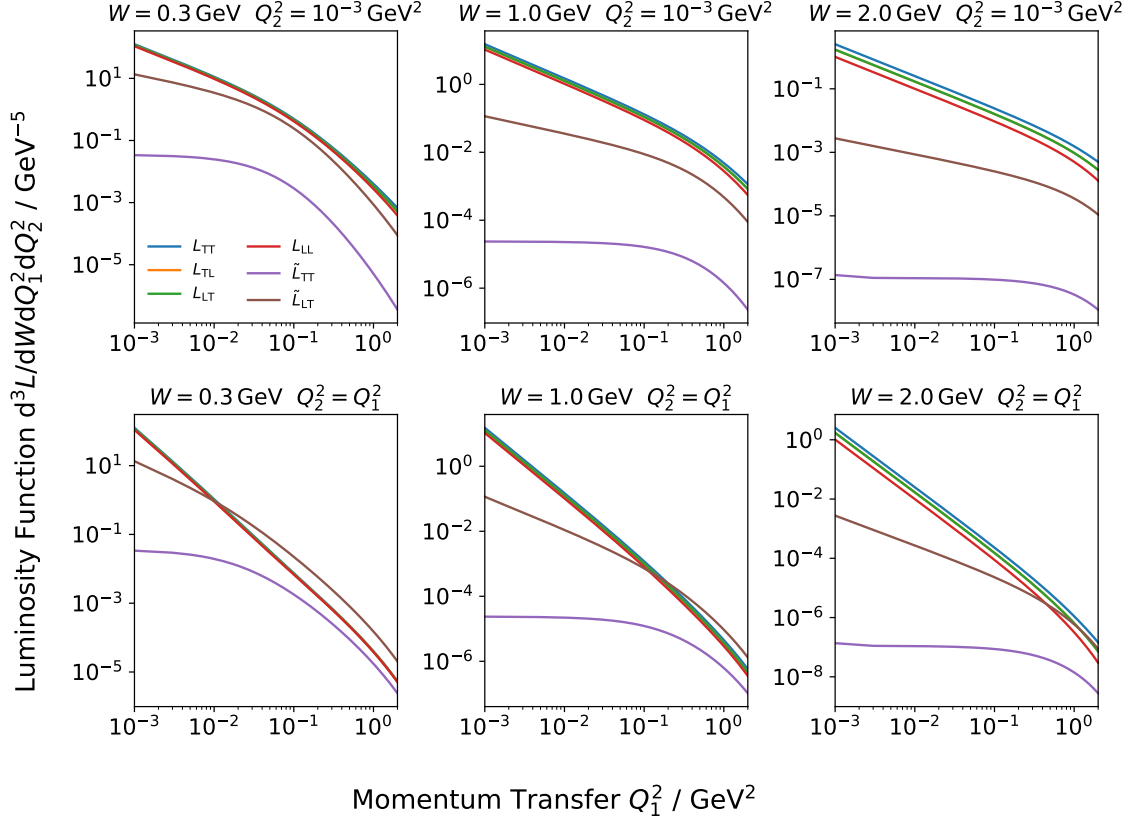


Figure 1.14: Comparison of the two-photon luminosity functions for different photon polarizations as function of the positron momentum transfer Q_1^2 for different two-photon center-of-mass energies W (columns) and electron momentum transfers Q_2^2 (rows). The luminosity functions are calculated following the procedure of Ref. [257]. All values are given for $\sqrt{s} = 3.773 \text{ GeV}$.

If one momentum transfer (in the following example Q_2^2) is minimal, the longitudinal polarization of the photon connected to this momentum transfer is strongly suppressed. The integration of the cross section over the connected angle $\tilde{\phi}_2$ leads to

$$\begin{aligned}
 d\sigma|_{Q_2^2 \rightarrow 0} &= \frac{\alpha^2}{8\pi^4 Q_1^2 Q_2^2} \frac{\sqrt{X}}{s(1-4m^2/s)^{1/2}} \frac{d^3\vec{p}'_1}{E'_1} \frac{d^3\vec{p}'_2}{E'_2} d\cos\theta^* \frac{4}{(1-\varepsilon_1)(1-\varepsilon_2)} \\
 &\times \left\{ \frac{1}{2} \left(\frac{d\sigma_0}{d\cos\theta^*} + \frac{d\sigma_2}{d\cos\theta^*} \right) + \left[\varepsilon_1 + \frac{2m^2}{Q_1^2} (1-\varepsilon_1) \right] \frac{d\sigma_{LT}}{d\cos\theta^*} \right. \\
 &\quad \left. - \varepsilon_1 \cos(2\tilde{\phi}_1) \frac{d\tau_{T2}}{d\cos\theta^*} \right.
 \end{aligned}$$

$$+ \left[\varepsilon_1(1 + \varepsilon_1) + \frac{4m^2}{Q_1^2} \varepsilon_1(1 - \varepsilon_1) \right]^{1/2} \cos \tilde{\phi}_1 \left(\frac{d\tau_{-12}}{d \cos \theta^*} - \frac{d\tau_{-1\Gamma}}{d \cos \theta^*} \right) \Big\} \quad (1.28)$$

offering an interesting possibility to measure some of the response functions independently of the other two-photon cross sections by studying a single additional angle.

Since the kinematic factors ρ_1^{++} , ρ_2^{++} , ρ_1^{00} , ρ_2^{00} , ε_1 , and ε_2 in the cross section formulas depend on the Lorentz invariants s_1 and s_2 while the two-photon cross sections do not, the two-photon production of hadrons is typically not studied as function of s_1 and s_2 and the measured spectra are integrated over these quantities. In Ref. [257], an analytical calculation of the integrals is presented, which includes a change of variables such that the resulting cross section becomes triple differential in W , Q_1^2 , Q_2^2 (and possibly some additional angles depending on the hadronic final state). Using the results of Ref. [257], Eq. (1.18) can be rewritten as

$$\begin{aligned} \frac{d^3\sigma}{dW dQ_1^2 dQ_2^2} &= \frac{d^3 L_{\text{TT}}}{dW dQ_1^2 dQ_2^2} \cdot \sigma_{\text{TT}} + \frac{d^3 L_{\text{TL}}}{dW dQ_1^2 dQ_2^2} \cdot \sigma_{\text{TL}} + \frac{d^3 L_{\text{LT}}}{dW dQ_1^2 dQ_2^2} \cdot \sigma_{\text{LT}} \\ &+ \frac{d^3 L_{\text{LL}}}{dW dQ_1^2 dQ_2^2} \cdot \sigma_{\text{LL}} + \frac{d^3 \tilde{L}_{\text{TT}}}{dW dQ_1^2 dQ_2^2} \cdot \tau_{\text{TT}} + \frac{d^3 \tilde{L}_{\text{LT}}}{dW dQ_1^2 dQ_2^2} \cdot \frac{1}{2} (\tau_0 + \tau_1) \quad . \end{aligned} \quad (1.29)$$

The analytically known functions $d^3 L_{AB}/dW dQ_1^2 dQ_2^2$ ($A, B \in \text{T, L}$) are called two-photon luminosity functions and only depend on the mass W , and both momentum transfers Q_1^2 and Q_2^2 . They fully characterize the QED couplings of the hadronic two-photon process at electron-positron colliders. Analogously, the two-photon luminosity functions of the exclusive pion production cross section (Eq. (1.27)) can be defined. In Ref. [257], a procedure for the analytic calculation of the two-photon luminosity functions derived from Eq. (1.18) is given. The results of this procedure are displayed in Fig. 1.14 for various hadronic masses and momentum transfers. All functions decrease strongly with both momentum transfers and the hadronic mass. This indicates a rapid drop of the $e^+e^- \rightarrow e^+e^- \mathcal{M}$ cross section with increasing momentum transfers and hadronic mass.

1.4 | The Two-Photon Production of Neutral-Pion Pairs

For the Standard Model prediction of a_μ^{HLbL} , the most interesting tensor state to study is the lightest tensor meson, $f_2(1270)$, which can be accessed in two-photon processes via its decay into two pions. The charged-pion channel contains a scalar QED Born contribution at low invariant masses. While this effect is likely negligible at the mass of the $f_2(1270)$, the absence of Born terms in the neutral two-pion channel simplifies a detailed study of the contributing resonances, including the tensor states.

Experimentally, the strong dependence of the kinematic factors in Eqs. (1.18) and (1.27) requires different approaches to study the two-photon production process in different kinematic regions. In general, the $e^+e^- \rightarrow e^+e^- \mathcal{M}$ cross sections decrease rapidly with

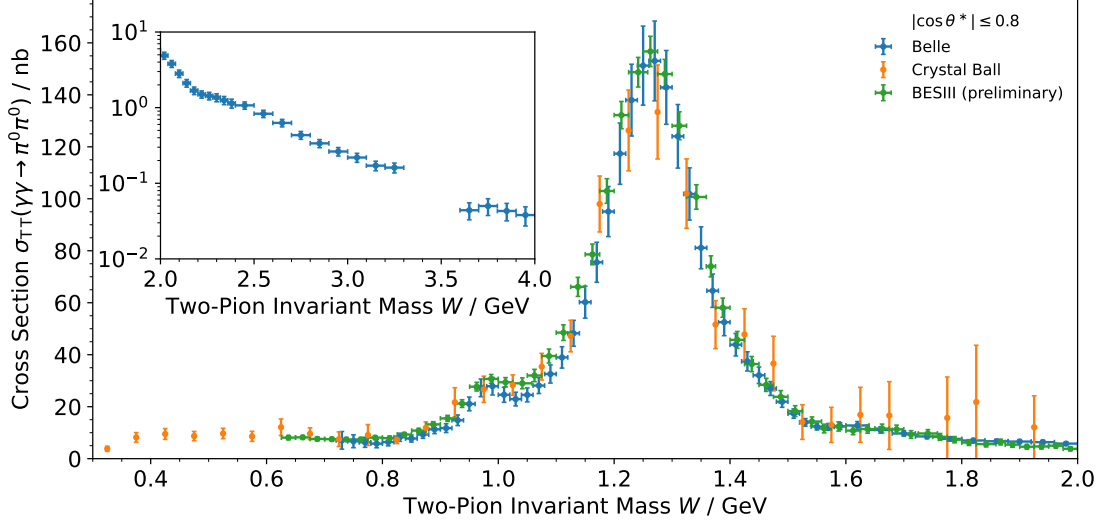


Figure 1.15: Measured two-photon production cross sections of neutral-pion pairs by the Belle collaboration [198] (blue), the Crystal Ball collaboration [193] (orange), and preliminary data from the BESIII collaboration [199] (green). In all cases, the helicity-angle-integrated cross sections are shown in the region $|\cos \theta^*| < 0.8$ as a function of the two-pion invariant mass W .

the lepton momentum transfers Q_1^2 and Q_2^2 , which depend on the initial and final lepton energies and on their scattering angles:

$$Q_i^2 \approx 4E_i E_i' \sin^2 \frac{\theta_i}{2} \quad ,$$

where E_i and E_i' represent the initial and final lepton energies and θ_i the scattering angle relative to the incoming beam. Detector geometry at collider experiments imposes gaps at small or large polar angles relative to the beam direction. Consequently, leptons emitted with small momentum transfers (and therefore small scattering angles) escape detection. Since there are two final-state leptons, three experimental configurations are possible depending on whether each lepton is measured or not, each covering different kinematic ranges.

In the untagged approach, both leptons escape the detector at small angles, so that the momentum transfers remain small. Additional requirements, such as cuts on the transverse momentum of the final-state hadrons, are used to ensure that the virtualities of both photons are minimal and the colliding photons are quasi-real (see, for example, Ref. [199]). This type of measurement does not provide access to the Q^2 dependence of two-photon production, and therefore transition form factors cannot be measured. However, because the virtualities are small and the corresponding cross sections are large, high-statistics measurements are feasible. Moreover, the cross section is directly related to

the radiative widths of the involved resonances, making the untagged mode particularly relevant for spectroscopy.

Since longitudinally polarized photons must be off-shell, most of the cross section and response terms in Eqs. (1.18) and (1.27) vanish. Furthermore, when integrating over the azimuthal angles $\tilde{\phi}$, $\tilde{\phi}_1$, and $\tilde{\phi}_2$, which are not accessible in untagged kinematics, only the transverse-transverse component σ_{TT} (i.e. σ_0 and σ_2) contributes to the total cross section.

For the production of neutral-pion pairs from real photons, measurements have been performed by the Crystal Ball collaboration [193], the Belle collaboration [198], and the BESIII collaboration [199], although the BESIII data are still preliminary. All three experiments are limited to the helicity angle range of $|\cos\theta^*| < 0.8$ and cover different two-pion invariant mass regions. The Crystal Ball measurement is the only one that covers the threshold region. The Belle and BESIII results do not cover this low-mass range but achieve significantly higher statistics than the Crystal Ball measurement at larger masses. Only the Belle collaboration provides data above two-pion invariant masses of $W > 2 \text{ GeV}$.

Unlike the other two collaborations, BESIII performed a coupled-channel partial-wave analysis of $\pi^0\pi^0$ production together with the two-photon production of $\pi^0\eta$ and K^+K^- , enabling a very precise extraction of the radiative widths of the contributing resonances. The data from all three collaborations are displayed in Fig. 1.15. In general, the available data are in good agreement. The most prominent feature is the $f_2(1270)$ resonance, with the $f_0(980)$ also clearly visible. At low invariant masses, the cross section is non-vanishing, indicating the presence of the $f_0(500)$ state. At higher masses, additional tensor and scalar states have been identified through partial wave analyses [198, 199].

Small discrepancies, particularly in the $f_0(980)$ mass region, are likely caused by smearing effects. A combined fit of the data will likely require taking these effects into account.

When one of the final-state leptons is detected while the other escapes at small angles, one of the photon virtualities remains finite. This leads to a significantly reduced cross section and lower statistics, but allows the study of the momentum-transfer dependence of two-photon production, with respect to one of photon virtualities. Unlike untagged measurements, these single-tagged measurements also include contributions from two-photon processes where one photon is longitudinally polarized. Consequently, there is an additional contribution from the helicity-1 component, σ_{LT} (or σ_{TL} if the second photon is off-shell).

According to Eqs. (1.18) and (1.27), the kinematic factors for the different contributions differ, resulting in two distinct luminosity functions for this process. Since these functions are not identical, one of the two-photon cross section terms is measured only up to a known scale factor ε . Because the σ_{LT} contribution arises only from tensor mesons, it is typically chosen to carry this additional factor. The measured observable is therefore $\sigma_{\text{TT}} + \varepsilon_{\text{LT}} \cdot \sigma_{\text{LT}}$. A partial-wave analysis enables the separation of these terms and the extraction of the transition form factors of the involved resonances.

Such a measurement has been performed by the Belle collaboration [200]. The observed helicity angle-integrated cross sections are shown in Fig. 1.16. Compared to untagged measurements, the statistics is significantly reduced. The accessible mass range

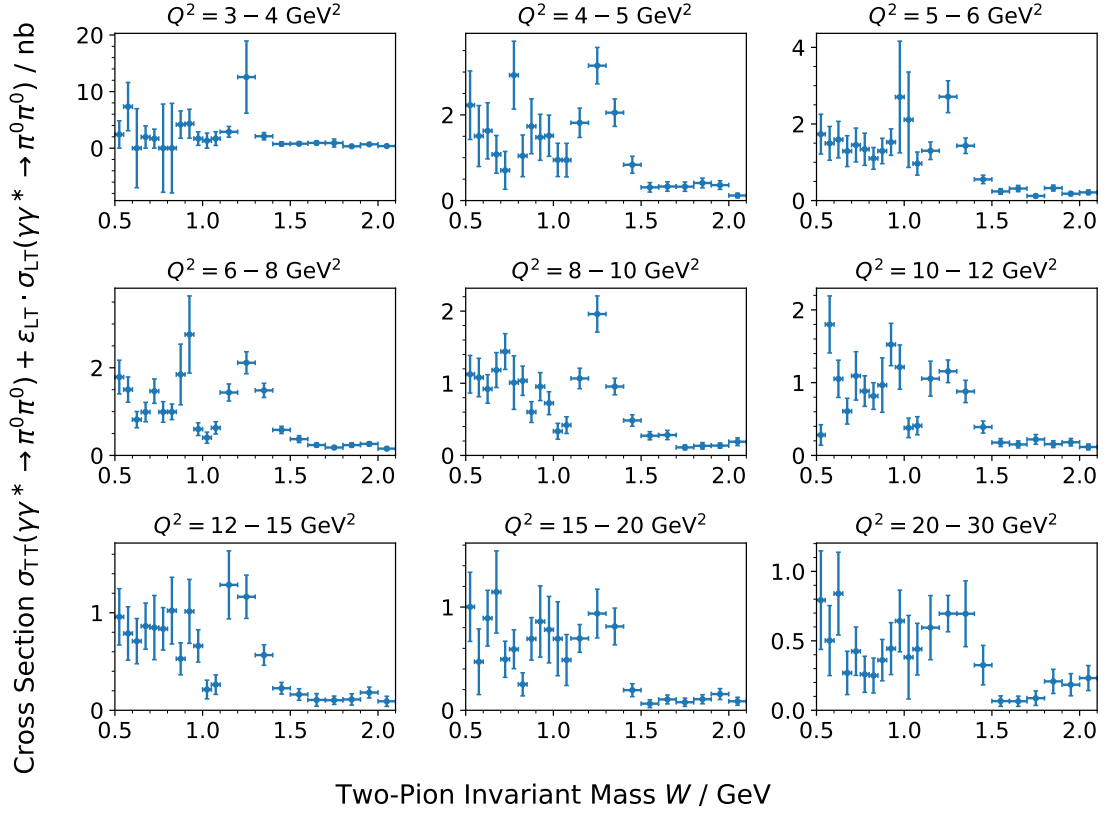


Figure 1.16: Cross section measurement of neutral-pion pair production by the Belle collaboration [200]. The two-photon production cross section is shown as a function of the two-pion invariant mass, integrated over the full helicity angle range. Each panel corresponds to a different momentum-transfer range.

is smaller, but the full helicity angle range is covered. A partial-wave analysis was used to extract the transition form factors of the $f_0(980)$ and $f_2(1270)$ states. The form factor of the most important scalar contribution to a_μ^{HLbL} (the $f_0(500)$) could not be measured because of the limited kinematic range. Moreover, because the measurement was performed at large center-of-mass energies, the momentum transfers were relatively high ($Q^2 > 3 \text{ GeV}^2$), which is not the ideal range for improving the Standard Model prediction of a_μ^{HLbL} .

Because of the drastically reduced statistics in double-tagged measurements, where both leptons are scattered at large angles and detected, the double-virtual production of neutral-pion pairs has not been studied. In fact, there is only one published double-tagged measurement: the determination of the doubly virtual η' transition form factor by the BaBar collaboration [174]. As a result, there is currently no available data on the doubly off-shell transition form factors of scalar or tensor states.

Besides experimental studies of the two-photon production of neutral pion pairs, sev-

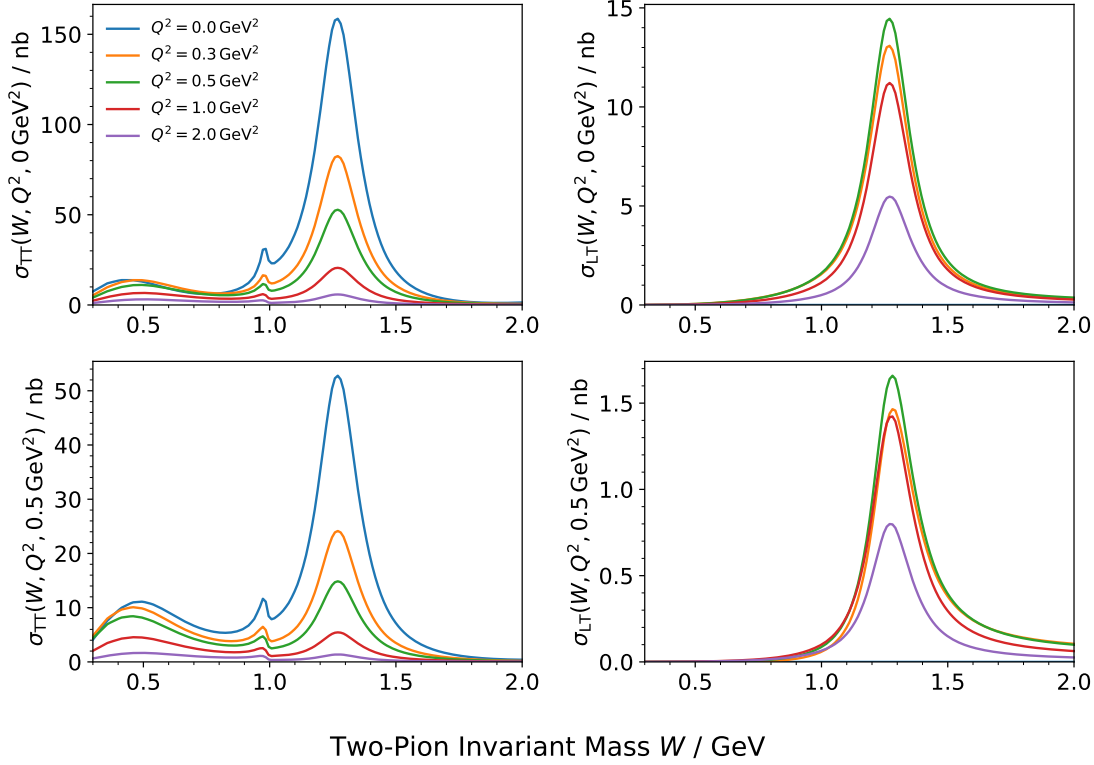


Figure 1.17: Dispersive theory prediction of the σ_{TT} (left) and σ_{LT} (right) cross sections in a single virtual (top) and double virtual (bottom) configuration as function of the two-pion invariant mass W . The data was kindly made available by the authors of Refs. [258–260].

eral theoretical investigations have been carried out to provide the necessary input for the determination of a_{μ}^{HLbL} (see, for example, Refs. [258–261]). In the works presented in Refs. [256, 258–260], the helicity amplitudes contributing to the two-photon process $\gamma^*\gamma^* \rightarrow \pi\pi$ are determined within a dispersive framework. In this approach, the scalar resonances $f_0(500)$ and $f_0(980)$ are treated in a coupled-channel formalism that incorporates both $\pi\pi$ and $K\bar{K}$ intermediate states, allowing for a unified description of the narrow $f_0(980)$ together with the broad $f_0(500)$. The tensor state $f_2(1270)$ is included in a single-channel ($\pi\pi$ only) treatment, and no additional states are considered at present. At large Q^2 , the theoretical description is matched to the available Belle data (see Ref. [200] and Fig. 1.16), while at small virtualities it is constrained by dispersive calculations and describes the untagged experimental data well (Fig. 1.15 and Refs. [193, 197, 199]). Since all relevant helicity amplitudes are determined within this framework, it provides predictions for all two-photon cross sections and response functions entering Eqs. (1.18) and (1.27). The resulting predictions for the σ_{TT} and σ_{LT} cross sections, which are the most relevant contributions in singly-virtual processes, are shown

in Fig. 1.17. In the most relevant virtuality range for a_μ , at $\lesssim 1 \text{ GeV}^2$, the framework is not yet constrained by experimental data, as none are currently available. Consequently, these predictions would benefit significantly from additional measurements of the $\gamma^*\gamma^* \rightarrow \pi^0\pi^0$ cross section at small momentum transfers.

1.5 | Goal of this Work

The goal of this work is to study the two-photon production of neutral-pion pairs using the BESIII detector and its large accumulated data samples. The results are intended to improve the precision of the Standard Model prediction of a_μ^{HLbL} . In particular, the main objective is the determination of the singly virtual transition form factors of the $f_2(1270)$ state, as well as the transition form factors of the scalar resonances accessible in $\gamma\gamma \rightarrow \pi^0\pi^0$ at virtualities relevant for a_μ^{HLbL} , below and around 2 GeV^2 .

If feasible, information on the double virtual production of neutral-pion pairs will be extracted using an event selection similar to that of the single-tag study.

The measurement of the two-photon production cross sections requires an efficiency-correction procedure, which is typically based on studies using Monte Carlo samples. For the $e^+e^- \rightarrow e^+e^-\pi^0\pi^0$ process considered here, the number of available Monte Carlo event generators capable of simulating the physics of the final state is strongly limited. Therefore, in this work, a new Monte Carlo event generator is developed. The goal of this generator is not only to produce reliable simulations of $e^+e^- \rightarrow e^+e^-\pi^0\pi^0$, but also to be easily extendable to other two-photon reactions, such as $e^+e^- \rightarrow e^+e^-\pi^0\eta$ or $e^+e^- \rightarrow e^+e^-f_1(1285)$, thereby enabling the study of these processes at BESIII and other electron–positron collision experiments in the future.

2 | Development of a Monte Carlo Event Generator for Hadronic Two-Photon Scattering in Electron Collisions

Contents

2.1	Basic Requirements on Monte Carlo Simulations for the Study of Hadronic Two-Photon Scattering	34
2.2	General Approach	35
2.3	Phase Space Generation	36
2.3.1	Generation of the $e^+e^- \rightarrow e^+e^- \mathcal{M}$ Phase Space	36
2.3.2	Generation of the Final State Hadronic Decay	39
2.3.3	Application of User Cuts and Consistency Checks	41
2.4	Two-Photon Cross Sections and Responses	41
2.4.1	Production through a Single Resonance of a Custom Final State	41
2.4.2	Luminosity Function Mode	44
2.4.3	$e^+e^- \rightarrow e^+e^- \pi\pi$ and $e^+e^- \rightarrow e^+e^- \pi\eta$ Modes	44
2.4.4	$e^+e^- \rightarrow e^+e^- KK$ and $e^+e^- \rightarrow e^+e^- \eta\eta$ Modes	45
2.4.5	$e^+e^- \rightarrow e^+e^- f_1(1285) \rightarrow e^+e^- \eta\pi^+\pi^-$ Mode	47
2.5	Program Structure	47
2.5.1	Double and Quadruple Precision Floating Numbers	49
2.5.2	Input Scheme	49
2.5.3	Output Scheme	49
2.5.4	Implementation of Three Vector and LorentzVector classes	50
2.5.5	Important Variables	50
2.5.6	Important Functions	50
2.6	Running the Simulation	52
2.7	Results	53
2.7.1	Luminosity Functions	53

2.7.2	Fixed Two-Photon Cross Sections and Luminosity Functions . . .	56
2.7.3	Cross Sections of Two-Hadron Final States	56
2.7.4	Cross Sections of the $e^+e^- \rightarrow e^+e^-\pi^0\pi^0$ Process	57
2.7.5	Cross Sections of the $e^+e^- \rightarrow e^+e^-f_1(1285) \rightarrow e^+e^-\eta\pi^+\pi^-$ Process	58
2.8	Summary of the Monte Carlo Event Generator	61

2.1 | Basic Requirements on Monte Carlo Simulations for the Study of Hadronic Two-Photon Scattering

The study of two-photon production of hadronic states in electron-positron collisions requires a Monte Carlo simulation of the process to evaluate both the signal purity in the selected sample and the reconstruction efficiency of the hadronic states. For hadronic final states with higher multiplicities, a partial-wave analysis is typically required to extract the relevant physics information from the data. Since the cross sections for such final states depend on many kinematic variables, the analysis is usually performed using an unbinned maximum-likelihood fit to the data. Software frameworks developed for this type of analysis generally require a Monte Carlo sample that follows a uniform phase-space distribution of the relevant final state (see, for example, Refs. [262, 263]).

In two-photon physics, using a uniform $e^+e^-\mathcal{M}$ sample results in an extremely inefficient event generation procedure, since two-photon cross sections are typically strongly peaked at small momentum transfers, as discussed in Sec. 1.3. Moreover, when only a basic phase-space Monte Carlo is employed, the complex dynamics described by Eqs. 1.18 and 1.27 must be implemented separately in each individual analysis. A more efficient strategy is to generate a Monte Carlo sample that maintains a flat phase-space distribution of the final-state hadrons while incorporating the QED part of the two-photon-hadron dynamics specified in Eqs. 1.18 and 1.27, thereby requiring only the hadronic two-photon dynamics to be implemented in the partial-wave analysis.

To simulate a complete physics process, a Monte Carlo generator that models two-photon production using the cross sections described in Sec. 1.3 and which can be easily adapted to incorporate improved physics descriptions as they become available is essential.

Currently, several MC event generators exist that simulate hadronic two-photon physics at electron-positron colliders. Among them, the EKHARA generator [264–268] provides the most detailed physics modeling. It simulates two-photon production of pseudoscalar particles at next-to-leading order and the production of charged and neutral pions, where the charged channel includes the irreducible background from Bhabha processes emitting additional virtual photons. It also models the production of several resonances in the charm region. The generator uses a Lorentz-covariant expression for the $e^+e^- \rightarrow e^+e^-\mathcal{M}$ cross section rather than the framework of Sec. 1.3, and therefore cannot be used to calculate the luminosity functions. Furthermore, because the matrix element depends strongly

on the specific hadronic final state, the generator cannot be extended simply by inserting two-photon cross sections.

There are other Monte Carlo event generators [269–272] available, typically based on the inclusive cross section formula of Eq. (1.18). These generators are often limited to specific kinematic configurations (e.g., untagged or single-tagged modes) and may rely on high-energy approximations or simplifying assumptions about the two-photon dynamics. Moreover, the exclusive production of two mesons described by Eq. (1.27) is not implemented in these generators.

The goal of this work is to develop a Monte Carlo event generator that models two-photon production within the framework presented in Sec. 1.3, without relying on high-energy approximations. The code will be capable of generating phase-space and luminosity-function samples suitable for use in partial-wave analyses and for physics simulations of two-pion final states, as required for the BESIII measurement presented later in this work. The implementation will be sufficiently flexible to accommodate additional final states in the future. For two-body hadronic final states, the theory input will be structured such that the relevant two-photon cross sections and response functions in Eq. (1.27) can be supplied numerically as functions of the two-photon center-of-mass energy, the two photon virtualities, and the cosine of the helicity angle, enabling straightforward updates of the theory input and extension to other hadronic final states.

2.2 | General Approach

The code, nicknamed HADROTOPS (Hadron production in TwO-Photon Scattering in electron-positron collisions), is designed to simulate the process $e^+e^- \rightarrow e^+e^-\mathcal{M}$, where \mathcal{M} denotes an arbitrary hadronic final state. For the phase-space generation, a modified version of the efficient algorithm presented in Ref. [271] and used by the GALUGA and EKHARA [264] event generators is employed. The differential two-photon cross sections and responses contributing to Eqs. 1.18 and 1.27 are implemented in different ways to simulate various underlying physics scenarios.

The two-photon cross sections can be specified through simple analytic models, extracted from experimental data, or supplied as numerical tables as for example done by the authors of Refs. [258, 273]. Since the cross sections are provided through look-up tables, the code is highly modular. The cross section and response function inputs are stored in external text files, allowing models to be modified easily by supplying alternative input files.

For easy integration into the BESIII software framework, the code is written in C++, using the quadruple-precision library `libquadmath` for additional numerical precision. The design philosophy prioritizes minimal dependence on external libraries. In its most basic configuration, the generated events can be written to an ASCII file or directly passed to an experimental framework. Optionally, classes from the ROOT framework [274] can be used to generate output in the form of histograms stored in ROOT files.

2.3 | Phase Space Generation

In this section, the procedure for generating four-vectors of the final state particles and the numerical determination of the phase-space element are described. The code employs a two-step approach to the generation of four-vectors. First, the $e^+e^- \rightarrow e^+e^- \mathcal{M}$ intermediate state is produced; subsequently, the decay of \mathcal{M} is simulated, if required.

The generator assumes that the four-vectors of the initial-state positron and electron are given by

$$p_1 = (\sqrt{s}/2, 0, 0, p)^T \quad \text{and} \quad p_2 = (\sqrt{s}/2, 0, 0, -p)^T, \quad (2.1)$$

respectively. The initial lepton momentum is denoted by $p = \sqrt{s/4 - m^2}$ and $m = 510.99895$ keV the electron mass [275].

2.3.1 | Generation of the $e^+e^- \rightarrow e^+e^- \mathcal{M}$ Phase Space

The generation of the $e^+e^- \mathcal{M}$ phase space is largely based on the highly efficient algorithm developed by Schuler, which is implemented in the GALUGA generator and described in detail in Ref. [271]. This algorithm has also been incorporated into the EKHARA event generator [264, 267], from which parts of the present phase space code have been adapted and reimplemented in C++. This section provides a brief overview of the phase-space generation procedure, with emphasis on the differences relative to the implementations in GALUGA and EKHARA. A comprehensive description of the algorithm can be found in Refs. [264, 271].

The algorithm generates the final-state four-vectors using five Lorentz invariants:

$$W = p_X^2 \quad (2.2)$$

$$t_1 = q_1^2 = -Q_1^2 \quad t_2 = q_2^2 = -Q_2^2 \quad (2.3)$$

$$s_1 = (p'_1 + p_{\mathcal{M}})^2 \quad s_2 = (p'_2 + p_{\mathcal{M}})^2, \quad (2.4)$$

together with the fixed center-of-mass energy \sqrt{s} .

In the first step, the $e^+e^- \mathcal{M}$ four-vectors are generated using the random numbers x_1, \dots, x_6 , uniformly distributed in the interval $[0, 1)$, such that the Lorentz-invariant phase-space element is mapped onto a six-dimensional unit hypercube:

$$\begin{aligned} d\text{Lips}_{ee\mathcal{M}} &= \int \frac{d^3\vec{p}'_1}{(2\pi)^3 2E'_1} \frac{d^3\vec{p}'_2}{(2\pi)^3 2E'_2} \frac{d^3\vec{p}_{\mathcal{M}}}{(2\pi)^3 2E_{\mathcal{M}}} (2\pi)^4 \delta^{(4)}(p_1 + p_2 - p'_1 - p'_2 - p_{\mathcal{M}}) \\ &= \frac{2W}{(2\pi)^5} \frac{\pi^2}{4\beta s} \delta \delta_1 \delta_2 \delta_W dx_1 \cdots dx_6, \end{aligned} \quad (2.5)$$

where $\beta = \sqrt{1 - 4m^2/s}$ denotes the electron velocity. The Jacobian factors δ , δ_1 , δ_2 , and δ_W in this equation – partially derived from the calculations in Refs. [264, 271] and dependent on the specific variable mappings employed – will be detailed later in this section. The factor $2W$ arises from the transformation of the differential cross section

from dW^2 (as used in Ref. [271]) to dW . This transformation is necessary since the hadronic input is typically provided in dependence on W rather than W^2 .

Using the random numbers $x_1 \dots x_6$, the three-body $e^+e^- \mathcal{M}$ final state is then generated in the following steps:

1. *Generation of the Hadronic Mass W :*

If the user specifies a fixed value, this step is skipped. Otherwise, W is constrained to lie within the boundaries W_{\min} and W_{\max} , as set by kinematic and user-defined conditions. For cross-checks, two alternative mappings are implemented:

(a) Flat Mapping:

Here, every mass between W_{\min} and W_{\max} is generated at equal probability:

$$W = W_{\min} + (W_{\max} - W_{\min}) x_6 \quad , \quad (2.6)$$

which leads to a Jacobian factor of

$$\delta_W \equiv \frac{dW}{dx_6} = W_{\max} - W_{\min} \quad . \quad (2.7)$$

(b) Logarithmic Mapping:

For better description of the kinematic factors in Eqs. (1.18) and (1.27), which generally drop rapidly with increasing W , a logarithmic mapping is implemented, which generates a larger fraction of events at small masses:

$$W = W_{\min} \exp \left(x_6 \log \left(\frac{W_{\max}}{W_{\min}} \right) \right) \quad . \quad (2.8)$$

The Jacobian factor becomes

$$\delta_W = W \log \left(\frac{W_{\max}}{W_{\min}} \right) \quad . \quad (2.9)$$

In general, the choice of mapping does not affect the final result if a reasonably large sample is generated, but can significantly influence the computational efficiency of the code. For the generation of samples including arbitrary final states produced with through a single resonance with a flat phase space, both mappings perform equally well. However, for channels that use hadronic input to model a specific physical process, typically including several resonances, the flat mapping is recommended.

2. *Generation of the Positron and Electron Momentum Transfers t_1 and t_2 :*

The electron momentum transfer t_2 is constrained by kinematic and user-defined limits to lie between $t_{2,\min}$ and $t_{2,\max}$. For this variable, both flat and logarithmic mappings are implemented, following the same structure as described for the hadronic mass W :

(a) Flat Mapping:

The momentum transfer is generated as

$$t_2 = t_{2,\min} + (t_{2,\max} - t_{2,\min}) x_1 \quad , \quad (2.10)$$

which results into a Jacobian factor of

$$\delta_2 = \frac{dt_2}{dx_1} = (t_{2,\max} - t_{2,\min}) \quad . \quad (2.11)$$

(b) Logarithmic Mapping:

$$t_2 = t_{2,\min} \exp \left(x_1 \log \left(\frac{t_{2,\max}}{t_{2,\min}} \right) \right) \quad . \quad (2.12)$$

$$\delta_2 = t_2 \log \left(\frac{t_{2,\max}}{t_{2,\min}} \right) \quad . \quad (2.13)$$

After generating the electron momentum transfer, the positron momentum transfer t_1 and its corresponding Jacobian factor δ_1 are generated in the same manner using the random variable x_2 . In principle, both flat and logarithmic mappings yield identical physics results. However, the logarithmic mapping is significantly more efficient, as it better describes the rapidly decreasing behavior of the kinematic factors in Eqs. (1.18) and (1.27) with increasing photon virtualities. Additionally, the logarithmic mapping cancels the poles at $t_1 = 0$ and $t_2 = 0$ in Eqs. (1.18) and (1.27), preventing potential numerical instabilities at small values of t_1 and t_2 . Thus, the usage of the logarithmic mapping is strongly recommended – especially when generating samples at small photon virtualities.

3. Generation of the Subsystem Center-of-Mass Energies s_1 and s_2 :

The generation of s_1 and s_2 follows the procedure outlined in Ref. [271]. Since these invariants are typically not used in experimental two-photon interaction studies because the hadronic dynamics do not depend on these variables, user-defined cuts are not applied to these values. Similarly, the option to directly restrict the final-state energies of the leptons during the generation of the subsystem center-of-mass energies – which would effectively constrain s_1 and s_2 – is not implemented for the same reason. Therefore, s_1 and s_2 are restricted solely by kinematics. User cuts on the final lepton energies can still be applied after the full final-state four-vectors have been generated. This alternative approach is included for completeness. The invariants are generated using the random numbers x_3 and x_4 , and the corresponding Jacobian contribution to the phase-space element is given by [271]:

$$\delta = \frac{s(1 + \beta)^2}{(\nu + \sqrt{X})(1 + y_1)(1 + y_2)}, \quad \text{with } y_{1/2} = \sqrt{1 - 4m^2/t_{1/2}} \quad . \quad (2.14)$$

and

$$\nu = q_1 \cdot q_2 = \frac{1}{2} (W^2 + Q_1^2 + Q_2^2) \quad X = \nu^2 - Q_1^2 Q_2^2 \quad . \quad (2.15)$$

4. *Calculation of the final-state four-vectors:*

Once all six Lorentz invariants are determined, the final-state four-vectors can be calculated, up to an overall rotation around the azimuthal angle. A numerically stable parametrization of the vectors is adopted from Ref. [271]. Since the vectors are initially defined only relative to one another, they are rotated around the azimuthal angle by a random number uniformly distributed between 0 and 2π , generated using the random variable x_5 .

At this point, the full final-state kinematics of the process $e^+e^- \rightarrow e^+e^-\mathcal{M}$ is generated, and the Lorentz-invariant phase space element of this process is calculated.

2.3.2 | Generation of the Final State Hadronic Decay

The subsequent decay of the hadronic final state \mathcal{M} into N particles with masses m_1, \dots, m_N and final-state four-vectors ℓ_1, \dots, ℓ_N is generated using a GENBOD-like algorithm [276]. In this approach, the N -body decay is split into a series of two-body decays until all final-state particles with the correct masses are produced. To facilitate this, a set of intermediate-state masses M_1 through M_N is defined as:

$$M_1^2 = m_1^2, \quad M_N = p_{\mathcal{M}}^2 = W^2, \quad \text{and} \quad M_i^2 = \left(\sum_{j=1}^i \ell_j \right)^2 \quad . \quad (2.16)$$

The intermediate masses $M_2 \dots M_{N-1}$ are randomly generated within their kinematic limits using $N - 2$ random numbers $\tilde{x}_2 \dots \tilde{x}_{N-1} \in [0, 1)$:

$$\begin{aligned} M_{i,\min} &= \sum_{j=1}^i m_j \\ M_{i,\max} &= M_{i+1} - m_{i+1} \\ M_i^2 &= M_{i,\min}^2 + (M_{i,\max}^2 - M_{i,\min}^2) \tilde{x}_i \quad . \end{aligned} \quad (2.17)$$

For each step, the magnitude of the three momentum in each two-body decay chain in the parent particle's rest frame is given by

$$p_i^*(M_{i+1}, M_i, m_{i+1}) = \frac{\sqrt{\lambda(M_{i+1}^2, M_i^2, m_{i+1}^2)}}{2M_{i+1}} \quad (2.18)$$

where

$$\lambda(x, y, z) = x^2 + y^2 + z^2 - 2xy - 2xz - 2yz \quad (2.19)$$

is the Källén triangle function. By using the additional random variables $\hat{x}_{i,1}, \hat{x}_{i,2} \in [0, 1)$, the azimuthal and polar angles in the parent particle's rest frame can be generated as

$$\begin{aligned}\cos \theta_i^* &= 2 \hat{x}_{i,1} - 1 \\ \phi_i^* &= 2\pi \hat{x}_{i,2} \\ d\Omega^* &= 4\pi d\hat{x}_{i,1} d\hat{x}_{i,2} \quad .\end{aligned}$$

Using the decay angles, three-momenta, and particle masses, the four-vectors of the decay products are initially constructed in the rest frame of the parent particle. These four-vectors are then boosted into the e^+e^- center-of-mass frame via a Lorentz transformation.

The Lorentz-invariant phase space element of the N body decay is given by

$$d\text{Lips}_N(\ell_1, \dots, \ell_N) = \int \prod_{i=1}^N \frac{d^3 \vec{\ell}_i}{(2\pi)^3 2E_i} (2\pi)^4 \delta^{(4)} \left(p_{\mathcal{M}} - \sum_{i=1}^N \ell_i \right) \quad . \quad (2.20)$$

This expression can be expressed recursively in terms of $d\text{Lips}_{N-1}$.

$$d\text{Lips}_N(M_N^2) = \frac{dM_{N-1}^2}{2\pi} d\text{Lips}_2(p_N; p_{N-1}, l_N) d\text{Lips}_{N-1}(M_{N-1}^2), \quad (2.21)$$

where $d\text{Lips}_2(p_N; p_{N-1}, l_N)$ is the two-body phase space for the decay

$$p_N \rightarrow p_{N-1} + l_N, \quad p_i \equiv \sum_{j=1}^i l_j, \quad (2.22)$$

and $d\text{Lips}_{N-1}(M_{N-1}^2)$ is the $(N-1)$ body phase space of the subsystem with total four-momentum p_{N-1} . Inserting the two-body element in spherical coordinates, one obtains

$$d\text{Lips}_N(M_N^2) = \frac{dM_{N-1}^2}{2\pi} d\Omega_{N-1}^* \frac{\sqrt{\lambda(M_N^2, M_{N-1}^2, m_N^2)}}{8\pi M_N^2} d\text{Lips}_{N-1}(M_{N-1}^2). \quad (2.23)$$

Iterating Eq. (2.21) results in the form

$$d\text{Lips}_N(M_N^2) = \left(\prod_{i=2}^{N-1} \frac{dM_i^2}{2\pi} \right) \left(\prod_{i=1}^{N-1} \frac{\sqrt{\lambda(M_{i+1}^2, M_i^2, m_{i+1}^2)}}{8\pi M_{i+1}^2} d\Omega_i^* \right), \quad (2.24)$$

which can be further modified using the random variables into a high-dimensional unit-hypercube:

$$d\text{Lips}_N(W^2) = \left(\prod_{i=2}^{N-1} \frac{(M_{i,\max}^2 - M_{i,\min}^2) d\tilde{x}_i}{2\pi} \right) \left(\prod_{i=1}^{N-1} \frac{\sqrt{\lambda(M_{i+1}^2, M_i^2, m_{i+1}^2)}}{2 M_{i+1}^2} d\hat{x}_{i,1} d\hat{x}_{i,2} \right). \quad (2.25)$$

The Lorentz invariant phase space of the full final state is obtained by

$$d\text{Lips} = d\text{Lips}_{ee\mathcal{M}} \times d\text{Lips}_N. \quad (2.26)$$

2.3.3 | Application of User Cuts and Consistency Checks

After all final-state four-vectors have been generated, they are numerically checked for energy and momentum conservation at the level of 1 eV, which is negligibly small for typical particle physics experiments. When the code is compiled using quadruple precision floating-point numbers, the final-state vectors consistently satisfy this requirement. No numerically unstable events have been observed. When using double precision instead of quadruple precision floating-point numbers, less than 0.001 % of events show deviations exceeding this threshold. Any event that fails the stability check is rejected, and a new event is generated.

Following the stability check, additional user-defined cuts are applied. These include cuts on the polar angles of the hadronic decay products and on the total transverse momentum of the hadronic system, the latter being commonly used in studies involving two quasi-real photons, see for example, Ref. [199].

After these steps, the generation of the final-state four-vectors and the calculation of the phase-space element are complete. Figure 2.1 presents a flow chart summarizing the four-vector generation procedure.

2.4 | Two-Photon Cross Sections and Responses

The two-photon cross sections and response functions appearing in Eqs. (1.18) and (1.27) must be specified to obtain physically accurate Monte Carlo predictions. To accommodate a wide range of processes, several generator modes are implemented to handle different classes of final states, as outlined in this section. An important feature of the generator is its flexibility: users can independently activate or deactivate individual cross sections and response functions, making it possible to explore each configuration separately or to study their combined effects within a unified framework.

This work focuses on the production of two final-state hadrons, specifically neutral pions. Consequently, particular attention is given to the dynamics and properties of two-body final states involving narrow hadronic resonances. Nevertheless, the code is designed with sufficient flexibility to be readily extended to include other final-state particles.

2.4.1 | Production through a Single Resonance of a Custom Final State

The most basic functionality of HADROTURNS is to simulate the production of a user-defined hadronic final state via a single resonance using a dedicated final-state mode. This allows experimental collaborations to estimate the reconstruction efficiency for a given final state and to use the generated events in partial-wave analysis tools such as AmpTools [263] and PAWIAN [262] without implementing the QED parts of Eqs. (1.18) and (1.27) into the analyses. Since no universal theoretical model exists for the production and decay of generic final states in two-photon collisions, simplified models are used to describe such processes. The two-photon cross sections are expressed in a factorized

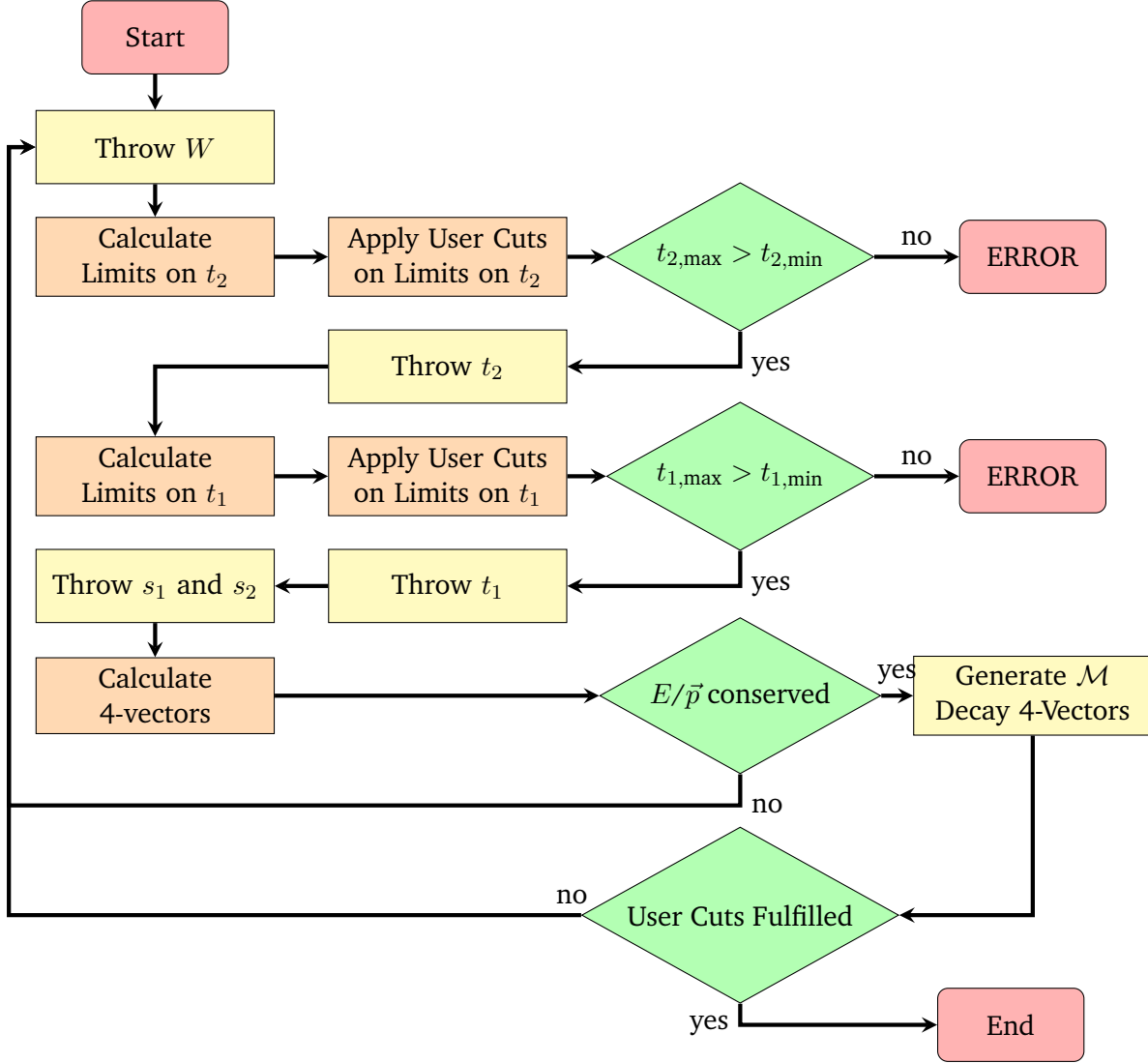


Figure 2.1: Flowchart of the four-vector generation of the $e^+e^-\mathcal{M}$ final state.

form consisting of a mass-dependent term, $f(W)$, and a transition form factor, $|\mathcal{F}_{AB}|^2$:

$$\sigma_{AB}(W, Q_1^2, Q_2^2) \approx f(W) |\mathcal{F}_{AB}(Q_1^2, Q_2^2)|^2, \quad A, B \in T, L. \quad (2.27)$$

The default expressions for $f(W)$ and $\mathcal{F}_{AB}(Q_1^2, Q_2^2)$ are given below. Setting both $\mathcal{F}_{AB}(Q_1^2, Q_2^2)$ and $f(W)$ to unity allows the generated sample to be used directly within partial-wave analysis frameworks, eliminating the need to explicitly include the luminosity functions in the amplitude definitions.

For the transition form factor, a factorized dependence on the photon virtualities is

assumed, ensuring the correct behavior in the real-photon limit:

$$|\mathcal{F}_{AB}(Q_1^2, Q_2^2)|^2 \approx h_A(Q_1^2) h_B(Q_2^2), \quad h_T(0) = 1, \quad h_L(0) = 0. \quad (2.28)$$

All other cross sections and response functions are implemented in analogy to σ_{TT} . Because experimental studies of these quantities involve azimuthal dependencies, normalizing them to unity allows the generation of Monte Carlo samples that incorporate the full lepton-side kinematics. This, in turn, facilitates the extraction of hadronic structure by fitting the simulated samples directly to the experimental data.

For the mass-dependent component, three options are available. The first option omits any explicit mass dependence, generating the mass distribution solely based on the kinematic factors in Eqs. (1.18) and (1.27), i.e., $f(W) = 1 \text{ GeV}^{-2}$. Alternatively, a fixed-mass scenario can be simulated using $f(W) = \delta(W^2 - W_{\text{user}}^2)$.

Furthermore, a Breit-Wigner mass distribution can be used:

$$f(W) = \frac{1}{(W^2 - M^2)^2 + \Gamma^2 M^2} \frac{M \Gamma}{\pi}, \quad (2.29)$$

where the resonance mass M and width Γ are chosen by the user.

Analogous to the treatment of the mass dependence, a constant transition form factor model is available: $|\mathcal{F}_{AB}| = 1$. For a more realistic description, a vector-pole-like model is implemented, following the approach used in the GALUGA2.0 generator [271]. In this case, the transition form factor is given by

$$h_T(Q^2) = \left(\frac{1}{1 + Q^2/m_V^2} \right)^2, \quad h_L(Q^2) = \xi \frac{Q^2}{m_V^2} \left(\frac{1}{1 + Q^2/m_V^2} \right)^2, \quad (2.30)$$

where the pole mass m_V and the scaling parameter ξ can be determined by the user. Alternatively, a simplified vector-meson-dominance (VMD) model with multiple poles is available [277]. In this case, the transition form factors are given by

$$h_T(Q^2) = \sum_{i=0}^3 r_i \left(\frac{m_{V_i}^2}{Q^2 + m_{V_i}^2} \right)^2, \quad h_L(Q^2) = \sum_{i=1}^3 \xi \frac{Q^2}{m_{V_i}^2} r_i \left(\frac{m_{V_i}^2}{Q^2 + m_{V_i}^2} \right)^2, \quad (2.31)$$

where the masses m_{V_0}, \dots, m_{V_3} and the parameters ξ, r_1, \dots, r_3 are free inputs, with the constraint $r_0 = 1 - r_1 - r_2 - r_3$ to ensure proper normalization. The resonance with index 0 normalizes the transverse term and does not contribute to the longitudinal term. A generalized VMD model [278] is also implemented:

$$\begin{aligned} h_T(Q^2) &= r \left(\frac{m_1^2}{Q^2 + m_1^2} \right)^2 + (1 - r) \frac{m_2^2}{Q^2 + m_2^2} \\ h_L(Q^2) &= \xi r \left(\frac{m_1^2}{Q^2 + m_1^2} \right)^2 + \xi(1 - r) \left[\frac{m_2^2}{Q^2} \log \left(1 + \frac{Q^2}{m_2^2} \right) - \frac{m_2^2}{Q^2 + m_2^2} \right] \end{aligned} \quad (2.32)$$

This implementation enables the code to reproduce the results of GALUGA2.0, while avoiding reliance on high-energy approximations. As before, all parameters are left as free inputs for the user.

Helicity-angle dependencies of the decay products have not been implemented. Instead, all final states are generated according to a isotropically populated phase-space distribution. Since no reliable theoretical information exists regarding the relative scaling between different cross sections for an arbitrary hadronic state, the absolute normalization is identical for all channels. Consequently, it is not meaningful to simulate multiple cross-section and response-function combinations simultaneously. However, ratios of independently generated Monte Carlo samples can be used to study differences arising from the lepton-side kinematics.

2.4.2 | Luminosity Function Mode

Besides generating arbitrary $e^+e^- \rightarrow e^+e^-\mathcal{M}$ events, the code can also be used to numerically calculate the luminosity functions introduced in Sec. 1.3. For this purpose, all two-photon cross sections or response functions are set to unity, effectively removing any hadronic dynamics, and only the $e^+e^- \rightarrow e^+e^-\mathcal{M}$ phase-space element is evaluated. Consequently, only $d\text{Lips}_{ee\mathcal{M}}$ is used in the weight calculation, while the hadronic decay factor is set to unity, thereby excluding any dynamics from the decay of \mathcal{M} . The same procedure can be applied to calculate the corresponding functions associated with the two-photon cross sections in Eq. (1.27).

2.4.3 | $e^+e^- \rightarrow e^+e^-\pi\pi$ and $e^+e^- \rightarrow e^+e^-\pi\eta$ Modes

To simulate the physics process $e^+e^- \rightarrow e^+e^-\pi\pi$ and $e^+e^- \rightarrow e^+e^-\pi\eta$, it is necessary to accurately model the differential response functions of the subprocesses $\gamma^*\gamma^* \rightarrow \pi\pi$ and $\gamma^*\gamma^* \rightarrow \pi\eta$. In the code, these are implemented using the dispersive formalism developed in Refs. [258–260], which has been briefly discussed in Sec. 1.4. For the process $e^+e^- \rightarrow e^+e^-\pi^0\eta$, the work presented in Ref. [190] was extended by the original authors to incorporate a second virtuality.

The cross sections are provided numerically as functions of W , Q_1^2 , Q_2^2 , and the pion scattering angle $|\cos\theta^*|$ in the two-photon center-of-mass system within the kinematic limits $2m_\pi < W < 2\text{ GeV}$ and $0 \leq Q_{1/2}^2 \leq 4\text{ GeV}^2$. To determine the cross section at an arbitrary point, the theory input is interpolated using three different methods. The most stable approach is a linear spline interpolation of the nearest neighbors in all four dimensions, which is recommended to use.

To generate events beyond the input theory range, the code can extrapolate the theoretical predictions. The cross section is assumed to decrease proportionally to $1/W^2$, while the high- Q^2 behavior is modeled using the form-factor frameworks introduced in Sec. 2.4.1. Both the form-factor model and its parameters can be freely adjusted, providing full flexibility.

It should be emphasized that the theory input is only valid within its specified kinematic range, and any extrapolation should be regarded as a rough estimate rather than an

accurate representation of the actual cross section.

For the $\pi^+\pi^-$ channel, only the two-photon production of the pion pair in $e^+e^- \rightarrow e^+e^-\pi^+\pi^-$ is simulated. Possible production of charged pion pairs from the radiation of a virtual photon in a Bhabha scattering event is not included, although it is expected to play an important role in experimental studies of this channel [279]. An updated version of the EKHARA event generator includes both production mechanisms and their interference [268]. This EKHARA version has not been published but was kindly made available for cross-checks by the original author Henryk Czyż.

2.4.4 | $e^+e^- \rightarrow e^+e^-KK$ and $e^+e^- \rightarrow e^+e^-\eta\eta$ Modes

In the absence of reliable theoretical input, these experimental measurements are used to model the two-photon cross sections for the corresponding final states. The Belle collaboration investigated the two-photon production of K^+K^- [280, 281], $K_S K_S$ [282], and $\eta\eta$ [283] in an untagged configuration with $Q_1^2 = Q_2^2 \approx 0$, covering a wide range of invariant masses. Additionally, the BESIII collaboration has performed a coupled-channel analysis of the $\pi^0\pi^0$, K^+K^- , and $\pi^0\eta$ final states [199, 284].

For the K^+K^- channel, the BESIII partial-wave analysis results provide a precise measurement of the $\sigma_{\text{TT}}(0, 0)$ cross section in the angular range $|\cos\theta^*| < 0.8$, with an extrapolation to the full angular range. These results are therefore used in the range $W < 2$ GeV. For $W > 2$ GeV, the Belle measurements are used. Since the Belle data do not cover the full angular range, an extrapolation is required. To perform this extrapolation, the differential cross section is described by

$$\frac{d\sigma}{d|\cos\theta^*|} \propto \left| S(W) Y_0^0(\theta^*, 0) + D_0(W) Y_2^0(\theta^*, 0) e^{i\phi(W)} \right|^2 + |D_2(W) Y_2^2(\theta^*, 0)|^2, \quad (2.33)$$

where $Y_n^m(\theta, \phi)$ are spherical harmonics, S , D_0 , and D_2 represent the relative strengths of the amplitudes, and ϕ describes the interference between the S and D_0 amplitudes at each mass point. Since the generator does not require information about the physical intermediate states, a quantitative information of the differential cross section at each energy point is sufficient to determine the numerical input.

Figure 2.2 shows the fit results for the Belle K^+K^- cross sections below $W < 2.4$ GeV. Equation (2.33) provides an accurate description of the data within its uncertainties. The same methodology is applied to the high-mass Belle K^+K^- cross section results [281], as well as to the $K_S K_S$ and $\eta\eta$ cross sections. The resulting curves are used to estimate cross sections outside the measured angular range ($|\cos\theta^*| > 0.6$ for K^+K^- , $|\cos\theta^*| > 0.8$ or > 0.6 for $K_S K_S$, and $|\cos\theta^*| > 0.9$ or full coverage for $\eta\eta$).

Figure 2.3 shows the numerical integration of the differential cross section over various helicity angle ranges. As expected, the integration of the Belle fits exhibits increasing uncertainties when extended beyond the range of experimental input. This effect is particularly pronounced in the intermediate mass region ($W < 2.4$ GeV) for the K^+K^- channel, which is limited by both statistics and helicity angle coverage.

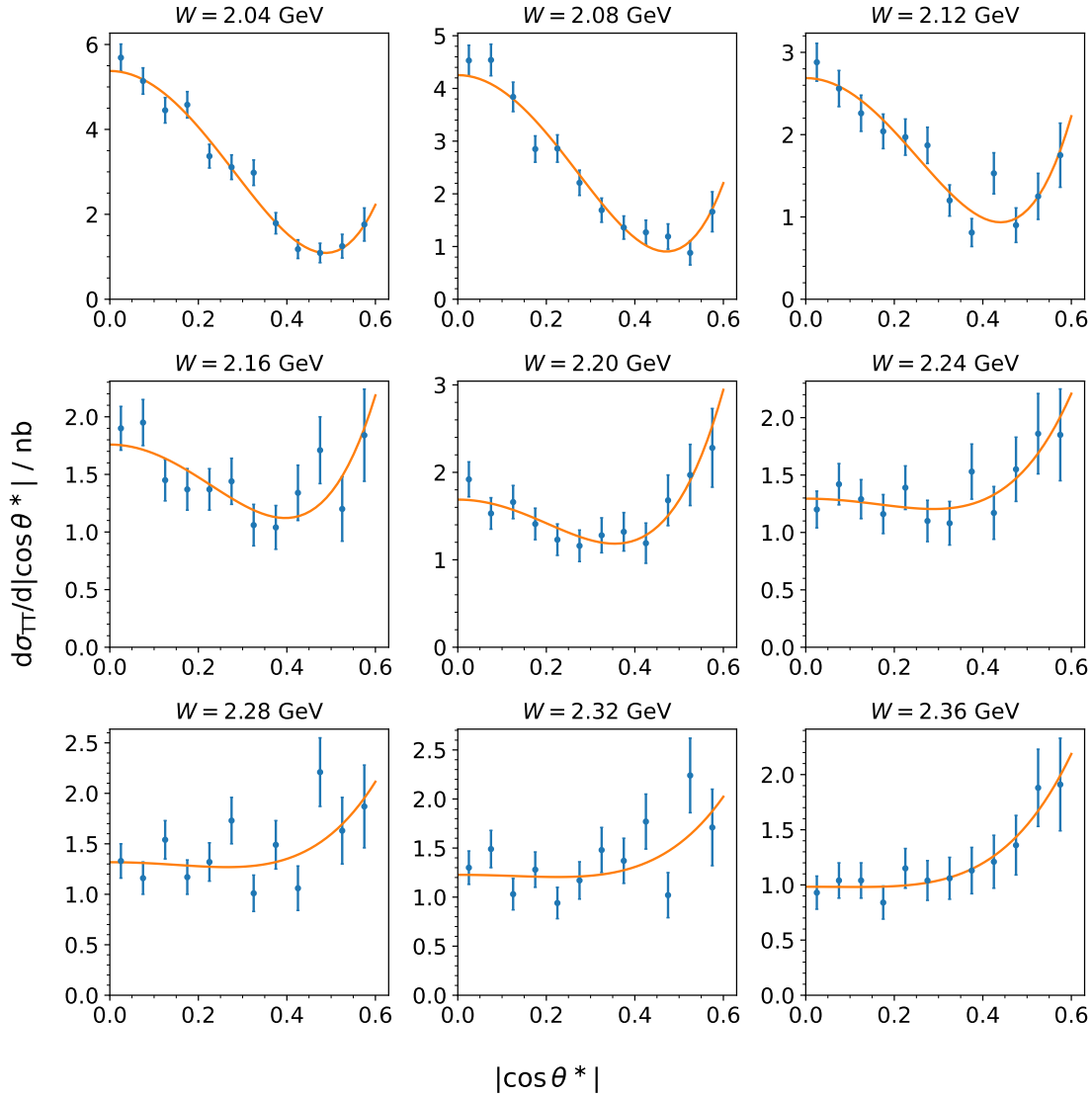


Figure 2.2: Fit of the cross section model (Eq. 2.33) to the Belle $\gamma\gamma \rightarrow K^+K^-$ cross sections [280, 281] as function of the helicity angle $|\cos\theta^*|$. The blue points are the Belle data presented in Ref. [280], the orange curve is the fit result. The different panels represent different K^+K^- invariant masses.

Since the BESIII and Belle collaborations performed untagged measurements, only the TT-polarized cross sections can be analyzed, and no information on the momentum-transfer dependence is provided. Consequently, the numerical input is available only at $Q_1^2 = Q_2^2 = 0$. The extrapolation methods described in Sec. 2.4.3 can be used to obtain Q^2 -dependent cross sections, though these results are highly model-dependent. Therefore, the implemented model is considered reliable only at $Q_{1/2}^2 \approx 0$.

2.4.5 | $e^+e^- \rightarrow e^+e^- f_1(1285) \rightarrow e^+e^- \eta\pi^+\pi^-$ Mode

So far, the discussion has focused exclusively on two-body hadronic final states. However, the generator is capable of producing final states with arbitrary multiplicity. In ongoing work by Jan Muskalla [285], the two-photon production of the $f_1(1285)$ via its decay into $\eta\pi^+\pi^-$ – including interfering intermediate states $f_0(500)\eta$ and $a_0^\pm(980)\pi^\mp$ – is being investigated. Implementing such a three-body decay using look-up tables, as done for the two-body channels, would be computationally expensive due to the high dimensionality of the differential two-photon cross sections. To address this, the two-photon production amplitudes from Ref. [286], which are employed in the partial-wave analysis of the $f_1(1285)$ transition form factors in Muskalla’s study, have been implemented and extended within the generator code to account for two virtualities.

2.5 | Program Structure

In the previous section, the implemented physics processes were discussed. Here, the technical details of the program are presented. HADROTOPS is distributed as source code organized into a structured directory layout. The core of the generator is implemented as a class, allowing straightforward integration into experiment software frameworks. The main header file, `HadroTOPS.hh`, is located in the `include/` folder. In the same directory, `common.hh` provides essential quadruple-precision functions, and the headers for the Lorentz and three-vector objects (`LorentzVector` and `Vector3`) are also included. The source code for the vector objects resides in `src/vector`, while the HADROTOPS generator’s implementation is located in `src/hadrotops`. The main function, which reads job options and instantiates the HADROTOPS object accordingly, is located in `src/main.cc`.

The HADROTOPS source code is organized across several files:

- `HadroTOPS.cc`: Implements the constructor of the HADROTOPS object and handles the initialization and finalization of the event generation procedure. Constants are defined here.
- `HadroTOPS.aux.cc`: Provides auxiliary functions, including consistency and sanity checks of user input, a convenience function for the random number generator, and status-bar display.
- `HadroTOPS.crosssection.cc`: Contains all functions for calculating the event weight, i.e., the full differential cross section, for the current kinematic configuration.

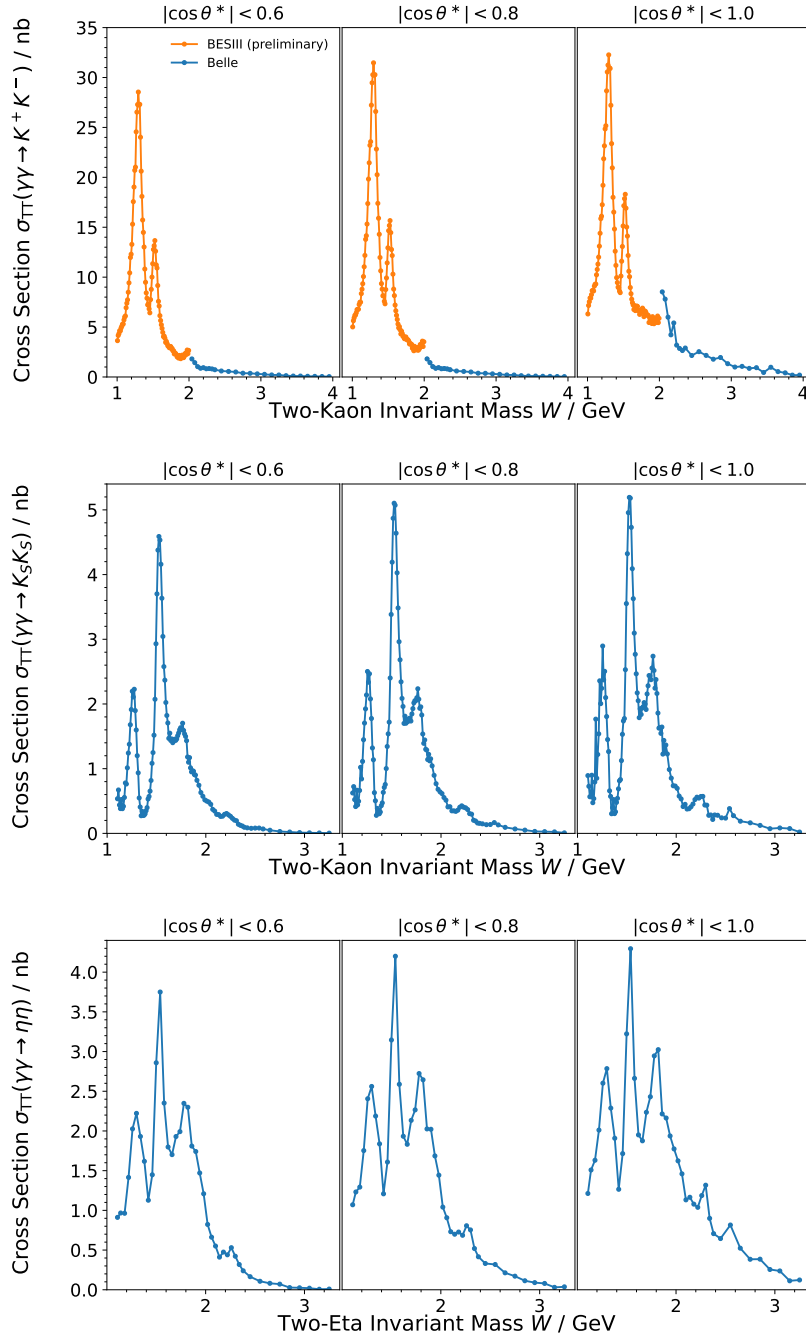


Figure 2.3: Integrated BESIII partial-wave analysis (orange) and fits to the $\gamma\gamma \rightarrow K^+K^-$ (top), $\gamma\gamma \rightarrow K_S K_S$ (center) and $\gamma\gamma \rightarrow \eta\eta$ (bottom) cross sections (blue) over different helicity angle ranges. The points (crosses) represent the actual mass points, the lines are linear interpolation between the results.

- `HadroTOPS.generate.cc`: Implements all functions required for generating final-state Lorentz vectors and computing the associated phase-space elements and other kinematic factors.
- `HadroTOPS.getters.cc`: Contains all getter functions.
- `HadroTOPS.mc.cc`: Implements functions for the Monte Carlo procedure, including weighted and unweighted event generation loops and Monte Carlo integration.
- `HadroTOPS.out.cc`: Provides all functions necessary for program output.
- `HadroTOPS.setters.cc`: Contains all setter functions.
- `HadroTOPS.theory.cc`: Implements all functions needed to read and interpolate the theory input for the two-photon cross sections.

2.5.1 | Double and Quadruple Precision Floating Numbers

The code can be compiled to run using either double or quadruple precision floating-point numbers. Quadruple precision provides improved numerical stability but comes at the cost of significantly longer execution times. Nevertheless, its use is recommended for the sake of numerical reliability. For quadruple precision, the `libquadmath` library and the `__float128` floating-point data type are employed. For convenience, this type is aliased as `quad`. When only double precision is needed, the preprocessor flag `-DDOUBLE_PREC` can be set during compilation. This makes the `quad` type equivalent to `long double` and replaces the quadruple-precision functions with their standard long-double counterparts.

2.5.2 | Input Scheme

The executable `HadroTOPS.exe` is generated in the `bin/` folder. When executed (in bash shells `./bin/HadroTOPS.exe`), it reads all settings from `config/jobOptions.txt`, unless a different file is specified (`./bin/HadroTOPS.exe path/to/file.txt`). This input file defines all necessary parameters for input, output, and the event generation process. A detailed description of the available settings is provided in the `HADROTOPS` manual distributed together with the source code.

It should be noted that the generator can also be used without a dedicated input file. When integrated into a larger software framework, all settings can be configured directly using the appropriate setter functions.

The numerical theory input is stored in the `data/` folder.

2.5.3 | Output Scheme

The program is capable of providing both event-by-event output and histograms of the (differential) cross section. The histogramming functionality requires a `ROOT [274]` installation.

Weighted and unweighted events are stored in separate ASCII files. Each file contains, for every event, the number of final-state particles, their labels, and the four-vectors of all particles in the e^+e^- center-of-mass frame. For weighted events, the weight is included in the output. The precise format is detailed in the manual.

Histograms are saved in a ROOT file, whose name and location are defined in the `jobOptions.txt` file.

In addition to these output files, information about the current run is displayed in the console, which can be used for logging purposes.

2.5.4 | Implementation of Three Vector and LorentzVector classes

Since the code may employ quadruple-precision floating-point calculations, the available classes for three- and four-vectors are not suitable. To address this, a simplified and very incomplete reimplementations of the most important functions from ROOT's [274] `TVector3` and `TLorentzVector` classes is provided, using quadruple-precision floats and functions. The source code for these reimplementations is located in the corresponding header files, as well as in `src/vector/Vector3.cc` and `src/vector/LorentzVector.cc`.

2.5.5 | Important Variables

The kinematic variables, required by different functions, are implemented as member variables of the `HadroTOPS` class. All quantities are handled in units of GeV for energies, masses, widths, and momenta, in radians for angles, and in GeV^{-2} for cross sections and responses. These include scalar variables of type `quad` for the center-of-mass energy (`Ecm` and `s`), the two-photon center-of-mass energy (`w`), lepton momentum transfers (`t1`, `t2`, `Q1s`, and `Q2s`), subsystem center-of-mass energies (`s1` and `s2`), the modulation angles $\tilde{\phi}$ (`phiTilde`), $\tilde{\phi}_1$ (`phiTilde1`), and $\tilde{\phi}_2$ (`phiTilde2`), and the polar and azimuthal angles of the final-state hadrons in the two-photon center-of-mass system (`cosThetaStar` and `phiStar`).

The four-vectors of the initial and final-state positron (`k1` and `p1`) and electron (`k2` and `p2`), the four-vector of the hadronic system $p_{\mathcal{M}}$ (`px`), and the final-state hadron four-vectors (`pdec`) are stored as `LorentzVector` objects, or as C++ `std::vectors` thereof. Other important quantities, such as the current event weight (`WEIGHT`), the maximum event weight observed during the weighted event loop (`maxWEIGHT`), and the phase-space elements `dLipseeM`, `dLipseeM/(t1t2)`, and `dLipsN` (`dLips`, `dLipsDiv`, `dLipsDec`) are also stored as member variables of type `quad`.

2.5.6 | Important Functions

A brief overview of a selected set of the most important functions in the `HADROTOPS` source code is provided below.

- Functions for the generation of final-state four-vectors

- void HadroTOPS::generateFixW():
Generates the $e^+e^-\mathcal{M}$ final-state vectors and calculates $dLips_{ee\mathcal{M}}$ as well as relevant kinematic variables at given (globally defined) values of s and W . User and kinematic limits of the final-state vectors are respected.
 - void HadroTOPS::decayFinalState():
Handles the decay of the hadronic final state \mathcal{M} into its final-state particles and calculates the corresponding phase-space element.
 - bool HadroTOPS::generateEvent():
Generates a numerically stable weighted event. If necessary, W is generated and the decay products of the hadronic final state \mathcal{M} are produced. Determines final-state Lorentz vectors in the center-of-mass system and calculates additional required kinematic variables. Returns a boolean indicating whether the generated event passes user constraints. Calls `calcXS()` to compute the event weight according to the chosen two-photon model and Eqs. (1.18) and (1.27).
 - bool HadroTOPS::acceptEvent():
Checks user-defined constraints and returns `false` if the event should be rejected. Additional user-specific constraints could be implemented here.
 - void HadroTOPS::generateWeightedEvent():
Generates a weighted event within user constraints, handles Monte Carlo integration and event output. Internally calls `generateEvent()` and `acceptEvent()`.
 - void HadroTOPS::runWeighted():
Implements the weighted event loop, generating the number of weighted events requested by the user while respecting user constraints. Determines the maximum event weight and stores it in `maxWEIGHT`.
 - void HadroTOPS::generateUnweightedEvent():
Generates an unweighted event using rejection sampling [287] while respecting user constraints. Requires that the maximum weight (`maxWEIGHT`) is known, which can be set by running `runWeighted()`. Calls `generateWeightedEvent()` internally and handles unweighted event output.
 - void HadroTOPS::runUnweighted():
Generates the number of unweighted events requested by the user, subject to user-defined constraints.
- Calculation of the cross section
 - void HadroTOPS::interpolateCrossSectionInput():
Wrapper function for the interpolation of the cross section input. It calls the necessary functions to interpolate the theory input at the current kinematic variables. The interpolated two-photon cross sections are stored in the member variable `quad itXS[18]`.

- `quad HadroTOPS::getFFTT()`:
Calculates the transition form factor for two transversely polarized virtual photons according to the model chosen by the user. For other photon-polarization combinations, the corresponding functions are implemented as `getFFTL()` (transverse-longitudinal), `getFFLT()` (longitudinal-transverse), and `getFFLL()` (longitudinal-longitudinal).
- `void HadroTOPS::calcXS()`:
Calculates the two-photon cross section using the current kinematic variables and the user-specified input model.

2.6 | Running the Simulation

HADROTOPS is executed using a four-step procedure:

1. Initialization
2. Weighted event generation and upper bound estimation loop
3. Unweighted event generation (optional)
4. Finalization

The general workflow of HADROTOPS is outlined here; detailed instructions for using the generator standalone or embedded within an external program structure are provided in the HADROTOPS manual. During initialization, a new HADROTOPS object is created and the simulation options are configured using setter functions. Subsequently, the function `void HadroTOPS::init()` must be called, which verifies the settings, initializes the output routines and the random number generator, and sets up the Monte Carlo integration variables.

Next, the function `HadroTOPS::runWeighted()` is called to generate a predefined number of weighted events satisfying the user-specified constraints. During this process, the maximum event weight within the user-defined constraints is determined, which is necessary for the subsequent unweighted-events loop. Alternatively, a user may call `HadroTOPS::generateWeightedEvent()` to generate a single weighted event that satisfies the user constraints. The current event weight, expressed in nanobarns or in GeV, when running in luminosity-function mode, can be obtained using `HadroTOPS::getWeight()`. It is important to note that `HadroTOPS::generateWeightedEvent()` cannot be used to determine the maximum weight. In all cases, events are recorded in histograms and/or written to the output file as specified by the user.

The weighted events loop is typically followed by an optional unweighted events loop. Analogous to the weighted events, `HadroTOPS::runUnweighted()` generates a predefined number of unweighted events, while `HadroTOPS::generateUnweightedEvent()` generates a single unweighted event that satisfies the user-defined cuts. The resulting events are recorded in histograms and/or written to the output file and must be scaled to the total

cross section using the same normalization procedure. The final step is program finalization, during which the total cross section of the simulated physics process is calculated and reported. The cross section and its corresponding uncertainty for the weighted events – including all trials in the unweighting procedure – are given by:

$$\sigma = \frac{1}{N_w} \sum_{i=1}^{N_w} d\sigma_i \quad (2.34)$$

$$(\Delta\sigma)^2 = \frac{1}{N_w - 1} \left(\frac{1}{N_w} \sum_{i=1}^{N_w} (d\sigma_i)^2 - \sigma^2 \right) , \quad (2.35)$$

where $d\sigma_i$ is the weight (cross section) of event i and N_w the number of generated weighted events within the user cuts. Alternatively, the cross section can be calculated from the unweighted events by

$$\sigma = d\sigma_{\max} \frac{N_{uw}}{N_t} \quad (2.36)$$

$$(\Delta\sigma)^2 = \frac{\sigma(d\sigma_{\max} - \sigma)}{N_{uw}} \quad (2.37)$$

with the maximum weight $d\sigma_{\max}$ and the number of unweighted events N_{uw} . Here, N_t denotes the number of trials, i.e., the number of generated weighted events during the unweighting procedure.

2.7 | Results

2.7.1 | Luminosity Functions

For cross-checks, the luminosity functions calculated using HADROTOPS can be compared to their analytically computed counterparts. The exact calculation is demonstrated in Ref. [257]. This comparison is only possible for the luminosity functions associated with the cross section in Eq. (1.18), as no analytical calculation has been performed for the formula in Eq. (1.27).

A comparison between the output of HADROTOPS and the analytical curves is performed over a wide range of center-of-mass energies, two-photon center-of-mass energies, and momentum transfers for all possible combinations of photon polarizations. The agreement is found to lie within the statistical fluctuations of the generated samples. Figure 2.4 shows a comparison of the double-transverse luminosity function as a function of momentum transfers and two-photon center-of-mass energy, taken at $\sqrt{s} = 4$ GeV. The momentum transfers and masses are chosen within their respective typically accessible ranges at this energy (see for example chapter 5 and Ref. [288]). The comparison demonstrates excellent agreement. A similar level of agreement is observed for the five other analytically known luminosity functions as well.

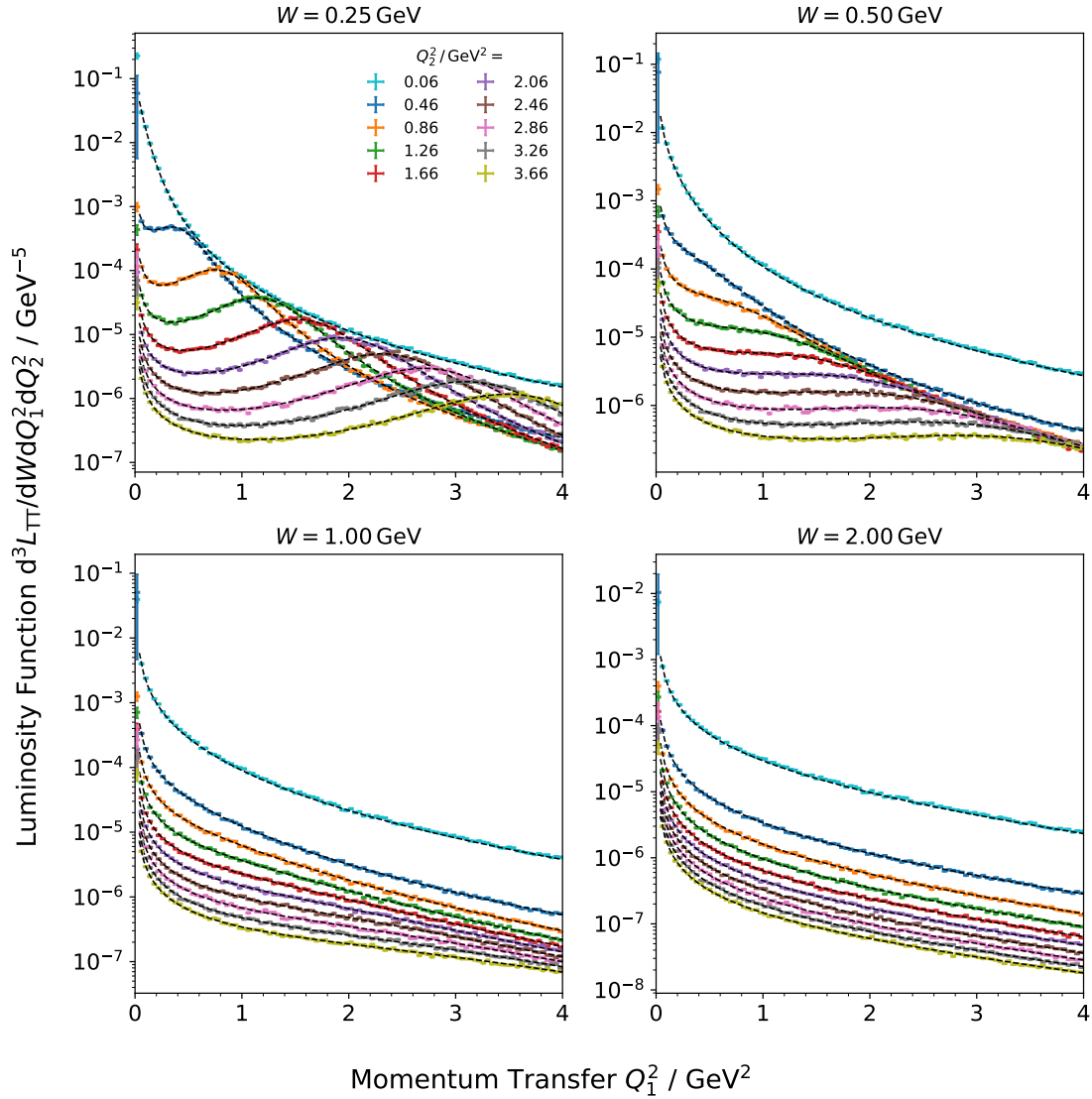


Figure 2.4: Comparison of the luminosity function of two transversely polarized photons calculated by HADROTOPS (data points) and analytical results (black dashed lines). The panels present different hadronic masses W , the different colors show different values of Q_2^2 . All functions are displayed as function of Q_1^2 and are determined at $\sqrt{s} = 4$ GeV.

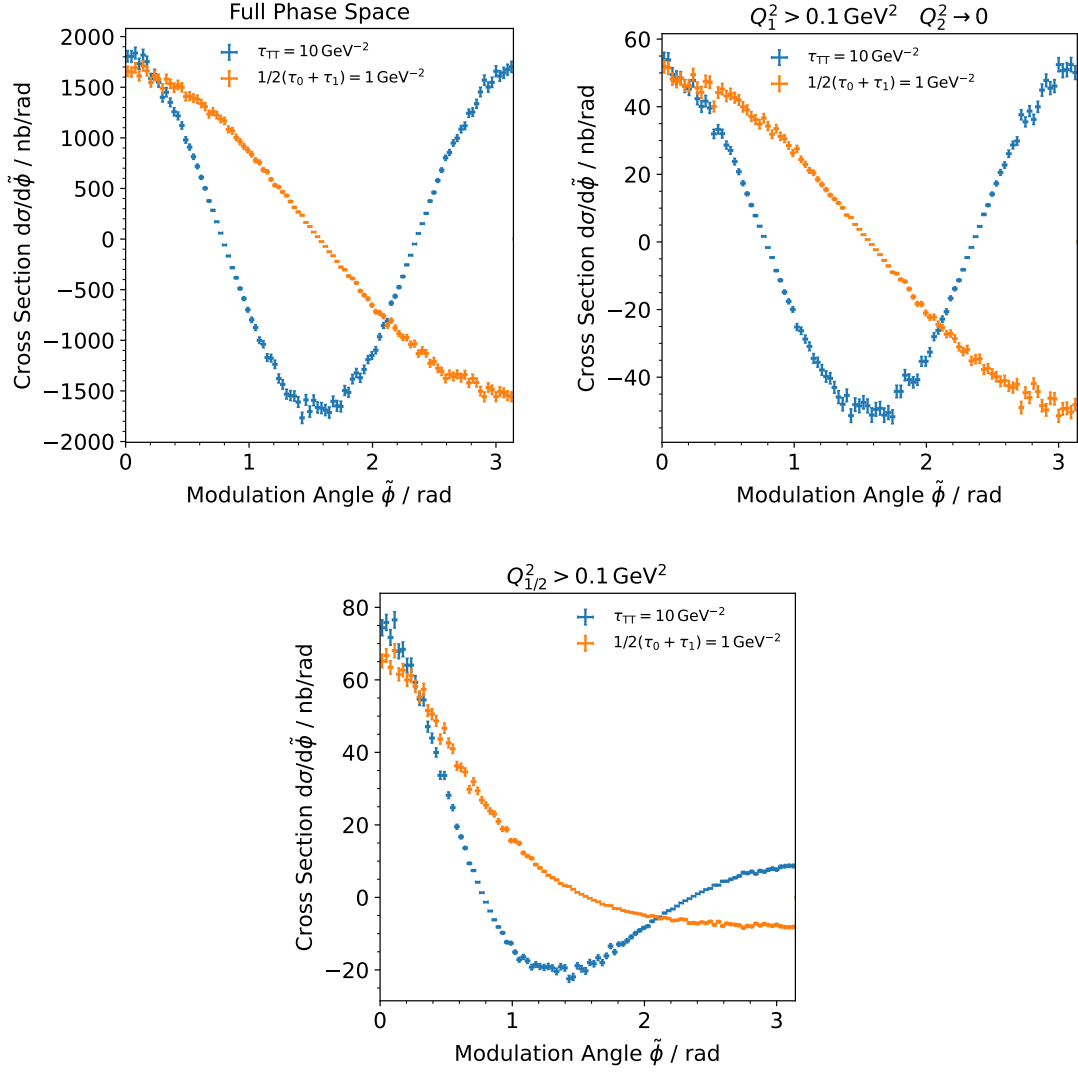


Figure 2.5: Differential cross section as function of the modulation angle $\tilde{\phi}$. The left panel shows the cross section when only τ_{TT} and $1/2(\tau_0 + \tau_1)$ are set to non-zero values. The right panel shows the same in a single-tagged configuration, the bottom panel in a double-tagged setup. All plots are produced at $\sqrt{s} = 4 \text{ GeV}$ for the production of a stable particle with mass $W = 1 \text{ GeV}$, with $\tau_{LT} = 1 \text{ GeV}^{-2}$ and (for better visibility) $\tau_{TT} = 10 \text{ GeV}^{-2}$.

2.7.2 | Fixed Two-Photon Cross Sections and Luminosity Functions

Calculating the $e^+e^- \rightarrow e^+e^- \mathcal{M}$ cross section at fixed two-photon cross sections not only enables the computation of the luminosity functions, but also allows the study of the behavior of the cross sections with respect to the modulation angles $\tilde{\phi}$, $\tilde{\phi}_1$, and $\tilde{\phi}_2$. Experimentally, examining the cross section dependence on these modulation angles provides the opportunity to extract distinct responses from the cross section. These responses are typically ignored due to the usual integration over the modulation angles, yet they still contain valuable information that has, so far, not been accessed in any experimental measurements. This is primarily because measuring $\tilde{\phi}$ requires tagging both final-state leptons, which leads to a small cross section and, consequently, limited statistics.

An additional complication arises, as illustrated in Fig. 2.5, where the $\tilde{\phi}$ -dependent contributions to the cross section are plotted as a function of this angle. When integrating over all virtualities and in a single-tag configuration, the cross sections exhibit the expected $\cos \tilde{\phi}$ and $\cos 2\tilde{\phi}$ behavior, but they are heavily distorted in the double-tag case. This distortion results from the complex dependence of the modulation angle on all Lorentz invariants, as described in Ref. [271]. Therefore, to exploit the dependence of the cross section on the modulation angles, it is insufficient to merely fit the functional dependence of these angles, as given in Eqs. (1.18) and (1.27), to the experimentally extracted differential cross section. Instead, one must fit the full kinematic dependence, as computed by HADROTOPS, to the experimental data.

2.7.3 | Cross Sections of Two-Hadron Final States

Figure 2.6 presents the two-pion invariant-mass distributions and the positron momentum-transfer distributions generated by HADROTOPS, simulating the full available phase space at $\sqrt{s} = 4, \text{GeV}$. The strong decrease of the cross section with increasing masses is clearly visible, as is the rapid drop of the cross section with increasing Q^2 . The limited coverage of the Q^2 and W dependencies for the $\pi\pi$ and $\pi\eta$ final states arising from the theory input is also evident. In contrast, the modeling of the Q^2 dependence for other states is simpler but less reliable when $Q_1^2, Q_2^2 > 0$, allowing coverage of larger momentum transfers.

The fluctuating behavior of the K^+K^- , $K_S K_S$, and $\eta\eta$ final states can only be partially attributed to intermediate resonances. It is primarily caused by the limited statistics of the experimental input, particularly evident for the K^+K^- final state. Compared to the neutral-pion counterpart, the charged-pion cross section is roughly twice as large in the $f_2(1270)$ mass region, as expected from isospin symmetry. However, at lower energies, the charged-pion contribution dominates the neutral-pion contribution by more than an order of magnitude due to the Born contribution. A similar effect is found for the charged and neutral kaons.

The helicity angle distributions, shown in Fig. 2.7, illustrate the distinct angular behaviors of the final states, which depend on the spin and helicity of the produced intermediate state. The $\pi^+\pi^-$ final state exhibits a maximum at $\cos \theta^* = \pm 1$, while all other channels reach their maximum at $\cos \theta^* = 0$. This behavior is again attributed to the Born contributions present in the charged modes.

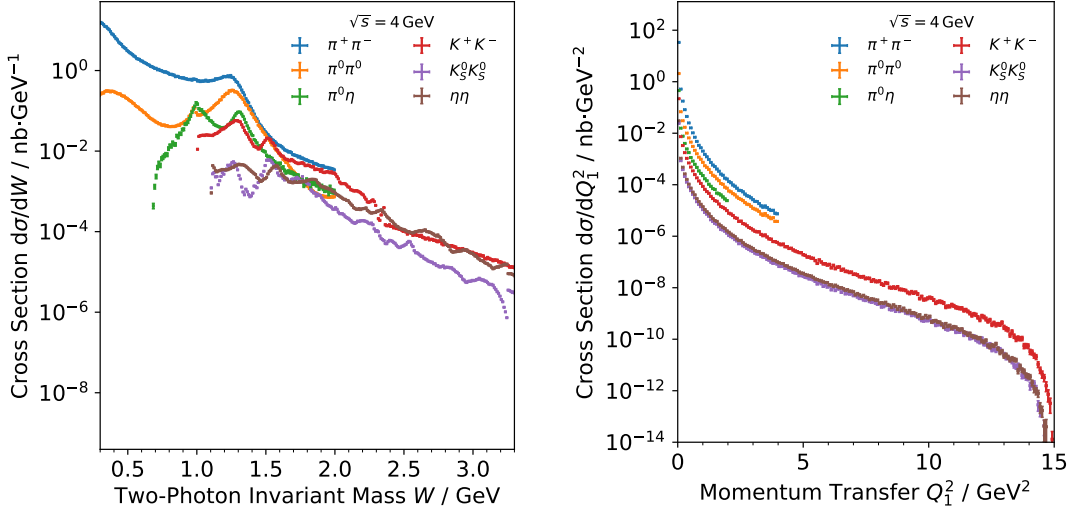


Figure 2.6: Two-Photon invariant mass distribution (left) and momentum transfer Q_1^2 distribution (right) for the simulation of two-hadron final states with HADROTOPS. All events are produced at $\sqrt{s} = 4$ GeV and cover the W and Q^2 ranges as described in Secs. 2.4.3 and 2.4.4. For the K^+K^- , $K_S^0K_S^0$, and $\eta\eta$ two-photon cross sections, the Q^2 dependence is described with a vector-pole model with $m_V = 775$ MeV.

2.7.4 | Cross Sections of the $e^+e^- \rightarrow e^+e^-\pi^0\pi^0$ Process

The author of the currently unpublished EKHARA3.2 generator, Henryk Czyż, has kindly provided access to the code, allowing a comparison between the two generators for the process $e^+e^- \rightarrow e^+e^-\pi^0\pi^0$. A comparison for the charged pion process is not feasible, as EKHARA3.2 includes pion-pair production from a virtual photon radiated in a Bhabha scattering event.

A comparison between HADROTOPS and EKHARA3.2 at $\sqrt{s} = 4$ GeV is shown in Fig. 2.8, as a function of the kinematic variables W , Q_1^2 , $\cos\theta^*$, and $\tilde{\phi}_1$. For HADROTOPS, two separate samples are generated using the cross section formulas for the inclusive process (Eq. (1.18)) and the exclusive process (Eq. (1.27)). The two resulting HADROTOPS distributions are in excellent agreement across all variables except for the modulation angle $\tilde{\phi}_1$, as expected, since this dependence enters only through the exclusive process formula, which exhibits a strong modulation.

Overall, the results are in good agreement, although minor differences remain. While both generators use the same theoretical input, these deviations originate from the implementations of the differential cross section. Unlike HADROTOPS, which derives the cross section from the analytic expressions in Eqs. (1.18) and (1.27) using the two-photon cross sections and response functions, EKHARA3.2 evaluates the $e^+e^- \rightarrow e^+e^-\pi^0\pi^0$ cross section directly from the Lorentz-covariant formulation of the $e^+e^- \rightarrow e^+e^-\pi^0\pi^0$ matrix

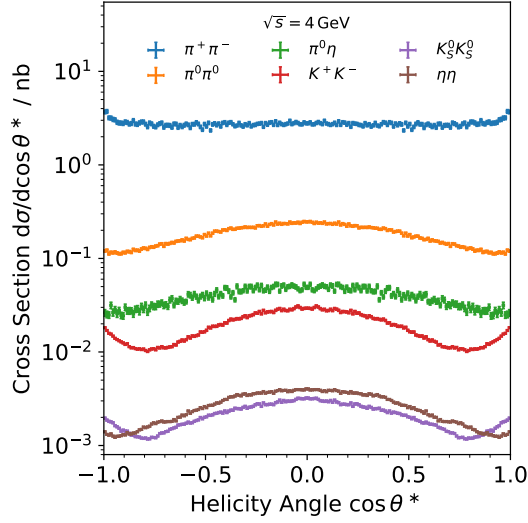


Figure 2.7: Helicity angle $\cos\theta^*$ distributions for the simulation of two-hadron final states with HADROTOPS. All events are produced at $\sqrt{s} = 4$ GeV and include the W and Q^2 ranges as described in Secs. 2.4.3 and 2.4.4 and shown in Fig. 2.6.

element.

Consequently, EKHARA3.2 uses the helicity amplitudes as direct input, whereas HADROTOPS requires interpolation of the combined helicity amplitudes and kinematic factors entering the two-photon cross sections and responses. EKHARA3.2, by contrast, interpolates only the helicity amplitudes and evaluates all remaining kinematic factors at the exact phase-space point of the event. With an infinitely dense grid for the numerical theory input, both generators are expected to yield identical results.

2.7.5 | Cross Sections of the $e^+e^- \rightarrow e^+e^- f_1(1285) \rightarrow e^+e^- \eta\pi^+\pi^-$ Process

Figure 2.9 shows example plots of the HADROTOPS prediction for the cross section of two-photon production of the $f_1(1285)$ and its subsequent decay into $\eta\pi^+\pi^-$. The mass-dependent cross section is found to be orders of magnitude smaller than that of the two-pion modes and is comparable in size to the $K\bar{K}$ and $\eta\eta$ cross sections shown in Fig. 2.6. Since the production of a spin-1 state is forbidden at $Q_1^2 = Q_2^2 = 0$, a smaller cross section is expected. The double-transversely polarized cross section decreases significantly more slowly than the cross section for one transverse and one longitudinal photon. Because the contribution involving one longitudinal photon is considerably larger, it dominates the total cross section at $\sqrt{s} = 4$ GeV, representative of a typical BESIII scenario.

Due to the faster decrease of the TT contribution, a BESIII measurement is expected to be more sensitive to the LT and TL contributions, whereas measurements at BaBar or

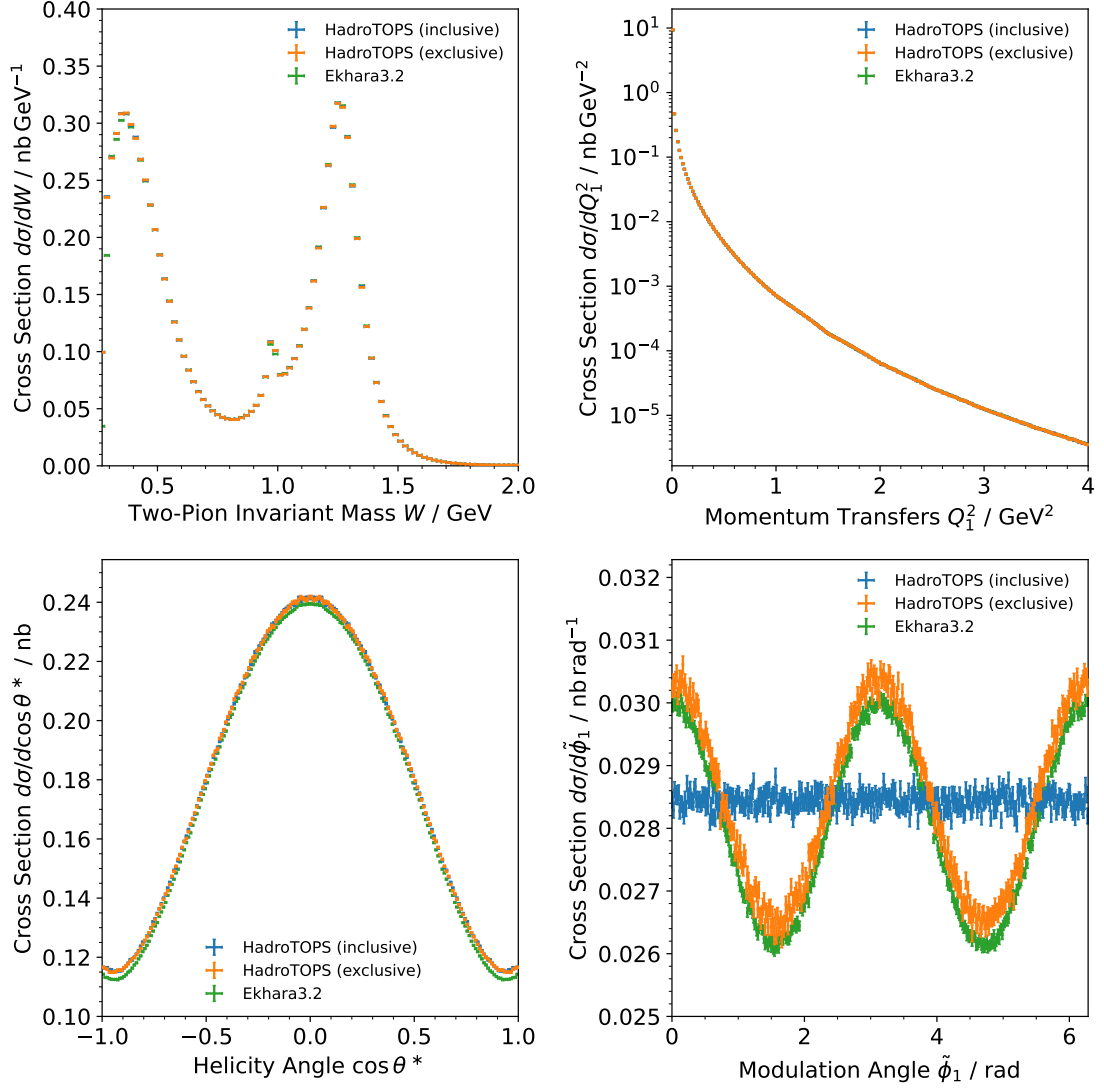


Figure 2.8: Comparison of the predicted cross sections for the process $e^+e^- \rightarrow e^+e^-\pi^0\pi^0$ calculated by HADROTOPS, using the inclusive (blue) and exclusive (orange) cross section formulas, and with EKHARA3.2 (green). The distributions are shown as functions of the two-pion invariant mass (upper left), positron momentum transfer (upper right), polar angle of one of the pions in the two-photon c.m. frame (lower left), and the modulation angle $\tilde{\phi}_1$ (lower right). The center-of-mass energy is fixed at $\sqrt{s} = 4$ GeV. The mass range is limited to $W = 0.27 - 2$ GeV, and the momentum transfers to $Q_{1/2}^2 = 0 - 4$ GeV².

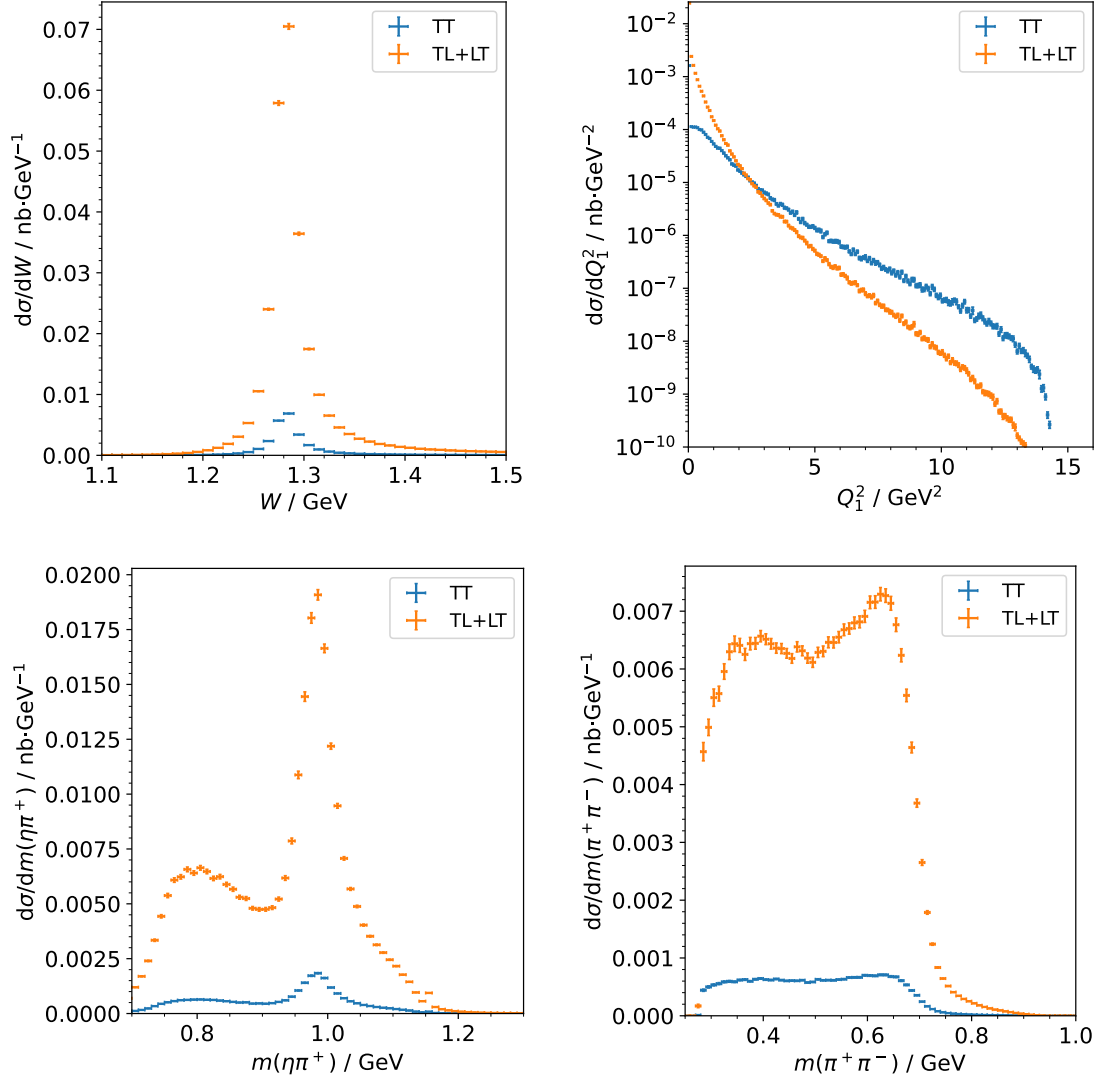


Figure 2.9: Differential cross sections of the process $e^+e^- \rightarrow e^+e^- f_1(1285) \rightarrow e^+e^- \eta \pi^+ \pi^-$ as a function of the two-photon invariant mass W (top left), the positron momentum transfer Q_1^2 (top right), the $\eta\pi^+$ invariant mass (bottom left), and the $\pi^+\pi^-$ invariant mass (bottom right), shown for two transversely polarized photons (blue) and for one transverse and one longitudinal photon (orange). All parameters follow Ref. [286]. The center-of-mass energy is $\sqrt{s} = 4 \text{ GeV}$.

Belle(II), with higher center-of-mass energies and consequently larger momentum transfers, will be more sensitive to TT polarizations. In the $\eta\pi^+$ mass spectrum, the $a_0(980)$ peak from the $f_1(1285) \rightarrow a_0(980)^\pm\pi^\mp$ decay and its kinematic reflection is clearly visible. There is no clear mass separation between the $a_0(980)^\pm\pi^\mp$ and $f_0(500)\eta$ final states. Consequently, a full partial-wave is necessary for future measurements of this channel, as already demonstrated in Ref. [285]. In the $\pi^+\pi^-$ mass spectrum, a pronounced destructive-interference pattern is observed. This interference can be controlled via the respective phase angle, which is set to $\phi = 180^\circ$ in this case; the destructive interference vanishes at $\phi = 0^\circ$.

2.8 | Summary of the Monte Carlo Event Generator

The HADROTURNS code provides simulations of the processes $e^+e^- \rightarrow e^+e^-\pi\pi$ and $e^+e^- \rightarrow e^+e^-\pi^0\eta$, using dispersive-theory input for the underlying two-photon dynamics. In addition, it supports the simulation of the reactions $e^+e^- \rightarrow e^+e^-K^+K^-$, $e^+e^- \rightarrow e^+e^-K_S K_S$, and $e^+e^- \rightarrow e^+e^-\eta\eta$ in untagged kinematics, based on available experimental data. For generic hadronic two-body final states, the framework allows straightforward updates by simply replacing the corresponding input files.

Furthermore, using a phenomenological model, HADROTURNS can simulate the two-photon production and decay of the $f_1(1285)$ resonance through the $a_0^\pm\pi^\mp$ and $f_0(500)\eta$ intermediate channels into $\eta\pi^+\pi^-$. The code also provides luminosity-function calculations and generates Monte Carlo samples based on phase-space and luminosity-function distributions, making it directly compatible with standard partial-wave analysis tools.

Throughout this work, the generator will be used to simulate the $e^+e^- \rightarrow e^+e^-\pi^0\pi^0$ process for background estimation and efficiency corrections, as well as the $e^+e^- \rightarrow e^+e^-\pi^0\eta$ process for background studies.

The HADROTURNS generator, together with the dispersive analysis and the theoretical work by Igor Danilkin, Xiu-Lei Ren, and Marc Vanderhaeghen, has been submitted for publication. The preprint is publicly available (Ref. [256]) and attached to this thesis.

3 | The BESIII Experiment

Contents

3.1	Beijing Electron Positron Collider II	63
3.2	Beijing Spectrometer III	63
3.2.1	Main Drift Chamber	64
3.2.2	Time-of-Flight System	65
3.2.3	Electromagnetic Calorimeter	66
3.2.4	Superconducting Solenoid	66
3.2.5	Muon Chambers	67
3.3	Trigger and Data Acquisition	67
3.4	The BESIII Offline Software System	67
3.5	Further Upgrades and Modifications	68

3.1 | Beijing Electron Positron Collider II

The Beijing Electron Positron Collider II (BEPC-II), situated at the Institute of High Energy Physics (IHEP) of the Chinese Academy of Sciences in Beijing, China, is an electron–positron collider operating in the τ –charm region. It incorporates a linear accelerator capable of propelling electrons and positrons to an energy level of 2.5 GeV. These particles are subsequently injected into two storage rings, each with a circumference of 237.5 m. At the interaction point, the beams cross with a total crossing angle of 22 milliradians, with a variable center-of-mass energy ranging from 2.0 GeV to 5.0 GeV. The designed luminosity of BEPCII is $\mathcal{L} = 1.0 \times 10^{33} \text{ cm}^{-2}\text{s}^{-1}$ at $\sqrt{s} = 3.77 \text{ GeV}$ [289]. Remarkably, this design luminosity has been surpassed by 10 % [290]. A schematic representation of the magnetic lattice of the storage rings is depicted in Fig. 3.1.

3.2 | Beijing Spectrometer III

The Beijing Spectrometer III (BESIII) is a cylindrical, multipurpose detector located at the interaction point of the BEPC-II accelerator complex. It comprises several essential components: a wire chamber for tracking charged particles, a time-of-flight system for particle

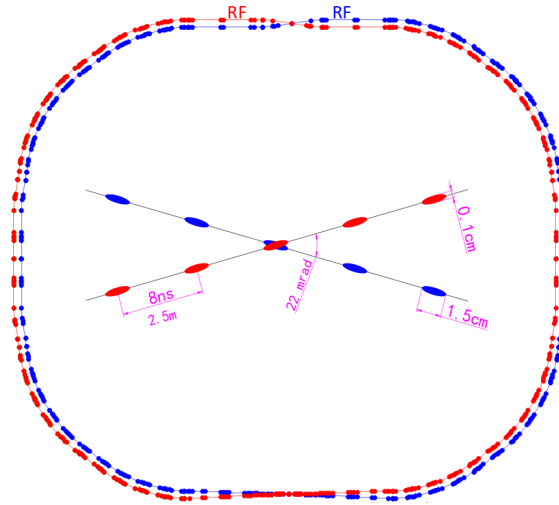


Figure 3.1: Schematic drawing of the storage ring. The diagram illustrates the floor plan of the magnetic lattice elements. The central cross indicates the crossing angle and beam geometry at the interaction point. Adapted from Ref. [291].

identification, an electromagnetic calorimeter for measuring the energy of electromagnetic showers, a superconducting solenoid to provide the magnetic field for tracking, and muon chambers for muon identification, located in the flux return yoke of the magnet. The detector covers 93 % of the full solid angle. A technical drawing of the BESIII detector system is presented in Fig. 3.2. The subsequent sections of this chapter will provide a comprehensive overview of the detector, beginning with the innermost subsystem and progressing outward from the interaction point.

3.2.1 | Main Drift Chamber

The main drift chamber (MDC) is the primary instrument for measuring the momentum of charged particles and is the innermost subsystem of BESIII. It achieves high-precision momentum determination by tracking the trajectories of charged particles within the magnetic field generated by the superconducting solenoid. The momentum is derived from the curvature of the particle tracks and the magnetic field strength. In addition to momentum, the MDC measures the specific energy loss dE/dx of particles traversing the chamber. This energy loss, which depends on the particle's velocity as described by the Bethe-Bloch formula [293, 294], when combined with the momentum measurement, contributes to particle identification.

A GEANT4 polygon representing the MDC, the inner time-of-flight system, and the inner drift chamber walls is depicted in Fig. 3.3a. In Fig. 3.2, the MDC is highlighted in green. The wires are strung between the inner drift chamber walls, some of them in a stereo configuration, enabling the three-dimensional reconstruction of particle trajectories and momentum. The MDC is divided into inner and outer regions. The eight innermost

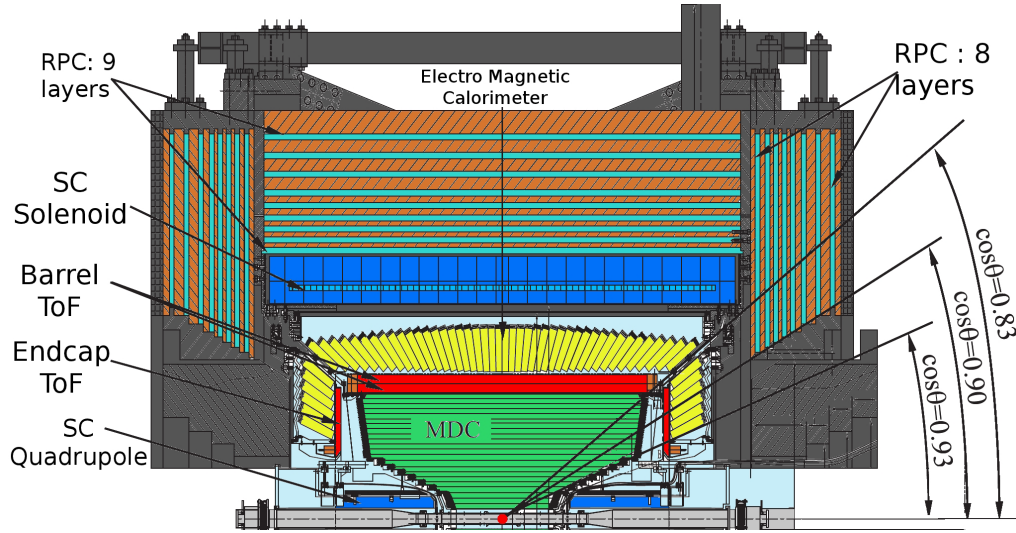


Figure 3.2: Schematic illustration of the upper half of the BESIII detector, colored for illustration purposes. Adapted from Ref. [292].

layers of wires are strung in a stereo configuration, while in the outer region, only 16 out of 35 layers adopt this configuration. In total, the chamber's 6796 wires enable the measurement of particle momentum across all polar angles satisfying $|\cos\theta| < 0.93$. Filled with a helium-based gas mixture (60% He / 40% C₃H₈), the chamber's gas minimizes multiple scattering effects. The resolution for charged-particle momentum at 1 GeV is 0.5%, and the dE/dx resolution for electrons from Bhabha scattering is 6% [292, 295].

3.2.2 | Time-of-Flight System

The Time-of-Flight system (TOF) is located outside of the Main Drift Chamber (MDC) and composed of two layers of plastic scintillators in the barrel region and one layer in each end-cap. Within the barrel TOF, each layer features 88 plastic scintillator bars, each 5 cm thick, designed with a trapezoidal cross section. The end-cap TOF is composed of 48 fan-shaped counters. Instrumentation of the MDC requires a small gap in the between the barrel and end-cap parts of the TOF system. A GEANT4 rendition of the TOF system is depicted in Fig. 3.3b, in the technical drawing of the detector system (Fig. 3.2) it is highlighted in red. The time resolution of the system is approximately 100 ps in the end-caps and 68 ps in the barrel region, thereby providing information for the effective differentiation of kaons from pions [292]. Furthermore, the end-cap TOF of BESIII has undergone recent upgrades to enhance time resolution. The plastic scintillators have been replaced with 36 overlapping multi-gap resistive plate chambers (MRPC), achieving an improved time resolution of 60 ps [296, 297]. The TOF system covers angles ranging from $|\cos\theta| < 0.83$ in the barrel region to $0.85 < |\cos\theta| < 0.95$ in the end caps. Crucially, the TOF signal serves as the time reference for the precise reconstruction of charged tracks [292].

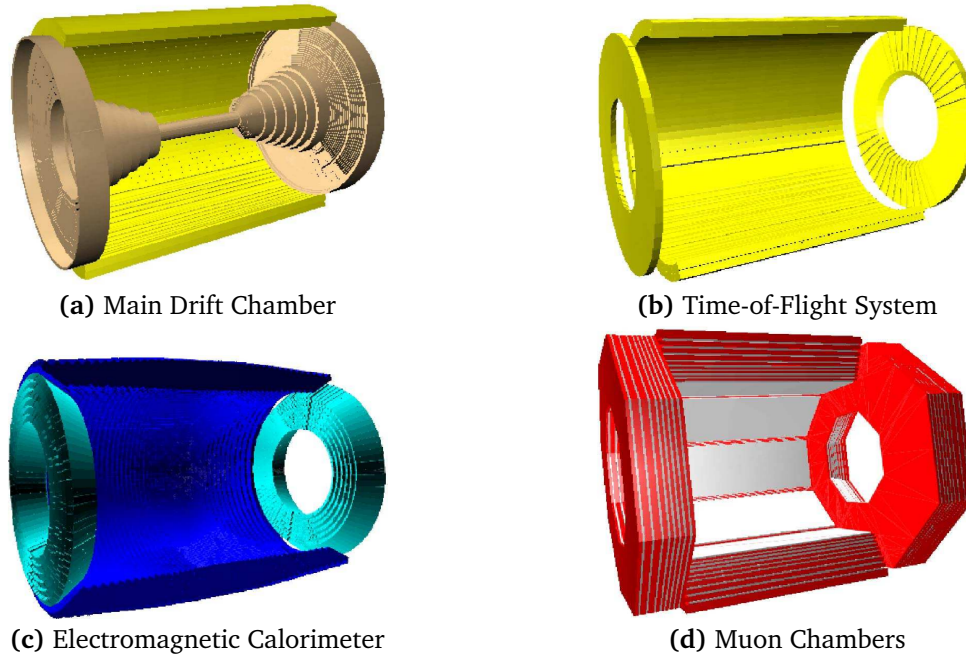


Figure 3.3: GEANT4 models of the main drift chamber (upper left), the time-of-flight system (upper right), the electromagnetic calorimeter (lower left), and the muon chambers (lower right). The model of the MDC includes the chamber wall, the end plates, and the TOF system in the barrel region of the detector. Adapted from Ref. [295].

3.2.3 | Electromagnetic Calorimeter

The electromagnetic calorimeter (EMC) is positioned between the TOF system and the solenoid, as illustrated in Fig. 3.2, where it is colored in yellow. Furthermore, a GEANT4 polygon of the EMC is provided in Fig. 3.3c. Comprising an arrangement of 6240 CsI(Tl) crystals, the calorimeter offers good precision in measuring the energy and position of electromagnetic showers with energies exceeding 20 MeV. Like the TOF system, the EMC is split into end-cap and barrel parts covering different polar angle ranges, specifically $|\cos \theta| \leq 0.83$ and $0.85 \leq |\cos \theta| \leq 0.94$. Notably, the energy resolution is given by $\sigma_E/E = 2.5\% \cdot \sqrt{E[\text{GeV}]}$. Additionally, for 1 GeV showers, the EMC has a position resolution of about 0.6 cm [292, 295].

3.2.4 | Superconducting Solenoid

The magnetic field necessary for charged track reconstruction with the MDC is provided by a superconducting solenoid. It is located outside the EMC. In Fig. 3.2 it is colored blue. The 848 turns of the coil are cooled to 4 K to provide the 1 T magnetic field [292, 295].

3.2.5 | Muon Chambers

The outermost detectors of BESIII are the muon chambers (MUC), situated within the flux return yoke of the electromagnetic solenoid. Comprising nine layers of resistive plate chambers (RPC) in the barrel region and eight layers in each end-cap, their primary function is the precise identification of charged particles traversing the EMC and the solenoid. Given that these particles predominantly consist of muons, with pions present to a lesser extent, the MUC data serves a critical role in separating muon tracks from other particle trajectories, particularly distinguishing between pions and muons. Encased within steel plates and positioned outside of both the solenoid and all other detector systems, the MUC requires a minimum momentum of approximately 0.4 GeV for muons and pions to penetrate the initial layers effectively. Utilizing the penetration depth within the MUC, in combination with the particles' momentum as determined by the MDC, enables a reliable differentiation between these two particle types [292, 295]. In Fig. 3.2, it is highlighted in cyan, Fig. 3.3d shows the GEANT4 polygon of the muon chambers.

3.3 | Trigger and Data Acquisition

The BESIII trigger and data acquisition (DAQ) system is designed for high-rate, low-dead-time operation in a challenging environment with closely spaced beam bunches and substantial background. A fully pipelined readout enables near dead-time-free performance and real-time data processing. The trigger architecture consists of a two-level system: a hardware-based trigger implemented primarily using FPGA logic, and a software-based trigger running on an online computer farm. Subdetector triggers from the TOF, MDC, and EMC are combined by global trigger logic operating synchronously [292]. The trigger conditions are configured to provide high trigger efficiency for a wide variety of physics event topologies, ranging from Bhabha events and multi-prong hadronic events to purely neutral final states [298, 299].

The DAQ system employs VME-bus-based electronics and high-speed optical links to transfer buffered subdetector data to an online computer farm, where events are assembled, reconstructed, and filtered. Multilevel buffering, parallel processing, and high-speed networking ensure efficient handling of large data volumes. The second-level event filter further suppresses background and classifies events before the data are written to permanent storage at rates of up to approximately 40 MB/s during operation at the J/ψ peak [292].

3.4 | The BESIII Offline Software System

The BESIII Offline Software System (BOSS) is the software framework that integrates all computing needs of the BESIII collaboration, including event reconstruction, simulation, and basic analysis routines. It is written in C++ and built on the GAUDI framework [300] and ROOT [274]. To ensure stability, consistent computational behavior, and reproducible

results, BOSS relies on specific versions of external libraries and is intended to be run on particular Linux distributions provided within a containerized environment.

For proper simulation, BOSS relies on the GEANT4 framework [301–303] for processing event-based (Monte Carlo) simulations. The Lorentz vectors and particle types of the final-state particles are passed to a GEANT4 model of the detector system, where their interactions with the active and passive detector materials are simulated. After applying models of the readout electronics and adding background noise, the simulation output is converted into the same file format produced by the real detector during data-taking campaigns. These files can then be processed identically by the reconstruction and analysis routines, providing high-quality event-based simulations for a wide range of physics processes.

The output of each data-taking run and simulation is then processed by a reconstruction algorithm, which combines the signals from the various subdetectors and traces them back to the original physical event. This includes track reconstruction in the MDC, after which the tracks are matched to signals in the TOF and MUC systems. By combining the results of track reconstruction with those from the EMC shower-reconstruction algorithm, signals originating from charged tracks and photon candidates can be distinguished. Afterwards, an offline calibration of all detector systems is performed to achieve the best possible resolution for key observables such as the momentum measured in the MDC, the energy deposition in the calorimeter, and other variables like the specific energy loss, flight time, penetration depth in the MUC, and many more.

Once the properties of the signals produced by different particles in each event have been reconstructed, analysis algorithms can be applied. Although the specific procedures vary depending on the analysis, they typically involve particle identification and the transformation of measured particle properties into Lorentz vectors to enable efficient physics studies. These steps may include advanced particle-identification routines that use a wide range of reconstructed observables, as well as tools such as kinematic and vertex fits to improve event reconstruction.

In this work, the event selection criteria are described in detail in Secs. 5.1 and 6.1. The results of the analysis are subsequently processed using the ROOT framework [274]. BOSS version 7.1.2 and ROOT version 6.34.04 were used for this study, and data visualizations were produced with the Python library matplotlib [304].

3.5 | Further Upgrades and Modifications

Aging effects lead to a significant degradation of performance of the inner MDC. During the accelerator shutdown in 2024, the inner MDC was replaced with a cylindrical gas electron multiplier detector (CGEM), further enabling high quality data taking. The new tracking device is constructed from three layers of GEM detectors, each made from three layers of GEM foils. It will improve tracking capabilities at high rates, aging resistance, and secondary vertex reconstruction, while maintaining the good tracking capabilities of the original MDC – ensuring high-quality momentum reconstruction [305–311].

At the east side of the detector setup, a zero-degree detectors is installed between

the beam pipes, positioned just before and after the BESIII detector setup to monitor the luminosity by detecting photons emitted at smallest angles. Unfortunately, the current design cannot be synchronized with the rest of the BESIII detector system. The Mainz group is currently working on replacing this detector to resolve the synchronization issues. With the new small-angle detectors, it will be possible not only to monitor the luminosity but also to detect photons emitted close to the beam axis, thereby improving the precision of hadronic cross section measurements using the initial state radiation technique [312].

4 | Data Sets and Simulations

Contents

4.1	Data Sets	71
4.2	Simulation of the Signal Process	71
4.3	Simulation of Other Two-Photon Processes	72
4.4	Simulation of Other Potential Background Processes	72

4.1 | Data Sets

Compared to other processes at electron–positron colliders, the total cross sections of hadronic two-photon reactions are typically small, particularly in singly- or doubly-virtual kinematics. An additional complication arises from the QED coupling factors in Eqs. 1.18 and 1.27, which must be taken into account and which depend explicitly on the center-of-mass energy of the data set in question. Consequently, combining measurements at different center-of-mass energies is not ideal, as it introduces additional systematic uncertainties. For this reason, using a single high-statistics data set at a fixed energy is strongly preferred.

The analyses presented in this work are based on a data sample corresponding to an integrated luminosity of $(20,235 \pm 80) \text{ pb}^{-1}$ collected at $\sqrt{s} = 3.773 \text{ GeV}$ [75, 313], which represents the highest-statistics data point acquired by the BESIII collaboration. The uncertainty on the integrated luminosity is dominated by systematic effects and amounts to less than 0.4%. The data were recorded in five running periods (03, 04, 15, 16, and 17). Monte Carlo samples are generated separately for each period, with the exception of the 03 and 04 data, which are combined due to their comparatively small integrated luminosities.

4.2 | Simulation of the Signal Process

The signal Monte Carlo samples are generated using the HADROTOPS event generator, described in detail in Chapter 2. It uses the dispersive theory input briefly discussed in Sec. 1.4. For each configuration, MC samples corresponding to approximately 40 times

Table 4.1: Summary of the generated Monte Carlo samples. All samples are produced without phase-space restrictions. The samples generated with EKHARA3.1 include radiative corrections, unweighting, and the triple-octet transition-form-factor model. The luminosity scaling factor (LSF) is defined as the ratio of the generated to the measured luminosity.

Round	Process	Generator	Number of Events	Cross Section / nb	LSF
03 & 04	$e^+e^-\pi^0\pi^0$	HadroTOPS	19400000	0.1659	39.83
15	$e^+e^-\pi^0\pi^0$	HadroTOPS	33100000	0.1659	39.94
16	$e^+e^-\pi^0\pi^0$	HadroTOPS	54100000	0.1659	39.97
17	$e^+e^-\pi^0\pi^0$	HadroTOPS	27800000	0.1659	39.98
03 & 04	$e^+e^-\pi^0\eta$	HadroTOPS	4141000	0.0357	39.58
15	$e^+e^-\pi^0\eta$	HadroTOPS	7140000	0.0357	40.11
16	$e^+e^-\pi^0\eta$	HadroTOPS	11424000	0.0357	39.30
17	$e^+e^-\pi^0\eta$	HadroTOPS	6000000	0.0357	40.17
03 & 04	$e^+e^-\eta$	EKHARA3.1	35000000	0.2879	41.41
15	$e^+e^-\eta$	EKHARA3.1	60000000	0.2879	41.72
16	$e^+e^-\eta$	EKHARA3.1	95200000	0.2879	40.53
17	$e^+e^-\eta$	EKHARA3.1	50160000	0.2879	41.56
03 & 04	$e^+e^-\eta'$	EKHARA3.1	32000000	0.2705	40.31
15	$e^+e^-\eta'$	EKHARA3.1	57100000	0.2705	42.25
16	$e^+e^-\eta'$	EKHARA3.1	86300000	0.2705	39.10
17	$e^+e^-\eta'$	EKHARA3.1	45200000	0.2705	39.82

the expected statistics (referred to as the luminosity scaling factor) are produced. The MC production for the signal channel is summarized, together with the other simulated samples, in Tab. 4.1.

4.3 | Simulation of Other Two-Photon Processes

The production of η and η' mesons is simulated with the EKHARA3.1 Monte Carlo event generator, which incorporates next-to-leading-order effects within the triple-octet transition-form-factor model [264–267]. The $\pi^0\eta$ final state is simulated using HADROTOPS. For each process and data-taking period, samples corresponding to approximately 40 times the expected statistics are generated.

4.4 | Simulation of Other Potential Background Processes

Other potentially relevant background processes – including Bhabha scattering, di-photon, di-muon, and di-tau production, $\psi(3770)$ decays, radiative return to the J/ψ and $\psi(2S)$

and their subsequent decays, as well as the hadronic continuum – are simulated using the corresponding samples provided by the BESIII collaboration. These samples are generated using Babayaga@NLO [314–318], KKMC [319], Phokhara [266, 320–337], and EventGen [338], and are partially tuned to reproduce physics observations at BESIII.

Typically, for each process a sample corresponding to 40 times the luminosity of the data set is produced, and the generated events cover the full phase space. In the case of Bhabha scattering, however, the strong increase of the cross section towards small angles and the generally large cross section restricts the size and phase-space coverage of the simulation. The generated sample includes only events in which both leptons are scattered at angles greater than 20° , and its effective integrated luminosity is limited to 0.25 times that of the data. For $\psi(3770) \rightarrow D^0 \bar{D}^0$ decays, the sample size is increased to 80 times the luminosity of the data set.

5 | Study of the $\gamma\gamma^* \rightarrow \pi^0\pi^0$ Cross Section and Measurement of Light Meson Transition Form Factors

Contents

5.1	Event Selection and Background Suppression	76
5.1.1	Good Charged Track Selection	76
5.1.2	Particle Identification	77
5.1.3	Photon Candidate Selection	79
5.1.4	Kinematic Fitting	81
5.1.5	Selection of Single-Virtual Events	81
5.1.6	Three Constraint Kinematic Fit	85
5.1.7	Suppression of Two-Photon Backgrounds	86
5.1.8	Total Event Yield	89
5.2	Background Subtraction	89
5.3	Reconstruction Efficiency	93
5.4	Determination of the Two-Photon Luminosity Function	98
5.5	Extraction of the Effective Two-Photon Production Cross Section	103
5.6	Study of Systematic Uncertainties	103
5.6.1	Integrated Luminosity	104
5.6.2	Electron/Positron Detection Efficiency and Particle Identification	104
5.6.3	Pion Detection Efficiency	105
5.6.4	Analysis Constraints	105
5.6.5	Fit of the χ_{3C}^2 Spectra	108
5.6.6	Subtraction of the Two-Photon Background	108
5.6.7	Efficiency Correction	111
5.6.8	Two-Photon Luminosity Function	111

5.6.9	Total Systematic Uncertainty	111
5.7	Measurement of Transition Form Factors	119
5.7.1	Parametrization of the $f_0(500)$ and $f_0(980)$ Amplitudes	120
5.7.2	Parametrization of the $f_2(1270)$ Amplitude	121
5.7.3	Resolution Effects	122
5.7.4	Fit Results	123
5.8	Summary of the Study of the $\gamma\gamma^* \rightarrow \pi^0\pi^0$ Cross Section . . .	125

The theoretical prediction of the hadronic Light-by-Light scattering contribution to the muon anomalous magnetic moment is strongly constrained by precise knowledge of the two-photon couplings of tensor mesons, as discussed in Sec. 1.2.2.4. In this first analysis chapter, the cross section of the two-photon process $\gamma\gamma \rightarrow \pi^0\pi^0$ is studied as a function of the virtuality of one photon, while the second photon is kept quasi-real. The reaction is dominated by the lightest tensor resonance, $f_2(1270)$, with additional contributions from the scalar states $f_0(500)$ and $f_0(980)$. A partial wave analysis of the cross section enables the extraction of the corresponding transition form factors as function of one photon virtuality.

5.1 | Event Selection and Background Suppression

The first step of the measurement is the selection of events. Since this is a single-tagged measurement, this includes the selection and identification of an electron or a positron, and four photons, which are the decay products of two neutral pions. In the following, the procedure for event selection and background suppression is discussed.

5.1.1 | Good Charged Track Selection

Charged particle tracks are reconstructed from their entries in the MDC, which provide the information necessary to determine the particle trajectories. In the presence of a magnetic field, the particles follow helical trajectories, and the curvature and orientation of these helices enable a precise determination of the momentum vector in three dimensions.

By extrapolating the helices, the point of closest approach of a charged particle track to the interaction point can be determined. In two-photon scattering events, the leptons are expected to scatter near the interaction point, and consequently, the mesons are also produced in its vicinity. To suppress potential background contributions, only charged tracks originating from a region close to the interaction point are considered. The point of closest approach of the reconstructed helix in the radial and beam directions is shown in Fig. 5.1. A clear accumulation of events at small distances from the interaction point is observed, while the sum of all Monte Carlo samples, as well as the signal Monte Carlo samples, exhibit an increase in intensity at larger distances. The data, however, show a roughly constant distribution at larger distances, indicating the presence of beam-related background and contamination from cosmic radiation. The point of closest approach of the extrapolated helix is required to lie within a cylinder of radius $|dr| < 1$ cm and length

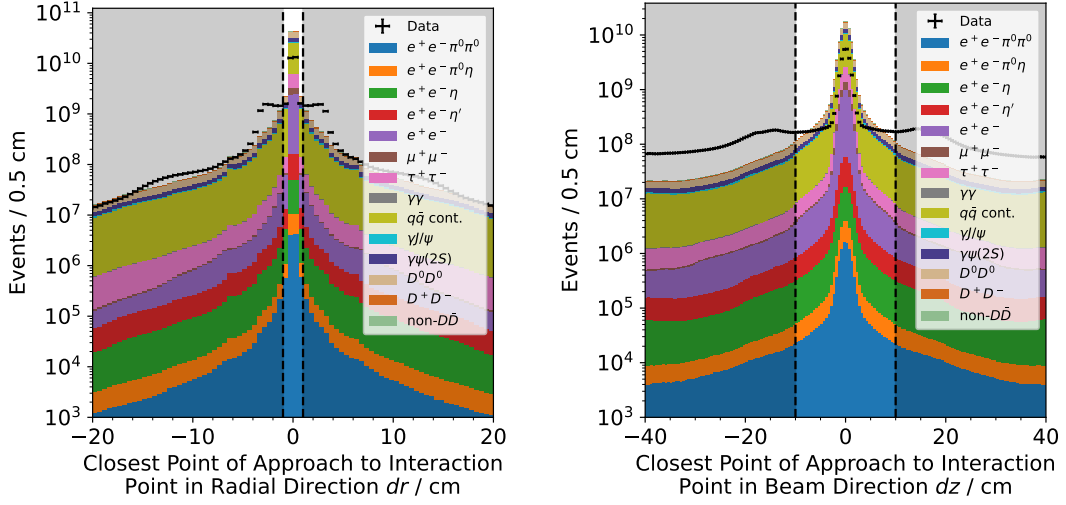


Figure 5.1: Comparison of the distributions of the distance of closest approach of the reconstructed helices of charged track candidates to the interaction point in the radial (left) and beam direction (right) of data (black points) and stacked Monte Carlo distributions. The dashed lines represent the constraint set to select good charged track candidates.

$|dz| < 10$ cm centered on the interaction point, as suggested by the data quality group of the BESIII collaboration. Tracks outside this region are discarded.

To avoid edge effects in the MDC and to ensure the selection of properly reconstructed tracks with high momentum resolution, the polar angle θ of a charged track with respect to the beam axis is required to lie within the active detector region, satisfying $|\cos \theta| < 0.93$.

The goal of this work is a single-virtual measurement of the $e^+e^- \rightarrow e^+e^-\pi^0\pi^0$ process. Since the pions predominantly decay into photons, the only charged track to be measured corresponds to one of the scattered leptons. Consequently, events are required to contain exactly one good charged track candidate.

5.1.2 | Particle Identification

To identify a charged track as an electron or positron, information from both the EMC and MDC is utilized. Electrons and positrons are expected to deposit the majority of their energy in the calorimeter. Given their negligible mass compared to the typical energy scales at BESIII, the ratio of the energy deposited in the calorimeter, E_{EMC} , to the momentum measured in the MDC, p_{MDC} , is expected to be close to unity. In contrast, muons, being significantly heavier than electrons, emit less bremsstrahlung and therefore deposit only a small fraction of their energy in the EMC. Hadrons, such as pions, kaons, and protons, predominantly interact via the strong force, producing hadronic showers that are generally broader than electromagnetic showers. Their masses are also substantially larger than

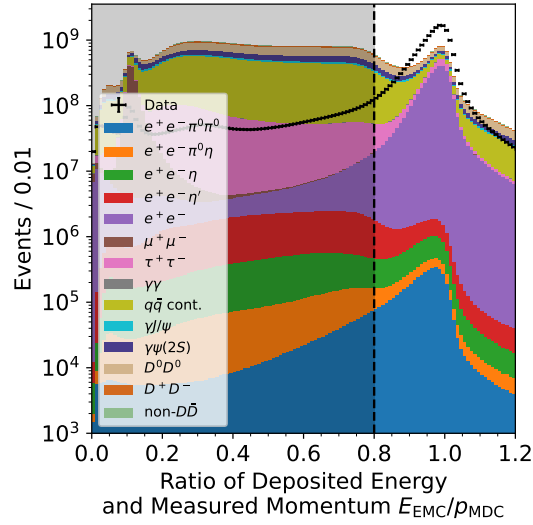


Figure 5.2: Comparison of the distributions of ratio of deposited energy in the calorimeter and measured momentum in the main drift chamber $E_{\text{EMC}}/p_{\text{MDC}}$ of charged track candidates in data (black points) and stacked Monte Carlo distributions. The black dashed line indicates the constraint to select tracks stemming from electrons or positrons.

the electron mass. As a result, the energy deposition of these particles in the calorimeter is expected to be smaller than their momentum.

Figure 5.2 shows the distribution of $E_{\text{EMC}}/p_{\text{MDC}}$ of the data, along with the corresponding Monte Carlo simulations. A strong accumulation of events with $E_{\text{EMC}}/p_{\text{MDC}} > 0.8$ is observed for processes involving electrons and positrons in the final state, such as Bhabha scattering or the signal channel $e^+e^- \rightarrow e^+e^-\pi^0\pi^0$, and the two-photon processes $e^+e^- \rightarrow e^+e^-\pi^0\eta$, $e^+e^- \rightarrow e^+e^-\eta$, and $e^+e^- \rightarrow e^+e^-\eta'$. At smaller ratios, processes involving charged hadrons or muons dominate. Since hadrons can decay (semi-)leptonically or hadronically, some processes contribute across the full range of $E_{\text{EMC}}/p_{\text{MDC}}$ values. This is particularly true for the continuum production of heavier hadrons, which may subsequently decay into electrons; for two-photon processes producing hadrons other than π^0 , which can decay into other charged hadrons (here mostly pions); and for the radiative production of J/ψ and $\psi(2S)$, which often include leptons in their decay chains. To select events in which the charged track candidate can be identified as an electron or positron, the track is required to satisfy $E_{\text{EMC}}/p_{\text{MDC}} > 0.8$. All other events are discarded from further analysis.

5.1.3 | Photon Candidate Selection

A photon candidate is defined as an energy deposition in the EMC that is not associated with any charged track candidate reconstructed in the MDC. The EMC is divided into barrel and end-cap regions. Most QED processes, as well as machine-related background, are expected to occur at small polar angles in the end-caps, which are located closer to the beam direction. The energy distribution of photon candidates is shown in the left panel of Fig. 5.3. A clear increase in the number of photon candidates towards lower energies is observed, as expected. Moreover, the data contain significantly more photon candidates than predicted by the Monte Carlo simulations, indicating a considerable contribution from beam-related background, pile-up events, unaccounted electronic noise, and cosmic rays, which are not fully modeled in the simulation. Therefore, imposing a constraint on the total number of photon candidates is not appropriate, and the correct combination of photons must be selected by other means.

To suppress the large number of low-energy background photons, a minimum cluster energy of 50 MeV is required for photon candidates detected in the end-cap region, while the threshold is lowered to 25 MeV for candidates in the barrel. To avoid threshold effects such as partial shower losses, the polar angle θ of photon candidates with respect to the beam axis is required to satisfy $0.86 < |\cos \theta| < 0.92$ for end-cap clusters and $|\cos \theta| < 0.8$ for those in the barrel. These constraints are consistent with the standard selection criteria recommended by the BESIII collaboration.

An additional complication in identifying photon candidates arises from the fact that they are measured solely with the calorimeter. If an energy deposition from a charged particle in the EMC is not correctly associated with its corresponding track reconstructed in the MDC, a fake photon candidate may be reconstructed. Moreover, very energetic EMC showers – such as those produced in Bhabha scattering events – can spread over a large number of crystals in the EMC. These may be reconstructed as two or more separate showers, thereby creating additional fake photon candidates.

To suppress both types of background, the angular separation between each photon candidate and the nearest charged track is studied. The corresponding distributions are shown in the right panel of Fig. 5.3. All Monte Carlo simulations, except for the Bhabha-scattering sample, show a decrease toward small separation angles, indicating that cluster splitting from high-energy electromagnetic showers can lead to misreconstructed photon candidates. To reject such reconstruction artifacts, the position of a photon shower is required to have an angular separation of at least 10° from the extrapolated helix of any charged track at the EMC surface.

The time-of-flight information from the EMC is also used to ensure a timing coincidence between charged tracks and photon candidates. The EMC signal is required to fall within a time window of 700 ns relative to the timing of the charged track.

Neutral pions are reconstructed via their decay into two photons. Since additional photon candidates may originate from noise, beam-related background, or other sources, each event is required to contain at least four good photon candidates. If six or more photon candidates are present in an event, an additional check is performed to determine

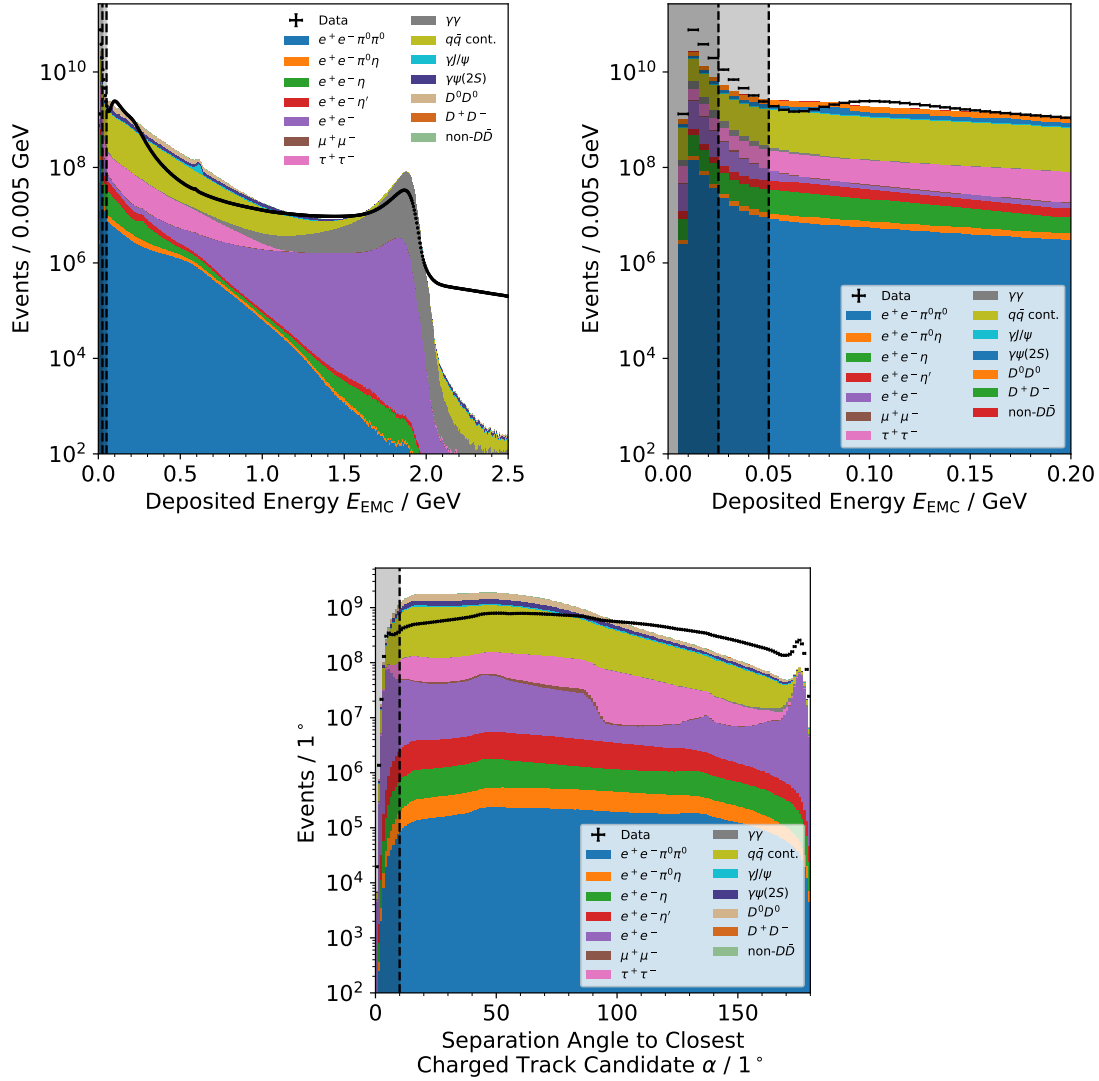


Figure 5.3: Comparison of the distributions of deposited energy in the calorimeter by photon candidates (top left), energy in the calorimeter by photon candidates in the cut-off region (top right), and separation angle between photon candidates and closest charged track (bottom) of data (black points) and stacked Monte Carlo distributions. The black dashed lines displayed in the top panels indicate the energy constraints applied to photon candidates in the barrel and end-cap region of the calorimeter. The dashed line in the bottom panel shows the constraint on the separation angle.

whether an additional π^0 candidate can be formed. If any additional pair of photons not used in the primary $\pi^0\pi^0$ reconstruction satisfies $0.11 \text{ GeV} \leq m(\gamma\gamma) \leq 0.16 \text{ GeV}$, the event is discarded from further analysis.

5.1.4 | Kinematic Fitting

So far, the event selection requires the presence of exactly one good charged track candidate, identified as either an electron or positron, and at least four good photon candidates. To select the most probable combination of four photons consistent with the process $e^+e^- \rightarrow e^+e^-\pi^0\pi^0 \rightarrow e^+e^-4\gamma$, a kinematic fit is performed.

In the first step, the kinematic fit is performed under the hypothesis that one of the scattered leptons remains undetected, while the four photon candidates and the charged track candidate correspond to the remaining final state particles. This results in a one-constraint (1C) fit, where the single constraint is the mass of the missing lepton, which is reconstructed using energy and momentum conservation.

To reduce computation time and suppress background, additional preselection criteria are applied. Specifically, the invariant masses of the two photon pairs formed from the four tested photons (prior to the fit) are required to lie within the range $0.05 \text{ GeV} < m(\gamma\gamma) < 0.3 \text{ GeV}$. This mass window covers the π^0 mass region while being sufficiently broad to account for detector resolution effects and reject background at large and small two-photon invariant masses. These two photon pairs are considered π^0 candidates. The relatively wide mass window is chosen to facilitate a data-driven background subtraction at a later stage. The lower bound of the mass requirement effectively suppresses background from low-energy photons, which typically produce very small invariant masses.

The fit is required to converge with a χ^2 value smaller than 200. If multiple photon combinations satisfy this condition, the combination yielding the smallest χ^2 is selected.

In a second kinematic fit, two additional constraints are introduced, resulting in a three-constraint (3C) kinematic fit. The two photon pairs are required to have invariant masses equal to the nominal neutral pion mass, $m_{\pi^0} = 134.9768 \text{ MeV}$ [275]. At this stage, convergence of this fit is not required. The fit results are used to improve the precision of the reconstructed observables. Requiring the fit to converge would enforce both photon pairs to have invariant masses fixed to the pion mass, which would preclude a data-driven background subtraction based on the two-photon invariant mass distributions. Unless stated otherwise, all observables are calculated from the final-state four-vectors obtained from the three-constraint kinematic fit.

5.1.5 | Selection of Single-Virtual Events

The goal of this analysis is to investigate the single-virtual production of neutral-pion pairs. Events must be selected such that the momentum transfer of the undetected lepton remains close to zero. In previous single-tag measurements (see, for example, Refs. [171, 173, 200, 288]), the momentum transfer was constrained either by limiting the scattering angle of the missing momentum to small values – ensuring that the momentum transfer, given by $Q_i^2 = -(p_i - p'_i)^2 \approx 4E_i E'_i \sin^2 \frac{\theta_i}{2}$, remains small – or by restricting the transverse

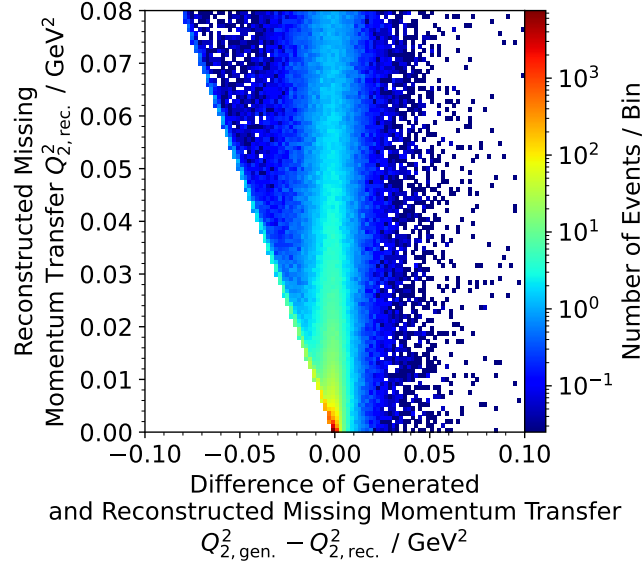


Figure 5.4: Comparison of the signal Monte Carlo distribution of the difference between generated and reconstructed missing momentum transfer as a function of the reconstructed missing momentum transfer.

momentum of the detected system. The latter approach, through energy-momentum conservation, likewise confines the missing momentum vector to small angles, thereby reducing the photon virtuality.

A direct constraint on the missing momentum transfer has not been applied in previous measurements (for example [288]), due to the limited resolution on this observable. However, this approach can introduce certain drawbacks. Inaccuracies in the determination of the missing particle’s four-momentum can result in a non-negligible residual virtuality, yielding quasi-single-virtual events rather than truly single-virtual ones. The kinematic fit is expected to improve the precision of the missing momentum transfer determination. Therefore, an essential first step of this analysis is to quantify the resolution effects on this quantity using signal Monte Carlo simulations.

Figure 5.4 shows the difference between reconstructed and generated values of the missing momentum transfer as a function of the reconstructed missing momentum transfer in the region where it is close to zero. A clear accumulation of events at $|Q_{2,gen.}^2 - Q_{2,rec.}^2| \lesssim 0.05 \text{ GeV}^2$ is observed across all values of $Q_{2,rec.}^2$. This indicates that the kinematic fit reconstructs the missing momentum transfer with an accuracy better than this threshold.

A second prominent feature is the sharp edge along $Q_{2,gen.}^2 \approx 0$, reflecting the smearing of events generated at minimal momentum transfer – where the cross section is largest and which represents the region of primary interest – towards higher reconstructed values. This behavior is expected, as the momentum transfer must always be positive, making upward smearing the only possible effect.

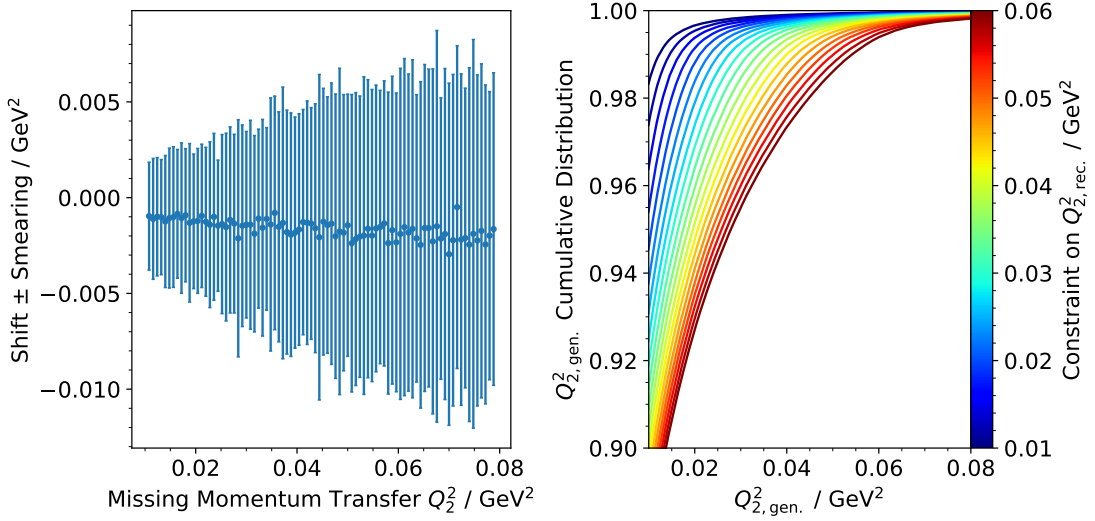


Figure 5.5: Results of the fits to the smearing matrix of the missing momentum transfer as function of the reconstructed value of Q_2^2 (left panel). The central values represent the obtained mean of the Gaussian curves, the error bars their standard deviations. Cumulative distributions of the generated missing momentum transfer $Q_{2,\text{gen.}}^2$ for different cuts on the reconstructed missing momentum transfer $Q_{2,\text{rec.}}^2$ (right panel).

To better estimate the uncertainty, a Gaussian function is fitted to the $Q_{2,\text{gen.}}^2 - Q_{2,\text{rec.}}^2$ distributions, together with an exponential and a first-degree polynomial background, for different ranges of reconstructed missing momentum transfer. The Gaussian component is intended to describe the central peak, determining its mean position and width considered to be the shift and smearing of this observable, while the exponential and polynomial terms account for the steep edge arising from events generated at minimal momentum transfer and other sources of contamination. The central value μ , which represents the systematic shift in the reconstruction of the missing momentum transfer, and the Gaussian width, which quantifies the smearing, are shown in the left panel of Fig. 5.5.

The shift is always observed to be negative with a dropping behavior towards larger values of $Q_{2,\text{rec.}}^2$. The absolute value of the shift remains one to two orders of magnitude smaller than $Q_{2,\text{rec.}}^2$. The smearing parameter shows an increasing trend with $Q_{2,\text{rec.}}^2$ and is about one order of magnitude smaller than the reconstructed value.

Generally, the smearing and shift of the reconstructed values can be considered sufficiently small to allow for a direct constraint on the missing lepton virtuality, even when the missing momentum transfer itself is to be studied. For a singly virtual analysis, however, the exact determination of the missing momentum transfer is not crucial, since the goal is merely to restrict it to values as small as possible. Therefore, the cumulative distributions of the generated missing momentum transfer $Q_{2,\text{gen.}}^2$ are studied for different cuts applied

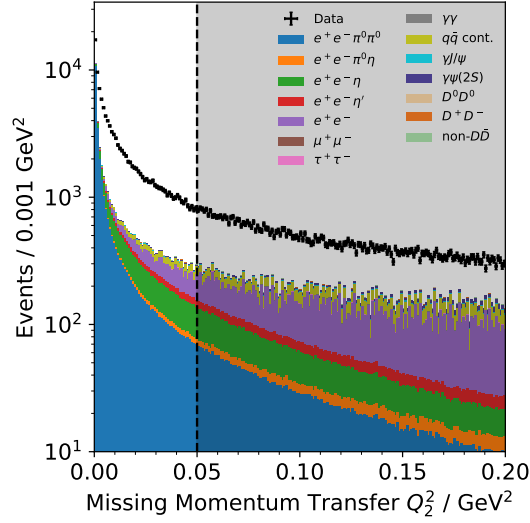


Figure 5.6: Comparison of distributions of missing momentum transfer of data (black points) and stacked Monte Carlo distributions. The black dashed line indicates the constraint set to select single-virtual events.

to $Q_{2,\text{rec.}}^2$. The corresponding curves are shown in the right panel of Fig. 5.5.

The curves rapidly approach unity and reach the 0.99 level close to the applied cut value on $Q_{2,\text{rec.}}^2$, indicating that the constraint is well controlled in the range $Q_{2,\text{gen.}}^2 \approx (0.01\text{--}0.06) \text{ GeV}^2$, and remains effective even beyond this region, with a resulting limit on $Q_{2,\text{gen.}}^2$ of similar magnitude. For comparison, a selection of singly virtual two-photon events based on a restriction of the scattering angle of the missing lepton θ_{miss} is tested. When requiring $|\cos \theta_{\text{miss}}| > 0.995$, the cumulative distribution of $Q_{2,\text{gen.}}^2$ reaches the 0.99 level only at about 0.2 GeV^2 – a significantly weaker constraint to singly virtual events. Therefore, the direct cut on $Q_{2,\text{rec.}}^2$ is adopted in this analysis.

In Fig. 5.6, data and Monte Carlo simulations are compared. The signal channel, along with the background processes arising from the two-photon production of η and η' , are peaked at small virtualities, as expected from the general kinematics of two-photon processes discussed in Sec. 1.3. The remaining Monte Carlo samples show a comparatively flat distribution. Consequently, applying a constraint to small virtualities also serves as an effective constraint to further suppress background contributions. All events with $Q_{2,\text{rec.}}^2 > 0.05 \text{ GeV}^2$ are therefore rejected. This boundary lies within the range estimated to be well controlled for ensuring a singly virtual configuration, as discussed at the beginning of this section. The cut value is later varied to evaluate the associated systematic uncertainty.

Most notably, however, a significant amount of unaccounted background remains in the spectrum even after applying the constraint. This excess likely originates from beam-related background or from an incomplete simulation of low-energy photons. It is evident that essential components of the simulation are missing, as the Bhabha scattering Monte

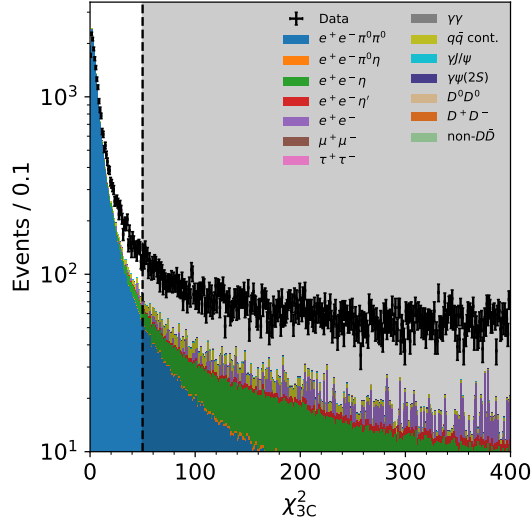


Figure 5.7: Comparison of the distributions of χ_{3C}^2 of data (black points) and stacked Monte Carlo distributions.

Carlo sample is generated in a double-tag configuration and is therefore strongly underestimated for the kinematics present in this analysis. Consequently, additional selection criteria are required to further suppress the remaining background contributions.

5.1.6 | Three Constraint Kinematic Fit

So far, no constraint has been applied to the three-constraint kinematic fit. The χ_{3C}^2 distributions for data and Monte Carlo samples are shown in Fig. 5.7. The signal-channel Monte Carlo simulation shows a clear peak at small values of χ_{3C}^2 , followed by a rapid decrease toward larger values. A similar, though less pronounced, trend is observed for the Monte Carlo samples for the $\gamma\gamma \rightarrow \eta$, $\gamma\gamma \rightarrow \eta'$, and $\gamma\gamma \rightarrow \pi^0\eta$ processes, indicating a mixture of peaking and non-peaking background contributions in these samples. A more detailed study reveals that these contributions are dominated by the $\eta \rightarrow \gamma\gamma$, $\eta \rightarrow 3\pi^0$, $\eta' \rightarrow \gamma\gamma$, and $\eta' \rightarrow \gamma\pi^0\pi^0$ decay channels, and hence some peaking behavior in the two-photon invariant mass spectrum is expected. In contrast, the Monte Carlo samples corresponding to the remaining background processes are nearly flat, showing only a slight downward slope. The unmodeled background in data also appears approximately constant, with only a gradual decrease at larger χ_{3C}^2 values.

To further suppress background contributions, all events with $\chi_{3C}^2 > 50$ are rejected. As in the case of the constraint on the missing momentum transfer, this requirement is later varied to evaluate the systematic effects of this selection on the final result. After applying the χ_{3C}^2 constraint, the dominant background contribution remaining originates from the $\gamma\gamma \rightarrow \eta$ process – besides some sources of contamination which are not modeled

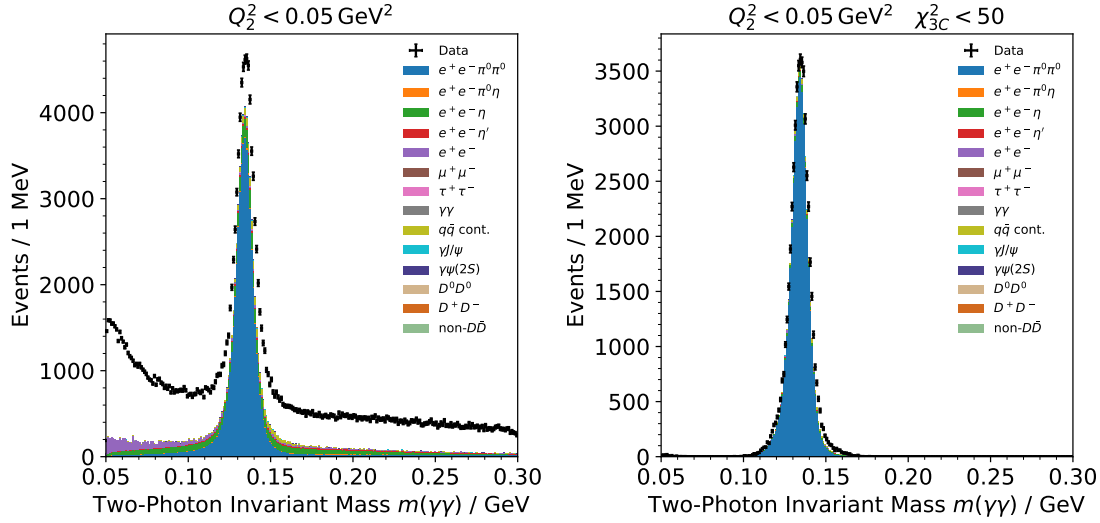


Figure 5.8: Comparison of distributions of the two-photon invariant mass calculated from the results of one-constraint kinematic fit of data (black points) and stacked Monte Carlo distributions before (left panel) and after (right panel) the constraint on χ_{3C}^2 .

by Monte Carlo.

This cut is equivalent to fixing the two-photon invariant masses to the pion mass, as illustrated in Fig. 5.8, which shows the two-photon invariant masses calculated from the results of the one-constraint kinematic fit before and after applying the constraint on the χ^2 value of the three-constraint kinematic fit. Consequently, it is no longer possible to perform a data-driven background subtraction based on the two-photon invariant masses, which would otherwise be the most straightforward approach to extract the number of signal events. Such a subtraction method requires the background distribution to be approximately flat, which, as shown in Fig. 5.8, is clearly not the case. Therefore, additional selection criteria, which may introduce further systematic uncertainties, must be employed. In this analysis, a data-driven background subtraction is performed using the χ_{3C}^2 distributions, which are easier to model than the two-dimensional two-photon invariant mass distributions. This procedure is described in Sec. 5.2.

5.1.7 | Suppression of Two-Photon Backgrounds

The most significant background contribution described by Monte Carlo simulations now originates from the two-photon process $\gamma\gamma \rightarrow \eta$. This background is expected to show a peaking behavior in the two-photon invariant mass spectrum as discussed earlier and, to some extent, in the χ_{3C}^2 distribution, making its suppression particularly challenging. Therefore, a strong suppression of these events is required. The transverse momentum

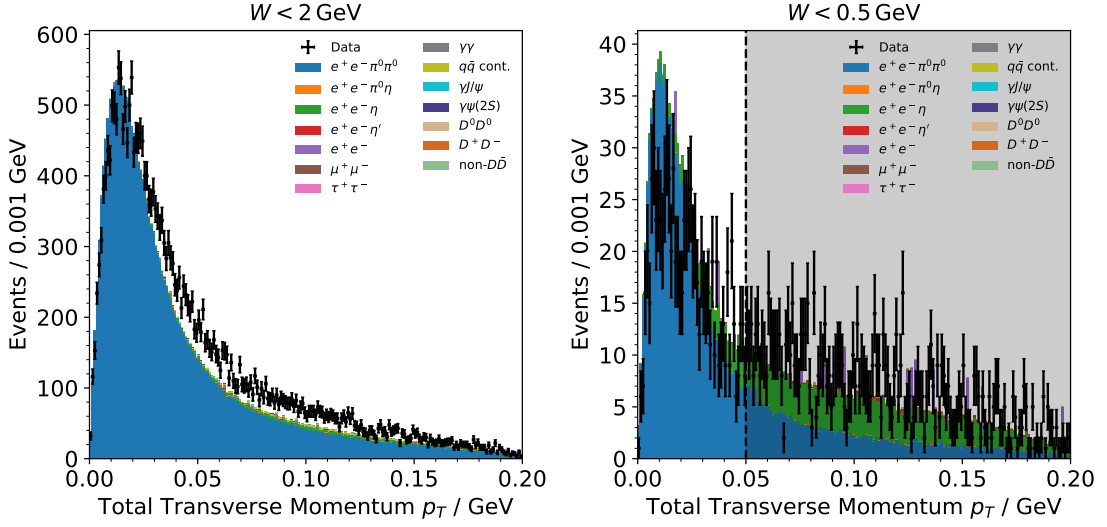


Figure 5.9: Comparison of distributions of total transverse momentum p_T of data (black points) and stacked Monte Carlo distributions for two-pion invariant masses below 2 GeV (left) and below 0.5 GeV (right). The black dashed line indicates the constraint to reject two-photon background.

of the detected final-state particles p_T has proven to be an effective tool for background reduction in untagged analyses [199]. Since the final-state leptons are scattered at small angles, their transverse momentum is also small. This property can be directly exploited in single-tagged analyses by restricting the transverse momentum of the combined $\pi^0\pi^0$ and tagged lepton system, rather than just the two-pion system, because the missing lepton is required to scatter at small angles.

The transverse momentum distributions are shown in the left and right panels of Fig. 5.9 for two-pion invariant masses below 2 GeV and 0.5 GeV, respectively. As expected, the signal-channel Monte Carlo distribution is strongly peaked at small values, with a tail extending up to approximately 200 MeV. Over the full mass spectrum, the two-photon background appears negligible, with the main background arising from unmodeled sources. However, for small invariant masses below 0.5 GeV, the two-photon background is dominant and shifted to slightly larger p_T values compared to the signal-channel simulation. Since this background is only significant in the low-mass region, suppression is required only there. Consequently, events with two-pion invariant masses $W < 0.5$ GeV are required to satisfy $p_T < 0.05$ GeV. As with the other selection criteria, the p_T constraint is later varied to assess its systematic impact.

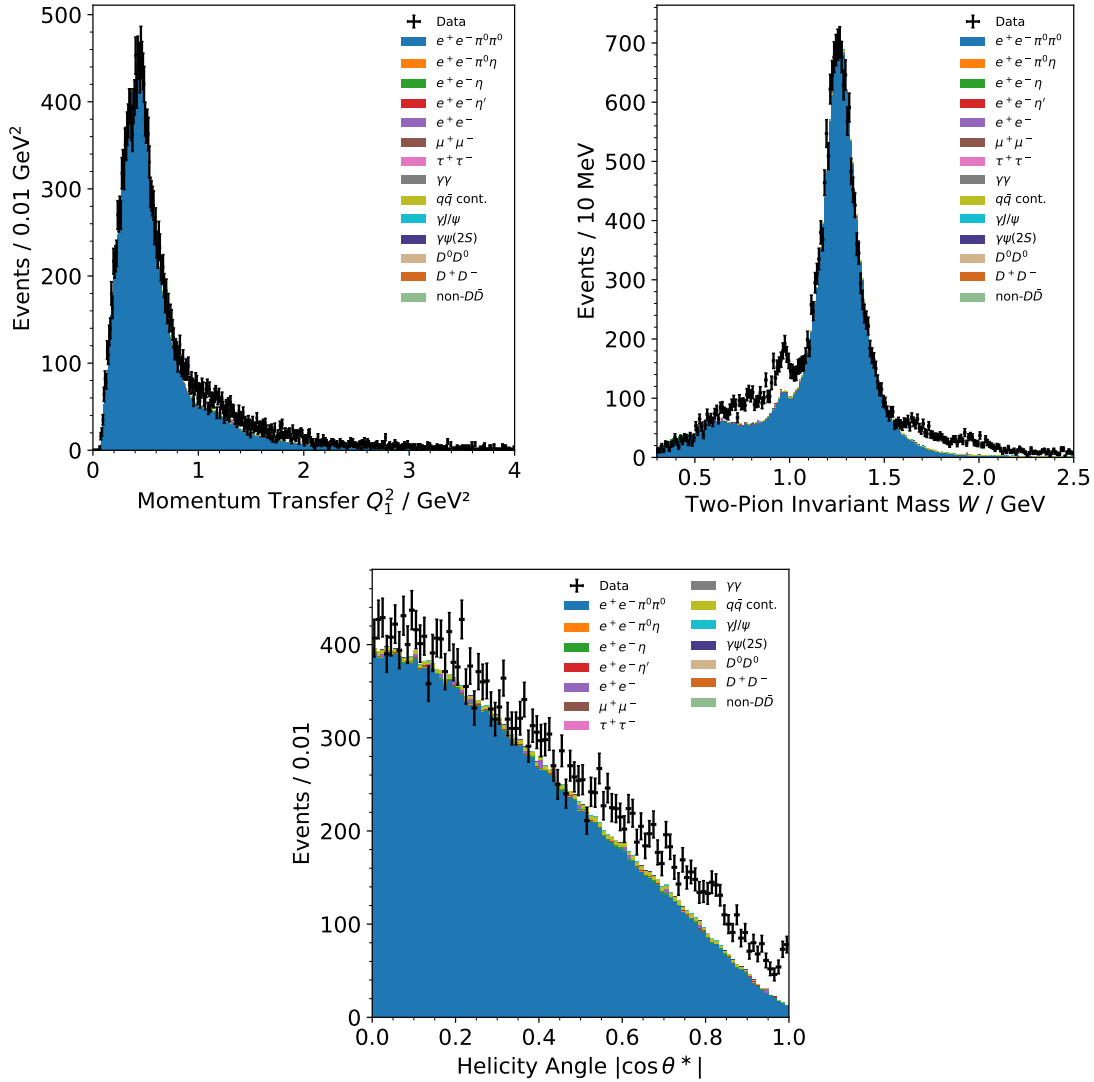


Figure 5.10: Comparison of distributions of momentum transfer Q_1^2 (upper left panel), two-pion invariant mass (upper right panel) and pion helicity angle $|\cos \theta^*|$ (bottom) of data (black points) and stacked Monte Carlo distributions after all analysis constraints.

5.1.8 | Total Event Yield

After the event selection and background suppression, the event yield can be studied. The event yield as a function of the three key variables – momentum transfer Q_1^2 , two-pion invariant mass W , and pion helicity angle $|\cos \theta^*|$ – is shown in Fig. 5.10. The two most prominent features in the mass spectrum, the $f_0(980)$ and $f_2(1270)$ resonances, are clearly visible. While the Monte Carlo description of the tensor state appears accurate, the predictions in the region of the $f_0(980)$ and lower masses are less satisfactory. This discrepancy may result from background contributions and from limited knowledge of the transition form factors of light mesons. At higher masses, additional structures are visible that are not described by the Monte Carlo simulation, as they are not included in the theoretical model input. These structures are most likely heavier scalar and tensors resonances, which have already been identified by previous works [199, 284].

The description of the momentum transfer distribution is largely accurate. The initial rise of the Q_1^2 spectrum is due to leptons at small momentum transfer not being scattered at sufficiently large angles to be detected, whereas the subsequent fall reflects the decrease of the two-photon cross section and luminosity function with increasing photon virtualities. The helicity angle spectrum generally follows the Monte Carlo prediction, although larger deviations are observed at small angles (large $|\cos \theta^*|$), indicating the presence of additional background. The overall decrease of the $|\cos \theta^*|$ distribution is consistent with the dominance of tensor mesons in the observed processes, which are expected to contribute predominantly via their helicity $\lambda = 2$ partial waves, since the helicity-2 contribution to the $f_2(1270)$ radiative width is dominant [199]. The reconstruction efficiency is expected to decrease at large $|\cos \theta^*|$, as this observable is strongly correlated with the polar angle in the lab frame, particularly for events with small momentum transfers.

5.2 | Background Subtraction

A data-driven background subtraction is performed to remove the remaining background contamination from the data. Here, the results of the three-constraint kinematic fit, specifically the χ_{3C}^2 distribution, are exploited. In principle, the χ_{3C}^2 distribution should be studied as a function of the two-pion invariant mass, the momentum transfer, and the helicity angle. Due to limited statistics – particularly at small helicity angles, large Q_1^2 , and W far from the $f_2(1270)$ resonance – an integrated approach is preferred. In Fig. 5.11, the observed χ_{3C}^2 distributions at very large values are compared for different ranges of momentum transfer, two-pion invariant mass, and pion helicity angles. Since these χ_{3C}^2 values are very large, the distributions can be expected to be signal-free and therefore dominated by background. Within $2\text{--}3\sigma$, the integrated distributions agree with the distributions obtained from cuts on each of the individual observables. Consequently, it is feasible to perform a combined fit to determine the background shape, which can then be applied to the data binned in all three observables.

One notable exception is the low-mass region. Here, the two-photon background is expected to exhibit a slight peaking behavior due to decay channels involving multiple

neutral pions, most notably the $\gamma\gamma \rightarrow \eta$ process, which is not observed in other invariant-mass regions. Therefore, the background fractions for the sideband subtraction are determined only in dependence of the two-pion invariant mass using fits to the χ_{3C}^2 spectra inclusive in Q^2 and $|\cos\theta^*|$. The χ_{3C}^2 distribution is modeled using the Monte Carlo distributions of all available background simulations, each scaled by an independent fit parameter, combined with a second-order polynomial. The polynomial component of the fit is later varied to estimate systematic uncertainties. To ensure a physically meaningful fit, the background Monte Carlo distributions are constrained to deviate by no more than 10% from their nominal values, and the polynomial background is required to be positive at all χ_{3C}^2 values. The functions are fitted to the χ_{3C}^2 spectra using a binned maximum likelihood method.

To validate the use of polynomials for describing the background shapes, it is necessary to select a sample enriched in background with minimal signal contamination. Background events are selected by removing the constraint on χ_{3C}^2 while retaining the constraint on the missing momentum transfer. Since this sample still contains signal events, an additional selection is applied to suppress them. To do so, the photon energy asymmetry is studied, defined as the absolute difference between the measured energies of the two photons, divided by their sum.

A large fraction of the unmodeled background is expected to originate from radiative Bhabha scattering events, which typically involve a high-energy photon that combines with low-energy noise to form a fake pion candidate; these events are therefore expected to exhibit large energy asymmetries. The Monte Carlo sample provided by the collaboration only includes events in which both leptons are scattered at large angles. Beam-related background events are expected to exhibit a similar behavior as the Bhabha background. They often include low-energy photons, which can be combined with other background photons to falsely reconstructed pion candidates. Figure 5.12 shows the energy asymmetry of the highest-energy photon and its counterpart in the respective pion candidate, before and after applying the χ_{3C}^2 constraint. After the χ_{3C}^2 requirement, the large asymmetry peak disappears, and the remaining distribution is generally well described, with only a small residual contribution at large asymmetries, indicating the presence of a minor remaining Bhabha scattering component in the selected signal sample.

To select background events, all events with an asymmetry below 0.8 are rejected. Since the signal fraction is expected to be small after applying the photon energy asymmetry constraint, the signal Monte Carlo contribution is subtracted to obtain the background shape. The total background distribution is then constructed by combining all background Monte Carlo samples for asymmetries below 0.8 with the data-driven background estimate for asymmetries above 0.8.

In Fig. 5.13, the χ_{3C}^2 distributions of the data, the the signal Monte Carlo, and the estimated background are compared. The sum of the signal Monte Carlo and the background estimate provides a good description of the observed data, with small discrepancies at low photon-energy asymmetries, as visible in the left panel of Fig. 5.12 likely arising from imperfections in the signal Monte Carlo and background selection. The background estimate itself is approximately flat, with only minor deviations from a straight line. The only

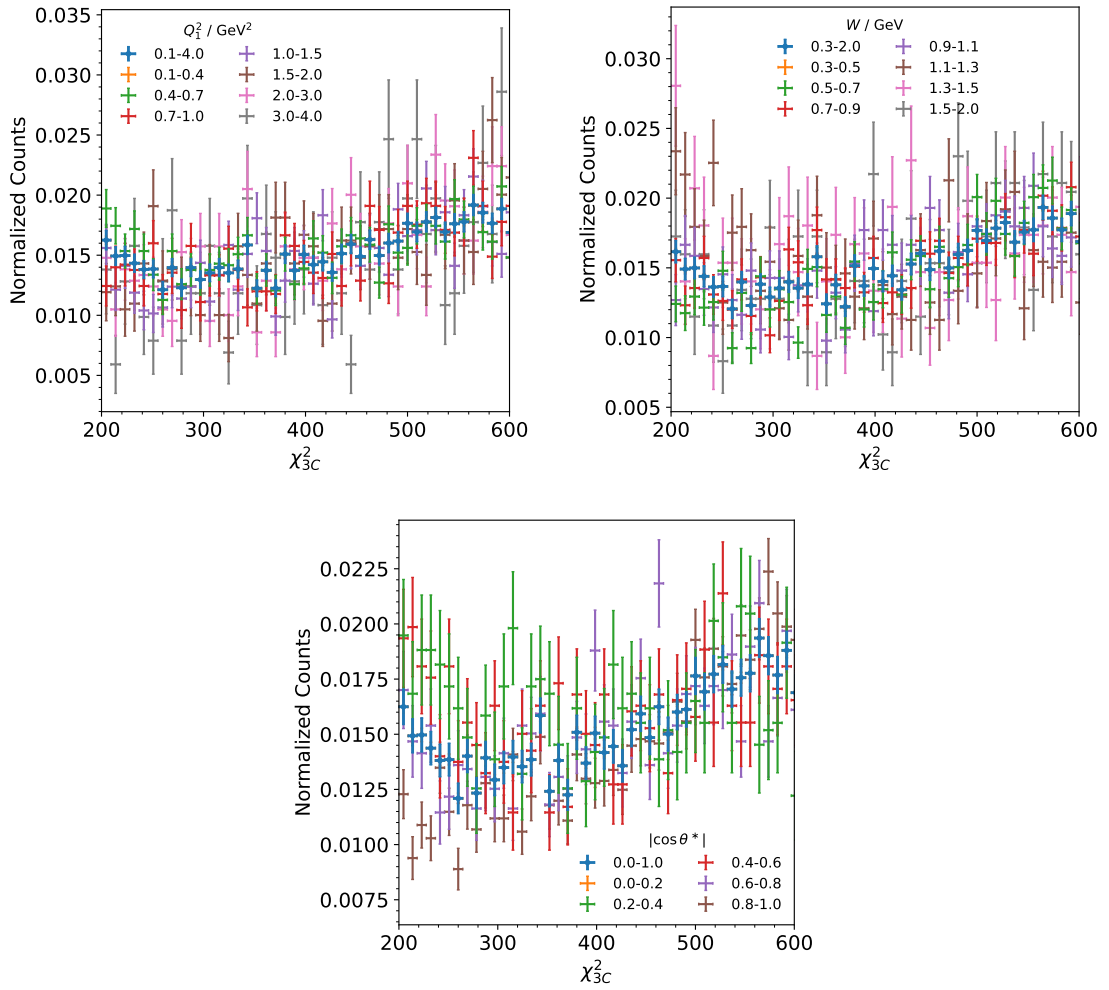


Figure 5.11: χ_{3C}^2 distributions at large values χ_{3C}^2 of the selected data for different momentum transfers (top left), two-pion invariant mass (top right), and helicity angle (bottom) ranges. All distributions are normalized. The blue points are the integrated distributions.

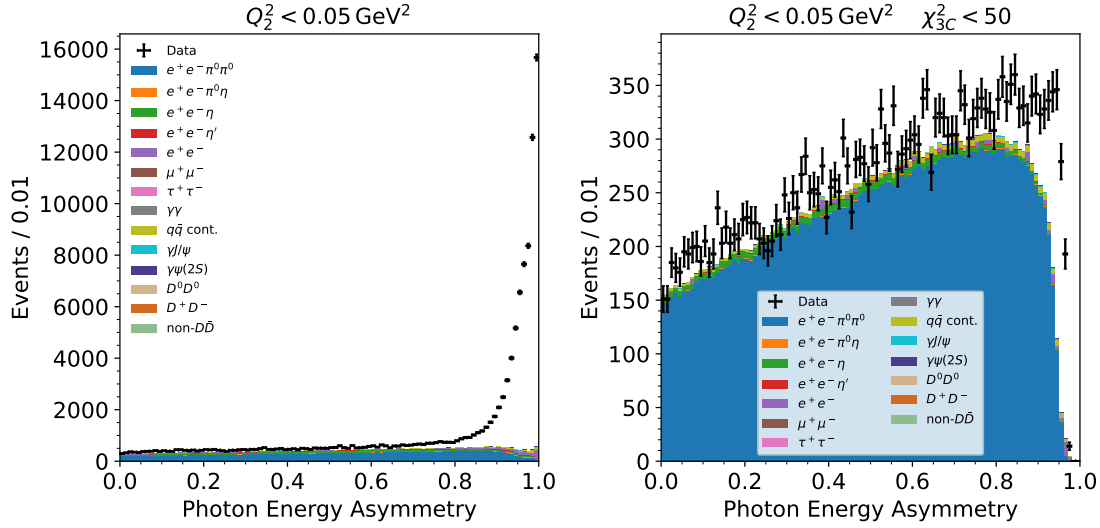


Figure 5.12: Comparison of the distributions of photon-energy asymmetry for the data (black points) and stacked Monte Carlo simulations (histograms) without (left panel) and with (right panel) a constraint on χ^2_{3C} . Only the energy asymmetry distributions stemming from the photons contributing to the pion candidate that contains the highest-energetic photon are shown.

statistically significant feature in the spectrum is the strong suppression of background events in the lowest χ^2_{3C} bin; however, since this effect occurs over a very limited parameter range, it is negligible relative to the remainder of the background. Therefore, a polynomial function can be used to describe the background contribution in the χ^2_{3C} distributions.

The fits to the different mass bins are shown in Fig. 5.14. At small masses, the background contribution is largely described by the χ^2_{3C} distributions of the background Monte Carlo samples, specifically the two-photon production of the η meson, whereas at higher masses, the spectra are fully described by the polynomial component. The minimum likelihood values correspond to $\chi^2/\text{n.d.f.} = 0.9\text{--}1.6$, depending on the mass bin, indicating a good fit quality. The background contribution in the signal region, defined as $\chi^2_{3C} < 50$, is determined by comparing the integral of the background function within the signal region to that in a sideband (background) window, and scaling according to the number of events observed in the sideband. This procedure is performed as a function of the three key observables: momentum transfer Q_1^2 , two-pion invariant mass W , and pion helicity angle $|\cos\theta^*|$. In the first step, the background window is defined by $100 < \chi^2_{3C} < 600$. This window is chosen to be sufficiently large to improve the statistical precision of the sideband estimation, while extending to sufficiently large χ^2_{3C} values to minimize any contamination from the signal. The constraints are later varied to assess any systematic effects arising from this procedure.

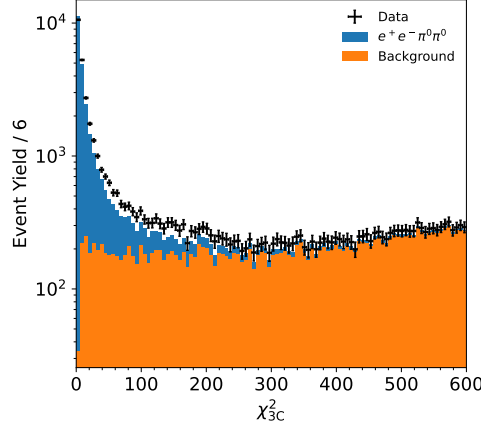


Figure 5.13: Comparison of χ^2_{3C} distributions for the data (black points) and the signal Monte Carlo (blue), stacked on top of the estimated background contribution (orange). All samples are subject to the constraints $Q_2^2 < 0.05 \text{ GeV}^2$ and $p_T < 0.05 \text{ GeV}$ for masses below $W < 0.5 \text{ GeV}$.

The event yield in the signal window is compared to the background contribution, determined from the fit results and the event yield in the background window, in Fig. 5.15 as a function of Q_1^2 and W . The corresponding helicity-angle-dependent distributions are provided in the appendix (Figs. A.1–A.5). The background fraction generally increases with increasing momentum transfer and decreasing helicity angles. At small momentum transfers and small $|\cos \theta^*|$, the background is negligible, whereas the highest Q_1^2 and $|\cos \theta^*|$ bins are almost entirely dominated by background. To determine the signal yield, both the sideband contribution and the residual $\gamma\gamma \rightarrow \eta$ component are subtracted. The systematic uncertainty associated with the subtraction of the $\gamma\gamma \rightarrow \eta$ Monte Carlo distribution is later evaluated by employing different transition form factor models implemented in the EKHARA event generator.

5.3 | Reconstruction Efficiency

To remove the effects of detection, event reconstruction, background subtraction and other detector effects from the final result, the signal event yield must be corrected for the reconstruction efficiency. The reconstruction efficiency is determined by comparing the generated and reconstructed signal Monte Carlo events. By definition, the branching fraction of the neutral pion to two photons, $Br(\pi^0 \rightarrow \gamma\gamma) = (98.823 \pm 0.034) \%$ [275], is included in the efficiency definition, such that the reconstruction efficiency is given by

$$\varepsilon(W, Q_1^2, |\cos \theta^*|) = Br(\pi^0 \rightarrow \gamma\gamma)^2 \frac{N_{\text{rec.}}(W, Q_1^2, |\cos \theta^*|)}{N_{\text{gen.}}(W, Q_1^2, |\cos \theta^*|)} . \quad (5.1)$$

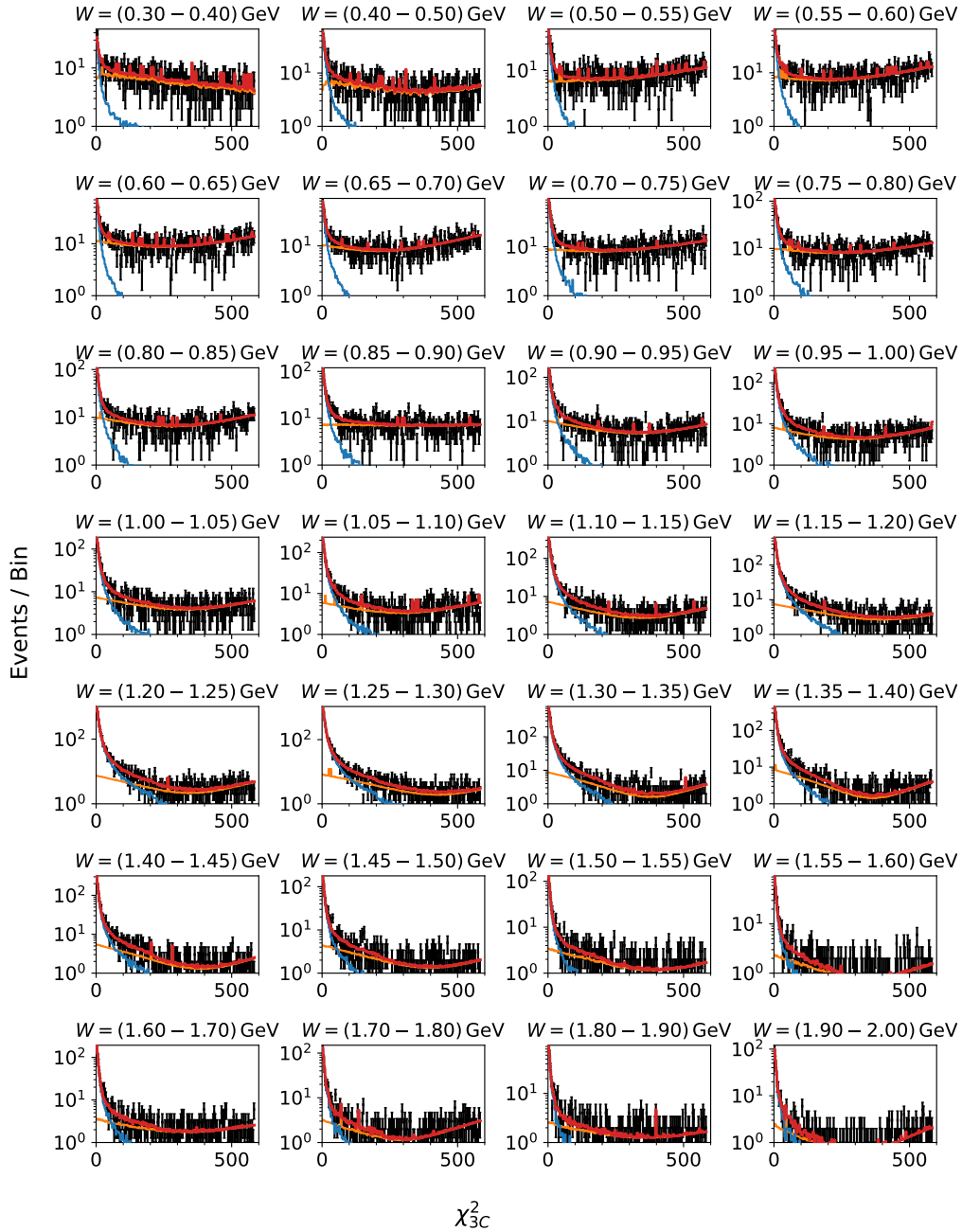


Figure 5.14: Fits to the χ^2_{3C} distributions for different two-pion invariant mass bins. The red line represents the total fit, the orange the background contribution, and blue the signal contribution.

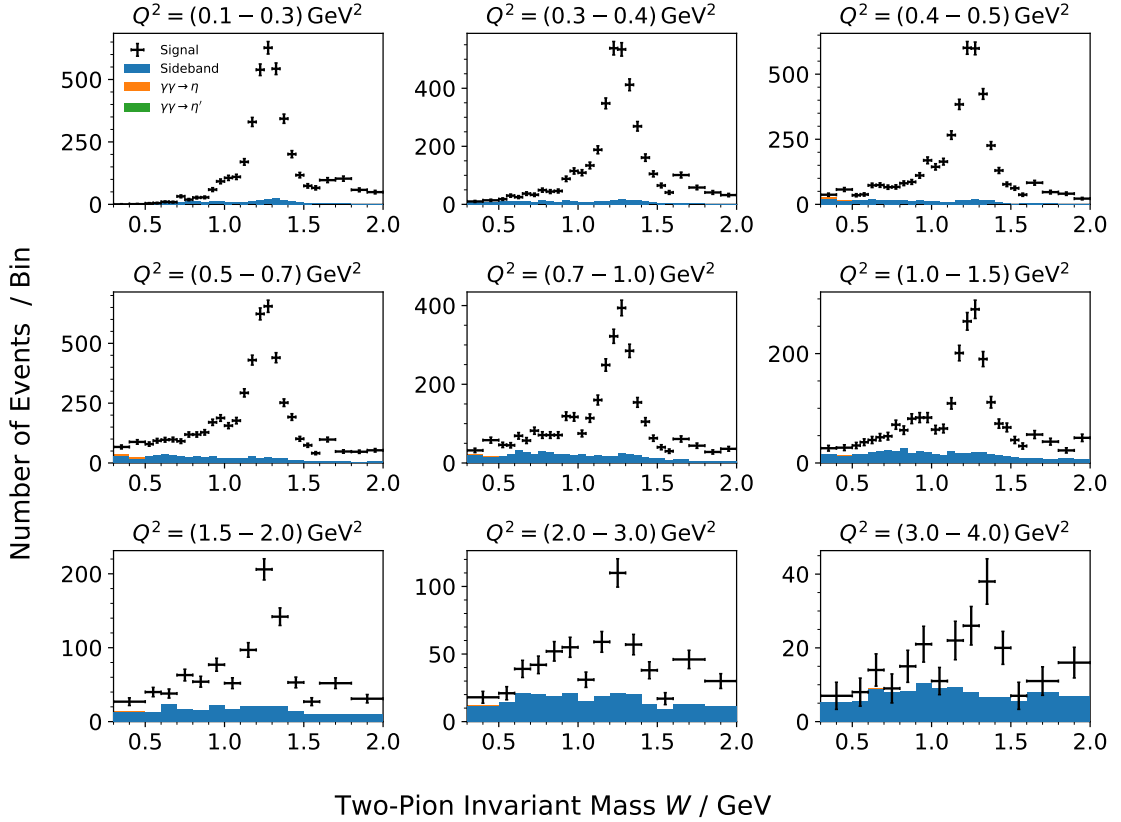


Figure 5.15: The event yield in signal window (black points) compared to the sideband extracted from the fitted background shape and event yield in the background window (blue histograms) stacked with the remaining contribution of $\gamma\gamma \rightarrow \eta$ and $\gamma\gamma \rightarrow \eta'$ Monte Carlo simulations in different momentum-transfer bins. The event yields are integrated over all helicity angles.

Since the reconstruction efficiency represents a probability of successful reconstruction, the statistical uncertainty is estimated using binomial statistics.

The effective cut on $Q_{2,\text{gen.}}^2$ is an important input for the determination of the reconstruction efficiency and the two-photon luminosity function. This constraint must be applied to the generated sample when determining the reconstruction efficiency, because the sample includes events over the full range of momentum transfers and is not exclusively singly virtual, while the efficiency needs to be evaluated for the singly virtual configuration. Without this constraint, the resulting estimation of the event yield and cross section would be highly model-dependent and correspond to all momentum transfers rather than the singly virtual configuration. The effective cut can be determined by scanning the cumulative distributions of the missing momentum transfer presented in Fig. 5.5. Although the cumulative distributions derived from the signal Monte Carlo eventually reach unity,

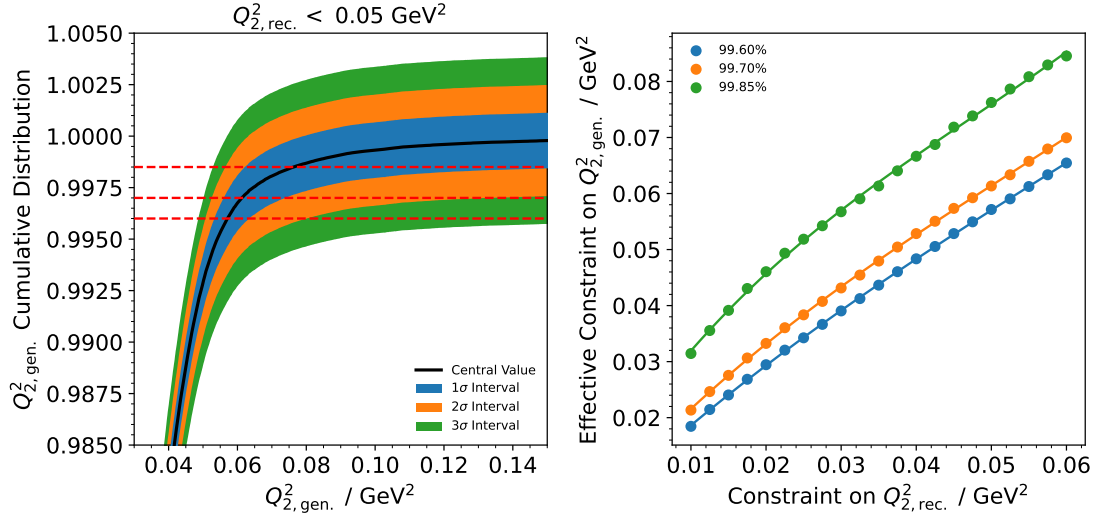


Figure 5.16: The cumulative distribution of $Q_{2,gen}^2$ for a constraint on $Q_{2,rec}^2 < 0.05 \text{ GeV}^2$ including the statistical uncertainty (left panel) and extracted effective constraints on $Q_{2,gen}^2$ as function of $Q_{2,rec}^2$ for different thresholds on the cumulative distributions (right). The red lines in the left panel indicate the 99.60 %, 99.70 %, and 99.85 % levels. The lines in the right figure represent the results of a fit of a fourth-order polynomial to the effective constraints at discrete values.

this value is strongly affected by the finite size of the Monte Carlo sample and is therefore unsuitable for direct use. The statistical uncertainty of the cumulative distributions must be taken into account.

The left panel of Fig. 5.16 shows one such cumulative distribution together with its statistical uncertainty (up to 3σ). At approximately 99.60 %, the 3σ uncertainty band of the cumulative distribution is reached, at 99.70 %, the 2σ interval is reached, and at 99.85 %, the 1σ interval is reached. Consequently, the effective cut can be defined as the point where the cumulative distribution reaches a value of at least 99.60 %. The effective constraints can be determined by scanning the cumulative distributions at the respective levels. The results of these scans are shown in the right panel of Fig. 5.16, together with a fourth-order polynomial fit to the scan points. As expected, the effective cut increases with both increasing constraints on $Q_{2,rec}^2$ and higher levels of the cumulative distribution from which the effective cut is defined. Only a small difference is observed between the 99.60 % and 99.70 % levels, whereas the 99.85 % level corresponds to significantly larger values and exhibits larger fluctuations, reflecting the limited statistics of the signal Monte Carlo in this high-value region. Therefore, the 99.60% level is adopted to define the effective cut on the missing momentum transfer.

In Fig. 5.17, the reconstruction efficiency is shown as a function of the three key ob-

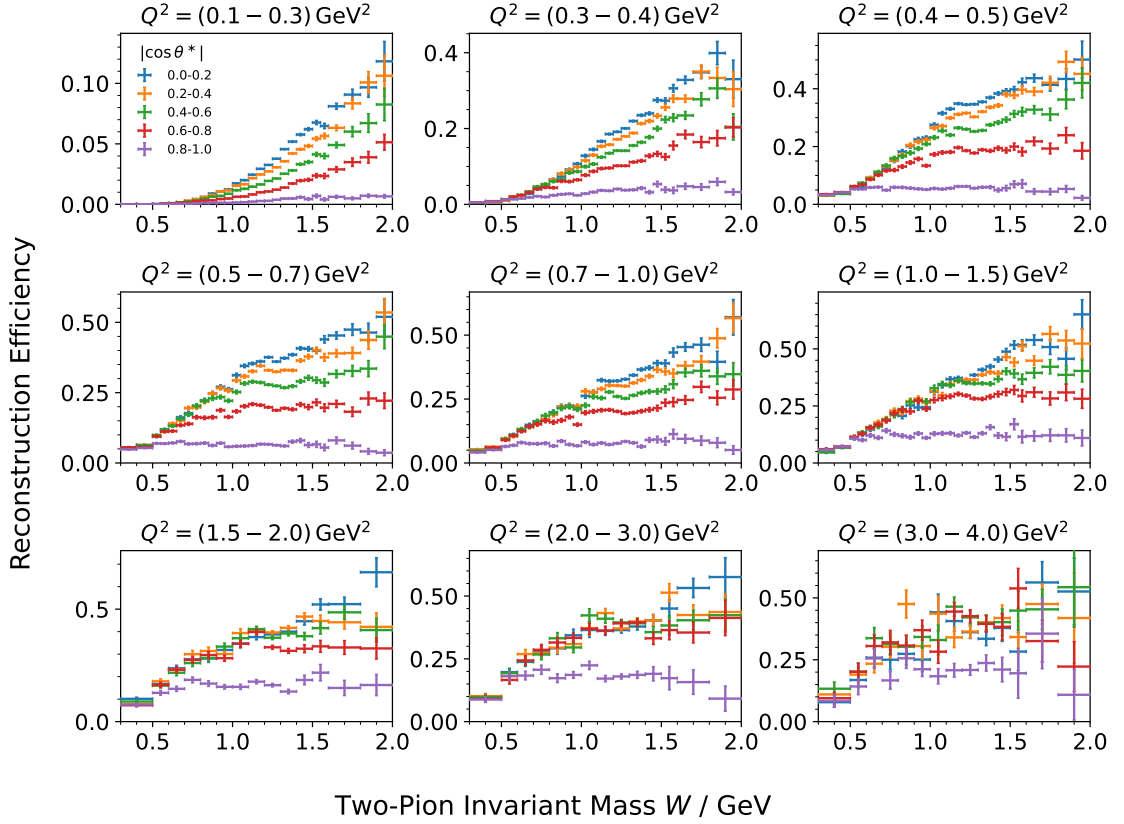


Figure 5.17: The reconstruction efficiency as function of two-pion invariant mass, momentum transfer, and pion helicity angle determined from signal Monte Carlo. The error bars represent the uncertainty evaluated using binomial statistics.

servables. The efficiency increases with increasing two-pion invariant mass, as expected, because of the smaller boost and the resulting greater isotropy of the hadronic decay products. At small masses, the stronger boost along the beam axis reduces the likelihood that the pion decay products are scattered into the active detector material. The efficiency is also smaller for the two smallest Q^2 bins, which is consistent with small momentum transfers corresponding to smaller scattering angles and, consequently, a reduced probability of reconstruction. Additionally, the efficiency decreases for large $|\cos \theta^*|$, with this effect being most pronounced at low Q^2 . For small Q^2 , the virtual photon is produced at a small angle, causing the pion helicity angle to be strongly correlated with the pion polar angles in the lab frame. As a result, events with small pion helicity angles are less likely to be reconstructed, since the decay products are less likely to be scattered into the EMC.

5.4 | Determination of the Two-Photon Luminosity Function

Since the goal of this work is the study of the $\gamma\gamma^* \rightarrow \pi^0\pi^0$ cross sections, it is necessary to determine the luminosity functions introduced in Sec. 1.3, which connects the $e^+e^- \rightarrow e^+e^-\pi^0\pi^0$ cross section to the $\gamma\gamma^* \rightarrow \pi^0\pi^0$ cross section. In Ref. [257], the authors provide fully analytical results for the different luminosity functions. The analytical expressions are obtained by rewriting Eq. (1.18) such that the kinematic factors in the cross section formula are expressed as two-dimensional polynomials in terms of the Lorentz invariants defined as

$$u_1 = 2p_1 \cdot q_2 \quad \text{and} \quad u_2 = 2p_2 \cdot q_1 \quad . \quad (5.2)$$

The change of variables allows the phase-space element to be rewritten as

$$\frac{d^3\vec{p}_1}{E_1} \frac{d^3\vec{p}_2}{E_2} \rightarrow \frac{\pi}{\sqrt{s(s-4m^2)}} dQ_1^2 dQ_2^2 dW^2 \frac{du_1 du_2}{\sqrt{A-4m^2B}} \quad (5.3)$$

with

$$A = 4Q_1^2 Q_2^2 (s - u_1)(s - u_2) - (u_1 u_2 + Q_1^2 Q_2^2 - 2s\nu)^2 \quad \text{and} \quad (5.4)$$

$$B = 4s(Q_1^2 Q_2^2 - \nu^2) + Q_1^2(u_2 - Q_2^2)^2 + Q_2^2(u_1 - Q_1^2)^2 + 2\nu(u_1 - Q_1^2)(u_2 - Q_2^2) \quad . \quad (5.5)$$

The hadronic dynamics itself does not depend on u_1 and u_2 , which allows integration of these observables over the full phase space. Reference [257] provides a straightforward procedure to perform this integration by expressing the kinematic factors in front of the two-photon cross section in Eq. (1.18) as second-order two-dimensional polynomials in u_1 and u_2 , and by providing master integrals for each possible combination of the two Lorentz invariants.

Since this is a single-tag measurement, the dependence on one of the momentum transfers must also be eliminated. A naive approach is to set the remaining virtuality (here, for simplicity, Q_2^2) to its minimum value, given by

$$Q_{2,\min}^2 = \frac{c}{a Q_{2,\max}^2} \quad \text{with} \quad (5.6)$$

$$Q_{2,\max}^2 = \frac{1}{2} \left(b/a + \sqrt{\Delta/a} \right) \quad (5.7)$$

$$\begin{aligned} \Delta &= (Q - Q_1^2 - W^2 + m_e W)(Q - Q_1^2 - W^2 - m_e W) \\ &\quad \times (Q^2 + 2Q(Q_1^2 + W^2) + Q_1^4 + W^4 + 16m_e^2 Q_1^2 + 2W^2 Q_1^2) \end{aligned} \quad (5.8)$$

$$Q = 4(s - Q_1^2 - 4m_e^2) / (1 + \beta_e y) + Q_1^2 - W^2 \quad (5.9)$$

$$\beta_e = \sqrt{1 - 4m_e^2/s} \quad (5.10)$$

$$y = \sqrt{1 + 4m_e^2/Q_1^2} \quad (5.11)$$

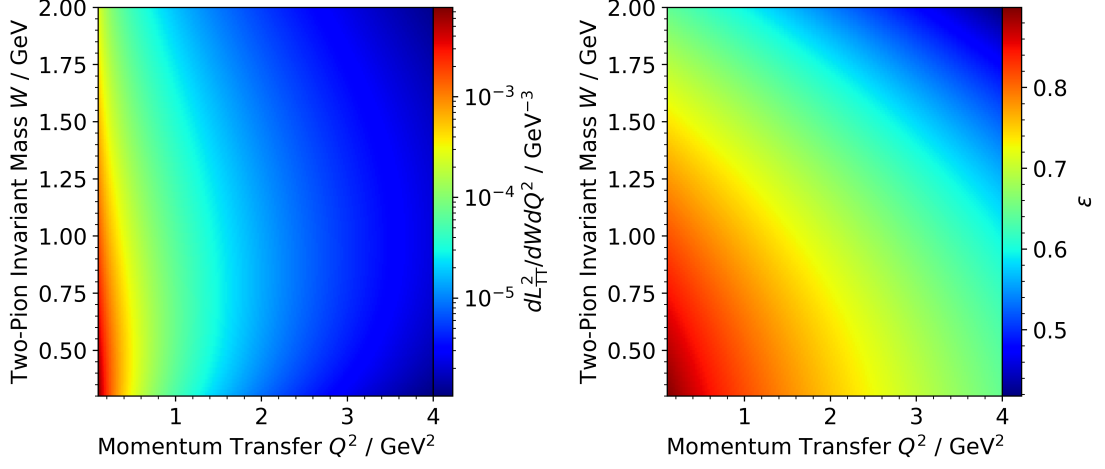


Figure 5.18: Model-averaged two-photon luminosity function (left) and factor ε (right) evaluated for $Q_{2,\text{rec.}}^2 < 0.05 \text{ GeV}^2$ as function of two-pion invariant mass and tagged lepton's momentum transfer.

$$a = 2(Q - Q_1^2 + 2m_e^2 + W^2) \quad (5.12)$$

$$b = Q^2 - W^4 - 2W^2Q_1^2 - Q_1^4 + 8m_e^2(Q_1^2 - W^2) \quad (5.13)$$

$$c = 4m_e^2(W^2 + Q_1^2)^2 \quad (5.14)$$

This, however, neglects resolution effects and the resulting residual virtuality of the pseudo-on-shell photon and its virtuality Q_2^2 . Consequently, the measurement would yield two-photon cross sections that are not defined for a fixed virtuality of zero, but rather correspond to the cross section integrated from the minimum value to the upper bound of the missing virtuality. To account for this effect, the luminosity functions are integrated from the minimum value of Q_2^2 up to the effective constraint $Q_{2,\text{cut}}^2$, which was determined in the previous section.

A second effect that must be accounted for in the integration of the luminosity functions is the expected decrease of the cross section with increasing momentum transfer Q_2^2 . To incorporate this, an additional factor $h_T(Q_2^2)$ is multiplied by the luminosity functions prior to integration. This factor is intended to model the reduction of the two-photon cross section as a function of the unmeasured virtuality:

$$\frac{d^2 L_{AB}(W, Q_1^2)}{dW dQ_1^2} = \int_{Q_{2,\text{min}}^2}^{Q_{2,\text{cut}}^2} dQ_2^2 \frac{d^3 L_{AB}(W, Q_1^2, Q_2^2)}{dW dQ_1^2 dQ_2^2} h_T(Q_2^2) \quad \text{with } A, B = T, L \quad (5.15)$$

The function $h_T(Q_2^2)$ must be modeled, and the impact of the chosen model needs to be carefully evaluated. Results on electromagnetic transition form factors (e.g., Ref. [288]) have shown that vector-meson-dominance-like models describe the data reasonably well.

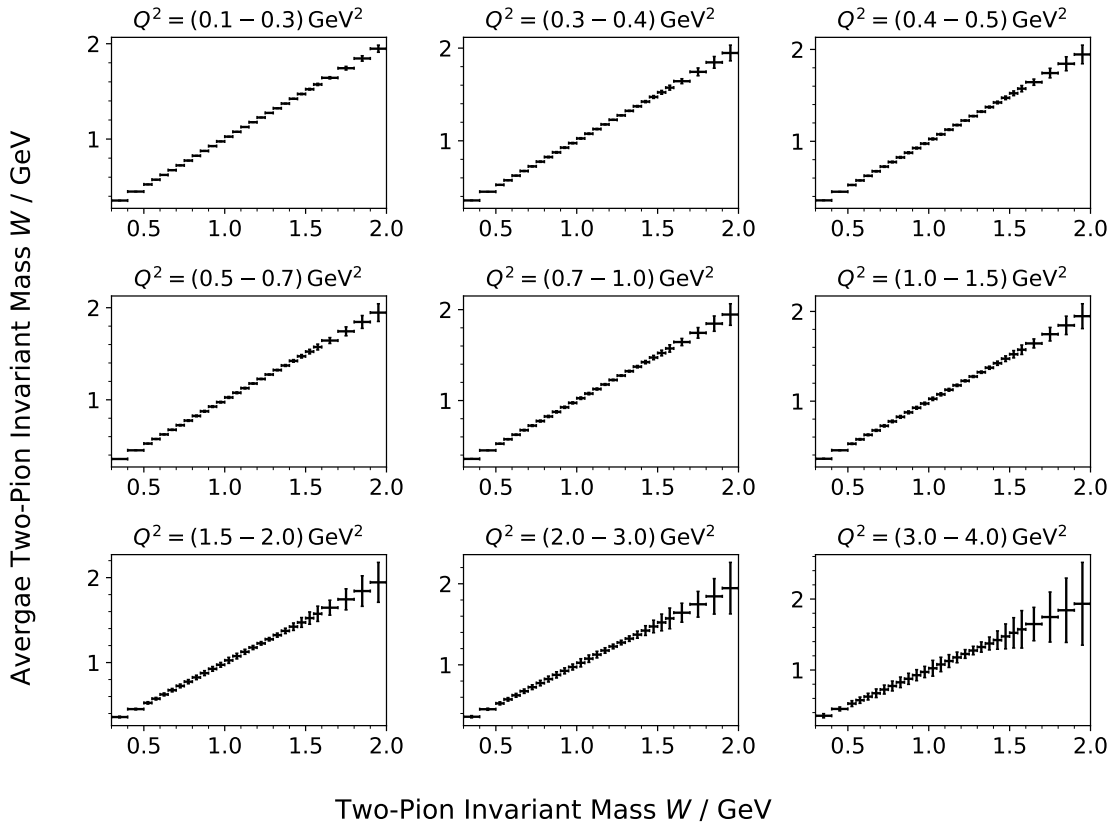


Figure 5.19: Average two-pion invariant mass calculated from the signal channel Monte Carlo simulation for different bins of reconstructed momentum transfer and two-pion invariant mass.

To estimate systematic uncertainties, three different models are tested, namely those implemented into HADROTOPS and defined in Sec. 2.4.1.

There is no model expected to describe the data better or worse than the others. Therefore, the nominal results for the calculation of the luminosity functions are obtained by averaging over the three models.

For convenience, the cross section formula is rewritten to contain only a single luminosity function and a dimensionless factor ε , defined as the ratio of the luminosity functions for LT- and TT-polarized photons. The TT luminosity function is chosen as the reference, since scalar resonances do not contribute to σ_{LT} and the helicity-2 component – contributing only to the σ_{TT} cross section – of the tensor states are expected to be dominant. Thus, in this measurement the sum of the cross sections $\sigma_{TT} + \varepsilon \sigma_{TL}$ is measured. The averaged luminosity function, together with the factor ε , are shown in Fig. 5.18. Both quantities were calculated numerically using Wolfram Mathematica [339], with a relative precision better than 10^{-6} , resulting in a negligible statistical uncertainty. The Mathemat-

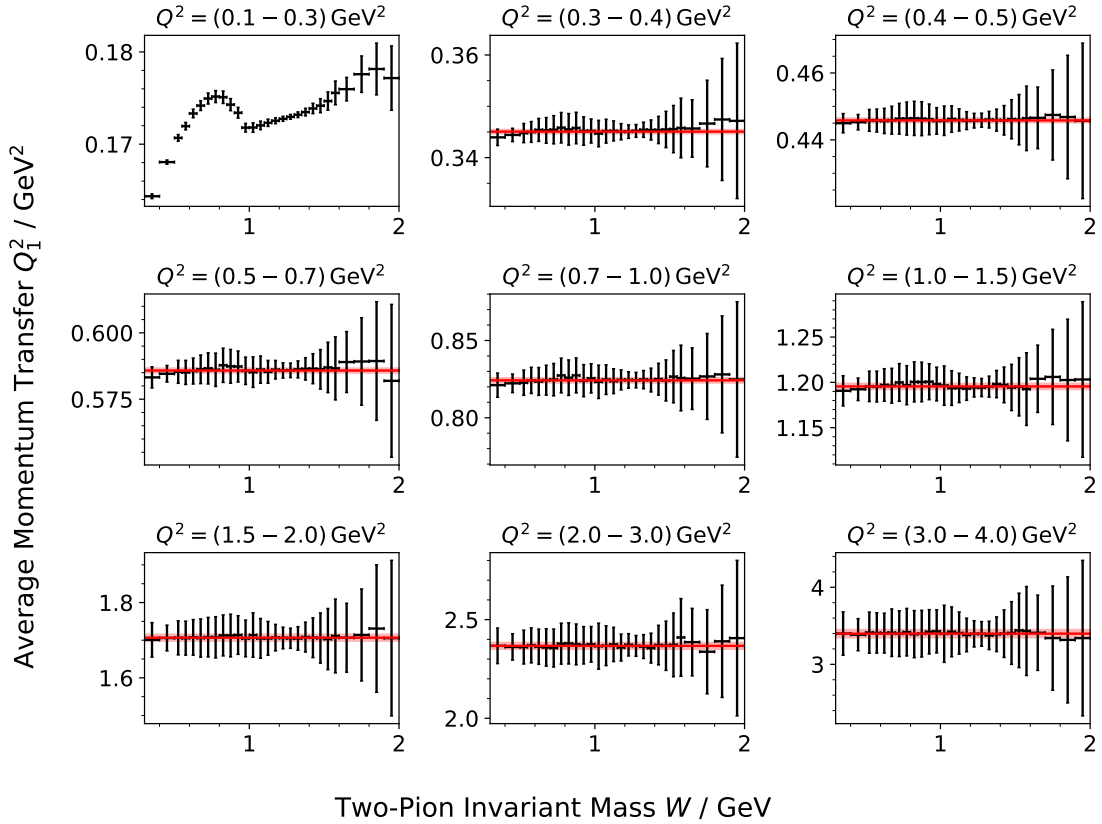


Figure 5.20: Average momentum transfer calculated from the signal channel Monte Carlo simulation for different bins of reconstructed momentum transfer and two-pion invariant mass. The red lines represent the fit of a constant to the observed average. The shaded area represents the fit uncertainty.

ica code is cross-checked using HADROTURNS.

The luminosity function shows the expected decrease with increasing momentum transfer and two-pion invariant mass – over the given parameter range, spanning more than seven orders of magnitude. In contrast, the scaling factor ε decreases much more slowly as a function of momentum transfer and two-pion invariant mass due to the overall similarity of the different luminosity functions.

Due to the strong dependence on momentum transfer, the luminosity functions – and therefore the measured cross sections – are highly sensitive to the point of evaluation. Simply evaluating the luminosity functions at the bin center would underestimate their true bin-representative values, leading to an overestimation of the final results. Therefore, the average momentum transfer and two-pion invariant mass in each bin are evaluated using the signal Monte Carlo simulation. As no significant dependence of these averages on the helicity angle was observed, this evaluation is performed only as a function of mass

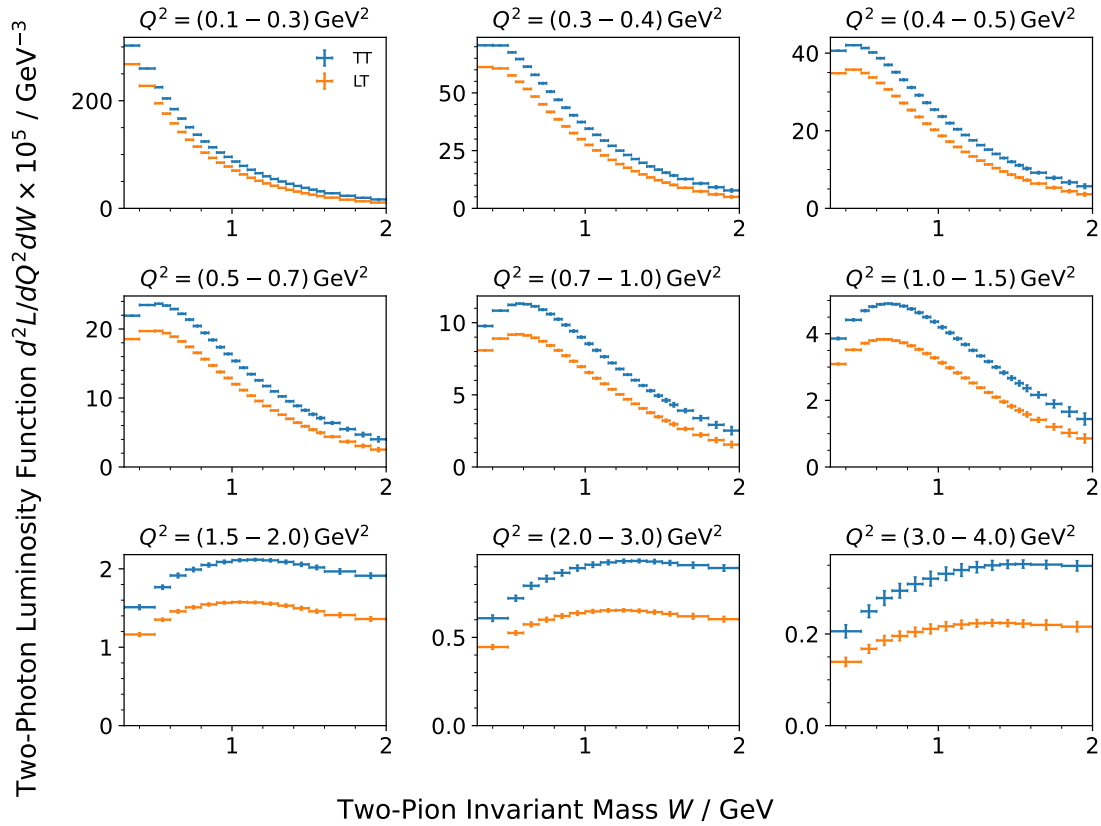


Figure 5.21: Two-photon luminosity functions for TT (blue) and LT (orange) photon polarizations in each bin. The statistical uncertainties are determined by evaluating the luminosity functions also at the average mass and momentum transfers varied by their respective uncertainties. The largest deviation from the central values is used as the statistical uncertainty.

and momentum transfer. The results are shown in Figs. 5.19 and 5.20, respectively.

While the average two-pion invariant mass distributions (Fig. 5.19) behave as expected: a linear increase with increasing reconstructed two-pion mass, the determined average momentum transfers (Fig. 5.20) show a more complex behavior. For reconstructed values above $Q_1^2 > 0.3 \text{ GeV}^2$, no significant Q^2 dependence is observed within the uncertainties, and a constant provides a good description of the results. The average momentum transfer lies systematically below the bin center, reflecting the strong Q^2 dependence within each bin and shifting the average to smaller values. A more complex pattern is observed in the smallest Q^2 bin, where a strong mass dependence appears. Here, the pole position of the $f_0(980)$ and the shape of the $f_0(500)$ clearly influence the average momentum transfer values. This mass dependence appears only at the smallest momentum transfers, where the scattering angle is confined to a very narrow region at

the edge of the detector acceptance. In this kinematic regime, the momentum transfer becomes more sensitive to variations in the energy of the final-state lepton, which in turn depends on the mass of the produced hadronic system.

The resulting luminosity functions are shown in Fig. 5.21. The statistical uncertainties are estimated by evaluating the luminosity functions at the average mass and momentum transfer, varied within their respective uncertainties. For momentum transfer bins larger than $Q^2 > 0.3 \text{ GeV}^2$, the results of the fit to the average momentum transfer are used. The largest deviation from the central value is taken as the statistical uncertainty. Since these uncertainties are relatively small compared to the statistical uncertainties of the event yield, this conservative estimate is sufficient and does not significantly increase the total uncertainty. The luminosity function for two transversely polarized photons is larger than that for one transverse and one longitudinally polarized photon across the entire parameter range. This effect becomes more pronounced at higher momentum transfers and is largely independent of the two-pion invariant mass.

5.5 | Extraction of the Effective Two-Photon Production Cross Section

Using the information discussed in the previous chapters, the effective two-photon production cross section of two neutral pions as a function of the two-pion invariant mass W , momentum transfer Q^2 , and pion helicity angle $|\cos \theta^*|$ can be calculated as

$$\frac{d(\sigma_{\text{TT}} + \varepsilon\sigma_{\text{LT}})}{d|\cos \theta^*|} = \frac{1}{2} \frac{N_{\text{sub}}}{\Delta_W \cdot \Delta_{Q^2} \cdot \Delta_{|\cos \theta^*|} \cdot \varepsilon(W, Q^2, |\cos \theta^*|) \cdot \frac{d^2L(W, Q^2)}{dW dQ^2} \cdot \mathcal{L}_{\text{int}}}, \quad (5.16)$$

where N_{sub} is the background-subtracted event yield, Δ_W , Δ_{Q^2} , and $\Delta_{|\cos \theta^*|}$ are the bin widths in mass, momentum transfer, and helicity angle, respectively, $\varepsilon(W, Q^2, |\cos \theta^*|)$ is the reconstruction efficiency, $\frac{d^2L(W, Q^2)}{dW dQ^2}$ is the two-photon luminosity function, and \mathcal{L}_{int} is the integrated luminosity of the data sample. The factor $1/2$ arises from the definition of the luminosity function and from the use of both electron- and positron-tagged events. The results for helicity-angle-integrated cross sections are shown in Fig. 5.22. The presence of the $f_2(1270)$ contribution is evident, and there is a clear indication of the $f_0(980)$ state. Since the cross sections remain non-zero near threshold, one can also assume the presence of the $f_0(500)$ meson.

5.6 | Study of Systematic Uncertainties

In addition to statistical fluctuations, systematic uncertainties arise from various analysis conditions, including particle reconstruction algorithms, the modeling of the detector in Monte Carlo simulations, and analysis procedures and applied constraints. These uncertainties are evaluated in this section.

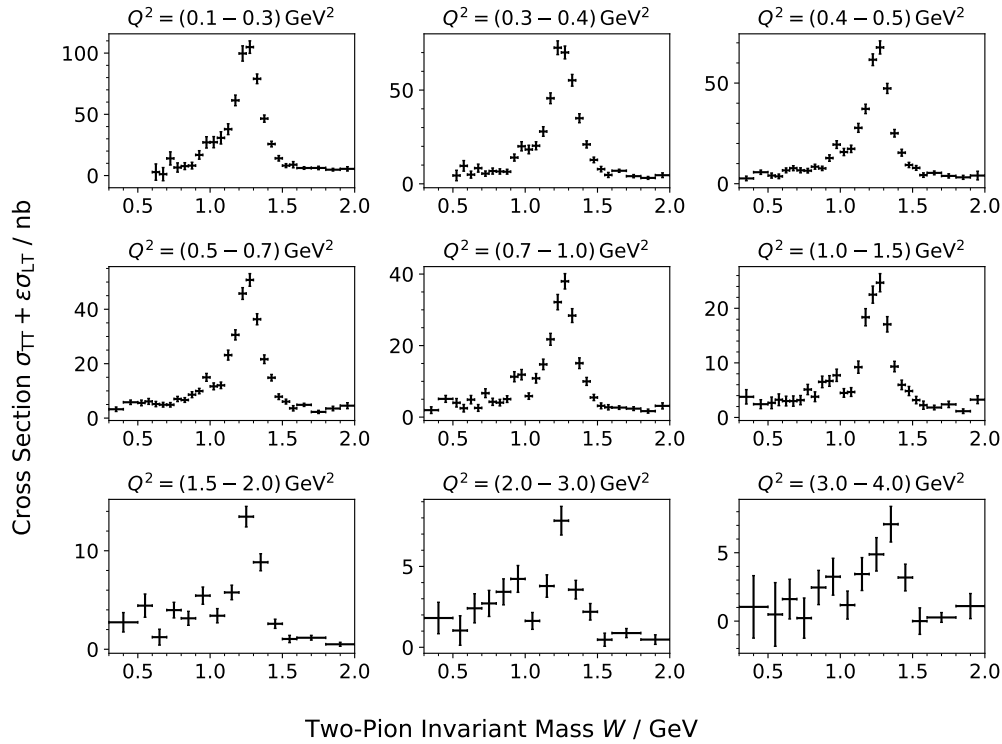


Figure 5.22: Singly virtual effective two-photon production cross section of two neutral pions. The shown uncertainties are purely statistical. The results are integrated over all helicity angles.

5.6.1 | Integrated Luminosity

The time-integrated luminosity of the round 03, round 04, round 15, round 16, and round 17 $\psi(3770)$ data sets has a combined total uncertainty of 0.4%, which is predominantly due to systematic effects [75, 313]. This value is used as a contribution to the systematic uncertainty of the cross section arising from the determination of the integrated luminosity.

5.6.2 | Electron/Positron Detection Efficiency and Particle Identification

The difference in electron and positron detection efficiency between data and Monte Carlo samples is studied, together with the effects of the particle identification procedure used in this work, in radiative Bhabha scattering events, as described in Ref. [340]. The detection efficiency difference between data and Monte Carlo is shown in the left panel of Fig. 5.23 as a function of lepton momentum and polar angle, while the corresponding distribution of the selected events is shown in the right panel. The event-weighted difference in reconstruction efficiency between data and Monte Carlo is determined to be less than 1.5%,

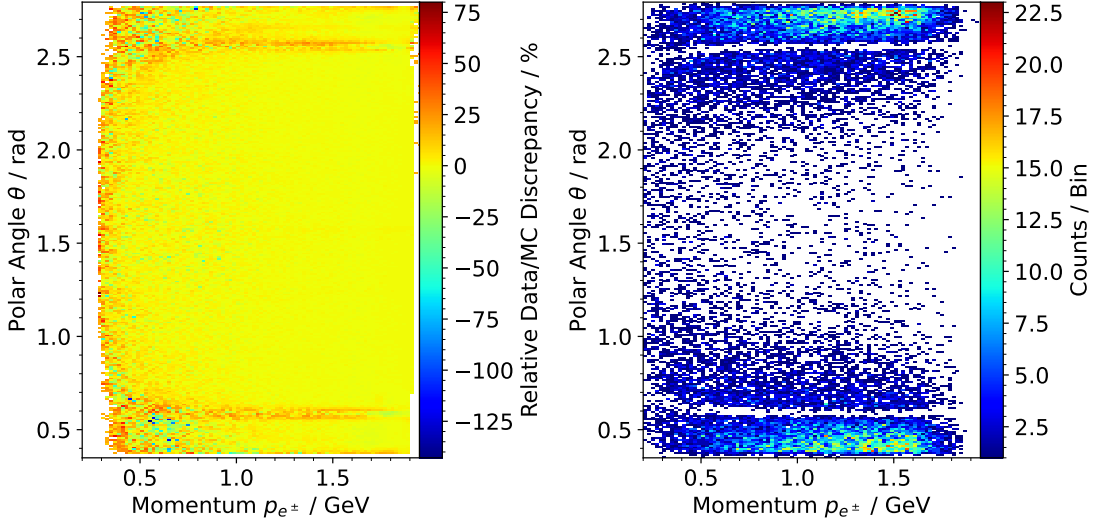


Figure 5.23: Data and Monte Carlo detection efficiency difference for electrons and positrons (left, taken from Ref. [340]) and distribution of the selected events (right) as function of lepton momentum and lepton polar angle.

which is taken as a systematic uncertainty on the measurement of the cross section.

5.6.3 | Pion Detection Efficiency

The pion detection efficiency for the $\sqrt{s} = 3.773$ GeV data has been studied using D^0 decays [341], employing π^0 selection criteria similar to those used in this work. The data-Monte Carlo efficiency differences were found to be 4% for pion momenta $p < 0.2$ GeV, 2.1% for $0.2 \text{ GeV} < p < 0.4 \text{ GeV}$, 2.3% for $0.4 \text{ GeV} < p < 0.6 \text{ GeV}$, 2.6% for $0.6 \text{ GeV} < p < 0.8 \text{ GeV}$, and 1.8% for $p > 0.8 \text{ GeV}$. Pion momenta above 1 GeV were not studied. Based on the observed trend, a 2.5% difference is assumed for higher momenta. The observed pion yields shown in Fig. 5.24 are used as weights to determine an average data-Monte Carlo difference of 2.3%. Since two pions are detected in this analysis, a systematic uncertainty of 4.6% is assigned.

5.6.4 | Analysis Constraints

The contributions to the systematic uncertainties arising from the constraints on the missing momentum transfer Q_2^2 , the transverse momentum p_T , the upper boundary of the signal window $\chi_{\text{Sig.}}^2$, the lower bound of the sideband window $\chi_{\text{Sid.}}^2$, the upper bound of the sideband window χ_{max}^2 , and the number of bins in the χ_{3C}^2 spectra used to determine the background ratios are studied simultaneously to account for any effects caused by correlations between these constraints.

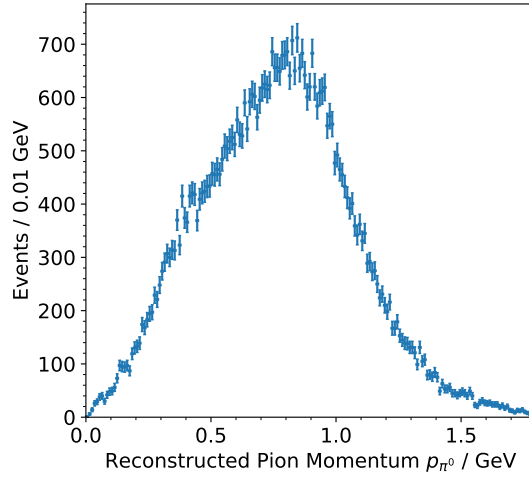


Figure 5.24: Measured π^0 momenta after all analysis cuts.

To determine the systematic effects, the analysis is repeated 1000 times with randomly varied constraints. The range over which the constraints are varied is chosen such that the background behavior remains under control for the least strict constraint and the statistical uncertainties remain reasonable for the tightest chosen constraint. If a constraint is chosen such that a significantly larger fraction of signal events is rejected, larger statistical uncertainties would be observed, which could be misidentified as systematic effects, leading to an overestimation of the total uncertainty.

Specifically, the constraint on the missing momentum transfer is varied between $Q_2^2 = (0.03 - 0.06) \text{ GeV}^2$, the transverse momentum cut is varied between $p_T = (0.04 - 0.06) \text{ GeV}$, the signal window size between $\chi_{\text{Sig.}}^2 = (30 - 50)$ the lower bound of the sideband window between $\chi_{\text{Sid.}}^2 = (80 - 120)$, the upper bound of the sideband window between $\chi_{\text{max}}^2 = (580 - 620)$, and the number of bins in the χ_{3C}^2 spectrum between 125 and 150. Since the luminosity function is highly sensitive to the constraint on the missing momentum transfer, it is evaluated for missing momentum cuts between 0.03 GeV^2 and 0.06 GeV^2 with a step size of 0.005 GeV^2 . If a randomly chosen cut lies between two evaluated values, the luminosity function is linearly interpolated between the neighboring points.

After this procedure, 1000 strongly correlated results are obtained. It is not possible to select a single “best” result from these samples to define the central value of the measured cross section in each bin. Therefore, the central values are taken as the arithmetic mean of all results. The statistical uncertainty of this average is calculated assuming full correlation between the results. Finally, the numerically determined standard deviation of the observed spread in each bin is used as a measure of the systematic effect of the applied constraints.

Mostly, the observed spreads are approximately Gaussian. In some cases, a predominantly non-Gaussian behavior is observed. However, the distributions still decrease with

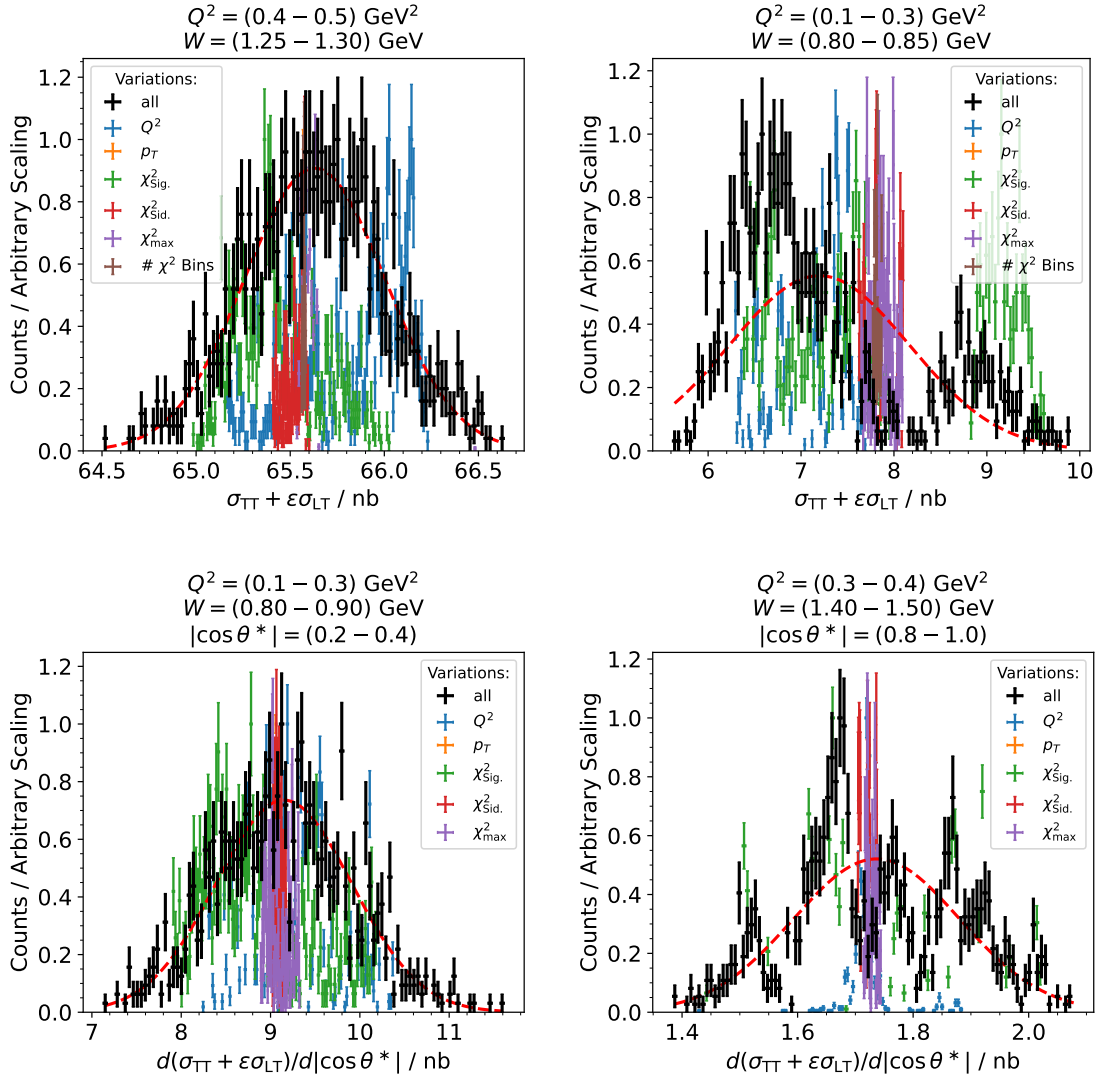


Figure 5.25: The observed variations for some bins compared to a Gaussian curve evaluated at the arithmetic mean and the calculated standard deviation. The left-hand panels show examples where the observed spread shows a Gaussian behavior, the right-hand plots show cases where there is a significant difference.

increasing distance from the arithmetic mean. Examples of both cases are shown in Fig. 5.25. While in both scenarios the determined standard deviation is used as a measure of the systematic uncertainty, in cases of non-Gaussian behavior, an additional scale factor of 2 is introduced. This situation mostly occurs in low-statistics bins and is naturally entangled with statistical effects. The dominant contributions to the systematic uncertainty stem from the constraints on the signal window size and the momentum transfer. The transverse momentum constraint is only relevant at small masses, while contributions connected to the number of bins in the χ_{3C}^2 spectra and the size of the sideband window are largely irrelevant.

The contributions to the systematic uncertainty are summarized in Tab. 5.1. The uncertainties are given in absolute numbers, since some measured cross sections are close to zero, such that relative uncertainties seem inflated. The relative uncertainties reported correspond to the value at the mass of the $f_2(1270)$, where the influence of statistical fluctuations on the systematic effect is expected to be minimal. For the helicity-angle-integrated cross section, the uncertainty is at the level of 5% for momentum transfers below 1 GeV^2 and remains below 10% for $Q^2 < 2 \text{ GeV}^2$. At larger momentum transfers, significant statistical fluctuations affect the systematic contributions. For the differential cross sections, the uncertainty is similar to the integrated cross section at small $|\cos\theta^*|$ and larger in the low-statistics, high- $|\cos\theta^*|$ bins.

5.6.5 | Fit of the χ_{3C}^2 Spectra

The contribution arising from the choice of fit function for the fit to the χ_{3C}^2 spectra is linked to the other analysis constraints and, in an ideal scenario, should be studied together with them. Since the background shape is already well described by a second-order polynomial, using very high-order polynomials in a semi-randomized study could lead to overfitting and to an overestimation of the systematic effects. Employing only a small number of different background functions may produce additional peaks in the variation plots, which are difficult to interpret. Therefore, a more conservative approach is adopted: the background shape is varied using polynomials of order 1 to 4, and the final results are compared.

Figure 5.26 shows the results for the integrated cross sections obtained using different background functions. The differences are generally found to lie within the statistical uncertainties. The Gaussian spread of these results is taken as the systematic uncertainty. The contributions are summarized in Tab. 5.2. In bins with relatively high statistics, the effect is largely negligible. In low-statistics bins, the effect is more pronounced and folded with the statistical uncertainty.

5.6.6 | Subtraction of the Two-Photon Background

The subtraction of the remaining two-photon background is dominated by the choice of transition form factor model in the EKARA3.1 event generator. To estimate its effect, the total cross section of the $\gamma\gamma \rightarrow \eta$ process in the relevant phase-space region is compared to that used in the simulation of the subtracted Monte Carlo sample. The largest deviation

Table 5.1: The absolute contributions of the analysis constraints to the systematic uncertainty of the integrated and differential cross sections in each Q^2 bin. The numbers in the brackets indicate the relative uncertainty at the $f_2(1270)$ mass.

Q^2 / GeV^2	$\Delta(\sigma_{\text{TT}} + \varepsilon\sigma_{\text{LT}}) / \text{nb}$	$\Delta d(\sigma_{\text{TT}} + \varepsilon\sigma_{\text{LT}})/d \cos\theta^* / \text{nb}$
0.1-0.3	1.0-6.5 (4%)	0.9-15.7 (4%-28%)
0.3-0.4	0.8-3.6 (5%)	0.9-6.9 (5%-20%)
0.4-0.5	0.9-3.2 (4%)	0.8-6.0 (5%-21%)
0.5-0.7	0.6-2.3 (4%)	0.6-4.8 (4%-19%)
0.7-1.0	0.5-2.1 (5%)	0.6-4.3 (7%-19%)
1.0-1.5	0.4-1.7 (7%)	0.5-3.6 (8%-23%)
1.5-2.0	0.2-1.2 (8%)	0.3-2.3 (10%-67%)
2.0-3.0	0.3-1.0 (14%)	0.3-2.1 (15%-92%)
3.0-4.0	0.4-2.4 (33%)	0.4-5.1 (23%-98%)

Table 5.2: Absolute contributions of the background function to the systematic uncertainty of the integrated and differential cross sections in different Q^2 bins. The numbers in brackets indicate the relative uncertainty at the $f_2(1270)$ mass.

Q^2 / GeV^2	$\Delta(\sigma_{\text{TT}} + \varepsilon\sigma_{\text{LT}}) / \text{nb}$	$\Delta d(\sigma_{\text{TT}} + \varepsilon\sigma_{\text{LT}})/d \cos\theta^* / \text{nb}$
0.1-0.3	0.0-2.0 (0%)	0.0-2.6 (0%-1%)
0.3-0.4	0.0-1.1 (0%)	0.0-1.7 (0%-1%)
0.4-0.5	0.0-0.6 (0%)	0.0-0.9 (0%-1%)
0.5-0.7	0.1-0.7 (0%)	0.0-1.1 (0%-1%)
0.7-1.0	0.1-1.2 (1%)	0.0-2.0 (0%-4%)
1.0-1.5	0.2-0.8 (2%)	0.0-2.1 (0%-8%)
1.5-2.0	0.1-1.0 (5%)	0.0-1.8 (0%-61%)
2.0-3.0	0.1-1.0 (16%)	0.0-2.5 (1%-137%)
3.0-4.0	0.2-1.2 (22%)	0.0-2.9 (1%-69%)

Table 5.3: Absolute contributions of the efficiency correction to the systematic uncertainty of the integrated and differential cross sections in different Q^2 bins. The numbers in brackets indicate the relative uncertainty at the $f_2(1270)$ mass.

Q^2 / GeV^2	$\Delta(\sigma_{\text{TT}} + \varepsilon\sigma_{\text{LT}}) / \text{nb}$	$\Delta d(\sigma_{\text{TT}} + \varepsilon\sigma_{\text{LT}})/d \cos\theta^* / \text{nb}$
0.10-0.30	0.04-1.70 (1%)	0.00-5.48 (0%-8%)
0.30-0.40	0.16-0.95 (1%)	0.09-1.99 (0%-5%)
0.40-0.50	0.10-0.75 (1%)	0.01-1.51 (0%-4%)
0.50-0.70	0.11-0.53 (1%)	0.00-1.54 (0%-4%)
0.70-1.00	0.10-0.54 (1%)	0.00-1.10 (1%-4%)
1.00-1.50	0.09-0.44 (1%)	0.00-0.99 (1%-4%)
1.50-2.00	0.05-0.30 (2%)	0.00-0.48 (2%-6%)
2.00-3.00	0.02-0.22 (3%)	0.01-0.49 (3%-6%)
3.00-4.00	0.00-0.49 (7%)	0.02-1.28 (7%-11%)

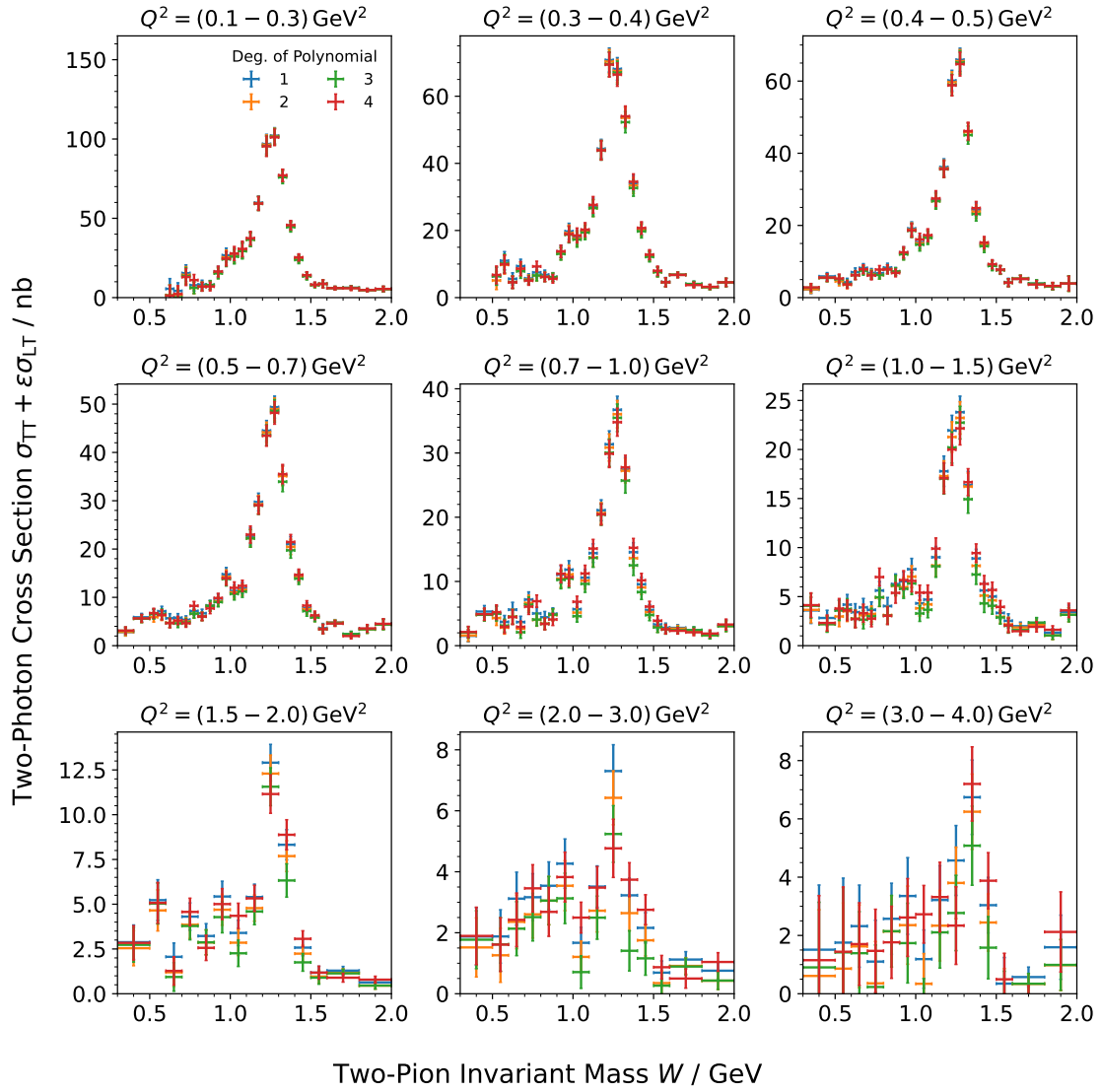


Figure 5.26: The extracted integrated two-photon cross section for different background functions.

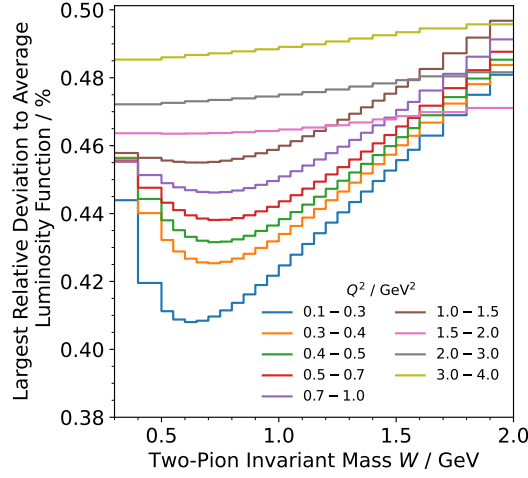


Figure 5.27: Maximum deviation of any model from the average luminosity function as a function of mass and momentum transfer.

is found to be below 5%. Therefore, 5% of the relative contribution of the $\gamma\gamma \rightarrow \eta$ Monte Carlo to the total event yield is taken as a systematic uncertainty. The average over all 1000 evaluations of the cross section is used. The contributions are always smaller than 0.03 nb and, thus, negligible.

5.6.7 | Efficiency Correction

Since the reconstruction efficiency is the probability of observing an event, the binomial uncertainty is used. The error therefore depends on the statistics of the signal-channel Monte Carlo simulation. The contributions are summarized in Tab. 5.3 and are significantly smaller than any statistical effect.

5.6.8 | Two-Photon Luminosity Function

The used two-photon luminosity function is determined by averaging the three models described in Secs. 5.3 and 2.4.1. The systematic uncertainty of the luminosity function can therefore be estimated from the difference of each model to the average. Again, the average over all 1000 evaluations is used. The maximum deviation of any model from the average is shown in Fig. 5.27. Since the differences are smaller than 0.5% in all bins, this value is used as a conservative estimate for the systematic uncertainty.

5.6.9 | Total Systematic Uncertainty

The total systematic uncertainty is calculated by summing the aforementioned contributions in quadrature. It is summarized in Tab. 5.4. At the $f_2(1270)$ resonance, the systematic uncertainty is below 10% for momentum transfers below 1.5 GeV^2 and for small $|\cos \theta^*|$.

Table 5.4: Absolute total systematic uncertainty of the helicity-angle-integrated and differential two-photon production cross sections. The numbers in the brackets indicate the relative uncertainty at the $f_2(1270)$ mass.

Q^2 / GeV^2	$\Delta(\sigma_{\text{TT}} + \varepsilon\sigma_{\text{LT}}) / \text{nb}$	$\Delta d(\sigma_{\text{TT}} + \varepsilon\sigma_{\text{LT}})/d \cos\theta^* / \text{nb}$
0.1-0.3	1.1-7.6 (6%)	0.9-15.9 (6%-30%)
0.3-0.4	0.8-5.0 (7%)	1.0-7.3 (6%-21%)
0.4-0.5	1.0-4.5 (6%)	0.9-6.3 (6%-22%)
0.5-0.7	0.6-3.3 (6%)	0.6-5.3 (6%-20%)
0.7-1.0	0.5-2.8 (7%)	0.6-4.6 (8%-20%)
1.0-1.5	0.5-2.1 (9%)	0.5-3.9 (9%-25%)
1.5-2.0	0.3-1.4 (11%)	0.3-2.8 (11%-91%)
2.0-3.0	0.4-1.4 (22%)	0.3-3.0 (16%-165%)
3.0-4.0	0.5-2.4 (41%)	0.4-5.3 (25%-121%)

At larger momentum transfers and large $|\cos\theta^*|$, the uncertainty increases due to the interplay with statistical effects and is dominated by the contributions from the applied analysis constraints. The total uncertainty is obtained by combining statistical and systematic uncertainties in quadrature. The final cross section results, including both statistical and total uncertainties, are presented in Figs. 5.28–5.33, compared to the dispersive theory calculations by Danilkin and Vanderhaeghen [258–260].

For the comparison, the theoretical curves, which have been provided in a lookup table that is also used in HADROTOPS, are averaged over the Q^2 bins and, for the differential cross sections, over the two-pion invariant mass bins. The σ_{LT} contribution is multiplied by the ε factor so that the effects of the different luminosity functions are taken into account in both the theoretical curves and the experimental data.

For the helicity-angle-integrated cross section, the theoretical curves describe the data well in the $f_2(1270)$ region. At larger masses, small deviations appear, likely due to heavier resonances not included in the model. More pronounced differences occur below $W < 1 \text{ GeV}$, where resolution effects distort the narrow $f_0(980)$ and discrepancies near threshold suggest limited knowledge of the two-photon coupling of the $f_0(500)$. For the differential cross sections, the deviations are generally larger but follow the same overall pattern as in the integrated case.

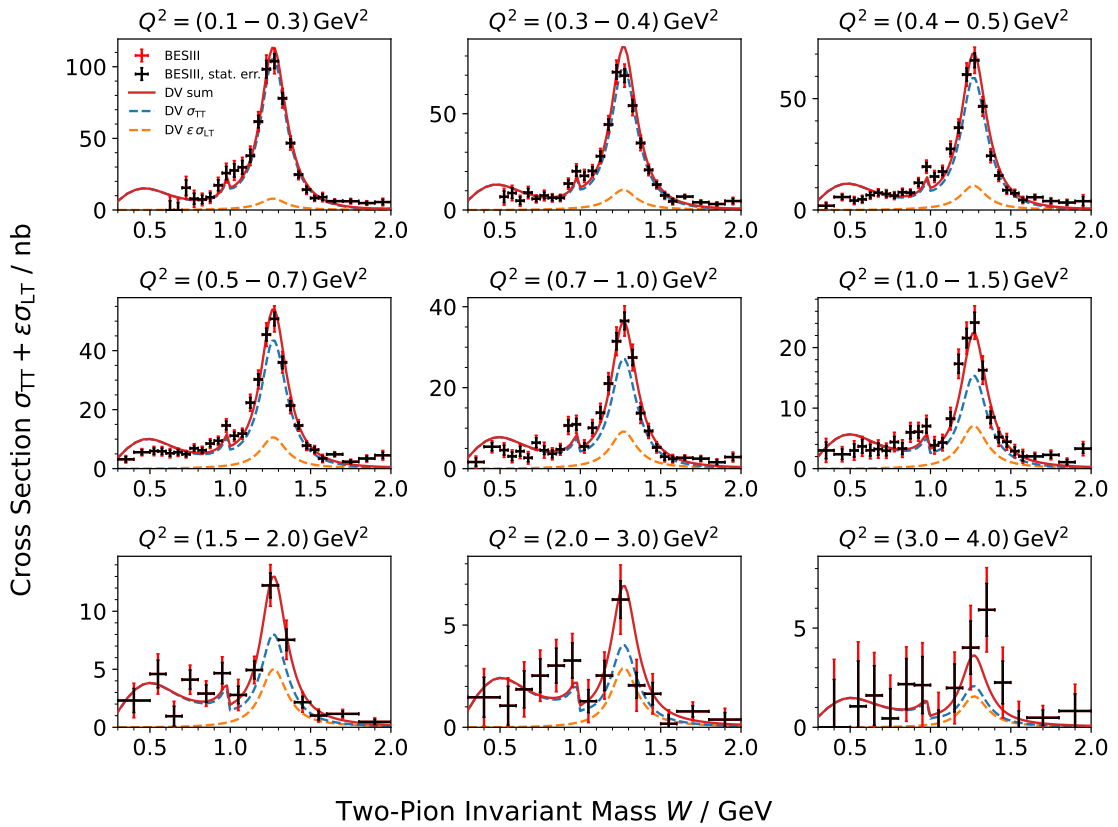


Figure 5.28: The singly virtual integrated two-photon production cross section of neutral pion pairs is shown with total uncertainties (red points) and statistical uncertainties (black points), compared to the theoretical prediction by Danilkin and Vanderhaeghen (DV, red line) [258–260]. The σ_{TT} (blue line) and $\epsilon\sigma_{\text{LT}}$ (orange line) contributions are shown separately.

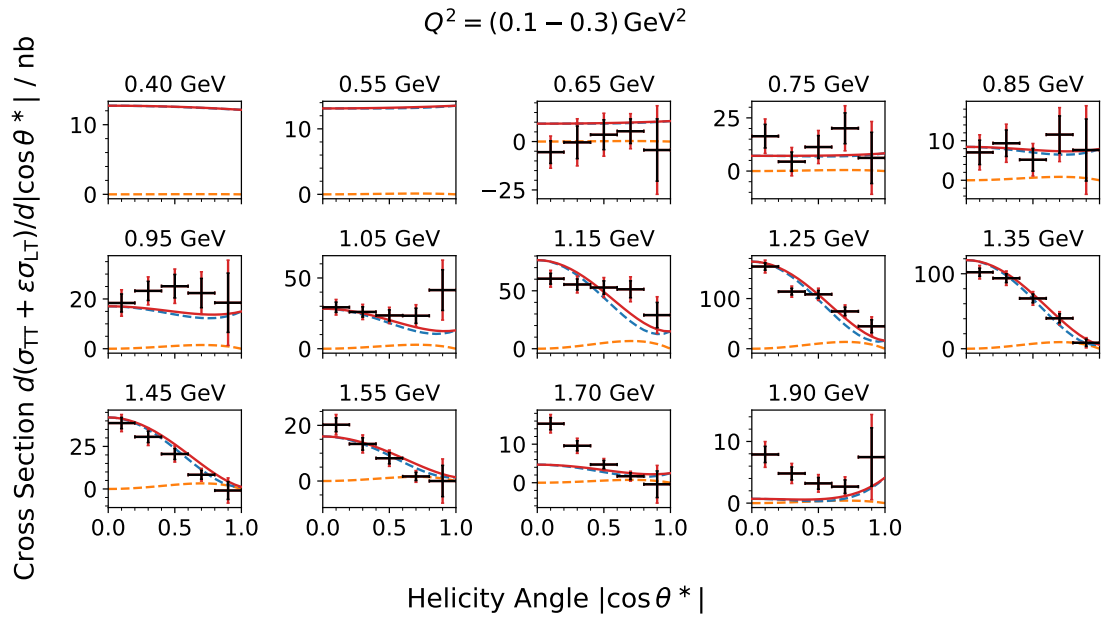


Figure 5.29: Singly virtual differential two-photon production cross section of neutral pion pairs in the virtuality range $Q^2 = (0.1-0.3), \text{ GeV}^2$, shown with total (red points) and statistical uncertainties (black points), compared to the theoretical prediction by Danilkin and Vanderhaeghen (DV, red line) [258–260]. The σ_{TT} (blue line) and $\varepsilon\sigma_{\text{LT}}$ (orange line) contributions are shown separately.

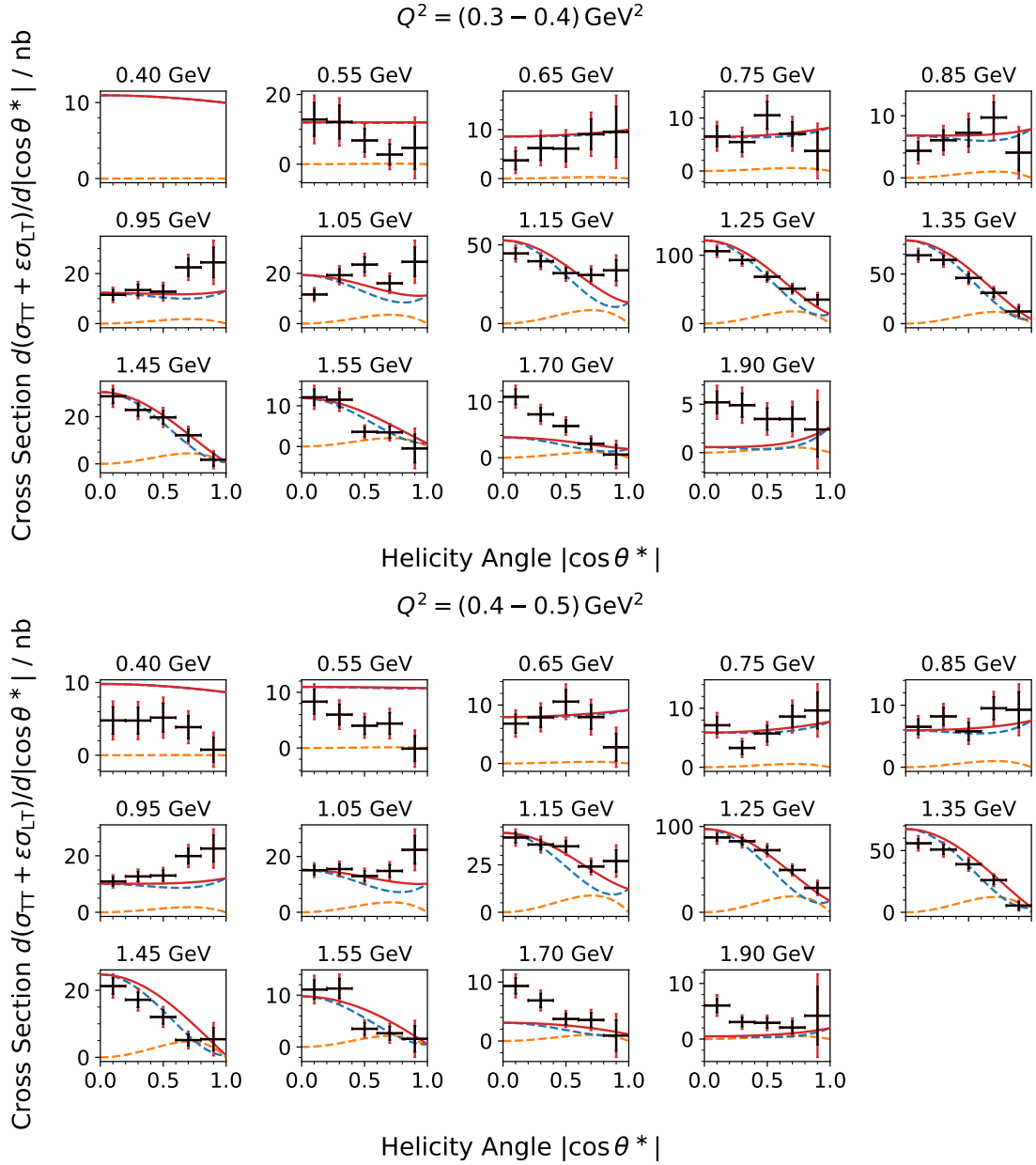


Figure 5.30: Singly virtual differential two-photon production cross section of neutral pion pairs in the virtuality ranges $Q^2 = (0.3-0.4) \text{ GeV}^2$ (top) and $Q^2 = (0.4-0.5) \text{ GeV}^2$ (bottom), shown with total (red points) and statistical uncertainties (black points), compared to the theoretical prediction by Danilkin and Vanderhaeghen (DV, red line) [258–260]. The σ_{TT} (blue line) and $\varepsilon\sigma_{\text{LT}}$ (orange line) contributions are shown separately.

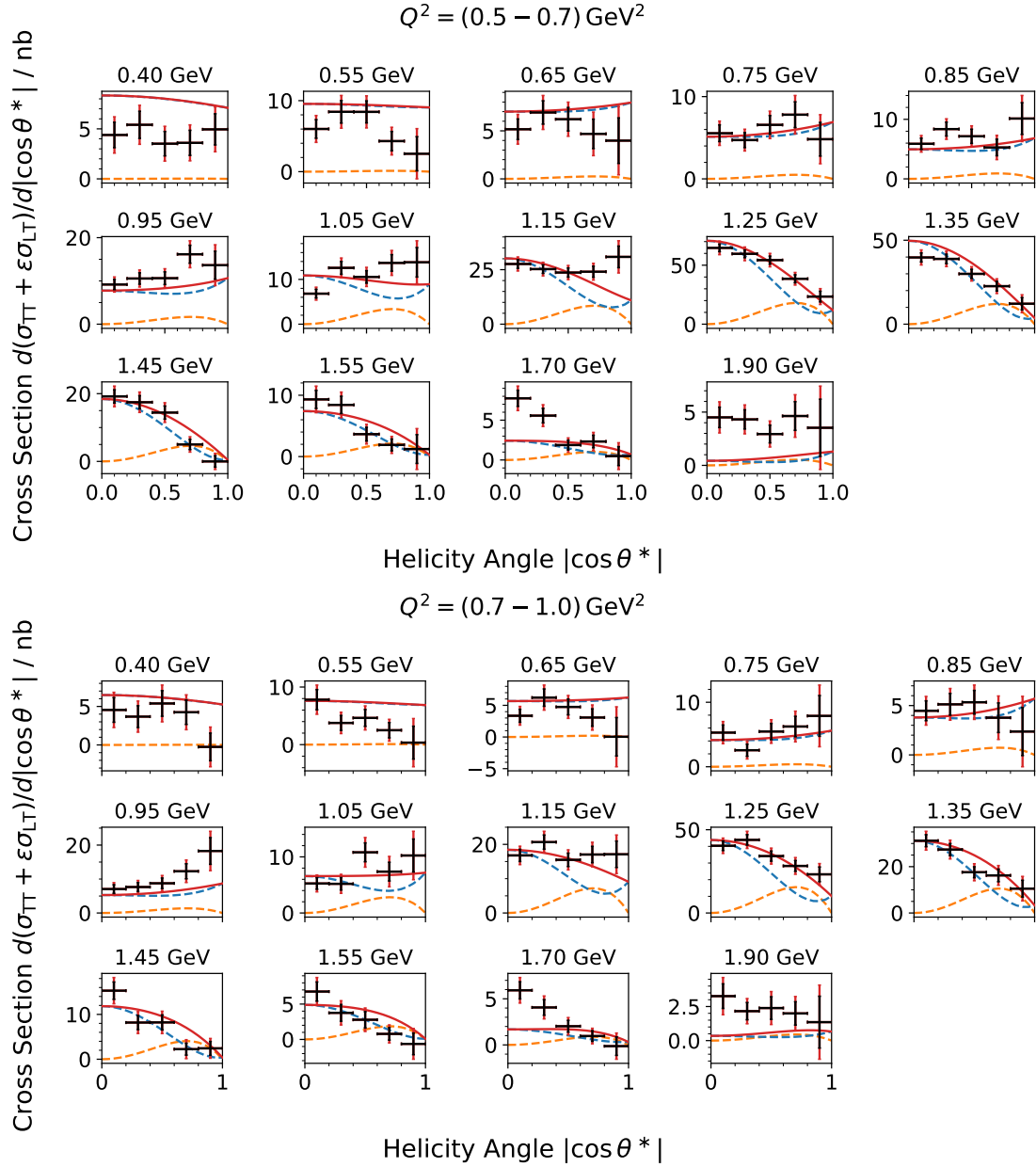


Figure 5.31: Singly virtual differential two-photon production cross section of neutral pion pairs in the virtuality ranges $Q^2 = (0.5-0.7) \text{ GeV}^2$ (top) and $Q^2 = (0.7-1.0) \text{ GeV}^2$ (bottom), shown with total (red points) and statistical uncertainties (black points), compared to the theoretical prediction by Danilkin and Vanderhaeghen (DV, red line) [258–260]. The σ_{TT} (blue line) and $\varepsilon\sigma_{\text{LT}}$ (orange line) contributions are shown separately.

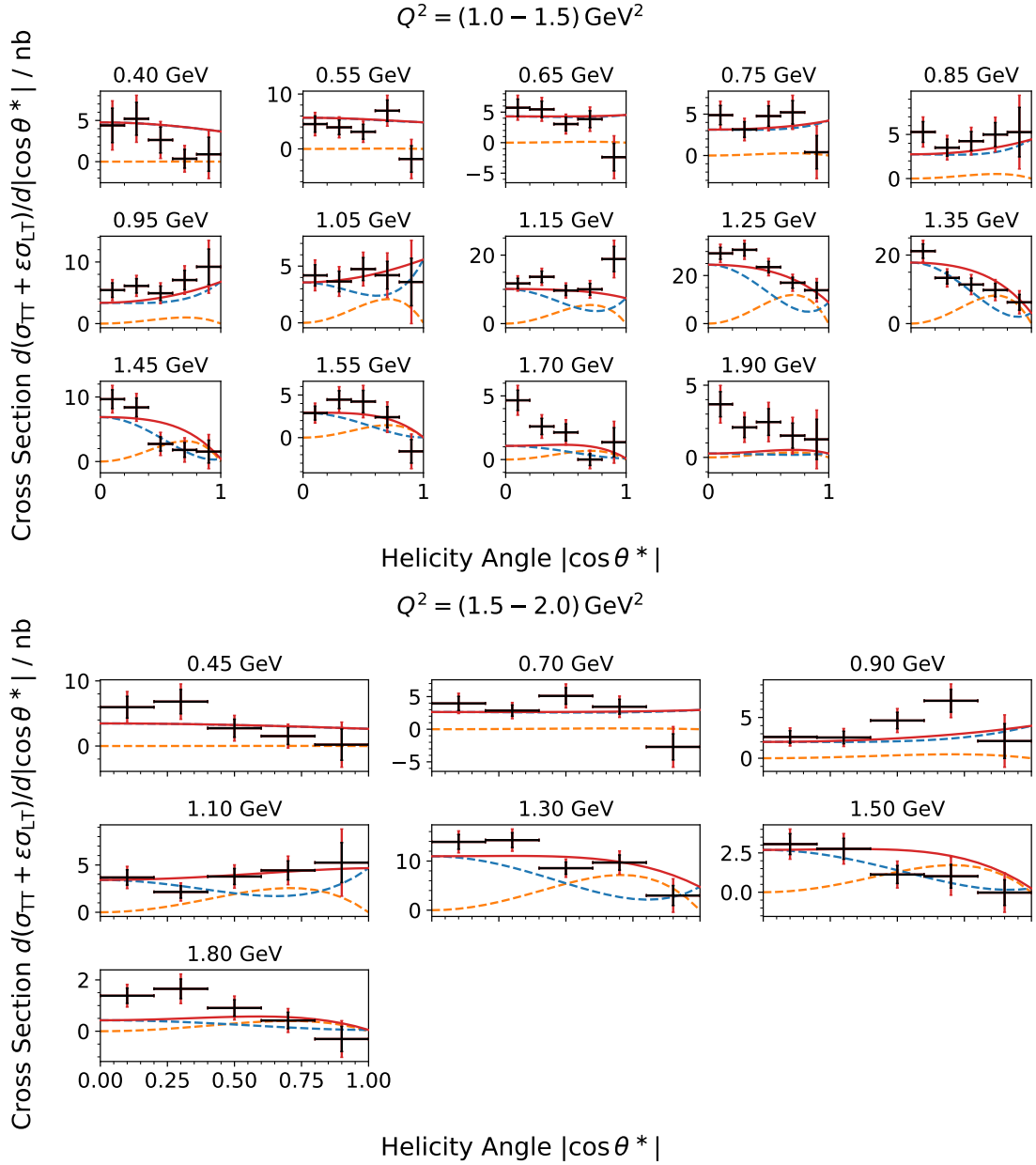


Figure 5.32: Singly virtual differential two-photon production cross section of neutral pion pairs in the virtuality ranges $Q^2 = (1.0-1.5) \text{ GeV}^2$ (top) and $Q^2 = (1.5-2.0) \text{ GeV}^2$ (bottom), shown with total (red points) and statistical uncertainties (black points), compared to the theoretical prediction by Danilkin and Vanderhaeghen (DV, red line) [258–260]. The σ_{TT} (blue line) and $\varepsilon\sigma_{LT}$ (orange line) contributions are shown separately.

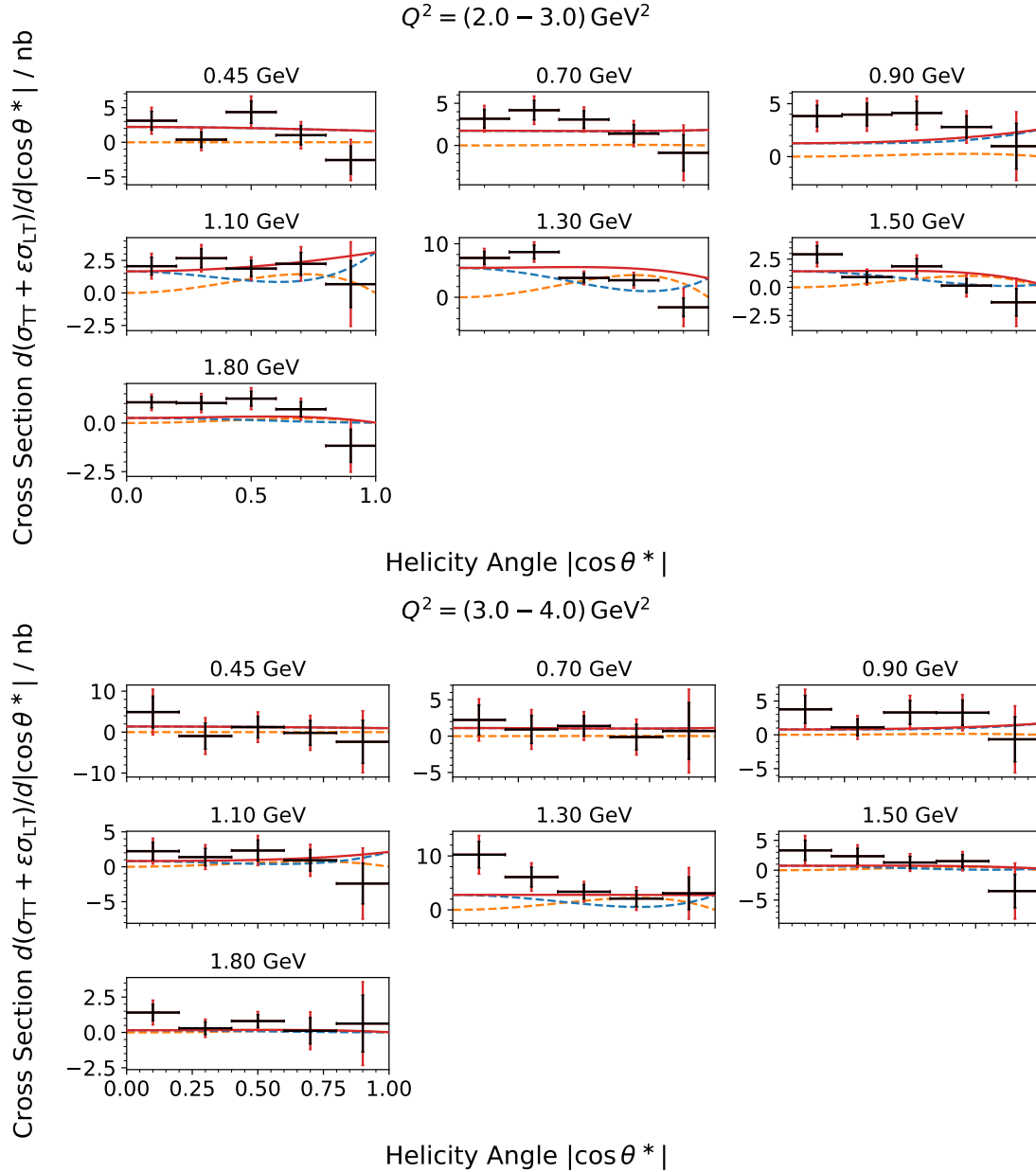


Figure 5.33: Singly virtual differential two-photon production cross section of neutral pion pairs in the virtuality ranges $Q^2 = (2.0-3.0) \text{ GeV}^2$ (top) and $Q^2 = (3.0-4.0) \text{ GeV}^2$ (bottom), shown with total (red points) and statistical uncertainties (black points), compared to the theoretical prediction by Danilkin and Vanderhaeghen (DV, red line) [258–260]. The σ_{TT} (blue line) and $\varepsilon\sigma_{\text{LT}}$ (orange line) contributions are shown separately.

5.7 | Measurement of Transition Form Factors

In the cross sections shown in Figs. 5.28–5.33, the $f_0(980)$ and $f_2(1270)$ resonances are clearly visible. At low invariant masses, a nonzero cross section suggests the presence of the $f_0(500)$ resonance, which has been previously identified in theoretical studies [188, 258, 273].

To extract the electromagnetic transition form factors of these mesons as a function of the momentum transfer Q^2 , a partial-wave analysis (PWA) is performed. The differential cross section is expressed in terms of the meson amplitudes, which depend on Q^2 and are proportional to the transition form factors. Since the transition form factors need to be normalized to their values at $Q^2 = 0$ and the normalization depends on the choice of signal shape, a simultaneous minimum χ^2 fit to the results presented in this chapter and the untagged results from BESIII (preliminary) [199], Belle [198], and Crystal Ball [193] is performed.

Heavier resonances observed in Ref. [199] do not appear to be statistically relevant in this single-tagged study, so the PWA only includes the $f_0(500)$, $f_0(980)$, and $f_2(1270)$ resonances. The untagged data are therefore limited to masses below $W < 1.5$ GeV.

Regarding helicities, scalar mesons contribute only via the S -wave (helicity-0) component. The tensor meson $f_2(1270)$ contributes at $Q^2 = 0$ through helicity-0 and helicity-2 components (D_0 and D_2 waves), with the helicity-2 contribution expected to be dominant [199]. At nonzero momentum transfer, helicity-1 contributions (D_1 waves) are also allowed, since the Landau-Yang theorem [342, 343] does not apply to virtual photons. Consequently, the PWA must include the S -wave contributions of the scalar mesons and the D_0 , D_1 , and D_2 waves of the $f_2(1270)$.

The soft photon zero theorem [259] imposes a specific behavior of the helicity amplitudes with respect to the two-pion invariant mass and the momentum transfer. For the scalar contributions, this dependence is exact, $S \propto (W^2 + Q^2)$, while for the tensor states it is more involved, with one contribution following the same behavior as the S -wave and the others being at least similar [344]. Therefore, the S -wave dependence is applied to all helicity contributions, following the convention of the existing Belle analysis [200]. The singly virtual two-photon cross sections are proportional to $(W^2 + Q^2)^{-1/2}$ [254]. Combining these two factors, a proportionality factor of $(W^2 + Q^2)^{1/2}$ must be applied to each helicity amplitude. Here, the factor is assumed to be identical for all helicity amplitudes and must be normalized to unity at $Q^2 = 0$. Thus, a global factor of $(1 + Q^2/W^2)$ is applied to the cross section. The Belle collaboration introduced a similar factor of $(1 + Q^2/M_r^2)^{1/2}$ to the helicity amplitudes in their measurement of the $f_0(980)$ and $f_2(1270)$ transition form factors [200], where M_r is the mass of the respective resonance. While this is a good approximation for narrow resonances like the $f_0(980)$, it can have a significant effect on broad states such as the $f_0(500)$.

The helicity-1 contributions correspond to the σ_{LT} cross sections, such that the factor ε must be included in the formula. σ_{TT} corresponds to half the sum of the helicity-0 and helicity-2 contributions. In the two-photon center-of-mass frame, the system is purely two-body. Therefore, no azimuthal angle ϕ^* needs to be included in the cross section

formula. The ϕ^* angular dependence introduced and studied in Ref. [200] likely arises from a misunderstanding of the luminosity functions for interference cross sections of the exclusive $e^+e^- \rightarrow e^+e^-\pi^0\pi^0$ (see Eq. (1.28)), which can induce such a dependence but are not directly related to σ_{TT} or σ_{LT} . Consequently, this effect is not included in this analysis. The angular dependence is described using the spherical harmonics Y_0^0 for the S wave, Y_2^0 for D_0 , Y_2^1 for D_1 , and Y_2^2 for D_2 . Taking all of this into account, the two-photon differential cross section is written as

$$\frac{d(\sigma_{\text{TT}} + \varepsilon\sigma_{\text{LT}})}{d|\cos\theta^*|} = 4\pi \left(1 + \frac{Q^2}{W^2}\right) \left(|S Y_0^0 + D_0 Y_2^0|^2 + 2\varepsilon |D_1 Y_2^1|^2 + |D_2 Y_2^2|^2\right). \quad (5.17)$$

An additional factor of 2 arises since the cross section is measured as function of the absolute of $\cos\theta^*$.

5.7.1 | Parametrization of the $f_0(500)$ and $f_0(980)$ Amplitudes

The complex S -wave dependencies are parameterized by the coupled-channel Omnès functions kindly provided by the authors of Refs. [188, 258], which provides a full description of the $\pi\pi$ (and KK) dynamics up to a polynomial factor in W^2 . The S -channel amplitude is given by

$$S = \sqrt{\beta_\pi} \left((a + bW^2) \Omega_{11}(W^2) + (c + dW^2) \Omega_{12}(W^2) \right), \quad (5.18)$$

where Ω_{11} and Ω_{12} denote the the Omnès functions associated with the $f_0(500)$ and $f_0(980)$ intermediate states, and the pion velocity is given by $\beta_\pi = \sqrt{1 - 4m_\pi^2/W^2}$.

The transition form factors are not parameters that are directly determined by the fit; they can, however, be obtained from the S -wave amplitudes at the respective pole masses. The transition form factors of the involved resonances are given by the ratio of the S -wave amplitudes at the respective poles [344]:

$$\frac{|F_{f_0}(Q^2)|}{|F_{f_0}(0)|} = \frac{|S(W^2 = s_{f_0}, Q^2)|}{|S(W^2 = s_{f_0}, 0)|}. \quad (5.19)$$

The poles of $f_0(500)$ and $f_0(980)$ are given by

$$\begin{aligned} \sqrt{s_{f_0(500)}} &= (0.458 - 0.256i) \text{ GeV} \\ \sqrt{s_{f_0(980)}} &= (0.993 - 0.021i) \text{ GeV} \end{aligned}$$

and the Omnès functions evaluated at the poles are [188, 344]

$$\begin{aligned} \Omega_{11}(s_{f_0(500)}) &= +0.797 - 0.406i \\ \Omega_{12}(s_{f_0(500)}) &= -0.020 - 0.099i \\ \Omega_{11}(s_{f_0(980)}) &= +0.679 - 0.194i \\ \Omega_{12}(s_{f_0(980)}) &= -1.095 - 0.261i \end{aligned} .$$

5.7.2 | Parametrization of the $f_2(1270)$ Amplitude

The helicity λ amplitude of the $f_2(1270)$ is modeled using a relativistic Breit-Wigner distribution [200]

$$D_\lambda^{f_2(1270)} = F_{f_2(1270)}^\lambda(Q^2) \sqrt{\frac{8\pi(2J+1)m_{f_2(1270)}}{W}} \frac{\sqrt{\Gamma_{\text{tot}}(W)\Gamma_{\gamma\gamma}(W)\text{Br}(\pi^0\pi^0)}}{m_{f_2(1270)}^2 - W^2 - im_{f_2(1270)}\Gamma_{\text{tot}}(W)} . \quad (5.20)$$

The energy dependent width is given by

$$\Gamma_{XX}(W) = \Gamma_{f_2(1270)}\text{Br}(XX) \left(\frac{q_X(W)}{q_X(m_{f_2(1270)})} \right)^{2J+1} \frac{D_2(q_X(W)r_R)}{D_2(q_X(m_{f_2(1270)})r_R)} \quad (5.21)$$

with the center-of-mass momentum

$$q_X(W)^2 = W^2/4 - m_X^2 \quad (5.22)$$

and the Blatt-Weisskopf barrier factor [345]

$$D_2(x) = \frac{1}{9 + 3x^2 + 4x^4} . \quad (5.23)$$

The effective range of the interaction is assumed to be $r_R = 5 \text{ GeV}^{-1}$. The total width is written as

$$\Gamma_{\text{tot}}(W) = \sum_X \Gamma_{XX}(W) + \Gamma_{\text{others}}(W) \quad (5.24)$$

with

$$\Gamma_{\text{others}}(W) = \Gamma_{f_2(1270)} \left(1 - \sum_X \text{Br}(XX) \right) \frac{W^2}{m_{f_2(1270)}^2} . \quad (5.25)$$

The branching ratios $\text{BR}(\pi\pi) = 0.877$, $\text{BR}(KK) = 0.026$, and $\text{BR}(\eta\eta) = 0.003$ are fixed to Ref. [275]; the radiative width $\Gamma_{\gamma\gamma} = 2.6 \text{ keV}$ is fixed to the preliminary BESIII results [199]. The total width and mass of the resonance are fitted to account for any resolution effects.

The helicity form factors must fulfill

$$\sum_\lambda \left(F_{f_2(1270)}^\lambda \right)^2 = \left(F_{f_2(1270)}^{\text{tot}} \right)^2 . \quad (5.26)$$

To accommodate this normalization in the fit function, the helicity form factors are written as

$$F_{f_2(1270)}^{\lambda=0} = \sqrt{\frac{r_0}{1+r_0+r_1}} F_{f_2(1270)}^{\text{tot}} \quad (5.27)$$

$$F_{f_2(1270)}^{\lambda=1} = \sqrt{\frac{r_1}{1+r_0+r_1}} F_{f_2(1270)}^{\text{tot}} \quad (5.28)$$

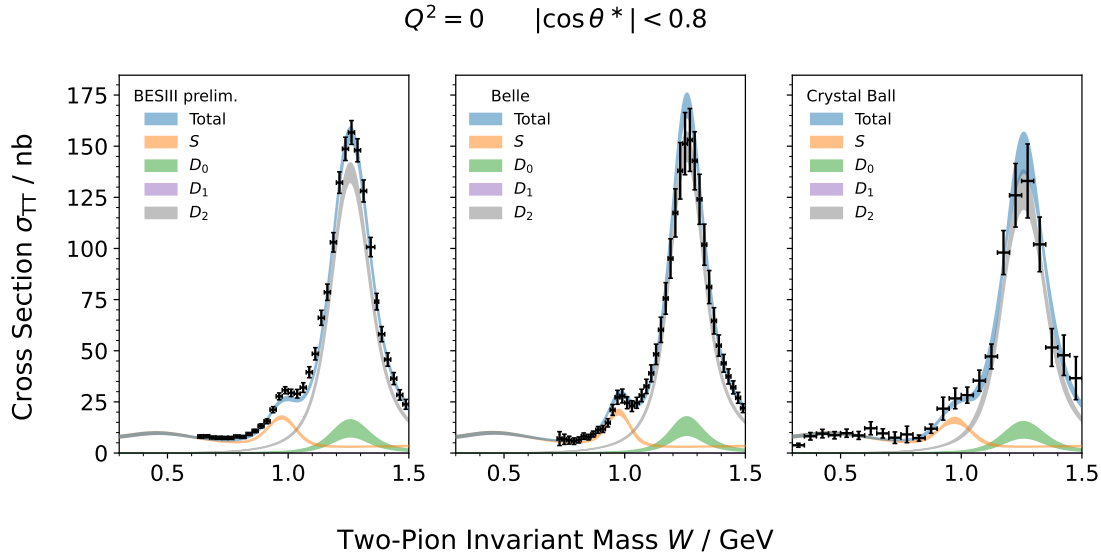


Figure 5.34: Comparison of the fit results (blue shaded area) and the S (orange), D_0 (green), and D_2 (grey) partial waves to the integrated untagged data by BESIII (left panel) [199], Belle (central panel) [198], and Crystal Ball (right panel) [193]. The curves in the three panels represent the same fit result; any differences originate exclusively from the distinct smearing parameters employed for each experiment.

$$F_{f_2(1270)}^{\lambda=2} = \sqrt{\frac{1}{1+r_0+r_1}} F_{f_2(1270)}^{\text{tot}} \quad (5.29)$$

with the parameters r_0 and r_1 , which may be zero or any positive number. The latter parameter, r_1 , must be zero at $Q^2 = 0$, as enforced by the Landau-Yang theorem [342, 343]. The form factor $F_{f_2(1270)}^{\text{tot}}(Q^2 = 0)$ is not fixed to unity but determined from the fit to the untagged data to gauge the single-tagged results. The helicity $\lambda = 0$ amplitude is multiplied by a factor $e^{i\phi_{D_0}}$ to account for possible interference with the scalar resonances.

5.7.3 | Resolution Effects

In both the single-virtual and the untagged measurements, the resolution effects are larger than the width of the $f_0(980)$. To accommodate this effect, the cross-section function is numerically convolved with a Gaussian distribution. For the BESIII single- and untagged measurements, a combined smearing parameter is used, while the Belle and Crystal Ball measurements each have their own smearing parameter. All smearing parameters are determined by the fit.

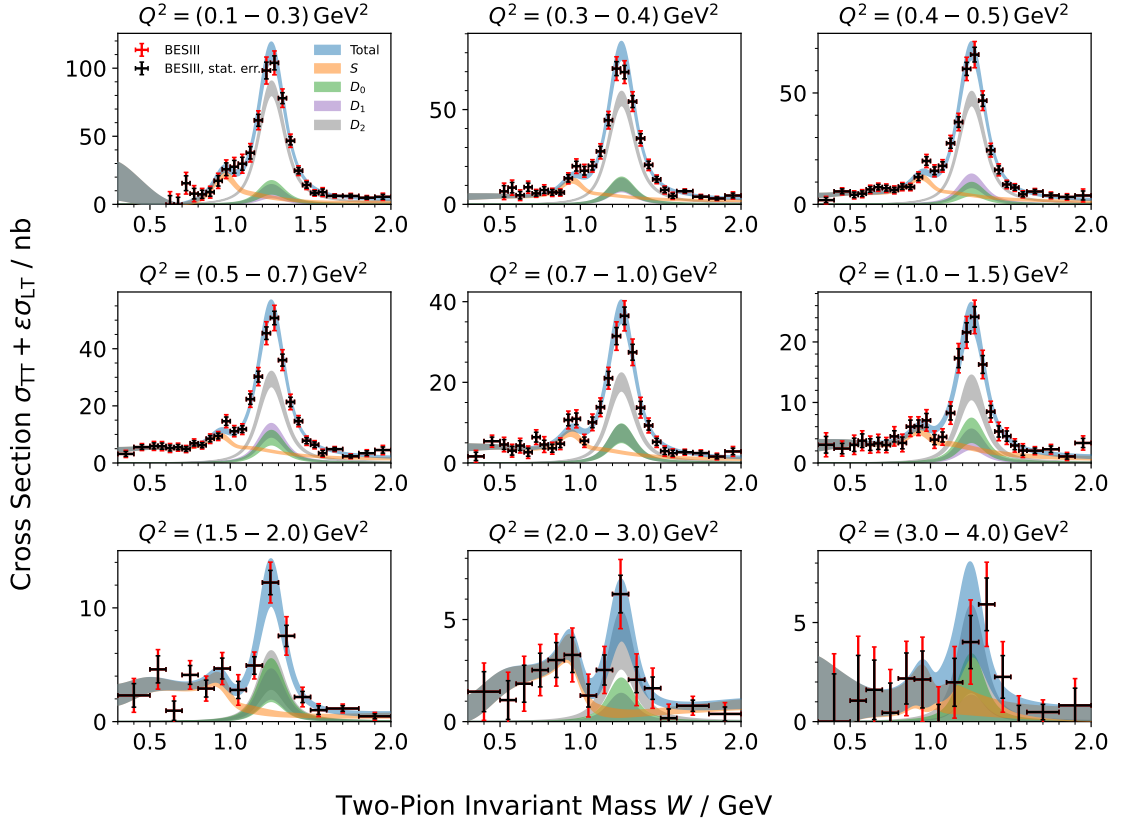


Figure 5.35: Comparison of the fit results (blue shaded area) and the S (orange), D_0 (green), D_1 (violet), and D_2 (grey) partial waves to the integrated singly virtual BESIII data.

5.7.4 | Fit Results

The fit converges with a minimum at $\chi^2/\text{n.d.f.} = 736/1449$, indicating an excellent description of the data. The unusually small $\chi^2/\text{n.d.f.}$ value arises from the large number of degrees of freedom contributed by the untagged Belle data, which, despite their very high statistics, have relatively large uncertainties that appear to be overestimated and are dominated by systematic effects. The projection of the best-fit result to the untagged data is shown in Fig. 5.34. All structures are well described, including the $f_0(980)$, which is significantly distorted by smearing effects. The results at $Q^2 = 0$ are primarily determined by the Belle measurement, which provides more than 700 data points. The non-differential BESIII and Crystal Ball measurements contribute only marginally to the χ^2 in the $f_0(980)$ and $f_2(1270)$ mass region, although they are crucial for determining the signal strength of the $f_0(500)$ at zero virtuality, as they cover lower masses than Belle, and for determining the smearing parameter for the BESIII single-tag measurement. The apparent discrepancies between the BESIII, Belle, and Crystal Ball measurements can be fully resolved by

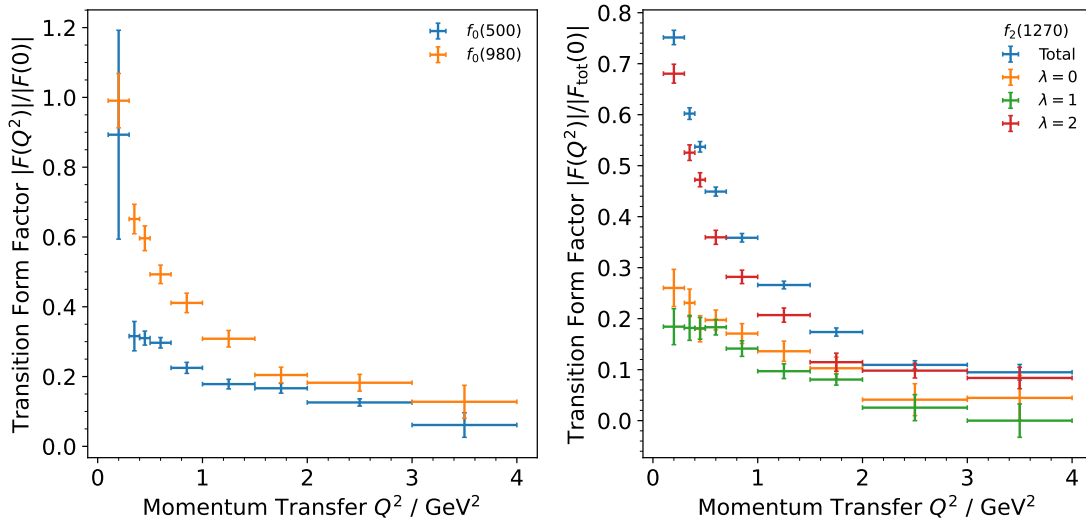


Figure 5.36: Transition form factors of $f_0(500)$ and $f_0(980)$ as a function of the momentum transfer Q^2 , normalized to their values at $Q^2 = 0$ (left), and the total form factor of $f_2(1270)$ together with its helicity contributions as a function of the momentum transfer Q^2 , normalized to the total form factor at $Q^2 = 0$ (right).

accounting for experiment-specific smearing parameters in the fit. The obtained smearing parameters are $\sigma = (49.0 \pm 2.5) \text{ MeV}$ for the BESIII results, $\sigma = (38.5 \pm 4.0) \text{ MeV}$ for the Belle measurement, and $\sigma = (56.5 \pm 7.0) \text{ MeV}$ for the data provided by the Crystal Ball collaboration.

The equivalent plots for the single-tagged measurement presented in this work are shown in Fig. 5.35 and, in the appendix, in Figs. B.1–B.5. All structures are well described, including the decrease of all amplitudes with increasing Q^2 . The bins at large $|\cos \theta^*|$ contribute very little to the χ^2 , with the dominant contribution arising from the bin with $|\cos \theta^*| < 0.6$. In particular, the $0.6 < |\cos \theta^*| < 0.8$ bin remains important for constraining the helicity contributions of the $f_2(1270)$.

The resulting transition form factors are shown in Fig. 5.36. The $f_0(500)$ and $f_0(980)$ form factors show different Q^2 behavior, indicating a different internal structure. At $Q^2 < 0.3 \text{ GeV}^2$, the $f_0(500)$ form factor has a very large uncertainty due to the poor reconstruction efficiency and the resulting limited statistics at small two-pion invariant masses at small virtualities. This is the first measurement of the $f_0(500)$ transition form factor and the first measurement of the $f_0(980)$ transition form factor for $Q^2 < 3 \text{ GeV}^2$.

The extracted form factors of the $f_2(1270)$, particularly the total form factor and the helicity-2 component, are determined more precisely due to the large signal strength of the $f_2(1270)$ compared to the scalar particles. As expected from measurements of the helicity contributions to the $f_2(1270)$ radiative widths [199], the helicity-2 contribution dominates

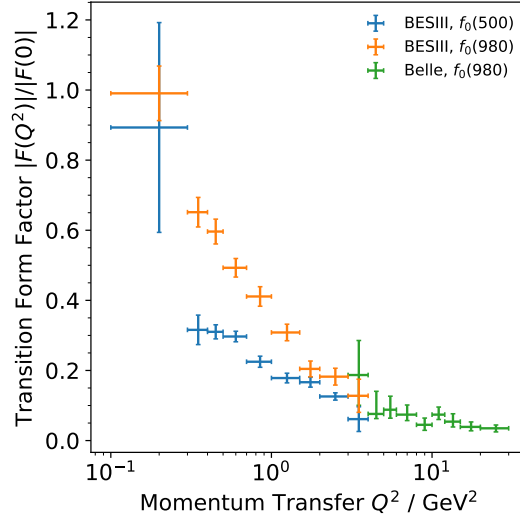


Figure 5.37: Comparison of the extracted $f_0(500)$ (blue) and $f_0(980)$ (orange) transition form factors as a function of the momentum transfer Q^2 with the results from Belle [200] (green). The transition form factors are normalized to their values at $Q^2 = 0$.

the total form factor across the entire momentum transfer range. Larger fluctuations are observed in the helicity-0 and helicity-1 contributions due to limited statistics. The expected drop of the helicity-1 contribution to zero at small virtualities, as required by the Landau-Yang theorem, is not observed within the measured Q^2 range.

The results for the $f_0(980)$ and $f_2(1270)$ transition form factors can be compared to the previous measurements by the Belle collaboration [200], which were performed at significantly larger Q^2 due to the higher electron–positron center-of-mass energy. The lowest- Q^2 Belle data point, however, coincides with the highest- Q^2 BESIII measurement, allowing for a limited comparison. The corresponding plots are shown in Figs. 5.37 and 5.38. Overall, the measurements of all form factors are in good agreement.

5.8 | Summary of the Study of the $\gamma\gamma^* \rightarrow \pi^0\pi^0$ Cross Section

In this chapter, the (differential) cross section of the process $\gamma\gamma^* \rightarrow \pi^0\pi^0$ was measured, and the electromagnetic transition form factors of the $f_0(500)$, $f_0(980)$, and $f_2(1270)$ resonances were extracted from the data. The measurement spans the photon virtuality range $Q^2 = (0.1-4.0) \text{ GeV}^2$, which is particularly relevant for improving the precision of the Standard Model prediction of the hadronic Light-by-Light contribution to the anomalous magnetic moment of the muon a_μ^{HLbL} .

The systematic uncertainty of the integrated cross section in the $f_2(1270)$ mass region remains below 10 % for photon virtualities below 1.5 GeV^2 . At higher virtualities, in other

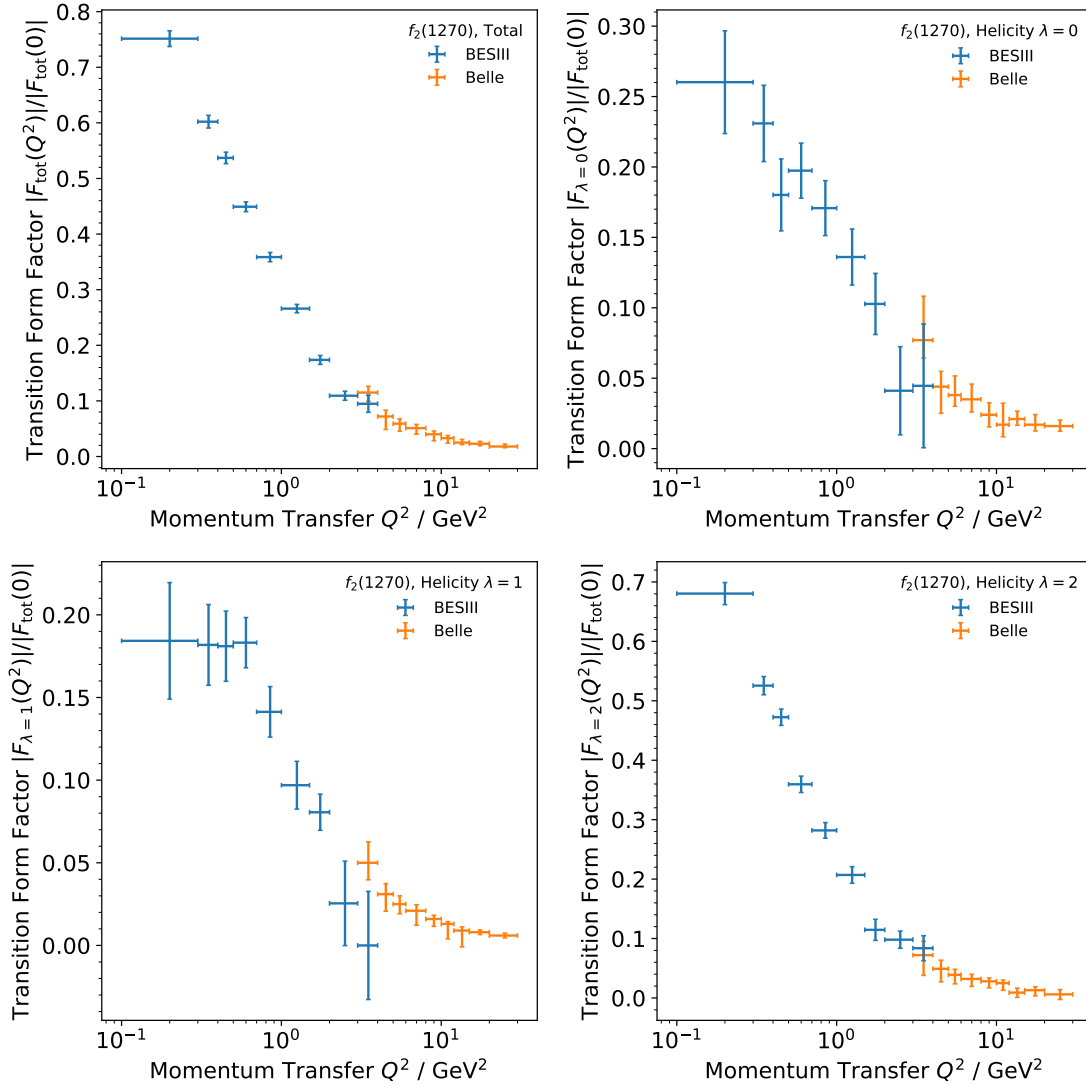


Figure 5.38: Comparison of the extracted $f_2(1270)$ transition form factor (blue) as a function of the momentum transfer Q^2 with the results from Belle [200] (orange). The total form factor (upper left), the helicity-0 contribution (upper right), the helicity-1 contribution (lower left), and the helicity-2 contribution (lower right) are presented separately. The transition form factors are normalized to the value of the total transition form factor at $Q^2 = 0$.

mass regions, or for the differential cross section, the uncertainty can be larger. The total uncertainty of the measurement is dominated by statistical effects. With the exception of the $f_0(500)$ mass region, the extracted cross sections are generally well described by the theoretical predictions of Danilkin and Vanderhaeghen [258–260].

The extracted transition form factors of the $f_0(980)$ and $f_2(1270)$ – including the separate helicity components of the latter – are consistent with the available Belle data [200] in the limited region of overlap. The transition form factor of the $f_0(500)$ was determined for the first time.

The numerical results of the two-photon production cross sections, the luminosity function ratio ε , and the extracted transition form factors can be found in the appendix C in tables C.1 to C.19.

6 | Measurement of the $\gamma^*\gamma^* \rightarrow \pi^0\pi^0$ Cross Section from Single Tagged Two-Photon Scattering Events

Contents

6.1	Event Selection and Background Suppression	130
6.2	Background Subtraction	132
6.3	Reconstruction Efficiency	136
6.4	Calculation Two-Photon Luminosity Functions	136
6.5	Extraction of the Two-Photon Production Cross Section	138
6.6	Study of Systematic Uncertainties	139
6.6.1	Integrated Luminosity	139
6.6.2	Electron/Positron Detection Efficiency and Particle Information	139
6.6.3	Pion Detection Efficiency	140
6.6.4	Analysis Conditions	141
6.6.5	Background Description in the Fits of the χ_{3C}^2 Distributions	143
6.6.6	Efficiency Correction	144
6.6.7	Total Systematic Uncertainty	144
6.7	Summary of the Measurement of the $\gamma^*\gamma^* \rightarrow \pi^0\pi^0$ Cross Section	146

The large uncertainty in the tensor contribution to the hadronic Light-by-Light contribution to the muon anomalous magnetic moment, discussed in Sec. 1.2.2.4, arises in part from the limited knowledge of the two-photon couplings of tensor states at arbitrary photon virtualities. In the previous chapter, the transition form factors of the $f_2(1270)$ were measured in a singly virtual configuration for photon virtualities $Q^2 < 4 \text{ GeV}^2$. Currently, no information is available on the doubly virtual two-photon production of tensor states.

In a conventional measurement of the doubly virtual production cross sections and transition form factors, both final-state leptons are detected. However, the relatively large lepton scattering angles θ typically more than 20° required in such a measurement lead to

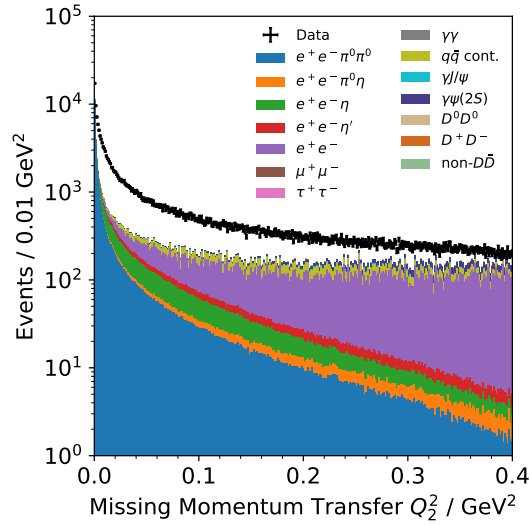


Figure 6.1: Comparison of the distributions of the missing momentum transfer for data (black points) and the stacked Monte Carlo distributions after the initial event selection.

large momentum transfers and, consequently, very small cross sections – and an infeasible measurement with the currently available BESIII data sets.

In Sec. 5.1.5, it is shown that with the applied event selection, which exploits a kinematic fit for single-tagged two-pion production, the missing momentum transfer is reconstructed with a reasonably small resolution. Since the undetected lepton is scattered at small angles, the associated momentum transfer is much smaller, resulting in a larger cross section and therefore higher event yields. This enables a study of the doubly virtual two-photon production of pion pairs using single-tagged events. This study is described in the following chapter.

6.1 | Event Selection and Background Suppression

The event selection closely follows the procedure used for the extraction of singly virtual events discussed in the previous chapter. However, unlike in the singly virtual case, the missing momentum transfer Q_2^2 – determined with improved precision using a three-constraint kinematic fit – is not restricted to small values, but is instead exploited to measure the doubly virtual effective production cross section. The distributions of the missing momentum transfer Q_2^2 in data and Monte Carlo simulations after the selection are shown in Fig. 6.1.

Due to the virtuality dependence of the luminosity functions and the transition form factors, the signal-channel Monte Carlo simulation peaks at small Q_2^2 values, corresponding to the singly virtual regime discussed in the previous chapter. At larger momentum

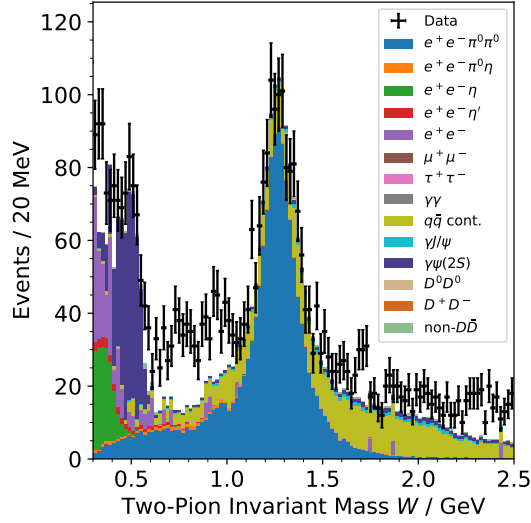


Figure 6.2: Comparison of the distributions of the two-pion invariant mass for data (black points) and the stacked Monte Carlo distributions after applying the $Q_2^2 = (0.08-0.35) \text{ GeV}^2$ and $\chi^2 < 50$ constraints.

transfers, the expected number of signal events decreases significantly. As discussed in Sec. 5.1.5, a substantial smearing of singly virtual events toward larger momentum transfers is observed. Consequently, if the measured Q_2^2 is too small, a strong contamination from singly virtual events is expected in the doubly virtual sample, which must be subtracted.

At large momentum transfers, background contributions from other processes increase rapidly, while the signal yield drops steeply. Therefore, in this measurement, the missing momentum transfer is restricted to the range $Q_2^2 = (0.08-0.30) \text{ GeV}^2$. Using the Monte Carlo simulation, this interval has been identified to be largely free from the contamination of singly virtual events. The fraction of events stemming from singly and doubly virtual two-pion productions drops below 5%.

If one additionally constrains χ_{3C}^2 to values smaller than 50, as in the singly virtual case, a clear signal of the $f_2(1270)$ resonance becomes visible, as shown in Fig. 6.2, which displays the two-pion invariant mass distribution after applying the constraints on Q_2^2 and χ_{3C}^2 . From the Monte Carlo study, one can identify contamination from the $q\bar{q}$ continuum at invariant masses above approximately 0.7 GeV. Close to threshold, there is also a significant contribution from the radiative production of the $\psi(2S)$ resonance and its subsequent decay $\psi(2S) \rightarrow \pi^0\pi^0 J/\psi \rightarrow \pi^0\pi^0 e^+e^-$, as well as from radiative Bhabha scattering and the two-photon production of η and η' .

Overall, the event yield is considerably reduced compared to the singly virtual selection – in the $f_2(1270)$ mass range by a factor of about 15. Since the cross section generally depends on at least four variables – the two-pion invariant mass, both virtualities, and the

helicity angle – only in the $f_2(1270)$ mass region are enough events available to extract the cross section with reasonable precision. At smaller and larger two-pion invariant masses, the background contamination is larger than the expected signal yield. Therefore, in this measurement, the two-pion invariant mass is restricted to the range $W = (1.0-1.5)$ GeV, and only a single mass bin is studied.

The observed event yield after applying the constraints is shown in Fig. 6.3. The momentum transfer spectrum of the tagged lepton, Q_1^2 , has a similar shape to that in the singly virtual case, depicted in Fig. 5.10. Due to the significantly smaller statistics, a measurement for $Q_1^2 > 1$ GeV² is infeasible, due also to the larger background contamination indicated by the Monte Carlo simulations. In the interval $1 \text{ GeV}^2 < Q_1^2 < 2 \text{ GeV}^2$, the signal to background ratio drops below one. Similar to the tagged lepton's momentum transfer, the missing lepton's momentum transfer distribution decreases rapidly. The helicity angle behavior is similar to that observed in the singly virtual case.

Compared to the singly virtual measurement, the sizes of the first Q_1^2 bins used in this measurement are doubled, except for the $Q_1^2 = (0.7-1.0)$ GeV² bin. This choice is made to ensure that a possible combined fit of the data does not need to account for unequal bin boundaries. The Q_2^2 bins are chosen such that the event yield remains roughly equal in all bins: $(0.08-0.15)$ GeV² and $(0.15-0.30)$ GeV². The five equally sized bins in the $|\cos\theta^*|$ distribution are the same as in the singly virtual measurement.

6.2 | Background Subtraction

The remaining background is subtracted from the data using a similar approach as in the measurement of the $\gamma\gamma^* \rightarrow \pi^0\pi^0$ cross section. Again, the χ_{3C}^2 distributions are used to determine the signal event count in each bin. In the singly virtual measurement, a signal and a sideband region were defined, and the number of background events in the signal window is determined from a weighted event count in the sideband region. This approach is modified here due to the contamination from singly virtual events.

The left panel of Fig. 6.4 shows the distribution of the generated missing momentum transfer $Q_{2,\text{gen.}}^2$ of the reconstructed signal Monte Carlo events after all applied analysis constraints. While most events are found roughly in the same range as the initial constraint of $Q_2^2 = (0.08-0.30)$ GeV² – with some edge effects due to limited resolution – there is a remaining contamination from singly virtual events in the selection, as indicated by the pronounced peak toward $Q_{2,\text{gen.}}^2 \approx 0$. It is crucial that this background is subtracted from the final event yield to avoid a significant overestimation of the final cross section. Naturally, the contamination from this background is largest at the smallest Q_2^2 . Since this background varies significantly with the momentum-transfer bin, a global evaluation of the background ratios in the signal and sideband regions, as done for the singly virtual measurement, is not possible. Instead, the χ_{3C}^2 distribution is fitted individually for each bin.

In the right panel of Fig. 6.4, the normalized χ_{3C}^2 distributions of the signal-channel Monte Carlo, for both true doubly virtual and singly virtual events, as well as the background Monte Carlo samples, are compared. The true doubly virtual and singly virtual

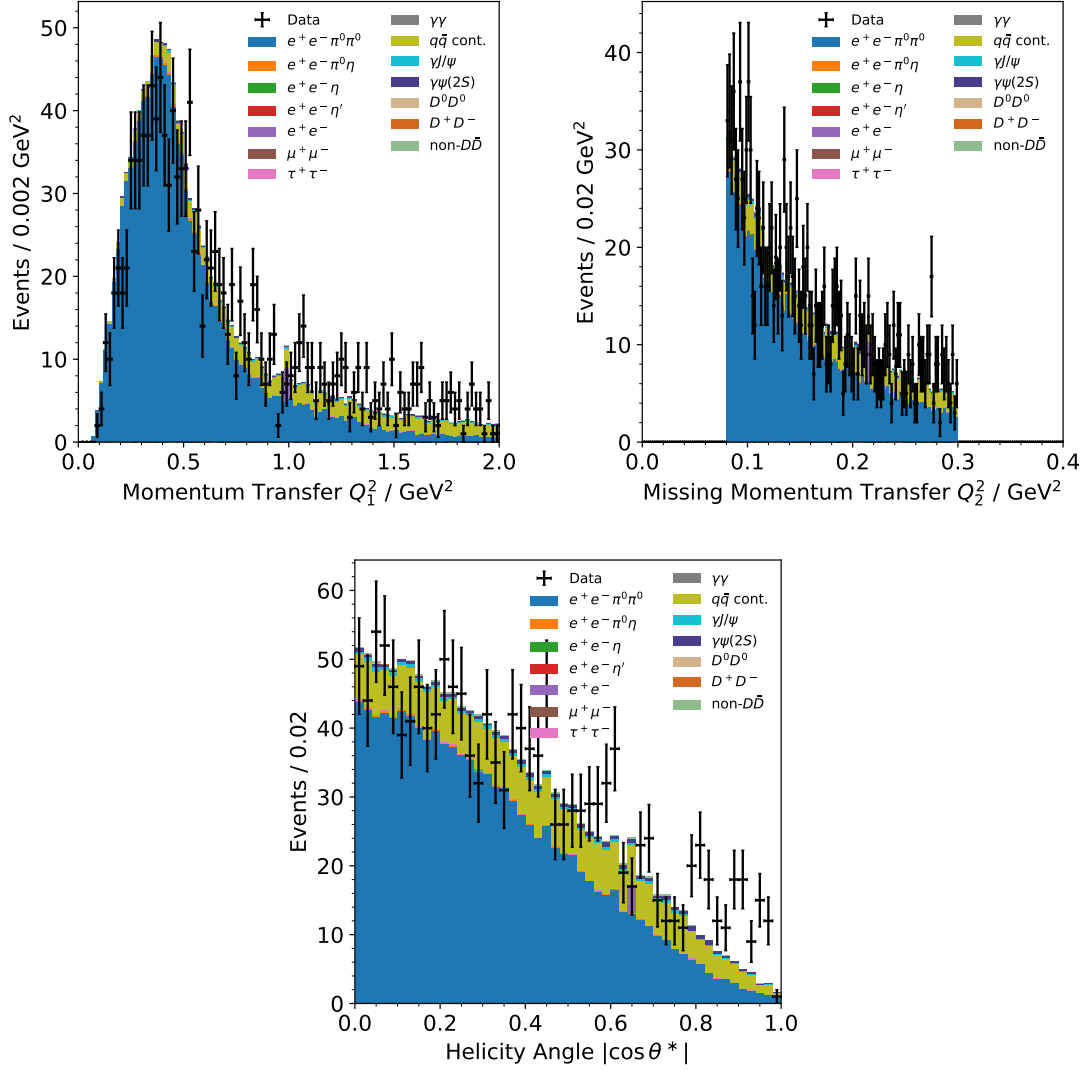


Figure 6.3: Comparison of the distributions of the momentum transfer Q_1^2 (left), the missing momentum transfer Q_2^2 (right), and the pion helicity angle $|\cos \theta^*|$ (bottom) for data (black points) and the stacked Monte Carlo distributions after applying the $Q_2^2 = (0.08-0.35) \text{ GeV}^2$, $\chi^2 < 50$, and $W = (1.0-1.5) \text{ GeV}$ constraints.

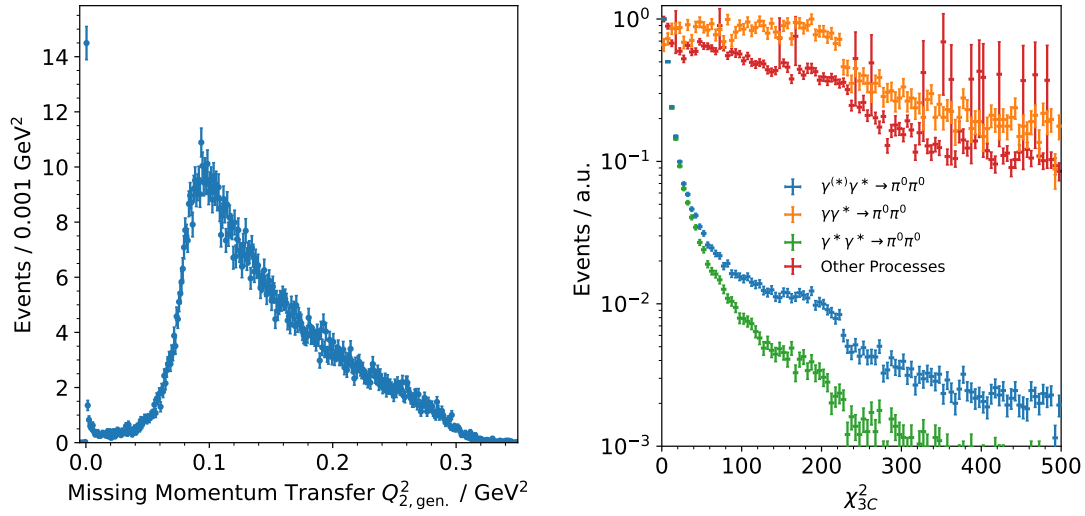


Figure 6.4: Generated distribution of the missing momentum transfer $Q_{2,\text{gen}}^2$ for the selected signal Monte Carlo events (left), and comparison of the normalized χ_{3C}^2 signal shapes (right) for the signal Monte Carlo (blue points), the signal Monte Carlo for real doubly virtual (green) and singly virtual (orange) events, and the background Monte Carlo samples (red).

Monte Carlo events are selected by applying $Q_{2,\text{gen}}^2 > 0.05 \text{ GeV}^2$ and $Q_{2,\text{gen}}^2 < 0.05 \text{ GeV}^2$, respectively. For doubly virtual signal-channel events, a clear accumulation of events at small χ^2 values is observed, as expected from the result of a kinematic fit applied to signal events. For the singly virtual background, this shape is significantly distorted. In this case, the remaining final-state lepton must be scattered at zero angle, so that reconstruction at a nonzero angle – i.e., at finite Q^2 – corresponds to a poor fit quality, resulting in significantly larger χ^2 values. The background Monte Carlo samples, dominated by the $q\bar{q}$ continuum contribution, show the same behavior.

As demonstrated in Fig. 6.5, the shape of the χ_{3C}^2 distributions for the different Monte Carlo samples does not depend significantly on the chosen mass or momentum-transfer bin, with the notable exception of the $\gamma\gamma^* \rightarrow \pi^0\pi^0$ channel. In this case, the distribution exhibits a rapid drop toward zero at larger values of Q_2^2 and therefore remains proportional to the global χ_{3C}^2 spectrum.

To extract the event yield from the χ_{3C}^2 spectra, the different Monte Carlo shapes are fitted to the data using a binned log-likelihood approach, together with the absolute value of a first-order polynomial. The polynomial component models a possible contribution from radiative Bhabha scattering, which is expected to show a smooth behavior, as observed in the singly-virtual measurement (Sec. 5.2). The parameters of the polynomial are later varied to evaluate the systematic uncertainty associated with the background subtraction.

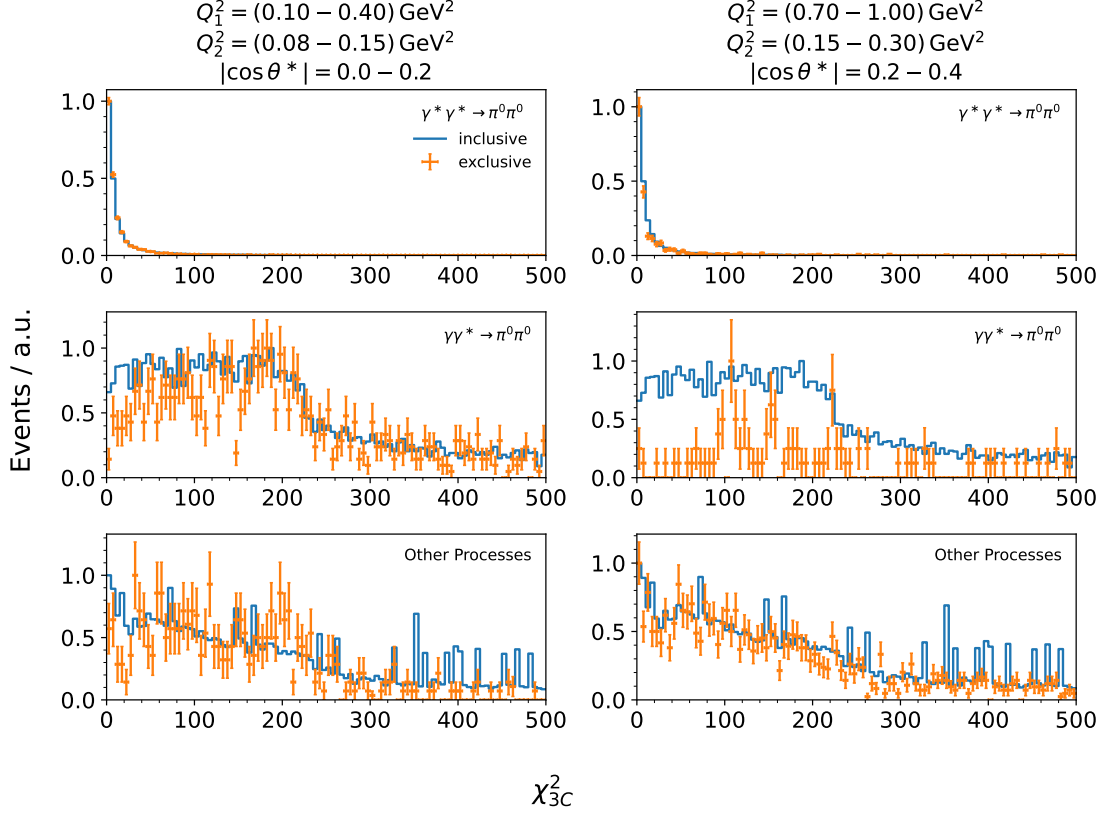


Figure 6.5: Comparison of the χ_{3C}^2 distributions for the $\gamma^* \gamma^* \rightarrow \pi^0 \pi^0$ signal (top), the $\gamma \gamma^* \rightarrow \pi^0 \pi^0$ background constamination (center), and the remaining background Monte Carlo (bottom) in two different momentum-transfer and invariant-mass bins (left and right). The exclusive shapes in each bin (blue) are compared to the corresponding inclusive (orange) χ_{3C}^2 distributions.

Figure 6.6 shows the fit results for two representative bins in momentum transfer and helicity angle. The contributions from the $\gamma \gamma^* \rightarrow \pi^0 \pi^0$ background and the remaining background exhibit similar shapes and are therefore typically strongly correlated. The resulting signal yields in each bin are displayed together with the signal-channel Monte Carlo prediction in Fig. 6.7.

As expected, the event yield decreases with both momentum transfer and the cosine of the helicity angle. In particular, in the bin of the largest momentum transfers, large statistical fluctuations are observed, leading to substantial statistical uncertainties which can reach more than 100%.

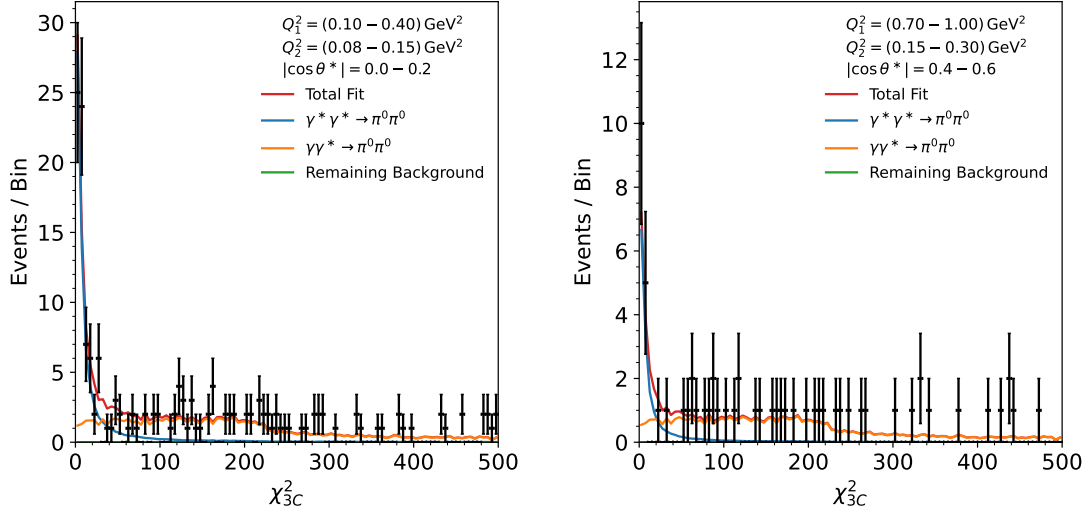


Figure 6.6: Comparison of the χ^2_{3C} distributions of the data with the fitted contributions from the signal and background Monte Carlo samples, together with the polynomial component, for two different momentum-transfer and helicity-angle bins.

6.3 | Reconstruction Efficiency

In order to determine the cross section, acceptance and detector effects need to be corrected for. The reconstruction efficiency – by which the observed event yield must be corrected – is determined by comparing the generated and reconstructed signal Monte Carlo events. The branching fraction of the neutral pion to two photons, $Br(\pi^0 \rightarrow \gamma\gamma) = (98.823 \pm 0.034) \%$ [275], is incorporated into the efficiency, such that the reconstruction efficiency is given by

$$\varepsilon(Q_1^2, Q_2^2, |\cos \theta^*|) = Br(\pi^0 \rightarrow \gamma\gamma)^2 \frac{N_{\text{rec}}(Q_1^2, Q_2^2, |\cos \theta^*|)}{N_{\text{gen}}(Q_1^2, Q_2^2, |\cos \theta^*|)} . \quad (6.1)$$

Since the reconstruction efficiency represents the probability of successful reconstruction, the statistical uncertainty is calculated using binomial statistics. The reconstruction efficiencies are displayed in Fig. 6.8.

6.4 | Calculation Two-Photon Luminosity Functions

The final necessary component to calculate the $\gamma^*\gamma^* \rightarrow \pi^0\pi^0$ cross section is the evaluation of the two-photon luminosity function introduced in Sec. 1.3. The luminosity functions are obtained from the analytical expressions derived in Ref. [257], as discussed in Sec. 5.3. In contrast to the singly virtual measurement, four two-photon cross section components

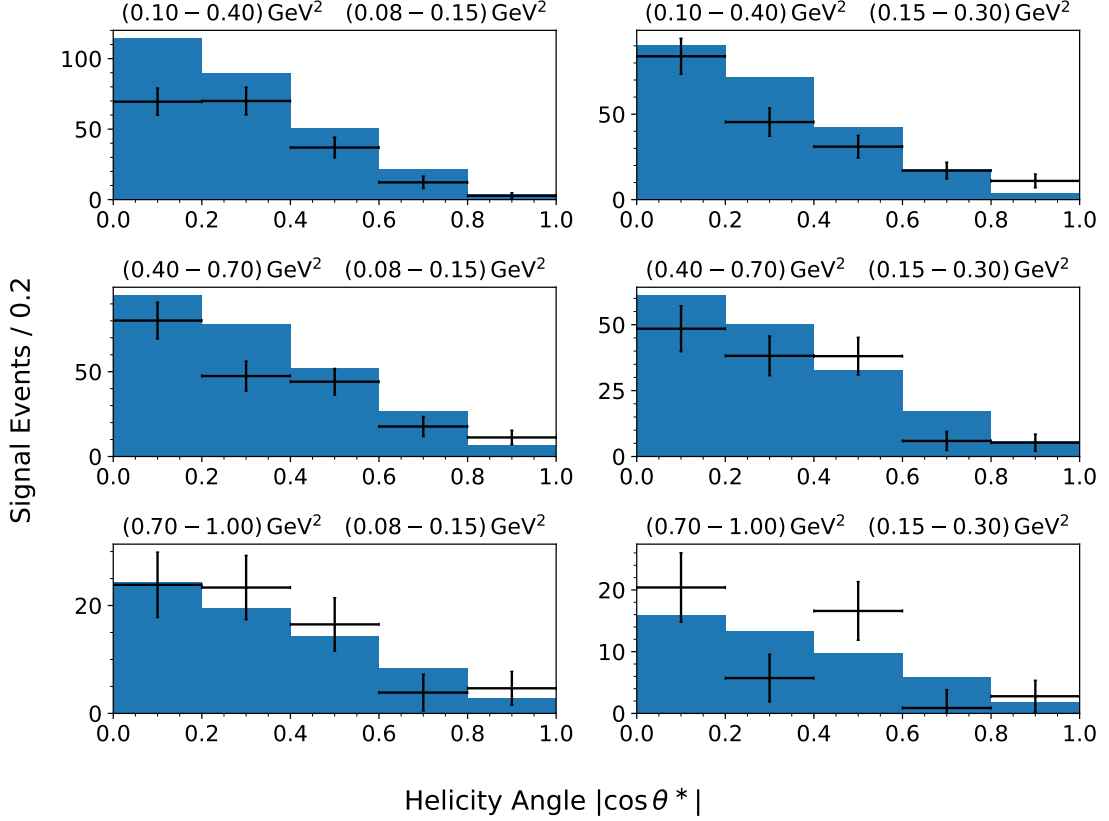


Figure 6.7: Signal event yields extracted from fits to the χ_{3C}^2 spectra in each momentum-transfer and helicity-angle bin, compared to the signal-channel Monte Carlo prediction.

contribute in this case. After integrating over the azimuthal angles $\tilde{\phi}_1$ and $\tilde{\phi}_2$, the contributions from σ_{TT} , σ_{TL} , σ_{LT} , and σ_{LL} remain.

The analytically known doubly virtual luminosity functions are numerically averaged over the momentum-transfer bins and the mass range.

As in the singly virtual case, four different two-photon luminosity functions contribute, and a specific function must be selected to compute the cross section. In this analysis, the luminosity function corresponding to two transversely polarized photons is used, as this contribution is expected to dominate. For the remaining three polarization components, the ratios of their respective luminosity functions are determined relative to the transverse-transverse one. This procedure ensures that the calculation incorporates the most relevant information from all polarization states, while remaining consistent with the dominant σ_{TT} component used in the $\gamma\gamma^* \rightarrow \pi^0\pi^0$ analysis. Therefore, the effective two-photon

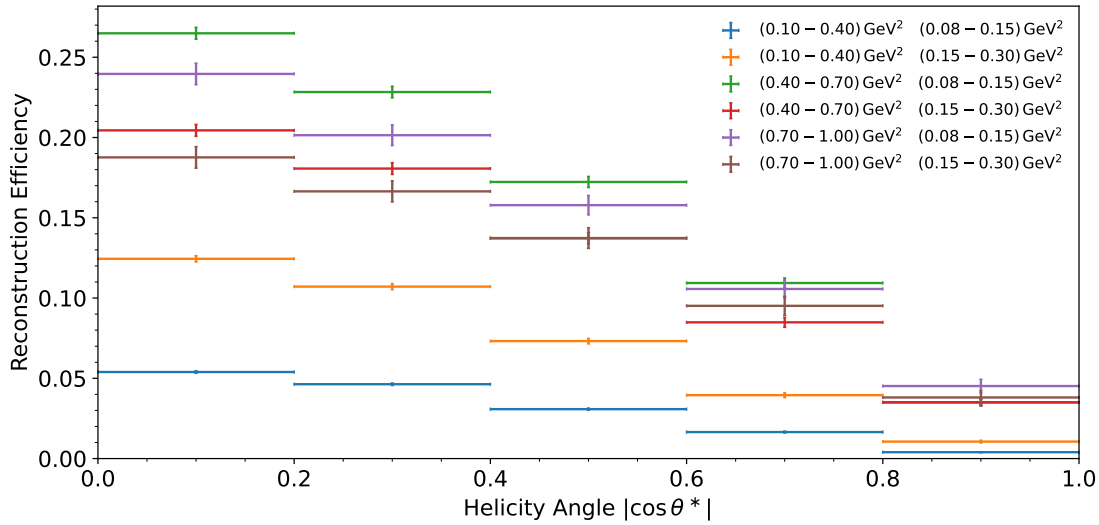


Figure 6.8: Reconstruction efficiency of $\gamma^*\gamma^* \rightarrow \pi^0\pi^0$ events as obtained from the signal Monte Carlo simulation, shown for each momentum-transfer and helicity-angle bin.

production cross section is given by

$$\frac{d\sigma}{d|\cos\theta^*|} \equiv \frac{d(\sigma_{\text{TT}} + \varepsilon_{\text{LT}}\sigma_{\text{LT}} + \varepsilon_{\text{TL}}\sigma_{\text{TL}} + \varepsilon_{\text{LL}}\sigma_{\text{LL}})}{d|\cos\theta^*|},$$

where the factors ε_{AB} ($A, B \in \{\text{T}, \text{L}\}$) represent the ratios of the luminosity functions for AB- and TT-polarized photons.

The numerical results of the luminosity functions and the ratios ε_{LT} , ε_{TL} , and ε_{LL} are summarized in Tab. 6.1. The typical decrease of the luminosity functions with increasing momentum transfer is clearly visible. The change of the ε_{AB} parameters with increasing momentum transfer indicates an increasing relative difference among the different luminosity functions.

6.5 | Extraction of the Two-Photon Production Cross Section

From the extracted number of signal events N , the reconstruction efficiency ε , the bin widths in momentum transfer, two-pion invariant mass, and helicity angle $\Delta_{Q_1^2}$, $\Delta_{Q_2^2}$, Δ_W , and $\Delta_{|\cos\theta^*|}$, the integrated luminosity of the data sample \mathcal{L}_{int} , and the luminosity function $d^3L_{\text{TT}}/dW dQ_1^2 dQ_2^2$, the differential two-photon production cross section is given by

$$\frac{d\sigma}{d|\cos\theta^*|} = \frac{1}{2} \frac{N}{\Delta_{Q_1^2} \Delta_{Q_2^2} \Delta_W \Delta_{|\cos\theta^*|} \varepsilon \frac{d^3L_{\text{TT}}}{dW dQ_1^2 dQ_2^2}}.$$

Table 6.1: Numerical values of the TT polarization luminosity functions and the luminosity function ratios ε_{LT} , ε_{TL} , and ε_{LL} are provided for each momentum-transfer bin. The values are obtained by numerically averaging the analytical expressions given in Ref. [257]. The relative uncertainties from the numerical averaging are smaller than 10^{-6} and are therefore negligible.

Q_1^2 / GeV^2	Q_2^2 / GeV^2	$10^5 \times \frac{d^3 L_{TT}}{dW dQ_1^2 dQ_2^2} / \text{GeV}^{-5}$	ε_{LT}	ε_{TL}	ε_{LL}
0.10–0.40	0.08–0.15	29.66	0.80	0.80	0.61
0.10–0.40	0.15–0.30	14.20	0.80	0.80	0.60
0.40–0.70	0.08–0.15	9.21	0.78	0.78	0.58
0.40–0.70	0.15–0.30	4.58	0.78	0.78	0.58
0.70–1.00	0.08–0.15	4.64	0.77	0.77	0.55
0.70–1.00	0.15–0.30	2.35	0.77	0.77	0.56

The factor $\frac{1}{2}$ is due to the usage of electron and positron tagged events. The differential cross section is shown in Fig. 6.9.

Due to the limited statistics, especially at large momentum transfer regions, significant statistical fluctuations are observed. The statistical uncertainties vary from 12% to more than 100%. In the bin corresponding to the smallest momentum transfers, the decreasing trend of the cross section can be an indication of the expected D -wave behavior.

6.6 | Study of Systematic Uncertainties

In addition to statistical uncertainties, systematic uncertainties arise from the applied analysis conditions and techniques, the particle detection, reconstruction, and identification algorithms, as well as from the determination of the time-integrated luminosity of the data sample.

6.6.1 | Integrated Luminosity

The combined time-integrated luminosity uncertainty for the round03, round04, round15, round16, and round17 $\psi(3770)$ datasets is 0.4%, dominated by systematic effects [75, 313]. This uncertainty is included as the contribution to the systematic uncertainty on the cross section associated with the determination of the integrated luminosity.

6.6.2 | Electron/Positron Detection Efficiency and Particle Information

The differences in the detection efficiencies for electrons and positrons between data and Monte Carlo samples, as well as the impact of the particle identification procedure used in this analysis, are studied using radiative Bhabha scattering events following the method described in Ref. [340]. The efficiency difference between data and Monte Carlo as a function of lepton momentum and polar angle is shown in the left panel of Fig. 6.10,

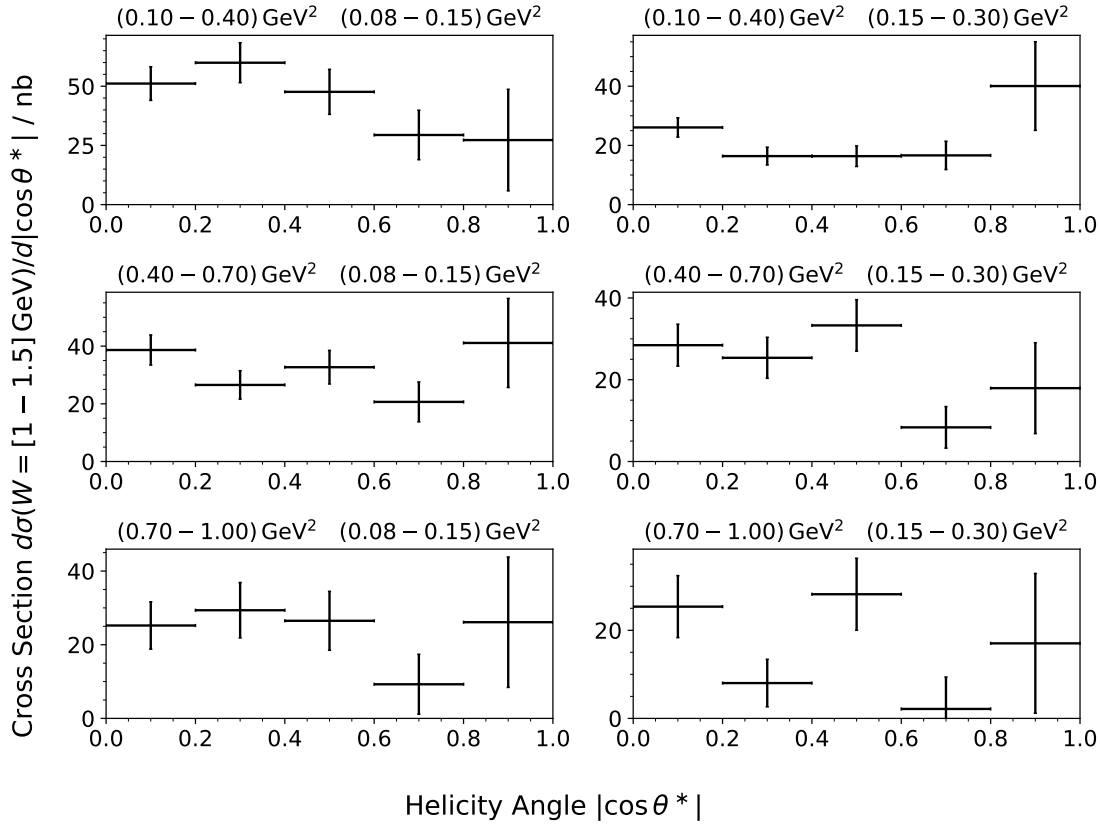


Figure 6.9: Differential $\gamma^*\gamma^* \rightarrow \pi^0\pi^0$ cross section in different momentum-transfer regions (separate panels), shown as a function of the cosine of the pion helicity angle in the two-pion invariant mass range $W = (1.0-1.5)$ GeV. The displayed uncertainties are purely statistical.

while the lepton momentum and polar angle distributions of selected events is presented in the right panel. The event-weighted reconstruction efficiency difference between data and Monte Carlo is determined to be less than 1.4%, which is assigned as the systematic uncertainty on the cross section measurement.

6.6.3 | Pion Detection Efficiency

The pion detection efficiency for the $\sqrt{s} = 3.773$ GeV data has been studied using D^0 decays in Ref. [341], employing selection criteria similar to those used in this work. The data-Monte Carlo efficiency differences were found to be 4% for pion momenta $p < 0.2$ GeV, 2.1% for $0.2 \text{ GeV} < p < 0.4$ GeV, 2.3% for $0.4 \text{ GeV} < p < 0.6$ GeV, 2.6% for $0.6 \text{ GeV} < p < 0.8$ GeV, and 1.8% for $p > 0.8$ GeV. Pion momenta above 1 GeV were not studied; based on the observed trend, a 2.5% difference is assumed for higher momenta. Averaging these values weighted by the observed pion yields, shown in Fig. 5.24,

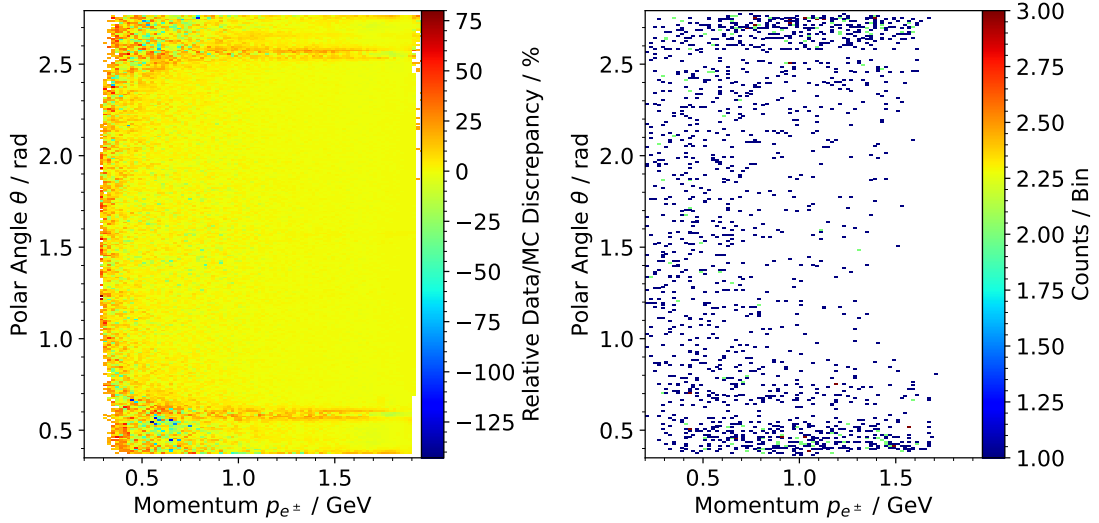


Figure 6.10: Difference in detection efficiency between data and Monte Carlo for electrons and positrons (left, taken from Ref. [340]) and distribution of the selected events (right), shown as a function of the lepton momentum and lepton polar angle.

an average data-Monte Carlo difference of 2.3 % is obtained. Since two pions are detected in this analysis, a systematic uncertainty of 4.6 % is assigned for pion detection.

6.6.4 | Analysis Conditions

The effects on the cross section measurement arising from the choice of fit range in the background subtraction, the number of bins used in the fitted χ_{3C}^2 distribution, and the cut value applied to distinguish singly- from doubly-virtual two-photon fusion events in the signal Monte Carlo sample are evaluated simultaneously. The analysis is repeated 1000 times with randomly varied conditions. Specifically, the fit range of the χ_{3C}^2 spectrum is varied within $\chi_{\text{max}}^2 = 550\text{-}650$, the number of bins is varied between 150 and 250, and the cut-off value in the Monte Carlo samples used to distinguish double and singly virtual events is varied between 0.02 GeV^2 and 0.06 GeV^2 . These ranges are selected to ensure that the effects of statistical fluctuations remain minimal while maintaining sufficiently wide variation intervals, thereby avoiding the introduction of statistical biases into the estimation of the systematic uncertainty.

Figure 6.12 shows the distributions of the observed differential cross section in two representative bins. The spreads obtained from the three individual variations are of comparable magnitude, indicating notable systematic contributions from each source. When all three conditions are randomly varied simultaneously (black points in Fig. 6.12), the resulting distribution is the broadest, though not wider by a factor of three compared to

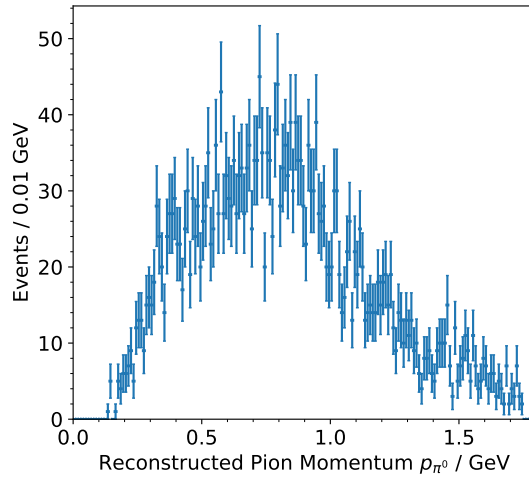


Figure 6.11: Measured π^0 momenta after applying all analysis constraints.

Table 6.2: Relative systematic uncertainties (%) of the differential cross section, obtained from variations in the analysis conditions, for each bin.

Q_1^2 / GeV^2	Q_2^2 / GeV^2	0.0 - 0.2	0.2 - 0.4	$ \cos \theta^* $ 0.4 - 0.6	0.6 - 0.8	0.8 - 1.0
0.10 - 0.40	0.08 - 0.15	3.8	3.5	3.2	6.4	12.6
0.10 - 0.40	0.15 - 0.30	3.0	3.1	4.0	3.7	4.6
0.40 - 0.70	0.08 - 0.15	3.1	3.6	4.6	6.8	4.3
0.40 - 0.70	0.15 - 0.30	3.8	4.7	3.7	12.2	5.7
0.70 - 1.00	0.08 - 0.15	3.9	5.0	6.1	13.4	12.0
0.70 - 1.00	0.15 - 0.30	4.6	15.4	4.7	58.7	15.4

those from the individual variations, suggesting the presence of significant correlations among the sources of uncertainty.

As in the singly-virtual measurement, the central value in each bin is taken as the mean of the 1000 individual measurements. The statistical uncertainty is calculated as the average of the statistical uncertainties from these measurements, which accounts for strong correlations among the individual measurements. The standard deviation of the resulting Gaussian distribution is used to estimate the systematic uncertainty.

In cases where the observed distribution deviates from a Gaussian shape, the standard deviation is still used as a baseline measure of the systematic uncertainty. To account for the non-Gaussian behavior, this uncertainty is conservatively inflated by a factor of two, ensuring that potential deviations are safely included in the systematic error estimate.

The relative uncertainties associated with the analysis conditions are summarized in Tab. 6.2. They range from 3% to nearly 60%, with the largest value appearing in a bin

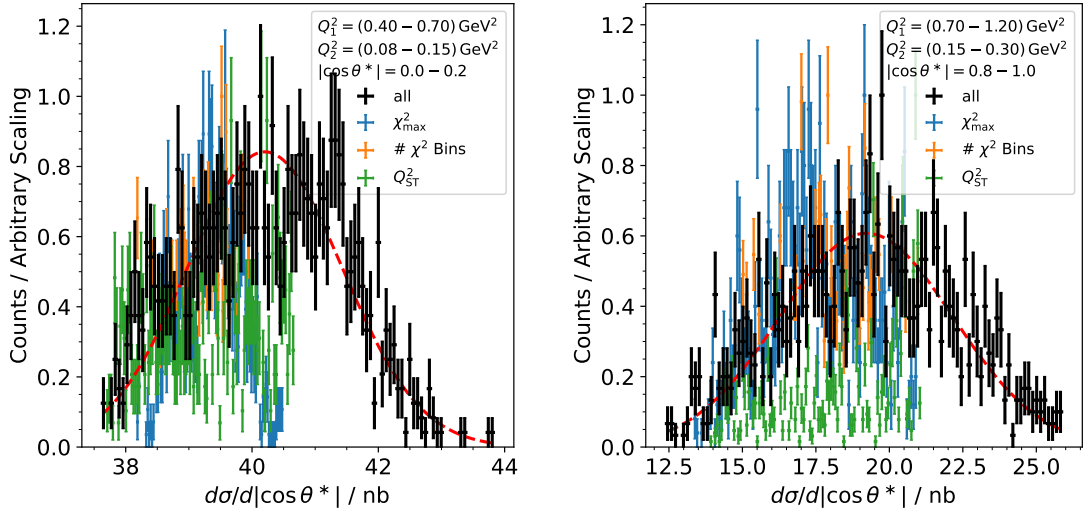


Figure 6.12: Observed variations in the measured cross section for two example bins compared to a Gaussian distribution evaluated using the arithmetic mean and the calculated standard deviation. The black data points represent the distribution obtained when all analysis parameters are varied simultaneously, while the blue, orange, and green points correspond to variations in which only the upper limit of the fitted χ^2_{3C} spectrum, the number of bins in that spectrum, and the virtuality constraint applied in the Monte Carlo sample are varied, respectively.

where the measured cross section is consistent with zero – although most uncertainties are smaller than 15%. In all cases, the statistical uncertainties exceed the systematic uncertainties arising from the analysis conditions.

6.6.5 | Background Description in the Fits of the χ^2_{3C} Distributions

The fit of the χ^2_{3C} distributions, used to estimate the number of signal events in each bin, includes a polynomial to model the radiative Bhabha scattering background. This polynomial was varied from a constant term up to a fourth-order polynomial to assess the systematic effect of this assumption. In all cases, the absolute of the polynomial is fitted to the data.

The resulting cross sections are generally unchanged – indicating only a minor dependence on the choice of fit function. Nevertheless, the standard deviation of the results is used to estimate the systematic uncertainty associated with the signal extraction from the fits to the χ^2_{3C} distributions.

The relative systematic uncertainties associated with the choice of fit function are summarized in Tab. 6.3. Compared to the uncertainties from the analysis conditions and the statistical errors, those from the fit function are generally small. Larger uncertainties are

Table 6.3: Relative systematic uncertainties (%) of the differential cross section arising from the background function used in the fit to the χ_{3C}^2 distributions.

Q_1^2 / GeV^2	Q_2^2 / GeV^2	0.0 - 0.2	0.2 - 0.4	$ \cos \theta^* $ 0.4 - 0.6	0.6 - 0.8	0.8 - 1.0
0.10 - 0.40	0.08 - 0.15	2.1	1.1	0.0	3.0	11.0
0.10 - 0.40	0.15 - 0.30	1.0	0.0	4.0	6.3	5.1
0.40 - 0.70	0.08 - 0.15	1.8	1.3	0.0	0.9	12.8
0.40 - 0.70	0.15 - 0.30	1.2	2.1	4.2	11.3	24.2
0.70 - 1.00	0.08 - 0.15	0.0	1.0	3.5	15.1	12.1
0.70 - 1.00	0.15 - 0.30	0.0	15.7	1.6	45.5	4.9

Table 6.4: Relative systematic uncertainties (%) of the differential cross section arising from the efficiency correction.

Q_1^2 / GeV^2	Q_2^2 / GeV^2	0.0 - 0.2	0.2 - 0.4	$ \cos \theta^* $ 0.4 - 0.6	0.6 - 0.8	0.8 - 1.0
0.10 - 0.40	0.08 - 0.15	1.4	1.6	2.2	3.4	7.8
0.10 - 0.40	0.15 - 0.30	1.6	1.8	2.3	3.7	7.9
0.40 - 0.70	0.08 - 0.15	1.4	1.6	2.0	2.9	5.9
0.40 - 0.70	0.15 - 0.30	1.8	2.0	2.6	3.7	6.5
0.70 - 1.00	0.08 - 0.15	2.8	3.2	3.8	5.2	9.2
0.70 - 1.00	0.15 - 0.30	3.6	4.0	4.7	6.2	11.2

only observed in bins where the measured cross section is consistent with zero.

6.6.6 | Efficiency Correction

The reconstruction efficiency represents the probability of observing an event. Its uncertainty is estimated using the binomial statistics. This uncertainty therefore depends on the statistics of the signal-channel Monte Carlo simulation. The resulting contributions are summarized in Tab. 6.4 and are considerably smaller than the statistical uncertainties and always smaller than 12%.

6.6.7 | Total Systematic Uncertainty

Unlike in the singly-virtual case, no systematic uncertainties arise from the calculation of the luminosity function, as the analytical expressions for the doubly-virtual case are known exactly. Furthermore, no $\gamma\gamma \rightarrow \eta^{(\prime)}$ background subtraction was applied because the mass window is positioned at higher values, and therefore this source does not contribute. The total systematic uncertainty of the differential cross section measurement is thus obtained by summing the contributions discussed in this section in quadrature. The resulting total

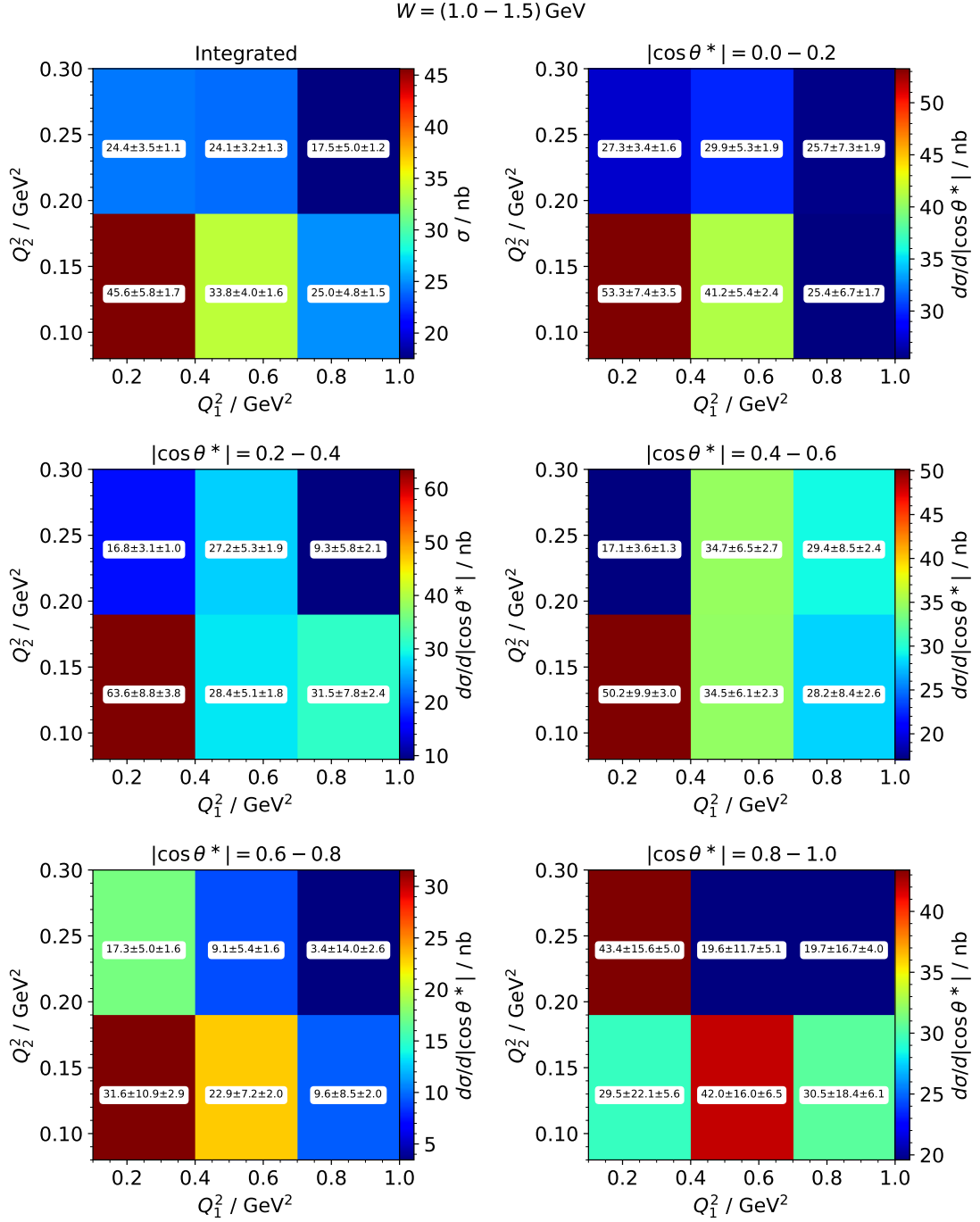


Figure 6.13: Measurement results for the integrated (upper left) and differential (remaining panels) cross sections of the $\gamma^*\gamma^* \rightarrow \pi^0\pi^0$ process in the two-pion invariant-mass range $W = (1.0 - 1.5) \text{ GeV}$, shown as functions of the tagged and untagged lepton momentum transfers Q_1^2 and Q_2^2 . The first uncertainty is statistical and the second is systematic.

Table 6.5: Relative systematic uncertainty (%) of the differential cross section.

Q_1^2 / GeV^2	Q_2^2 / GeV^2	0.0 - 0.2	0.2 - 0.4	$ \cos \theta^* $ 0.4 - 0.6	0.6 - 0.8	0.8 - 1.0
0.10 - 0.40	0.08 - 0.15	6.5	6.1	6.0	9.0	19.1
0.10 - 0.40	0.15 - 0.30	5.7	5.8	7.7	9.3	11.4
0.40 - 0.70	0.08 - 0.15	5.9	6.2	6.8	8.7	15.4
0.40 - 0.70	0.15 - 0.30	6.3	7.2	7.6	17.6	26.1
0.70 - 1.00	0.08 - 0.15	6.6	7.5	9.2	21.3	19.9
0.70 - 1.00	0.15 - 0.30	7.4	22.8	8.2	74.7	20.2

relative uncertainties are summarized in Tab. 6.5. They range from 5.7% to 26.1%, with the exception of one bin showing a much larger uncertainty of 74.7% due to the bin content's consistency with zero. Overall, the systematic uncertainties are smaller than the statistical uncertainties and, at low momentum transfers, are dominated by the pion reconstruction. At large momentum transfers, the leading source of uncertainty arises from the analysis conditions, which are likely folded with statistical effects.

The virtuality dependence of the measured differential and integrated cross sections is shown in Fig. 6.13. In particular, for the helicity-angle-integrated cross section, the decrease of the observable with increasing momentum transfer is apparent. In Fig. 6.14, the measured differential cross sections are compared with the theoretical predictions by Danilkin and Vanderhaeghen [258–260]. The data show overall good agreement with the theoretical predictions. By integrating the differential cross section over the helicity angle, the total cross section can be obtained. The comparison of this integrated observable with the theoretical predictions is presented in Fig. 6.15, where the agreement remains consistently good.

6.7 | Summary of the Measurement of the $\gamma^*\gamma^* \rightarrow \pi^0\pi^0$ Cross Section

In this chapter, a measurement of the space-like differential two-photon production of two neutral pions in the vicinity of the $f_2(1270)$ resonance is presented. This is the first measurement of this kind. The analysis explored the dependence of the cross section on both momentum transfers and the pion helicity angle. A novel approach was employed: instead of determining both momentum transfers by detecting both final-state leptons, a single-tag technique was used. The momentum transfer of the undetected lepton was reconstructed with high precision using a kinematic fit. This method enabled a measurement of the cross section at two finite momentum transfers.

Due to the limited statistics and difficult background situations, the analysis is restricted to the $f_2(1270)$ mass region. This range is particularly relevant given the large theoretical uncertainties in the tensor-meson contribution to the hadronic Light-by-Light

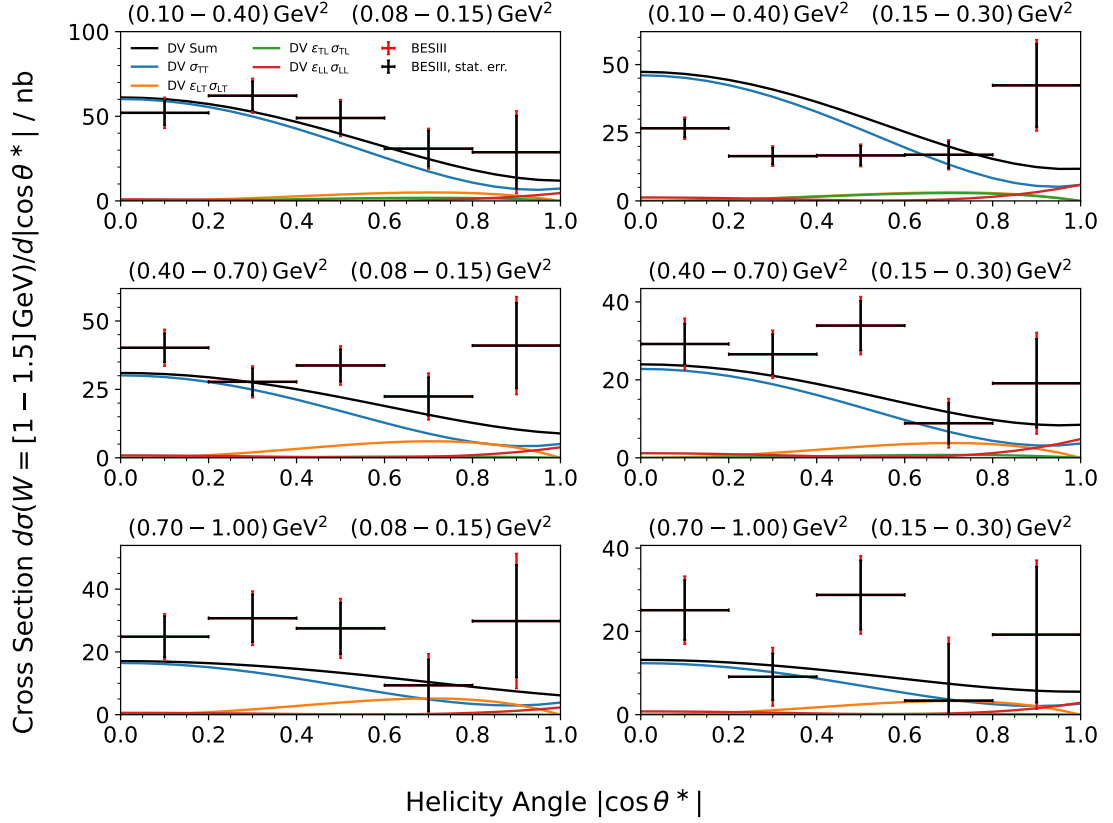


Figure 6.14: Result of the measurement of the differential cross section of the $\gamma^*\gamma^* \rightarrow \pi^0\pi^0$ process in the mass range $W = (1.0 - 1.5) \text{ GeV}$ for different momentum-transfer bins (panels), shown as a function of the cosine of the pion helicity angle $|\cos \theta^*|$. The black error bars represent the statistical uncertainty of the measurement, while the red error bars indicate the total uncertainty. The black line shows the full theoretical prediction by Danilkin and Vanderhaeghen (DV) [258–260], averaged over the mass and virtuality bins. The colored lines represent the individual cross section contributions, each combined with the corresponding correction factor for the respective luminosity functions.

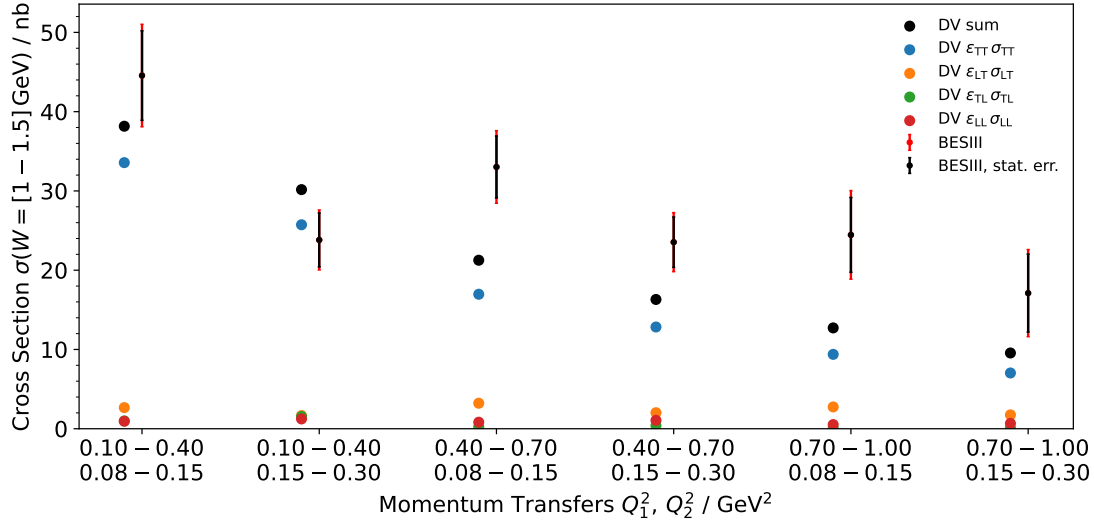


Figure 6.15: Result of the measurement of the integrated cross section of the $\gamma^*\gamma^* \rightarrow \pi^0\pi^0$ process in the mass range $W = (1.0-1.5)$ GeV for different momentum-transfer bins. The black error bars represent the statistical uncertainty of the measurement, while the red error bars indicate the total uncertainty. The black points show the full theoretical prediction by Danilkin and Vanderhaeghen (DV) [258–260], averaged over the mass and virtuality bins. The colored points represent the individual cross section contributions, each combined with the corresponding correction factor for the respective luminosity functions.

scattering part of the muon anomalous magnetic moment, a_μ^{HLbL} . Although the measurement is statistically limited – mainly due to the reduced event yield compared to the singly virtual case – it demonstrates the feasibility of such a study and would greatly benefit from larger data samples.

Overall, the dispersive theoretical predictions from Refs. [258–260] show good agreement with the measured data, indicating that the dispersive framework provides a reliable estimate of the tensor-meson contribution to a_μ^{HLbL} .

In the doubly virtual case, five different meson transition form factors contribute to the total cross section [254]. The form factors entering the σ_{LT} and σ_{TL} components, as well as the σ_0 and σ_{LL} components, contribute through the same helicity amplitudes (D_1 and D_0 , respectively), making it challenging to extract all five form factors directly from the available data without implementing assumptions and simplifications. In addition, possible S -wave contributions in this mass range, along with interference between the S and D_0 waves, further increase the number of fit parameters – exceeding the number of differential cross sections measured per momentum-transfer bin. Therefore, no partial-wave analysis is performed.

6.7. SUMMARY OF THE MEASUREMENT OF THE $\gamma^*\gamma^* \rightarrow \pi^0\pi^0$ CROSS SECTION 149

The numerical results of the extracted integrated and differential two-photon production cross sections can be found in Tab. C.20. The luminosity function ratios are given in Tab. 6.1.

7 | Conclusion and Outlook

In this work, the singly virtual production cross section of $\gamma\gamma^* \rightarrow \pi^0\pi^0$ is measured in the virtuality range $Q^2 = (0.1 - 4.0) \text{ GeV}^2$ – the region relevant for the Standard Model prediction of the hadronic Light-by-Light contribution to the muon’s anomalous magnetic moment – and for two-pion invariant masses $W < 2 \text{ GeV}$. The measurement covers the full pion helicity-angle range, thereby providing complete information on the angular distributions of the final-state pions. The analysis is based on a single-tagged event selection of $e^+e^- \rightarrow e^+e^-\pi^0\pi^0$, in which either the electron or positron is required to escape the detector at small angles such that the corresponding momentum transfer remains small. By applying a three-constraint kinematic fit to the selected event candidates, the resolution of the untagged lepton momentum is improved, allowing a direct constraint to singly virtual events. The background contribution is estimated using a data-driven approach based on sideband subtraction. After correcting the event yield for efficiency and numerically integrating the luminosity functions that connect the $e^+e^- \rightarrow e^+e^-\pi^0\pi^0$ and $\gamma\gamma^* \rightarrow \pi^0\pi^0$ cross sections, the differential and helicity-integrated quantity $\sigma_{\text{TT}} + \varepsilon \sigma_{\text{LT}}$ cross section is determined. A partial-wave analysis of the measured cross section is then performed to extract the electromagnetic transition form factors of the $f_0(500)$, $f_0(980)$, and $f_2(1270)$ intermediate states. For the $f_2(1270)$, all three helicity components are determined separately. In the partial-wave analysis, the tensor contribution is modeled using relativistic Breit-Wigner distributions, while the scalar contribution is described using Omnès functions provided by the authors of Refs. [188, 258]. A comparison with the Belle data [200] was possible in the overlapping virtuality range, corresponding to the highest virtuality bin. The statistical and systematic uncertainties of the measurement presented in this thesis are of comparable size; however, the determination of the contribution of analysis constraints to the systematic uncertainties may be biased by statistical effects. Consequently, the analysis will benefit from larger data sets, which will become available at future super- τ -charm factories.

The selection of $\gamma\gamma^* \rightarrow \pi^0\pi^0$ events via the decay of each pion into two photons in principle allows for a straightforward extension to the measurement of $\gamma\gamma^* \rightarrow \pi^0\eta$, where the η meson is reconstructed through its decay into two photons. The resulting two-photon invariant mass spectrum, obtained after an initial event selection based on the procedure described in Chapter 5, is shown in the left panel of Fig. 7.1.

In the mass spectrum, the $a_0(980)$ and $a_2(1320)$ are clearly visible, but the $a_0(980)$ contribution is not properly described by the HADROTOPS prediction. This discrepancy may

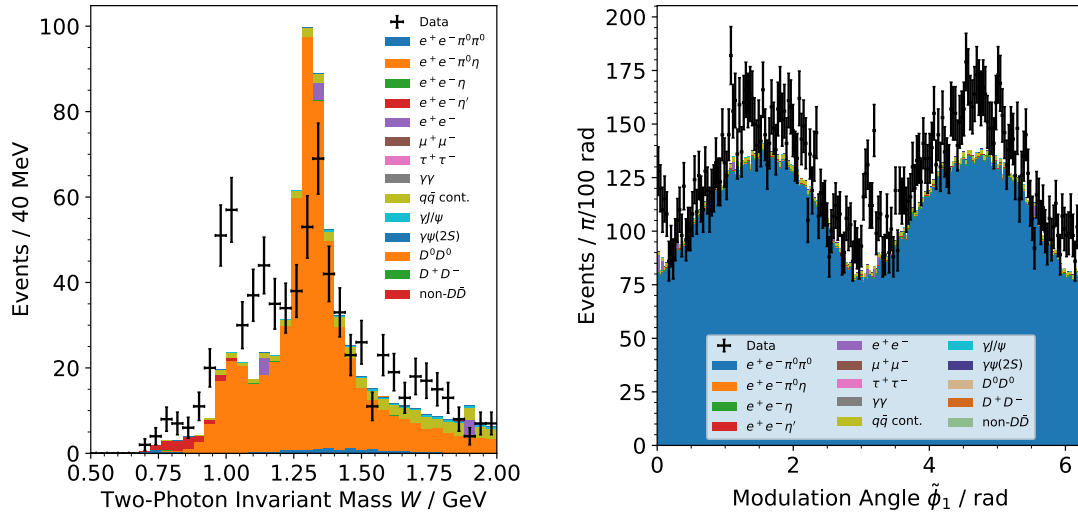


Figure 7.1: Two-photon invariant mass spectrum after the initial event selection of the $\gamma\gamma^* \rightarrow \pi^0\eta$ process, based on the selection procedure for $\gamma\gamma^* \rightarrow \pi^0\pi^0$ events presented in Chapter 5 (left panel), and the $\tilde{\phi}_1$ distribution of the selected $\gamma\gamma^* \rightarrow \pi^0\pi^0$ events compared to the HADROTOPS prediction (right panel).

indicate either additional peaking background contributions in the $a_0(980)$ mass range or an insufficient description by the underlying dispersive theory input. Furthermore, the overall event yield is significantly reduced compared to the $\gamma\gamma^* \rightarrow \pi^0\pi^0$ measurement. To achieve results with higher accuracy, the η meson may be reconstructed through additional decay channels, such as $\eta \rightarrow \pi^+\pi^-\pi^0$ or $\eta \rightarrow \pi^0\pi^0\pi^0$. By considering these three decay channels, 94.81% of η decays are included in the analysis, compared to only 39.36% when only the two-photon decay is reconstructed [275]. While the three-pion decay channels suffer from reduced geometric acceptance and therefore lower reconstruction efficiency, they provide a cleaner signature in the detector than the two-photon decay channel. As a result, the background conditions are expected to improve, thereby offering increased statistics and additional control over previously unknown background channels.

The development of the Monte Carlo event generator HADROTOPS not only enables an accurate description of the two-photon production of neutral pions, but also allows for the prediction of the dependence of the single-virtual $e^+e^- \rightarrow e^+e^-\pi^0\pi^0$ cross section (Eq. (1.28)) on the modulation angle $\tilde{\phi}_1$, as illustrated in the right panel of Fig. 7.1. In future, a dedicated study of this angular dependence will enable the extraction of the τ_{T2} and $\tau_{-12} - \tau_{-1T}$ response functions from the data. This will provide additional – and so far completely unmeasured – information on the two-photon couplings of the involved resonances, thereby significantly enhancing our understanding of their electromagnetic structure. The numerical determination of the two-photon coupling provided by HADROTOPS will play a key role in this study. The generator will also be used in future BESIII studies

of other two-photon processes such as $\gamma^{(*)}\gamma^* \rightarrow K^+K^-$, $\gamma^{(*)}\gamma^* \rightarrow K_S K_S$, $\gamma^{(*)}\gamma^* \rightarrow \pi^0\eta$, $\gamma^{(*)}\gamma^* \rightarrow \eta\eta$, and $\gamma^{(*)}\gamma^* \rightarrow f_1(1285)$. In its current state, it is able to deliver Monte Carlo samples suitable for the use in partial wave analysis tool for any hadronic final state.

The singly tagged selection was further extended to extract the doubly virtual cross section of $\gamma^*\gamma^* \rightarrow \pi^0\pi^0$. The number of signal events is determined by fitting the signal Monte Carlo distribution to the χ^2_{3C} distribution in each bin of the measurement. The luminosity functions are numerically determined. Due to limited statistics, this cross section measurement is restricted to the mass region $1.0 \text{ GeV} < W < 1.5 \text{ GeV}$ – covering the $f_2(1270)$ resonance. The full pion helicity angle range is covered and the virtuality ranges are $Q_1^2 \in [0.1, 1.0] \text{ GeV}^2$ and $Q_2^2 \in [0.08, 0.30] \text{ GeV}^2$. This novel approach enables the first measurement of double-virtual, space-like two-photon production of any tensor meson. Due to the single tag selection, the measured virtuality range is fully complementary to a possible double tagged selection. The uncertainty is statistically dominated and would profit enormously from larger data sets which will be available at future facilities.

Together, the singly and doubly virtual measurements presented in this thesis provide essential input for the dispersive evaluation of the hadronic Light-by-Light contribution to a_μ by supplying transition form factor measurements of scalar and tensor states, as well as partial waves of $\gamma^*\gamma^{(*)} \rightarrow \pi^0\pi^0$. The experimental results of this thesis therefore fulfill one item on the "wishlist" published by the $g - 2$ Theory Initiative for the determination of a_μ^{HLbL} [47]. By integrating the results of this thesis into the existing theoretical framework, the accuracy of the scalar contributions to a_μ^{HLbL} – the fourth-largest long-distance contribution – can be improved. In addition, the uncertainty of the tensor contributions, which constitute one of the dominant sources of uncertainty in the Standard Model prediction of the hadronic Light-by-Light scattering contribution, will be reduced using the results of this work.

The experimental results of this thesis are currently under internal review by the BESIII collaboration and prepared for publication. A Monte Carlo study of the $\gamma\gamma^* \rightarrow \pi^0\pi^0$ process, based on datasets different from those used in this thesis, was presented at the MENU2023 conference and documented in the corresponding proceedings (Ref. [346]), which are attached to this work. Similar Monte Carlo studies based on this work have also been presented at the plenary workshops of the Muon $g - 2$ Theory Initiative: in Bern (2023) by Max Lellmann, in Tsukuba (2024) by Max Lellmann and Dr. Christoph F. Redmer, and in Orsay (2025) by Dr. Christoph F. Redmer. The HADROTOPS generator, together with the dispersive analysis and the theoretical work by Igor Danilkin, Xiu-Lei Ren, and Marc Vanderhaeghen, has been submitted for publication. The preprint is publicly available (Ref. [256]) and also attached to this thesis.

Bibliography

- [1] I. Newton, *Philosophiae naturalis principia mathematica*. W. Dawson, 1687.
- [2] M. Sharratt, *Galileo - Decisive Innovator*, pp. 204–205. Cambridge: Cambridge University Press, 1996.
- [3] J. Maxwell, “On physical lines of force,” *Philosophical Magazine*, vol. 90, no. sup1, pp. 11–23, 2010.
- [4] J. Maxwell, “VIII. A dynamical theory of the electromagnetic field,” *Philosophical Transactions of the Royal Society of London*, vol. 155, pp. 459–512, 1865.
- [5] A. Einstein, “Zur Elektrodynamik bewegter Körper,” *Annalen der Physik und Chemie*, vol. 17, pp. 891–921, 1905.
- [6] A. Einstein, “Über das Relativitätsprinzip und die aus demselben gezogenen Folgerungen,” *Jahrbuch der Radioaktivität und Elektronik*, vol. IV, pp. 441–462, 1908.
- [7] A. Einstein, “Über den Einfluß der Schwerkraft auf die Ausbreitung des Lichtes,” *Annalen der Physik*, vol. 35, pp. 898–908, 1911.
- [8] A. Einstein and M. Grossmann, “Entwurf einer verallgemeinerten Relativitätstheorie und einer Theorie der Gravitation,” *Zeitschrift für Mathematik und Physik*, vol. 62, pp. 225–261, 1913.
- [9] A. Einstein, “Erklärung der Perihelbewegung des Merkur aus der allgemeinen Relativitätstheorie,” *Sitzungsberichte der Preussischen Akademie der Wissenschaften*, pp. 831–839, 1915.
- [10] A. Einstein, “Die Grundlage der allgemeinen Relativitätstheorie,” *Annalen der Physik*, vol. 354, pp. 769–822, 1916.
- [11] M. Planck, “Über das Gesetz der Energieverteilung im Normalspectrum,” *Annalen der Physik*, vol. 4, pp. 553–563, 1901.
- [12] M. Planck, *Acht Vorlesungen über theoretische Physik - gehalten an der Columbia University in the city of New York im Frühjahr 1909*. Stuttgart: S. Hirzel, 1910.

- [13] P. A. M. Dirac, “The quantum theory of the electron,” *Proc. Roy. Soc. Lond. A*, vol. 117, pp. 610–624, 1928.
- [14] P. A. M. Dirac, “The Quantum theory of electron. 2.,” *Proc. Roy. Soc. Lond. A*, vol. 118, p. 351, 1928.
- [15] P. A. M. Dirac, “A Theory of Electrons and Positrons,” *Proc. Roy. Soc. Lond. A*, vol. 126 (801), pp. 360–365, 1928.
- [16] C. D. Anderson, “The Positive Electron,” *Phys. Rev.*, vol. 43, pp. 491–494, Mar 1933.
- [17] S. L. Glashow and S. Weinberg, “Natural conservation laws for neutral currents,” *Phys. Rev. D*, vol. 15, pp. 1958–1965, Apr 1977.
- [18] G. 't Hooft, “Dimensional regularization and the renormalization group,” *Nuclear Physics B*, vol. 61, pp. 455–468, 1973.
- [19] D. J. Gross and F. Wilczek, “Asymptotically Free Gauge Theories. I,” *Phys. Rev. D*, vol. 8, pp. 3633–3652, Nov 1973.
- [20] D. J. Gross and F. Wilczek, “Asymptotically Free Gauge Theories. II,” *Phys. Rev. D*, vol. 9, pp. 980–993, Feb 1974.
- [21] H. D. Politzer, “Reliable Perturbative Results for Strong Interactions?,” *Phys. Rev. Lett.*, vol. 30, pp. 1346–1349, Jun 1973.
- [22] Wikimedia Commons, “Standard Model of Elementary Particles,” 2019.
- [23] G. Arnison *et al.*, “Experimental observation of isolated large transverse energy electrons with associated missing energy at $\sqrt{s} = 540$ GeV,” *Physics Letters B*, vol. 122, no. 1, pp. 103–116, 1983.
- [24] G. Arnison *et al.*, “Experimental observation of lepton pairs of invariant mass around 95 GeV/c² at the CERN SPS collider,” *Physics Letters B*, vol. 126, no. 5, pp. 398–410, 1983.
- [25] F. Abe *et al.*, “Observation of Top Quark Production in $\bar{p}p$ Collisions with the Collider Detector at Fermilab,” *Phys. Rev. Lett.*, vol. 74, pp. 2626–2631, Apr 1995.
- [26] J. E. Augustin *et al.*, “Discovery of a Narrow Resonance in e^+e^- Annihilation,” *Phys. Rev. Lett.*, vol. 33, pp. 1406–1408, Dec 1974.
- [27] ATLAS Collaboration, “Observation of a new particle in the search for the Standard Model Higgs boson with the ATLAS detector at the LHC,” *Physics Letters B*, vol. 716, no. 1, pp. 1–29, 2012.
- [28] CMS Collaboration, “Observation of a new boson at a mass of 125 GeV with the CMS experiment at the LHC,” *Physics Letters B*, vol. 716, no. 1, pp. 30–61, 2012.

- [29] A. Friedman, “Über die Krümmung des Raumes,” *Zeitschrift für Physik*, vol. 10, no. 1, pp. 377–386, 1922.
- [30] G. Lemaître, “Un Univers homogène de masse constante et de rayon croissant rendant compte de la vitesse radiale des nébuleuses extra-galactiques,” *Annales de la Société Scientifique de Bruxelles*, vol. 47, pp. 49–59, Jan. 1927.
- [31] F. Zwicky, “Die Rotverschiebung von extragalaktischen Nebeln,” *Helvetica Physica Acta*, vol. 6, pp. 110–127, 1933.
- [32] F. Zwicky, “On the Masses of Nebulae and of Clusters of Nebulae,” *The Astrophysical Journal*, vol. 86, pp. 217–246, 1937.
- [33] M. Kobayashi and T. Maskawa, “CP-Violation in the Renormalizable Theory of Weak Interaction,” *Progress of Theoretical Physics*, vol. 49, pp. 652–657, 02 1973.
- [34] L. Canetti, M. Drewes, and M. Shaposhnikov, “Matter and Antimatter in the Universe,” *New J. Phys.*, vol. 14, p. 095012, 2012.
- [35] R. Aliberti *et al.*, “The anomalous magnetic moment of the muon in the Standard Model: an update,” *Phys. Rept.*, vol. 1143, pp. 1–158, 2025.
- [36] D. P. Aguillard *et al.*, “Measurement of the Positive Muon Anomalous Magnetic Moment to 127 ppb,” 6 2025.
- [37] J. S. Schwinger, “On Quantum electrodynamics and the magnetic moment of the electron,” *Phys. Rev.*, vol. 73, pp. 416–417, 1948.
- [38] D. P. Aguillard *et al.*, “Measurement of the Positive Muon Anomalous Magnetic Moment to 0.20 ppm,” *Phys. Rev. Lett.*, vol. 131, no. 16, p. 161802, 2023.
- [39] D. P. Aguillard *et al.*, “Detailed report on the measurement of the positive muon anomalous magnetic moment to 0.20 ppm,” *Phys. Rev. D*, vol. 110, no. 3, p. 032009, 2024.
- [40] B. Abi *et al.*, “Measurement of the Positive Muon Anomalous Magnetic Moment to 0.46 ppm,” *Phys. Rev. Lett.*, vol. 126, no. 14, p. 141801, 2021.
- [41] T. Albahri *et al.*, “Measurement of the anomalous precession frequency of the muon in the Fermilab Muon $g - 2$ Experiment,” *Phys. Rev. D*, vol. 103, no. 7, p. 072002, 2021.
- [42] T. Albahri *et al.*, “Magnetic-field measurement and analysis for the Muon $g - 2$ Experiment at Fermilab,” *Phys. Rev. A*, vol. 103, no. 4, p. 042208, 2021.
- [43] T. Albahri *et al.*, “Beam dynamics corrections to the Run-1 measurement of the muon anomalous magnetic moment at Fermilab,” *Phys. Rev. Accel. Beams*, vol. 24, no. 4, p. 044002, 2021.

- [44] G. W. Bennett *et al.*, “Final Report of the Muon E821 Anomalous Magnetic Moment Measurement at BNL,” *Phys. Rev. D*, vol. 73, p. 072003, 2006.
- [45] F. Jegerlehner and A. Nyffeler, “The Muon $g-2$,” *Phys. Rept.*, vol. 477, pp. 1–110, 2009.
- [46] M. Abe *et al.*, “A New Approach for Measuring the Muon Anomalous Magnetic Moment and Electric Dipole Moment,” *PTEP*, vol. 2019, no. 5, p. 053C02, 2019.
- [47] T. Aoyama *et al.*, “The anomalous magnetic moment of the muon in the Standard Model,” *Phys. Rept.*, vol. 887, pp. 1–166, 2020.
- [48] T. Aoyama, M. Hayakawa, T. Kinoshita, and M. Nio, “Complete Tenth-Order QED Contribution to the Muon $g - 2$,” *Phys. Rev. Lett.*, vol. 109, p. 111808, 2012.
- [49] T. Aoyama, T. Kinoshita, and M. Nio, “Theory of the Anomalous Magnetic Moment of the Electron,” *Atoms*, vol. 7, no. 1, p. 28, 2019.
- [50] R. H. Parker, C. Yu, W. Zhong, B. Estey, and H. Müller, “Measurement of the fine-structure constant as a test of the standard model,” *Science*, vol. 360, pp. 191–195, Apr. 2018.
- [51] L. Morel, Z. Yao, P. Cladé, and S. Guellati-Khélifa, “Determination of the fine-structure constant with an accuracy of 81 parts per trillion,” *Nature*, vol. 588, no. 7836, pp. 61–65, 2020.
- [52] J. S. Schelfhout, T. M. Hird, K. M. Hughes, and C. J. Foot, “A single-photon large-momentum-transfer atom interferometry scheme for Sr or Yb atoms with application to determining the fine-structure constant,” *Phys. Rev. A*, vol. 110, p. 053309, 2024.
- [53] P. J. Mohr, D. B. Newell, B. N. Taylor, and E. Tiesinga, “CODATA recommended values of the fundamental physical constants: 2022*,” *Rev. Mod. Phys.*, vol. 97, no. 2, p. 025002, 2025.
- [54] W. J. Huang, M. Wang, F. G. Kondev, G. Audi, and S. Naimi, “The AME 2020 atomic mass evaluation (I). Evaluation of input data, and adjustment procedures,” *Chin. Phys. C*, vol. 45, no. 3, p. 030002, 2021.
- [55] M. Wang, W. J. Huang, F. G. Kondev, G. Audi, and S. Naimi, “The AME 2020 atomic mass evaluation (II). Tables, graphs and references,” *Chin. Phys. C*, vol. 45, no. 3, p. 030003, 2021.
- [56] A. Czarnecki, B. Krause, and W. J. Marciano, “Electroweak corrections to the muon anomalous magnetic moment,” *Phys. Rev. Lett.*, vol. 76, pp. 3267–3270, 1996.
- [57] S. Peris, M. Perrottet, and E. de Rafael, “Two loop electroweak corrections to the muon $g-2$: A New class of hadronic contributions,” *Phys. Lett. B*, vol. 355, pp. 523–530, 1995.

- [58] G. Degrossi and G. F. Giudice, “QED logarithms in the electroweak corrections to the muon anomalous magnetic moment,” *Phys. Rev. D*, vol. 58, p. 053007, 1998.
- [59] A. Czarnecki, W. J. Marciano, and A. Vainshtein, “Refinements in electroweak contributions to the muon anomalous magnetic moment,” *Phys. Rev.*, vol. D67, p. 073006, 2003. [Erratum: *Phys. Rev.* **D73**, 119901 (2006)].
- [60] S. Heinemeyer, D. Stockinger, and G. Weiglein, “Electroweak and supersymmetric two-loop corrections to $(g-2)(\mu)$,” *Nucl. Phys. B*, vol. 699, pp. 103–123, 2004.
- [61] T. Gribouk and A. Czarnecki, “Electroweak interactions and the muon $g-2$: Bosonic two-loop effects,” *Phys. Rev. D*, vol. 72, p. 053016, 2005.
- [62] C. Gnendiger, D. Stöckinger, and H. Stöckinger-Kim, “The electroweak contributions to $(g-2)_\mu$ after the Higgs boson mass measurement,” *Phys. Rev.*, vol. D88, p. 053005, 2013.
- [63] R. R. Akhmetshin *et al.*, “Measurement of $e^+e^- \rightarrow \pi^+\pi^-$ cross-section with CMD-2 around rho meson,” *Phys. Lett. B*, vol. 527, pp. 161–172, 2002.
- [64] R. R. Akhmetshin *et al.*, “Reanalysis of hadronic cross-section measurements at CMD-2,” *Phys. Lett. B*, vol. 578, pp. 285–289, 2004.
- [65] V. M. Aul’chenko *et al.*, “Measurement of the pion form-factor in the range 1.04 GeV to 1.38 GeV with the CMD-2 detector,” *JETP Lett.*, vol. 82, pp. 743–747, 2005.
- [66] R. R. Akhmetshin *et al.*, “High-statistics measurement of the pion form factor in the rho-meson energy range with the CMD-2 detector,” *Phys. Lett. B*, vol. 648, pp. 28–38, 2007.
- [67] M. N. Achasov *et al.*, “Study of the process $e^+e^- \rightarrow \pi^+\pi^-$ in the energy region $400 < \sqrt{s} < 1000$ MeV,” *J. Exp. Theor. Phys.*, vol. 101, no. 6, pp. 1053–1070, 2005.
- [68] M. N. Achasov *et al.*, “Update of the $e^+e^- \rightarrow \pi^+\pi^-$ cross-section measured by SND detector in the energy region $400\text{-MeV} < s^{**}(1/2) < 1000\text{-MeV}$,” *J. Exp. Theor. Phys.*, vol. 103, pp. 380–384, 2006.
- [69] J. P. Lees *et al.*, “Precise Measurement of the $e^+e^- \rightarrow \pi^+\pi^-(\gamma)$ Cross Section with the Initial-State Radiation Method at BABAR,” *Phys. Rev. D*, vol. 86, p. 032013, 2012.
- [70] A. Aloisio *et al.*, “Measurement of $\sigma(e^+e^- \rightarrow \pi^+\pi^-\gamma)$ and extraction of $\sigma(e^+e^- \rightarrow \pi^+\pi^-)$ below 1-GeV with the KLOE detector,” *Phys. Lett. B*, vol. 606, pp. 12–24, 2005.
- [71] F. Ambrosino *et al.*, “Measurement of $\sigma(e^+e^- \rightarrow \pi^+\pi^-\gamma(\gamma))$ and the dipion contribution to the muon anomaly with the KLOE detector,” *Phys. Lett. B*, vol. 670, pp. 285–291, 2009.

- [72] F. Ambrosino *et al.*, “Measurement of $\sigma(e^+e^- \rightarrow \pi^+\pi^-)$ from threshold to 0.85 GeV² using Initial State Radiation with the KLOE detector,” *Phys. Lett. B*, vol. 700, pp. 102–110, 2011.
- [73] D. Babusci *et al.*, “Precision measurement of $\sigma(e^+e^- \rightarrow \pi^+\pi^-\gamma)/\sigma(e^+e^- \rightarrow \mu^+\mu^-\gamma)$ and determination of the $\pi^+\pi^-$ contribution to the muon anomaly with the KLOE detector,” *Phys. Lett. B*, vol. 720, pp. 336–343, 2013.
- [74] A. Anastasi *et al.*, “Combination of KLOE $\sigma(e^+e^- \rightarrow \pi^+\pi^-\gamma(\gamma))$ measurements and determination of $a_\mu^{\pi^+\pi^-}$ in the energy range $0.10 < s < 0.95$ GeV²,” *JHEP*, vol. 03, p. 173, 2018.
- [75] M. Ablikim *et al.*, “Measurement of the $e^+e^- \rightarrow \pi^+\pi^-$ cross section between 600 and 900 MeV using initial state radiation,” *Phys. Lett. B*, vol. 753, pp. 629–638, 2016. [Erratum: *Phys.Lett.B* 812, 135982 (2021)].
- [76] M. N. Achasov *et al.*, “Measurement of the $e^+e^- \rightarrow \pi^+\pi^-$ process cross section with the SND detector at the VEPP-2000 collider in the energy region $0.525 < \sqrt{s} < 0.883$ GeV,” *JHEP*, vol. 01, p. 113, 2021.
- [77] F. V. Ignatov *et al.*, “Measurement of the $e^+e^- \rightarrow \pi^+\pi^-$ cross section from threshold to 1.2 GeV with the CMD-3 detector,” *Phys. Rev. D*, vol. 109, no. 11, p. 112002, 2024.
- [78] F. V. Ignatov *et al.*, “Measurement of the Pion Form Factor with CMD-3 Detector and its Implication to the Hadronic Contribution to Muon ($g-2$),” *Phys. Rev. Lett.*, vol. 132, no. 23, p. 231903, 2024.
- [79] S. J. Brodsky and E. De Rafael, “Suggested boson-lepton pair couplings and the anomalous magnetic moment of the muon,” *Phys. Rev.*, vol. 168, pp. 1620–1622, 1968.
- [80] B. E. Lautrup and E. De Rafael, “Calculation of the sixth-order contribution from the fourth-order vacuum polarization to the difference of the anomalous magnetic moments of muon and electron,” *Phys. Rev.*, vol. 174, pp. 1835–1842, 1968.
- [81] V. Auslander, G. Budker, J. Pestov, V. Sidorov, A. Skrinsky, and A. Khabakhpashev, “Investigation of the ρ -meson resonance with electron-positron colliding beams,” *Physics Letters B*, vol. 25, no. 6, pp. 433–435, 1967.
- [82] V. L. Auslander, G. I. Budker, E. V. Pakhtusova, Y. N. Pestov, V. A. Sidorov, A. N. Skrinsky, and A. G. Khabakhpashev, “Investigation of the ρ -meson resonance with electron-positron colliding beams,” *Yad. Fiz.*, vol. 9, pp. 114–119, 1969.
- [83] V. Balakin, G. Budker, E. Pakhtusova, V. Sidorov, A. Skrinsky, G. Tumaikin, and A. Khabakhpashev, “Investigation of the ϕ -meson resonance by electron-positron colliding beams,” *Physics Letters B*, vol. 34, no. 4, pp. 328–332, 1971.

- [84] V. Balakin, G. Budker, L. Kurdadze, A. Onuchin, E. Pakhtusova, S. Serednyakov, V. Sidorov, and A. Skrinsky, "Measurement of the electron-positron annihilation cross-section into $\pi^+\pi^-$, K^+K^- -pairs at the total energy 1.18–1.34 GeV," *Physics Letters B*, vol. 41, no. 2, pp. 205–208, 1972.
- [85] D. Benaksas, G. Cosme, B. Jean-Marie, S. Jullian, F. Laplanche, J. Lefrançois, A. Liberman, G. Parrou, J. Repellin, and G. Sauvage, " $\pi^+\pi^-$ production by e^+e^- annihilation in the ρ energy range with the Orsay storage ring," *Physics Letters B*, vol. 39, no. 2, pp. 289–293, 1972.
- [86] G. Cosme *et al.*, "Measurement of the electron-Positron Annihilation Cross-Section Into $\pi^+\pi^-$ at the Energies 915-MeV, 990-MeV and 1076-MeV," 7 1976.
- [87] D. Bollini, P. Giusti, T. Massam, L. Monari, F. Palmonari, G. Valenti, and A. Zichichi, "The Pion Electromagnetic Form-Factor in the Timelike Range 1.44 GeV²-9.0 GeV²," *Lett. Nuovo Cim.*, vol. 14, p. 418, 1975.
- [88] A. Quenzer *et al.*, "Pion Form-Factor from 480 MeV to 1100 MeV," *Phys. Lett. B*, vol. 76, pp. 512–516, 1978.
- [89] B. Esposito *et al.*, "Momentum Analysis of Kaon and Pion Pairs Produced from Timelike Photons at 1.6-GeV Energy," *Phys. Lett. B*, vol. 67, pp. 239–242, 1977.
- [90] B. Esposito *et al.*, "Measurements of the e.m. timelike form-factors for kaon and pion at $\sqrt{s} = 1.5$ GeV," *Lett. Nuovo Cim.*, vol. 28, pp. 337–342, 1980.
- [91] I. B. Vasserman, P. M. Ivanov, G. Y. Kezerashvili, I. A. Koop, A. P. Lysenko, Y. N. Pestov, A. N. Skrinsky, G. V. Fedotov, and Y. M. Shatunov, "Pion Form-factor Measurement in the Reaction $e^+e^- \rightarrow \pi^+\pi^-$ for Energies Within the Range From 0.4-GeV to 0.46-GeV," *Yad. Fiz.*, vol. 33, pp. 709–714, 1981.
- [92] S. R. Amendolia *et al.*, "Measurement of the Pion Form-factor in the Timelike Region for q^2 Values Between 0.1 GeV/c² and 0.18 GeV/c²," *Phys. Lett. B*, vol. 138, pp. 454–458, 1984.
- [93] D. Bisello *et al.*, "The Pion Electromagnetic Form-factor in the Timelike Energy Range $1.35 \text{ GeV} \leq \sqrt{s} \leq 2.4 \text{ GeV}$," *Phys. Lett. B*, vol. 220, pp. 321–327, 1989.
- [94] L. M. Barkov *et al.*, "Electromagnetic Pion Form-Factor in the Timelike Region," *Nucl. Phys. B*, vol. 256, pp. 365–384, 1985.
- [95] V. M. Aul'chenko *et al.*, "Measurement of the $e^+e^- \rightarrow \pi^+\pi^-$ cross section with the CMD-2 detector in the 370 - 520-MeV c.m. energy range," *JETP Lett.*, vol. 84, pp. 413–417, 2006.
- [96] T. K. Pedlar *et al.*, "Precision measurements of the timelike electromagnetic form-factors of pion, kaon, and proton," *Phys. Rev. Lett.*, vol. 95, p. 261803, 2005.

- [97] K. K. Seth, S. Dobbs, Z. Metreveli, A. Tomaradze, T. Xiao, and G. Bonvicini, “Electromagnetic Structure of the Proton, Pion, and Kaon by High-Precision Form Factor Measurements at Large Timelike Momentum Transfers,” *Phys. Rev. Lett.*, vol. 110, no. 2, p. 022002, 2013.
- [98] T. Xiao, S. Dobbs, A. Tomaradze, K. K. Seth, and G. Bonvicini, “Precision Measurement of the Hadronic Contribution to the Muon Anomalous Magnetic Moment,” *Phys. Rev. D*, vol. 97, no. 3, p. 032012, 2018.
- [99] S. Schael *et al.*, “Branching ratios and spectral functions of tau decays: Final ALEPH measurements and physics implications,” *Phys. Rept.*, vol. 421, pp. 191–284, 2005.
- [100] M. Davier, A. Höcker, B. Malaescu, C.-Z. Yuan, and Z. Zhang, “Update of the ALEPH non-strange spectral functions from hadronic τ decays,” *Eur. Phys. J. C*, vol. 74, no. 3, p. 2803, 2014.
- [101] K. Ackerstaff *et al.*, “Measurement of the strong coupling constant $\alpha(s)$ and the vector and axial vector spectral functions in hadronic tau decays,” *Eur. Phys. J. C*, vol. 7, pp. 571–593, 1999.
- [102] S. Anderson *et al.*, “Hadronic structure in the decay $\tau^- \rightarrow \pi^- \pi^0 \nu_\tau$,” *Phys. Rev. D*, vol. 61, p. 112002, 2000.
- [103] M. Fujikawa *et al.*, “High-Statistics Study of the $\tau^- \rightarrow \pi^- \pi^0 \nu_\tau$ Decay,” *Phys. Rev. D*, vol. 78, p. 072006, 2008.
- [104] M. Davier, A. Hoecker, G. Lopez Castro, B. Malaescu, X. H. Mo, G. Toledo Sanchez, P. Wang, C. Z. Yuan, and Z. Zhang, “The Discrepancy Between τ and e^+e^- Spectral Functions Revisited and the Consequences for the Muon Magnetic Anomaly,” *Eur. Phys. J. C*, vol. 66, pp. 127–136, 2010.
- [105] M. Davier, A. Hoecker, B. Malaescu, and Z. Zhang, “Reevaluation of the Hadronic Contributions to the Muon $g-2$ and to $\alpha(M_Z)$,” *Eur. Phys. J. C*, vol. 71, p. 1515, 2011. [Erratum: *Eur.Phys.J.C* 72, 1874 (2012)].
- [106] M. Davier, A. Hoecker, B. Malaescu, C. Z. Yuan, and Z. Zhang, “Reevaluation of the hadronic contribution to the muon magnetic anomaly using new $e^+e^- \rightarrow \pi^+\pi^-$ cross section data from BABAR,” *Eur. Phys. J. C*, vol. 66, pp. 1–9, 2010.
- [107] M. Davier, A. Hoecker, B. Malaescu, and Z. Zhang, “Reevaluation of the hadronic vacuum polarisation contributions to the Standard Model predictions of the muon $g-2$ and $\alpha(m_Z^2)$ using newest hadronic cross-section data,” *Eur. Phys. J. C*, vol. 77, no. 12, p. 827, 2017.
- [108] M. Davier, A. Hoecker, B. Malaescu, and Z. Zhang, “A new evaluation of the hadronic vacuum polarisation contributions to the muon anomalous magnetic moment and to $\alpha(m_Z^2)$,” *Eur. Phys. J. C*, vol. 80, no. 3, p. 241, 2020. [Erratum: *Eur.Phys.J.C* 80, 410 (2020)].

- [109] M. Davier, A. Hoecker, A.-M. Lutz, B. Malaescu, and Z. Zhang, “Tensions in $e^+e^- \rightarrow \pi^+\pi^-(\gamma)$ measurements: the new landscape of data-driven hadronic vacuum polarization predictions for the muon $g - 2$,” *Eur. Phys. J. C*, vol. 84, no. 7, p. 721, 2024.
- [110] G. Colangelo, M. Hoferichter, and P. Stoffer, “Two-pion contribution to hadronic vacuum polarization,” *JHEP*, vol. 02, p. 006, 2019.
- [111] G. Colangelo, M. Hoferichter, B. Kubis, and P. Stoffer, “Isospin-breaking effects in the two-pion contribution to hadronic vacuum polarization,” *JHEP*, vol. 10, p. 032, 2022.
- [112] P. Stoffer, G. Colangelo, and M. Hoferichter, “Puzzles in the hadronic contributions to the muon anomalous magnetic moment,” *JINST*, vol. 18, no. 10, p. C10021, 2023.
- [113] T. P. Leplumey and P. Stoffer, “Dispersive analysis of the pion vector form factor without zeros,” 1 2025.
- [114] A. Keshavarzi, D. Nomura, and T. Teubner, “Muon $g - 2$ and $\alpha(M_Z^2)$: a new data-based analysis,” *Phys. Rev. D*, vol. 97, no. 11, p. 114025, 2018.
- [115] A. Keshavarzi, D. Nomura, and T. Teubner, “ $g - 2$ of charged leptons, $\alpha(M_Z^2)$, and the hyperfine splitting of muonium,” *Phys. Rev. D*, vol. 101, no. 1, p. 014029, 2020.
- [116] T. Blum, P. A. Boyle, V. Gülpers, T. Izubuchi, L. Jin, C. Jung, A. Jüttner, C. Lehner, A. Portelli, and J. T. Tsang, “Calculation of the hadronic vacuum polarization contribution to the muon anomalous magnetic moment,” *Phys. Rev. Lett.*, vol. 121, no. 2, p. 022003, 2018.
- [117] D. Giusti, V. Lubicz, G. Martinelli, F. Sanfilippo, and S. Simula, “Electromagnetic and strong isospin-breaking corrections to the muon $g - 2$ from Lattice QCD+QED,” *Phys. Rev. D*, vol. 99, no. 11, p. 114502, 2019.
- [118] S. Borsanyi *et al.*, “Leading hadronic contribution to the muon magnetic moment from lattice QCD,” *Nature*, vol. 593, no. 7857, pp. 51–55, 2021.
- [119] C. Lehner and A. S. Meyer, “Consistency of hadronic vacuum polarization between lattice QCD and the R-ratio,” *Phys. Rev. D*, vol. 101, p. 074515, 2020.
- [120] G. Wang, T. Draper, K.-F. Liu, and Y.-B. Yang, “Muon $g-2$ with overlap valence fermions,” *Phys. Rev. D*, vol. 107, no. 3, p. 034513, 2023.
- [121] C. Aubin, T. Blum, M. Golterman, and S. Peris, “Muon anomalous magnetic moment with staggered fermions: Is the lattice spacing small enough?,” *Phys. Rev. D*, vol. 106, no. 5, p. 054503, 2022.

- [122] M. Cè *et al.*, “Window observable for the hadronic vacuum polarization contribution to the muon $g-2$ from lattice QCD,” *Phys. Rev. D*, vol. 106, no. 11, p. 114502, 2022.
- [123] C. Alexandrou *et al.*, “Lattice calculation of the short and intermediate time-distance hadronic vacuum polarization contributions to the muon magnetic moment using twisted-mass fermions,” *Phys. Rev. D*, vol. 107, no. 7, p. 074506, 2023.
- [124] T. Blum *et al.*, “Update of Euclidean windows of the hadronic vacuum polarization,” *Phys. Rev. D*, vol. 108, no. 5, p. 054507, 2023.
- [125] S. Kuberski, M. Cè, G. von Hippel, H. B. Meyer, K. Ottnad, A. Risch, and H. Wittig, “Hadronic vacuum polarization in the muon $g - 2$: the short-distance contribution from lattice QCD,” *JHEP*, vol. 03, p. 172, 2024.
- [126] A. Boccaletti *et al.*, “High precision calculation of the hadronic vacuum polarisation contribution to the muon anomaly,” 7 2024.
- [127] S. Spiegel and C. Lehner, “High-precision continuum limit study of the HVP short-distance window,” *Phys. Rev. D*, vol. 111, no. 11, p. 114517, 2025.
- [128] T. Blum *et al.*, “Long-Distance Window of the Hadronic Vacuum Polarization for the Muon $g-2$,” *Phys. Rev. Lett.*, vol. 134, no. 20, p. 201901, 2025.
- [129] D. Djukanovic, G. von Hippel, S. Kuberski, H. B. Meyer, N. Miller, K. Ottnad, J. Parrino, A. Risch, and H. Wittig, “The hadronic vacuum polarization contribution to the muon $g - 2$ at long distances,” *JHEP*, vol. 04, p. 098, 2025.
- [130] C. Alexandrou *et al.*, “Strange and charm quark contributions to the muon anomalous magnetic moment in lattice QCD with twisted-mass fermions,” *Phys. Rev. D*, vol. 111, no. 5, p. 054502, 2025.
- [131] A. Bazavov *et al.*, “Hadronic vacuum polarization for the muon $g-2$ from lattice QCD: Complete short and intermediate windows,” *Phys. Rev. D*, vol. 111, no. 9, p. 094508, 2025.
- [132] A. Bazavov *et al.*, “Hadronic Vacuum Polarization for the Muon $g-2$ from Lattice QCD: Long-Distance and Full Light-Quark Connected Contribution,” *Phys. Rev. Lett.*, vol. 135, no. 1, p. 011901, 2025.
- [133] L. Di Luzio, A. Keshavarzi, A. Masiero, and P. Paradisi, “Model-Independent Tests of the Hadronic Vacuum Polarization Contribution to the Muon $g-2$,” *Phys. Rev. Lett.*, vol. 134, no. 1, p. 011902, 2025.
- [134] A. Kurz, T. Liu, P. Marquard, and M. Steinhauser, “Hadronic contribution to the muon anomalous magnetic moment to next-to-next-to-leading order,” *Phys. Lett. B*, vol. 734, pp. 144–147, 2014.

- [135] C. M. Carloni Calame, M. Passera, L. Trentadue, and G. Venanzoni, “A new approach to evaluate the leading hadronic corrections to the muon $g-2$,” *Phys. Lett. B*, vol. 746, pp. 325–329, 2015.
- [136] G. Colangelo, M. Hoferichter, M. Procura, and P. Stoffer, “Dispersion relation for hadronic light-by-light scattering: theoretical foundations,” *JHEP*, vol. 09, p. 074, 2015.
- [137] R. Tarrach, “Invariant Amplitudes for Virtual Compton Scattering Off Polarized Nucleons Free from Kinematical Singularities, Zeros and Constraints,” *Nuovo Cim. A*, vol. 28, p. 409, 1975.
- [138] K. Melnikov and A. Vainshtein, “Hadronic light-by-light scattering contribution to the muon anomalous magnetic moment revisited,” *Phys. Rev. D*, vol. 70, p. 113006, 2004.
- [139] J. Aldins, T. Kinoshita, S. J. Brodsky, and A. J. Dufner, “Photon-photon scattering contribution to the sixth order magnetic moments of the muon and electron,” *Phys. Rev. D*, vol. 1, p. 2378, 1970.
- [140] G. Colangelo, M. Hoferichter, M. Procura, and P. Stoffer, “Dispersion relation for hadronic light-by-light scattering: two-pion contributions,” *JHEP*, vol. 04, p. 161, 2017.
- [141] M. Hoferichter, G. Colangelo, M. Procura, and P. Stoffer, “Virtual photon-photon scattering,” *Int. J. Mod. Phys. Conf. Ser.*, vol. 35, p. 1460400, 2014.
- [142] G. Colangelo, M. Hoferichter, B. Kubis, M. Procura, and P. Stoffer, “Towards a data-driven analysis of hadronic light-by-light scattering,” *Phys. Lett. B*, vol. 738, pp. 6–12, 2014.
- [143] G. Colangelo, M. Hoferichter, M. Procura, and P. Stoffer, “Dispersive approach to hadronic light-by-light scattering,” *JHEP*, vol. 09, p. 091, 2014.
- [144] G. Colangelo, M. Hoferichter, M. Procura, and P. Stoffer, “Rescattering effects in the hadronic-light-by-light contribution to the anomalous magnetic moment of the muon,” *Phys. Rev. Lett.*, vol. 118, no. 23, p. 232001, 2017.
- [145] M. Hoferichter, B.-L. Hoid, B. Kubis, S. Leupold, and S. P. Schneider, “Dispersion relation for hadronic light-by-light scattering: pion pole,” *JHEP*, vol. 10, p. 141, 2018.
- [146] M. Hoferichter, B.-L. Hoid, B. Kubis, S. Leupold, and S. P. Schneider, “Pion-pole contribution to hadronic light-by-light scattering in the anomalous magnetic moment of the muon,” *Phys. Rev. Lett.*, vol. 121, no. 11, p. 112002, 2018.
- [147] E. de Rafael, “Hadronic contributions to the muon $g-2$ and low-energy QCD,” *Phys. Lett. B*, vol. 322, pp. 239–246, 1994.

- [148] J. Bijnens, N. Hermansson-Truedsson, and A. Rodríguez-Sánchez, “Short-distance constraints for the HLbL contribution to the muon anomalous magnetic moment,” *Phys. Lett. B*, vol. 798, p. 134994, 2019.
- [149] J. Bijnens, N. Hermansson-Truedsson, L. Laub, and A. Rodríguez-Sánchez, “Short-distance HLbL contributions to the muon anomalous magnetic moment beyond perturbation theory,” *JHEP*, vol. 10, p. 203, 2020.
- [150] J. Bijnens, N. Hermansson-Truedsson, L. Laub, and A. Rodríguez-Sánchez, “The two-loop perturbative correction to the $(g - 2)_\mu$ HLbL at short distances,” *JHEP*, vol. 04, p. 240, 2021.
- [151] J. Bijnens, N. Hermansson-Truedsson, and A. Rodríguez-Sánchez, “Constraints on the hadronic light-by-light in the Melnikov-Vainshtein regime,” *JHEP*, vol. 02, p. 167, 2023.
- [152] J. Bijnens, N. Hermansson-Truedsson, and A. Rodríguez-Sánchez, “Constraints on the hadronic light-by-light tensor in corner kinematics for the muon $g - 2$,” *JHEP*, vol. 03, p. 094, 2025.
- [153] G. P. Lepage and S. J. Brodsky, “Exclusive Processes in Quantum Chromodynamics: Evolution Equations for Hadronic Wave Functions and the Form-Factors of Mesons,” *Phys. Lett. B*, vol. 87, pp. 359–365, 1979.
- [154] S. J. Brodsky and G. P. Lepage, “Large Angle Two Photon Exclusive Channels in Quantum Chromodynamics,” *Phys. Rev. D*, vol. 24, p. 1808, 1981.
- [155] I. I. Balitsky and A. V. Yung, “Proton and Neutron Magnetic Moments from QCD Sum Rules,” *Phys. Lett. B*, vol. 129, pp. 328–334, 1983.
- [156] B. L. Ioffe and A. V. Smilga, “Nucleon Magnetic Moments and Magnetic Properties of Vacuum in QCD,” *Nucl. Phys. B*, vol. 232, pp. 109–142, 1984.
- [157] N. I. Usyukina and A. I. Davydychev, “New results for two loop off-shell three point diagrams,” *Phys. Lett. B*, vol. 332, pp. 159–167, 1994.
- [158] F. Chavez and C. Duhr, “Three-mass triangle integrals and single-valued polylogarithms,” *JHEP*, vol. 11, p. 114, 2012.
- [159] G. Colangelo, F. Hagelstein, M. Hoferichter, L. Laub, and P. Stoffer, “Short-distance constraints on hadronic light-by-light scattering in the anomalous magnetic moment of the muon,” *Phys. Rev. D*, vol. 101, no. 5, p. 051501, 2020.
- [160] K. Melnikov and A. Vainshtein, “On dispersion relations and hadronic light-by-light scattering contribution to the muon anomalous magnetic moment,” 11 2019.
- [161] G. Colangelo, F. Hagelstein, M. Hoferichter, L. Laub, and P. Stoffer, “Longitudinal short-distance constraints for the hadronic light-by-light contribution to $(g - 2)_\mu$ with large- N_c Regge models,” *JHEP*, vol. 03, p. 101, 2020.

- [162] M. Knecht, “On some short-distance properties of the fourth-rank hadronic vacuum polarization tensor and the anomalous magnetic moment of the muon,” *JHEP*, vol. 08, p. 056, 2020.
- [163] J. Lüdtke and M. Procura, “Effects of longitudinal short-distance constraints on the hadronic light-by-light contribution to the muon $g - 2$,” *Eur. Phys. J. C*, vol. 80, no. 12, p. 1108, 2020.
- [164] L. Cappiello, O. Catà, and G. D’Ambrosio, “Scalar resonances in the hadronic light-by-light contribution to the muon ($g-2$),” *Phys. Rev. D*, vol. 105, no. 5, p. 056020, 2022.
- [165] G. Colangelo, F. Hagelstein, M. Hoferichter, L. Laub, and P. Stoffer, “Short-distance constraints for the longitudinal component of the hadronic light-by-light amplitude: an update,” *Eur. Phys. J. C*, vol. 81, no. 8, p. 702, 2021.
- [166] A. Nyffeler, “Precision of a data-driven estimate of hadronic light-by-light scattering in the muon $g - 2$: Pseudoscalar-pole contribution,” *Phys. Rev. D*, vol. 94, no. 5, p. 053006, 2016.
- [167] P. Masjuan and P. Sanchez-Puertas, “Pseudoscalar-pole contribution to the $(g_\mu - 2)$: a rational approach,” *Phys. Rev. D*, vol. 95, no. 5, p. 054026, 2017.
- [168] H. J. Behrend *et al.*, “A Measurement of the π^0 , eta and eta-prime electromagnetic form-factors,” *Z. Phys. C*, vol. 49, pp. 401–410, 1991.
- [169] J. Gronberg *et al.*, “Measurements of the meson - photon transition form-factors of light pseudoscalar mesons at large momentum transfer,” *Phys. Rev. D*, vol. 57, pp. 33–54, 1998.
- [170] M. Acciarri *et al.*, “Measurement of eta-prime (958) formation in two photon collisions at LEP-1,” *Phys. Lett. B*, vol. 418, pp. 399–410, 1998.
- [171] B. Aubert *et al.*, “Measurement of the $\gamma\gamma^* \rightarrow \pi^0$ transition form factor,” *Phys. Rev. D*, vol. 80, p. 052002, 2009.
- [172] P. del Amo Sanchez *et al.*, “Measurement of the $\gamma\gamma^* \rightarrow \eta$ and $\gamma\gamma^* \rightarrow \eta'$ transition form factors,” *Phys. Rev. D*, vol. 84, p. 052001, 2011.
- [173] S. Uehara *et al.*, “Measurement of $\gamma\gamma^* \rightarrow \pi^0$ transition form factor at Belle,” *Phys. Rev. D*, vol. 86, p. 092007, 2012.
- [174] J. P. Lees *et al.*, “Measurement of the $\gamma^*\gamma^* \rightarrow \eta'$ transition form factor,” *Phys. Rev. D*, vol. 98, no. 11, p. 112002, 2018.
- [175] G. Peter Lepage and S. J. Brodsky, “Exclusive processes in quantum chromodynamics: Evolution equations for hadronic wavefunctions and the form factors of mesons,” *Physics Letters B*, vol. 87, no. 4, pp. 359–365, 1979.

- [176] G. P. Lepage and S. J. Brodsky, “Exclusive processes in perturbative quantum chromodynamics,” *Phys. Rev. D*, vol. 22, pp. 2157–2198, Nov 1980.
- [177] S. P. Schneider, B. Kubis, and F. Niecknig, “The $\omega \rightarrow \pi^0\gamma^*$ and $\phi \rightarrow \pi^0\gamma^*$ transition form factors in dispersion theory,” *Phys. Rev. D*, vol. 86, p. 054013, 2012.
- [178] C. Hanhart, A. Kupść, U. G. Meißner, F. Stollenwerk, and A. Wirzba, “Dispersive analysis for $\eta \rightarrow \gamma\gamma^*$,” *Eur. Phys. J. C*, vol. 73, no. 12, p. 2668, 2013. [Erratum: *Eur.Phys.J.C* 75, 242 (2015)].
- [179] M. Hoferichter, B. Kubis, S. Leupold, F. Niecknig, and S. P. Schneider, “Dispersive analysis of the pion transition form factor,” *Eur. Phys. J. C*, vol. 74, p. 3180, 2014.
- [180] S. Holz, J. Plenter, C. W. Xiao, T. Dato, C. Hanhart, B. Kubis, U. G. Meißner, and A. Wirzba, “Towards an improved understanding of $\eta \rightarrow \gamma^*\gamma^*$,” *Eur. Phys. J. C*, vol. 81, no. 11, p. 1002, 2021.
- [181] S. Holz, M. Hoferichter, B.-L. Hoid, and B. Kubis, “Dispersion relation for hadronic light-by-light scattering: η and η' poles,” *JHEP*, vol. 04, p. 147, 2025.
- [182] S. Holz, M. Hoferichter, B.-L. Hoid, and B. Kubis, “Precision Evaluation of the η - and η' -Pole Contributions to Hadronic Light-by-Light Scattering in the Anomalous Magnetic Moment of the Muon,” *Phys. Rev. Lett.*, vol. 134, no. 17, p. 171902, 2025.
- [183] D. Stamen, D. Hariharan, M. Hoferichter, B. Kubis, and P. Stoffer, “Kaon electromagnetic form factors in dispersion theory,” *Eur. Phys. J. C*, vol. 82, no. 5, p. 432, 2022.
- [184] D. Drechsel, G. Knochlein, A. Y. Korchin, A. Metz, and S. Scherer, “Structure analysis of the virtual Compton scattering amplitude at low-energies,” *Phys. Rev. C*, vol. 57, pp. 941–952, 1998.
- [185] G. Colangelo, J. Gasser, and H. Leutwyler, “ $\pi\pi$ scattering,” *Nucl. Phys. B*, vol. 603, pp. 125–179, 2001.
- [186] J. F. de Troconiz and F. J. Yndurain, “The Hadronic contributions to the anomalous magnetic moment of the muon,” *Phys. Rev. D*, vol. 71, p. 073008, 2005.
- [187] C. Hanhart, “A New Parameterization for the Pion Vector Form Factor,” *Phys. Lett. B*, vol. 715, pp. 170–177, 2012.
- [188] I. Danilkin, O. Deineka, and M. Vanderhaeghen, “Data-driven dispersive analysis of the $\pi\pi$ and πK scattering,” *Phys. Rev. D*, vol. 103, no. 11, p. 114023, 2021.
- [189] I. Danilkin, M. Hoferichter, and P. Stoffer, “A dispersive estimate of scalar contributions to hadronic light-by-light scattering,” *Phys. Lett. B*, vol. 820, p. 136502, 2021.

- [190] O. Deineka, I. Danilkin, and M. Vanderhaeghen, “Dispersive estimate of the $a_0(980)$ contribution to $(g-2)_\mu$,” *Phys. Rev. D*, vol. 111, no. 3, p. 034009, 2025.
- [191] M. Hoferichter, P. Stoffer, and M. Zillinger, “Dispersion relation for hadronic light-by-light scattering: subleading contributions,” *JHEP*, vol. 02, p. 121, 2025.
- [192] M. Hoferichter, P. Stoffer, and M. Zillinger, “Complete Dispersive Evaluation of the Hadronic Light-by-Light Contribution to Muon $g-2$,” *Phys. Rev. Lett.*, vol. 134, no. 6, p. 061902, 2025.
- [193] H. Marsiske *et al.*, “A Measurement of $\pi^0\pi^0$ Production in Two Photon Collisions,” *Phys. Rev. D*, vol. 41, p. 3324, 1990.
- [194] J. Boyer *et al.*, “Two photon production of pion pairs,” *Phys. Rev. D*, vol. 42, pp. 1350–1367, 1990.
- [195] H. J. Behrend *et al.*, “An Experimental study of the process $\gamma\gamma \rightarrow \pi^+\pi^-$,” *Z. Phys. C*, vol. 56, pp. 381–390, 1992.
- [196] T. Mori *et al.*, “High statistics measurement of the cross-sections of $\gamma\gamma \rightarrow \pi^+\pi^-$ production,” *J. Phys. Soc. Jap.*, vol. 76, p. 074102, 2007.
- [197] S. Uehara *et al.*, “High-statistics measurement of neutral pion-pair production in two-photon collisions,” *Phys. Rev. D*, vol. 78, p. 052004, 2008.
- [198] S. Uehara *et al.*, “High-statistics study of neutral-pion pair production in two-photon collisions,” *Phys. Rev. D*, vol. 79, p. 052009, 2009.
- [199] M. K usner, *Coupled channel partial wave analysis of two-photon reactions at BESIII*. doctoralthesis, Ruhr-Universit at Bochum, Universit atsbibliothek, 2022.
- [200] M. Masuda *et al.*, “Study of π^0 pair production in single-tag two-photon collisions,” *Phys. Rev. D*, vol. 93, no. 3, p. 032003, 2016.
- [201] M. Hoferichter, P. Stoffer, and M. Zillinger, “An optimized basis for hadronic light-by-light scattering,” *JHEP*, vol. 04, p. 092, 2024.
- [202] M. Hoferichter and P. Stoffer, “Asymptotic behavior of meson transition form factors,” *JHEP*, vol. 05, p. 159, 2020.
- [203] G. A. Schuler, F. A. Berends, and R. van Gulik, “Meson photon transition form-factors and resonance cross-sections in e^+e^- collisions,” *Nucl. Phys. B*, vol. 523, pp. 423–438, 1998.
- [204] M. Hoferichter, B. Kubis, and M. Zanke, “Axial-vector transition form factors and $e^+e^- \rightarrow f_1\pi^+\pi^-$,” *JHEP*, vol. 08, p. 209, 2023.
- [205] M. Zanke, M. Hoferichter, and B. Kubis, “On the transition form factors of the axial-vector resonance $f_1(1285)$ and its decay into e^+e^- ,” *JHEP*, vol. 07, p. 106, 2021.

- [206] P. Achard *et al.*, “ $f_1(1285)$ formation in two photon collisions at LEP,” *Phys. Lett. B*, vol. 526, pp. 269–277, 2002.
- [207] J. M. Maldacena, “The Large N limit of superconformal field theories and supergravity,” *Adv. Theor. Math. Phys.*, vol. 2, pp. 231–252, 1998.
- [208] O. Aharony, S. S. Gubser, J. M. Maldacena, H. Ooguri, and Y. Oz, “Large N field theories, string theory and gravity,” *Phys. Rept.*, vol. 323, pp. 183–386, 2000.
- [209] J. Erlich, E. Katz, D. T. Son, and M. A. Stephanov, “QCD and a holographic model of hadrons,” *Phys. Rev. Lett.*, vol. 95, p. 261602, 2005.
- [210] L. Da Rold and A. Pomarol, “Chiral symmetry breaking from five dimensional spaces,” *Nucl. Phys. B*, vol. 721, pp. 79–97, 2005.
- [211] J. Hirn and V. Sanz, “Interpolating between low and high energy QCD via a 5-D Yang-Mills model,” *JHEP*, vol. 12, p. 030, 2005.
- [212] A. Karch, E. Katz, D. T. Son, and M. A. Stephanov, “Linear confinement and AdS/QCD,” *Phys. Rev. D*, vol. 74, p. 015005, 2006.
- [213] D. K. Hong and D. Kim, “Pseudo scalar contributions to light-by-light correction of muon $g-2$ in AdS/QCD,” *Phys. Lett. B*, vol. 680, pp. 480–484, 2009.
- [214] O. Domenech, G. Panico, and A. Wulzer, “Massive Pions, Anomalies and Baryons in Holographic QCD,” *Nucl. Phys. A*, vol. 853, pp. 97–123, 2011.
- [215] L. Cappiello, O. Cata, and G. D’Ambrosio, “The hadronic light by light contribution to the $(g - 2)_\mu$ with holographic models of QCD,” *Phys. Rev. D*, vol. 83, p. 093006, 2011.
- [216] L. Cappiello, O. Catà, G. D’Ambrosio, D. Greynat, and A. Iyer, “Axial-vector and pseudoscalar mesons in the hadronic light-by-light contribution to the muon $(g - 2)$,” *Phys. Rev. D*, vol. 102, no. 1, p. 016009, 2020.
- [217] J. Leutgeb, J. Mager, and A. Rebhan, “Pseudoscalar transition form factors and the hadronic light-by-light contribution to the anomalous magnetic moment of the muon from holographic QCD,” *Phys. Rev. D*, vol. 100, no. 9, p. 094038, 2019. [Erratum: *Phys.Rev.D* 104, 059903 (2021)].
- [218] J. Leutgeb and A. Rebhan, “Hadronic light-by-light contribution to the muon $g-2$ from holographic QCD with massive pions,” *Phys. Rev. D*, vol. 104, no. 9, p. 094017, 2021.
- [219] J. Leutgeb, J. Mager, and A. Rebhan, “Hadronic light-by-light contribution to the muon $g-2$ from holographic QCD with solved $U(1)_A$ problem,” *Phys. Rev. D*, vol. 107, no. 5, p. 054021, 2023.

- [220] J. Lüdtke, M. Procura, and P. Stoffer, “Dispersion relations for the hadronic VVA correlator,” *JHEP*, vol. 04, p. 130, 2025.
- [221] J. Leutgeb, J. Mager, and A. Rebhan, “Superconnections in AdS/QCD and the hadronic light-by-light contribution to the muon $g-2$,” *Phys. Rev. D*, vol. 111, no. 11, p. 114001, 2025.
- [222] S. Peris, “Large- $N(c)$ QCD and Pade approximant theory,” *Phys. Rev. D*, vol. 74, p. 054013, 2006.
- [223] M. Golterman and S. Peris, “On the relation between low-energy constants and resonance saturation,” *Phys. Rev. D*, vol. 74, p. 096002, 2006.
- [224] P. Masjuan and S. Peris, “A Rational approach to resonance saturation in large- $N(c)$ QCD,” *JHEP*, vol. 05, p. 040, 2007.
- [225] P. Masjuan and S. Peris, “A Rational approximation to $\langle VV-AA \rangle$ and its $O(p^6)$ low-energy constant,” *Phys. Lett. B*, vol. 663, pp. 61–65, 2008.
- [226] P. Masjuan and S. Peris, “Pade Theory applied to the vacuum polarization of a heavy quark,” *Phys. Lett. B*, vol. 686, pp. 307–312, 2010.
- [227] P. Masjuan, “ $\gamma^*\gamma \rightarrow \pi^0$ transition form factor at low-energies from a model-independent approach,” *Phys. Rev. D*, vol. 86, p. 094021, 2012.
- [228] R. Escribano, S. González-Solís, P. Masjuan, and P. Sanchez-Puertas, “ η' transition form factor from space- and timelike experimental data,” *Phys. Rev. D*, vol. 94, no. 5, p. 054033, 2016.
- [229] R. Escribano, P. Masjuan, and P. Sanchez-Puertas, “ η and η' transition form factors from rational approximants,” *Phys. Rev. D*, vol. 89, no. 3, p. 034014, 2014.
- [230] R. Escribano, P. Masjuan, and P. Sanchez-Puertas, “The η transition form factor from space- and time-like experimental data,” *Eur. Phys. J. C*, vol. 75, no. 9, p. 414, 2015.
- [231] P. Masjuan Queralt, “Rational Approximations in Quantum Chromodynamics,” other thesis, 5 2010.
- [232] E. J. Estrada, S. González-Solís, A. Guevara, and P. Roig, “Improved π^0 , η , η' transition form factors in resonance chiral theory and their a_μ^{HLbL} contribution,” *JHEP*, vol. 12, p. 203, 2024.
- [233] E. J. Estrada and P. Roig, “Tensor Meson Pole contributions to the HLbL piece of a_μ^{HLbL} within $R\chi T$,” 4 2025.
- [234] P. Masjuan, P. Roig, and P. Sanchez-Puertas, “The interplay of transverse degrees of freedom and axial-vector mesons with short-distance constraints in $g - 2$,” *J. Phys. G*, vol. 49, no. 1, p. 015002, 2022.

- [235] G. Eichmann, C. S. Fischer, and R. Williams, “Kaon-box contribution to the anomalous magnetic moment of the muon,” *Phys. Rev. D*, vol. 101, no. 5, p. 054015, 2020.
- [236] G. Eichmann, C. S. Fischer, E. Weil, and R. Williams, “Single pseudoscalar meson pole and pion box contributions to the anomalous magnetic moment of the muon,” *Phys. Lett. B*, vol. 797, p. 134855, 2019. [Erratum: *Phys.Lett.B* 799, 135029 (2019)].
- [237] G. Eichmann, C. S. Fischer, T. Haeuser, and O. Regenfelder, “Axial-vector and scalar contributions to hadronic light-by-light scattering,” *Eur. Phys. J. C*, vol. 85, no. 4, p. 445, 2025.
- [238] L. Cappiello, J. Leutgeb, J. Mager, and A. Rebhan, “Tensor meson transition form factors in holographic QCD and the muon $g - 2$,” *JHEP*, vol. 07, p. 033, 2025.
- [239] J. Leutgeb and A. Rebhan, “Axial vector transition form factors in holographic QCD and their contribution to the anomalous magnetic moment of the muon,” *Phys. Rev. D*, vol. 101, no. 11, p. 114015, 2020.
- [240] G. Colangelo, M. Hoferichter, A. Nyffeler, M. Passera, and P. Stoffer, “Remarks on higher-order hadronic corrections to the muon $g-2$,” *Phys. Lett. B*, vol. 735, pp. 90–91, 2014.
- [241] X.-d. Ji and C.-w. Jung, “Studying hadronic structure of the photon in lattice QCD,” *Phys. Rev. Lett.*, vol. 86, p. 208, 2001.
- [242] X. Feng, S. Aoki, H. Fukaya, S. Hashimoto, T. Kaneko, J.-i. Noaki, and E. Shintani, “Two-photon decay of the neutral pion in lattice QCD,” *Phys. Rev. Lett.*, vol. 109, p. 182001, 2012.
- [243] A. Gérardin, H. B. Meyer, and A. Nyffeler, “Lattice calculation of the pion transition form factor $\pi^0 \rightarrow \gamma^* \gamma^*$,” *Phys. Rev. D*, vol. 94, no. 7, p. 074507, 2016.
- [244] A. Gérardin, H. B. Meyer, and A. Nyffeler, “Lattice calculation of the pion transition form factor with $N_f = 2+1$ Wilson quarks,” *Phys. Rev. D*, vol. 100, no. 3, p. 034520, 2019.
- [245] C. Alexandrou *et al.*, “ $\eta \rightarrow \gamma^* \gamma^*$ transition form factor and the hadronic light-by-light η -pole contribution to the muon $g-2$ from lattice QCD,” *Phys. Rev. D*, vol. 108, no. 5, p. 054509, 2023.
- [246] A. Gérardin, W. E. A. Verplanke, G. Wang, Z. Fodor, J. N. Guenther, L. Lellouch, K. K. Szabo, and L. Varnhorst, “Lattice calculation of the π_0 , η and η' transition form factors and the hadronic light-by-light contribution to the muon $g-2$,” *Phys. Rev. D*, vol. 111, no. 5, p. 054511, 2025.

- [247] C. Alexandrou *et al.*, “Pion transition form factor from twisted-mass lattice QCD and the hadronic light-by-light π^0 -pole contribution to the muon $g-2$,” *Phys. Rev. D*, vol. 108, no. 9, p. 094514, 2023.
- [248] J. Koponen, A. Gérardin, H. B. Meyer, K. Ottnad, and G. von Hippel, “Status update: $\pi^0 \rightarrow \gamma^* \gamma^*$ transition form factor on CLS ensembles,” *PoS*, vol. LATTICE2023, p. 254, 2024.
- [249] T. Blum, N. Christ, M. Hayakawa, T. Izubuchi, L. Jin, C. Jung, and C. Lehner, “The hadronic light-by-light scattering contribution to the muon anomalous magnetic moment from lattice QCD,” *Phys. Rev. Lett.*, vol. 124, no. 13, p. 132002, 2020.
- [250] E.-H. Chao, R. J. Hudspith, A. Gérardin, J. R. Green, H. B. Meyer, and K. Ottnad, “Hadronic light-by-light contribution to $(g-2)_\mu$ from lattice QCD: a complete calculation,” *Eur. Phys. J. C*, vol. 81, no. 7, p. 651, 2021.
- [251] E.-H. Chao, R. J. Hudspith, A. Gérardin, J. R. Green, and H. B. Meyer, “The charm-quark contribution to light-by-light scattering in the muon $(g-2)$ from lattice QCD,” *Eur. Phys. J. C*, vol. 82, no. 8, p. 664, 2022.
- [252] T. Blum, N. Christ, M. Hayakawa, T. Izubuchi, L. Jin, C. Jung, C. Lehner, and C. Tu, “Hadronic light-by-light contribution to the muon anomaly from lattice QCD with infinite volume QED at physical pion mass,” *Phys. Rev. D*, vol. 111, no. 1, p. 014501, 2025.
- [253] Z. Fodor, A. Gérardin, L. Lellouch, K. K. Szabó, B. C. Toth, and C. Zimmermann, “Hadronic light-by-light scattering contribution to the anomalous magnetic moment of the muon at the physical pion mass,” *Phys. Rev. D*, vol. 111, no. 11, p. 114509, 2025.
- [254] V. Pascalutsa, V. Pauk, and M. Vanderhaeghen, “Light-by-light scattering sum rules constraining meson transition form factors,” *Phys. Rev. D*, vol. 85, p. 116001, 2012.
- [255] M. Vanderhaeghen. private communication, 2024.
- [256] M. Lellmann, I. Danilkin, A. Denig, J. Muskalla, C. F. Redmer, X.-L. Ren, and M. Vanderhaeghen, “HadroTOPS: A Monte Carlo Event Generator For Hadron Production In Two-Photon Scattering In Electron Positron Collisions,” 11 2025.
- [257] G. Bonneau, M. Gourdin, and F. Martin, “Inelastic lepton anti-lepton scattering and the two photon exchange approximation,” *Nucl. Phys. B*, vol. 54, pp. 573–597, 1973.
- [258] I. Danilkin, O. Deineka, and M. Vanderhaeghen, “Dispersive analysis of the $\gamma^* \gamma^* \rightarrow \pi\pi$ process,” *Phys. Rev. D*, vol. 101, no. 5, p. 054008, 2020.
- [259] I. Danilkin and M. Vanderhaeghen, “Dispersive analysis of the $\gamma\gamma^* \rightarrow \pi\pi$ process,” *Phys. Lett. B*, vol. 789, pp. 366–372, 2019.

- [260] I. Danilkin, C. F. Redmer, and M. Vanderhaeghen, “The hadronic light-by-light contribution to the muon’s anomalous magnetic moment,” *Prog. Part. Nucl. Phys.*, vol. 107, pp. 20–68, 2019.
- [261] M. Hoferichter and P. Stoffer, “Dispersion relations for $\gamma^*\gamma^* \rightarrow \pi\pi$: helicity amplitudes, subtractions, and anomalous thresholds,” *JHEP*, vol. 07, p. 073, 2019.
- [262] M. Fritsch, M. Michel, S. Pflüger, R. de Boer, L. Wollenberg, W. Gradl, P. Weidenkaff, K. Peters, and K. Götzen, “Common partial wave analysis: A collaboration-independent organisation for amplitude analysis software,” 2022.
- [263] M. Shepherd, J. Stevens, R. Mitchell, M. Albrecht, B. Grube, A. Austregesilo, N. D. Hoffman, and N. Hüsken, “AmpTools: Version 0.15.2,” 2023.
- [264] H. Czyz and S. Ivashyn, “EKHARA: A Monte Carlo generator for $e^+e^- \rightarrow e^+e^-\pi^0$ and $e^+e^- \rightarrow e^+e^-\pi^+\pi^-$ processes,” *Comput. Phys. Commun.*, vol. 182, pp. 1338–1349, 2011.
- [265] H. Czyz, S. Ivashyn, A. Korchin, and O. Shekhovtsova, “Two-photon form factors of the π^0 , η and η' mesons in the chiral theory with resonances,” *Phys. Rev. D*, vol. 85, p. 094010, 2012.
- [266] H. Czyż, P. Kiswa, and S. Tracz, “Modeling interactions of photons with pseudoscalar and vector mesons,” *Phys. Rev. D*, vol. 97, no. 1, p. 016006, 2018.
- [267] H. Czyz and P. Kiswa, “EKHARA 3.0: an update of the EKHARA Monte Carlo event generator,” *Comput. Phys. Commun.*, vol. 234, pp. 245–255, 2019.
- [268] H. Czyż. personal communication, 2023.
- [269] A. Courau, “A fast monte carlo generator for $ee \rightarrow eeX$ untagged experiments,” in *6th International Conference on Photon-Photon Collisions*, 6 1984.
- [270] S. Uehara, “TREPS: A Monte-Carlo Event Generator for Two-photon Processes at e^+e^- Colliders using an Equivalent Photon Approximation,” 7 1996.
- [271] G. A. Schuler, “Two-photon physics with GALUGA 2.0,” *Computer Physics Communications*, vol. 108, no. 2, pp. 279–303, 1998.
- [272] V. Druzhinin, L. Kardapoltsev, and V. Tayursky, “GGRESRC: A Monte Carlo generator for the two-photon process $e^+e^- \rightarrow e^+e^-R(J^{PC} = 0^{-+})$ in the single-tag mode,” *Computer Physics Communications*, vol. 185, no. 1, pp. 236–243, 2014.
- [273] O. Deineka, I. Danilkin, and M. Vanderhaeghen, “Theoretical analysis of the $\gamma\gamma^{(*)} \rightarrow \pi^0\eta$ process,” *EPJ Web Conf.*, vol. 199, p. 02005, 2019.
- [274] R. Brun and F. Rademakers, “Root - an object oriented data analysis framework,” June 2020.

- [275] S. Navas *et al.*, “Review of particle physics,” *Phys. Rev. D*, vol. 110, no. 3, p. 030001, 2024.
- [276] F. James, “Monte-Carlo phase space,” 5 1968.
- [277] J. J. Sakurai and D. Schildknecht, “Generalized vector dominance and inelastic electron - proton scattering,” *Phys. Lett. B*, vol. 40, pp. 121–126, 1972.
- [278] L. B. Bezurkov and E. V. Bugaev, “Inelastic scattering of muons on nucleons in diffractive regions,” *Sov. J. Nucl. Phys.*, vol. 32, p. 847, 1980.
- [279] Y. Guo, “Two photon physics at BESIII,” *J. Phys. Conf. Ser.*, vol. 1137, no. 1, p. 012008, 2019.
- [280] K. Abe *et al.*, “Measurement of K^+K^- production in two photon collisions in the resonant mass region,” *Eur. Phys. J. C*, vol. 32, pp. 323–336, 2003.
- [281] H. Nakazawa *et al.*, “Measurement of the $\gamma\gamma \rightarrow \pi^+\pi^-$ and $\gamma\gamma \rightarrow K^+K^-$ processes at energies of 2.4-GeV to 4.1-GeV,” *Phys. Lett. B*, vol. 615, pp. 39–49, 2005.
- [282] S. Uehara *et al.*, “High-statistics study of K_S^0 pair production in two-photon collisions,” *PTEP*, vol. 2013, no. 12, p. 123C01, 2013.
- [283] S. Uehara *et al.*, “Measurement of $\eta\eta$ production in two-photon collisions,” *Phys. Rev. D*, vol. 82, p. 114031, 2010.
- [284] M. Küßner, “Recent Highlights on Meson Spectroscopy at BESIII,” *EPJ Web Conf.*, vol. 291, p. 01002, 2024.
- [285] J. Muskalla, A. Denig, and C. F. Redmer, “Measurement of the Singly Virtual Transition Form Factor of the $f_1(1285)$ in a Partial Wave Analysis at BESIII,” in *Eighth Plenary Workshop of the Muon g-2 Theory Initiative*, 2025.
- [286] X.-L. Ren, I. Danilkin, and M. Vanderhaeghen, “Phenomenological model for the $\gamma^*\gamma \rightarrow \eta\pi^+\pi^-$ reaction in the $f_1(1285)$ energy region,” *Phys. Rev. D*, vol. 110, no. 9, p. 094043, 2024.
- [287] J. von Neumann, “Various techniques used in connection with random digits. Monte Carlo methods. ,” *Nat. Bureau Standards*, vol. 12, pp. 36–38, 1951.
- [288] M. Ablikim *et al.*, “Measurement of the space-like π^0 transition form factor,” 9 2025.
- [289] C.H. Yu and others, “BEPcII Performance and Beam Dynamics Studies on Luminosity,” in *Proc. of International Particle Accelerator Conference (IPAC’16), Busan, Korea, May 8-13, 2016*, no. 7 in International Particle Accelerator Conference, (Geneva, Switzerland), pp. 1014–1018, JACoW, June 2016.
- [290] Ablikim, M. and others, “Future Physics Programme of BESIII,” *Chin. Phys. C*, vol. 44, no. 4, p. 040001, 2020.

- [291] Guangshun Huang, “Timelike form factor measurements at besiii,” 2015.
- [292] Ablikim, M. and others, “Design and Construction of the BESIII Detector,” *Nucl. Instrum. Meth. A*, vol. 614, pp. 345–399, 2010.
- [293] H. Bethe, “Zur Theorie des Durchgangs schneller Korpuskularstrahlen durch Materie,” *Annalen der Physik*, vol. 397, no. 3, pp. 325–400, 1930.
- [294] F. Bloch, “Zur Bremsung rasch bewegter Teilchen beim Durchgang durch Materie,” *Annalen der Physik*, vol. 408, no. 3, pp. 285–320, 1933.
- [295] D. M. Asner *et al.*, “Physics at BES-III,” *Int. J. Mod. Phys.*, vol. A24, pp. S1–794, 2009.
- [296] X. Wang *et al.*, “The upgrade system of BESIII ETOF with MRPC technology,” *JINST*, vol. 11, no. 08, p. C08009, 2016.
- [297] P. Cao *et al.*, “Design and construction of the new BESIII endcap Time-of-Flight system with MRPC Technology,” *Nucl. Instrum. Meth. A*, vol. 953, p. 163053, 2020.
- [298] S.-J. Wei *et al.*, “Introduction to BESIII EMC sub-trigger system,” *Nucl. Instrum. Meth. A*, vol. 598, pp. 323–327, 2009.
- [299] N. Berger, K. Zhu, Z.-A. Liu, D.-P. Jin, H. Xu, W.-X. Gong, K. Wang, and G.-F. Cao, “Trigger efficiencies at BES III,” *Chin. Phys. C*, vol. 34, pp. 1779–1784, 2010.
- [300] G. Barrand *et al.*, “GAUDI - A software architecture and framework for building HEP data processing applications,” *Comput. Phys. Commun.*, vol. 140, pp. 45–55, 2001.
- [301] S. Agostinelli *et al.*, “GEANT4 - A Simulation Toolkit,” *Nucl. Instrum. Meth. A*, vol. 506, pp. 250–303, 2003.
- [302] J. Allison *et al.*, “Geant4 developments and applications,” *IEEE Trans. Nucl. Sci.*, vol. 53, p. 270, 2006.
- [303] J. Allison *et al.*, “Recent developments in Geant4,” *Nucl. Instrum. Meth. A*, vol. 835, pp. 186–225, 2016.
- [304] J. D. Hunter, “Matplotlib: A 2d graphics environment,” *Computing in Science & Engineering*, vol. 9, no. 3, pp. 90–95, 2007.
- [305] R. Farinelli *et al.*, “Preliminary results from the cosmic data taking of the BESIII cylindrical GEM detectors,” *JINST*, vol. 15, no. 08, p. C08004, 2020.
- [306] S. Gramigna, “Operation of the new CGEM Inner Tracker for the Upgrade of the BESIII Experiment,” *PoS*, vol. EPS-HEP2021, p. 766, 2022.

- [307] A. Bortone, “Development and operation of the CGEM Inner Tracker for the BESIII experiment,” *Nucl. Instrum. Meth. A*, vol. 1048, p. 167957, 2023.
- [308] I. Balossino, F. Cossio, R. Farinelli, and L. Lavezzi, “The CGEM-IT: An Upgrade for the BESIII Experiment,” *Symmetry*, vol. 14, no. 5, p. 905, 2022.
- [309] R. Farinelli, “Operation and readout of the CGEM inner tracker,” *JINST*, vol. 18, no. 05, p. C05022, 2023.
- [310] F. M. Melendi, “Operation and readout of CGEM inner Tracker,” *PoS*, vol. ICHEP2024, p. 1086, 2025.
- [311] S. Gramigna, “Construction, Commissioning, and Installation of the Cylindrical GEM Inner Tracker of the BESIII Experiment,” 5 2025.
- [312] Frederic Stieler, *Construction and testing of the crystal Zero Degree Detector for BE-III*. Master’s thesis, Johannes Gutenberg-Universität Mainz, September 2021.
- [313] M. Ablikim *et al.*, “Measurement of integrated luminosity of data collected at 3.773 GeV by BESIII from 2021 to 2024*,” *Chin. Phys. C*, vol. 48, no. 12, p. 123001, 2024.
- [314] C. M. Carloni Calame, C. Lunardini, G. Montagna, O. Nicosini, and F. Piccinini, “Large angle Bhabha scattering and luminosity at flavor factories,” *Nucl. Phys. B*, vol. 584, pp. 459–479, 2000.
- [315] C. M. Carloni Calame, “An Improved parton shower algorithm in QED,” *Phys. Lett. B*, vol. 520, pp. 16–24, 2001.
- [316] C. M. Carloni Calame, G. Montagna, O. Nicosini, and F. Piccinini, “The BABAYAGA event generator,” *Nucl. Phys. B Proc. Suppl.*, vol. 131, pp. 48–55, 2004.
- [317] G. Balossini, C. M. Carloni Calame, G. Montagna, O. Nicosini, and F. Piccinini, “Matching perturbative and parton shower corrections to Bhabha process at flavour factories,” *Nucl. Phys. B*, vol. 758, pp. 227–253, 2006.
- [318] G. Balossini, C. Bignamini, C. M. C. Calame, G. Montagna, O. Nicosini, and F. Piccinini, “Photon pair production at flavour factories with per mille accuracy,” *Phys. Lett. B*, vol. 663, pp. 209–213, 2008.
- [319] S. Jadach, B. F. L. Ward, and Z. Was, “The Precision Monte Carlo event generator K K for two fermion final states in $e^+ e^-$ collisions,” *Comput. Phys. Commun.*, vol. 130, pp. 260–325, 2000.
- [320] G. Rodrigo, A. Gehrmann-De Ridder, M. Guillaume, and J. H. Kuhn, “NLO QED corrections to ISR in $e^+ e^-$ annihilation and the measurement of $\sigma(e^+ e^- \rightarrow \text{hadrons})$ using tagged photons,” *Eur. Phys. J. C*, vol. 22, pp. 81–88, 2001.

- [321] G. Rodrigo, H. Czyz, J. H. Kuhn, and M. Szopa, “Radiative return at NLO and the measurement of the hadronic cross-section in electron positron annihilation,” *Eur. Phys. J. C*, vol. 24, pp. 71–82, 2002.
- [322] J. H. Kuhn and G. Rodrigo, “The Radiative return at small angles: Virtual corrections,” *Eur. Phys. J. C*, vol. 25, pp. 215–222, 2002.
- [323] H. Czyz, A. Grzelinska, J. H. Kuhn, and G. Rodrigo, “The Radiative return at phi and B factories: Small angle photon emission at next-to-leading order,” *Eur. Phys. J. C*, vol. 27, pp. 563–575, 2003.
- [324] H. Czyz, A. Grzelinska, J. H. Kuhn, and G. Rodrigo, “The Radiative return at Phi and B factories: FSR at next-to-leading order,” *Eur. Phys. J. C*, vol. 33, pp. 333–347, 2004.
- [325] H. Czyz, J. H. Kuhn, E. Nowak, and G. Rodrigo, “Nucleon form-factors, B meson factories and the radiative return,” *Eur. Phys. J. C*, vol. 35, pp. 527–536, 2004.
- [326] H. Czyz, A. Grzelinska, J. H. Kuhn, and G. Rodrigo, “The Radiative return at phi and B factories: FSR for muon pair production at next-to-leading order,” *Eur. Phys. J. C*, vol. 39, pp. 411–420, 2005.
- [327] H. Czyz, A. Grzelinska, and J. H. Kuhn, “Charge asymmetry and radiative phi decays,” *Phys. Lett. B*, vol. 611, pp. 116–122, 2005.
- [328] H. Czyz, A. Grzelinska, J. H. Kuhn, and G. Rodrigo, “Electron-positron annihilation into three pions and the radiative return,” *Eur. Phys. J. C*, vol. 47, pp. 617–624, 2006.
- [329] H. Czyz, A. Grzelinska, and J. H. Kuhn, “Spin asymmetries and correlations in lambda-pair production through the radiative return method,” *Phys. Rev. D*, vol. 75, p. 074026, 2007.
- [330] H. Czyz, J. H. Kuhn, and A. Wapientnik, “Four-pion production in tau decays and e^+e^- annihilation: An Update,” *Phys. Rev. D*, vol. 77, p. 114005, 2008.
- [331] H. Czyz and J. H. Kuhn, “Strong and Electromagnetic J/psi and psi(2S) Decays into Pion and Kaon Pairs,” *Phys. Rev. D*, vol. 80, p. 034035, 2009.
- [332] H. Czyz, A. Grzelinska, and J. H. Kuhn, “Narrow resonances studies with the radiative return method,” *Phys. Rev. D*, vol. 81, p. 094014, 2010.
- [333] F. Campanario, H. Czyz, J. Gluza, M. Gunia, T. Riemann, G. Rodrigo, and V. Yundin, “Complete QED NLO contributions to the reaction $e^+e^- \rightarrow \mu^+\mu^-\gamma$ and their implementation in the event generator PHOKHARA,” *JHEP*, vol. 02, p. 114, 2014.
- [334] H. Czyz, M. Gunia, and J. H. Kühn, “Simulation of electron-positron annihilation into hadrons with the event generator PHOKHARA,” *JHEP*, vol. 08, p. 110, 2013.

- [335] H. Czyz, J. H. Kühn, and S. Tracz, “Nucleon form factors and final state radiative corrections to $e^+e^- \rightarrow p\bar{p}\gamma$,” *Phys. Rev. D*, vol. 90, no. 11, p. 114021, 2014.
- [336] H. Czyz, J. H. Kühn, and S. Tracz, “ χ_{c1} and χ_{c2} production at e^+e^- colliders,” *Phys. Rev. D*, vol. 94, no. 3, p. 034033, 2016.
- [337] F. Campanario, H. Czyz, J. Gluza, T. Jeliński, G. Rodrigo, S. Tracz, and D. Zhuridov, “Standard model radiative corrections in the pion form factor measurements do not explain the a_μ anomaly,” *Phys. Rev. D*, vol. 100, no. 7, p. 076004, 2019.
- [338] R.-G. Ping, “Event generators at BESIII,” *Chin. Phys. C*, vol. 32, p. 599, 2008.
- [339] W. R. Inc., “Mathematica, Version 14.2.” Champaign, IL, 2024.
- [340] S. B. Debus, *Investigation of the Track Reconstruction Performance of Electrons at the BESIII Experiment*. Bachelor’s thesis, Johannes Gutenberg-Universität Mainz, 2025.
- [341] L. Yang, Z. Li, and L. Dong, “Study of π^0 reconstruction efficiency for 20fb^{-1} $\psi(3773)$ data under BOSS 7.1.2,” *BESIII Analysis Memo*, vol. 408, 2024.
- [342] L. D. Landau, “On the angular momentum of a system of two photons,” *Dokl. Akad. Nauk SSSR*, vol. 60, no. 2, pp. 207–209, 1948.
- [343] C. N. Yang, “Selection rules for the dematerialization of a particle into two photons,” *Phys. Rev.*, vol. 77, pp. 242–245, Jan 1950.
- [344] I. Danilkin. private communication, 2025.
- [345] J. M. Blatt and V. F. Weisskopf, *Theoretical Nuclear Physics*. New York, NY: Springer, Nov. 2011.
- [346] M. Lellmann, “Study of Neutral-Pion Pair Production in Two-Photon Scattering at BESIII,” *EPJ Web Conf.*, vol. 303, p. 01017, 2024.

List of Figures

1.1	Schematic drawing of the Standard Model	3
1.2	Schematic illustration of the storage ring, detector instrumentation, and the decay pattern of a muon inside the storage ring at the BNL and FNAL experiments.	5
1.3	Observed event rate as a function of time after injection (inset), and Fourier transform of the residuals from the fits to the last three runs of the FNAL muon $g - 2$ experiment.	6
1.4	Feynman Graph of the leading order QED correction.	8
1.5	Leading-order Feynman graphs of the contributions from the weak interaction to the muon anomalous magnetic moment.	8
1.6	Leading-order Feynman graph of the hadronic vacuum polarization contribution.	9
1.7	Comparison of the leading-order contribution of the pion form factor to the muon anomalous magnetic moment $a_{\mu}^{\pi\pi,LO}$ in the energy range $\sqrt{s} = (600 - 880) \text{ MeV}$	10
1.8	Leading-order Feynman graph of the hadronic Light-by-Light scattering contribution.	11
1.9	Feynman graphs of the leading order long distance contributions to the HLbL contribution to a_{μ}^{HLbL} [147].	13
1.10	Comparison of the different contributions to the central value and the uncertainty of the phenomenologically determined a_{μ}^{HLbL}	17
1.11	Comparison of the Standard Model predictions of the muon anomalous magnetic moment to the experimental measurements and to the world average.	19
1.12	Feynman graph of the space-like two-photon process $e^+e^- \rightarrow e^+e^- \mathcal{M}$	20
1.13	Definition of the coordinate system and angles in the two-photon center-of-mass system.	22
1.14	Comparison of the two-photon luminosity functions for different photon polarizations as function of the positron momentum transfer Q_1^2 for different two-photon center-of-mass energies W and electron momentum transfers Q_2^2	25

1.15	Measured two-photon production cross sections of neutral-pion pairs by the Belle collaboration, the Crystal Ball collaboration, and preliminary data from the BESIII collaboration.	27
1.16	Cross section measurement of singly virtual neutral-pion pair production by the Belle collaboration.	29
1.17	Dispersive theory prediction of the σ_{TT} (left) and σ_{LT} (right) cross sections in a single virtual and double virtual configuration.	30
2.1	Flowchart of the four-vector generation of the $e^+e^-\mathcal{M}$ final state.	42
2.2	Fit of the cross section model to the Belle $\gamma\gamma \rightarrow K^+K^-$ cross sections as function of the helicity angle $ \cos\theta^* $	46
2.3	Integrated BESIII partial-wave analysis and fits to the $\gamma\gamma \rightarrow K^+K^-$, $\gamma\gamma \rightarrow K_S K_S$ and $\gamma\gamma \rightarrow \eta\eta$ cross sections over different helicity angle ranges.	48
2.4	Comparison of the luminosity function of two transversely polarized photons calculated by HADROTOPS and analytical results.	54
2.5	Differential cross section as function of the modulation angle $\tilde{\phi}$	55
2.6	Two-Photon invariant mass distribution and momentum transfer Q_1^2 distribution for the simulation of two-hadron final states with HADROTOPS	57
2.7	Helicity angle $\cos\theta^*$ distributions for the simulation of two-hadron final states with HADROTOPS	58
2.8	Comparison of the predicted cross sections for the process $e^+e^- \rightarrow e^+e^-\pi^0\pi^0$ calculated by HADROTOPS , using the inclusive and exclusive cross section formulas, and with EKHARA3.2.	59
2.9	Differential cross sections of the process $e^+e^- \rightarrow e^+e^-f_1(1285) \rightarrow e^+e^-\eta\pi^+\pi^-$ as a function of the two-photon invariant mass W , the positron momentum transfer Q_1^2 , the $\eta\pi^+$ invariant mass, and the $\pi^+\pi^-$ invariant mass.	60
3.1	Schematic drawing of the storage ring.	64
3.2	Schematic illustration of the upper half of the BESIII detector.	65
3.3	textsGeant4 models of the main drift chamber, the time-of-flight system, the electromagnetic calorimeter, and the muon chambers.	66
5.1	Comparison of the distributions of the distance of closest approach of the reconstructed helices of charged track candidates to the interaction point in the radial (left) and beam direction of data and Monte Carlo distributions.	77
5.2	Comparison of the distributions of ratio of deposited energy in the calorimeter and measured momentum in the main drift chamber $E_{\text{EMC}}/p_{\text{MDC}}$ of charged track candidates in data (black points) and Monte Carlo distributions.	78
5.3	Comparison of the distributions of deposited energy in the calorimeter by photon candidates, energy in the calorimeter by photon candidates in the cut-off region, and separation angle between photon candidates and closest charged track of data and Monte Carlo distributions.	80

5.4	Comparison of the signal Monte Carlo distribution of the difference between generated and reconstructed missing momentum transfer as a function of the reconstructed missing momentum transfer.	82
5.5	Results of the fits to the smearing matrix of the missing momentum transfer as function of the reconstructed value of Q_2^2 and cumulative distributions of the generated missing momentum transfer $Q_{2,\text{gen.}}^2$	83
5.6	Comparison of distributions of missing momentum transfer of data and Monte Carlo distributions	84
5.7	Comparison of the distributions of χ_{3C}^2 of data and Monte Carlo distributions.	85
5.8	Comparison of distributions of the two-photon invariant mass calculated from the results of one-constraint kinematic fit of data and stacked Monte Carlo distributions before and after the constraint on χ_{3C}^2	86
5.9	Comparison of distributions of total transverse momentum p_T of data and stacked Monte Carlo distributions for two-pion invariant masses below 2 GeV and below 0.5 GeV.	87
5.10	Comparison of distributions of momentum transfer Q_1^2 , two-pion invariant mass, and pion helicity angle $ \cos\theta^* $ of data and stacked Monte Carlo distributions after all analysis constraints.	88
5.11	χ_{3C}^2 distributions at large values χ_{3C}^2 of the selected data for different momentum transfers, two-pion invariant mass, and helicity angle ranges.	91
5.12	Comparison of the distributions of photon-energy asymmetry for the data and stacked Monte Carlo simulations without and with a constraint on χ_{3C}^2	92
5.13	Comparison of χ_{3C}^2 distributions for the data and the signal Monte Carlo, stacked on top of the estimated background contribution.	93
5.14	Fits to the χ_{3C}^2 distributions for different two-pion invariant mass bins.	94
5.15	The event yield in signal window compared to the sideband extracted from the fitted background shape and event yield in the background window stacked with the remaining contribution of $\gamma\gamma \rightarrow \eta$ and $\gamma\gamma \rightarrow \eta'$ Monte Carlo simulations in different momentum-transfer bins.	95
5.16	The cumulative distribution of $Q_{2,\text{gen.}}^2$ for a constraint on $Q_{2,\text{rec.}}^2 < 0.05 \text{ GeV}^2$ including the statistical uncertainty and extracted effective constraints on $Q_{2,\text{gen.}}^2$ as function of $Q_{2,\text{rec.}}^2$	96
5.17	The reconstruction efficiency as function of two-pion invariant mass, momentum transfer, and pion helicity angle determined from signal Monte Carlo.	97
5.18	Model-averaged two-photon luminosity function and factor ε	99
5.19	Average two-pion invariant mass calculated from the signal channel Monte Carlo simulation.	100
5.20	Average momentum transfer calculated from the signal channel Monte Carlo simulation.	101
5.21	Two-photon luminosity functions for TT and LT photon polarizations in each bin.	102

5.22	Singly virtual effective two-photon production cross section of two neutral pions with purely statistical uncertainties.	104
5.23	Data and Monte Carlo detection efficiency difference for electrons and positrons and selected events as function of lepton momentum and lepton polar angle.	105
5.24	Measured π^0 momenta after all analysis cuts.	106
5.25	The observed variations for some bins compared to a Gaussian curve evaluated at the arithmetic mean and the calculated standard deviation.	107
5.26	The extracted integrated two-photon cross section for different background functions.	110
5.27	Maximum deviation of any model from the average luminosity function as a function of mass and momentum transfer.	111
5.28	The singly virtual integrated two-photon production cross section of neutral pion pairs is shown with total uncertainties and statistical uncertainties (black points), compared to the theoretical prediction by Danilkin and Vanderhaeghen.	113
5.29	Singly virtual differential two-photon production cross section of neutral pion pairs in the virtuality range $Q^2 = (0.1-0.3)$, GeV^2 , shown with total and statistical uncertainties, compared to the theoretical prediction by Danilkin and Vanderhaeghen.	114
5.30	Singly virtual differential two-photon production cross section of neutral pion pairs in the virtuality ranges $Q^2 = (0.3-0.4)$ GeV^2 and $Q^2 = (0.4-0.5)$ GeV^2 , shown with total and statistical uncertainties, compared to the theoretical prediction by Danilkin and Vanderhaeghen.	115
5.31	Singly virtual differential two-photon production cross section of neutral pion pairs in the virtuality ranges $Q^2 = (0.5-0.7)$ GeV^2 and $Q^2 = (0.7-1.0)$ GeV^2 , shown with total and statistical uncertainties, compared to the theoretical prediction by Danilkin and Vanderhaeghen.	116
5.32	Singly virtual differential two-photon production cross section of neutral pion pairs in the virtuality ranges $Q^2 = (1.0-1.5)$ GeV^2 and $Q^2 = (1.5-2.0)$ GeV^2 , shown with total (red points) and statistical uncertainties, compared to the theoretical prediction by Danilkin and Vanderhaeghen.	117
5.33	Singly virtual differential two-photon production cross section of neutral pion pairs in the virtuality ranges $Q^2 = (2.0-3.0)$ GeV^2 and $Q^2 = (3.0-4.0)$ GeV^2 , shown with total and statistical uncertainties, compared to the theoretical prediction by Danilkin and Vanderhaeghen.	118
5.34	Comparison of the fit results to the integrated untagged data by BESIII, Belle, and Crystal Ball.	122
5.35	Comparison of the fit results to the integrated singly virtual BESIII data.	123
5.36	Transition form factors of $f_0(500)$, $f_0(980)$, and $f_2(1270)$ as a function of the momentum transfer Q^2	124
5.37	Comparison of the $f_0(500)$ and $f_0(980)$ transition form factor to the Belle results.	125
5.38	Comparison of the $f_2(1270)$ transition form factors to the Belle results.	126

6.1	Comparison of the distributions of the missing momentum transfer for data and the stacked Monte Carlo distributions after the initial event selection.	130
6.2	Comparison of the distributions of the two-pion invariant mass for data and the stacked Monte Carlo distributions after applying the $Q_2^2 = (0.08-0.35) \text{ GeV}^2$ and $\chi^2 < 50$ constraints.	131
6.3	Comparison of the distributions of the momentum transfer Q_1^2 (left), the missing momentum transfer Q_2^2 (right), and the pion helicity angle $ \cos \theta^* $ (bottom) for data (black points) and the stacked Monte Carlo distributions after applying the $Q_2^2 = (0.08-0.35) \text{ GeV}^2$, $\chi^2 < 50$, and $W = (1.0-1.5) \text{ GeV}$ constraints.	133
6.4	Generated distribution of the missing momentum transfer $Q_{2,\text{gen.}}^2$ for the selected signal Monte Carlo events, and comparison of the normalized χ_{3C}^2 signal shapes for the signal Monte Carlo, the signal Monte Carlo for real doubly virtual and singly virtual events, and the background Monte Carlo samples.	134
6.5	Comparison of the χ_{3C}^2 distributions for the $\gamma^*\gamma^* \rightarrow \pi^0\pi^0$ signal, the $\gamma\gamma^* \rightarrow \pi^0\pi^0$ background constamination, and the remaining background Monte Carlo in two different momentum-transfer and invariant-mass bins. The exclusive shapes in each bin (blue) are compared to the corresponding inclusive χ_{3C}^2 distributions.	135
6.6	Comparison of the χ_{3C}^2 distributions of the data with the fitted contributions from the signal and background Monte Carlo samples, together with the polynomial component, for two different momentum-transfer and helicity-angle bins.	136
6.7	Signal event yields extracted from fits to the χ_{3C}^2 spectra in each momentum-transfer and helicity-angle bin.	137
6.8	Reconstruction efficiency of $\gamma^*\gamma^* \rightarrow \pi^0\pi^0$ events as obtained from the signal Monte Carlo simulation.	138
6.9	Differential $\gamma^*\gamma^* \rightarrow \pi^0\pi^0$ cross section with statistical uncertainties in different momentum-transfer regions, shown as a function of the cosine of pion helicity angle.	140
6.10	Difference in detection efficiency between data and Monte Carlo for electrons and positrons and distribution of the selected events, shown as a function of the lepton momentum and lepton polar angle.	141
6.11	Measured π^0 momenta after applying all analysis constraints.	142
6.12	Observed variations in the measured cross section for two example bins compared to a Gaussian distribution evaluated using the arithmetic mean and the calculated standard deviation.	143
6.13	Measurement results for the integrated and differential cross sections of the $\gamma^*\gamma^* \rightarrow \pi^0\pi^0$ process in the two-pion invariant-mass range $W = (1.0 - 1.5) \text{ GeV}$	145

6.14	Result of the measurement of the differential cross section of the $\gamma^*\gamma^* \rightarrow \pi^0\pi^0$ process in the mass range $W = (1.0-1.5)$ GeV for different momentum-transfer bins.	147
6.15	Result of the measurement of the integrated cross section of the $\gamma^*\gamma^* \rightarrow \pi^0\pi^0$ process in the mass range $W = (1.0-1.5)$ GeV for different momentum-transfer bins.	148
7.1	Two-photon invariant mass spectrum after the initial event selection of the $\gamma\gamma^* \rightarrow \pi^0\eta$ process and the $\tilde{\phi}_1$ distribution of the selected $\gamma\gamma^* \rightarrow \pi^0\pi^0$ events compared to the HADROTOPS prediction.	152
A.1	Comparison of the event yield in the signal window to the sideband contribution as function of two-pion invariant mass and momentum transfer for $ \cos\theta = 0.0 - 0.2$	189
A.2	Comparison of the event yield in the signal window to the sideband contribution as function of two-pion invariant mass and momentum transfer for $ \cos\theta = 0.2 - 0.4$	190
A.3	Comparison of the event yield in the signal window to the sideband contribution as function of two-pion invariant mass and momentum transfer for $ \cos\theta = 0.4 - 0.6$	191
A.4	Comparison of the event yield in the signal window to the sideband contribution as function of two-pion invariant mass and momentum transfer for $ \cos\theta = 0.6 - 0.8$	192
A.5	Comparison of the event yield in the signal window to the sideband contribution as function of two-pion invariant mass and momentum transfer for $ \cos\theta = 0.8 - 1.0$	193
B.1	Comparison of the fit results to the single virtual data BESIII data at $Q^2 = (0.1 - 0.3)$ GeV ²	195
B.2	Comparison of the fit results to the single virtual data BESIII data at $Q^2 = (0.3 - 0.4)$ GeV ² and $Q^2 = (0.4 - 0.5)$ GeV ²	196
B.3	Comparison of the fit results to the single virtual data BESIII data at $Q^2 = (0.5 - 0.7)$ GeV ² and $Q^2 = (0.7 - 1.0)$ GeV ²	197
B.4	Comparison of the fit results to the single virtual data BESIII data at $Q^2 = (1.0 - 1.5)$ GeV ² and $Q^2 = (1.5 - 2.0)$ GeV ²	198
B.5	Comparison of the fit results to the single virtual data BESIII data at $Q^2 = (2.0 - 3.0)$ GeV ² and $Q^2 = (3.0 - 4.0)$ GeV ²	199

List of Tables

4.1	Summary of the generated Monte Carlo samples.	72
5.1	The absolute contributions of the analysis constraints to the systematic uncertainty of the integrated and differential cross sections in each Q^2 bin. . .	109
5.2	Absolute contributions of the background function to the systematic uncertainty of the integrated and differential cross sections in different Q^2 bins. .	109
5.3	Absolute contributions of the efficiency correction to the systematic uncertainty of the integrated and differential cross sections in different Q^2 bins.	109
5.4	Absolute total systematic uncertainty of the helicity-angle-integrated and differential two-photon production cross sections.	112
6.1	Numerical values of the TT polarization luminosity functions and the luminosity function ratios ε_{LT} , ε_{TL} , and ε_{LL}	139
6.2	Relative systematic uncertainties (%) of the differential cross section, obtained from variations in the analysis conditions, for each bin.	142
6.3	Relative systematic uncertainties (%) of the differential cross section arising from the background function used in the fit to the χ^2_{3C} distributions. . . .	144
6.4	Relative systematic uncertainties (%) of the differential cross section arising from the efficiency correction.	144
6.5	Relative systematic uncertainty (%) of the differential cross section.	146
C.1	Numerical results of the extracted transition form factors.	201
C.2	Numerical results for the integrated cross section in the momentum transfer range $Q_1^2 = (0.1 - 0.3) \text{ GeV}^2$	201
C.3	Numerical results for the integrated cross section in the momentum transfer range $Q_1^2 = (0.3 - 0.4) \text{ GeV}^2$	202
C.4	Numerical results for the integrated cross section in the momentum transfer range $Q_1^2 = (0.4 - 0.5) \text{ GeV}^2$	203
C.5	Numerical results for the integrated cross section in the momentum transfer range $Q_1^2 = (0.5 - 0.7) \text{ GeV}^2$	203
C.6	Numerical results for the integrated cross section in the momentum transfer range $Q_1^2 = (0.7 - 1.0) \text{ GeV}^2$	204

C.7	Numerical results for the integrated cross section in the momentum transfer range $Q_1^2 = (1.0 - 1.5) \text{ GeV}^2$	204
C.8	Numerical results for the integrated cross section in the momentum transfer range $Q_1^2 = (1.5 - 2.0) \text{ GeV}^2$	205
C.9	Numerical results for the integrated cross section in the momentum transfer range $Q_1^2 = (2.0 - 3.0) \text{ GeV}^2$	205
C.10	Numerical results for the integrated cross section in the momentum transfer range $Q_1^2 = (3.0 - 4.0) \text{ GeV}^2$	205
C.11	Numerical results for the differential cross section in the momentum transfer range $Q_1^2 = (0.1 - 0.3) \text{ GeV}^2$	206
C.12	Numerical results for the differential cross section in the momentum transfer range $Q_1^2 = (0.3 - 0.4) \text{ GeV}^2$	207
C.13	Numerical results for the differential cross section in the momentum transfer range $Q_1^2 = (0.4 - 0.5) \text{ GeV}^2$	208
C.14	Numerical results for the differential cross section in the momentum transfer range $Q_1^2 = (0.5 - 0.7) \text{ GeV}^2$	209
C.15	Numerical results for the differential cross section in the momentum transfer range $Q_1^2 = (0.7 - 1.0) \text{ GeV}^2$	210
C.16	Numerical results for the differential cross section in the momentum transfer range $Q_1^2 = (1.0 - 1.5) \text{ GeV}^2$	211
C.17	Numerical results for the differential cross section in the momentum transfer range $Q_1^2 = (1.5 - 2.0) \text{ GeV}^2$	212
C.18	Numerical results for the differential cross section in the momentum transfer range $Q_1^2 = (2.0 - 3.0) \text{ GeV}^2$	212
C.19	Numerical results for the differential cross section in the momentum transfer range $Q_1^2 = (3.0 - 4.0) \text{ GeV}^2$	213
C.20	Numerical results for the integrated and differential double virtual cross section as function of Q_1^2 , Q_2^2 , and, $ \cos \theta^* $	213

A | Additional Plots: Background Subtraction for the $\gamma\gamma^* \rightarrow \pi^0\pi^0$ Process

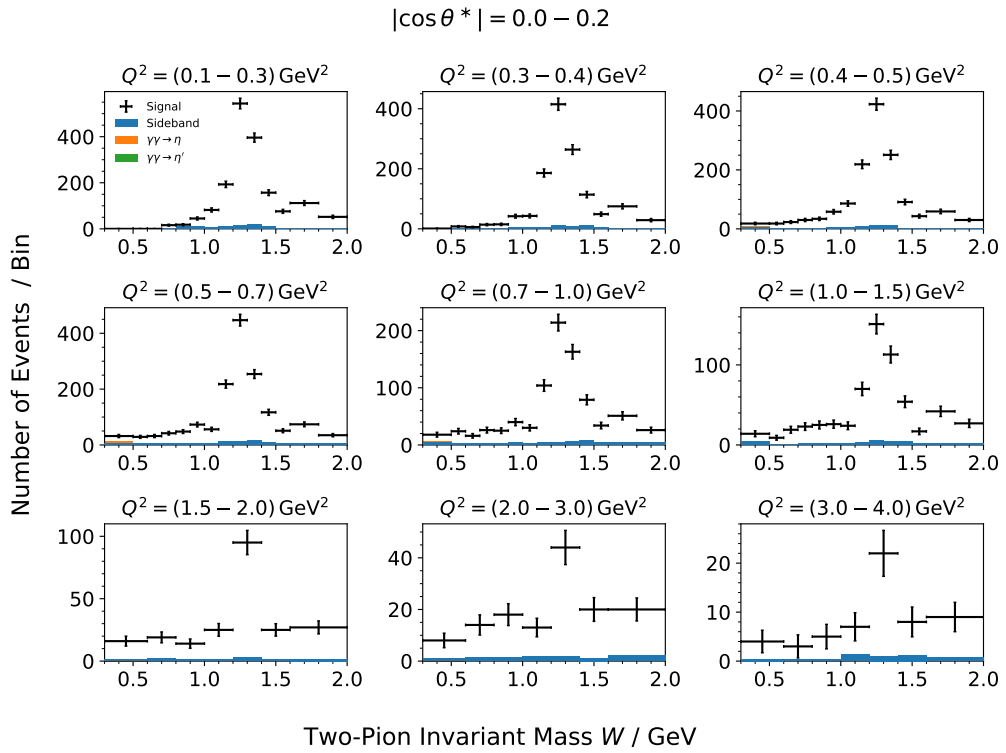


Figure A.1: Event yield in signal window (black points) compared to sideband extracted from fitted background shape and event yield in the background window (blue histograms) stacked with the remaining contribution of $\gamma\gamma \rightarrow \eta$ and $\gamma\gamma \rightarrow \eta'$ Monte Carlo simulations in different momentum transfer bins. The helicity angle is restricted to $|\cos\theta| = 0.0 - 0.2$.

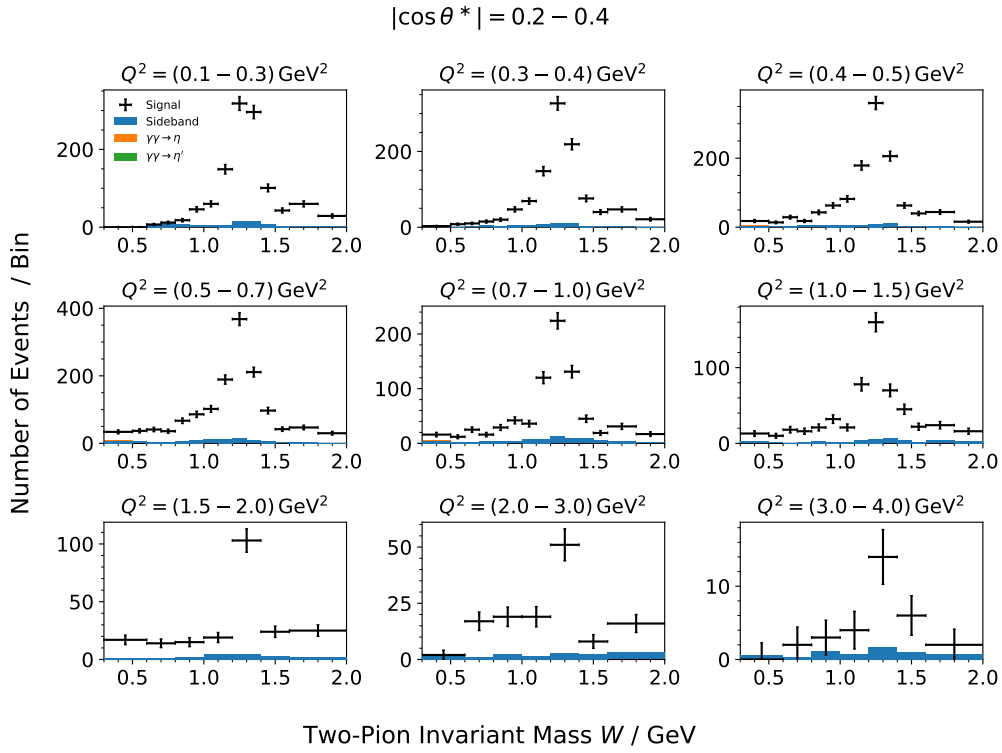


Figure A.2: Event yield in signal window (black points) compared to sideband extracted from fitted background shape and event yield in the background window (blue histograms) stacked with the remaining contribution of $\gamma\gamma \rightarrow \eta$ and $\gamma\gamma \rightarrow \eta'$ Monte Carlo simulations in different momentum transfer bins. The helicity angle is restricted to $|\cos\theta| = 0.2 - 0.4$.

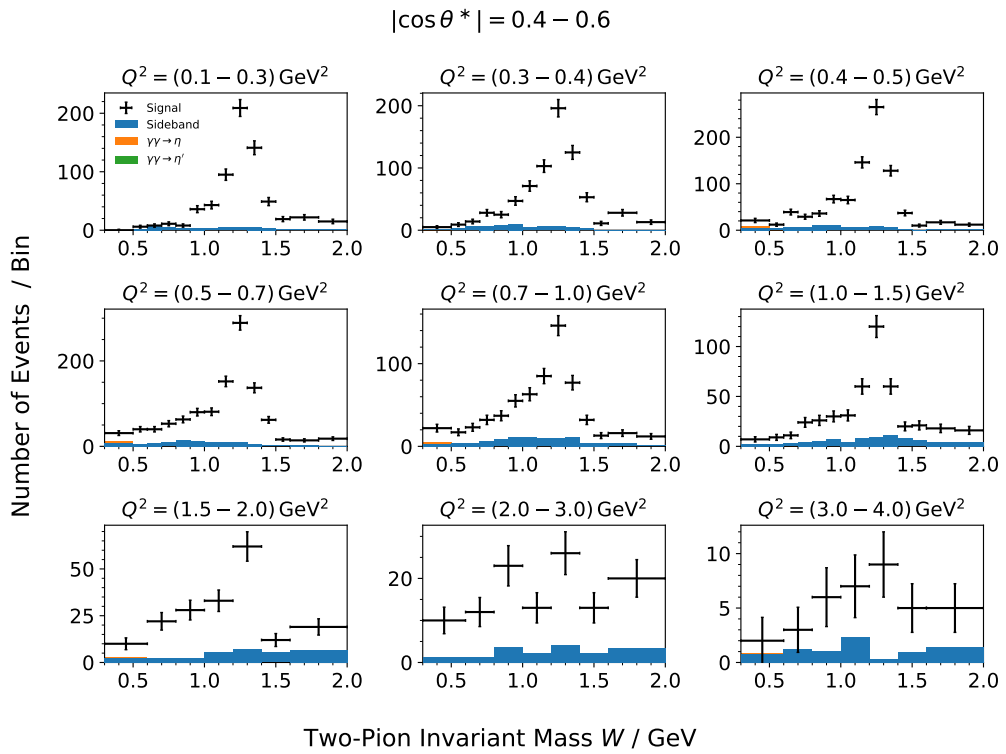


Figure A.3: Event yield in signal window (black points) compared to sideband extracted from fitted background shape and event yield in the background window (blue histograms) stacked with the remaining contribution of $\gamma\gamma \rightarrow \eta$ and $\gamma\gamma \rightarrow \eta'$ Monte Carlo simulations in different momentum transfer bins. The helicity angle is restricted to $|\cos \theta| = 0.4 - 0.6$.

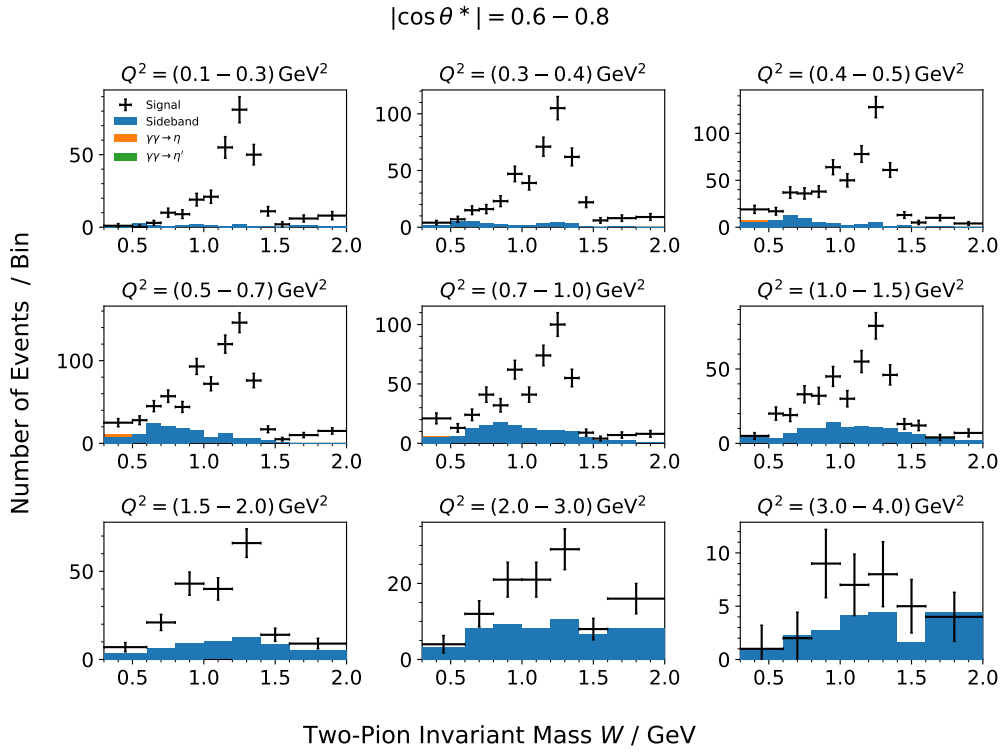


Figure A.4: Event yield in signal window (black points) compared to sideband extracted from fitted background shape and event yield in the background window (blue histograms) stacked with the remaining contribution of $\gamma\gamma \rightarrow \eta$ and $\gamma\gamma \rightarrow \eta'$ Monte Carlo simulations in different momentum transfer bins. The helicity angle is restricted to $|\cos\theta| = 0.6 - 0.8$.

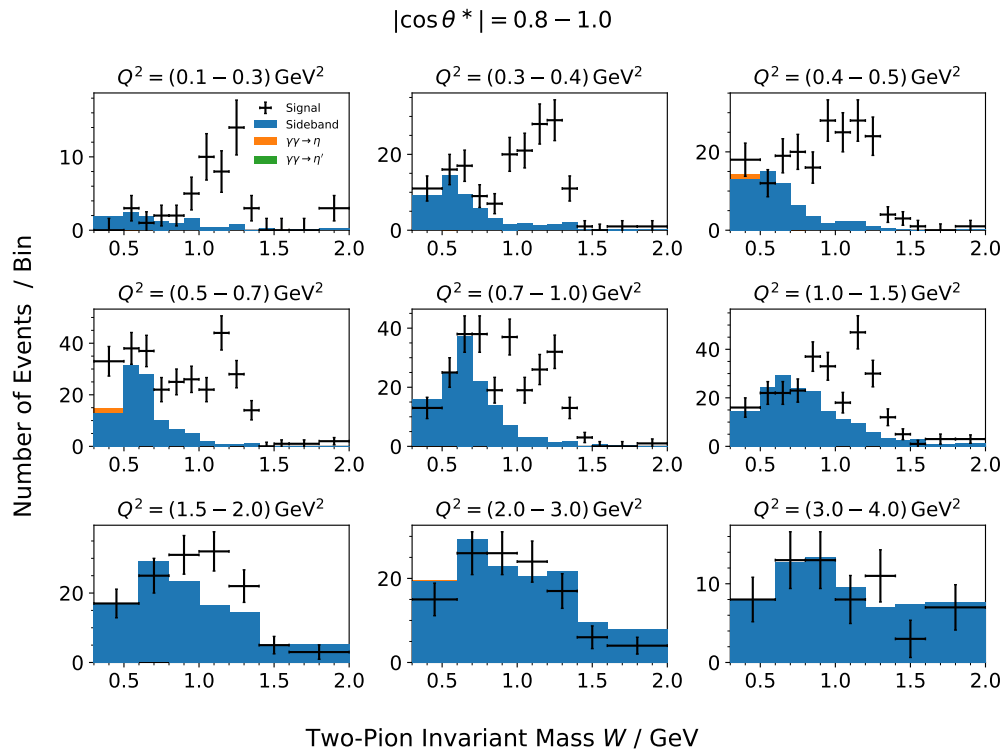


Figure A.5: Event yield in signal window (black points) compared to sideband extracted from fitted background shape and event yield in the background window (blue histograms) stacked with the remaining contribution of $\gamma\gamma \rightarrow \eta$ and $\gamma\gamma \rightarrow \eta'$ Monte Carlo simulations in different momentum transfer bins. The helicity angle is restricted to $|\cos\theta| = 0.8 - 1.0$.

B | Additional Plots: Partial-Wave Analysis of the $\gamma\gamma^* \rightarrow \pi^0\pi^0$ Process

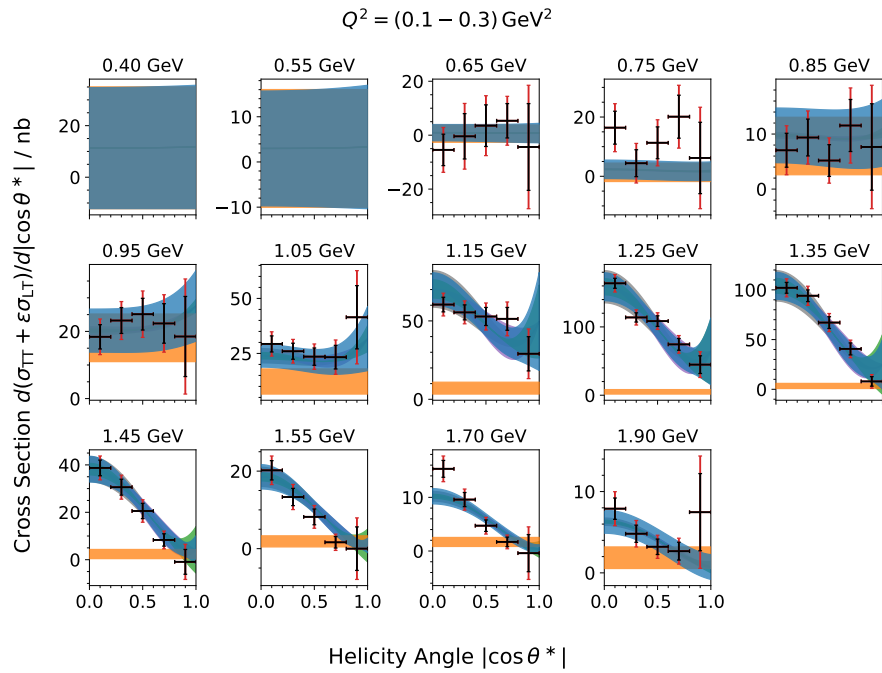


Figure B.1: Comparison of the fit results (blue shaded area) and the S (orange), D_0 (green), D_1 (violet), and D_2 (grey) partial wave to the single virtual data BESIII data at $Q^2 = (0.1 - 0.3) \text{ GeV}^2$ with total (red points) and statistical (black) uncertainties.

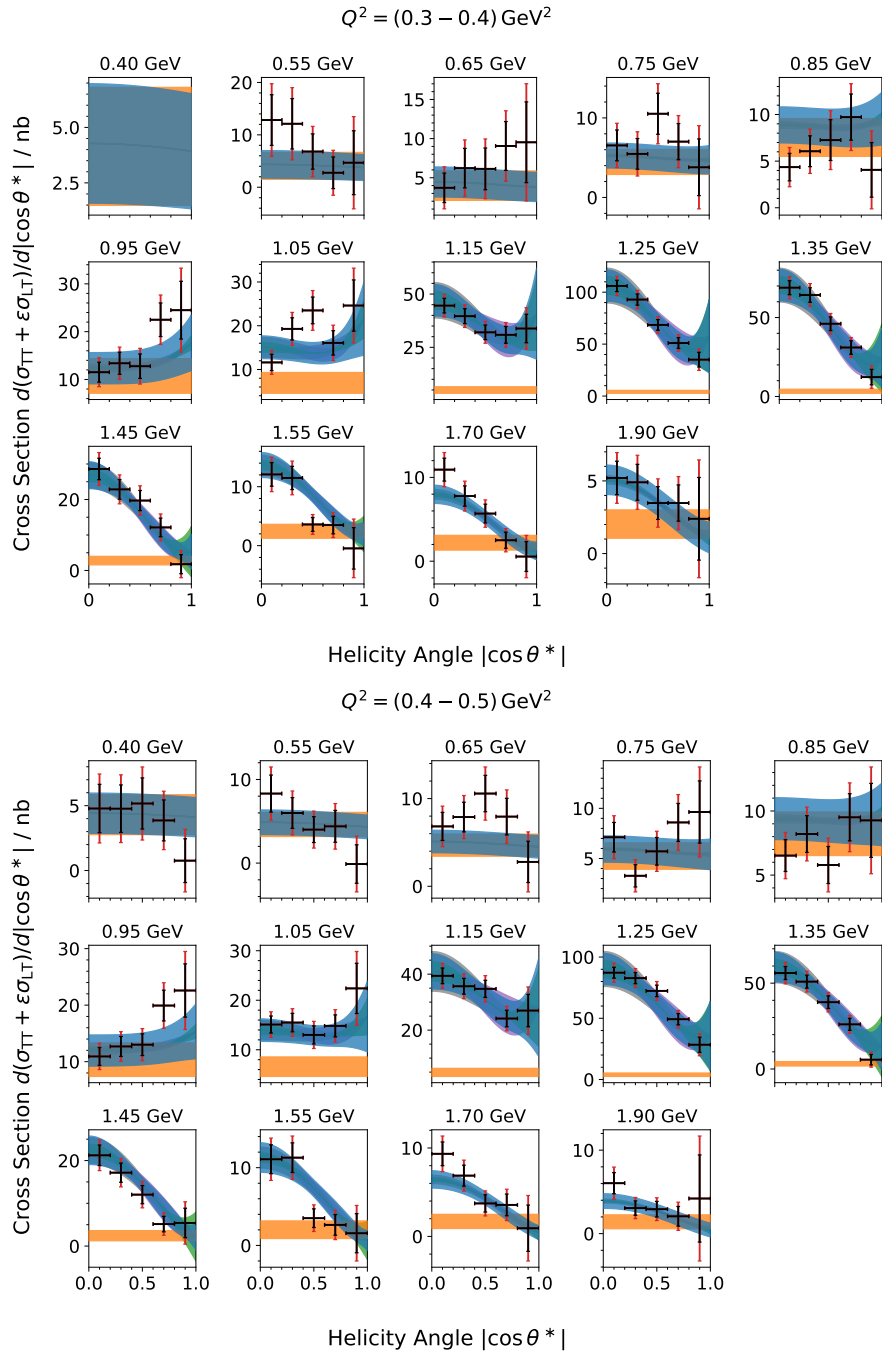


Figure B.2: Comparison of the fit results (blue shaded area) and the S (orange), D_0 (green), D_1 (violet), and D_2 (grey) partial wave to the single virtual data BESIII data at $Q^2 = (0.3 - 0.4) \text{ GeV}^2$ (top) and $Q^2 = (0.4 - 0.5) \text{ GeV}^2$ (bottom) with total (red points) and statistical (black) uncertainties.

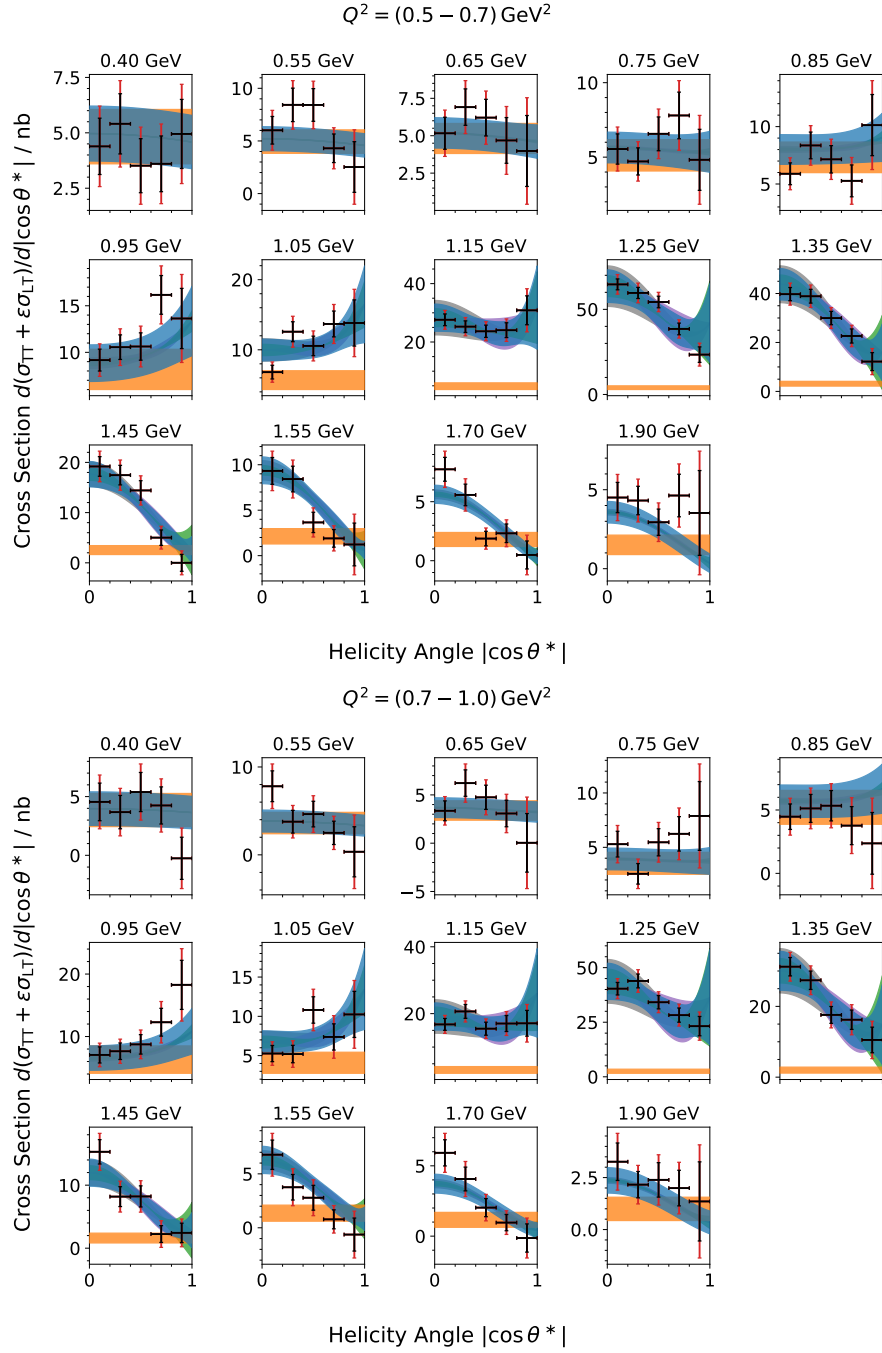


Figure B.3: Comparison of the fit results (blue shaded area) and the S (orange), D_0 (green), D_1 (violet), and D_2 (grey) partial wave to the single tagged data BESIII data at $Q^2 = (0.5 - 0.7) \text{ GeV}^2$ (top) and $Q^2 = (0.7 - 1.0) \text{ GeV}^2$ (bottom) with total (red points) and statistical (black) uncertainties.

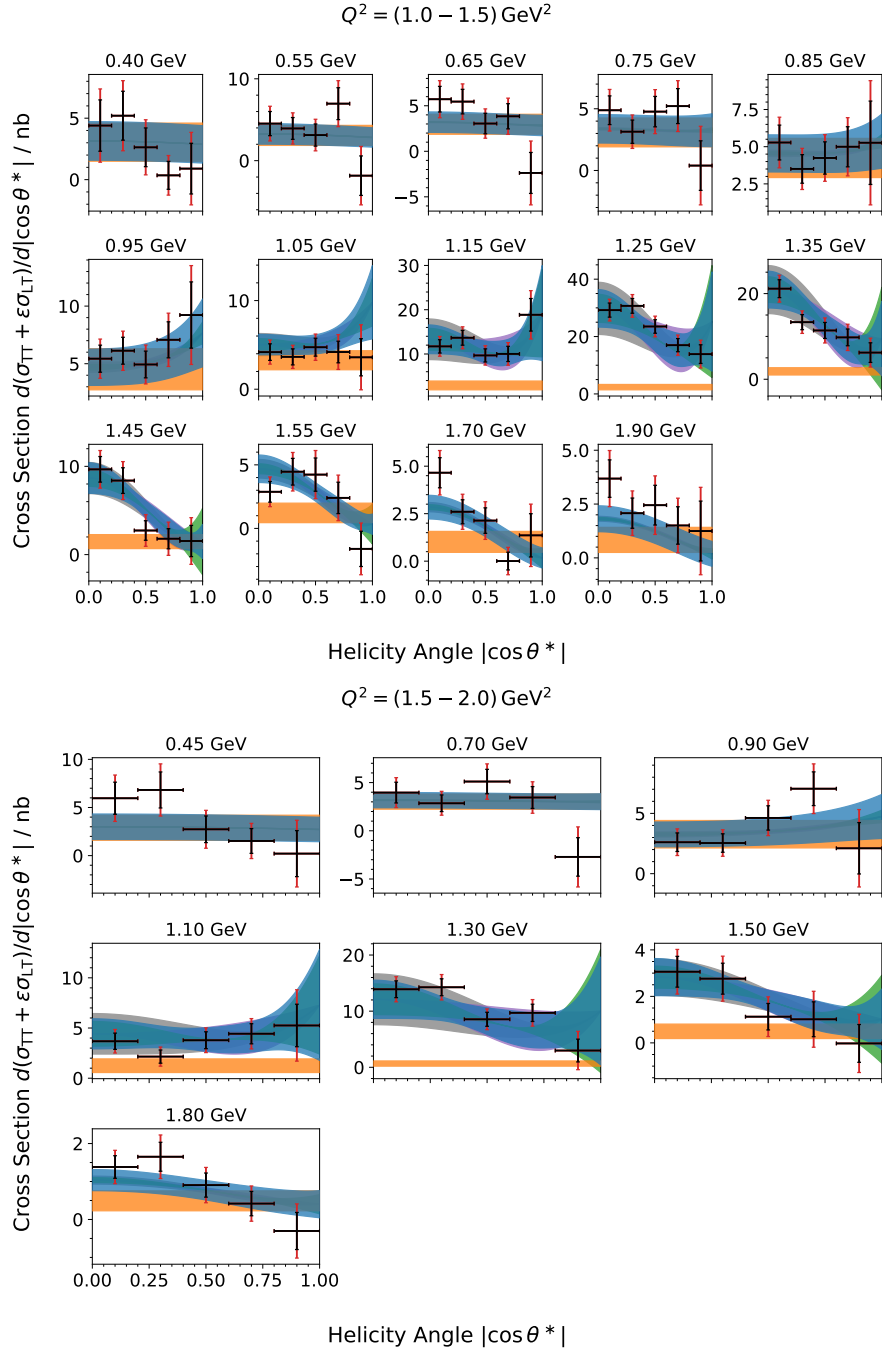


Figure B.4: Comparison of the fit results (blue shaded area) and the S (orange), D_0 (green), D_1 (violet), and D_2 (grey) partial wave to the single virtual data BESIII data at $Q^2 = (1.0 - 1.5) \text{ GeV}^2$ (top) and $Q^2 = (1.5 - 2) \text{ GeV}^2$ (bottom) with total (red points) and statistical (black) uncertainties.

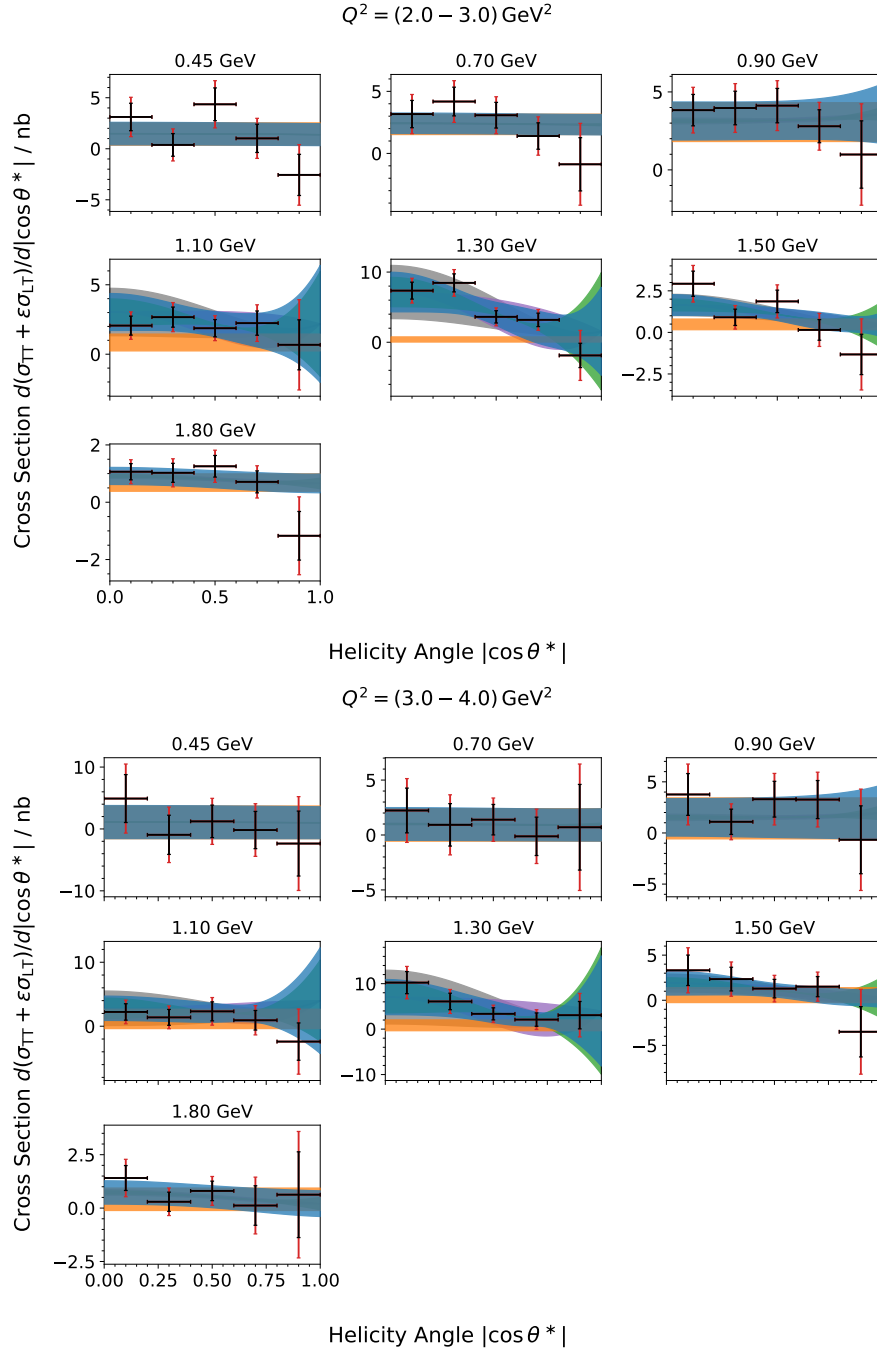


Figure B.5: Comparison of the fit results (blue shaded area) and the S (orange), D_0 (green), D_1 (violet), and D_2 (grey) partial wave to the single virtual data BESIII data at $Q^2 = (2 - 3) \text{ GeV}^2$ (top) and $Q^2 = (3 - 4) \text{ GeV}^2$ (bottom) with total (red points) and statistical (black) uncertainties.

C | Numerical Results

Table C.1: Numerical results of the extracted transition form factors and total uncertainty in dependence on the momentum transfer Q^2 .

Q^2 / GeV^2	$\frac{ F_{f_0(500)}(Q^2) }{ F_{f_0(500)}(0) }$	$\frac{ F_{f_0(980)}(Q^2) }{ F_{f_0(980)}(0) }$	$\frac{ F_{f_2(1270)}^{\text{tot}}(Q^2) }{ F_{f_2(1270)}^{\text{tot}}(0) }$	$\frac{ F_{f_2(1270)}^{\lambda=0}(Q^2) }{ F_{f_2(1270)}^{\text{tot}}(0) }$	$\frac{ F_{f_2(1270)}^{\lambda=1}(Q^2) }{ F_{f_2(1270)}^{\text{tot}}(0) }$	$\frac{ F_{f_2(1270)}^{\lambda=2}(Q^2) }{ F_{f_2(1270)}^{\text{tot}}(0) }$
0.1–0.3	0.89±0.30	0.99±0.08	0.75±0.01	0.26±0.04	0.18±0.04	0.68±0.02
0.3–0.4	0.32±0.04	0.65±0.04	0.60±0.01	0.23±0.03	0.18±0.02	0.53±0.02
0.4–0.5	0.31±0.02	0.60±0.04	0.54±0.01	0.18±0.03	0.18±0.02	0.47±0.01
0.5–0.7	0.30±0.02	0.49±0.03	0.45±0.01	0.20±0.02	0.18±0.02	0.36±0.01
0.7–1.0	0.22±0.02	0.41±0.03	0.36±0.01	0.17±0.02	0.14±0.02	0.28±0.01
1.0–1.5	0.18±0.01	0.31±0.02	0.27±0.01	0.14±0.02	0.10±0.01	0.21±0.01
1.5–2.0	0.17±0.01	0.20±0.02	0.17±0.01	0.10±0.02	0.08±0.01	0.11±0.02
2.0–3.0	0.13±0.01	0.18±0.02	0.11±0.01	0.04±0.03	0.03±0.03	0.10±0.01
3.0–4.0	0.06±0.04	0.13±0.05	0.09±0.02	0.04±0.04	0.00±0.03	0.08±0.02

Table C.2: Numerical results of the integrated cross section $\sigma_{\text{TT}} + \varepsilon \sigma_{\text{LT}}$ and luminosity function ratio ε in dependence of the two-pion invariant mass W in the momentum transfer range $Q_1^2 = (0.1–0.3) \text{ GeV}^2$. The first uncertainty is statistical, the second one is systematic.

W / GeV	ε	$\sigma_{\text{TT}} + \varepsilon \sigma_{\text{LT}} / \text{nb}$	W / GeV	ε	$\sigma_{\text{TT}} + \varepsilon \sigma_{\text{LT}} / \text{nb}$
0.60 – 0.65	0.86	-0.29±6.68±6.94	1.20 – 1.25	0.78	98.28±6.16±7.78
0.65 – 0.70	0.85	-0.27±5.45±5.65	1.25 – 1.30	0.77	103.90±5.14±7.12
0.70 – 0.75	0.84	15.51±5.43±5.82	1.30 – 1.35	0.76	77.98±4.01±5.49
0.75 – 0.80	0.84	7.85±3.88±4.47	1.35 – 1.40	0.76	46.71±3.05±3.83
0.80 – 0.85	0.83	7.37±3.02±3.16	1.40 – 1.45	0.75	24.72±2.34±2.70
0.85 – 0.90	0.83	8.96±3.00±3.13	1.45 – 1.50	0.74	14.20±2.29±2.43
0.90 – 0.95	0.82	17.25±3.82±4.07	1.50 – 1.55	0.73	8.34±1.63±1.70
0.95 – 1.00	0.81	25.79±4.66±5.03	1.55 – 1.60	0.72	9.01±2.28±2.34
1.00 – 1.05	0.81	27.61±4.67±5.03	1.60 – 1.70	0.71	6.22±1.06±1.12
1.05 – 1.10	0.80	29.82±4.75±5.08	1.70 – 1.80	0.69	6.15±1.33±1.41
1.10 – 1.15	0.79	37.87±4.55±5.00	1.80 – 1.90	0.67	4.86±1.10±1.21
1.15 – 1.20	0.79	61.73±4.40±5.36	1.90 – 2.00	0.65	5.56±1.78±1.99

Table C.3: Numerical results of the integrated cross section $\sigma_{\text{TT}} + \varepsilon \sigma_{\text{LT}}$ and luminosity function ratio ε in dependence of the two-pion invariant mass W in the momentum transfer range $Q_1^2 = (0.3-0.4) \text{ GeV}^2$. The first uncertainty is statistical, the second one is systematic.

W / GeV	ε	$\sigma_{\text{TT}} + \varepsilon \sigma_{\text{LT}} / \text{nb}$	W / GeV	ε	$\sigma_{\text{TT}} + \varepsilon \sigma_{\text{LT}} / \text{nb}$
0.50 – 0.55	0.85	$6.86 \pm 3.01 \pm 3.15$	1.15 – 1.20	0.77	$44.40 \pm 2.90 \pm 3.62$
0.55 – 0.60	0.85	$8.82 \pm 2.76 \pm 2.91$	1.20 – 1.25	0.77	$71.62 \pm 3.68 \pm 5.06$
0.60 – 0.65	0.84	$4.82 \pm 1.95 \pm 2.04$	1.25 – 1.30	0.76	$69.77 \pm 3.52 \pm 4.88$
0.65 – 0.70	0.84	$9.05 \pm 2.18 \pm 2.38$	1.30 – 1.35	0.75	$54.23 \pm 3.15 \pm 4.14$
0.70 – 0.75	0.83	$5.79 \pm 1.43 \pm 1.52$	1.35 – 1.40	0.75	$34.79 \pm 2.51 \pm 3.11$
0.75 – 0.80	0.83	$7.55 \pm 1.75 \pm 2.17$	1.40 – 1.45	0.74	$20.83 \pm 1.96 \pm 2.26$
0.80 – 0.85	0.82	$6.32 \pm 1.49 \pm 1.59$	1.45 – 1.50	0.73	$13.20 \pm 1.54 \pm 1.71$
0.85 – 0.90	0.81	$6.26 \pm 1.30 \pm 1.39$	1.50 – 1.55	0.72	$7.58 \pm 1.45 \pm 1.52$
0.90 – 0.95	0.81	$13.72 \pm 1.95 \pm 2.17$	1.55 – 1.60	0.71	$4.50 \pm 1.31 \pm 1.34$
0.95 – 1.00	0.80	$20.15 \pm 2.57 \pm 2.86$	1.60 – 1.70	0.70	$6.96 \pm 0.81 \pm 0.90$
1.00 – 1.05	0.80	$17.73 \pm 2.25 \pm 2.52$	1.70 – 1.80	0.68	$4.02 \pm 0.86 \pm 0.91$
1.05 – 1.10	0.79	$20.30 \pm 2.18 \pm 2.46$	1.80 – 1.90	0.66	$3.12 \pm 0.78 \pm 0.84$
1.10 – 1.15	0.78	$27.97 \pm 2.63 \pm 3.03$	1.90 – 2.00	0.64	$4.66 \pm 1.26 \pm 1.47$

Table C.4: Numerical results of the integrated cross section $\sigma_{\text{TT}} + \varepsilon \sigma_{\text{LT}}$ and luminosity function ratio ε in dependence of the two-pion invariant mass W in the momentum transfer range $Q_1^2 = (0.4-0.5) \text{ GeV}^2$. The first uncertainty is statistical, the second one is systematic.

W / GeV	ε	$\sigma_{\text{TT}} + \varepsilon \sigma_{\text{LT}} / \text{nb}$	W / GeV	ε	$\sigma_{\text{TT}} + \varepsilon \sigma_{\text{LT}} / \text{nb}$
0.30 – 0.40	0.86	1.91±1.17±1.21	1.10 – 1.15	0.78	27.42±2.26±2.73
0.40 – 0.50	0.85	5.83±1.10±1.18	1.15 – 1.20	0.77	36.95±2.37±3.11
0.50 – 0.55	0.84	4.25±1.26±1.34	1.20 – 1.25	0.76	60.80±2.94±4.34
0.55 – 0.60	0.84	4.79±1.24±1.32	1.25 – 1.30	0.75	67.20±3.30±4.89
0.60 – 0.65	0.83	6.70±1.28±1.41	1.30 – 1.35	0.75	46.53±2.54±3.61
0.65 – 0.70	0.83	7.71±1.23±1.39	1.35 – 1.40	0.74	24.32±1.92±2.42
0.70 – 0.75	0.82	7.26±1.28±1.42	1.40 – 1.45	0.73	15.48±1.79±2.01
0.75 – 0.80	0.82	6.48±1.15±1.38	1.45 – 1.50	0.72	8.91±1.30±1.40
0.80 – 0.85	0.81	7.95±1.24±1.37	1.50 – 1.55	0.72	7.54±1.18±1.27
0.85 – 0.90	0.81	7.76±1.11±1.24	1.55 – 1.60	0.71	4.49±1.12±1.16
0.90 – 0.95	0.80	12.20±1.59±1.78	1.60 – 1.70	0.70	5.76±0.93±1.01
0.95 – 1.00	0.80	19.46±1.93±2.25	1.70 – 1.80	0.68	4.01±1.06±1.12
1.00 – 1.05	0.79	15.05±1.76±2.04	1.80 – 1.90	0.66	3.34±1.00±1.06
1.05 – 1.10	0.78	17.27±1.84±2.10	1.90 – 2.00	0.64	3.98±2.02±2.11

Table C.5: Numerical results of the integrated cross section $\sigma_{\text{TT}} + \varepsilon \sigma_{\text{LT}}$ and luminosity function ratio ε in dependence of the two-pion invariant mass W in the momentum transfer range $Q_1^2 = (0.5-0.7) \text{ GeV}^2$. The first uncertainty is statistical, the second one is systematic.

W / GeV	ε	$\sigma_{\text{TT}} + \varepsilon \sigma_{\text{LT}} / \text{nb}$	W / GeV	ε	$\sigma_{\text{TT}} + \varepsilon \sigma_{\text{LT}} / \text{nb}$
0.30 – 0.40	0.85	3.17±0.87±0.91	1.10 – 1.15	0.77	22.35±1.81±2.22
0.40 – 0.50	0.84	5.58±0.82±0.90	1.15 – 1.20	0.76	30.24±1.91±2.54
0.50 – 0.55	0.83	5.97±1.06±1.17	1.20 – 1.25	0.75	45.45±2.19±3.36
0.55 – 0.60	0.83	5.90±1.08±1.19	1.25 – 1.30	0.75	50.76±2.36±3.76
0.60 – 0.65	0.82	5.24±1.04±1.18	1.30 – 1.35	0.74	36.01±2.10±2.99
0.65 – 0.70	0.82	5.54±0.92±1.08	1.35 – 1.40	0.73	21.37±1.65±2.17
0.70 – 0.75	0.81	4.88±0.84±0.94	1.40 – 1.45	0.72	14.64±1.23±1.54
0.75 – 0.80	0.81	6.89±0.93±1.23	1.45 – 1.50	0.72	7.79±1.06±1.26
0.80 – 0.85	0.80	6.23±0.89±1.01	1.50 – 1.55	0.71	6.39±0.97±1.08
0.85 – 0.90	0.80	8.50±1.11±1.25	1.55 – 1.60	0.70	3.43±0.97±1.01
0.90 – 0.95	0.79	9.43±1.02±1.21	1.60 – 1.70	0.69	4.86±0.59±0.69
0.95 – 1.00	0.79	14.63±1.47±1.74	1.70 – 1.80	0.67	2.34±0.58±0.63
1.00 – 1.05	0.78	11.14±1.27±1.51	1.80 – 1.90	0.65	3.44±0.81±0.89
1.05 – 1.10	0.77	11.84±1.21±1.44	1.90 – 2.00	0.63	4.53±1.08±1.23

Table C.6: Numerical results of the integrated cross section $\sigma_{\text{TT}} + \varepsilon \sigma_{\text{LT}}$ and luminosity function ratio ε in dependence of the two-pion invariant mass W in the momentum transfer range $Q_1^2 = (0.7-1.0) \text{ GeV}^2$. The first uncertainty is statistical, the second one is systematic.

W / GeV	ε	$\sigma_{\text{TT}} + \varepsilon \sigma_{\text{LT}} / \text{nb}$	W / GeV	ε	$\sigma_{\text{TT}} + \varepsilon \sigma_{\text{LT}} / \text{nb}$
0.30 – 0.40	0.83	1.64±1.03±1.08	1.10 – 1.15	0.75	13.82±1.48±1.79
0.40 – 0.50	0.82	5.41±1.01±1.11	1.15 – 1.20	0.75	21.02±1.70±2.10
0.50 – 0.55	0.82	4.58±1.22±1.32	1.20 – 1.25	0.74	31.47±2.13±2.82
0.55 – 0.60	0.81	3.05±1.09±1.16	1.25 – 1.30	0.73	36.49±2.17±3.05
0.60 – 0.65	0.81	4.31±1.22±1.36	1.30 – 1.35	0.73	27.45±1.98±2.63
0.65 – 0.70	0.80	2.67±1.00±1.18	1.35 – 1.40	0.72	13.72±1.56±2.04
0.70 – 0.75	0.80	6.41±1.21±1.37	1.40 – 1.45	0.71	9.31±1.15±1.45
0.75 – 0.80	0.79	4.57±1.07±1.64	1.45 – 1.50	0.70	5.24±0.89±1.06
0.80 – 0.85	0.79	3.66±0.98±1.11	1.50 – 1.55	0.70	2.95±0.84±0.96
0.85 – 0.90	0.78	4.77±0.97±1.08	1.55 – 1.60	0.69	2.44±0.73±0.76
0.90 – 0.95	0.78	10.66±1.45±1.67	1.60 – 1.70	0.67	2.68±0.50±0.56
0.95 – 1.00	0.77	10.94±1.45±1.70	1.70 – 1.80	0.66	2.46±0.53±0.58
1.00 – 1.05	0.77	5.48±0.95±1.32	1.80 – 1.90	0.64	1.60±0.57±0.61
1.05 – 1.10	0.76	10.07±1.32±1.59	1.90 – 2.00	0.62	2.87±0.82±0.91

Table C.7: Numerical results of the integrated cross section $\sigma_{\text{TT}} + \varepsilon \sigma_{\text{LT}}$ and luminosity function ratio ε in dependence of the two-pion invariant mass W in the momentum transfer range $Q_1^2 = (1.0-1.5) \text{ GeV}^2$. The first uncertainty is statistical, the second one is systematic.

W / GeV	ε	$\sigma_{\text{TT}} + \varepsilon \sigma_{\text{LT}} / \text{nb}$	W / GeV	ε	$\sigma_{\text{TT}} + \varepsilon \sigma_{\text{LT}} / \text{nb}$
0.30 – 0.40	0.80	3.01±1.37±1.43	1.10 – 1.15	0.73	8.26±1.16±1.46
0.40 – 0.50	0.80	2.38±0.86±0.92	1.15 – 1.20	0.73	17.32±1.57±1.85
0.50 – 0.55	0.79	3.00±1.10±1.17	1.20 – 1.25	0.72	21.58±1.59±2.10
0.55 – 0.60	0.79	3.68±1.13±1.19	1.25 – 1.30	0.71	24.14±1.70±2.18
0.60 – 0.65	0.78	3.04±0.96±1.03	1.30 – 1.35	0.71	16.28±1.47±1.83
0.65 – 0.70	0.78	3.24±1.00±1.13	1.35 – 1.40	0.70	8.47±1.02±1.40
0.70 – 0.75	0.78	2.96±0.84±0.94	1.40 – 1.45	0.69	5.21±0.92±1.22
0.75 – 0.80	0.77	4.40±0.93±1.31	1.45 – 1.50	0.68	4.44±0.85±1.08
0.80 – 0.85	0.77	3.31±0.97±1.09	1.50 – 1.55	0.68	2.90±0.70±0.85
0.85 – 0.90	0.76	6.00±1.08±1.22	1.55 – 1.60	0.67	2.05±0.79±0.83
0.90 – 0.95	0.76	6.08±1.02±1.17	1.60 – 1.70	0.65	2.03±0.44±0.50
0.95 – 1.00	0.75	7.03±1.15±1.36	1.70 – 1.80	0.64	2.27±0.54±0.60
1.00 – 1.05	0.75	3.86±0.83±1.18	1.80 – 1.90	0.62	1.08±0.44±0.51
1.05 – 1.10	0.74	4.29±0.82±1.08	1.90 – 2.00	0.60	3.31±0.76±0.90

Table C.8: Numerical results of the integrated cross section $\sigma_{\text{TT}} + \varepsilon \sigma_{\text{LT}}$ and luminosity function ratio ε in dependence of the two-pion invariant mass W in the momentum transfer range $Q_1^2 = (1.5-2.0) \text{ GeV}^2$. The first uncertainty is statistical, the second one is systematic.

W / GeV	ε	$\sigma_{\text{TT}} + \varepsilon \sigma_{\text{LT}} / \text{nb}$	W / GeV	ε	$\sigma_{\text{TT}} + \varepsilon \sigma_{\text{LT}} / \text{nb}$
0.30 – 0.50	0.77	$2.31 \pm 1.04 \pm 1.07$	1.10 – 1.20	0.74	$4.94 \pm 0.77 \pm 0.90$
0.50 – 0.60	0.77	$4.59 \pm 1.19 \pm 1.27$	1.20 – 1.30	0.74	$12.23 \pm 1.07 \pm 1.44$
0.60 – 0.70	0.76	$0.96 \pm 0.85 \pm 0.96$	1.30 – 1.40	0.73	$7.53 \pm 0.93 \pm 1.41$
0.70 – 0.80	0.76	$4.10 \pm 0.83 \pm 0.95$	1.40 – 1.50	0.73	$2.16 \pm 0.49 \pm 0.71$
0.80 – 0.90	0.75	$2.90 \pm 0.74 \pm 0.81$	1.50 – 1.60	0.72	$1.01 \pm 0.38 \pm 0.41$
0.90 – 1.00	0.75	$4.67 \pm 0.92 \pm 1.07$	1.60 – 1.80	0.72	$1.15 \pm 0.25 \pm 0.30$
1.00 – 1.10	0.75	$2.78 \pm 0.76 \pm 1.11$	1.80 – 2.00	0.71	$0.47 \pm 0.22 \pm 0.27$

Table C.9: Numerical results of the integrated cross section $\sigma_{\text{TT}} + \varepsilon \sigma_{\text{LT}}$ and luminosity function ratio ε in dependence of the two-pion invariant mass W in the momentum transfer range $Q_1^2 = (2.0-3.0) \text{ GeV}^2$. The first uncertainty is statistical, the second one is systematic.

W / GeV	ε	$\sigma_{\text{TT}} + \varepsilon \sigma_{\text{LT}} / \text{nb}$	W / GeV	ε	$\sigma_{\text{TT}} + \varepsilon \sigma_{\text{LT}} / \text{nb}$
0.30 – 0.50	0.73	$1.47 \pm 0.98 \pm 1.01$	1.10 – 1.20	0.71	$2.53 \pm 0.74 \pm 0.89$
0.50 – 0.60	0.73	$1.06 \pm 0.95 \pm 0.98$	1.20 – 1.30	0.70	$6.25 \pm 0.92 \pm 1.42$
0.60 – 0.70	0.72	$1.86 \pm 0.91 \pm 1.00$	1.30 – 1.40	0.70	$2.05 \pm 0.63 \pm 1.10$
0.70 – 0.80	0.72	$2.53 \pm 0.82 \pm 0.95$	1.40 – 1.50	0.69	$1.64 \pm 0.55 \pm 0.82$
0.80 – 0.90	0.72	$3.02 \pm 0.85 \pm 0.95$	1.50 – 1.60	0.69	$0.17 \pm 0.45 \pm 0.52$
0.90 – 1.00	0.71	$3.27 \pm 0.86 \pm 1.00$	1.60 – 1.80	0.68	$0.78 \pm 0.28 \pm 0.37$
1.00 – 1.10	0.71	$1.28 \pm 0.56 \pm 0.89$	1.80 – 2.00	0.68	$0.38 \pm 0.34 \pm 0.43$

Table C.10: Numerical results of the integrated cross section $\sigma_{\text{TT}} + \varepsilon \sigma_{\text{LT}}$ and luminosity function ratio ε in dependence of the two-pion invariant mass W in the momentum transfer range $Q_1^2 = (3.0-4.0) \text{ GeV}^2$. The first uncertainty is statistical, the second one is systematic.

W / GeV	ε	$\sigma_{\text{TT}} + \varepsilon \sigma_{\text{LT}} / \text{nb}$	W / GeV	ε	$\sigma_{\text{TT}} + \varepsilon \sigma_{\text{LT}} / \text{nb}$
0.30 – 0.50	0.68	$0.00 \pm 2.41 \pm 2.43$	1.10 – 1.20	0.65	$1.98 \pm 1.21 \pm 1.34$
0.50 – 0.60	0.67	$1.06 \pm 2.28 \pm 2.32$	1.20 – 1.30	0.65	$4.01 \pm 1.34 \pm 1.65$
0.60 – 0.70	0.67	$1.60 \pm 1.50 \pm 1.56$	1.30 – 1.40	0.64	$5.92 \pm 1.33 \pm 1.66$
0.70 – 0.80	0.66	$0.45 \pm 1.50 \pm 1.59$	1.40 – 1.50	0.64	$2.26 \pm 1.08 \pm 1.42$
0.80 – 0.90	0.66	$2.18 \pm 1.29 \pm 1.37$	1.50 – 1.60	0.63	$-0.27 \pm 1.09 \pm 1.14$
0.90 – 1.00	0.66	$2.13 \pm 1.44 \pm 1.58$	1.60 – 1.80	0.63	$0.48 \pm 0.39 \pm 0.48$
1.00 – 1.10	0.65	$-0.20 \pm 1.07 \pm 1.64$	1.80 – 2.00	0.62	$0.82 \pm 0.87 \pm 1.03$

Table C.11: Numerical results of the differential cross section $d(\sigma_{\text{TT}} + \varepsilon \sigma_{\text{TT}})/d|\cos \theta^*|$ and luminosity function ratio ε in dependence of the two-pion invariant mass W and the helicity angle $|\cos \theta^*|$ in the momentum transfer range $Q_1^2 = (0.1 - 0.3) \text{ GeV}^2$. The first uncertainty is statistical, the second one is systematic.

W / GeV	ε	$ \cos \theta^* = 0.0-0.2$	$ \cos \theta^* = 0.2-0.4$	$d(\sigma_{\text{TT}} + \varepsilon \sigma_{\text{TT}})/d \cos \theta^* / \text{nb}$	$ \cos \theta^* = 0.6-0.8$	$ \cos \theta^* = 0.8-1.0$
0.6-0.7	0.85	-5.46±5.83±5.93	-0.41±8.41±8.81	3.53±7.72±7.99	5.34±6.38±6.45	-4.38±16.10±16.27
0.7-0.8	0.84	16.40±5.56±5.90	4.42±4.55±4.89	11.30±5.38±5.62	20.11±7.25±7.74	6.18±12.04±12.17
0.8-0.9	0.83	7.05±3.08±3.21	9.37±3.35±3.48	5.19±2.88±2.94	11.55±4.73±4.93	7.65±7.85±8.00
0.9-1.0	0.82	18.39±3.62±3.88	23.24±3.85±4.13	25.13±4.72±5.05	22.37±5.88±6.20	18.48±11.92±12.31
1.0-1.1	0.80	29.31±3.66±4.14	25.99±3.64±3.96	23.53±3.93±4.21	23.30±5.37±5.67	41.44±14.37±15.57
1.1-1.2	0.79	60.42±4.66±5.56	55.44±4.78±5.52	52.81±5.76±6.40	51.30±7.28±7.94	29.03±10.93±11.47
1.2-1.3	0.77	163.86±7.31±10.53	113.87±6.77±8.82	108.50±7.78±9.41	74.46±8.63±9.54	44.76±12.95±13.64
1.3-1.4	0.76	102.04±5.45±7.22	94.05±5.88±7.58	67.09±5.93±6.91	40.60±6.02±6.47	7.93±4.79±4.87
1.4-1.5	0.74	38.72±3.31±3.79	30.60±3.36±3.80	20.55±3.23±3.47	8.34±2.60±2.69	-0.91±5.23±5.25
1.5-1.6	0.73	20.21±2.49±2.72	13.32±2.22±2.36	8.20±2.03±2.11	1.65±1.48±1.49	0.00±5.61±5.61
1.6-1.8	0.70	15.31±1.57±1.80	9.58±1.32±1.45	4.72±1.07±1.13	1.70±0.89±0.92	-0.40±3.46±3.47
1.8-2.0	0.66	7.89±1.31±1.63	4.81±1.06±1.24	3.21±0.95±1.06	2.67±1.10±1.16	7.47±4.75±5.02

Table C.12: Numerical results of the differential cross section $d(\sigma_{\text{TT}} + \varepsilon \sigma_{\text{LT}})/d|\cos\theta^*|$ and luminosity function ratio ε in dependence of the two-pion invariant mass W and the helicity angle $|\cos\theta^*|$ in the momentum transfer range $Q_1^2 = (0.3 - 0.4) \text{ GeV}^2$. The first uncertainty is statistical, the second one is systematic.

$W / \text{ GeV}$	ε	$ \cos\theta^* = 0.0-0.2$	$ \cos\theta^* = 0.2-0.4$	$d(\sigma_{\text{TT}} + \varepsilon \sigma_{\text{LT}})/d \cos\theta^* / \text{ nb}$ $ \cos\theta^* = 0.4-0.6$	$ \cos\theta^* = 0.6-0.8$	$ \cos\theta^* = 0.8-1.0$
0.5-0.6	0.85	12.82±4.84±4.97	12.11±4.81±4.94	6.81±3.37±3.42	2.76±3.02±3.05	4.68±6.10±6.35
0.6-0.7	0.84	3.71±1.88±1.91	6.23±2.52±2.57	6.13±2.67±2.74	9.06±3.12±3.24	9.53±5.16±5.42
0.7-0.8	0.83	6.54±1.93±2.00	5.47±1.93±2.00	10.52±2.58±2.76	7.02±2.27±2.36	3.79±3.56±3.83
0.8-0.9	0.82	4.36±1.47±1.51	6.06±1.65±1.71	7.25±2.19±2.27	9.72±2.47±2.59	4.06±2.93±2.98
0.9-1.0	0.80	11.52±2.08±2.20	13.39±2.31±2.46	12.77±2.56±2.73	22.49±3.51±3.79	24.49±6.04±6.39
1.0-1.1	0.79	11.61±1.86±1.99	19.28±2.54±2.77	23.50±3.05±3.35	16.07±2.78±2.94	24.61±5.85±6.23
1.1-1.2	0.78	44.57±3.43±4.07	39.62±3.49±3.99	32.04±3.43±3.80	30.86±3.92±4.24	33.83±6.67±7.13
1.2-1.3	0.76	106.00±5.43±7.44	92.89±5.38±7.00	68.48±5.12±6.09	51.05±5.25±5.83	35.05±7.07±7.47
1.3-1.4	0.75	68.91±4.42±5.50	64.27±4.57±5.59	46.06±4.31±4.89	31.03±4.27±4.60	12.28±4.90±5.14
1.4-1.5	0.73	28.60±3.02±3.51	22.85±2.76±3.00	19.70±2.84±3.04	12.13±2.62±2.74	1.78±2.69±2.70
1.5-1.6	0.72	12.09±2.01±2.12	11.49±1.97±2.07	3.59±1.18±1.20	3.49±1.48±1.51	-0.47±3.51±3.52
1.6-1.8	0.69	10.93±1.37±1.51	7.77±1.21±1.30	5.68±1.12±1.19	2.50±0.96±0.99	0.56±1.78±1.79
1.8-2.0	0.65	5.20±1.15±1.31	4.90±1.23±1.39	3.48±1.13±1.22	3.48±1.25±1.33	2.39±2.84±2.89

Table C.13: Numerical results of the differential cross section $d(\sigma_{\text{TT}} + \varepsilon \sigma_{\text{TR}})/d|\cos \theta^*|$ and luminosity function ratio ε in dependence of the two-pion invariant mass W and the helicity angle $|\cos \theta^*|$ in the momentum transfer range $Q_1^2 = (0.4 - 0.5) \text{ GeV}^2$. The first uncertainty is statistical, the second one is systematic.

$W / \text{ GeV}$	ε	$ \cos \theta^* = 0.0-0.2$	$ \cos \theta^* = 0.2-0.4$	$d(\sigma_{\text{TT}} + \varepsilon \sigma_{\text{TR}})/d \cos \theta^* / \text{ nb}$	$ \cos \theta^* = 0.6-0.8$	$ \cos \theta^* = 0.8-1.0$
0.3-0.5	0.85	4.78±1.86±1.90	4.77±1.83±1.86	5.17±1.97±2.01	3.86±1.58±1.61	0.76±1.69±1.72
0.5-0.6	0.84	8.31±2.21±2.29	5.99±1.84±1.88	4.00±1.55±1.58	4.39±1.90±1.95	-0.11±2.30±2.41
0.6-0.7	0.83	6.83±1.60±1.67	7.89±1.69±1.78	10.57±2.08±2.21	7.94±2.09±2.22	2.78±2.36±2.48
0.7-0.8	0.82	7.12±1.47±1.55	3.27±1.11±1.16	5.71±1.38±1.45	8.59±1.89±2.03	9.63±3.10±3.25
0.8-0.9	0.81	6.52±1.24±1.31	8.20±1.43±1.53	5.79±1.44±1.52	9.51±1.84±1.95	9.27±2.88±3.00
0.9-1.0	0.80	10.92±1.58±1.71	12.69±1.77±1.93	13.00±1.92±2.10	19.93±2.72±2.98	22.59±4.72±5.04
1.0-1.1	0.79	15.09±1.71±1.92	15.49±1.86±2.09	13.00±1.82±2.05	14.82±2.22±2.40	22.39±5.07±5.45
1.1-1.2	0.77	39.39±2.79±3.50	35.68±2.80±3.40	34.74±3.05±3.60	24.15±2.95±3.25	26.98±5.78±6.16
1.2-1.3	0.76	87.20±4.43±6.43	82.79±4.55±6.30	72.35±4.70±6.03	49.27±4.63±5.35	28.40±6.17±6.51
1.3-1.4	0.74	55.90±3.77±4.95	50.87±3.78±4.72	38.92±3.67±4.29	26.01±3.49±3.80	5.42±3.04±3.10
1.4-1.5	0.73	21.24±2.40±2.67	17.17±2.25±2.45	12.03±2.12±2.24	5.14±1.81±1.89	5.41±3.44±3.56
1.5-1.6	0.71	11.08±1.86±1.99	11.29±1.91±2.03	3.51±1.20±1.22	2.64±1.33±1.35	1.57±2.52±2.53
1.6-1.8	0.69	9.34±1.34±1.50	6.87±1.18±1.29	3.73±0.98±1.02	3.56±1.23±1.28	0.93±2.61±2.62
1.8-2.0	0.65	6.05±1.27±1.45	3.06±0.86±0.93	2.93±0.93±1.00	2.08±1.18±1.21	4.21±5.22±5.36

Table C.14: Numerical results of the differential cross section $d(\sigma_{\text{TT}} + \varepsilon \sigma_{\text{LT}})/d|\cos\theta^*|$ and luminosity function ratio ε in dependence of the two-pion invariant mass W and the helicity angle $|\cos\theta^*|$ in the momentum transfer range $Q_1^2 = (0.5 - 0.7) \text{ GeV}^2$. The first uncertainty is statistical, the second one is systematic.

$W / \text{ GeV}$	ε	$ \cos\theta^* = 0.0-0.2$	$ \cos\theta^* = 0.2-0.4$	$ \cos\theta^* = 0.4-0.6$	$ \cos\theta^* = 0.6-0.8$	$ \cos\theta^* = 0.8-1.0$
0.3-0.5	0.84	4.39±1.27±1.30	5.41±1.36±1.40	3.52±1.22±1.24	3.60±1.26±1.29	4.95±1.56±1.61
0.5-0.6	0.83	6.01±1.31±1.36	8.43±1.59±1.67	8.42±1.55±1.64	4.30±1.36±1.40	2.52±2.41±2.59
0.6-0.7	0.82	5.17±1.07±1.12	6.91±1.22±1.28	6.21±1.22±1.29	4.69±1.53±1.67	3.98±2.37±2.66
0.7-0.8	0.81	5.55±1.02±1.07	4.71±0.91±0.96	6.56±1.13±1.22	7.80±1.57±1.74	4.82±2.05±2.17
0.8-0.9	0.80	5.89±0.95±1.02	8.36±1.16±1.27	7.15±1.19±1.29	5.27±1.39±1.49	10.13±2.66±2.81
0.9-1.0	0.79	9.17±1.17±1.29	10.56±1.32±1.46	10.63±1.47±1.62	16.17±2.08±2.32	13.63±3.23±3.45
1.0-1.1	0.78	6.82±0.98±1.07	12.58±1.42±1.68	10.55±1.39±1.62	13.68±1.84±2.08	13.83±3.29±3.50
1.1-1.2	0.76	27.61±2.01±2.52	25.26±1.98±2.41	23.68±2.10±2.48	24.06±2.54±2.89	30.86±4.95±5.48
1.2-1.3	0.75	64.67±3.19±4.78	59.64±3.27±4.75	54.32±3.39±4.56	38.49±3.43±4.11	23.40±4.55±4.94
1.3-1.4	0.74	39.75±2.70±3.60	38.89±2.81±3.62	29.97±2.73±3.27	22.64±2.88±3.29	12.18±3.67±3.87
1.4-1.5	0.72	19.19±1.96±2.34	17.46±1.94±2.30	14.42±1.94±2.17	5.01±1.53±1.67	0.00±1.68±1.68
1.5-1.6	0.70	9.32±1.47±1.60	8.43±1.41±1.54	3.66±1.12±1.15	1.90±0.97±0.99	1.23±2.35±2.36
1.6-1.8	0.68	7.75±1.01±1.16	5.57±0.91±1.02	1.87±0.62±0.65	2.32±0.79±0.82	0.49±1.18±1.19
1.8-2.0	0.64	4.50±0.96±1.11	4.32±0.90±1.01	2.94±0.83±0.90	4.63±1.35±1.48	3.53±2.69±2.85

Table C.15: Numerical results of the differential cross section $d(\sigma_{\text{TT}} + \varepsilon \sigma_{\text{TR}})/d|\cos \theta^*|$ and luminosity function ratio ε in dependence of the two-pion invariant mass W and the helicity angle $|\cos \theta^*|$ in the momentum transfer range $Q_1^2 = (0.7 - 1.0) \text{ GeV}^2$. The first uncertainty is statistical, the second one is systematic.

$W / \text{ GeV}$	ε	$ \cos \theta^* = 0.0-0.2$	$ \cos \theta^* = 0.2-0.4$	$d(\sigma_{\text{TT}} + \varepsilon \sigma_{\text{TR}})/d \cos \theta^* / \text{ nb}$	$ \cos \theta^* = 0.6-0.8$	$ \cos \theta^* = 0.8-1.0$
0.3-0.5	0.82	4.55±1.60±1.64	3.68±1.42±1.44	5.39±1.67±1.71	4.25±1.58±1.62	-0.26±1.79±1.85
0.5-0.6	0.81	7.81±1.75±1.84	3.77±1.29±1.32	4.64±1.46±1.50	2.50±1.33±1.35	0.35±2.85±3.07
0.6-0.7	0.81	3.35±1.03±1.06	6.22±1.37±1.43	4.75±1.25±1.30	3.08±1.37±1.44	0.04±3.03±3.64
0.7-0.8	0.80	5.29±1.18±1.24	2.56±0.94±0.97	5.46±1.25±1.33	6.24±1.58±1.78	7.88±3.16±3.59
0.8-0.9	0.79	4.47±1.00±1.05	5.12±1.10±1.17	5.34±1.20±1.26	3.77±1.50±1.61	2.37±2.43±2.61
0.9-1.0	0.78	7.05±1.29±1.38	7.65±1.32±1.41	8.75±1.56±1.69	12.29±2.22±2.46	18.27±3.93±4.26
1.0-1.1	0.76	5.26±1.03±1.08	5.20±1.11±1.28	10.81±1.68±2.04	7.37±1.67±2.13	10.25±2.93±3.16
1.1-1.2	0.75	16.78±1.77±2.01	20.66±2.07±2.38	15.49±1.95±2.18	17.04±2.39±2.65	17.11±3.85±4.09
1.2-1.3	0.74	40.36±2.87±3.60	43.90±3.17±4.07	34.17±3.06±3.69	28.26±3.25±3.83	23.21±4.43±4.70
1.3-1.4	0.72	31.21±2.60±3.12	27.38±2.60±3.12	17.59±2.37±2.80	16.22±2.73±3.26	10.51±3.62±3.85
1.4-1.5	0.71	15.29±1.93±2.20	8.18±1.58±1.87	8.22±1.68±1.85	2.24±1.33±1.64	2.43±1.54±1.58
1.5-1.6	0.69	6.77±1.36±1.44	3.76±1.18±1.24	2.78±1.15±1.20	0.78±0.88±0.92	-0.63±1.53±1.54
1.6-1.8	0.67	5.92±0.93±1.03	4.06±0.84±0.91	2.03±0.64±0.69	0.96±0.58±0.61	-0.13±1.00±1.01
1.8-2.0	0.63	3.26±0.90±1.02	2.16±0.63±0.68	2.39±0.83±0.88	2.00±0.86±0.90	1.35±1.90±1.95

Table C.16: Numerical results of the differential cross section $d(\sigma_{\text{TT}} + \varepsilon \sigma_{\text{LT}})/d|\cos\theta^*|$ and luminosity function ratio ε in dependence of the two-pion invariant mass W and the helicity angle $|\cos\theta^*|$ in the momentum transfer range $Q_1^2 = (1.0 - 1.5) \text{ GeV}^2$. The first uncertainty is statistical, the second one is systematic.

$W / \text{ GeV}$	ε	$ \cos\theta^* = 0.0-0.2$	$ \cos\theta^* = 0.2-0.4$	$d(\sigma_{\text{TT}} + \varepsilon \sigma_{\text{LT}})/d \cos\theta^* / \text{ nb}$	$ \cos\theta^* = 0.6-0.8$	$ \cos\theta^* = 0.8-1.0$
0.3-0.5	0.80	4.40±2.09±2.13	5.20±1.99±2.04	2.63±1.58±1.59	0.35±1.14±1.14	0.90±2.06±2.11
0.5-0.6	0.79	4.53±1.48±1.52	3.93±1.33±1.36	3.13±1.35±1.38	6.96±1.95±2.02	-1.83±2.41±2.63
0.6-0.7	0.78	5.72±1.41±1.47	5.46±1.35±1.40	3.05±1.13±1.15	3.85±1.38±1.43	-2.38±2.25±2.69
0.7-0.8	0.77	4.88±1.16±1.22	3.14±0.94±0.97	4.77±1.23±1.29	5.22±1.42±1.50	0.40±2.01±2.47
0.8-0.9	0.76	5.28±1.17±1.24	3.51±0.96±1.00	4.24±1.08±1.13	4.99±1.35±1.42	5.26±2.80±3.09
0.9-1.0	0.75	5.44±1.17±1.23	6.13±1.17±1.23	4.93±1.16±1.22	7.07±1.56±1.70	9.22±2.87±3.18
1.0-1.1	0.74	4.19±0.93±0.98	3.65±0.90±0.94	4.74±1.01±1.09	4.20±1.22±1.54	3.60±2.09±3.01
1.1-1.2	0.73	11.72±1.51±1.64	13.66±1.67±1.83	9.68±1.48±1.60	10.02±1.72±1.89	18.85±3.68±4.03
1.2-1.3	0.72	29.22±2.47±2.87	30.69±2.56±3.00	23.51±2.35±2.73	17.00±2.28±2.67	13.88±3.26±3.60
1.3-1.4	0.70	21.15±2.09±2.34	13.33±1.76±1.95	11.39±1.87±2.25	9.78±1.96±2.36	6.22±2.29±2.47
1.4-1.5	0.69	9.66±1.45±1.56	8.39±1.45±1.59	2.73±1.11±1.41	1.80±1.14±1.50	1.54±1.77±1.97
1.5-1.6	0.67	2.88±0.81±0.84	4.46±1.05±1.09	4.23±1.31±1.37	2.40±1.23±1.30	-1.61±1.39±1.49
1.6-1.8	0.65	4.65±0.79±0.86	2.60±0.63±0.67	2.14±0.67±0.73	0.01±0.47±0.55	1.36±1.14±1.18
1.8-2.0	0.61	3.68±0.87±0.97	2.08±0.70±0.76	2.45±0.92±1.00	1.51±0.87±0.92	1.25±1.39±1.48

Table C.17: Numerical results of the differential cross section $d(\sigma_{\text{TT}} + \varepsilon \sigma_{\text{LT}})/d|\cos\theta^*|$ and luminosity function ratio ε in dependence of the two-pion invariant mass W and the helicity angle $|\cos\theta^*|$ in the momentum transfer range $Q_1^2 = (1.5 - 2.0)$ GeV². The first uncertainty is statistical, the second one is systematic.

W / GeV	ε	$ \cos\theta^* = 0.0-0.2$	$ \cos\theta^* = 0.2-0.4$	$d(\sigma_{\text{TT}} + \varepsilon \sigma_{\text{LT}})/d \cos\theta^* $ / nb	$ \cos\theta^* = 0.4-0.6$	$ \cos\theta^* = 0.6-0.8$	$ \cos\theta^* = 0.8-1.0$
0.3-0.6	0.77	5.96±1.67±1.74	6.82±1.87±1.96	2.74±1.38±1.40	1.52±1.29±1.30	0.21±2.39±2.51	
0.6-0.8	0.76	3.96±1.08±1.12	2.85±0.86±0.89	5.11±1.27±1.33	3.45±1.13±1.18	-2.71±2.00±2.39	
0.8-1.0	0.75	2.61±0.77±0.79	2.54±0.77±0.79	4.62±1.01±1.06	7.05±1.40±1.52	2.11±2.13±2.40	
1.0-1.2	0.74	3.68±0.81±0.85	2.15±0.66±0.69	3.78±0.84±0.90	4.43±1.00±1.13	5.25±2.12±2.85	
1.2-1.4	0.74	13.90±1.50±1.66	14.26±1.51±1.69	8.55±1.25±1.36	9.70±1.54±1.80	2.98±2.03±2.74	
1.4-1.6	0.73	3.06±0.66±0.70	2.76±0.67±0.70	1.13±0.57±0.64	1.02±0.75±0.94	-0.02±0.81±0.95	
1.6-2.0	0.71	1.38±0.30±0.32	1.65±0.38±0.43	0.91±0.32±0.34	0.42±0.32±0.34	-0.30±0.49±0.52	

Table C.18: Numerical results of the differential cross section $d(\sigma_{\text{TT}} + \varepsilon \sigma_{\text{LT}})/d|\cos\theta^*|$ and luminosity function ratio ε in dependence of the two-pion invariant mass W and the helicity angle $|\cos\theta^*|$ in the momentum transfer range $Q_1^2 = (2.0 - 3.0)$ GeV². The first uncertainty is statistical, the second one is systematic.

W / GeV	ε	$ \cos\theta^* = 0.0-0.2$	$ \cos\theta^* = 0.2-0.4$	$d(\sigma_{\text{TT}} + \varepsilon \sigma_{\text{LT}})/d \cos\theta^* $ / nb	$ \cos\theta^* = 0.4-0.6$	$ \cos\theta^* = 0.6-0.8$	$ \cos\theta^* = 0.8-1.0$
0.3-0.6	0.73	3.11±1.35±1.38	0.38±1.11±1.11	4.36±1.60±1.67	1.02±1.38±1.39	-2.56±2.02±2.18	
0.6-0.8	0.72	3.17±1.10±1.13	4.18±1.16±1.22	3.08±1.03±1.07	1.40±1.06±1.12	-0.88±2.14±2.51	
0.8-1.0	0.72	3.83±1.01±1.06	3.97±1.08±1.14	4.12±1.10±1.16	2.80±1.06±1.11	0.99±2.16±2.43	
1.0-1.2	0.71	2.06±0.68±0.71	2.67±0.72±0.76	1.87±0.62±0.65	2.24±0.87±0.99	0.68±1.80±2.71	
1.2-1.4	0.70	7.35±1.21±1.29	8.46±1.28±1.39	3.62±0.88±0.92	3.19±0.96±1.12	-1.88±1.73±3.11	
1.4-1.6	0.69	2.93±0.76±0.80	0.91±0.49±0.51	1.86±0.68±0.73	0.15±0.62±0.78	-1.32±1.21±1.76	
1.6-2.0	0.68	1.06±0.28±0.31	1.03±0.33±0.36	1.25±0.38±0.42	0.71±0.38±0.41	-1.17±0.85±1.06	

Table C.19: Numerical results of the differential cross section $d(\sigma_{\text{TT}} + \varepsilon \sigma_{\text{LR}})/d|\cos\theta^*|$ and luminosity function ratio ε in dependence of the two-pion invariant mass W and the helicity angle $|\cos\theta^*|$ in the momentum transfer range $Q_1^2 = (3.0 - 4.0) \text{ GeV}^2$. The first uncertainty is statistical, the second one is systematic.

W / GeV	ε	$ \cos\theta^* = 0.0-0.2$	$ \cos\theta^* = 0.2-0.4$	$d(\sigma_{\text{TT}} + \varepsilon \sigma_{\text{LR}})/d \cos\theta^* / \text{nb}$	$ \cos\theta^* = 0.4-0.6$	$ \cos\theta^* = 0.6-0.8$	$ \cos\theta^* = 0.8-1.0$
0.3-0.6	0.67	$4.91 \pm 3.87 \pm 4.02$	$-0.95 \pm 3.17 \pm 3.17$	$1.23 \pm 2.63 \pm 2.64$	$-0.18 \pm 3.01 \pm 3.01$	$-2.36 \pm 5.25 \pm 5.47$	
0.6-0.8	0.67	$2.23 \pm 2.04 \pm 2.07$	$0.92 \pm 1.93 \pm 1.94$	$1.39 \pm 1.39 \pm 1.40$	$-0.12 \pm 1.75 \pm 1.75$	$0.70 \pm 3.90 \pm 4.23$	
0.8-1.0	0.66	$3.76 \pm 2.04 \pm 2.16$	$1.09 \pm 1.24 \pm 1.25$	$3.30 \pm 1.75 \pm 1.82$	$3.26 \pm 1.86 \pm 1.92$	$-0.67 \pm 3.32 \pm 3.68$	
1.0-1.2	0.65	$2.23 \pm 1.28 \pm 1.33$	$1.38 \pm 1.24 \pm 1.27$	$2.32 \pm 1.49 \pm 1.57$	$0.93 \pm 1.53 \pm 1.70$	$-2.40 \pm 2.92 \pm 4.18$	
1.2-1.4	0.64	$10.23 \pm 2.43 \pm 2.60$	$6.09 \pm 1.82 \pm 1.91$	$3.36 \pm 1.33 \pm 1.37$	$2.09 \pm 1.47 \pm 1.60$	$3.07 \pm 3.01 \pm 3.72$	
1.4-1.6	0.63	$3.32 \pm 1.69 \pm 1.84$	$2.34 \pm 1.31 \pm 1.37$	$1.29 \pm 1.02 \pm 1.06$	$1.51 \pm 1.12 \pm 1.16$	$-3.49 \pm 2.79 \pm 3.78$	
1.6-2.0	0.62	$1.41 \pm 0.58 \pm 0.65$	$0.30 \pm 0.45 \pm 0.46$	$0.80 \pm 0.46 \pm 0.50$	$0.12 \pm 0.93 \pm 0.95$	$0.63 \pm 2.01 \pm 2.17$	

Table C.20: Numerical results of the differential cross section $d\sigma/d|\cos\theta^*| = d(\sigma_{\text{TT}} + \varepsilon_{\text{LR}}\sigma_{\text{LR}} + \varepsilon_{\text{TL}}\sigma_{\text{TL}} + \varepsilon_{\text{LL}}\sigma_{\text{LL}})/d|\cos\theta^*|$ and integrated cross section $\sigma = \sigma_{\text{TT}} + \varepsilon_{\text{LR}}\sigma_{\text{LR}} + \varepsilon_{\text{TL}}\sigma_{\text{TL}} + \varepsilon_{\text{LL}}\sigma_{\text{LL}}$ in dependence on the momentum transfers Q_1^2 and Q_2^2 and the helicity angle $|\cos\theta^*|$ in the two-pion invariant mass range $W = (1.0 - 1.5) \text{ GeV}$. The first uncertainty is statistical, the second one is systematic.

Q_1^2 / GeV^2	Q_2^2 / GeV^2	σ / nb	$d\sigma/d \cos\theta^* / \text{nb}$			
		$ \cos\theta^* = 0.0-0.2$	$ \cos\theta^* = 0.2-0.4$	$ \cos\theta^* = 0.4-0.6$	$ \cos\theta^* = 0.6-0.8$	$ \cos\theta^* = 0.8-1.0$
0.1-0.4	0.08-0.15	$45.6 \pm 5.8 \pm 1.7$	$53.3 \pm 7.4 \pm 3.5$	$63.6 \pm 8.8 \pm 3.8$	$50.2 \pm 9.9 \pm 3.0$	$29.5 \pm 22.1 \pm 5.6$
0.1-0.4	0.15-0.30	$24.4 \pm 3.5 \pm 1.1$	$27.3 \pm 3.4 \pm 1.6$	$16.8 \pm 3.1 \pm 1.0$	$17.1 \pm 3.6 \pm 1.3$	$43.4 \pm 15.6 \pm 5.0$
0.4-0.7	0.08-0.15	$33.8 \pm 4.0 \pm 1.6$	$41.2 \pm 5.4 \pm 2.4$	$28.4 \pm 5.1 \pm 1.8$	$34.5 \pm 6.1 \pm 2.3$	$42.0 \pm 16.0 \pm 6.5$
0.4-0.7	0.15-0.30	$24.1 \pm 3.2 \pm 1.3$	$29.9 \pm 5.3 \pm 1.9$	$27.2 \pm 5.3 \pm 1.9$	$34.7 \pm 6.5 \pm 2.7$	$19.6 \pm 11.7 \pm 5.1$
0.7-1.0	0.08-0.15	$25.0 \pm 4.8 \pm 1.5$	$25.4 \pm 6.7 \pm 1.7$	$31.5 \pm 7.8 \pm 2.4$	$28.2 \pm 8.4 \pm 2.6$	$30.5 \pm 18.4 \pm 6.1$
0.7-1.0	0.15-0.30	$17.5 \pm 5.0 \pm 1.2$	$25.7 \pm 7.3 \pm 1.9$	$9.3 \pm 5.8 \pm 2.1$	$29.4 \pm 8.5 \pm 2.4$	$19.7 \pm 16.7 \pm 4.0$

Danksagung / Acknowledgments

Aus datenschutzrechtlichen Gründen entfernt.
Removed due to data protection regulations.

Curriculum Vitae

Aus datenschutzrechtlichen Gründen entfernt.
Removed due to data protection regulations.

HADROTOPS: A Monte Carlo Event Generator For Hadron Production In Two-Photon Scattering In Electron Positron Collisions

Max Lellmann ^{a,b,*}, Igor Danilkin ^{a,b}, Achim Denig ^{a,b,c}, Jan Muskalla ^{a,b}, Christoph F. Redmer ^{a,b}, Xiu-Lei Ren ^{b,c,d}, Marc Vanderhaeghen ^{a,b,c}

^a*Institute for Nuclear Physics, Johannes Gutenberg University, D-55099 Mainz*

^b*PRISMA⁺ Cluster of Excellence, Johannes Gutenberg University, D-55099 Mainz*

^c*Helmholtz Institute Mainz, Johannes Gutenberg University, D-55099 Mainz*

^d*Shandong Provincial Key Laboratory of Nuclear Science, Nuclear Energy Technology and Comprehensive Utilization & School of Nuclear Science, Energy and Power Engineering, Shandong University, Jinan 250061, China*

Abstract

We present a Monte Carlo event generator specifically developed for the study of hadronic two-photon scattering events in two-photon scattering at electron-positron colliders. The code enables the generation of events with exact leading-order QED coupling and a flat phase space decay of the hadronic state into an arbitrary number of final state particles as selected by the user. Thus, this generator is well-suited for the use of partial wave analyses tools to study the two-photon production of higher-multiplicity final states across a wide range of energies and photon virtualities. Furthermore, the code integrates both experimental and theoretical inputs on the two-photon couplings of hadrons to simulate two-photon production processes. Motivated by the investigations of the BESIII collaboration, the final states $\pi^+\pi^-$, $\pi^0\pi^0$, $\pi^0\eta$, K^+K^- , $K_S^0K_S^0$, $\eta\eta$, and $f_1(1285) \rightarrow \eta\pi^+\pi^-$ via $a_0^\pm(980)\pi^\mp$ and $f_0(500)\eta$ are currently included. The code is sufficiently flexible to easily add additional final states as well as quickly change the already included channels.

Keywords: Monte Carlo; Event Generator; Two-Photon Physics; Electron Positron Collisions; Pion Pair Production; Hadronic Two-Photon Scattering;

PROGRAM SUMMARY

Program Title: HadroTOPS

CPC Library link to program files: (to be added by Technical Editor)

Code Ocean capsule: (to be added by Technical Editor)

Licensing provisions: GPLv3

Programming language: C++

Nature of problem:

The analysis of hadronic two-photon interactions at electron-positron colliders necessitates the use of a Monte Carlo generator capable of modeling the complex hadronic processes involved in the fusion mechanism across a broad kinematic spectrum. In particular, the study of multi-hadron production is hindered by the lack of suitable simulation tools. Partial wave analyses of various hadronic final states require a Monte Carlo simulation that precisely predicts the quantum electrodynamics (QED) components of the process,

*E-mail address: lellmann@uni-mainz.de

while simultaneously generating a uniform phase space distribution for two-photon to multi-hadron transitions. This allows for a correct description of the known QED couplings while providing an easy decay model, which can be utilized in partial wave analyses and allows for the two-photon cross section to be replaced by the relevant observables.

Solution method:

In this code, the leading-order QED calculation from Refs. [1–3] for the inclusive and single-meson production process $e^+e^- \rightarrow e^+e^-X$ is extended to the fully exclusive two-meson (M_1M_2) production process $e^+e^- \rightarrow e^+e^-M_1M_2$, and combined with the highly efficient phase-space generation algorithm outlined in Ref. [4]. This combination enables an accurate leading QED description of two-photon production for any hadronic final state, with a uniform decay distribution, making it a suitable tool for partial wave analyses. Being able to incorporate theoretical calculations and experimental results of the cross section of two-photon processes, the generator can simulate the two-photon production of any hadronic final states for which the relevant information is provided. For the two-meson production channels, explicit estimates are given based on a dispersive formalism to incorporate the (virtual) two-photon fusion process $\gamma^{(*)}\gamma^{(*)} \rightarrow M_1M_2$. The program is designed to be easily extendable, allowing for the inclusion of additional hadronic final states or more refined hadronic models in future developments.

1. Physics Case and Theoretical Foundation

Two-photon processes in e^+e^- collisions of the form $e^+e^- \rightarrow e^+e^-X$ are a well established tool to study hadronic structure in photon-photon interactions. In such processes, each e^\pm emit a quasi-real or virtual photon, and the photon-photon fusion produces a hadronic final state X . In this work, we focus on the exclusive production of pion pairs ($X = \pi^+\pi^-, \pi^0\pi^0$), $X = \pi^0\eta$, and the production of the axial state $f_1(1285)$ ($f_1(1285) \rightarrow \eta\pi^+\pi^-$). Other final states ($K\bar{K}, \eta\eta$) are purely described by available experimental measurements. All these reactions proceed via $\gamma^{(*)}\gamma^{(*)}$ fusion, where γ^* denotes an off-shell photon. At e^+e^- colliders, two-photon production of hadrons has been studied in detail to extract two-photon couplings and properties of the $f_0(500)$, $f_0(980)$, $a_0(980)$, $f_2(1270)$, $a_2(1320)$ and other resonances in the hadronic system [5–11]. There is renewed interest in accurate theoretical descriptions of $\gamma^*\gamma^* \rightarrow X$ type hadronic reactions, driven by the role of the processes in hadronic light-by-light (HLbL) contribution [12–41] to the muon anomalous magnetic moment $(g-2)_\mu$ [42]. In particular, an accurate modeling of the $\gamma^*\gamma^* \rightarrow \pi\pi$ amplitudes, including the effects of strong final-state interactions (FSI) between pions, is essential for precision HLbL computations [14, 23, 43]. Dispersive approaches have been developed to address this need, providing partial wave (p.w.) amplitudes that incorporate $\pi\pi$ rescattering unitarily and tie into experimental $\pi\pi$ scattering data [44–49].

On the experimental side, current and future e^+e^- facilities, such as BESIII and Belle II, can perform detailed measurements of two-photon processes, including kinematic configurations where one or both outgoing leptons are detected (single-tag or double-tag modes). To fully leverage these measurements, a Monte Carlo (MC) event generator that includes the state-of-the-art two-photon amplitudes is required. The existing generator EKHARA3.0 [50–53] has been used for simulating two-photon production of charged pion pairs. However, EKHARA3.0 includes only the lowest-order Born contribution for $\gamma^*\gamma^* \rightarrow \pi^+\pi^-$ and neglects the strong-interaction dynamics that generate resonances in the $\pi^+\pi^-$ invariant mass spectrum. The latest version EKHARA3.2 has updated its $\gamma^*\gamma^* \rightarrow \pi\pi$ input to include the full dispersive amplitudes for $\pi\pi$ final states, thereby greatly improving the physical accuracy of the simulation. The further development of the EKHARA event generator beyond the version 3.2 will likely not continue [54].

Ongoing or foreseen studies of multi-hadron final states other than pion pairs require equivalent activities. Therefore, the generator presented in this work is configured to simulate the

production of $\pi^0\eta$, $K\bar{K}$, $\eta\eta$, and $f_1(1285) \rightarrow \eta\pi^+\pi^-$. To achieve this, various experimental measurements and theoretical predictions are incorporated.

As mentioned above, beyond their relevance for precision tests, two-photon production processes are of particular importance for hadron spectroscopy. They provide a clean environment for the formation of non-vector states in electron-positron collisions. In the light-meson sector, the density of resonances demands partial-wave analyses (PWA) to extract the relevant resonance contributions. Such analyses rely on

MC simulations which evenly cover all dimensions of the phase space for fitting and normalization [55, 56]. When using a fully phase-space-distributed MC sample to analyze a two-photon process, one must incorporate the QED couplings into the amplitudes. This introduces an additional complication, which can be avoided by using a MC generator that provides a phase-space-distributed sample while already taking into account the QED couplings. However, many available generators capable of producing such MC samples have different kinematic limitations and therefore cannot be used in all cases (see, for example, Refs [57–59]).

1.1. Theoretical Formulation

To provide such a tool, we begin by formulating the general process

$$e^+(p_1) + e^-(p_2) \rightarrow e^+(p'_1) + e^-(p'_2) + X(p_X), \quad (1)$$

where the quantities in parentheses denote four-momenta. In the overall center-of-mass (c.m.) frame of the initial e^+e^- , the initial four-momenta are $p_1 = (E, \mathbf{p})$ and $p_2 = (E, -\mathbf{p})$ with beam energy $E = \sqrt{s}/2$ and $s = (p_1 + p_2)^2$. The outgoing leptons carry momenta p'_1 and p'_2 , and we define the momentum transfers as $q_1 = p_1 - p'_1$ and $q_2 = p_2 - p'_2$. Consequently, q_1 and q_2 are the four-momenta of the photons emitted by the e^+ and e^- , respectively, that fuse into the X system. The effective squared $\gamma^*\gamma^*$ center-of-mass energy is $W^2 = (q_1 + q_2)^2 = p_X^2$. The photon virtualities are defined as $Q_1^2 \equiv -q_1^2$ and $Q_2^2 \equiv -q_2^2$, with $Q_{1,2}^2 \geq 0$. If Q^2 is near zero, the photon is considered as *quasi-real* (such photons are emitted at very small angles and carry very low momentum transfer in the e^+e^- c.m. frame). When Q^2 is substantial, the photon is virtual, as is the case when an outgoing lepton is detected at large scattering angle at experiments like BESIII ($\theta \gtrsim 20^\circ$, $Q^2 \gtrsim 0.1 \text{ GeV}^2$) or Belle II ($\theta \gtrsim 17^\circ$, $Q^2 \gtrsim 3 \text{ GeV}^2$).

The polarized cross section for the process $e^+e^- \rightarrow e^+e^-X$, which explicitly depends on the helicities h_1, h_2 of the incoming leptons, can be written as

$$d\sigma_{h_1 h_2} = \frac{1}{F} d\text{Lips} \sum_{h'_1, h'_2} |\mathcal{M}|^2, \quad (2)$$

where \mathcal{M} denotes the full scattering amplitude, F is the flux factor, and $d\text{Lips}$ is the Lorentz-invariant phase space measure for the final state

$$d\text{Lips} = \frac{d^3\vec{p}'_1}{(2\pi)^3 2E'_1} \frac{d^3\vec{p}'_2}{(2\pi)^3 2E'_2} d\Gamma_X (2\pi)^4 \delta(p_1 + p_2 - p'_1 - p'_2 - p_X). \quad (3)$$

The factor $d\Gamma_X$ denotes the phase space element for the intermediate hadronic state. At tree level, the amplitude takes the form

$$\mathcal{M} = \frac{e^2}{Q_1^2 Q_2^2} [\bar{v}(p_1, h_1) \gamma^\mu v(p'_1, h'_1)] [\bar{u}(p'_2, h'_2) \gamma^\nu u(p_2, h_2)] H_{\mu\nu}, \quad (4)$$

where $H_{\mu\nu}$ is the hadronic tensor associated with the subprocess $\gamma^*\gamma^* \rightarrow X$. The squared amplitude, summed over the final-state lepton helicities, becomes

$$\sum_{h'_1, h'_2} |\mathcal{M}|^2 = \frac{e^4}{Q_1^4 Q_2^4} L_{h_1, \mu\mu'} L_{h_2, \nu\nu'} H^{\mu\nu} (H^{\mu'\nu'})^*, \quad (5)$$

where $L_{h_1, \mu\mu'}$ is the leptonic tensor associated with the positron currents,

$$L_{h_1, \mu\mu'} = (p_1 + p'_1)_\mu (p_1 + p'_1)_{\mu'} + (q_1^2 g_{\mu\mu'} - q_{1\mu} q_{1\mu'}) + h_1 2i \varepsilon_{\mu\mu' \kappa\lambda} q_1^\kappa p_1^\lambda, \quad (6)$$

with $\varepsilon_{0123} = +1$, and helicity $h_1 = \pm 1$ (in units $\hbar/2$). There is an analogous definition for the leptonic tensor $L_{h_2, \nu\nu'}$ associated with the electron currents.

There are two conceptually distinct ways to compute the $e^+e^- \rightarrow e^+e^-X$ cross section at this stage. The first proceeds covariantly, using the hadronic tensor $H^{\mu\nu}$ as shown above, and is incorporated in EKHARA3.2 for $X = \pi\pi$. The second approach, which we adopt here, involves decomposing the hadronic tensor in terms of helicity amplitudes for the fusion of two virtual photons into a hadronic system

$$H_{\lambda_1\lambda_2} \equiv \varepsilon^\mu(q_1, \lambda_1) \varepsilon^\nu(q_2, \lambda_2) H_{\mu\nu}, \quad (7)$$

with virtual photon helicities $\lambda_{1,2} = \pm 1, 0$. By inserting complete sets of photon polarization states into Eq. (5) and employing electromagnetic gauge invariance, the squared amplitude can be rewritten as

$$\sum_{h'_1, h'_2} |\mathcal{M}|^2 = \frac{e^4}{Q_1^2 Q_2^2} \sum_{\lambda_1, \lambda_2, \lambda'_1, \lambda'_2} \rho_{h_1}^{\lambda_1\lambda'_1} \rho_{h_2}^{\lambda_2\lambda'_2} H_{\lambda_1\lambda_2} H_{\lambda'_1\lambda'_2}^*, \quad (8)$$

where $\rho_{h_1}^{\lambda_1\lambda'_1}$ and $\rho_{h_2}^{\lambda_2\lambda'_2}$ are the photon density matrices, which encode the polarization information of the virtual photons, defined as:

$$\rho_{h_1}^{\lambda_1\lambda'_1} \equiv \frac{(-1)^{\lambda_1+\lambda'_1}}{Q_1^2} \varepsilon^{\mu*}(q_1, \lambda_1) \varepsilon^{\mu'}(q_1, \lambda'_1) L_{h_1, \mu\mu'}, \quad (9)$$

and an analogous definition for $\rho_{h_2}^{\lambda_2\lambda'_2}$.

The central object in this representation is the imaginary part of the forward light-by-light scattering amplitude $\gamma^*(q_1, \lambda_1) \gamma^*(q_2, \lambda_2) \rightarrow \gamma^*(q_1, \lambda'_1) \gamma^*(q_2, \lambda'_2)$

$$\text{Im } M_{\lambda'_1\lambda'_2, \lambda_1\lambda_2} \equiv W_{\lambda'_1\lambda'_2, \lambda_1\lambda_2}, \quad (10)$$

which defines the helicity-dependent response functions. According to unitarity, these response functions can be written as a sum over all possible intermediate hadronic states X , yielding

$$\begin{aligned} W_{\lambda'_1\lambda'_2, \lambda_1\lambda_2} &= \frac{1}{2} \sum_X \int d\Gamma_X (2\pi)^4 \delta^4(q_1 + q_2 - p_X) H_{\lambda_1\lambda_2}(q_1, q_2, p_X) H_{\lambda'_1\lambda'_2}^*(q_1, q_2, p_X), \\ &\equiv \sum_X W_{\lambda'_1\lambda'_2, \lambda_1\lambda_2}^X. \end{aligned} \quad (11)$$

The response functions satisfy several symmetry relations due to discrete symmetries and angular momentum conservation. First, angular momentum conservation along the photon-photon axis

implies that, in the forward limit, only transitions with equal total helicity $\Lambda = \Lambda'$ contribute, where $\Lambda = \lambda_1 - \lambda_2$ and $\Lambda' = \lambda'_1 - \lambda'_2$. Parity invariance imposes the condition

$$W_{-\lambda'_1, -\lambda'_2, -\lambda_1, -\lambda_2} = W_{\lambda'_1, \lambda'_2, \lambda_1, \lambda_2},$$

and time-reversal symmetry leads to

$$W_{\lambda'_1, \lambda'_2, \lambda_1, \lambda_2} = W_{\lambda_1, \lambda_2, \lambda'_1, \lambda'_2}.$$

As a result of these constraints, the number of independent response functions is reduced from 81 to 8. This reduced set corresponds to distinct cross sections and interference terms, forming the basis for expressing the full cross section in terms of measurable response functions.

1.1.1. General cross section for the inclusive $e^+e^- \rightarrow e^+e^-X$ process

We begin by considering the inclusive case, in which a sum is taken over all possible hadronic final states X in Eq.(11). Compared to the exclusive $X = \pi\pi$ process, which will be presented in detail in the next subsection, the inclusive cross section can be written compactly as¹ [1, 2]

$$\begin{aligned} d\sigma_{h_1, h_2} = & \frac{\alpha^2}{8\pi^4 Q_1^2 Q_2^2} \frac{\sqrt{X}}{s(1-4m^2/s)^{1/2}} \frac{d^3\vec{p}'_1}{E'_1} \frac{d^3\vec{p}'_2}{E'_2} \left\{ 4\rho_1^{++}\rho_2^{++} \frac{1}{2}(\sigma_0 + \sigma_2) + \rho_1^{00}\rho_2^{00}\sigma_{LL} \right. \\ & + 2\rho_1^{++}\rho_2^{00}\sigma_{TL} + 2\rho_1^{00}\rho_2^{++}\sigma_{LT} + 2(\rho_1^{++} - 1)(\rho_2^{++} - 1)\cos(2\tilde{\phi})\tau_{TT} \\ & + 8[(\rho_1^{00} + 1)(\rho_2^{00} + 1)(\rho_1^{++} - 1)(\rho_2^{++} - 1)]^{1/2}\cos\tilde{\phi}\frac{1}{2}(\tau_0 + \tau_1) \\ & + h_1h_2 4[(\rho_1^{00} + 1)(\rho_2^{00} + 1)]^{1/2}\frac{1}{2}(\sigma_0 - \sigma_2) \\ & \left. + h_1h_2 8[(\rho_1^{++} - 1)(\rho_2^{++} - 1)]^{1/2}\cos\tilde{\phi}\frac{1}{2}(\tau_0 - \tau_1) \right\}, \end{aligned} \quad (12)$$

where $X \equiv (q_1 \cdot q_2)^2 - q_1^2 q_2^2$, $\tilde{\phi}$ is the azimuthal angle between the two leptonic planes in the $\gamma^*\gamma^*$ center-of-mass frame (later called the $\gamma\gamma$ frame), and m is the lepton mass. The eight independent response functions that enter the cross section encapsulate the full structure of the $\gamma^*\gamma^* \rightarrow X$ sub-processes, and are defined as:

$$\begin{aligned} \sigma_0 &= \frac{1}{2\sqrt{X}} W_{++++}, & \sigma_2 &= \frac{1}{2\sqrt{X}} W_{+-,-+}, & \sigma_{TT} &\equiv \frac{1}{2}(\sigma_0 + \sigma_2), \\ \sigma_{TL} &= \frac{1}{2\sqrt{X}} W_{+0,+0}, & \sigma_{LT} &= \frac{1}{2\sqrt{X}} W_{0+,0+}, & \sigma_{LL} &= \frac{1}{2\sqrt{X}} W_{00,00}, \\ \tau_{TT} &= \frac{1}{2\sqrt{X}} W_{++,-+}, & \tau_0 &= \frac{1}{2\sqrt{X}} W_{++00}, & \tau_1 &= -\frac{1}{2\sqrt{X}} W_{0+,-0}. \end{aligned} \quad (13)$$

These response functions depend on three independent kinematic variables: the two-photon center-of-mass energy W and the virtualities Q_1^2 and Q_2^2 .

¹This formulation follows a slightly different convention from Refs. [2], avoiding the use of τ_{TL} and τ_{TL}^a in favor of the τ_0 and τ_1 . Also, several typos have appeared in subsequent works [3, 60], which are fixed here.

For specific quantum numbers of the final state X , parity conservation imposes the following condition on the helicity amplitudes

$$H_{\lambda_1 \lambda_2} = P_X (-1)^{-J_X} H_{-\lambda_1 - \lambda_2}, \quad (14)$$

where P_X is the parity and J_X is the spin of the hadronic system X . Using this relation, one finds the following relation between the transverse-transverse interference term and the helicity-0 amplitude for production of states with different J^{PC} :

$$\tau_{TT} = \begin{cases} \sigma_0 & \text{for } X = 0^{++}, 2^{++}, 3^{-+}, \dots \\ -\sigma_0 & \text{for } X = 0^{-+}, 1^{++}, 2^{-+}, \dots \end{cases} \quad (15)$$

The virtual-photon density matrix elements $\rho_i^{\lambda_i \lambda_i'}$ capture the polarization structure of the virtual photons. The components relevant for Eq. (12) are given by the unpolarized part of $\rho_{h_i}^{\lambda_i \lambda_i'}$, which reads

$$\begin{aligned} \rho_1^{++} &= \frac{1}{2} \left\{ 1 - \frac{4m^2}{Q_1^2} + \frac{1}{X} (2 p_1 \cdot q_2 - q_1 \cdot q_2)^2 \right\}, \\ \rho_2^{++} &= \frac{1}{2} \left\{ 1 - \frac{4m^2}{Q_2^2} + \frac{1}{X} (2 p_2 \cdot q_1 - q_1 \cdot q_2)^2 \right\}, \\ \rho_1^{00} &= \frac{1}{X} (2 p_1 \cdot q_2 - q_1 \cdot q_2)^2 - 1, \\ \rho_2^{00} &= \frac{1}{X} (2 p_2 \cdot q_1 - q_1 \cdot q_2)^2 - 1. \end{aligned} \quad (16)$$

From these expressions, one can define the familiar virtual-photon polarization parameters ($0 \leq \varepsilon_i \leq 1$)

$$\varepsilon_i \equiv \frac{\rho_i^{++} - 1}{\rho_i^{00}}, \quad i = 1, 2,$$

which allow to express Eq. (12) in a form that conveniently allows to separate the response functions

$$\begin{aligned} d\sigma_{h_1 h_2} &= \frac{\alpha^2}{8\pi^4 Q_1^2 Q_2^2} \frac{\sqrt{X}}{s(1-4m^2/s)^{1/2}} \frac{d^3 \vec{p}'_1}{E'_1} \frac{d^3 \vec{p}'_2}{E'_2} \frac{4}{(1-\varepsilon_1)(1-\varepsilon_2)} \\ &\times \left\{ \frac{1}{2} (\sigma_0 + \sigma_2) + \left[\varepsilon_1 + \frac{2m^2}{Q_1^2} (1-\varepsilon_1) \right] \left[\varepsilon_2 + \frac{2m^2}{Q_2^2} (1-\varepsilon_2) \right] \sigma_{LL} \right. \\ &\quad + \left[\varepsilon_2 + \frac{2m^2}{Q_2^2} (1-\varepsilon_2) \right] \sigma_{TL} + \left[\varepsilon_1 + \frac{2m^2}{Q_1^2} (1-\varepsilon_1) \right] \sigma_{LT} + \frac{1}{2} \varepsilon_1 \varepsilon_2 \cos(2\tilde{\phi}) \tau_{TT} \\ &\quad + 2 \left[\varepsilon_1 (1+\varepsilon_1) + \frac{4m^2}{Q_1^2} \varepsilon_1 (1-\varepsilon_1) \right]^{1/2} \left[\varepsilon_2 (1+\varepsilon_2) + \frac{4m^2}{Q_2^2} \varepsilon_2 (1-\varepsilon_2) \right]^{1/2} \cos \tilde{\phi} \frac{1}{2} (\tau_0 + \tau_1) \\ &\quad + h_1 h_2 \left[1 - \varepsilon_1^2 + \frac{4m^2}{Q_1^2} (1-\varepsilon_1)^2 \right]^{1/2} \left[1 - \varepsilon_2^2 + \frac{4m^2}{Q_2^2} (1-\varepsilon_2)^2 \right]^{1/2} \frac{1}{2} (\sigma_0 - \sigma_2) \\ &\quad \left. + 2 h_1 h_2 [\varepsilon_1 (1-\varepsilon_1)]^{1/2} [\varepsilon_2 (1-\varepsilon_2)]^{1/2} \cos \tilde{\phi} \frac{1}{2} (\tau_0 - \tau_1) \right\}. \end{aligned} \quad (17)$$

1.1.2. General cross section for the exclusive $e^+e^- \rightarrow e^+e^-\pi\pi$ process

We next consider the exclusive process

$$e^+(p_1) + e^-(p_2) \rightarrow e^+(p'_1) + e^-(p'_2) + \pi_1(p_{\pi_1}) + \pi_2(p_{\pi_2}), \quad (18)$$

where $\pi_1\pi_2$ stands for the $\pi^+\pi^-$ or $\pi^0\pi^0$ state, or in general stands for any two-meson state M_1M_2 . In contrast to the fully inclusive case, for which the cross section is given by Eq. (12), for the exclusive process of Eq. (18), we need to retain the full kinematic information on the pion pair, including their polar and azimuthal angular distributions. This allows for a more differential analysis of the reaction dynamics.

It is convenient to work in the $\gamma\gamma$ frame. By convention, the z -axis is chosen along the direction of \vec{q}_1 (the momentum of the photon emitted by the e^+), as shown in Fig. 1. In this frame, the two photons travel back-to-back along $\pm\hat{z}$. The pions are produced with momenta

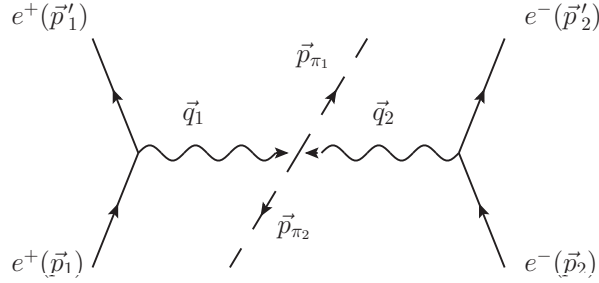


Figure 1: The $e^+e^- \rightarrow e^+e^-\pi_1\pi_2$ process in the $\gamma^*\gamma^*$ c.m. frame

p_{π_1}, p_{π_2} such that $\vec{p}_{\pi_1} + \vec{p}_{\pi_2} = 0$. We define the polar angle θ_π of the π_1 in the $\gamma\gamma$ frame as the angle between \vec{p}_{π_1} and \vec{q}_1 , so

$$\cos \theta_\pi = \hat{z} \cdot \hat{q}_1. \quad (19)$$

Azimuthal angles are introduced to describe the orientation of the outgoing lepton planes relative to the hadronic plane. First, the hadron plane is defined as the plane containing the $\gamma^*\gamma^*$ axis (\hat{z}) and the π_1 momentum; by this definition, the hadron plane is taken to be the xz -plane, i.e. $\phi_\pi = 0$. The x axis is fixed in the direction of the transverse component of \vec{p}_{π_1} (with respect to the direction of \vec{q}_1).

Next, the positron plane is defined as the plane containing \hat{z} and the three-momentum of the incoming e^+ (\vec{p}_1). The angle between the hadron plane and the positron plane is denoted by $\tilde{\phi}_1$. Similarly, the angle between the hadron plane and the electron plane (containing \vec{p}_2 and \hat{z}) is $\tilde{\phi}_2$. By construction, $\tilde{\phi}_{1,2}$ lie in $[0, 2\pi)$. It is convenient to define the components of lepton momenta p_i transverse to the $\gamma\gamma$ axis in the $\gamma\gamma$ rest frame

$$\vec{p}_{i\perp} \equiv \vec{p}_i - \frac{\vec{p}_i \cdot \vec{q}_1}{|\vec{q}_1|^2} \vec{q}_1, \quad i = 1, 2 \quad (20)$$

and express $\tilde{\phi}_{1,2}$ in terms of these quantities

$$\hat{p}_{i\perp} \cdot (\hat{q}_1 \times \hat{p}_{\pi^+}) = \sin \theta_\pi \sin \tilde{\phi}_i. \quad (21)$$

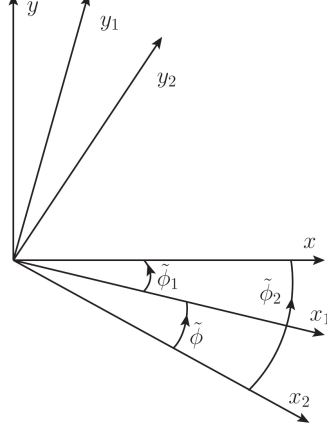


Figure 2: The azimuthal angles $\tilde{\phi}_1$ and $\tilde{\phi}_2$ in the $\gamma^*\gamma^*$ c.m. frame between the lepton planes and the hadron plane. The latter is chosen as the xz -plane. The momenta \vec{p}_1 and \vec{q}_1 define the x_1z -plane, whereas the momenta \vec{p}_2 and \vec{q}_2 define the x_2z -plane.

The difference $\tilde{\phi} = \tilde{\phi}_2 - \tilde{\phi}_1$ is the relative azimuthal angle between the two lepton scattering planes. Equivalently, $\cos \tilde{\phi}$ can also be obtained from the scalar product of the two leptons transverse momentum vectors in the $\gamma\gamma$ frame:

$$\cos(\tilde{\phi}_2 - \tilde{\phi}_1) = \hat{p}_{1\perp} \cdot \hat{p}_{2\perp}, \quad (22)$$

as shown in Fig. 2.

For the exclusive $e^+e^- \rightarrow e^+e^-\pi_1\pi_2$ process, one can introduce the angular integrated hadronic response function, contributing to the inclusive sum in Eq. (11), as:

$$W_{\lambda'_1\lambda'_2,\lambda_1\lambda_2}^{\pi\pi} = \int d\Omega_\pi \tilde{W}_{\lambda'_1\lambda'_2,\lambda_1\lambda_2}^{\pi\pi}, \quad (23)$$

while the non-integrated hadronic response function $\tilde{W}_{\lambda'_1\lambda'_2,\lambda_1\lambda_2}^{\pi\pi}$ can be expressed in terms of the $\gamma^*\gamma^* \rightarrow \pi_1\pi_2$ amplitudes as:

$$\tilde{W}_{\lambda'_1\lambda'_2,\lambda_1\lambda_2}^{\pi\pi} \equiv \frac{1}{2\pi} \frac{\beta_\pi}{32\pi} H_{\lambda_1\lambda_2} H_{\lambda'_1\lambda'_2}^*, \quad \beta_\pi = \left(1 - \frac{4m_\pi^2}{W^2}\right)^{1/2}, \quad (24)$$

with m_π the pion mass.

Using parity invariance for the $\gamma^*\gamma^* \rightarrow \pi_1\pi_2$ process, the hadronic response functions $\tilde{W}_{\lambda'_1\lambda'_2,\lambda_1\lambda_2}^{\pi\pi}$ have the property:

$$\tilde{W}_{-\lambda'_1-\lambda'_2,-\lambda_1-\lambda_2}^{\pi\pi} = (-1)^{\Lambda-\Lambda'} \tilde{W}_{\lambda'_1\lambda'_2,\lambda_1\lambda_2}^{\pi\pi}, \quad (25)$$

whereas hermiticity of the hadronic tensor leads to the relation:

$$\tilde{W}_{\lambda'_1\lambda'_2,\lambda_1\lambda_2}^{\pi\pi} = (\tilde{W}_{\lambda_1\lambda_2,\lambda'_1\lambda'_2}^{\pi\pi})^*. \quad (26)$$

The process $e^+e^- \rightarrow e^+e^-\pi_1\pi_2$ allows for contributions from helicity transitions with $\Lambda - \Lambda' = 0, \pm 1, \pm 2, \pm 3, \pm 4$. Accordingly, the fully differential $e^+e^- \rightarrow e^+e^-\pi_1\pi_2$ cross section, i.e. also differential in the pion solid angle $d\Omega_\pi$, can be expressed in terms of 25 helicity-dependent cross sections and so-called interference response functions for the subprocess $\gamma^*\gamma^* \rightarrow \pi_1\pi_2$. The (positive definite) differential cross sections are defined as follows:

$$\begin{aligned}\frac{d\sigma_0}{d\cos\theta_\pi} &\equiv \frac{\beta_\pi}{64\pi\sqrt{X}}|H_{++}|^2, & \frac{d\sigma_2}{d\cos\theta_\pi} &\equiv \frac{\beta_\pi}{64\pi\sqrt{X}}|H_{+-}|^2, \\ \frac{d\sigma_{TL}}{d\cos\theta_\pi} &\equiv \frac{\beta_\pi}{64\pi\sqrt{X}}|H_{+0}|^2, & \frac{d\sigma_{LT}}{d\cos\theta_\pi} &\equiv \frac{\beta_\pi}{64\pi\sqrt{X}}|H_{0+}|^2, \\ \frac{d\sigma_{LL}}{d\cos\theta_\pi} &\equiv \frac{\beta_\pi}{64\pi\sqrt{X}}|H_{00}|^2,\end{aligned}\tag{27}$$

while the interference terms are represented by the real and imaginary parts of products of helicity amplitudes:

$$\begin{aligned}\frac{d\tau_0}{d\cos\theta_\pi} &\equiv \frac{\beta_\pi}{64\pi\sqrt{X}}\operatorname{Re}(H_{++}^*H_{00}), & \frac{d\tau_1}{d\cos\theta_\pi} &\equiv \frac{\beta_\pi}{64\pi\sqrt{X}}\operatorname{Re}(H_{0+}^*H_{+0}), \\ \frac{d\tau_{12}}{d\cos\theta_\pi} &\equiv \frac{\beta_\pi}{64\pi\sqrt{X}}\operatorname{Re}(H_{+0}^*H_{+-}), & \frac{d\tau_{-12}}{d\cos\theta_\pi} &\equiv \frac{\beta_\pi}{64\pi\sqrt{X}}\operatorname{Re}(H_{0+}^*H_{+-}), \\ \frac{d\tau_{T2}}{d\cos\theta_\pi} &\equiv \frac{\beta_\pi}{64\pi\sqrt{X}}\operatorname{Re}(H_{++}^*H_{+-}), & \frac{d\tau_{L2}}{d\cos\theta_\pi} &\equiv \frac{\beta_\pi}{64\pi\sqrt{X}}\operatorname{Re}(H_{00}^*H_{+-}), \\ \frac{d\tau_{1T}}{d\cos\theta_\pi} &\equiv \frac{\beta_\pi}{64\pi\sqrt{X}}\operatorname{Re}(H_{+0}^*H_{++}), & \frac{d\tau_{-1T}}{d\cos\theta_\pi} &\equiv \frac{\beta_\pi}{64\pi\sqrt{X}}\operatorname{Re}(H_{0+}^*H_{++}), \\ \frac{d\tau_{1L}}{d\cos\theta_\pi} &\equiv \frac{\beta_\pi}{64\pi\sqrt{X}}\operatorname{Re}(H_{+0}^*H_{00}), & \frac{d\tau_{-1L}}{d\cos\theta_\pi} &\equiv \frac{\beta_\pi}{64\pi\sqrt{X}}\operatorname{Re}(H_{0+}^*H_{00}),\end{aligned}\tag{28}$$

where the subscripts used in the interference terms denote the total $\gamma^*\gamma^*$ helicity of the contributing $\gamma^*\gamma^* \rightarrow \pi_1\pi_2$ amplitudes, with $T(L)$ subscripts denote a helicity-zero amplitude arising from transverse (longitudinal) photons respectively. The remaining 10 interference response functions are given by the corresponding imaginary parts of the same helicity amplitude combinations. We denote them with a bar. For example,

$$\frac{d\bar{\tau}_0}{d\cos\theta_\pi} \equiv \frac{\beta_\pi}{64\pi\sqrt{X}}\operatorname{Im}(H_{++}^*H_{00}).\tag{29}$$

The fully differential polarized cross section for the exclusive process $e^+e^- \rightarrow e^+e^-\pi_1\pi_2$ can be expressed as:

$$d\sigma_{h_1,h_2} = d\sigma^{(0)} + h_1 d\sigma^{(1)} + h_2 d\sigma^{(2)} + h_1 h_2 d\sigma^{(12)},\tag{30}$$

where $h_{1,2} = \pm 1$ denote the helicities of the incoming leptons (in units $\hbar/2$).

The lepton helicity averaged (unpolarized) differential cross section $d\sigma^{(0)}$ is then obtained as:

$$\begin{aligned}d\sigma^{(0)} &= \frac{\alpha^2}{8\pi^4 Q_1^2 Q_2^2} \frac{\sqrt{X}}{s(1-4m^2/s)^{1/2}} \frac{d^3\vec{p}'_1}{E'_1} \frac{d^3\vec{p}'_2}{E'_2} d\cos\theta_\pi \frac{4}{(1-\varepsilon_1)(1-\varepsilon_2)} \\ &\times \left\{ \frac{1}{2} \left(\frac{d\sigma_0}{d\cos\theta_\pi} + \frac{d\sigma_2}{d\cos\theta_\pi} \right) + \left[\varepsilon_1 + \frac{2m^2}{Q_1^2} (1-\varepsilon_1) \right] \left[\varepsilon_2 + \frac{2m^2}{Q_2^2} (1-\varepsilon_2) \right] \frac{d\sigma_{LL}}{d\cos\theta_\pi} \right\}\end{aligned}$$

$$\begin{aligned}
& + \left[\varepsilon_2 + \frac{2m^2}{Q_2^2}(1 - \varepsilon_2) \right] \left(1 + \varepsilon_1 \cos(2\tilde{\phi}_1) \right) \frac{d\sigma_{TL}}{d \cos \theta_\pi} + \left[\varepsilon_1 + \frac{2m^2}{Q_1^2}(1 - \varepsilon_1) \right] \left(1 + \varepsilon_2 \cos(2\tilde{\phi}_2) \right) \frac{d\sigma_{LT}}{d \cos \theta_\pi} \\
& + \frac{1}{2} \varepsilon_1 \varepsilon_2 \left[\cos 2(\tilde{\phi}_2 - \tilde{\phi}_1) \frac{d\sigma_0}{d \cos \theta_\pi} + \cos 2(\tilde{\phi}_1 + \tilde{\phi}_2) \frac{d\sigma_2}{d \cos \theta_\pi} \right] - \left[\varepsilon_1 \cos(2\tilde{\phi}_1) + \varepsilon_2 \cos(2\tilde{\phi}_2) \right] \frac{d\tau_{T2}}{d \cos \theta_\pi} \\
& + \left[\varepsilon_1(1 + \varepsilon_1) + \frac{4m^2}{Q_1^2} \varepsilon_1(1 - \varepsilon_1) \right]^{1/2} \left[\varepsilon_2(1 + \varepsilon_2) + \frac{4m^2}{Q_2^2} \varepsilon_2(1 - \varepsilon_2) \right]^{1/2} \\
& \times \left[\cos(\tilde{\phi}_2 - \tilde{\phi}_1) \left(\frac{d\tau_0}{d \cos \theta_\pi} + \frac{d\tau_1}{d \cos \theta_\pi} \right) + \cos(\tilde{\phi}_1 + \tilde{\phi}_2) \left(\frac{d\tau_1}{d \cos \theta_\pi} - \frac{d\tau_{L2}}{d \cos \theta_\pi} \right) \right] \\
& + \left[\varepsilon_1(1 + \varepsilon_1) + \frac{4m^2}{Q_1^2} \varepsilon_1(1 - \varepsilon_1) \right]^{1/2} \left[\cos \tilde{\phi}_1 \left(\frac{d\tau_{-12}}{d \cos \theta_\pi} - \frac{d\tau_{-1T}}{d \cos \theta_\pi} \right) \right. \\
& \quad - 2 \left[\varepsilon_2 + \frac{2m^2}{Q_2^2}(1 - \varepsilon_2) \right] \cos \tilde{\phi}_1 \frac{d\tau_{1L}}{d \cos \theta_\pi} \\
& \quad \left. + \varepsilon_2 \cos(\tilde{\phi}_1 + 2\tilde{\phi}_2) \frac{d\tau_{-12}}{d \cos \theta_\pi} - \varepsilon_2 \cos(2\tilde{\phi}_2 - \tilde{\phi}_1) \frac{d\tau_{-1T}}{d \cos \theta_\pi} \right] \\
& + \left[\varepsilon_2(1 + \varepsilon_2) + \frac{4m^2}{Q_2^2} \varepsilon_2(1 - \varepsilon_2) \right]^{1/2} \left[\cos \tilde{\phi}_2 \left(\frac{d\tau_{12}}{d \cos \theta_\pi} - \frac{d\tau_{1T}}{d \cos \theta_\pi} \right) \right. \\
& \quad - 2 \left[\varepsilon_1 + \frac{2m^2}{Q_1^2}(1 - \varepsilon_1) \right] \cos \tilde{\phi}_2 \frac{d\tau_{-1L}}{d \cos \theta_\pi} \\
& \quad \left. + \varepsilon_1 \cos(2\tilde{\phi}_1 + \tilde{\phi}_2) \frac{d\tau_{12}}{d \cos \theta_\pi} - \varepsilon_1 \cos(2\tilde{\phi}_1 - \tilde{\phi}_2) \frac{d\tau_{1T}}{d \cos \theta_\pi} \right] \Bigg\}. \tag{31}
\end{aligned}$$

The helicity dependent cross section for the exclusive $e^+e^- \rightarrow e^+e^-\pi_1\pi_2$ process in the case of polarized lepton beams, proportional to $h_1 = \pm 1$ and $h_2 = \pm 1$ in Eq. (30), cannot be exploited at present due to missing beam polarization at existing experimental facilities. For future reference, we present these expressions for completeness in the Appendix.

Note that upon integrating Eq. (31) over $d\Omega_\pi$ ² yields the $\pi\pi$ contribution to the fully inclusive cross section given in Eq. (17). It is important to keep in mind that for the exclusive case $X = \pi\pi$, only final states with quantum numbers $J^P = 0^{++}, 2^{++}, 4^{++}, \dots$ are allowed. Consequently, the transverse-transverse interference term satisfies $\tau_{TT} = \sigma_0$ as indicated in Eq.(15).

The cross section for the single-tagged exclusive $e^+e^- \rightarrow e^+e^-\pi\pi$ process, where photon 1 has finite virtuality is obtained by integrating Eq. (31) over $\tilde{\phi}_2$ and taking the limit $Q_2^2 \rightarrow 0$. This yields:

$$\begin{aligned}
d\sigma^{(0)}|_{Q_2^2 \rightarrow 0} & = \frac{\alpha^2}{8\pi^4 Q_1^2 Q_2^2} \frac{\sqrt{X}}{s(1 - 4m^2/s)^{1/2}} \frac{d^3\vec{p}'_1}{E'_1} \frac{d^3\vec{p}'_2}{E'_2} d \cos \theta_\pi \frac{4}{(1 - \varepsilon_1)(1 - \varepsilon_2)} \\
& \times \left\{ \frac{1}{2} \left(\frac{d\sigma_0}{d \cos \theta_\pi} + \frac{d\sigma_2}{d \cos \theta_\pi} \right) + \left[\varepsilon_1 + \frac{2m^2}{Q_1^2}(1 - \varepsilon_1) \right] \frac{d\sigma_{LT}}{d \cos \theta_\pi} - \varepsilon_1 \cos(2\tilde{\phi}_1) \frac{d\tau_{T2}}{d \cos \theta_\pi} \right.
\end{aligned}$$

²To restore the trivial ϕ_π dependence in the kinematic factors in Eq. (31), which is shown for the choice $\phi_\pi = 0$, one needs to replace $\tilde{\phi}_1 \rightarrow \tilde{\phi}_1 - \phi_\pi$ and $\tilde{\phi}_2 \rightarrow \tilde{\phi}_2 - \phi_\pi$.

$$+ \left[\varepsilon_1(1 + \varepsilon_1) + \frac{4m^2}{Q_1^2} \varepsilon_1(1 - \varepsilon_1) \right]^{1/2} \cos \tilde{\phi}_1 \left(\frac{d\tau_{-12}}{d \cos \theta_\pi} - \frac{d\tau_{-1T}}{d \cos \theta_\pi} \right), \quad (32)$$

which is fully consistent with the cross section equation for the unpolarized electron scattering off an unpolarized target [61]. An important feature of the expression above is its explicit dependence on the azimuthal correlations between the lepton and hadronic planes. In particular, the terms proportional to $\cos(\tilde{\phi}_1)$ and $\cos(2\tilde{\phi}_1)$ reflect characteristic angular modulations of the cross section. These contributions arise from interference response functions such as τ_{T2} , τ_{-12} , and τ_{1L} . While τ_{T2} describes interference between two different transverse photon amplitudes, τ_{-12} and τ_{1L} result from interferences between transverse and longitudinal photons. The presence of these azimuthal modulations therefore provides a novel opportunity to experimentally access the differential distributions of these response functions, thereby offering additional information.

The equations above constitute a convenient starting point for experimental investigations aimed at isolating and interpreting different response functions.

1.1.3. Two-Photon Luminosity Functions

The experimentally measurable quantities, namely the two-photon cross sections and response functions, depend only on a limited set of variables: the two-photon center-of-mass energy W the photon virtualities Q_1^2 and Q_2^2 , and, in the case of multi-hadron final states, certain scattering angles of the decay products. Consequently, the differential cross sections given in Eqs. (12) and (31) are typically studied after suitable change of variables and integration over the remaining lepton variables, see Ref. [1]. In this way, the inclusive cross section of Eq. (12) can be written, for unpolarized beams, as

$$\begin{aligned} \frac{d^3\sigma}{dW dQ_1^2 dQ_2^2} &= \frac{d^3 L_{TT}}{dW dQ_1^2 dQ_2^2} \sigma_{TT} + \frac{d^3 L_{LL}}{dW dQ_1^2 dQ_2^2} \sigma_{LL} + \frac{d^3 L_{TL}}{dW dQ_1^2 dQ_2^2} \sigma_{TL} \\ &+ \frac{d^3 L_{LT}}{dW dQ_1^2 dQ_2^2} \sigma_{LT} + \frac{d^3 \tilde{L}_{TT}}{dW dQ_1^2 dQ_2^2} \tau_{TT} + \frac{d^3 \tilde{L}_{TL}}{dW dQ_1^2 dQ_2^2} \frac{1}{2} (\tau_0 + \tau_1), \end{aligned} \quad (33)$$

where L_{TT} , L_{LL} , L_{TL} , L_{LT} , \tilde{L}_{TT} , and \tilde{L}_{TL} are the two-photon luminosity functions, which collect all lepton-side kinematics. These functions provide the link between the measurable cross section of the process $e^+e^- \rightarrow e^+e^-X$ and the underlying photon-photon subprocess. For the inclusive case, these functions have been obtained analytically in Ref. [1]. In exclusive processes, however, the same approach is only applicable for the parts without explicit $\tilde{\phi}_{1,2}$ dependence. The terms involving $\tilde{\phi}_1$ and $\tilde{\phi}_2$ generally require numerical evaluation.

1.2. Related Monte Carlo Generators

Having established the theory framework, we briefly review existing two-photon MC tools to motivate our choices in HADROTOPS. Over the years, several generators have been developed for studies of two-photon physics, each optimized for specific processes and subject to certain limitations:

- The KLOE collaboration used the code by A. Courau [62] for untagged measurements of $e^+e^- \rightarrow e^+e^-\pi^0\pi^0$ [63]. The code is based on the double equivalent-photon approximation.

- A code written by F. Nguyen, F. Piccinini, and A.D. Polosa for two-photon physics at DAΦNE [64]. It has been used, for example, in the measurement of the η radiative width at KLOE-2 [65].
- The Belle and Belle II collaborations use the code by S. Uehara [66]. It has been applied in several studies, including those presented in Refs.[5, 9, 67]. It uses an equivalent photon approximation in which the photon virtualities are taken into account.
- The code GALUGA2.0 by S. Schuler [57] is intended for LEP-type physics and uses appropriate models for high energies and a highly efficient code to generate the $e^+e^- \rightarrow e^+e^-X$ phase space, taking into account the strong dependence of the cross section on the momentum transfers.
- The BaBar collaboration used the GGR_{ESRC} Monte Carlo generator [68] developed by the Novosibirsk group in their studies of transition form factors of pseudoscalars [8, 69]. The generator includes radiative corrections as described in Ref. [70].
- The EK_{HARA} code by H. Czyż [50, 53] and collaborators implements the same highly efficient phase-space generation algorithm as GALUGA2.0 and pairs it with the determination of the cross section using the actual matrix element for $e^+e^- \rightarrow e^+e^-(\pi^0, \eta, \eta', \eta_c)$, including NLO radiative corrections. An updated version of the generator (EK_{HARA}3.2) incorporates the double-virtual $\gamma^*\gamma^* \rightarrow \pi\pi$ amplitudes from Ref. [49] and, unlike other generators, also simulates $e^+e^- \rightarrow e^+e^-\pi^+\pi^-$ via a virtual photon radiated in Bhabha scattering in addition to two-photon scattering. It ensures a complete description of the $\pi^+\pi^-$ channel.

2. Phase Space Generation

2.1. Generation of the e^+e^-X Phase Space

The generation of the e^+e^-X phase space is largely based on the highly efficient algorithm developed by Schuler, which is implemented in the GALUGA generator and described in detail in Ref. [57]. The same method was later incorporated into the EK_{HARA} event generator [50, 53], from which parts of the code have been adapted for this work. This section provides a brief overview of the phase-space generation, with a focus on the differences from the implementations in GALUGA and EK_{HARA}. A full description of the algorithm can be found in Refs. [50, 57].

The algorithm produces the final-state vectors by using five Lorentz invariants

$$W^2 = p_X^2, \quad (34)$$

$$t_1 = -Q_1^2, \quad t_2 = -Q_2^2, \quad (35)$$

$$s_1 = (p'_1 + p_X)^2, \quad s_2 = (p'_2 + p_X)^2, \quad (36)$$

together with the constant center-of-mass energy \sqrt{s} .

In the first step, the e^+e^-X four vectors are generated from six numbers $x_1 \dots x_6$ randomly distributed in $[0, 1)$. This maps the Lorentz invariant phase space element onto a six-dimensional unit-1 hypercube:

$$d\text{Lips}_{eeX} = \frac{d^3 \vec{p}'_1}{(2\pi)^3 2E'_1} \frac{d^3 \vec{p}'_2}{(2\pi)^3 2E'_2} \frac{d^3 \vec{p}_X}{(2\pi)^3 2E_X} (2\pi)^4 \delta^{(4)}(p_1 + p_2 - p'_1 - p'_2 - p_X)$$

$$= \frac{2W}{(2\pi)^5} \frac{\pi^2}{4\beta s} \delta \delta_1 \delta_2 \delta_W dx_1 \dots dx_6, \quad (37)$$

where $\beta = \sqrt{1 - 4m^2/s}$ is the electron velocity in the e^+e^- c.m. frame. The remaining terms in this equation, which stem partially from the calculations in Refs. [50, 57] and depend on the use of different mappings, will be explained later in this section. The factor $2W$ arises from transforming the differential cross section from dW^2 (as used in Ref. [57]) to dW . The Jacobian factors $\delta, \delta_1, \delta_2$ and δ_W are detailed below. Using random numbers, the three-body final state is generated in the following steps:

1. *Generation of the hadronic mass W :*

If W is not fixed by the user to a constant value, it is restricted to the range $[W_{\min}, W_{\max}]$ by kinematic and user-defined conditions. For cross-checks, two different mappings have been implemented:

(a) Flat mapping:

In this case, every mass between W_{\min} and W_{\max} is generated with equal probability:

$$W = W_{\min} + (W_{\max} - W_{\min}) x_6, \quad (38)$$

which leads to a contribution to the phase space element of

$$\delta_W \equiv \frac{dW}{dx_6} = W_{\max} - W_{\min}. \quad (39)$$

(b) Logarithmic Mapping:

For better description of the kinematic factors in Eqs. (12) and (31), which typically drop rapidly with increasing W , a Logarithmic mapping is implemented. This enhances the generation of events at smaller masses:

$$W = W_{\min} \exp\left(x_6 \log\left(\frac{W_{\max}}{W_{\min}}\right)\right). \quad (40)$$

The corresponding contribution to the phase space element is

$$\delta_W = W \log\left(\frac{W_{\max}}{W_{\min}}\right). \quad (41)$$

In general, the choice of mapping does not affect the final physics result but have a significant influence the efficiency of the code. For the generation of arbitrary final states used in PWAs, both mappings perform equally well. For channels that use hadronic input to describe a physical process (see Sec. 3), the flat mapping is recommended.

2. *Generation of the lepton momentum transfers t_1 and t_2 :*

The electron momentum transfer t_2 is limited by kinematic and user-defined constraints to the range $[t_{2,\min}, t_{2,\max}]$. For this variable, both flat and logarithmic mappings are implemented, following the same structure as for the hadronic mass.

(a) Flat Mapping:

The momentum transfer is generated as

$$t_2 = t_{2,\min} + (t_{2,\max} - t_{2,\min}) x_1, \quad (42)$$

which leads to a contribution to the phase-space element of

$$\delta_2 = \frac{dt_2}{dx_1} = (t_{2,\max} - t_{2,\min}) . \quad (43)$$

(b) Logarithmic Mapping:

$$t_2 = t_{2,\min} \exp\left(x_1 \log\left(\frac{t_{2,\max}}{t_{2,\min}}\right)\right) \quad (44)$$

$$\delta_2 = t_2 \log\left(\frac{t_{2,\max}}{t_{2,\min}}\right) . \quad (45)$$

After the generation of the electron momentum transfer t_2 , the positron momentum transfer t_1 (and its contribution to the phase-space element δ_1) is obtained in the same manner using the random variable x_2 . In principle, both mappings yield the same physical result, but the logarithmic mapping is significantly more efficient, since it better describes the rapidly dropping behavior of the kinematic factor in Eqs. (12) and (31). Moreover, the logarithmic mapping cancels the pole in Eqs. (12) and (31) at $t_1 t_2 = 0$, which may otherwise cause numeric instabilities at small values of t_1 and t_2 .

3. Generation of the subsystem center-of-mass energies s_1 and s_2 :

The generation of s_1 and s_2 follow the procedure described in Ref. [57]. Since these invariants are typically not used in studies of two-photon interactions, user cuts on these variables are not implemented. The possibility to directly restrict the energy of the final state leptons during the generation of the sub-system center-of-mass energies, which would act on the limits s_1 and s_2 are generated in, is not implemented for the same reason. Thus, s_1 and s_2 are restricted only by kinematics. User-defined cuts on the final lepton's energies are possible once the final state vectors are generated. The less efficient option is provided for completeness, but is assumed to be unnecessary for normal use cases. The invariants are generated using the random numbers x_3 and x_4 . Their contribution to the phase space element is given by [57]

$$\delta = \frac{s(1+\beta)^2}{(v + \sqrt{X})(1+y_1)(1+y_2)}, \quad y_{1/2} \equiv \sqrt{1 - 4m^2/t_{1/2}} . \quad (46)$$

with

$$v \equiv (q_1 \cdot q_2) = \frac{1}{2}(W^2 - t_1 - t_2), \quad X = v^2 - t_1 t_2$$

4. Calculation of the final state four-vectors:

When all six Lorentz invariants are known, the four-vectors of the final state can be calculated, except for some rotation around the azimuthal angle. The numerically stable form of the vectors is taken from Ref. [57]. As the vectors are determined only relative to one another, they need to be rotated around the azimuthal angle by a random number between 0 and 2π , which is determined using x_5 .

At this point, the final state kinematics of the process $e^+e^- \rightarrow e^+e^-X$ is generated, and the Lorentz invariant phase space element of this process is calculated.

2.2. Generation of the Final State Hadronic Decay

After generating the overall four-momentum of the hadronic system X with invariant mass W , its decay into N final-state particles with masses $m_1 \dots m_N$ and four-momenta $\ell_1 \dots \ell_N$ needs to be simulated. This is achieved using a recursive method (similar to the Genbod algorithm [71]), where the N -body decay is constructed as a sequence of two-body decays. The sequence is realized by introducing a set of intermediate invariant masses:

$$\begin{aligned} M_1^2 &= m_1^2, \\ M_i^2 &= \left(\sum_{j=1}^i \ell_j \right)^2, \quad i = 2, \dots, N-1 \\ M_N^2 &= p_X^2 \equiv W^2 \end{aligned} \quad (47)$$

where each M_i corresponds to the invariant mass of a subsystem composed of the first i particles. The key idea is that at each step an intermediate state of mass M_{i+1} decay into two bodies: one real particle of mass m_{i+1} and a residual system of invariant mass M_i . To generate the actual values of the intermediate masses $i = 2, \dots, N-1$, they are randomly sampled within their kinematic limits

$$\begin{aligned} M_{i,\min} &= \sum_{j=1}^i m_j, \quad M_{i,\max} = M_{i+1} - m_{i+1} \\ M_i^2 &= M_{i,\min}^2 + (M_{i,\max}^2 - M_{i,\min}^2) \tilde{x}_i, \end{aligned} \quad (48)$$

In each two-body step, the magnitude of the three-momentum of the decay products in the rest frame of the parent (M_{i+1}) is given by

$$p_i^* (M_{i+1}, M_i, m_{i+1}) = \frac{\sqrt{\lambda(M_{i+1}^2, M_i^2, m_{i+1}^2)}}{2M_{i+1}} \quad (49)$$

where

$$\lambda(x, y, z) = x^2 + y^2 + z^2 - 2xy - 2xz - 2yz \quad (50)$$

is the Källén triangle function. By using the additional random variables $\hat{x}_{i,1}, \hat{x}_{i,2} \in [0, 1]$, the azimuthal and polar angles of the particle in the parent rest frame can be generated as

$$\begin{aligned} \cos \theta_i^* &= 2 \hat{x}_{i,1} - 1, \quad \phi_i^* = 2\pi \hat{x}_{i,2}, \\ d\Omega_i^* &= d \cos \theta_i^* d\phi_i^* = 4\pi d\hat{x}_{i,1} d\hat{x}_{i,2} \end{aligned} \quad (51)$$

Using the generated decay angles, two-body momentum, and the particle masses, the four-vectors of the decay products are first constructed in the rest frame of their parent particle. At each stage of the recursive decay chain, these four-vectors are then boosted from the parent rest frame to the overall e^+e^- center-of-mass frame by a Lorentz transformation.

The Lorentz invariant phase space element for the decay of a state X into N particles is given by

$$d\text{Lips}_N(M_N^2) = \left(\prod_{i=1}^N \frac{d^3 \vec{\ell}_i}{(2\pi)^3 2E_i} \right) (2\pi)^4 \delta^{(4)} \left(p_X - \sum_{i=1}^N \ell_i \right) . \quad (52)$$

This expression can be written recursively in terms of $d\text{Lips}_{N-1}$

$$d\text{Lips}_N(M_N^2) = \frac{dM_{N-1}^2}{2\pi} d\text{Lips}_2(p_N; p_{N-1}, l_N) d\text{Lips}_{N-1}(M_{N-1}^2), \quad (53)$$

where $d\text{Lips}_2(p_N; p_{N-1}, l_N)$ is the two-body phase space for the decay

$$p_N \rightarrow p_{N-1} + l_N, \quad p_i \equiv \sum_{j=1}^i l_j, \quad (54)$$

and $d\text{Lips}_{N-1}(M_{N-1}^2)$ is the $(N-1)$ body phase space of the subsystem with total four-momentum p_{N-1} (satisfying $p_{N-1}^2 = M_{N-1}^2$). Inserting the two-body element in the spherical coordinates, one obtains

$$d\text{Lips}_N(M_N^2) = \frac{dM_{N-1}^2}{2\pi} d\Omega_{N-1}^* \frac{\sqrt{\lambda(M_N^2, M_{N-1}^2, m_N^2)}}{8\pi M_N^2} d\text{Lips}_{N-1}(M_{N-1}^2). \quad (55)$$

Iterating (53) yields the standard product form

$$d\text{Lips}_N(M_N^2) = \left(\prod_{i=2}^{N-1} \frac{dM_i^2}{2\pi} \right) \left(\prod_{i=1}^{N-1} \frac{\sqrt{\lambda(M_{i+1}^2, M_i^2, m_{i+1}^2)}}{8\pi M_{i+1}^2} d\Omega_i^* \right). \quad (56)$$

Using the random variables introduced earlier (\tilde{x}_i for the invariant masses, and $\hat{x}_{i,1}, \hat{x}_{i,2}$ for the angles), the full recursive expression for the N -body phase space can be written as

$$d\text{Lips}_N(W^2) = \left(\prod_{i=2}^{N-1} \frac{(M_{i,\max}^2 - M_{i,\min}^2) d\tilde{x}_i}{2\pi} \right) \left(\prod_{i=1}^{N-1} \frac{\sqrt{\lambda(M_{i+1}^2, M_i^2, m_{i+1}^2)}}{2 M_{i+1}^2} d\hat{x}_{i,1} d\hat{x}_{i,2} \right) \quad (57)$$

The Lorentz invariant phase space of the full final state (which is given in Eq.(3)) can then be obtained by

$$d\text{Lips} = d\text{Lips}_{eeX} \times d\text{Lips}_N. \quad (58)$$

2.3. Application of User Cuts and Consistency Checks

After all final state four-vectors have been generated, they are numerically checked for energy and momentum conservation with a tolerance of 1 eV, which is negligible for typical particle physics experiments. When the code is compiled using quadruple precision floating point numbers, the final state vectors always fulfill this requirement, and no unstable events have been observed. With double precision, less than 0.001 % of events show a larger deviation, and these events are rejected and regenerated.

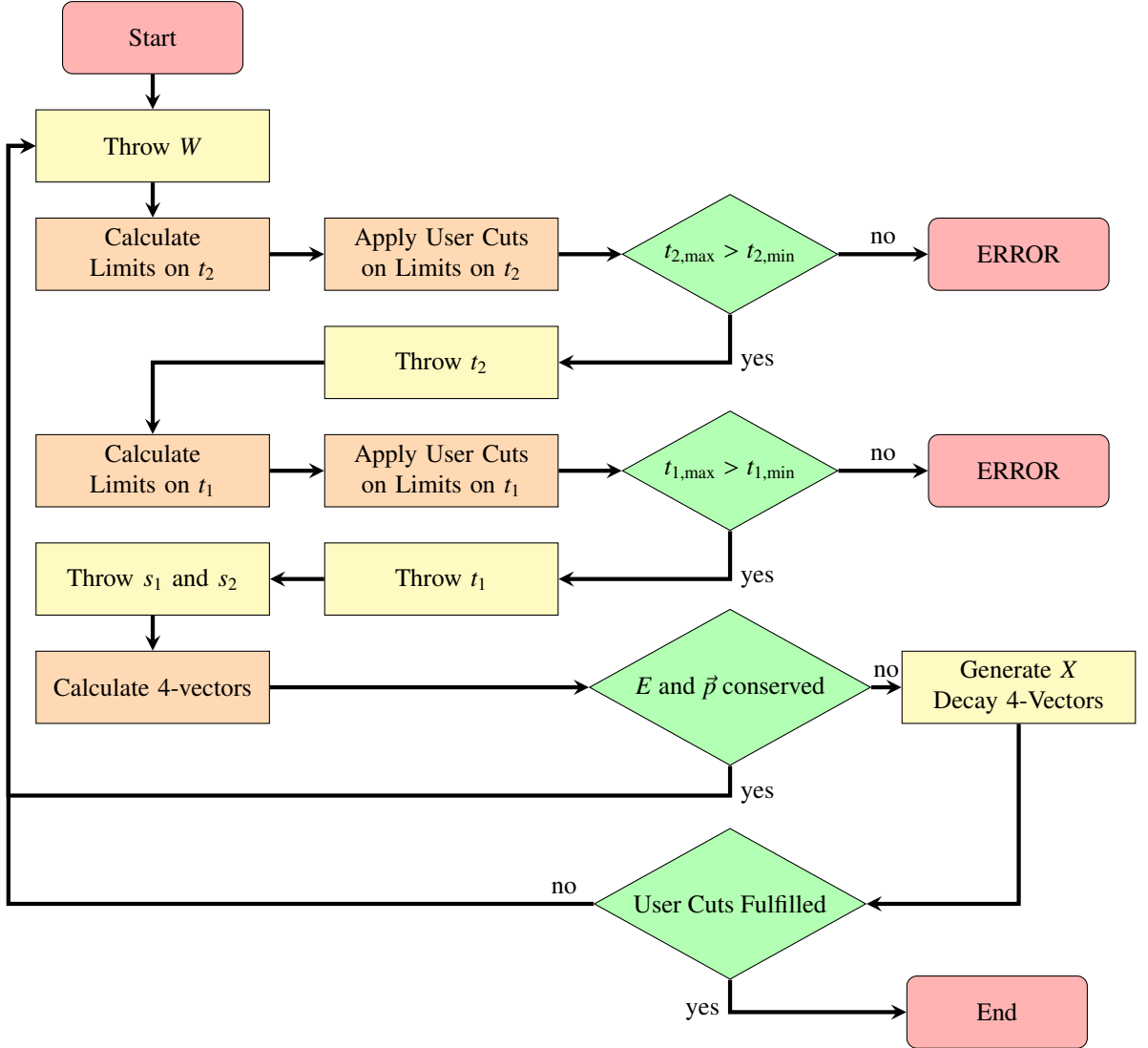


Figure 3: Flowchart of the four-vector generation of the e^+e^-X final state

Following the stability check, several user-defined cuts are applied. These include cuts on the polar angles of the hadronic decay products as well as on the total transverse momentum of the hadronic final state. The latter is a commonly used observable in studies involving two quasi-real photons.

Once these steps are completed, the generation of the final state four vectors and the calculation of the phase-space element are finished. Figure 3 illustrates the four-vector generation procedure as a flow chart.

3. Two-Photon cross sections and Responses

The two-photon cross sections and response functions entering Eqs. (12) and (31) must be specified in order to obtain physically meaningful results. Several modes are implemented to describe different classes of final states, which are briefly discussed in this section. A key feature of the generator is its flexibility: users can selectively switch between different cross sections and response functions, enabling the study of each contribution either independently or in combination.

3.1. $e^+e^- \rightarrow e^+e^-\pi\pi$ Modes

To simulate the process $e^+e^- \rightarrow e^+e^-\pi\pi$, one must accurately model the differential response functions of the subprocess $\gamma^*\gamma^* \rightarrow \pi\pi$. In HADROTOPS, these are implemented using the dispersive formalism developed in Refs. [47, 49, 60], which are summarized in this section. In the $\gamma\gamma$ frame, the helicity amplitudes $H_{\lambda_1\lambda_2}$ are decomposed into partial waves according to

$$H_{\lambda_1\lambda_2} = e^{i\phi_\pi(\lambda_1-\lambda_2)} \sum_{J \text{ even}} (2J+1) h_{\lambda_1\lambda_2}^{(J)}(W) d_{\Lambda,0}^{(J)}(\theta_\pi), \quad (59)$$

where $\Lambda = \lambda_1 - \lambda_2$ and $d_{\Lambda,0}^{(J)}(\theta_\pi)$ are Wigner rotation functions. The hadronic plane is fixed by choosing $\phi_\pi = 0$, so that all azimuthal dependence arises through $\tilde{\phi}_1$ and $\tilde{\phi}_2$ on the lepton side as in Eq.(31). The main idea of the dispersive approach is to impose analyticity and unitarity on the partial-wave amplitudes. This is achieved using a modified Muskhelishvili–Omnès representation [44], applied to specific linear combinations of partial-wave amplitudes that are free from kinematic singularities [72]. For the scalar channel ($J = 0, I = 0$), a coupled-channel dispersive analysis is employed to account for both $\pi\pi$ and $K\bar{K}$ intermediate states. This allows a unified treatment of the broad $f_0(500)$ and narrow $f_0(980)$ resonances. For the tensor channel ($J = 2, I = 0$), dominated by the $f_2(1270)$ resonance, a single-channel Omnès representation based on $\pi\pi$ rescattering is sufficient. Contributions from isospin-2 channels are also treated within a single-channel approach. Re-scattering effects for higher partial waves ($J \geq 4$) are expected to be suppressed at low to moderate energies and are approximated by their Born contributions. The S-wave left-hand cut is dominated by the Born terms, while for the D-wave, additional contributions from vector-meson exchange (e.g., ρ, ω) are included. As input for the pion and kaon vector form factors, standard VMD parameterizations are used, following the treatment in Ref. [23]. The $\pi\rho$ and $\pi\omega$ transition form factors (TFFs) are modeled using a phenomenological extension of VMD [60], designed to reproduce the correct asymptotic behavior at large photon virtualities. The parameters of these TFFs are determined by matching to low Q^2 input from VMD for $\pi\rho$ and dispersive results for $\pi\omega$ [73–75], and by matching to high $Q^2 = 4.5 \text{ GeV}^2$ experimental data from the Belle collaboration [76]. Unsubtracted dispersion relations are employed to ensure predictive power for virtual photons with $Q_i^2 \neq 0$, while respecting low-energy theorems and matching smoothly to real-photon data. The dispersively constructed amplitude for the scalar-isoscalar channel ($J = 0, I = 0$), which includes the $f_0(500)$ and $f_0(980)$ resonances, is currently used as input for computing their contributions to hadronic light-by-light scattering contribution of the muon anomalous magnetic moment $(g-2)_\mu$ [42].

The cross sections are provided in numerical form as functions of W, Q_1^2, Q_2^2 , and the scattering angle $|\cos\theta_\pi|$, within the kinematic limits $2m_\pi < W < 2 \text{ GeV}$ and $0 \leq Q_{1,2}^2 \leq 4 \text{ GeV}^2$. The results for the differential cross sections and response functions used in Section 1.1 for $\gamma^*\gamma^* \rightarrow \pi^0\pi^0$ are illustrated in Figs. 4, 5, 6, and 7. As expected, the dominant contributions are

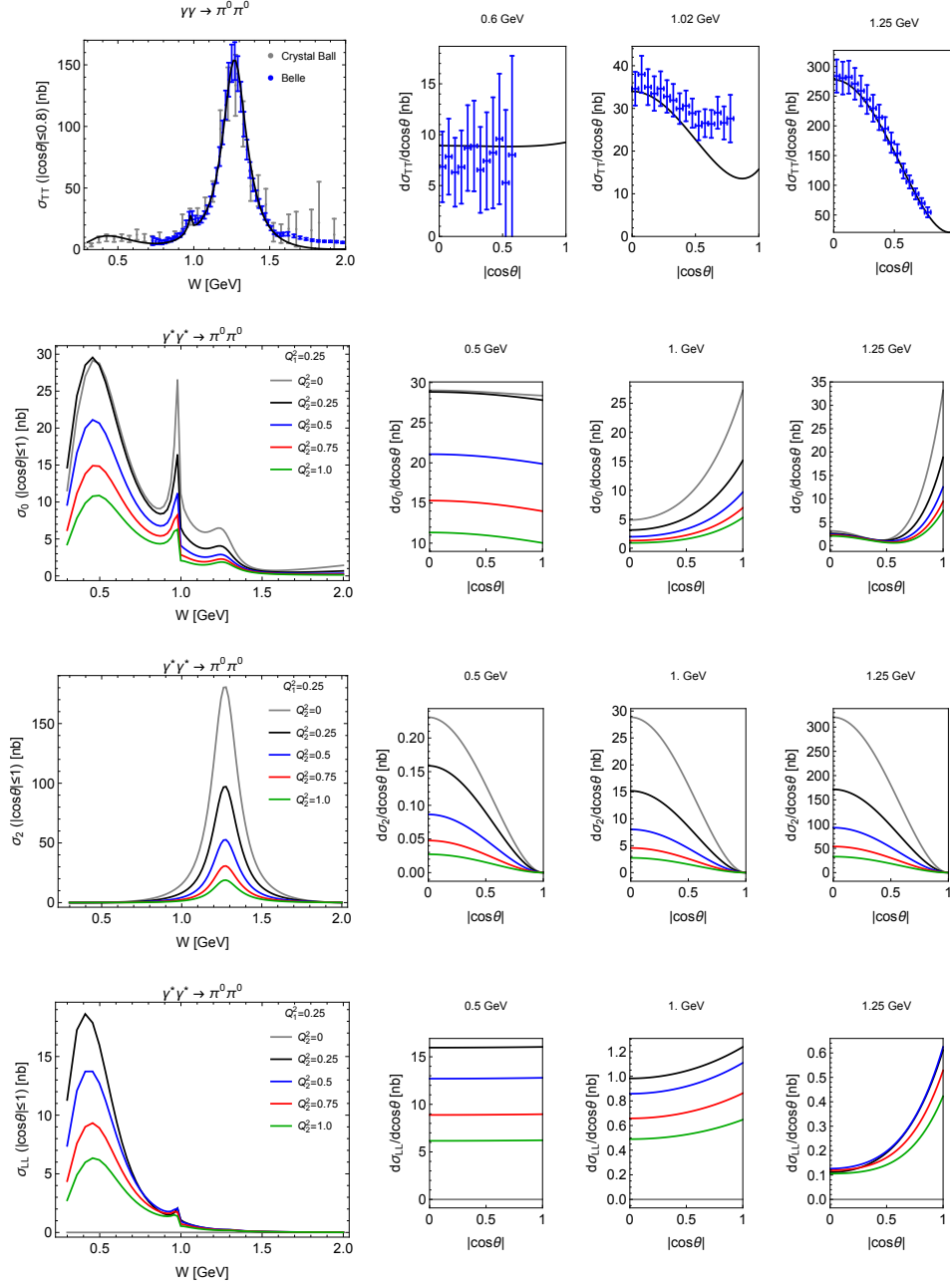


Figure 4: Top row of panels: prediction for σ_{TT} for $\gamma\gamma \rightarrow \pi^0\pi^0$ compared with data. Lower panels: predictions for σ_0 , σ_2 , and σ_{LL} for $\gamma^*\gamma^* \rightarrow \pi^0\pi^0$ with $Q_1^2 = 0.25 \text{ GeV}^2$ and $Q_2^2 = 0, 0.25, 0.5, 0.75, 1.0 \text{ GeV}^2$, shown for full angular coverage ($|\cos\theta| \leq 1$).

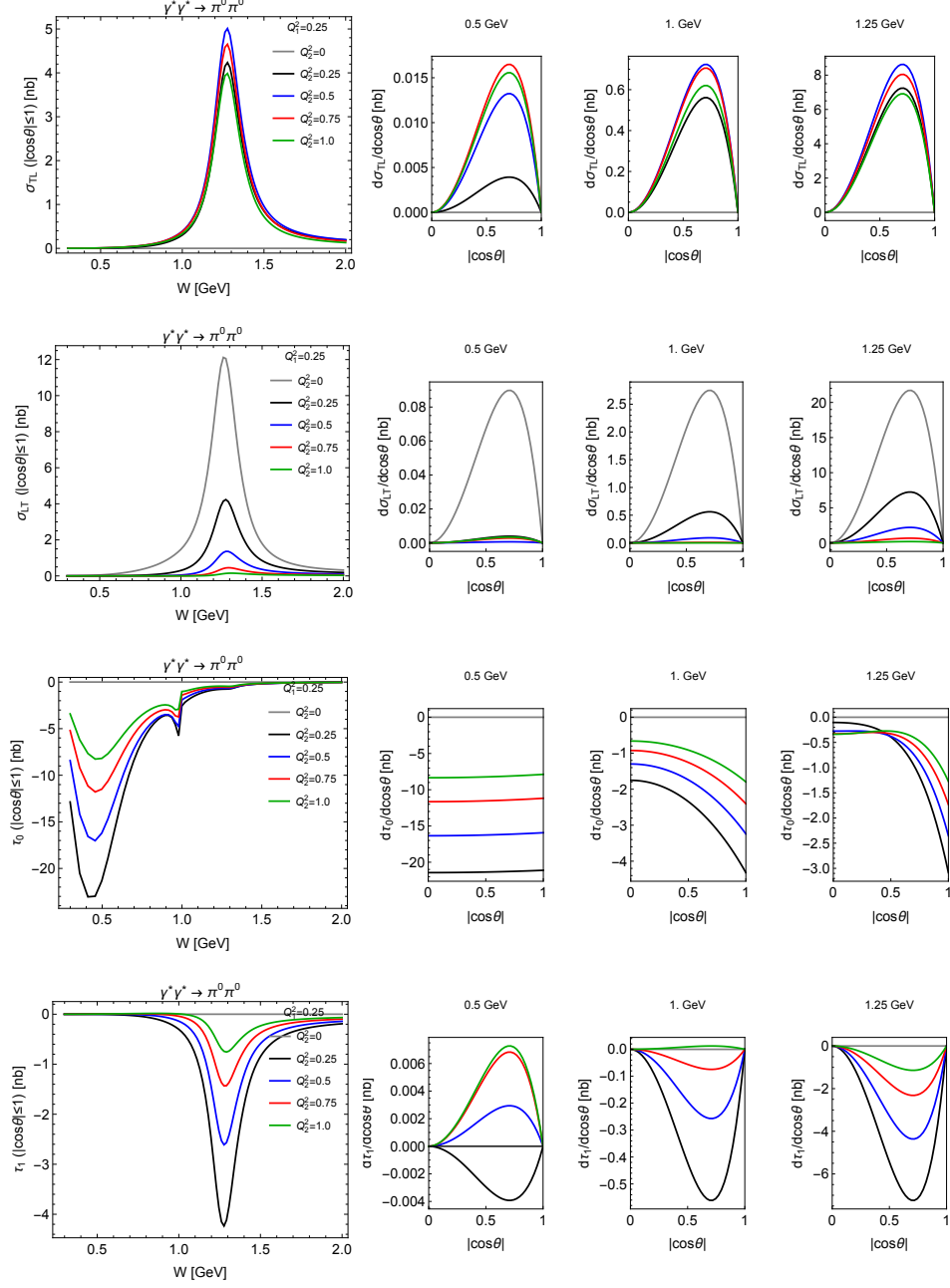


Figure 5: Predictions for σ_{TL} , σ_{LT} , τ_0 , and τ_1 for $\gamma^* \gamma^* \rightarrow \pi^0 \pi^0$ with $Q_1^2 = 0.25 \text{ GeV}^2$ and $Q_2^2 = 0, 0.25, 0.5, 0.75, 1.0 \text{ GeV}^2$, shown for full angular coverage ($|\cos \theta| \leq 1$).

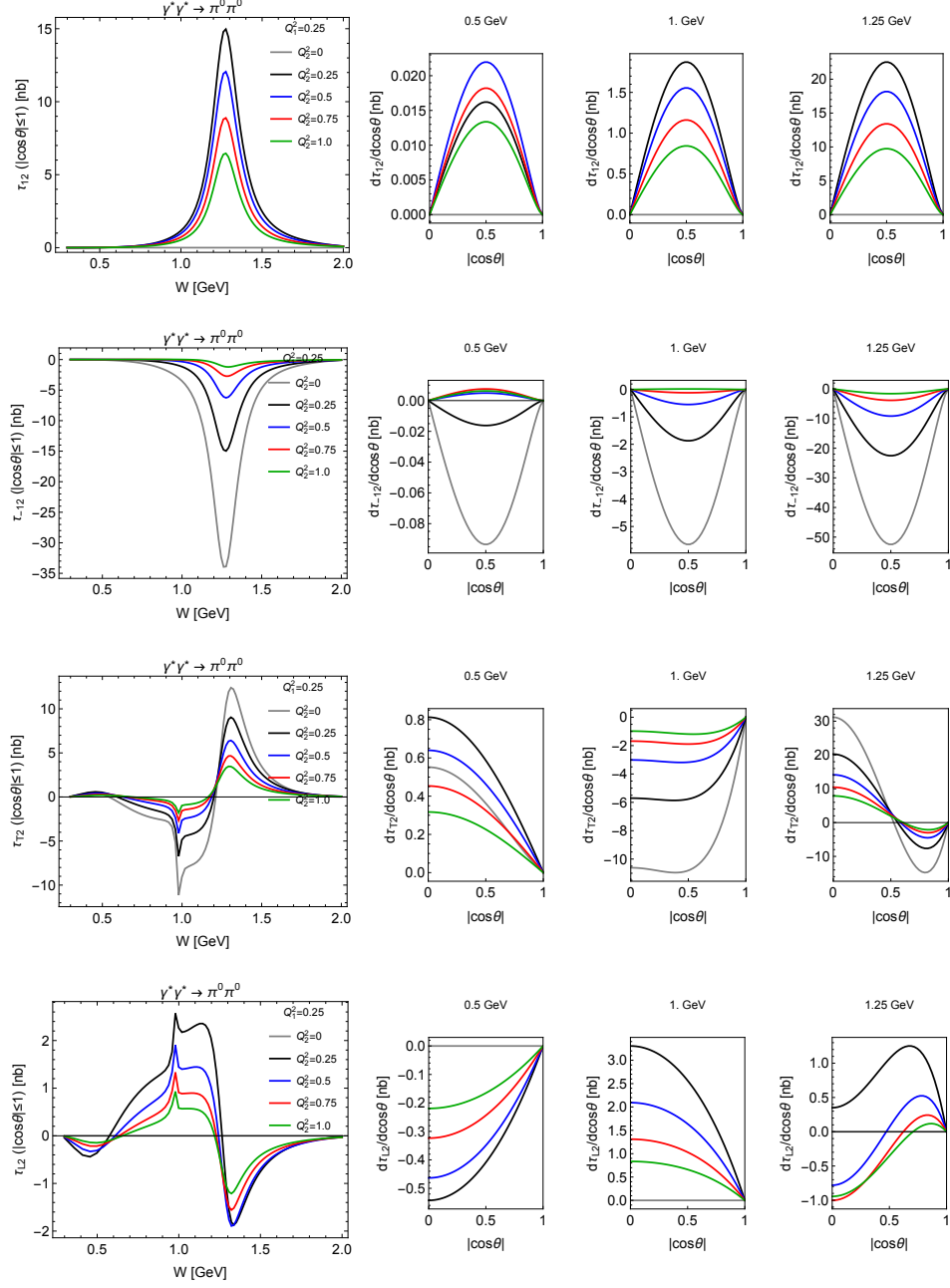


Figure 6: Predictions for τ_{12} , τ_{-12} , τ_{T2} , and τ_{L2} for $\gamma^* \gamma^* \rightarrow \pi^0 \pi^0$ with $Q_1^2 = 0.25 \text{ GeV}^2$ and $Q_2^2 = 0, 0.25, 0.5, 0.75, 1.0 \text{ GeV}^2$, shown for full angular coverage ($|\cos\theta| \leq 1$).

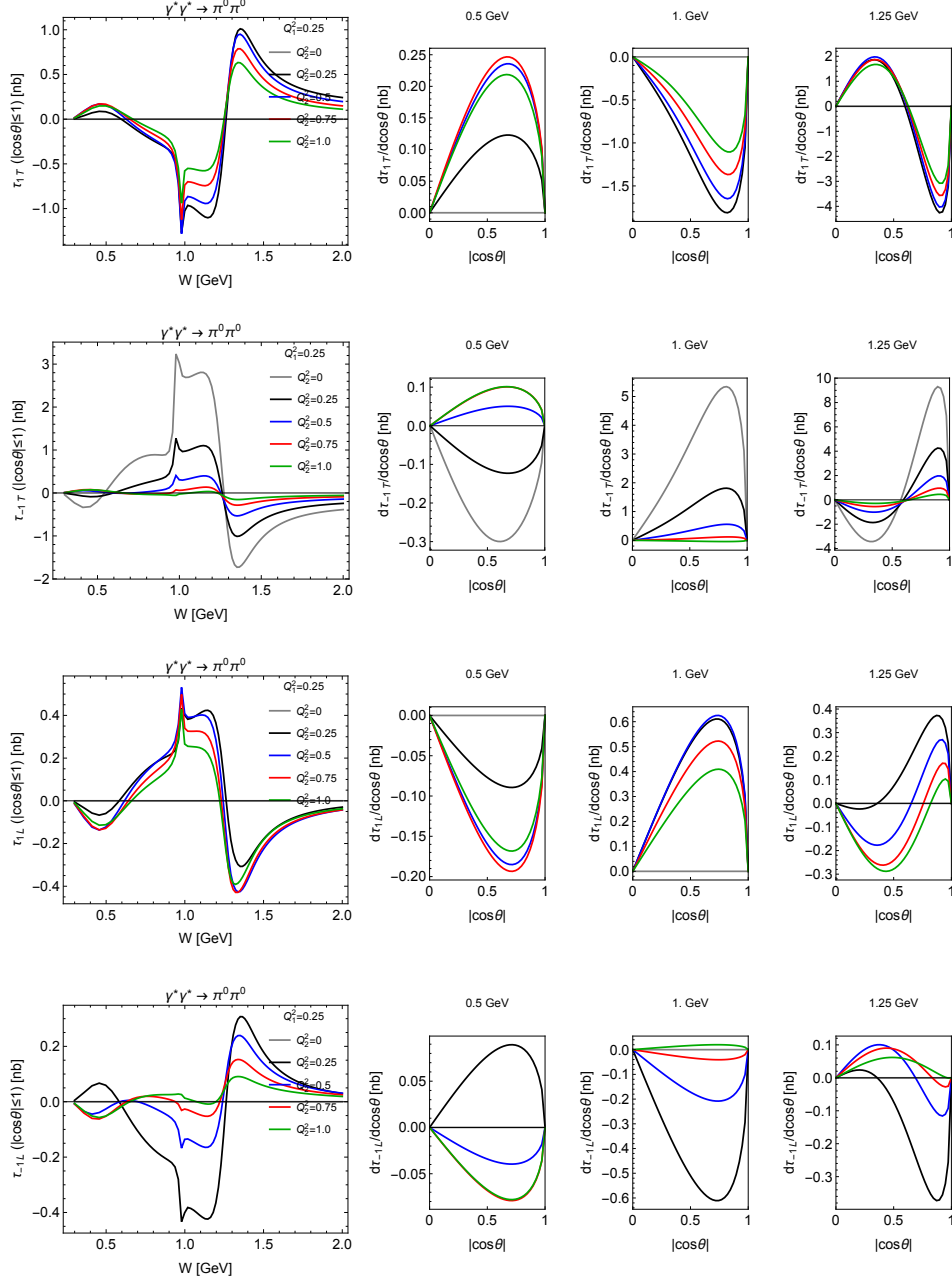


Figure 7: Predictions for τ_{1T} , τ_{-1T} , τ_{1L} , and τ_{-1L} for $\gamma^*\gamma^* \rightarrow \pi^0\pi^0$ with $Q_1^2 = 0.25$ GeV² and $Q_2^2 = 0, 0.25, 0.5, 0.75, 1.0$ GeV², shown for full angular coverage ($|\cos\theta| \leq 1$).

σ_0 and σ_2 , which survive in the real-photon limit. In single-virtual kinematics, σ_{TL} also becomes sizable. Owing to the new exclusive treatment of the $\pi\pi$ channel presented in Eq. (32), it will be possible to resolve the dependence on the azimuthal angle through terms proportional to $\cos\tilde{\phi}_1$ and $\cos 2\tilde{\phi}_1$, where the interference responses τ_{T2} and τ_{-12}, τ_{12} emerge as dominant structures. For differential responses that involve helicity flip, the differential distributions vanish in the forward and backward directions and, in some cases, also at $\cos\theta_\pi = 0$. The latter is a direct consequence of the odd helicity-flip nature of the entering amplitudes.

Cross sections at any given kinematic point are obtained by interpolating the theoretical input using three methods: linear spline interpolation, a nearest-neighbour approach, and an inverse-distance weighted average. The primary method is a linear spline interpolation of the nearest neighbors across all four dimensions ($W, Q_1^2, Q_2^2, \cos\theta_\pi$), which is validated against a simple nearest-neighbor algorithm and an inverse distanceweighted average, where the nearest points in all dimensions are averaged, weighted by the inverse of their Euclidean distance raised to a user-defined power. While all three approaches yield comparable results, linear spline interpolation consistently demonstrates superior stability with the available input and is therefore recommended.

To generate events beyond the theory range, the user can extrapolate the theory curves. The cross section is assumed to decrease with a $1/W^2$ behavior, while the large Q^2 behavior is modeled using the form factor frameworks discussed in the subsection on the production through a single resonance (Sec. 3.5). Both the choice of form factor model and its parameters can be adjusted by the user. We emphasize that the theoretical input is valid only within its specified kinematic range and any extrapolation should therefore be regarded as a rough estimate rather than an accurate prediction.

For the $\pi^+\pi^-$ channel, it should be noted that the simulation currently includes only the two-photon production of pions in the reaction $e^+e^- \rightarrow e^+e^-\pi^+\pi^-$. The production of charged pion pairs via the radiation of a virtual photon in Bhabha scattering events is not simulated, although it is expected to play an important role in experimental studies of this channel [77]. An updated version of the EKHARA event generator is expected to incorporate both production mechanisms as well as their interference [54].

3.2. $e^+e^- \rightarrow e^+e^-\pi^0\eta$ Mode

For the S -wave contribution to $\gamma^*\gamma^* \rightarrow \pi^0\eta$, the double-virtual partial waves from the dispersive analysis of [30] are used, which enforces analyticity, coupled-channel $\pi\eta/K\bar{K}_{l=1}$ unitarity, and the necessary kinematic constraints. This treatment is analogous to the two-pion mode discussed in the previous section, with the only difference being that real-photon data are used to constrain the coupled-channel Omnès representation. The dispersively constructed S -wave amplitude is currently employed as input for computing the $a_0(980)$ contribution to hadronic light-by-light (HLbL) scattering in $(g-2)_\mu$ [42].

The D -wave is modeled with a relativistic BreitWigner representation of the $a_2(1320)$, including an energy-dependent width and $L = 2$ BlattWeisskopf barrier factors. To extend the result for the real-photon production of a tensor meson (T) of Ref. [30] to the double-virtual case, the $\gamma^*\gamma^* \rightarrow T$ Lorentz decomposition is taken from Ref. [78], with the transition form factors provided by the quark-model calculation of Ref. [79], where only $F_1^T(Q_1^2, Q_2^2)$ is nonzero. The normalization $|F_1^T(0, 0)|$ is fixed by the on-shell decay width $\Gamma_{a_2 \rightarrow \gamma\gamma}$, and the sign is chosen by comparing to the dispersive description of $\gamma^*\gamma^* \rightarrow \pi^0\pi^0$ in the vicinity of the $f_2(1270)$. This construction ensures helicity-2 dominance in the real-photon limit and provides a controlled continuation to the double-virtual case. The mass scale is taken as $m_T \equiv m_{a_2}$, as in the original

quark-model calculation. This differs from [33], which adopted a VMD scale for the $(g-2)_\mu$ calculation. Currently, tensor-meson contributions to the hadronic light-by-light in $(g-2)_\mu$ are attributed an uncertainty of about 400% [42], making the reduction of model dependence in tensor form factors particularly timely.

This $\gamma^*\gamma^* \rightarrow \pi^0\eta$ input yields a reliable description of the $a_0(980)$ and $a_2(1320)$ regions and can be directly interpolated on a (W, Q_1^2, Q_2^2) grid using the same interpolation and extrapolation algorithms as discussed for the $\gamma^*\gamma^* \rightarrow \pi^0\pi^0$ case. The $\gamma^*\gamma^* \rightarrow \pi^0\eta$ response functions are shown in Figs. 8, 9, 10, and 11 as functions of the momentum transfers $Q_{1,2}^2$ in the range $0 - 2 \text{ GeV}^2$, and invariant masses from threshold up to 2 GeV.

3.3. $e^+e^- \rightarrow e^+e^-K^+K^-$, $e^+e^- \rightarrow e^+e^-K_S^0K_S^0$, and $e^+e^- \rightarrow e^+e^-\eta\eta$ Modes

Combined dispersive analyses discussed in Secs. 3.1 and 3.2, can provide Q^2 -dependent estimates for the $K\bar{K}$ channel, but are presently restricted to invariant masses below 1.4 GeV [30]. To extend the generator coverage, it is also possible to employ experimental data as direct input for the generator.

The modes $e^+e^- \rightarrow e^+e^-K^+K^-$, $e^+e^- \rightarrow e^+e^-K_S^0K_S^0$, and $e^+e^- \rightarrow e^+e^-\eta\eta$ are thus modeled using available experimental results from Belle and preliminary data from BESIII. Since both collaborations have performed untagged measurements with $Q_1^2 = Q_2^2 \approx 0$, only the TT-polarized cross sections are accessible, and information on the momentum-transfer dependence is not available. Nonetheless, such estimates are experimentally valuable: for example, the ongoing BESIII initial state radiation determination of the kaon form factor suffers from background due to two-photon production of charged kaon pairs in $e^+e^- \rightarrow e^+e^-K^+K^-$ [80]. Providing cross section inputs for $e^+e^- \rightarrow e^+e^-K^+K^-$ and the related $K_S^0K_S^0$ and $\eta\eta$ channels based on available untagged data thus aids background modeling.

The Belle collaboration investigated the two-photon production of K^+K^- [5, 6], $K_S^0K_S^0$ [67], and $\eta\eta$ [9], covering invariant-mass ranges of 1.4 – 4.1 GeV, 1.5 – 4.0 GeV, and 1.1 – 3.8 GeV, respectively. The measurements cover different angular regions: $|\cos\theta_K| < 0.6$ for K^+K^- , $|\cos\theta_K| < 0.8$ or $|\cos\theta_K| < 0.6$ for $K_S K_S$, and $|\cos\theta_\eta| < 0.9$ or with full angular coverage for $\eta\eta$. Furthermore, the BESIII collaboration has released preliminary results of a coupled-channel partial-wave analysis of the $\pi^0\pi^0$, K^+K^- , and $\pi^0\eta$ final states for masses below 2 GeV and within the angular range $|\cos\theta_{\pi,\eta,K}| < 0.8$. These results can be extrapolated to full angular coverage [10, 11].

For the K^+K^- channel, the preliminary BESIII results are used up to masses of 2 GeV as they cover the threshold region. At higher masses, the Belle results are employed. For the $K_S K_S$ and $\eta\eta$ modes, the available Belle data are used exclusively.

Since the Belle measurements do not cover the full angular range and the collaboration has not supplied results extended to full coverage, an extrapolation must be implemented. To achieve this, the differential cross section is described by

$$\frac{d\sigma}{d|\cos\theta_h|} \propto |S(W)Y_0^0(\theta_h, 0) + D_0(W)Y_2^0(\theta_h, 0)e^{i\phi(W)}|^2 + |D_2(W)Y_2^2(\theta_h, 0)|^2, \quad h = K, \eta \quad (60)$$

where $Y_n^m(\theta_h, \phi)$ are spherical harmonics, S , D_0 , and D_2 denote the relative strengths of the corresponding amplitudes, and $\phi(W)$ denotes the relative phase between the S and D_0 amplitudes at a given invariant mass W . Since HadroTOPS does not require knowledge of the actual intermediate states, a quantitative fit at each energy point is sufficient to determine the numerical input.

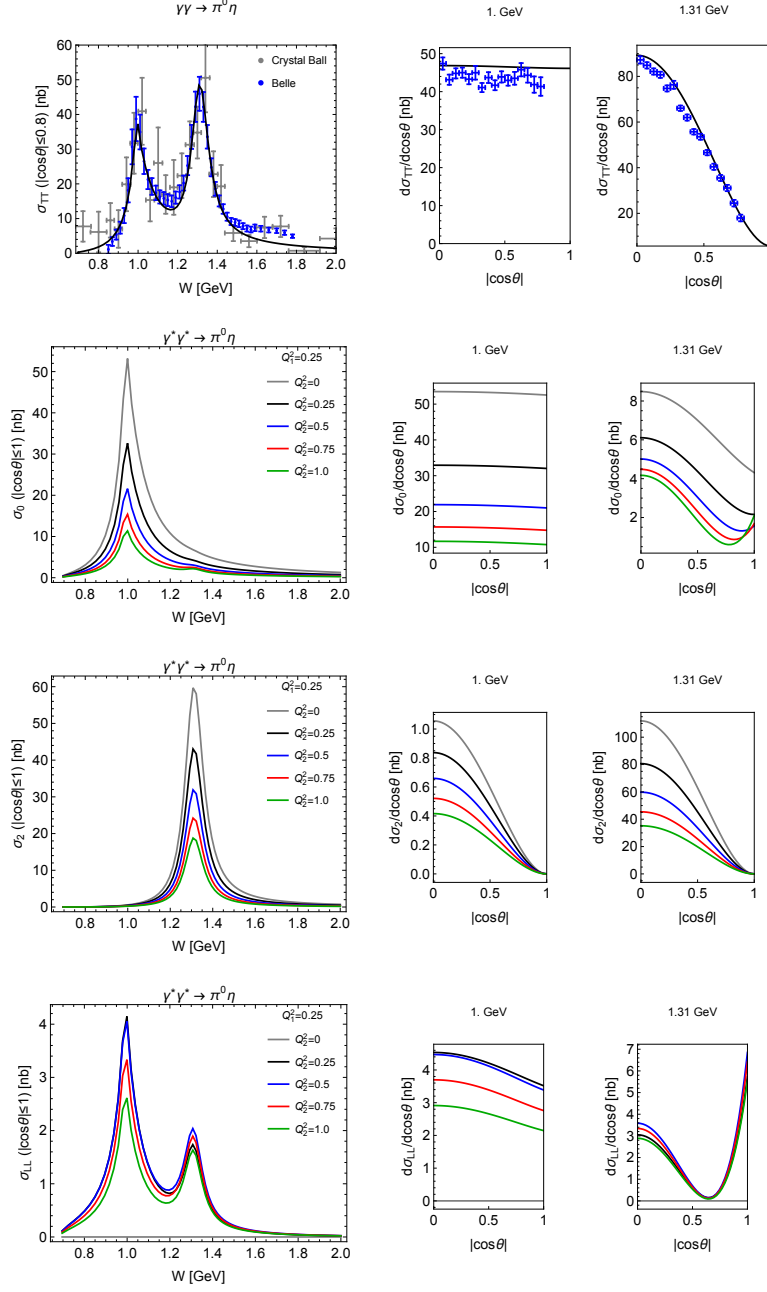


Figure 8: Top row of panels: predictions for σ_{TT} for $\gamma\gamma \rightarrow \pi^0\eta$ compared with data. Lower panels: predictions for σ_0 , σ_2 and σ_{LL} for $\gamma^*\gamma^* \rightarrow \pi^0\eta$ with $Q_1^2 = 0.25$ GeV² and $Q_2^2 = 0, 0.25, 0.5, 0.75, 1.0$ GeV², shown for full angular coverage ($|\cos\theta| \leq 1$).

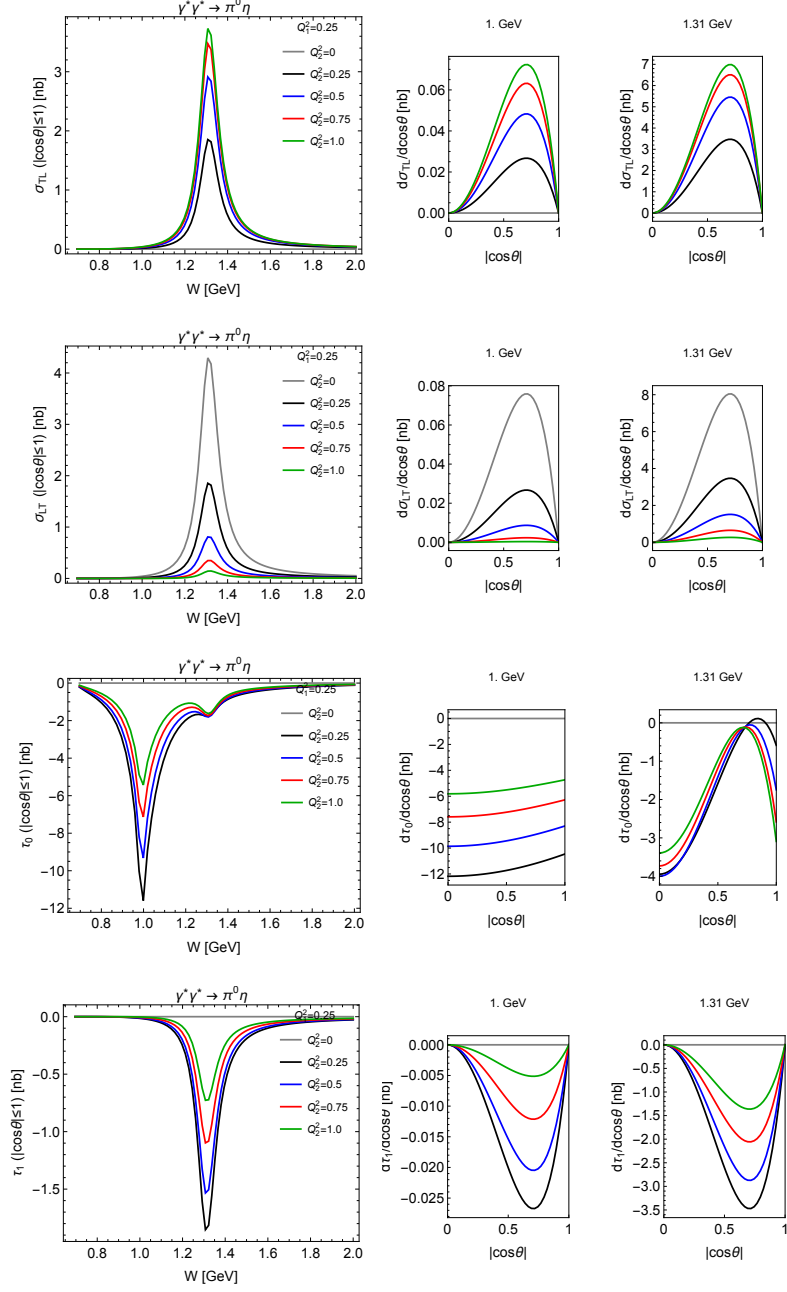


Figure 9: Predictions for σ_{TL} , σ_{LT} , τ_0 , and τ_1 for $\gamma^* \gamma^* \rightarrow \pi^0 \eta$ with $Q_1^2 = 0.25 \text{ GeV}^2$ and $Q_2^2 = 0, 0.25, 0.5, 0.75, 1.0 \text{ GeV}^2$, shown for full angular coverage ($|\cos\theta| \leq 1$).

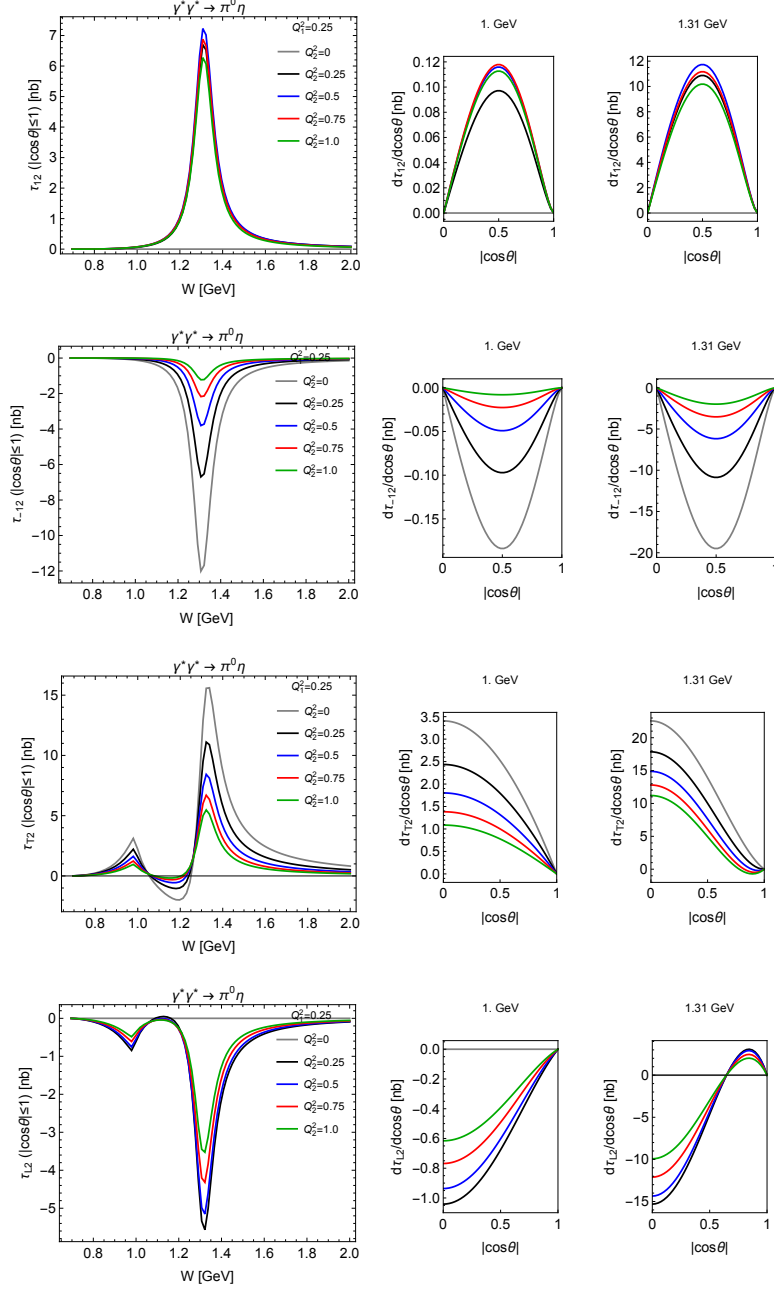


Figure 10: Predictions for τ_{12} , τ_{-12} , τ_{T2} , and τ_{L2} for $\gamma^* \gamma^* \rightarrow \pi^0 \eta$ with $Q_1^2 = 0.25 \text{ GeV}^2$ and $Q_2^2 = 0, 0.25, 0.5, 0.75, 1.0 \text{ GeV}^2$, shown for full angular coverage ($|\cos \theta| \leq 1$).

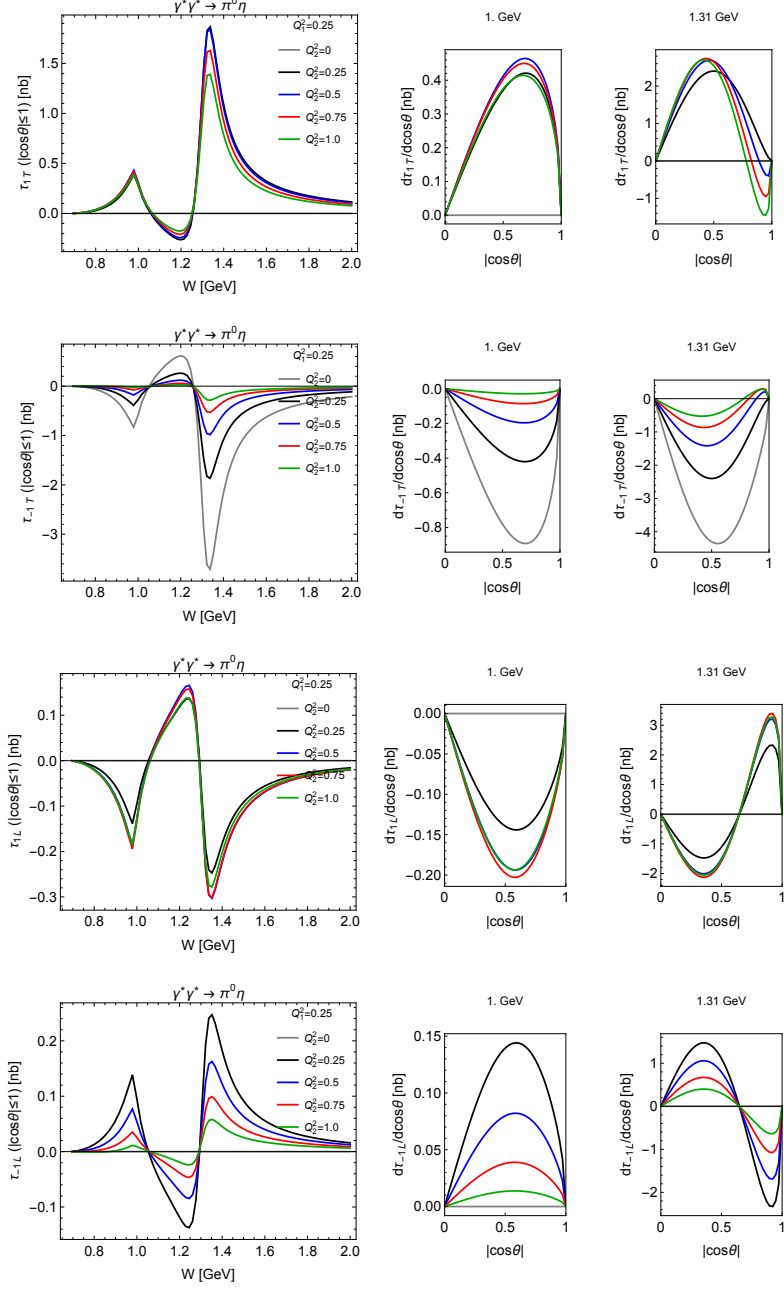


Figure 11: Predictions for τ_{1T} , τ_{-1T} , τ_{1L} , and τ_{-1L} response functions for $\gamma^*\gamma^* \rightarrow \pi^0\eta$ for $Q_1^2 = 0.25 \text{ GeV}^2$ and $Q_2^2 = 0, 0.25, 0.5, 0.75, 1.0 \text{ GeV}^2$ and for full angular coverage $|\cos\theta| \leq 1$.

Figure 12 presents the fit results for the Belle measurement of the K^+K^- cross section below $W < 2.4$ GeV. Equation (60) reproduces the data within the quoted experimental uncertainties. The same fitting procedure is applied to the higher-mass K^+K^- data from Belle [6], as well as to the $K_S^0 K_S^0$ and $\eta\eta$ cross sections.

Figure 13 shows the numerical integration of the differential cross section over various helicity angle ranges. The integration of the fits to the Belle data shows larger scattering when extended beyond the range of the experimental input. This is particularly evident in the intermediate mass region ($W < 2.4$ GeV) and $|\cos\theta_K| < 1$ for the K^+K^- channel, which is constrained by limited statistics and helicity angle coverage.

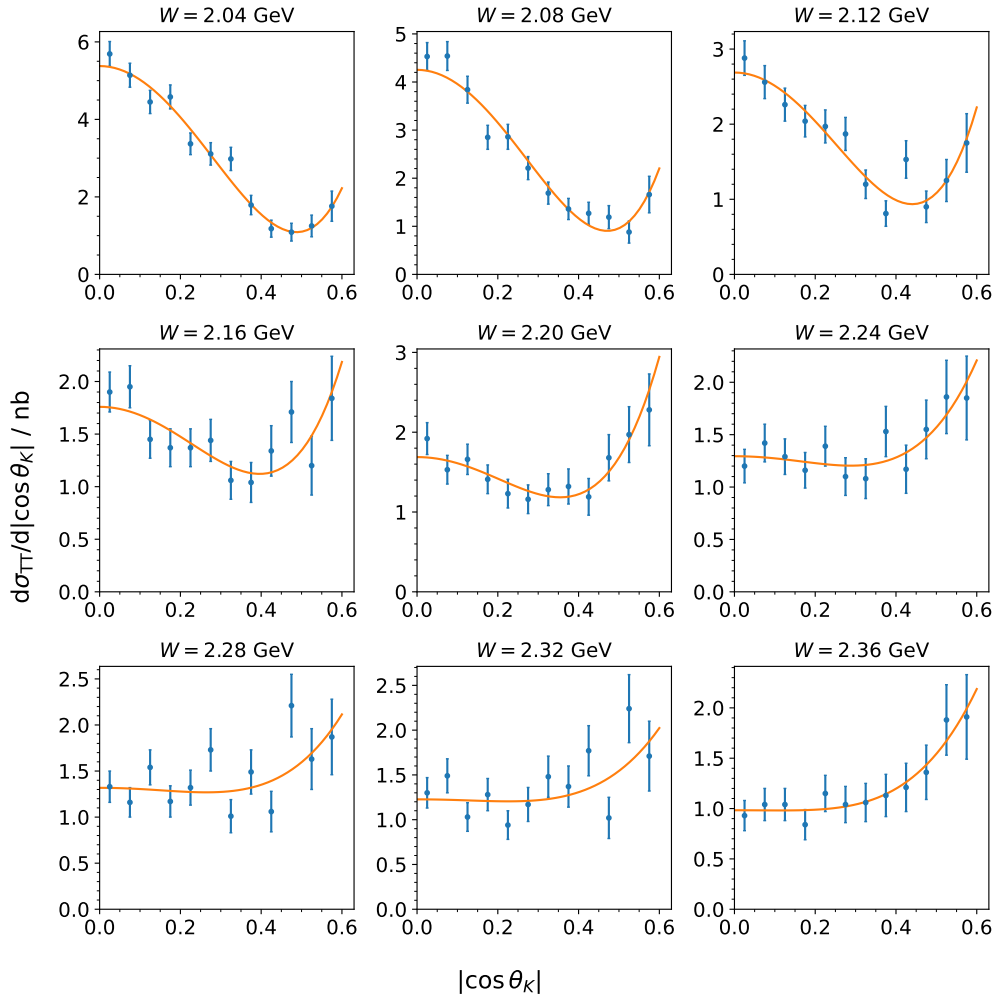


Figure 12: Fit of the cross section model (Eq. 60) to the Belle $\gamma\gamma \rightarrow K^+K^-$ cross sections as a function of the helicity angle $|\cos\theta_K|$. The blue points show the Belle data from Ref. [5], while the orange curve denotes the fit result. The different panels correspond to different K^+K^- invariant masses.

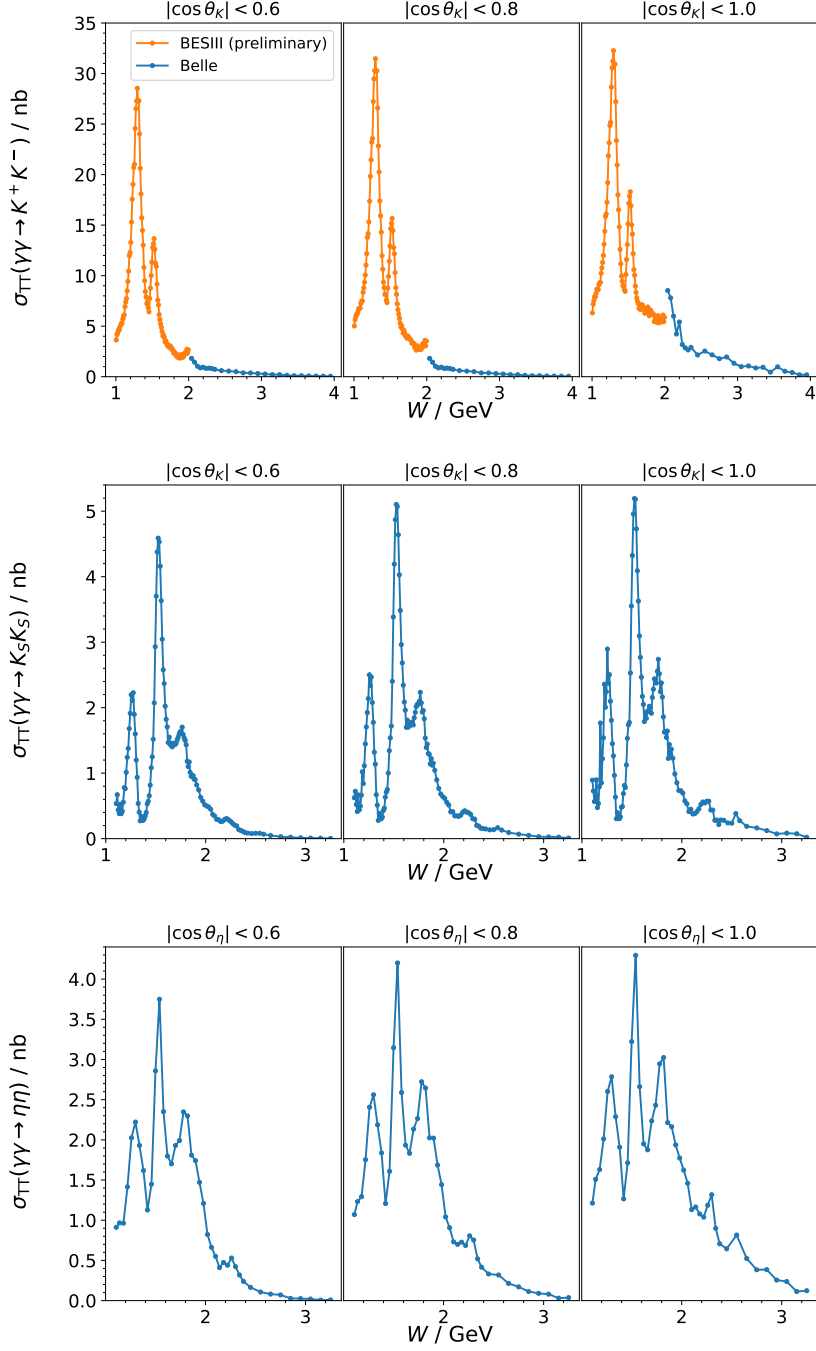


Figure 13: Integrated BESIII partial wave analysis (orange) and fits to the $\gamma\gamma \rightarrow K^+K^-$ (top), $\gamma\gamma \rightarrow K_S^0 K_S^0$ (center) and $\gamma\gamma \rightarrow \eta\eta$ (bottom) cross sections (blue) over different helicity angle ranges. The points (crosses) represent the actual mass points, the lines are linear interpolation between the results.

3.4. $e^+e^- \rightarrow e^+e^- f_1(1285) \rightarrow e^+e^- \eta \pi^+ \pi^-$ Mode

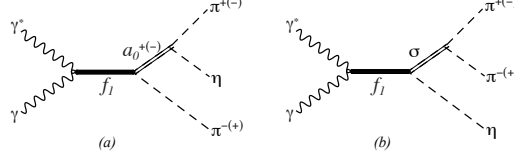


Figure 14: Feynman diagrams of the $\gamma^* \gamma \rightarrow \eta \pi^+ \pi^-$ process via the $f_1(1285) \rightarrow a_0(980)^\pm \pi^\mp$ and $f_1(1285) \rightarrow f_0(500) \eta$ decays.

In addition to the two-body modes, HADROTOPS can simulate the two-photon production of the axial-vector state $f_1(1285)$ and its subsequent decay into $\eta \pi^+ \pi^-$ via the intermediate states $a_0^\pm(980) \pi^\mp$ and $f_0(500) \eta$. The theoretical basis for this process follows Ref. [81], where the single-virtual process $\gamma^* \gamma \rightarrow \eta \pi^+ \pi^-$ is studied within an effective Lagrangian framework. As illustrated in Fig. 14, the two dominant channels $\gamma^* \gamma \rightarrow f_1(1285) \rightarrow a_0(980)^\pm \pi^\mp$ and $\gamma^* \gamma \rightarrow f_1(1285) \rightarrow f_0(500) \eta$ are included. The total two-photon amplitude is given by

$$\mathcal{M} = \mathcal{M}_{a_0^\pm(980) \pi^\mp} + \mathcal{M}_{a_0^-(980) \pi^+} + \mathcal{M}_{f_0(500) \eta} e^{i\phi}, \quad (61)$$

where the relative phase ϕ controls the interference between the channels. Motivated by the L3 measurement [82], Ref. [81] assumes fully destructive interference with $\phi = 180^\circ$. Using effective couplings fixed by the relevant decay widths, the model predicts invariant-mass spectra, angular distributions, and total cross sections. In the current implementation, the user has a full flexibility to specify coupling constants, branching fractions, scaling factors, and phase ϕ . Default values correspond to those used in Ref. [81].

In the current implementation, the framework is extended to account for a small but nonzero second virtuality Q_2^2 (which is assumed to be smaller than Q_1^2), thereby generalizing the original single-tagged study to more realistic experimental conditions. Specifically, the matrix elements in Eqs. (22) and (31) of Ref. [81] are modified to incorporate a symmetric Q_2^2 -dependent term. For the dominant LT contribution, the corresponding transition form factor $F_{LT}(Q_1^2, Q_2^2)$ amounts to the dipole parameterization

$$F_{LT}(Q_1^2, Q_2^2) = \frac{F_{LT}(0, 0)}{(1 + (Q_1^2 + Q_2^2)/\Lambda_{f_1}^2)^2}, \quad (62)$$

where $F_{LT}(0, 0)$ and the scale parameter Λ_{f_1} are defined as in Ref. [81]. For the subdominant TT contribution, the transition form factor $F_{TT}(Q_1^2, Q_2^2)$ is estimated via the quark model relation:

$$F_{TT}(Q_1^2, Q_2^2) = -\frac{X}{\nu(\nu + Q_2^2)} F_{LT}(Q_1^2, Q_2^2), \quad (63)$$

with $\nu \equiv q_1 \cdot q_2 = (W^2 + Q_1^2 + Q_2^2)/2$, and $X = \nu^2 - Q_1^2 Q_2^2$. Finally, the TL contribution is obtained using the symmetry relation

$$\frac{d\sigma_{TL}}{d|\cos \theta^*|}(Q_2^2, Q_1^2) = \frac{d\sigma_{LT}}{d|\cos \theta^*|}(Q_1^2, Q_2^2), \quad (64)$$

while the LL contribution is not included. The model is optimized for use in single-tagged studies. The Omnès function, which is used to describe the $f_0(500)$ amplitude in the matrix element of the $f_0(500) \eta$ intermediate state, is linearly interpolated and set to zero outside of its defined range.

3.5. Production through a Single Resonance

So far, only the simulation of specific final states has been discussed. HADROTOPS also offers the possibility to simulate the production of arbitrary hadronic final states through a single resonance using a custom final state mode. This feature enables experimental collaborations to estimate reconstruction efficiencies for arbitrary final states and to use the generated events in standard partial-wave analysis tools. Since no universal theoretical model exists for the production and decay of generic final states in two-photon collisions, simplified phenomenological models are implemented for such processes.

The two-photon cross sections are factorized into a mass-dependent part, $f(W)$, and a transition form factor, $|\mathcal{F}_{AB}|^2$,

$$\sigma_{AB}(W, Q_1^2, Q_2^2) \approx f(W) |\mathcal{F}_{AB}(Q_1^2, Q_2^2)|^2, \quad A, B \in \{T, L\}. \quad (65)$$

The default functional forms for $f(W)$, h_T and h_L are given below. When both are set to unity, the generated can be directly used in partial-wave analysis frameworks such as AmpTools [55] or Pawian [56], without explicitly incorporating the two-photon luminosity functions into the amplitudes.

For the transition form factor, a factorized dependence on the photon virtualities is assumed, with correct real-photon limits

$$|\mathcal{F}_{AB}(Q_1^2, Q_2^2)|^2 \approx h_A(Q_1^2) h_B(Q_2^2), \quad h_T(0) = 1, \quad h_L(0) = 0. \quad (66)$$

All other cross sections and response functions are implemented analogously to σ_{TT} . Since experimental studies of these cross sections and responses involve studies analyzing the azimuthal dependence, normalizing them to unity allows Monte Carlo samples to include the full lepton-side kinematics. This, in turn, enables the extraction of hadronic structure information from fits of the Monte Carlo samples to experimental data.

For the mass-dependent part, three options are available. The first one excludes any explicit mass dependence and simulates the mass distribution solely from the kinematic factors in Eqs. (12) and (31), i.e. $f(W) = 1 \text{ GeV}^{-2}$. A simulation at a fixed mass, $f(W) = \delta(W^2 - W_{\text{user}}^2)$, is also possible. Alternatively, a Breit-Wigner mass distribution can be used,

$$f(W) = \frac{1}{(W^2 - M^2)^2 + \Gamma^2 M^2} \frac{M\Gamma}{\pi}, \quad (67)$$

where the resonance mass M and width Γ are specified by the user.

Similarly to the mass dependency, a constant transition form factor model has also been implemented, $|\mathcal{F}_{AB}| = 1$. For a more realistic description of the transition form factor, a vector-pole model following the approach of the GALUGA2.0 code [57] is implemented

$$h_T(Q^2) = \left(\frac{1}{1 + Q^2/M_V^2} \right)^2, \quad h_L(Q^2) = \xi \frac{Q^2}{M_V^2} \left(\frac{1}{1 + Q^2/M_V^2} \right)^2, \quad (68)$$

where the pole mass M_V and the scaling parameter ξ can be freely chosen. Alternatively, a simplified vector meson dominance (VMD) model with multiple poles is available [83]. In this case, the functions are

$$h_T(Q^2) = \sum_{i=0}^3 r_i \left(\frac{1}{1 + Q^2/M_{V_i}^2} \right)^2, \quad h_L(Q^2) = \sum_{i=1}^3 \xi \frac{Q^2}{M_{V_i}^2} r_i \left(\frac{1}{1 + Q^2/M_{V_i}^2} \right)^2, \quad (69)$$

where the masses $M_{V_0} \dots M_{V_3}$ and the parameters $\xi, r_1 \dots r_3$ are free inputs, constrained by $r_0 = 1 - r_1 - r_2 - r_3$ to ensure normalization. The resonance with index 0 normalizes the transverse term and does not contribute to the longitudinal one. A generalized VMD model [84] is also included:

$$\begin{aligned} h_T &= r \left(\frac{1}{1 + Q^2/M_1^2} \right)^2 + (1 - r) \frac{1}{1 + Q^2/M_2^2} \\ h_L &= \xi r \left(\frac{1}{1 + Q^2/M_1^2} \right)^2 + \xi(1 - r) \left[\frac{M_2^2}{Q^2} \log \left(1 + \frac{Q^2}{M_2^2} \right) - \frac{1}{1 + Q^2/M_2^2} \right]. \end{aligned} \quad (70)$$

This implementation reproduces the results of GALUGA2.0 without relying on high-energy approximations. All parameters are configurable by the user.

Helicity-angle dependencies of the decay products in the final state have not been implemented. Instead, all final states decay according to a completely flat phase-space distribution. Since no reliable theoretical information exists on the relative normalization of the different cross sections for arbitrary hadronic states, a common absolute scale is used for all. Therefore, simulating combinations of cross sections simultaneously is not meaningful. Ratios of generated Monte Carlo samples can instead be used to study effects arising from lepton-side kinematics.

The previously introduced TFF models can be employed to extrapolate the numerical input for the $\pi\pi$, $\pi\eta$, $K\bar{K}$, and $\eta\eta$ channels beyond their defined virtuality range. The two-photon cross sections and response functions are assumed to continue proportional to $h_T(Q_1^2)h_T(Q_2^2)$ outside of their defined range. The mass dependence is modeled as $\sim 1/W^2$. This extrapolation should, however, be regarded only as a rough estimate rather than a reliable prediction of the cross sections outside the defined input region. In particular, for the $K\bar{K}$ and $\eta\eta$ channels, only the σ_{TT} cross section is available, meaning that essential components of the required information are missing for simulations at finite virtuality.

3.6. Luminosity Function Mode

Besides generating $e^+e^- \rightarrow e^+e^-X$ events, the code can also be used to calculate the luminosity functions introduced in Sec. 1.1.3. For this purpose, every two-photon cross section or response is set to unity thereby removing hadronic dynamics, and only the $e^+e^- \rightarrow e^+e^-X$ phase-space element is evaluated. In other words, the $d\text{Lips}_{e^+e^-X}$ is used and the hadronic decay factor is set to unity to exclude any dynamics from the decay of X . The same type of calculation can be performed for the corresponding functions associated with the two-photon cross sections in Eq. (31).

4. Program Structure

HADROTOPS is distributed as source code organized into a specific directory structure. The core of the generator is implemented as a class, enabling straightforward integration into detector software frameworks. The main header file for HADROTOPS, `HadroTOPS.hh`, is located in the `include/` folder. Alongside it, the `common.hh` header file includes essential quadruple precision functions, while the header files for the Lorentz and three-vector objects (`LorentzVector` and `Vector3`) are also located in this directory. The source code for the vector objects resides in the `src/vector` directory, while the HADROTOPS generator's source code is located in

`src/hadrotops`. The main function, which reads the job options and instantiates the `HADROTOPS` object accordingly, is implemented in `src/main.cc`.

The `HADROTOPS` source code is split into several files:

- `HadroTOPS.cc`: Contains the constructor of the `HADROTOPS` object and handles the initialization and finalization of the event generation procedure. All constants are defined here.
- `HadroTOPS.aux.cc`: Contains auxiliary functions such as consistency checks of user input, a convenience function for the random number generator, and the display of status bars.
- `HadroTOPS.crosssection.cc`: Implements all functions that calculate the event weight, which is the full cross section element, for the current kinematic setting.
- `HadroTOPS.generate.cc`: Includes all necessary functions for the generation of the final-state Lorentz vectors and the calculation of the associated phase space elements and other kinematic factors.
- `HadroTOPS.getters.cc`: Contains all getters.
- `HadroTOPS.mc.cc`: Contains all functions necessary to handle the Monte Carlo procedure. The weighted and unweighted event generation loops, as well as the Monte Carlo integration procedure, are implemented here.
- `HadroTOPS.out.cc`: Includes all functions necessary for the output of the program.
- `HadroTOPS.setters.cc`: Includes all setters.
- `HadroTOPS.theory.cc`: Contains all functions necessary to read and interpolate the theory input for the two-photon cross sections.

4.1. Double and Quadruple Precision Floating Point Numbers

The code can be compiled to be executed either in double or quadruple precision. The latter offers a slight improvement in stability, but results in significantly longer execution times. Nevertheless, using quadruple precision is generally recommended.

For quadruple precision, the `libquadmath` library and its quadruple precision floating-point type `__float128` are used. For convenience, this is set as the custom data type `quad`. When only double precision is required, the precompiler flag `-DDOUBLE_PREC` can be set during compilation, making the `quad` data type equivalent to `long double` and replacing the quadruple precision functions with their standard, double-precision counterparts.

4.2. Input Scheme

The executable `HadroTOPS.exe` is produced in the `bin/` directory. When executed, it reads the configuration settings from the file `jobOptions.txt`, unless a different file is specified by the user. The input file defines all necessary settings for input, output, and the generation process itself. The available settings are discussed in the `HADROTOPS` manual.

It should be noted that the generator can also operate without a dedicated input file. If integrated into a larger framework, all settings can be adjusted using the appropriate setter functions. The numerical theory input is placed in the folder `data/`.

4.3. Output Scheme

The program is capable of providing event-by-event output as well as histograms filled with the (differential) cross section output. The histogram functionality requires a ROOT installation [85] with properly set \$ROOTSYS variables.

Weighted and unweighted events are stored in two different ASCII files. Each file contains, for each event, the number of final state particles, their used defined labels (typically the IDs from the PDG's Monte Carlo numbering scheme), and the four-vectors of all particles in the e^+e^- center-of-mass frame, with the positron traveling along the positive z -axis. If a weighted event is reported, its corresponding weight is included in the output. The exact format is explained in the manual.

Histograms are stored in a ROOT file, the name and path of which is set in the `jobOptions.txt` file.

In addition to the output files, information about the current run is displayed in the console, which can also serve for logging purposes.

4.4. Implementation of Vector3 and LorentzVector classes

Since the code may use quadruple precision floating-point calculations, the standard double precision classes implementing three- and four-vectors are not suitable. Therefore, a simplified and very incomplete re-implementation of the most important functions of the `TVector3` and `TLorentzVector` classes of the ROOT framework [85], using quadruple precision floats and functions, is utilized. The code for these re-implementations can be found in the respective header files and `src/vector/Vector3.cc` and `src/vector/LorentzVector.cc`, respectively.

4.5. Important Variables

The most important kinematic variables required for by many functions are implemented as member variables. All of them are stored in units of GeV for energies, masses, widths, and momenta, and in radians for angles. These variables include the scalar (type quad) variables for the center-of-mass energy (`Ecm` and its square `s`), the two-photon center-of-mass energy (`W`), the lepton momentum transfers (`t1`, `t2`, `Q1s`, and `Q2s`), the subsystem center-of-mass energies (`s1` and `s2`), the modulation angles $\tilde{\phi}$, $\tilde{\phi}_1$, and $\tilde{\phi}_2$ (`phiTilde`, `phiTilde1`, `phiTilde2`), and the polar and azimuthal angles of the final state hadrons in the two-photon center-of-mass system (`cosThetaStar` and `phiStar`).

The four-vectors of the initial and final state positron (p_1 denoted in the code as `k1` and p'_1 denoted as `p1`) and electron (p_2 denoted as `k2` and p'_2 denoted as `p2`), the hadronic system four-vector p_X (`pX`), and the final state hadrons (`pDec`) are stored as `LorentzVector` (or `vector` thereof) objects.

Objects, such as the current event weight (`WEIGHT`), the maximum event weight observed during the weighted event loop (`maxWEIGHT`), and the phase space elements `dLipseeX`, $\frac{dLipseeX}{(t_1 \cdot t_2)}$, and `dLipsN` (`dLips`, `dLipsDiv`, `dLipsDec`) are also member variables of type quad.

4.6. Important Functions

This subsection provides an overview of a selected set of key functions implemented in the `HADROTOPS` source code.

- Functions for the generation of final state four-vectors

- `void HadroTOPS::generateFixW()`
Generates the e^+e^-X final state four-vectors and calculates $dLips_{eeX}$, along with several kinematic variables, at given (globally defined) values of s and W . The function takes into account user-defined and kinematic limits of the final-state vectors.
- `void HadroTOPS::decayFinalState()`
Handles the decay of the hadronic system X into its final-state particles and calculates the corresponding phase-space element.
- `bool HadroTOPS::generateEvent()`
Generates a numerically stable weighted event. If necessary, W is generated and decay products of the hadronic final state X are generated. The function determines final state Lorentz vectors in the two-photon center-of-mass system and calculates remaining necessary kinematic variables. It returns a Boolean value indicating whether the generated event satisfies the user-defined cuts and calls `calcXS()` to determine event weight.
- `bool HadroTOPS::acceptEvent()`
Checks user-defined constraints and returns `false` if the event shall be rejected. Additional user-specific constraints can be implemented within this function.
- `void HadroTOPS::generateWeightedEvent()`
Generates a weighted event under the specified user conditions. This function handles Monte Carlo integration and event output, and internally calls `generateEvent()` and `acceptEvent()`.
- `void HadroTOPS::runWeighted()`
Implements the weighted events loop. It generates as many weighted events as requested by the user within user constraints and determines the maximum event weight and stores it in `maxWEIGHT`.
- `void HadroTOPS::generateUnweightedEvent()`
Generates an unweighted event within user-specific conditions using the rejection sampling method [86]. This function performs Monte Carlo integration and produces unweighted event output. The maximum event weight (`maxWEIGHT`) must be predefined by running `runWeighted()`. It internally calls `generateWeightedEvent()`.
- `void HadroTOPS::runUnweighted()`
Generates as many unweighted events within user-specific constraints as requested.

- Functions for the calculation of the cross section

- `void HadroTOPS::interpolateCrossSectionInput()`
Wrapper function for the interpolation of the cross section input. It calls the necessary functions to interpolate the theory input to the current kinematic variables. The interpolated two-photon cross sections are stored in the member variable `quaditXS[18]`.
- `quad HadroTOPS::getFFTT()`
Calculates the transition form factor for two transversely polarized virtual photons, according to the user-selected model. Corresponding functions for transverselongitudinal, longitudinaltransverse, and longitudinallongitudinal photon polarizations are provided as `getFFTL()`, `getFFLT()`, and `getFFLL()`, respectively.

- `void HadroTOPS::calcXS()`
Calculates the cross section using the current kinematics and the user-defined theoretical model.

5. Running the Simulation

HADROTOPS operates in a four-step procedure:

1. Initialization
2. Weighted-event generation and upper bound estimation loop
3. Unweighting loop (optional)
4. Finalization

Detailed instructions for running the generator both as a standalone application and as an embedded component in a C++ program are provided in the HADROTOPS manual. During the initialization process, a new HADROTOPS object is created, and the simulation options are set using the setter functions, which are summarized in detail in the manual. Afterwards, the function `void HadroTOPS::init()` must be called to validate the settings and initialize the output functionalities, the random-number generator, and the Monte Carlo integration variables.

Next, the function `void HadroTOPS::runWeighted()` is called to generate a predefined number of weighted events within the user-defined cuts. In this way, the maximum weight within user cuts is determined, which is necessary for the unweighting loop. Alternatively, the user may call the `void HadroTOPS::generateWeightedEvent()` function to generate a single weighted event that satisfies the user constraints. The function `double HadroTOPS::getWeight()` returns the current event weight in units of nanobarns (or dimensionless in luminosity function mode, with the correct dimension of the luminosity function of GeV^{-5} arising from bin normalization). Note that the single-event function cannot be used to determine the maximum event weight. For all functions, the events are filled into histograms and/or written to the output files, as specified by the user.

The weighted-event loop may optionally be followed by the unweighting loop. Similar to the weighted-events procedure, the function `void HadroTOPS::runUnweighted()` generates a predefined number of unweighted events, while `void HadroTOPS::generateUnweightedEvent()` produces a single unweighted event within the user-defined cuts. The results are also reported to the histogram and output files as specified by the user. All events must be scaled to the total cross section using the same event weight.

The last step is the program finalization, in which the total cross section of the simulated physics process is calculated and reported. The cross section and its corresponding uncertainty for the weighted events (which also takes into account all trials needed in the unweighting procedure) are given by

$$\sigma = \frac{1}{N_w} \sum_{i=1}^{N_w} d\sigma_i$$

$$(\Delta\sigma)^2 = \frac{1}{N_w - 1} \left(\frac{1}{N_w} \sum_{i=1}^{N_w} (d\sigma_i)^2 - \sigma^2 \right), \quad (71)$$

where $d\sigma_i$ is the weight (cross section) of event i , and N_w is the number of generated weighted event within the user cuts. Alternatively, the cross section can be calculated from the unweighted events using

$$\begin{aligned}\sigma &= d\sigma_{\max} \cdot \frac{N_{uw}}{N_t} \\ (\Delta\sigma)^2 &= \frac{\sigma(d\sigma_{\max} - \sigma)}{N_{uw}},\end{aligned}\tag{72}$$

where $d\sigma_{\max}$ is the maximum event weight, N_{uw} is the number of unweighted events. N_t represents the number of trials, which is the number of generated weighted events during the unweighting procedure.

6. Results

6.1. Luminosity Functions

For validation purposes, the luminosity functions calculated using HADROTOPS can be compared with their analytically calculated counterparts. The exact analytical expressions are given in Ref.[1]. Such a comparison is possible only for the luminosity functions associated with the inclusive cross section in Eq. (12), as no analytical calculation exists for the exclusive formula in Eq. (31).

A systematic comparison between the HADROTOPS output and the analytical curves was performed over a wide range of center-of-mass energies, two-photon invariant masses, and momentum transfers, covering all possible combinations of photon polarizations. The agreement was found to be within the statistical fluctuations of the generated samples. Figure 15 shows the comparison of the double-transverse luminosity function as a function of both momentum transfers and the two-photon center-of-mass energy (W), evaluated at $\sqrt{s} = 4$ GeV. The chosen momentum transfers and masses lie within a typical range accessible at this energy. The comparison demonstrates excellent agreement, even at very high statistics. The same level of agreement is observed for the remaining five polarization combinations. All luminosity functions have been tested at a five per-mille level.

6.2. Fixed Two-Photon Cross Sections and Luminosity Functions

Calculating the $e^+e^- \rightarrow e^+e^-X$ cross section with constant two-photon cross sections not only enables a direct determination of the luminosity functions, but also cleanly isolates the lepton-side kinematics that govern the modulation angles $\tilde{\phi}$, $\tilde{\phi}_1$, and $\tilde{\phi}_2$. As argued at the end of Section 1.1.2, by analyzing the angular-harmonic content of the cross section in $\tilde{\phi}$ (the 1, $\cos \tilde{\phi}$ and $\cos 2\tilde{\phi}$ components) one can project out individual response components. In analyses integrating over the modulation angles, the cosine terms are removed by construction, leaving only the angle-averaged contribution. Practically, accessing $\tilde{\phi}$ requires double-tagging (both outgoing leptons reconstructed), which yields lower event rates.

An additional complication arises, as shown in Fig. 16, where the $\tilde{\phi}$ -dependent parts of the cross section are plotted as a function of $\tilde{\phi}$. In the full phase space and a single-tag environment, the distributions exhibit the expected $\cos \tilde{\phi}$ and $\cos 2\tilde{\phi}$ behavior. In the double-tag case, however, the shapes are significantly distorted. This distortion stems from the non-trivial dependence of $\tilde{\phi}$ on the full set of Lorentz invariants, as given in Ref. [57]. Therefore, to exploit the modulation-angle dependence, it is not sufficient to simply fit the functional dependencies

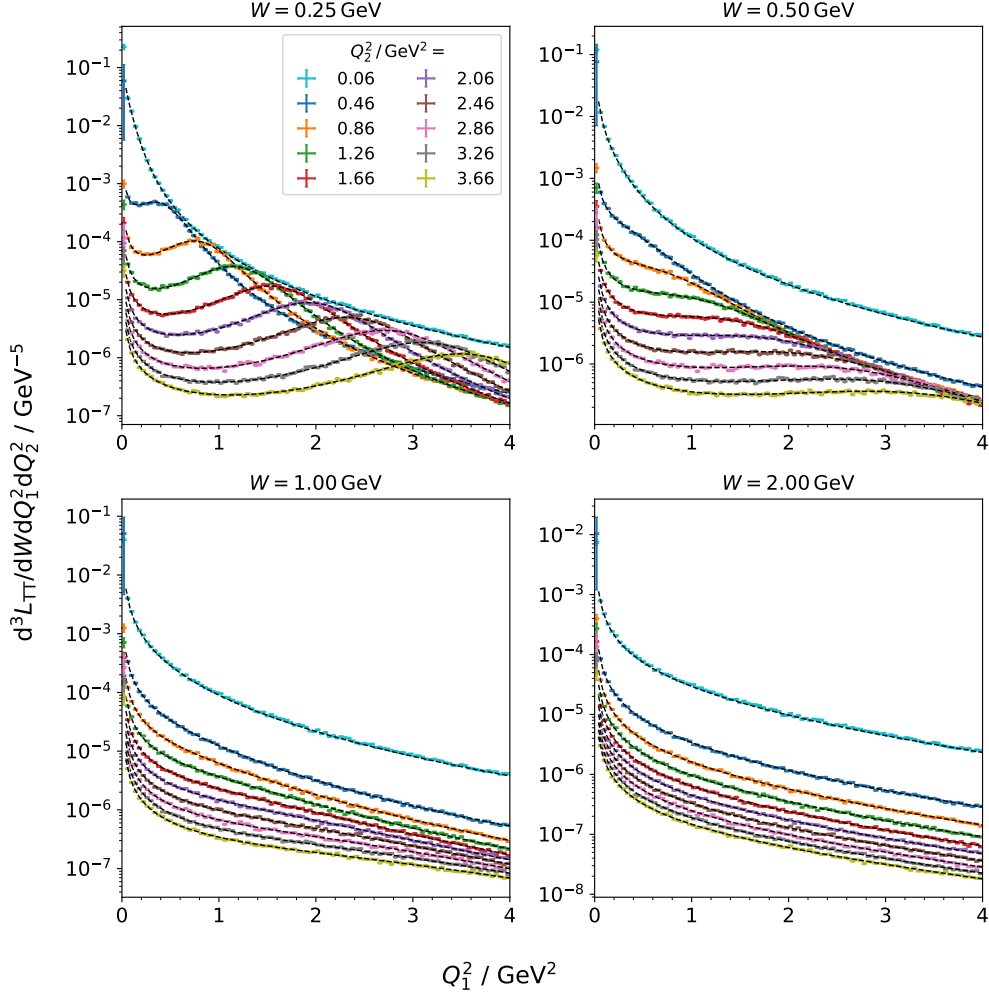


Figure 15: Comparison of the luminosity function of two transversely polarized photons calculated by HADROTOPS (data points) and the analytical result (black dashed lines) from Ref. [1]. The panels correspond to different two-photon center-of-mass energies W , while the colors represent different values of Q_2^2 . All functions are displayed in dependence on Q_1^2 and are evaluated at $\sqrt{s} = 4$ GeV.

on these modulation angles, as given in Eqs. (12) and (31), to the experimentally extracted differential cross section. Instead, one must fit the full kinematic dependence, as calculated by HADROTOPS, to the experimental data.

6.3. Cross Sections of Two-Hadron Final States

Figure 17 presents the two-photon invariant mass distributions and the positron momentum transfer distributions generated by HADROTOPS, when simulating the fully available phase space at $\sqrt{s} = 4$ GeV. A strong decrease of the cross section with increasing masses is clearly visible, as is the rapid drop with increasing Q^2 . The limited coverage in Q^2 for the $\pi\pi$ and $\pi\eta$ final states,

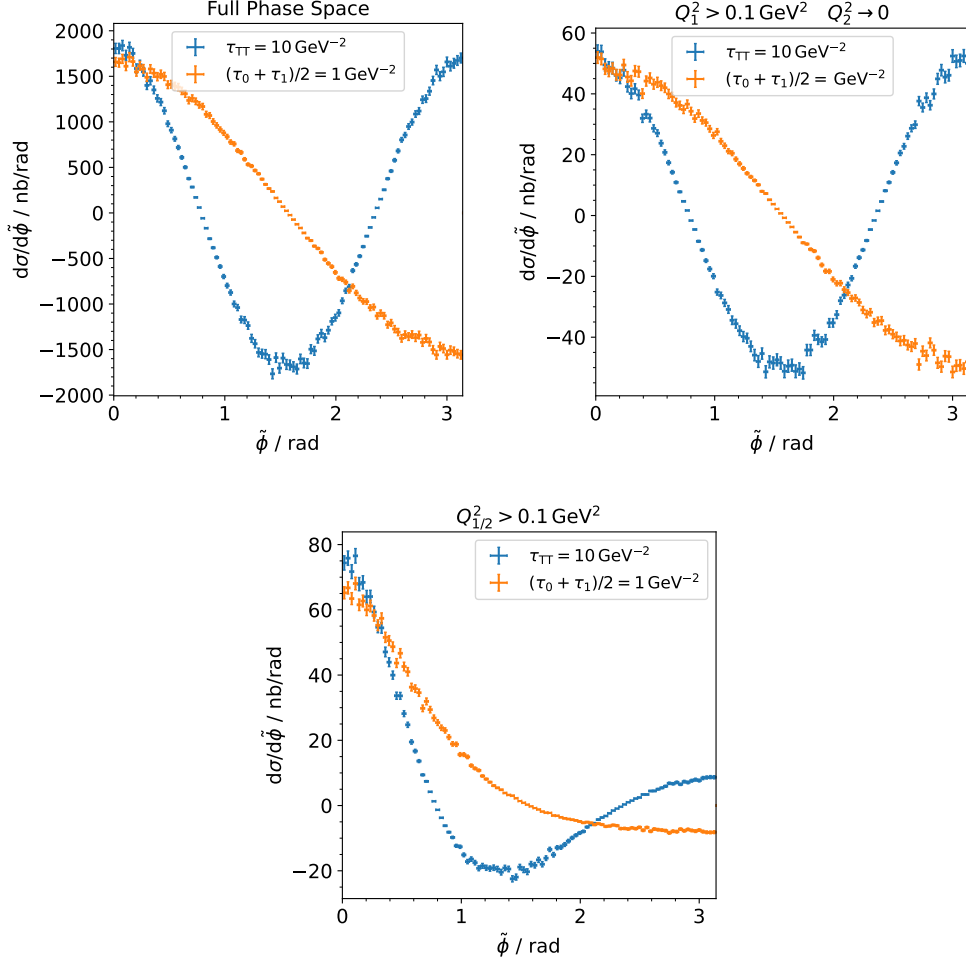


Figure 16: Differential cross section as a function of the modulation angle $\tilde{\phi}$. The top-left panel shows the cross section when only τ_{TT} and $(\tau_0 + \tau_1)/2$ are set to non-zero values. The top-right panel shows the same in the single-tag configuration, and the bottom panel in the double-tag setup. All plots are produced at $\sqrt{s} = 4$ GeV for the production of a stable particle with $W = 1$ GeV, with $(\tau_0 + \tau_1)/2 = 1$ GeV $^{-2}$ and (for better visibility) $\tau_{TT} = 10$ GeV $^{-2}$.

which originates from the theoretical input, is also apparent. In contrast, the modeling of the Q^2 dependence for other final states extends the coverage to larger momentum transfers, but relies on the simplified models described in Sec. 3.5.

The fluctuations observed in the K^+K^- , $K_S^0K_S^0$, and $\eta\eta$ final states can only partially be attributed to the intermediate resonances. They are primarily caused by the limited statistics of the experimental input, which is particularly evident for the K^+K^- channel. Compared to the neutral-pion case, the charged-pion cross section is roughly twice as large in the $f_2(1270)$ mass region, as expected from isospin symmetry. At lower invariant masses, however, the charged-pion contribution exceeds the neutral-pion one by more than an order of magnitude. This difference arises

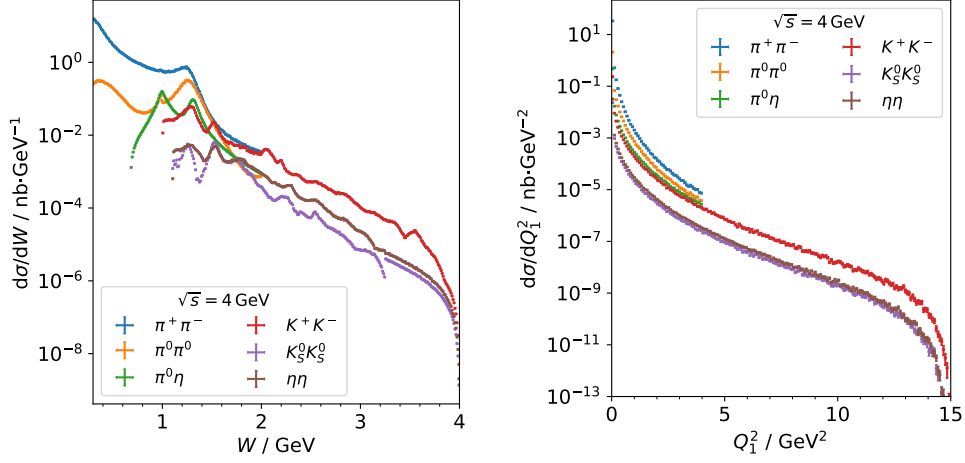


Figure 17: Two-Photon invariant mass distribution (left) and momentum transfer Q_1^2 distribution (right) for simulated two-hadron final states generated with HADROTOPS . All events are produced at $\sqrt{s} = 4$ GeV and cover the W and Q^2 ranges described in Secs. 3.1, 3.2 and 3.3. For the K^+K^- , $K_s^0K_s^0$, and $\eta\eta$ channels, the Q^2 dependence of the two-photon cross section is modeled using a vector-pole parametrization with $M_V=775$ MeV.

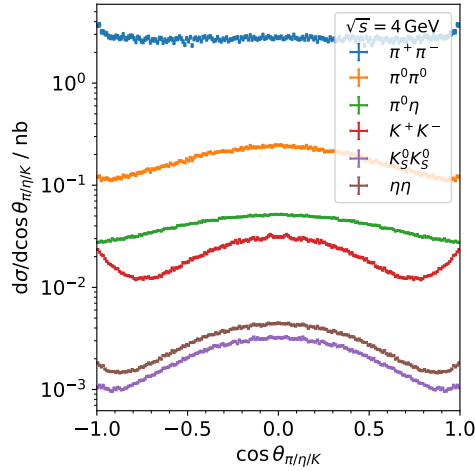


Figure 18: Helicity angle $\cos \theta_{\pi|\eta|K}$ distributions for simulated two-hadron final states generated with HADROTOPS . All events are produced at $\sqrt{s} = 4$ GeV and cover the W and Q^2 ranges described in Secs. 3.1, 3.2 and 3.3, and correspond to those shown in Fig. 17.

from the presence of the Born contribution, which is absent for neutral pions. A similar effect is expected for the charged and neutral kaon states, but the available experimental input does not cover the threshold region, and this feature is therefore not produced in HADROTOPS . The helicity-angle distributions shown in Fig. 18 illustrate the characteristic angular patterns of the final states, which depend on the spin and helicity configuration of the intermediate resonance.

For the charged channels, the pronounced forward and backward peaking originates mainly from the Born contribution.

6.3.1. Cross Sections of the $e^+e^- \rightarrow e^+e^-\pi^0\pi^0$ Process

The authors of the forthcoming EKHARA3.2 generator have kindly provided early access to the code, allowing a comparison between the two generators for the process $e^+e^- \rightarrow e^+e^-\pi^0\pi^0$. A corresponding comparison for the charged-pion channel is not feasible, since EKHARA3.2 also includes pion-pair production from a virtual photon radiated in Bhabha scattering.

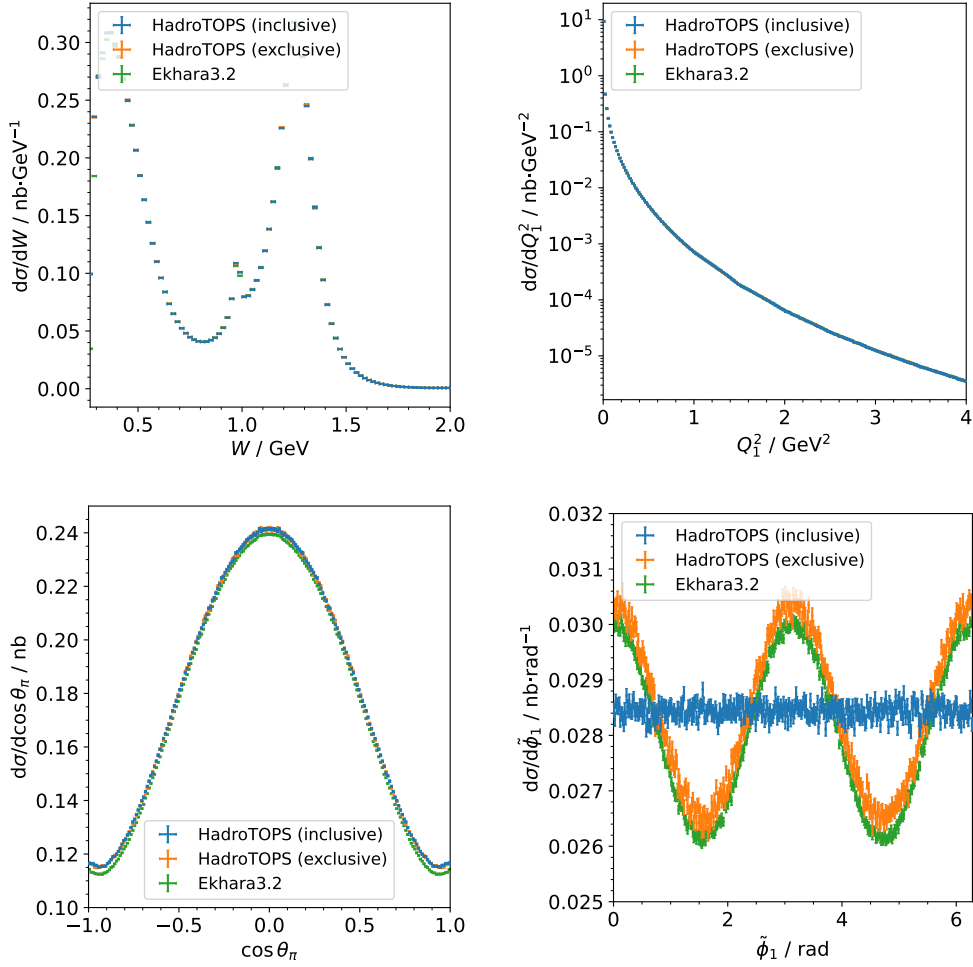


Figure 19: Comparison of the predicted cross sections for the process $e^+e^- \rightarrow e^+e^-\pi^0\pi^0$ calculated with HADROTOPS, using the inclusive (blue) and exclusive (orange) cross-section formulas, and with EKHARA3.2 (green). The distributions are shown as functions of the two-pion invariant mass (upper left), positron momentum transfer (upper right), pion polar angle $\cos\theta_\pi$ in the two-photon c.m. frame (lower left), and the modulation angle $\tilde{\phi}_1$ (lower right). The center-of-mass energy is fixed at $\sqrt{s} = 4$ GeV, with W limited to $W = 0 - 2$ GeV, and the momentum transfers to $Q_{1,2}^2 = 0 - 4$ GeV².

A comparison between HADROTOPS and EKHARA3.2 at $\sqrt{s} = 4 \text{ GeV}$ is shown in Fig. 19, as a function of the kinematic variables W , Q_1^2 , $\cos \theta_\pi$, and $\tilde{\phi}_1$. For HADROTOPS, two separate samples are generated using the cross-section formulas for the inclusive process Eq. (12) and the exclusive process Eq. (31). The two resulting HADROTOPS distributions agree perfectly across all variables except for the modulation angle $\tilde{\phi}_1$ between one of the lepton scattering planes and the hadron production plane. This is expected since this dependence only enters through the exclusive process formula.

Overall, the results from HADROTOPS are in good agreement with those from EKHARA3.2 apart from some minor differences. Both generators rely on the same theoretical input, but these discrepancies originate from differences in how the differential cross section is evaluated. Unlike HADROTOPS, where the cross section is analytically computed from Eqs. (12) and (31) using the two-photon cross sections and response functions, EKHARA3.2 evaluates the full $e^+e^- \rightarrow e^+e^-\pi\pi$ cross section directly from the matrix element in Eq. (7). Consequently, EKHARA3.2 uses the helicity amplitudes as direct input, whereas HADROTOPS interpolates the combination of helicity amplitudes and the kinematic factors arising from the two-photon dynamics. In contrast, EKHARA3.2 interpolates only the helicity amplitudes and evaluates all remaining kinematic factors at the exact point in phase space where the event is generated. With a very fine (or infinitely dense) grid for the numerical theory input, both generators are expected to yield identical results.

6.4. Cross Sections of the $e^+e^- \rightarrow e^+e^-f_1(1285) \rightarrow e^+e^-\eta\pi^+\pi^-$ Process

Figure 20 shows example distributions of the HADROTOPS prediction for the two-photon production cross section of the $f_1(1285)$ and its decay into $\eta\pi^+\pi^-$. The W dependent cross section is found to be around an order of magnitude smaller than the two-pion modes and comparable to the $K\bar{K}$ and $\eta\eta$ channels, as seen from Fig. 17. This behavior is expected, since the production of a spin-1 state by two real photons is forbidden by the LandauYang theorem [87, 88], and a nonzero cross section arises only for photons with finite virtualities.

The doubly-transverse polarized cross section (TT) decreases more slowly with Q^2 than the transverselongitudinal (TL/LT) one. At small momentum transfers, typical of BESIII at $\sqrt{s} = 4 \text{ GeV}$, the TL+LT contribution is numerically larger and dominates the cross section. At higher \sqrt{s} , as at BaBar or Belle II, where the average Q^2 is larger, the TT component becomes relatively more important.

In the $\eta\pi^+$ mass spectrum, the $a_0(980)$ resonance from the $f_1(1285) \rightarrow a_0(980)^\pm\pi^\mp$ decay and its kinematic reflection are clearly visible. There is no distinct mass separation between the $a_0(980)^\pm\pi^\mp$ and $f_0(500)\eta$ final states. Consequently, a full partial-wave analysis will be needed in future measurements. In the $\pi^+\pi^-$ mass spectrum, a clear destructive interference pattern is observed. The interference can be controlled by the relative phase angle, which in this case is set to $\phi = 180^\circ$. The destructive interference disappears for $\phi = 0^\circ$. Experimental input is necessary to determine the correct interference between the two intermediate states.

7. Summary

We present a Monte Carlo event generator capable of computing two-photon luminosity functions and simulating samples of the inclusive process $e^+e^- \rightarrow e^+e^-X$, including the QED couplings and assuming a flat phase-space distribution. The framework is suitable for supporting partial-wave analyses in two-photon reactions and for estimating reconstruction efficiencies. Furthermore, the code is also extended to simulate the exclusive processes $e^+e^- \rightarrow e^+e^-\pi^+\pi^-$,

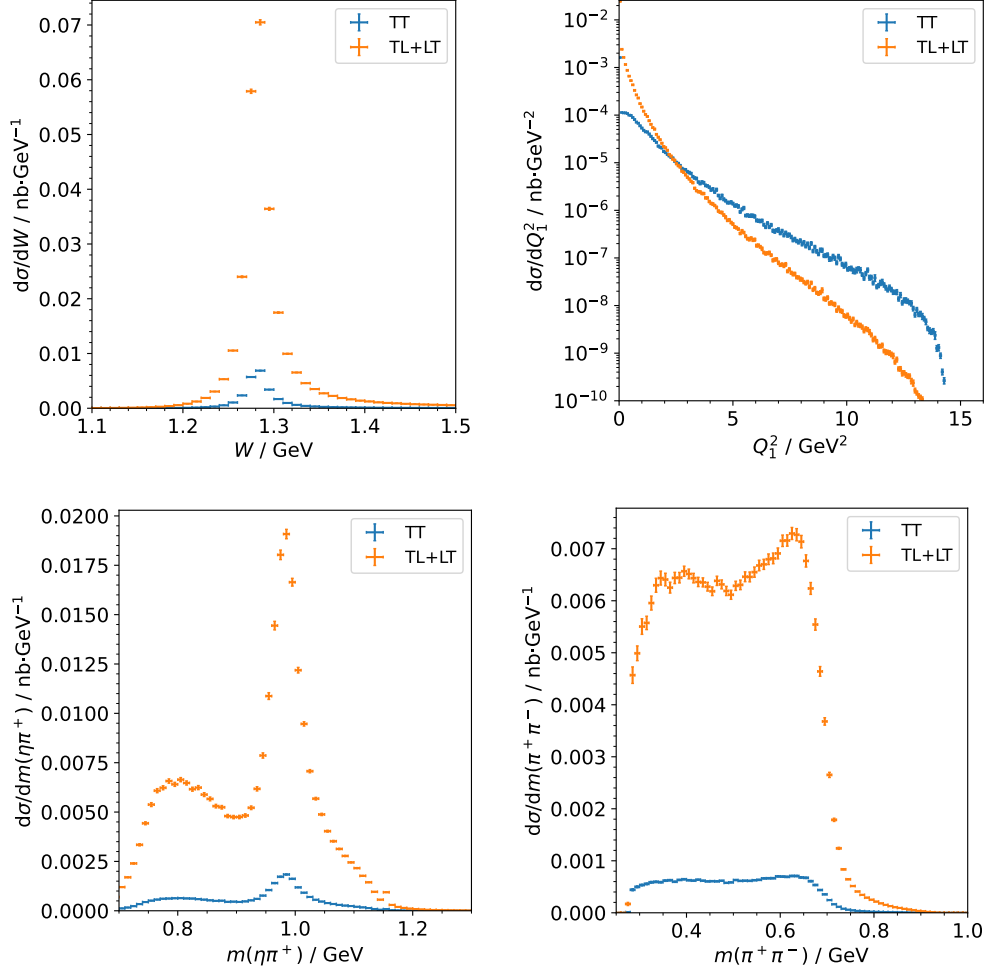


Figure 20: Differential cross sections of the $e^+e^- \rightarrow e^+e^- f_1(1285) \rightarrow e^+e^- \eta \pi^+ \pi^-$ in dependence on two-photon invariant mass W (top left), positron momentum transfer Q_1^2 (top right), $\eta\pi^+$ invariant mass (bottom left) and $\pi^+\pi^-$ invariant mass (bottom right) for the case of two transversely polarized photons (blue) and one transversely and one longitudinally polarized photon (orange). All parameters are set as in Ref. [81] for a value $\sqrt{s} = 4$ GeV.

$e^+e^- \rightarrow e^+e^- \pi^0 \pi^0$, $e^+e^- \rightarrow e^+e^- \pi^0 \eta$, $e^+e^- \rightarrow e^+e^- K^+ K^-$, $e^+e^- \rightarrow e^+e^- K_S^0 K_S^0$, $e^+e^- \rightarrow e^+e^- \eta \eta$, and $e^+e^- \rightarrow e^+e^- f_1(1285) \rightarrow e^+e^- \eta \pi^+ \pi^-$ via the two-photon production mechanism. For the exclusive two-meson production processes $e^+e^- \rightarrow e^+e^- M_1 M_2$ the full cross section formula is implemented in terms of $\gamma^* \gamma^* \rightarrow M_1 M_2$ response functions. The exclusive formulation retains the full azimuthal-angle modulations, enabling studies of interference response functions that are usually washed out by integration over modulation angles. For the $\pi\pi$ and $\pi\eta$ channels, the estimate of the $\gamma^* \gamma^* \rightarrow M_1 M_2$ response functions relies on dispersion theory input to describe the dependence on energy and photon virtualities. For $K^+ K^-$, $K_S^0 K_S^0$, and $\eta\eta$ the input is data-driven from untagged measurements (TT), with a user-configurable form-factor

model to describe the Q^2 fall-off when needed. The $f_1(1285)$ mode, accessed through the $e^+e^- \rightarrow e^+e^-f_1(1285) \rightarrow e^+e^-\eta\pi^+\pi^-$ process, is implemented based on an effective-Lagrangian description and includes LT and TT contributions (and TL by symmetry) with a small but nonzero second virtuality. In the future, the code can be easily extended to accommodate additional hadronic final states, when corresponding theoretical models become available.

Acknowledgements

We thank Meike Küssner for the discussion of the BESIII results and for providing of the experimental two-photon cross sections and Henryk Czyż for discussing results and providing the updated EKHARA Monte Carlo Event Generator.

This work was supported by the Deutsche Forschungsgemeinschaft (DFG, German Research Foundation) through the Research Unit FOR 5327 (Photon-photon interactions in the Standard Model and beyond, Projektnummer 458854507).

References

- [1] G. Bonneau, M. Gourdin, F. Martin, Inelastic lepton anti-lepton scattering and the two photon exchange approximation, Nucl. Phys. B 54 (1973) 573–597. doi:10.1016/0550-3213(73)90440-9.
- [2] V. M. Budnev, I. F. Ginzburg, G. V. Meledin, V. G. Serbo, The Two photon particle production mechanism. Physical problems. Applications. Equivalent photon approximation, Phys. Rept. 15 (1975) 181–281. doi:10.1016/0370-1573(75)90009-5.
- [3] V. Pascalutsa, V. Pauk, M. Vanderhaeghen, Light-by-light scattering sum rules constraining meson transition form factors, Phys. Rev. D 85 (2012) 116001. arXiv:1204.0740, doi:10.1103/PhysRevD.85.116001.
- [4] G. A. Schuler, Two photon physics with GALUGA 2.0, Comput. Phys. Commun. 108 (1998) 279–303. arXiv:hep-ph/9710506, doi:10.1016/S0010-4655(97)00127-6.
- [5] K. Abe, et al., Measurement of K^+K^- production in two photon collisions in the resonant mass region, Eur. Phys. J. C 32 (2003) 323–336. arXiv:hep-ex/0309077, doi:10.1140/epjc/s2003-01468-9.
- [6] H. Nakazawa, et al., Measurement of the $\gamma\gamma \rightarrow \pi^+\pi^-$ and $\gamma\gamma \rightarrow K^+K^-$ processes at energies of 2.4-GeV to 4.1-GeV, Phys. Lett. B 615 (2005) 39–49. arXiv:hep-ex/0412058, doi:10.1016/j.physletb.2005.03.067.
- [7] S. Uehara, et al., High-statistics measurement of neutral pion-pair production in two-photon collisions, Phys. Rev. D 78 (2008) 052004. arXiv:0805.3387, doi:10.1103/PhysRevD.78.052004.
- [8] B. Aubert, et al., Measurement of the $\gamma\gamma^* \rightarrow \pi^0$ transition form factor, Phys. Rev. D 80 (2009) 052002. arXiv:0905.4778, doi:10.1103/PhysRevD.80.052002.
- [9] S. Uehara, et al., Measurement of $\eta\eta$ production in two-photon collisions, Phys. Rev. D 82 (2010) 114031. arXiv:1007.3779, doi:10.1103/PhysRevD.82.114031.

- [10] M. Küßner, Coupled channel partial wave analysis of two-photon reactions at besiii, doctoralthesis, Ruhr-Universität Bochum, Universitätsbibliothek (2022). doi:10.13154/294-8590.
- [11] M. Küßner, Recent Highlights on Meson Spectroscopy at BESIII, EPJ Web Conf. 291 (2024) 01002. doi:10.1051/epjconf/202429101002.
- [12] G. Colangelo, M. Hoferichter, M. Procura, P. Stoffer, Dispersion relation for hadronic light-by-light scattering: theoretical foundations, JHEP 09 (2015) 074. arXiv:1506.01386, doi:10.1007/JHEP09(2015)074.
- [13] P. Masjuan, P. Sánchez-Puertas, Pseudoscalar-pole contribution to the $(g_\mu - 2)$: a rational approach, Phys. Rev. D 95 (5) (2017) 054026. arXiv:1701.05829, doi:10.1103/PhysRevD.95.054026.
- [14] G. Colangelo, M. Hoferichter, M. Procura, P. Stoffer, Dispersion relation for hadronic light-by-light scattering: two-pion contributions, JHEP 04 (2017) 161. arXiv:1702.07347, doi:10.1007/JHEP04(2017)161.
- [15] M. Hoferichter, B.-L. Hoid, B. Kubis, S. Leupold, S. P. Schneider, Dispersion relation for hadronic light-by-light scattering: pion pole, JHEP 10 (2018) 141. arXiv:1808.04823, doi:10.1007/JHEP10(2018)141.
- [16] G. Eichmann, C. S. Fischer, E. Weil, R. Williams, Single pseudoscalar meson pole and pion box contributions to the anomalous magnetic moment of the muon, Phys. Lett. B 797 (2019) 134855, [Erratum: Phys. Lett. B **799**, 135029 (2019)]. arXiv:1903.10844, doi:10.1016/j.physletb.2019.134855.
- [17] J. Bijnens, N. Hermansson-Truedsson, A. Rodríguez-Sánchez, Short-distance constraints for the HLbL contribution to the muon anomalous magnetic moment, Phys. Lett. B 798 (2019) 134994. arXiv:1908.03331, doi:10.1016/j.physletb.2019.134994.
- [18] J. Leutgeb, A. Rebhan, Axial vector transition form factors in holographic QCD and their contribution to the anomalous magnetic moment of the muon, Phys. Rev. D 101 (11) (2020) 114015. arXiv:1912.01596, doi:10.1103/PhysRevD.101.114015.
- [19] L. Cappiello, O. Catà, G. D’Ambrosio, D. Greynat, A. Iyer, Axial-vector and pseudoscalar mesons in the hadronic light-by-light contribution to the muon $(g - 2)$, Phys. Rev. D 102 (1) (2020) 016009. arXiv:1912.02779, doi:10.1103/PhysRevD.102.016009.
- [20] P. Masjuan, P. Roig, P. Sánchez-Puertas, The interplay of transverse degrees of freedom and axial-vector mesons with short-distance constraints in $g - 2$, J. Phys. G 49 (1) (2022) 015002. arXiv:2005.11761, doi:10.1088/1361-6471/ac3892.
- [21] J. Bijnens, N. Hermansson-Truedsson, L. Laub, A. Rodríguez-Sánchez, Short-distance HLbL contributions to the muon anomalous magnetic moment beyond perturbation theory, JHEP 10 (2020) 203. arXiv:2008.13487, doi:10.1007/JHEP10(2020)203.
- [22] J. Bijnens, N. Hermansson-Truedsson, L. Laub, A. Rodríguez-Sánchez, The two-loop perturbative correction to the $(g - 2)_\mu$ HLbL at short distances, JHEP 04 (2021) 240. arXiv:2101.09169, doi:10.1007/JHEP04(2021)240.

- [23] I. Danilkin, M. Hoferichter, P. Stoffer, A dispersive estimate of scalar contributions to hadronic light-by-light scattering, *Phys. Lett. B* 820 (2021) 136502. [arXiv:2105.01666](#), [doi:10.1016/j.physletb.2021.136502](#).
- [24] D. Stamen, D. Hariharan, M. Hoferichter, B. Kubis, P. Stoffer, Kaon electromagnetic form factors in dispersion theory, *Eur. Phys. J. C* 82 (5) (2022) 432. [arXiv:2202.11106](#), [doi:10.1140/epjc/s10052-022-10348-3](#).
- [25] J. Leutgeb, J. Mager, A. Rebhan, Hadronic light-by-light contribution to the muon $g - 2$ from holographic QCD with solved $U(1)_A$ problem, *Phys. Rev. D* 107 (5) (2023) 054021. [arXiv:2211.16562](#), [doi:10.1103/PhysRevD.107.054021](#).
- [26] M. Hoferichter, B. Kubis, M. Zanke, Axial-vector transition form factors and $e^+e^- \rightarrow f_1\pi^+\pi^-$, *JHEP* 08 (2023) 209. [arXiv:2307.14413](#), [doi:10.1007/JHEP08\(2023\)209](#).
- [27] M. Hoferichter, P. Stoffer, M. Zillinger, An optimized basis for hadronic light-by-light scattering, *JHEP* 04 (2024) 092. [arXiv:2402.14060](#), [doi:10.1007/JHEP04\(2024\)092](#).
- [28] E. J. Estrada, S. González-Solís, A. Guevara, P. Roig, Improved π^0 , η , η' transition form factors in resonance chiral theory and their a_μ^{HLbL} contribution, *JHEP* 12 (2024) 203. [arXiv:2409.10503](#), [doi:10.1007/JHEP12\(2024\)203](#).
- [29] J. Lütke, M. Procura, P. Stoffer, Dispersion relations for the hadronic VVA correlator, *JHEP* 04 (2025) 130. [arXiv:2410.11946](#), [doi:10.1007/JHEP04\(2025\)130](#).
- [30] O. Deineka, I. Danilkin, M. Vanderhaeghen, Dispersive estimate of the $a_0(980)$ contribution to $(g-2)_\mu$, *Phys. Rev. D* 111 (3) (2025) 034009. [arXiv:2410.12894](#), [doi:10.1103/PhysRevD.111.034009](#).
- [31] G. Eichmann, C. S. Fischer, T. Haeuser, O. Regenfelder, Axial-vector and scalar contributions to hadronic light-by-light scattering, *Eur. Phys. J. C* 85 (4) (2025) 445. [arXiv:2411.05652](#), [doi:10.1140/epjc/s10052-025-14055-7](#).
- [32] J. Bijnens, N. Hermansson-Truedsson, A. Rodríguez-Sánchez, Constraints on the hadronic light-by-light tensor in corner kinematics for the muon $g - 2$, *JHEP* 03 (2025) 094. [arXiv:2411.09578](#), [doi:10.1007/JHEP03\(2025\)094](#).
- [33] M. Hoferichter, P. Stoffer, M. Zillinger, Dispersion relation for hadronic light-by-light scattering: subleading contributions, *JHEP* 02 (2025) 121. [arXiv:2412.00178](#), [doi:10.1007/JHEP02\(2025\)121](#).
- [34] S. Holz, M. Hoferichter, B.-L. Hoid, B. Kubis, Dispersion relation for hadronic light-by-light scattering: η and η' poles, *JHEP* 04 (2025) 147. [arXiv:2412.16281](#), [doi:10.1007/JHEP04\(2025\)147](#).
- [35] L. Cappiello, J. Leutgeb, J. Mager, A. Rebhan, Tensor meson transition form factors in holographic QCD and the muon $g - 2$ Accepted for publication in *JHEP* (1 2025). [arXiv:2501.09699](#).
- [36] G. Colangelo, M. Hoferichter, A. Nyffeler, M. Passera, P. Stoffer, Remarks on higher-order hadronic corrections to the muon $g-2$, *Phys. Lett. B* 735 (2014) 90–91. [arXiv:1403.7512](#), [doi:10.1016/j.physletb.2014.06.012](#).

- [37] T. Blum, N. Christ, M. Hayakawa, T. Izubuchi, L. Jin, C. Jung, C. Lehner, The hadronic light-by-light scattering contribution to the muon anomalous magnetic moment from lattice QCD, *Phys. Rev. Lett.* 124 (13) (2020) 132002. [arXiv:1911.08123](#), [doi:10.1103/PhysRevLett.124.132002](#).
- [38] E.-H. Chao, R. J. Hudspith, A. Gérardin, J. R. Green, H. B. Meyer, K. Ottnad, Hadronic light-by-light contribution to $(g-2)_\mu$ from lattice QCD: a complete calculation, *Eur. Phys. J. C* 81 (7) (2021) 651. [arXiv:2104.02632](#), [doi:10.1140/epjc/s10052-021-09455-4](#).
- [39] E.-H. Chao, R. J. Hudspith, A. Gérardin, J. R. Green, H. B. Meyer, The charm-quark contribution to light-by-light scattering in the muon $(g-2)$ from lattice QCD, *Eur. Phys. J. C* 82 (8) (2022) 664. [arXiv:2204.08844](#), [doi:10.1140/epjc/s10052-022-10589-2](#).
- [40] T. Blum, N. Christ, M. Hayakawa, T. Izubuchi, L. Jin, C. Jung, C. Lehner, C. Tu, Hadronic light-by-light contribution to the muon anomaly from lattice QCD with infinite volume QED at physical pion mass, *Phys. Rev. D* 111 (1) (2025) 014501. [arXiv:2304.04423](#), [doi:10.1103/PhysRevD.111.014501](#).
- [41] Z. Fodor, A. Gérardin, L. Lellouch, K. K. Szabó, B. C. Toth, C. Zimmermann, Hadronic light-by-light scattering contribution to the anomalous magnetic moment of the muon at the physical pion mass, *Phys. Rev. D* 111 (11) (2025) 114509. [arXiv:2411.11719](#), [doi:10.1103/wdrk-7nrt](#).
- [42] R. Aliberti, et al., The anomalous magnetic moment of the muon in the Standard Model: an update (5 2025). [arXiv:2505.21476](#).
- [43] G. Colangelo, M. Hoferichter, M. Procura, P. Stoffer, Rescattering effects in the hadronic-light-by-light contribution to the anomalous magnetic moment of the muon, *Phys. Rev. Lett.* 118 (23) (2017) 232001. [arXiv:1701.06554](#), [doi:10.1103/PhysRevLett.118.232001](#).
- [44] R. Garcia-Martin, B. Moussallam, MO analysis of the high statistics Belle results on $\gamma\gamma \rightarrow \pi^+\pi^-, \pi^0\pi^0$ with chiral constraints, *Eur. Phys. J. C* 70 (2010) 155–175. [arXiv:1006.5373](#), [doi:10.1140/epjc/s10052-010-1471-7](#).
- [45] M. Hoferichter, D. R. Phillips, C. Schat, Roy-Steiner equations for $\gamma\gamma \rightarrow \pi\pi$, *Eur. Phys. J. C* 71 (2011) 1743. [arXiv:1106.4147](#), [doi:10.1140/epjc/s10052-011-1743-x](#).
- [46] B. Moussallam, Unified dispersive approach to real and virtual photon-photon scattering at low energy, *Eur. Phys. J. C* 73 (2013) 2539. [arXiv:1305.3143](#), [doi:10.1140/epjc/s10052-013-2539-y](#).
- [47] I. Danilkin, M. Vanderhaeghen, Dispersive analysis of the $\gamma\gamma^* \rightarrow \pi\pi$ process, *Phys. Lett. B* 789 (2019) 366–372. [arXiv:1810.03669](#), [doi:10.1016/j.physletb.2018.12.047](#).
- [48] M. Hoferichter, P. Stoffer, Dispersion relations for $\gamma^*\gamma^* \rightarrow \pi\pi$: helicity amplitudes, subtractions, and anomalous thresholds, *JHEP* 07 (2019) 073. [arXiv:1905.13198](#), [doi:10.1007/JHEP07\(2019\)073](#).

- [49] I. Danilkin, O. Deineka, M. Vanderhaeghen, Dispersive analysis of the $\gamma^*\gamma^* \rightarrow \pi\pi$ process, *Phys. Rev. D* 101 (5) (2020) 054008. [arXiv:1909.04158](https://arxiv.org/abs/1909.04158), [doi:10.1103/PhysRevD.101.054008](https://doi.org/10.1103/PhysRevD.101.054008).
- [50] H. Czyz, S. Ivashyn, EKHARA: A Monte Carlo generator for $e^+e^- \rightarrow e^+e^-\pi^0$ and $e^+e^- \rightarrow e^+e^-\pi^+\pi^-$ processes, *Comput. Phys. Commun.* 182 (2011) 1338–1349. [arXiv:1009.1881](https://arxiv.org/abs/1009.1881), [doi:10.1016/j.cpc.2011.01.029](https://doi.org/10.1016/j.cpc.2011.01.029).
- [51] H. Czyz, S. Ivashyn, A. Korchin, O. Shekhovtsova, Two-photon form factors of the π^0 , η and η' mesons in the chiral theory with resonances, *Phys. Rev. D* 85 (2012) 094010. [arXiv:1202.1171](https://arxiv.org/abs/1202.1171), [doi:10.1103/PhysRevD.85.094010](https://doi.org/10.1103/PhysRevD.85.094010).
- [52] H. Czyz, P. Kiswa, S. Tracz, Modeling interactions of photons with pseudoscalar and vector mesons, *Phys. Rev. D* 97 (1) (2018) 016006. [arXiv:1711.00820](https://arxiv.org/abs/1711.00820), [doi:10.1103/PhysRevD.97.016006](https://doi.org/10.1103/PhysRevD.97.016006).
- [53] H. Czyz, P. Kiswa, EKHARA 3.0: an update of the EKHARA Monte Carlo event generator, *Comput. Phys. Commun.* 234 (2019) 245–255. [arXiv:1805.07756](https://arxiv.org/abs/1805.07756), [doi:10.1016/j.cpc.2018.07.021](https://doi.org/10.1016/j.cpc.2018.07.021).
- [54] H. Czyz, private communication (2024).
- [55] M. Shepherd, J. Stevens, R. Mitchell, M. Albrecht, B. Grube, A. Austregesilo, N. D. Hoffman, N. Hüsken, AmpTools: Version 0.15.2 (2023). [doi:10.5281/zenodo.10223330](https://doi.org/10.5281/zenodo.10223330).
- [56] M. Fritsch, M. Michel, S. Pflüger, R. de Boer, L. Wollenberg, W. Gradl, P. Weidenkaff, K. Peters, K. Götzen, Common partial wave analysis: A collaboration-independent organisation for amplitude analysis software (2022). [doi:10.5281/zenodo.6908150](https://doi.org/10.5281/zenodo.6908150).
- [57] G. A. Schuler, Two-photon physics with GALUGA 2.0, *Computer Physics Communications* 108 (2) (1998) 279–303. [doi:https://doi.org/10.1016/S0010-4655\(97\)00127-6](https://doi.org/10.1016/S0010-4655(97)00127-6).
- [58] B. Aubert, et al., Observation of the $\chi_{c2}(2p)$ Meson in the Reaction $\gamma\gamma \rightarrow D\bar{D}$ at BaBar, *Phys. Rev. D* 81 (2010) 092003. [arXiv:1002.0281](https://arxiv.org/abs/1002.0281), [doi:10.1103/PhysRevD.81.092003](https://doi.org/10.1103/PhysRevD.81.092003).
- [59] A. Mustafa, Analyse der systeme $\pi^+\pi^-\eta$, η' π^0 sowie $\pi^+\pi^-\pi^0$ in zwei-photon-reaktionen bei besiii, doctoralthesis, Ruhr-Universität Bochum, Universitätsbibliothek (2019). [doi:10.13154/294-6287](https://doi.org/10.13154/294-6287).
- [60] I. Danilkin, C. F. Redmer, M. Vanderhaeghen, The hadronic light-by-light contribution to the muon's anomalous magnetic moment, *Prog. Part. Nucl. Phys.* 107 (2019) 20–68. [arXiv:1901.10346](https://arxiv.org/abs/1901.10346), [doi:10.1016/j.pnpnp.2019.05.002](https://doi.org/10.1016/j.pnpnp.2019.05.002).
- [61] D. Drechsel, L. Tiator, Threshold pion photoproduction on nucleons, *J. Phys. G* 18 (1992) 449–497. [doi:10.1088/0954-3899/18/3/004](https://doi.org/10.1088/0954-3899/18/3/004).
- [62] A. Courau, A FAST MONTE CARLO GENERATOR FOR $ee \rightarrow eeX$ UNTAGGED EXPERIMENTS, in: 6th International Conference on Photon-Photon Collisions, 1984.

- [63] S. Bellucci, A. Courau, S. Ong, Azimuthal correlations in $\gamma\gamma \rightarrow \pi^0\pi^0$ at DAPHNE, in: SIS-Pubblicazioni, INFN Laboratori Nazionali di Frascati, 1994.
- [64] F. Nguyen, F. Piccinini, A. D. Polosa, $e^+e^- \rightarrow e^+e^-\pi^0\pi^0$ at DAPHNE, Eur. Phys. J. C 47 (2006) 65–70. arXiv:hep-ph/0602205, doi:10.1140/epjc/s2006-02567-9.
- [65] D. Babusci, et al., Measurement of η meson production in $\gamma\gamma$ interactions and $\Gamma(\eta \rightarrow \gamma\gamma)$ with the KLOE detector, JHEP 01 (2013) 119. arXiv:1211.1845, doi:10.1007/JHEP01(2013)119.
- [66] S. Uehara, TREPS: A Monte-Carlo Event Generator for Two-photon Processes at e^+e^- Colliders using an Equivalent Photon Approximation (7 1996). arXiv:1310.0157.
- [67] S. Uehara, et al., High-statistics study of K_S^0 pair production in two-photon collisions, PTEP 2013 (12) (2013) 123C01. arXiv:1307.7457, doi:10.1093/ptep/ptt097.
- [68] V. Druzhinin, L. Kardapoltsev, V. Tayursky, GGRESRC: A Monte Carlo generator for the two-photon process $e^+e^- \rightarrow e^+e^-R(J^{PC} = 0^{++})$ in the single-tag mode, Computer Physics Communications 185 (1) (2014) 236–243. doi:https://doi.org/10.1016/j.cpc.2013.07.017.
URL <https://www.sciencedirect.com/science/article/pii/S0010465513002452>
- [69] J. P. Lees, et al., Measurement of the $\gamma^*\gamma^* \rightarrow \eta'$ transition form factor, Phys. Rev. D 98 (11) (2018) 112002. arXiv:1808.08038, doi:10.1103/PhysRevD.98.112002.
- [70] S. Ong, P. Kessler, A Process Independent Radiative Correction Formula for Single Tag and Double Tag Measurements of $\gamma\gamma$ Reactions, Phys. Rev. D 38 (1988) 2280. doi:10.1103/PhysRevD.38.2280.
- [71] F. James, Monte-Carlo phase space (5 1968).
- [72] I. Danilkin, O. Deineka, M. Vanderhaeghen, Data-driven dispersive analysis of the $\pi\pi$ and πK scattering, Phys. Rev. D 103 (11) (2021) 114023. arXiv:2012.11636, doi:10.1103/PhysRevD.103.114023.
- [73] F. Niecknig, B. Kubis, S. P. Schneider, Dispersive analysis of $\omega^- \rightarrow 3\pi$ and $\phi^- \rightarrow 3\pi$ decays, Eur. Phys. J. C 72 (2012) 2014. arXiv:1203.2501, doi:10.1140/epjc/s10052-012-2014-1.
- [74] S. P. Schneider, B. Kubis, F. Niecknig, The $\omega^- \rightarrow \pi^0\gamma^*$ and $\phi^- \rightarrow \pi^0\gamma^*$ transition form factors in dispersion theory, Phys. Rev. D 86 (2012) 054013. arXiv:1206.3098, doi:10.1103/PhysRevD.86.054013.
- [75] I. V. Danilkin, C. Fernández-Ramírez, P. Guo, V. Mathieu, D. Schott, M. Shi, A. P. Szczepaniak, Dispersive analysis of $\omega/\phi \rightarrow 3\pi, \pi\gamma^*$, Phys. Rev. D 91 (9) (2015) 094029. arXiv:1409.7708, doi:10.1103/PhysRevD.91.094029.
- [76] M. Masuda, et al., Study of π^0 pair production in single-tag two-photon collisions, Phys. Rev. D 93 (3) (2016) 032003. arXiv:1508.06757, doi:10.1103/PhysRevD.93.032003.

- [77] Y. Guo, Two photon physics at BESIII, J. Phys. Conf. Ser. 1137 (1) (2019) 012008. doi: 10.1088/1742-6596/1137/1/012008.
- [78] M. Hoferichter, P. Stoffer, Asymptotic behavior of meson transition form factors, JHEP 05 (2020) 159. arXiv:2004.06127, doi:10.1007/JHEP05(2020)159.
- [79] G. A. Schuler, F. A. Berends, R. van Gulik, Meson photon transition form-factors and resonance cross-sections in e^+e^- collisions, Nucl. Phys. B 523 (1998) 423–438. arXiv: hep-ph/9710462, doi:10.1016/S0550-3213(98)00128-X.
- [80] W. Wang, private communication (2025).
- [81] X.-L. Ren, I. Danilkin, M. Vanderhaeghen, Phenomenological model for the $\gamma^*\gamma \rightarrow \eta\pi^+\pi^-$ reaction in the $f_1(1285)$ energy region, Phys. Rev. D 110 (9) (2024) 094043. arXiv: 2409.07235, doi:10.1103/PhysRevD.110.094043.
- [82] P. Achard, et al., $f_1(1285)$ formation in two photon collisions at LEP, Phys. Lett. B 526 (2002) 269–277. arXiv:hep-ex/0110073, doi:10.1016/S0370-2693(01)01477-0.
- [83] J. J. Sakurai, D. Schildknecht, Generalized vector dominance and inelastic electron - proton scattering, Phys. Lett. B 40 (1972) 121–126. doi:10.1016/0370-2693(72)90300-0.
- [84] L. B. Bezurkov, E. V. Bugaev, Inelastic scattering of muons on nucleons in diffractive regions, Sov. J. Nucl. Phys. 32 (1980) 847.
- [85] R. Brun, F. Rademakers, Root - an object oriented data analysis framework (June 2020). doi:10.5281/zenodo.3895860. URL <https://doi.org/10.5281/zenodo.3895860>
- [86] J. von Neumann, Various techniques used in connection with random digits. Monte Carlo methods. , Nat. Bureau Standards 12 (1951) 36–38.
- [87] L. D. Landau, On the angular momentum of a system of two photons, Dokl. Akad. Nauk SSSR 60 (2) (1948) 207–209. doi:10.1016/B978-0-08-010586-4.50070-5.
- [88] C. N. Yang, Selection rules for the dematerialization of a particle into two photons, Phys. Rev. 77 (1950) 242–245. doi:10.1103/PhysRev.77.242. URL <https://link.aps.org/doi/10.1103/PhysRev.77.242>

Appendix A. Polarized cross section for the exclusive $e^+e^- \rightarrow e^+e^-\pi_1\pi_2$ process

The polarized differential cross section for the exclusive process $e^+e^- \rightarrow e^+e^-\pi_1\pi_2$ is expressed as:

$$d\sigma_{h_1,h_2} = d\sigma^{(0)} + h_1 d\sigma^{(1)} + h_2 d\sigma^{(2)} + h_1 h_2 d\sigma^{(12)} \quad (\text{A.1})$$

where $h_{1,2} = \pm 1$ denote the helicities (in units $\hbar/2$) of the incoming leptons, and $d\sigma^{(0)}$ represents the unpolarized cross section, which is provided in the main text. The terms $d\sigma^{(1)}$, $d\sigma^{(2)}$, and $d\sigma^{(12)}$ correspond to the polarization-dependent contributions and are given by:

$$d\sigma^{(12)} = \frac{\alpha^2}{8\pi^4 Q_1^2 Q_2^2} \frac{\sqrt{X}}{s(1-4m^2/s)^{1/2}} \cdot \frac{d^3\vec{p}'_1}{E'_1} \cdot \frac{d^3\vec{p}'_2}{E'_2} d\cos\theta_\pi \frac{4}{(1-\varepsilon_1)(1-\varepsilon_2)}$$

$$\begin{aligned}
& \times \left\{ \left[1 - \varepsilon_1^2 + \frac{4m^2}{Q_1^2} (1 - \varepsilon_1)^2 \right]^{1/2} \left[1 - \varepsilon_2^2 + \frac{4m^2}{Q_2^2} (1 - \varepsilon_2)^2 \right]^{1/2} \frac{1}{2} \left(\frac{d\sigma_0}{d \cos \theta_\pi} - \frac{d\sigma_2}{d \cos \theta_\pi} \right) \right. \\
& + [\varepsilon_1(1 - \varepsilon_1)]^{1/2} [\varepsilon_2(1 - \varepsilon_2)]^{1/2} \left[\cos(\tilde{\phi}_2 - \tilde{\phi}_1) \left(\frac{d\tau_0}{d \cos \theta_\pi} - \frac{d\tau_1}{d \cos \theta_\pi} \right) \right. \\
& \quad \left. \left. + \cos(\tilde{\phi}_1 + \tilde{\phi}_2) \left(\frac{d\tau_1}{d \cos \theta_\pi} + \frac{d\tau_{L2}}{d \cos \theta_\pi} \right) \right] \right. \\
& - [\varepsilon_1(1 - \varepsilon_1)]^{1/2} \left[1 - \varepsilon_2^2 + \frac{4m^2}{Q_2^2} (1 - \varepsilon_2)^2 \right]^{1/2} \cos \tilde{\phi}_1 \left(\frac{d\tau_{-12}}{d \cos \theta_\pi} + \frac{d\tau_{-1T}}{d \cos \theta_\pi} \right) \\
& \left. - \left[1 - \varepsilon_1^2 + \frac{4m^2}{Q_1^2} (1 - \varepsilon_1)^2 \right]^{1/2} [\varepsilon_2(1 - \varepsilon_2)]^{1/2} \cos \tilde{\phi}_2 \left(\frac{d\tau_{12}}{d \cos \theta_\pi} + \frac{d\tau_{1T}}{d \cos \theta_\pi} \right) \right\}, \quad (\text{A.2})
\end{aligned}$$

and

$$\begin{aligned}
d\sigma^{(1)} &= \frac{\alpha^2}{8\pi^4 Q_1^2 Q_2^2} \frac{\sqrt{X}}{s(1 - 4m^2/s)^{1/2}} \cdot \frac{d^3 \vec{p}'_1}{E'_1} \cdot \frac{d^3 \vec{p}'_2}{E'_2} d \cos \theta_\pi \frac{4}{(1 - \varepsilon_1)(1 - \varepsilon_2)} \\
& \times \left\{ [\varepsilon_1(1 - \varepsilon_1)]^{1/2} \left[\varepsilon_2(1 + \varepsilon_2) + \frac{4m^2}{Q_2^2} \varepsilon_2(1 - \varepsilon_2) \right]^{1/2} \right. \\
& \quad \times \left[\sin(\tilde{\phi}_2 - \tilde{\phi}_1) \left(\frac{d\bar{\tau}_0}{d \cos \theta_\pi} - \frac{d\bar{\tau}_1}{d \cos \theta_\pi} \right) + \sin(\tilde{\phi}_1 + \tilde{\phi}_2) \left(\frac{d\bar{\tau}_1}{d \cos \theta_\pi} - \frac{d\bar{\tau}_{L2}}{d \cos \theta_\pi} \right) \right] \\
& - \left[\varepsilon_1(1 + \varepsilon_1) + \frac{4m^2}{Q_1^2} \varepsilon_1(1 - \varepsilon_1) \right]^{1/2} \varepsilon_2 \sin(2\tilde{\phi}_2) \frac{d\bar{\tau}_{T2}}{d \cos \theta_\pi} \\
& + [\varepsilon_1(1 - \varepsilon_1)]^{1/2} \left[\sin \tilde{\phi}_1 \left(\frac{d\bar{\tau}_{-12}}{d \cos \theta_\pi} - \frac{d\bar{\tau}_{-1T}}{d \cos \theta_\pi} \right) + 2 \left[\varepsilon_2 + \frac{2m^2}{Q_2^2} (1 - \varepsilon_2) \right]^{1/2} \sin \tilde{\phi}_1 \frac{d\bar{\tau}_{1L}}{d \cos \theta_\pi} \right. \\
& \quad \left. + \varepsilon_2 \sin(\tilde{\phi}_1 + 2\tilde{\phi}_2) \frac{d\bar{\tau}_{-12}}{d \cos \theta_\pi} + \varepsilon_2 \sin(2\tilde{\phi}_2 - \tilde{\phi}_1) \frac{d\bar{\tau}_{-1T}}{d \cos \theta_\pi} \right] \\
& \left. + \left[1 - \varepsilon_1^2 + \frac{4m^2}{Q_1^2} (1 - \varepsilon_1)^2 \right]^{1/2} \left[\varepsilon_2(1 + \varepsilon_2) + \frac{4m^2}{Q_2^2} \varepsilon_2(1 - \varepsilon_2) \right]^{1/2} \sin \tilde{\phi}_2 \left(\frac{d\bar{\tau}_{12}}{d \cos \theta_\pi} + \frac{d\bar{\tau}_{1T}}{d \cos \theta_\pi} \right) \right\}, \quad (\text{A.3})
\end{aligned}$$

$$\begin{aligned}
d\sigma^{(2)} &= \frac{\alpha^2}{8\pi^4 Q_1^2 Q_2^2} \frac{\sqrt{X}}{s(1 - 4m^2/s)^{1/2}} \cdot \frac{d^3 \vec{p}'_1}{E'_1} \cdot \frac{d^3 \vec{p}'_2}{E'_2} d \cos \theta_\pi \frac{4}{(1 - \varepsilon_1)(1 - \varepsilon_2)} \\
& \times \left\{ \left[\varepsilon_1(1 + \varepsilon_1) + \frac{4m^2}{Q_1^2} \varepsilon_1(1 - \varepsilon_1) \right]^{1/2} [\varepsilon_2(1 - \varepsilon_2)]^{1/2} \right. \\
& \quad \times \left[\sin(\tilde{\phi}_2 - \tilde{\phi}_1) \left(\frac{d\bar{\tau}_0}{d \cos \theta_\pi} + \frac{d\bar{\tau}_1}{d \cos \theta_\pi} \right) + \sin(\tilde{\phi}_1 + \tilde{\phi}_2) \left(\frac{d\bar{\tau}_1}{d \cos \theta_\pi} + \frac{d\bar{\tau}_{L2}}{d \cos \theta_\pi} \right) \right] \\
& + \varepsilon_1 \left[\varepsilon_2(1 + \varepsilon_2) + \frac{4m^2}{Q_2^2} \varepsilon_2(1 - \varepsilon_2) \right]^{1/2} \sin(2\tilde{\phi}_1) \frac{d\bar{\tau}_{T2}}{d \cos \theta_\pi} \\
& - [\varepsilon_2(1 - \varepsilon_2)]^{1/2} \left[\sin \tilde{\phi}_2 \left(\frac{d\bar{\tau}_{12}}{d \cos \theta_\pi} - \frac{d\bar{\tau}_{1T}}{d \cos \theta_\pi} \right) + 2 \left[\varepsilon_1 + \frac{2m^2}{Q_1^2} (1 - \varepsilon_1) \right]^{1/2} \sin \tilde{\phi}_2 \frac{d\bar{\tau}_{-1L}}{d \cos \theta_\pi} \right. \\
& \quad \left. + \varepsilon_1 \sin(2\tilde{\phi}_1 + \tilde{\phi}_2) \frac{d\bar{\tau}_{12}}{d \cos \theta_\pi} + \varepsilon_1 \sin(2\tilde{\phi}_1 - \tilde{\phi}_2) \frac{d\bar{\tau}_{1T}}{d \cos \theta_\pi} \right] \\
& \left. - \left[\varepsilon_1(1 + \varepsilon_1) + \frac{4m^2}{Q_1^2} \varepsilon_1(1 - \varepsilon_1) \right]^{1/2} \left[1 - \varepsilon_2^2 + \frac{4m^2}{Q_2^2} (1 - \varepsilon_2)^2 \right]^{1/2} \sin \tilde{\phi}_1 \left(\frac{d\bar{\tau}_{-12}}{d \cos \theta_\pi} + \frac{d\bar{\tau}_{-1T}}{d \cos \theta_\pi} \right) \right\}. \quad (\text{A.4})
\end{aligned}$$

Study of Neutral-Pion Pair Production in Two-Photon Scattering at BESIII

Max Lellmann^{1,*} on behalf of the BESIII collaboration

¹Institute for Nuclear Physics, Johannes Gutenberg-Universität Mainz

Abstract. The anomalous magnetic moment of the muon, $a_\mu = (g-2)_\mu/2$, is one of the most precisely measured observables of the Standard Model. However, its value shows a sizeable discrepancy to the Standard Model prediction. It is still under discussion whether this discrepancy is a hint for New Physics or proof of the limited understanding of strong interaction at low energies. To get a better understanding of this discrepancy, one needs to reduce the uncertainty of both, the Standard Model prediction and the direct measurement.

Information on the production of pion pairs in two-photon fusion processes plays an important role in the dispersive calculation of the hadronic light-by-light scattering contribution to a_μ , which is one of the two large contributions to the Standard Model predictions uncertainty. The BESIII experiment, located at the Institute of High Energy Physics in Beijing/China, offers a perfect testbed for the investigation of two-photon processes at small momentum transfers. The process $e^+e^- \rightarrow e^+e^-\pi^0\pi^0$ is measured at the BESIII experiment at center-of-mass energies between 3.77 and 4.59 GeV with a total integrated luminosity of more than 13 fb^{-1} , with more data being available in future. This presentation will discuss the current status of the analysis.

1 Introduction

The anomalous magnetic moment of the muon $a_\mu = (g-2)_\mu/2$ is one of the most precisely determined properties of a fundamental particle. The Standard Model (SM) prediction reaches uncertainties better than 0.5 ppm [1], while the uncertainty of the best direct measurement is better than 0.2 ppm [2]. Between, the latest world average and the 2020 theory consensus value of a_μ presented in Ref [1], there is a 5σ discrepancy, which hints at possible physics beyond the SM. New developments in lattice QCD [3] and new measurements of the pion form factor by CMD-3 [4] suggest a larger SM value, which is closer to the direct measurement. Therefore, it is necessary to scrutinize the SM prediction and get a better understanding of the uncertainties, to find out whether the discrepancy stems from new physics or a limited understanding of QCD.

The SM prediction is limited by the hadronic contributions. The hadronic Light-by-Light (hLbL) scattering contribution is the second most important hadronic contribution to a_μ after the hadronic vacuum polarization. To improve the uncertainty of the hLbL contribution, a good understanding of photons coupling to hadrons is necessary, especially electromagnetic

*e-mail: lellmann@uni-manz.de

transition form factors of light pseudoscalars, scalars, tensor, and axial mesons at photon virtualities in the vicinity of $Q^2 \approx 1 \text{ GeV}^2$ [5].

The transition form factors of the light scalars $f_0(500)$ and $f_0(980)$ as well as the tensor $f_2(1270)$ can be accessed by the two-photon production of two neutral pions in electron positron collisions. The energy range available at BESIII is optimal to cover the low Q^2 necessary for a_μ^{hLbL} [1, 5] and is, thus, perfectly suited to extend the existing measurement of the $\gamma\gamma^* \rightarrow \pi^0\pi^0$ cross section by the Belle collaboration, which covers momentum transfers above 3 GeV^2 , [6] towards smaller photon virtualities between 0.1 GeV^2 and 2 GeV^2 .

The intention of this work is the study of the $\gamma\gamma^* \rightarrow \pi^0\pi^0$ cross section in the a_μ relevant region in the process $e^+e^- \rightarrow e^+e^-\pi^0\pi^0$ using the BESIII detector.

2 The BESIII Experiment, Data Sets, and Simulations

The BESIII detector [7] records symmetric e^+e^- collisions provided by the BEPCII storage ring [8] in the center-of-mass energy range from 2.0 to 4.95 GeV, with a peak luminosity of $1 \times 10^{33} \text{ cm}^{-2}\text{s}^{-1}$ achieved at $\sqrt{s} = 3.77 \text{ GeV}$. BESIII has collected large data samples in this energy region [9]. The cylindrical core of the BESIII detector covers 93% of the full solid angle and consists of a helium-based multilayer drift chamber (MDC), a plastic scintillator time-of-flight system (TOF), and a CsI(Tl) electromagnetic calorimeter (EMC), which are all enclosed in a superconducting solenoid providing a 1.0 T magnetic field. The solenoid is supported by an octagonal flux-return yoke with resistive plate counter muon identification modules interleaved with steel. The charged particle momentum resolution at $1 \text{ GeV}/c$ is 0.5%, and the dE/dx resolution is 6% for electrons from Bhabha scattering. The EMC measures photon energies with a resolution of 2.5% (5%) at 1 GeV in the barrel (end cap) region. The time resolution in the TOF barrel region is 68 ps, while that in the end cap region was 110 ps. The end cap TOF system was upgraded in 2015 using multigap resistive plate chamber technology, providing a time resolution of 60 ps, which benefits the data used in this analysis [10].

Currently, the analysis is based on more than 13 fb^{-1} of electron positron collision data collected by BESIII with center-of-mass energies between 3.773 GeV and 4.599 GeV. An overview of the used data sets and their energies and integrated luminosities is given in Tab. 1. For each data set, extensive studies of the signal channel $e^+e^- \rightarrow e^+e^-\pi^0\pi^0$ as well as for all background channels are performed. The most relevant background channels $e^+e^- \rightarrow e^+e^-\eta$ and $e^+e^- \rightarrow e^+e^-\eta'$ are simulated using the EKHARA 3.0 Monte Carlo Generator [11], the signal channel Monte Carlo simulation is performed using a modified version

Table 1. Center-of-mass energies \sqrt{s} and integrated luminosity of data sets used in this work. The first uncertainty is statistical the second systematical. The uncertainties of the center-of-mass energies are in the sub-percent level and negligible in this analysis. [12–16]

\sqrt{s} / GeV	$\mathcal{L}_{\text{int}} / \text{pb}^{-1}$	\sqrt{s} / GeV	$\mathcal{L}_{\text{int}} / \text{pb}^{-1}$
3.773	$2931.8 \pm 0.2 \pm 13.8$	4.226	$1047.34 \pm 0.1 \pm 10.1$
4.007	$482.0 \pm 0.1 \pm 4.7$	4.236	$530.3 \pm 0.1 \pm 2.7$
4.178	$3189.5 \pm 0.2 \pm 31.9$	4.244	$538.1 \pm 0.1 \pm 2.6$
4.189	$526.7 \pm 0.1 \pm 2.2$	4.267	$531.1 \pm 0.1 \pm 3.1$
4.199	$526.0 \pm 0.1 \pm 2.1$	4.358	$539.8 \pm 0.1 \pm 5.2$
4.209	$517.1 \pm 0.1 \pm 1.8$	4.416	$1028.9 \pm 0.1 \pm 10.0$
4.219	$514.6 \pm 0.1 \pm 1.8$	4.599	$566.9 \pm 0.1 \pm 5.5$
Total luminosity:		$13470.16 \pm 0.5 \pm 97.6 \text{ pb}^{-1}$	

of EKHARA 3.0 which takes into account the dispersive analysis of Danilkin, Deineka, and Vanderhaeghen [17] for the description of the $\gamma\gamma \rightarrow \pi^0\pi^0$ dynamics. Background processes are studied using inclusive Monte Carlo samples including QED processes like $e^+e^- \rightarrow e^+e^-$, $e^+e^- \rightarrow \mu^+\mu^-$, and $e^+e^- \rightarrow \tau^+\tau^-$ including radiative effects, radiative return to charmonium resonances, decays of the charmonium resonances into charmed mesons, hadronic charmonium transitions, and $q\bar{q}$ continuum processes.

3 Event Selection

This analysis attempts the measurement of the $\gamma\gamma^* \rightarrow \pi^0\pi^0$ cross sections via a single tagged measurement of the $e^+e^- \rightarrow e^+e^-\pi^0\pi^0$ channel. Here, one of the two final state leptons is measured while the remaining one is required to escape the detector at small angles and, thus, fixing the virtuality of the corresponding exchange photon to small values. The neutral pions are reconstructed using their decays into two photons.

The electron or positron is detected in the MDC and is required to be within a polar angle range of $|\cos\theta| < 0.93$ to ensure a good momentum measurement. Furthermore, the closest point of approach of the reconstructed helix to the interaction point is required to be within 10 cm along the beam axis and 1 cm in radial direction to reject background such as cosmics. The track is identified as electron/positron by comparing the momentum measured in the MDC $|\vec{p}|$ to the energy deposition in the EMC E_{EMC} . Since electrons/positrons are light particles, the ratio $E_{\text{EMC}}/|\vec{p}|$ is expected to be close to one, while for heavier and weakly interacting particles (i.e. all other directly detectable, charged particles) is expected to be smaller. The charged track is required to fulfill $E_{\text{EMC}}/|\vec{p}| > 0.8$. In this analysis, exactly one charged track is required, which must be identified as an electron/positron.

The photons are detected with the EMC. Their energy deposit is required to be at least 25 MeV in the barrel region and 50 MeV in the end caps of the detector to noise and low energy background. To exclude showers that originate from charged tracks, the angle subtended by the EMC shower and the position of the closest charged track at the EMC must be larger than 10° as measured from the interaction point. To suppress noise and reject showers unrelated to the event, the difference between the EMC time and the event start time is required to be within 700 ns. Since there might be additional photons besides the four photon stemming from the pion decays, at least four photons are required per event.

To find the correct combination of the photons to be from pion decays a kinematic fit is applied. In the fit, it is required that two pairs of two photons combine to the neutral pion mass and that the missing momentum is associated to the electron mass. To reduce background contributions and obtain a better resolution on the final four-vectors, the χ^2 of the fit must be smaller than 20.

The virtuality of the photon connected to the untagged lepton is directly constrained to $Q^2 < 0.03 \text{ GeV}^2$. The direct constraint of this observable is possible due to the improved resolution by the kinematic fit. In earlier single tagged measurements (see for example Refs. [6, 18–22]) the constraint on the photon virtuality was performed indirectly by applying conditions on observable connected to the momentum transfer, but not the momentum transfer directly. One option is the constraint of the scattering angle of the missing lepton to $\cos\theta > 0.99$. By doing this instead of the direct cut on Q^2 , the maximum observed virtuality is ten times larger. The direct cut on Q^2 in combination with the kinematic fit is therefore a much better option to enforce a single tagged condition.

Remaining background contributions of the $e^+e^- \rightarrow e^+e^-\eta$ and $e^+e^- \rightarrow e^+e^-\eta'$ are suppressed by restricting the total transverse momentum of the detected particles. The remainder is subtracted using Monte Carlo simulations.

4 Event Yield and Phase Space Coverage

Using this event selection scheme, more than 10000 events are reconstructed in the 13 fb^{-1} used in this analysis. The two-pion invariant mass spectrum is covered from threshold to 2 GeV and, therefore, covers the most important resonances $f_0(500)$, $f_0(980)$, and $f_2(1270)$. Momentum transfers between 0.1 GeV^2 and 2 GeV^2 can be accessed. Therefore, this measurement extends the existing Belle measurement to smaller virtualities and, thus, provides valuable information to the $(g - 2)_\mu$ puzzle. Furthermore, the entire helicity angle range is covered. In Fig. 1 the expected event yield from the Monte Carlo simulations in dependence on the two-pion invariant mass W and the momentum transfer Q^2 is shown.

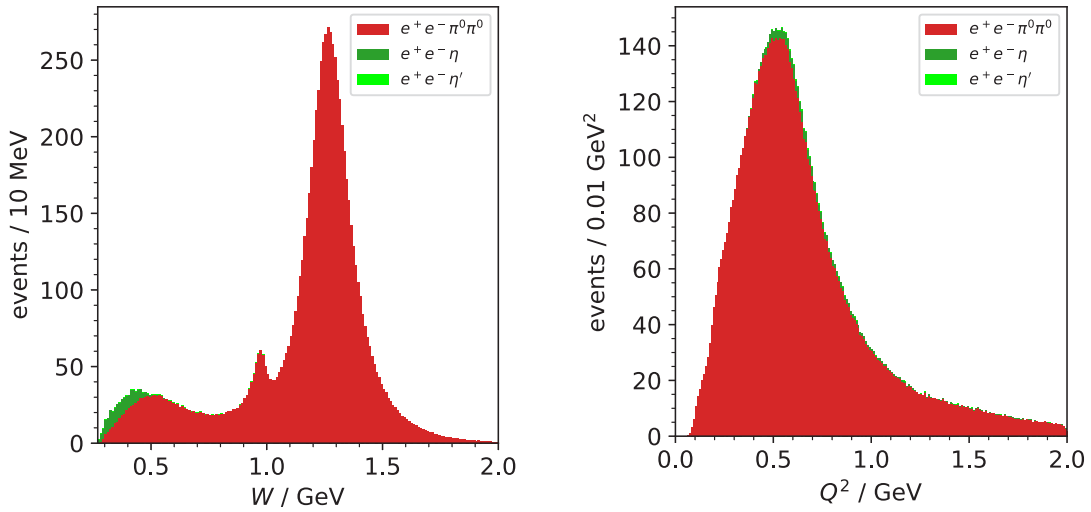


Figure 1. Expected event yield for 13.4 fb^{-1} of data for two-pion invariant mass W (left) and momentum transfer Q^2 (right). The histograms for the signal channel (red) and background channels $e^+e^-\eta$ (green) and $e^+e^-\eta'$ (lime green) are stacked.

5 Extraction of the Two-Photon Cross Section

From the selected events the cross section of $e^+e^- \rightarrow e^+e^-\pi^0\pi^0$ is determined. It can be connected to the relevant $\gamma\gamma^* \rightarrow \pi^0\pi^0$ cross section as demonstrated in Refs. [23–25]:

$$\frac{d^2\sigma_{e^+e^- \rightarrow e^+e^-\pi^0\pi^0}}{dQ^2 dW} = 2 \frac{d^2L_{\text{TT}}}{dQ^2 dW} \sigma_{\text{TT}} + 2 \frac{d^2L_{\text{TL}}}{dQ^2 dW} \sigma_{\text{TL}} \quad . \quad (1)$$

Here, σ_{TT} and σ_{TL} denote the two-photon cross sections for two transversely polarized photons and one transversely and one linearly polarized photon, respectively. The functions L_{TT} and L_{TL} are the two-photon luminosity functions and can be calculated as explained in Ref. [23]. Due to the specific dependence of the $e^+e^- \rightarrow e^+e^-\pi^0\pi^0$ cross section on the $\gamma\gamma^* \rightarrow \pi^0\pi^0$ cross sections for different photon polarizations, the first step will be a measurement of the sum of the two-photon cross sections $\sigma_{\text{TT}} + \varepsilon_{\text{TL}} \cdot \sigma_{\text{TL}}$ alongside the factor ε_{TL} , which is precisely known. A partial wave analysis can separate the two cross sections and the measurement of the electromagnetic transition form factors of the involved resonances is possible.

6 Summary and Outlook

The BESIII detector is uniquely situated to study the single tagged two-photon production of hadrons and provide information needed for the data driven approach to calculate the hLbL contribution to the anomalous magnetic moment of the muon. The acquired high luminosity data sets enable a high statistics study of the said processes in the momentum transfer range most relevant for a_μ . It is also the first single tagged measurement which can cover the two-pion production threshold. It will accompany the BESIII measurement of the π^0 transition form factor [22] as the world leading result in the a_μ relevant momentum transfer range. The measurement can easily be extended to $e^+e^- \rightarrow e^+e^-\pi^0\eta$ when considering the decay of the η meson to two photons. Using similar techniques, the charged pion final state is studied, too. In the future, higher multiplicity will be studied. All of the mentioned measurements will benefit from the new 20 fb^{-1} of data collected at the $\psi(3770)$ measurement. By exploiting the improved resolution of the missing lepton's momentum transfer, first studies of the measurement of the double virtual two-photon cross sections $\gamma^*\gamma^* \rightarrow \pi^0\pi^0$ are ongoing.

References

- [1] T. Ayoma *et al.*, Physics Reports **887**, 1-166 (2020)
- [2] D. P. Aguillard *et al.*, Phys. Rev. Lett. **131**, 161802 (2023)
- [3] Sz. Borsanyi *et al.*, Nature (London) **593**, 51 (2021).
- [4] F. V. Ignatov *et al.* (CMD-3 Collaboration), arXiv:2302.08834
- [5] I. Danilkin, C. F. Redmer, and M. Vanderhaeghen, Prog. Part. Nucl. Phys. **107**, 20-68 (2019)
- [6] M. Masuda *et al.* (Belle Collaboration), Phys. Rev. D **93** (2016) 3, 032003
- [7] M. Ablikim *et al.* (BESIII Collaboration), Nucl. Instrum. Meth. A **614**, 345 (2010).
- [8] C. H. Yu *et al.*, Proceedings of IPAC2016, Busan, Korea, 2016
- [9] M. Ablikim *et al.* (BESIII Collaboration), Chin. Phys. C **44**, 040001 (2020).
- [10] X. Li *et al.*, Radiat. Detect. Technol. Methods **1**, 13 (2017); Y. X. Guo *et al.*, Radiat. Detect. Technol. Methods **1**, 15 (2017); P. Cao *et al.*, Nucl. Instrum. Meth. A **953**, 163053 (2020).
- [11] H. Czyz and P. Kiszka, Comput. Phys. Commun. **234**, 245-255 (2019)
- [12] M. Ablikim *et al.* (BESIII Collaboration), Chin. Phys. C **39** 093001 (2015)
- [13] M. Ablikim *et al.* (BESIII Collaboration), Phys. Lett. B **753** 629–638 (2016). [Erratum: Phys.Lett.B **812**, 135982 (2021)]
- [14] M. Ablikim *et al.* (BESIII Collaboration), Chin. Phys. C **40** 063001 (2016)
- [15] M. Ablikim *et al.* (BESIII Collaboration), Chin. Phys. C **45** 103001 (2021)
- [16] M. Ablikim *et al.* (BESIII Collaboration), Chin. Phys. C **46** 113002 (2022)
- [17] I. Danilkin, O. Deineka, and M. Vanderheaghen, Phys. Rev. D **101**, 054008 (2020)
- [18] B. Aubert *et al.* (BaBar Collaboration), Phys. Rev. D **80**, 052002, (2009)
- [19] S. Uehara *et al.* (Belle Collaboration), Phys. Rev. D **86**, 092007, (2012)
- [20] C.F. Redmer, Nucl. Par. Phy. Proc. **287-288**, 99-102 (2017)
- [21] C.F. Redmer, EPJ Web Conf. **218**, 03004 (2019)
- [22] C.F. Redmer, EPJ Web Conf. **212**, 04004 (2019)
- [23] G. Bonneau, M. Gourdin, F. Martin, Nucl. Phys. B **54**, 573-597 (1973)
- [24] V.M. Budnev, I.F. Ginzburg, G.V. Meledin, V.G. Serbo, Phys. Rept. **15** 181-281 (1975)
- [25] V. Pascalutsa, V. Pauk, M. Vanderhaeghen, Phys. Rev. D **85** 116001 (2012)